Safety in Mines Research Advisory Committee

Final Project Report

Deep gold mine fracture zone behaviour

J A L Napier, D F Malan, E Sellers, A Daehnke,
M W Hildyard, T Dede, K-J Shou

Research agency : CSIR Division of Mining Technology

Project number : GAP332

Date : December 1998

Executive Summary

The investigation of the behaviour of the fracture zone surrounding deep level gold mine stopes is detailed in three main sections of this report.

Section 2 outlines the ongoing study of fundamental fracture processes and their numerical representation. Microscopic studies of fracture nucleation in rock confirm that the basic fracture initiation mechanisms are driven by the local grain structure and by the nature of the interfaces between grains. Observations of the fracture surface reveal a complex array of fracture nuclei which appear to propagate in a dynamic mode for short distances, sometimes leaving small scale mist and hackle traces. The microfractures, in all cases, appear to be controlled by splitting or extensile failure mechanisms and tend to be aligned to the direction of the major principal stress. For engineering purposes, it is found that the macro material behaviour can be represented effectively by a random mesh of discontinuities that are activated in sequence. This has been termed a tessellation model. This model can be applied at the stope scale to simulate fracture zone deformation mechanisms.

The time-dependent testing of quartzite and lava rock samples is described as well in Section 2. It is observed that the quartzites are more prone to creep than hard lavas. Experimental tests of the creep behaviour of rock discontinuities have been carried out using a novel shear test rig. These tests demonstrate that extension fractures in hard lava exhibit negligible creep compared to bedding planes or gouge filled discontinuities. It is found that the tessellation model provides a satisfactory numerical framework for representing the overall creep behaviour of the fracture zone. The initial extension of this work to three-dimensional modelling of fracture growth is reported, together with some preliminary studies of the selection of optimal mine layout sequences.

Section 3 presents a detailed summary of wave propagation and blast fracture processes. The interaction of plane waves with a number of distinct interface conditions is classified in terms of frequency dependent reflection and transmission behaviour. A detailed model of the blast gas driven propagation of a penny shaped crack is developed, taking into account coupled fluid flow and heat transfer effects, as well as the importance of dynamic fracture toughness properties. This model is demonstrated to provide a good description of dynamic photoelastic observations of the propagation of blast induced fracturing in a cubic block of transparent PMMA material. The implications of these studies in determining the range of influence of axi-radial fractures from blast holes are outlined. Work on the interaction of seismic waves with the stope fracture zone is reported, together with preliminary modelling of a field experiment in which the interaction of stress waves, induced from a set of blast holes, is monitored at the surface of an adjacent tunnel. A number of enhancements to the computer program WAVE have been implemented, including a hyperbolic joint stiffness model and facilities for designing the finite difference mesh to facilitate the setting of background stress fields.

Section 4 contains a description of model calibration experiments and the important application of acoustic emission monitoring techniques in tracking laboratory scale fracture processes. It is demonstrated that the stope fracture zone can be modelled successfully using the random mesh tessellation approach. These fracture zone simulations provide direct insights into the mechanisms of parting plane slip on the extent of the fracture zone and the effect of the field stress orientation on keyblock fracture angles. Parting plane undulations are shown also to increase the stope closure and to affect the formation of the fracture zone ahead of the stope face.

One of the most important findings in the research project, is the potential use of continuous stope closure measurements as a diagnostic measure of stope face stresses in different geotechnical environments. Continuous closure measurements offer a means of quantifying the effectiveness of preconditioning blasting and provide a well founded and practical means for

rock mechanics personnel to assess the seismic implications of different rates of mining mechanisation strategies or multi-shift production options.

Acknowledgements

The authors would like to acknowledge the SIMRAC sponsorship of the work reported here for the period 1996 to 1998. This work extends the studies carried out under SIMRAC project GAP029 and has enabled considerable progress to be made in achieving significant mechanistic understanding of the stope fracture zone. The cooperation of the rock mechanics personnel at Hartebeestfontein Mine, Western Deep Levels South Mine and Kloof Mine in supporting field observations of continuous stope closure is gratefully acknowledged. In addition, we would like to acknowledge the invaluable assistance of the external collaborators Professor H P Rossmanith, Professor M U Ozbay, Professor A P Peirce and Dr P A Cundall as well as the observational studies of microfracturing conducted by Mr P A Turner.

Glossary of abbreviations, symbols and terms

Abbreviations

Acoustic emission	AE
Closure ratio	CR
Uniaxial compressive strength	UCS
Velocity of detonation	VOD

Symbols

Cohesion	S_0
Compressional wave speed	C_P
Elastic stope face stiffness	k_e
Intermediate principal stress	σ_2
Major principal stress	σ_1
Minor principal stress	σ_3
Normal stiffness	k_n
Peak friction angle	ϕ
Poisson's ratio	ν
Rate of steady-state closure	$\dot{S}_{ss}$
Rayleigh wave speed	C_R
Residual cohesion	S_m
Residual friction angle	ϕ_m
Shear stiffness	k_s
Shear strength	τ_s
Shear stress	τ
Shear wave speed	C_S
Steady-state closure	S_{ss}
Uniaxial compressive strength	σ_c
Young's modulus	E

Terminology

Creep

Continued deformation of intact rock specimens or single discontinuities due to a constant applied stress. In this report, the term creep is only used in relation to the deformation of laboratory rock samples.

Time-dependent behaviour

Continued deformation of the rock mass around mine openings when subjected to a constant far-field stress. This behaviour is a complex result of the creep of intact rock, creep of bedding planes, delayed growth and initiation of new fractures and the rheology of the fracture zone. Time-dependency is also understood to refer to deformations not related to geometric changes in the dimensions of an excavation. It occurs on a time scale of days to years and is not related to elastodynamic behaviour.

Primary stope closure

The initial closure phase in a stope following a blast or a seismic event. It consists of an instantaneous jump in closure followed by a period of decelerating rate of closure. This phase is

a reflection of the transient response of the rock mass due to a sudden change in the applied stress conditions.

Steady-state stope closure
The continuous time-dependent closure phase which follows after the primary closure phase. The rate of closure in this phase remains virtually constant in the short term but may decrease slowly in the long term. This closure phase occurs in the absence of any mining or seismic activity and is the gradual time-dependent response of the rock mass when subjected to constant far-field stresses.

CONTENTS

LIST OF FIGURES

LIST OF TABLES

1 Introduction

The SIMRAC project GAP332 (Deep gold mine fracture zone behaviour) was planned in terms of three enabling outputs which are summarized briefly as follows.

(i) Gain sufficient knowledge of the fundamental physics of fracture initiation and growth to characterize and model the fracture zone and incorporate time-dependent creep effects in numerical models.

(ii) Study the interaction of seismic waves with the fracture zone to improve the design of rockburst resistant mining strategies and produce a report on dynamic fracture propagation and the modelling of dynamic fracturing.

(iii) Use the knowledge of fracture mechanisms to formulate strategies to reduce fall of ground injuries and fatalities, and produce a computer based fracture zone simulator to evaluate mining strategies.

A fourth enabling output was planned, to issue a two-dimensional version of the DIGS fracture simulation code. This output was dropped from the project proposal following the recommendations of the official SIMRAC project audit carried out by Professor S L Crouch in February 1996.

This final report for project GAP332 is structured in three main sections (Specifically Sections 2, 3 and 4) which cover the main features of the outputs (i), (ii) and (iii) respectively. A number of appendices are included as well to provide detailed descriptions of certain experimental procedures and field observations. The material presented in Sections 2, 3 and 4 is essentially a self-contained summary of the project work carried out over the three year period 1996 to 1998. Much more detailed descriptions of aspects of these studies are presented in supplementary documents. A list of these supplementary documents is given at the end of the report.

2 Development of physical and numerical models for the understanding of fracture growth processes

2.1 Introduction

The selection of engineering strategies to control the behaviour and stability of the stope fracture zone can be motivated by a fundamental understanding of basic fracture physics. To assist rock engineering and mining personnel, it is essential to be able to embody such understanding in a framework that will allow different mining strategies and existing problems to be analysed. This section sets out to describe the main steps that have been followed to satisfy these requirements.

At a basic level, attention has been given to examining the impact of the rock fabric on small scale failure processes and to validate the numerical representation of these effects using a random mesh discontinuity model. The numerical procedure is developed as a special version of the computer program DIGS and is termed the tessellation approach. The utility of the tessellation method has been enhanced by using the multipole influence computation technique developed under SIMRAC project GAP029 and by providing guidelines for the choice of numerical parameters which optimise the performance of the code.

One of the most important advances reported here is the quantification of the time-dependent behaviour of individual discontinuities on a laboratory scale. Large stope scale measurements of time-dependent stope closure are reported in Section 4. The basic understanding of both creep like and seismic processes in the stope fracture zone, allows the realistic simulation of seismic recurrence effects and provides a simulation tool for examining both the consequences of selected mining rate strategies and the implications of the stope closure rate on the life cycle of support units.

It is demonstrated in this section that the time-dependent behaviour of the stope fracture zone can be modelled by using either a continuum viscoplastic model implemented in the computer code FLAC or by adapting the DIGS tessellation model. The DIGS model is able to reproduce qualitative features of observed stope closure as well as characteristic seismic activity cycles between successive face advance increments. An extension of this model to include multiple layers with different material properties is described.

Finally, the initial steps in the design and coding of a three dimensional version of the DIGS code (3DIGS) are reported. A special hierarchical lumping scheme has been devised for the computation of influences between interacting cracks to allow the analysis of large assemblies of discontinuities. The first version of the 3DIGS code allows arbitrarily shaped but constant variation displacement discontinuity elements to be modelled. Initial results have demonstrated that the constant strength discontinuity elements are satisfactory for some specific intersection geometries (such as a single fault/ stope intersection) but are inadequate in solving problems with many acutely angled, intersecting cracks. Some novel applications of the program to the generation of automatic mining sequences have been explored and have highlighted the consequences of selecting different extraction policies.

2.2 Literature survey

2.2.1 Experimental and numerical observations of fracture growth processes

2.2.1.1 Fracture growth in triaxial extension tests

The initiation of distributed microfractures in cylindrical specimens of Witwatersrand quartzites under triaxial compression (major principal stress $\sigma 1$ in axial direction and intermediate and minor stresses applied as equal, radial, confinement $\sigma 2 = \sigma 3$) was studied by Hallbauer et al. (1973). A considerable number of subsequent studies have extended and confirmed these results (e.g. Kranz, 1983; Lockner et al., 1992). However, although such conventional triaxial testing of cylindrical specimens is easily performed in the laboratory, the fracturing is very different from that developed in a true triaxial stress environment found underground, where three different principal stresses ($\sigma 1$, $\sigma 2$ and $\sigma 3$) are present. In the triaxial compression tests, there is no clearly defined $\sigma 3$, normal to which, planar fractures are induced to grow (Jaeger & Cook, 1969). Fractures that develop under the conventional triaxial testing conditions are found to curve about the axis of maximum compressive stress σ_{max} axis. For example, the fractures in specimens of limestone were found by Zheng (1991) to curve parallel to the edges of the cylindrical specimen. From present and previous studies it has been found that, while the microfractures in triaxial test specimens are aligned parallel to σ_{max}, the overall failure is diagonally across the specimen, from end to end.

In contrast, the fractures in triaxial extension tests (minor principal stress $\sigma 3$ in axial direction with major and intermediate stresses applied as equal, radial, confinement $\sigma 1 = \sigma 2$) are predominantly rectilinear and planar (Briggs & Vieler, 1984) like the fractures developed ahead of deep level stope faces. This is because the least compressive stress ($\sigma 3$) direction is well defined. The microfracturing in some of these quartzites has been previously studied by Briggs and Vieler (1984) using polished half core sections, viewed with incident, dark-field illumination, reflected light techniques. These techniques, however, failed to reveal much of the finer and internal detail that provides a basis for understanding the fracture growth mechanisms.

The generally accepted descriptions of microfractures (e.g. by Simmons & Richter, 1976, Briggs & Vieler, 1984) define microfractures or microcracks (the terms are treated as synonymous) as being

- intra-granular fractures where they remain within a single grain,
- inter-granular fractures where they pass uninterruptedly between two grains across the grain boundaries,
- multi-grain fractures where they consecutively cross the boundaries of a number of grains,
- grain boundary fractures where they traverse a sinuous route along the boundaries of the grains.

In the tests performed by Briggs & Vieler (1984) on extremely strong siliceous quartzites, the confining stresses ranged from 400 to 600 MPa, while the axial stress at failure ranged from 2 to 20 MPa. Linear axial strains ranged from 5 to 9 microstrain and the total axial strain (comprising both linear and non-linear axial strain) ranged from 7 to 15 microstrain. Briggs & Vieler (1984) hydrostatically confined specimens of this siliceous quartzite to 600 MPa and allowed axial strain to various percentages of their estimated axial strain at failure. To unload the sample, the axial stress was increased to a hydrostatic state, then the axial and confining stresses were

reduced equally to zero. They found that intra-granular fractures could be observed in a few grains from about 42 per cent of the estimated strain at failure (i.e. 13 microstrain of axial extension strain from the hydrostatic, 600 MPa, compressively strained, length and 8 microstrain of axial extension strain from the initial, unconfined, unstrained condition). They observed that intra-granular fracture commenced at about 42 per cent of the estimated failure strain while inter-granular and multi-grain fractures occurred abundantly from about 86 per cent of the failure strain

2.2.1.2 Nucleation and growth of fractures

The initiation of fracture growth has been ascribed to the mechanical interaction between the advancing crack tip and potential nucleation points ahead of it. The fracture tip growth is terminated by mechanical interaction between the fractures of an en echelon fracture pair (Kranz, 1979a,b). Cracks parallel to and out of plane with each other are distinguished as

- en echelon where they do not overlap
- en passant where they overlap.

Calculations showed that the stress concentrations associated with the crack tips can dominate the crack growth locally (Kranz, 1979b). In the case of en passant cracks, one crack may shield the tip of the other. If the maximum stress is at a small angle to the cracks, a shear stress may result between the cracks. Thus, the observed links between the cracks may be shear fractures.

The surface topography of fractures, is a permanent record of the fracture process, providing both qualitative and quantitative information on crack propagation and failure mechanisms. Fractography, the science of the interpretation of fracture surface topography, is the major basis for failure analysis of materials. Typically, the nucleation point of the fracture is surrounded by a smooth almost featureless mirror zone (Bahat, 1996). Outside this mirror zone, linear fracture steps, aligned radially from the nucleation point, form hackle lines or ridges. Between the mirror and the hackle zone, a narrow zone of much finer, radially elongate structures is often apparent, and is called the mist zone.

The hackle lines are steps between segments of the fracture surface that are parallel to, but slightly out of plane with each other. They faithfully represent the local path of crack propagation (Frechette, 1998). They have also been termed cleavage steps but, as they are unrelated to the crystallographic cleavage, which is a potentially significant phenomenon, this term is avoided. The terms cleavage steps, river line, striae and lances are synonymous terms that are used to define the step faces that bridge between echelon segments of the fracture surface. Striae has been used to designate the radial rectangular steps in the mirror plane and are distinguished from radial hackles that appear beyond the mirror (Bahat, 1996). Both striae and hackle lines exhibit river line convergence features in the direction of fracture growth.

In studies of brittle materials it has been inferred that splitting up of the fracture surface is a manifestation of bifurcation that occurs when the fracture velocity becomes too high and propagation occurs as an unstable fracture (Bienawski, 1967). The mist zone that precedes the hackle zone is considered to form as the fracture growth approaches the terminal velocity and the formation of the hackle steps themselves is considered as being a form of crack branching: Bahat considers that branching only occurs as a continuation of hackles. The fine features of the mist zone are commonly a finer form of hackle, termed a velocity hackle. There is a tendency, in some cases, for the mist and hackle zones to repeat themselves. The repeating mist and hackle zones were produced experimentally by Ravi-Chandar & Knauss (1984) using a crack-parallel stress wave in Homalite. Investigations showed that the interactions of a reflected compressive wave with the crack tip caused the second mist zone.

The mist zone is sometimes very narrow, but there is usually an arcuate rib between it and the hackle zone, which is present even where the mist zone itself cannot be clearly distinguished. It has been shown, for example, by Levengood (1958) that, using the radius from the fracture origin to the mirror-mist or mist-hackle boundary, it is possible to calculate the tensile stress that caused fracture. The width of the mist zone has been found by Ball et al (1984) to be inversely related to the square of the fracture stress. Thus, information regarding the stresses involved during the fracture growth can be obtained from the fractographic observation of many of the grains. Such fracture stress determination was beyond the immediate scope of this study.

Although the hackle lines generally diverge as they extend outward, away from the source, there is often a tendency for the steps between some of the adjacent levels to converge in the direction of growth; they join like the tributaries of a river. This is the source of the term river lines. This convergence is regarded as being one of the most unambiguous indicators of fracture growth direction. Some river lines are found to extend from the source, across the mirror and mist zones. These should be regarded as radial striae rather than hackles.

On much of the fracture surface there are arcuate features. These features, which are sometimes described as rib marks or ripple marks, are arcuate about the fracture origin, i.e. convex in the direction of fracture growth. The rib marks may be due to an abrupt change in the fracture velocity (a rib mark is usually present at the edge of the mist zone). They may also reflect a local change in the direction of tension along the crack tip, which is, in turn accompanied by a change in the direction of fracture.

The interaction of the stress wave from an adjacent crack with the stress at the crack tip may also cause arcuate lines of a different nature; the stress wave momentarily distorts the stress field at the crack tip as it passes. These are termed Wallner lines. Whereas ribmarks do not cross each other, Wallner lines are seen to do so (Frechette, 1998). Another feature of Wallner lines is that the section across them is a smooth sinoidal curve, whereas the other ribmark lines have more acute crests. While Wallner lines are an important feature of the fractographic interpretation of the growth of fractures in glass, they are only rarely seen and are poorly defined on the fracture surfaces of the quartz grains. All these arcuate lines indicate the position and approximate shape of the crack front, at some stage during its growth (Frechette,1998).

2.2.1.3 Explicit modelling of the growth of fractures

Previous physical modelling of fracture propagation in a compressive stress field as well as numerical modelling e.g. Nemat-Nasser & Horii (1982) and Kemeny & Cook (1987), has incorporated cracks, at an angle of about 70° to the direction of maximum compressive stress, on which sliding has been able to occur. This has generated tensile stresses adjacent to the tips of the initial cracks. These have produced what have been termed kinked (straight segments) or kinked-curved crack extensions (Nemat-Nasser & Horii, 1982) or wing cracks (Fairhurst & Cook, 1966) that are at an angle to their parent crack and usually curve into alignment with the maximum compressive stress. A comparison of the various formulations is provided by Lehner and Kachanov (1996). Myer et al (1992), in modelling of fracture growth in specimens under compression, used small sliding cracks to induce fracture growth. Numerical and analytical studies by Willemse & Pollard (1998) suggested that the wing crack initiation angle depends on the type of fracture growth rule, and showed that the cohesive end zone models could explain field observations that could not be predicted by the conventional linear elastic fracture mechanics approach.

The en echelon fracture arrays observed along some of the grain-boundary segments are another manifestation of sliding on the micaceous veneer on a grain boundary. Such arrays of fractures are similar to those generated by Bieniawski (1967) when loading an oblique crack in glass. He attributed them to the tensile foci along the oblique crack induced by lock-ups of the

asperities, as the opposing surfaces of the crack slid past each other. The irregularities on the grain boundaries, where such en echelon crack arrays were developed, are thought to have behaved in the same way.

Whilst plastic distortions in micaceous granules are not the same as sliding cracks their mechanical influence on each other, and the cracks that grow from them, are probably not dissimilar. Malan & Napier (1995) modelled extension tests on quartzite using a pattern of Voronoi tessellations to simulate the grain boundaries and discrete cracks to represent the intragranular fracturing. Another approach to modelling the small granular quartzite samples was taken by Sellers & Napier (1997), in which they used a tessellation of Voronoi polygons to simulate the quartzite. Portions of the Voronoi grain boundaries were considered to be weaker material and weak flaws were distributed through the material. The flaws and intergranular sites had non-zero residual cohesion to simulate ductile flow such as could be expected in micaceous material. Pre-existing, intragranular, crack paths through the grains, which were permitted only to fail in tension, joined the apices of the grain boundaries. The models permitted the simulation of the processes of distributed microcracking and subsequent en echelon concatenation of microfractures that seems to be the manner of fracture growth in compression test specimens.

Dey & Wang (1981) found that when two different minerals, in effectively welded contact, are subjected to the same externally applied stress, the stiffer or least compressible mineral will also be subjected to additional boundary tractions. These can exceed the local tensile strength of bonds at the boundary and lead to extensional cracks in the stiffer material. The micaceous material being softer and more compressible than the quartz could induce the initial microfractures in the quartz grains.

Olson & Pollard (1991) modelled fracture growth from randomly distributed nuclear fractures but assumed an internal fluid pressurization of the fractures, which is a mechanism for fracture growth due to tectonic activity, but is absent in the fractures developed during extension tests. These, and other studies (e.g. Renshaw & Pollard, 1994) indicate that the interactions between preferentially located microcracks can initiate a macroscopic failure zone. Similar interactions between extensile microcracks have been postulated as reasons for the growth of shear cracks in compression (Lockner et al., 1992, Dyskin & Germanovich, 1995).

Myer et al (1992), with their randomly distributed sliding cracks, found that growth was favoured, forward of, but laterally adjacent to the growing fracture tip, as opposed to co-linearly with the growing fracture. Evidence was found of mechanical interaction between the advancing fracture and the next fracture growing from a position at a small angle laterally from the tip of advancing fracture.

2.2.2 Creep behaviour of intact rock and discontinuities

A vast amount of data on the laboratory creep of intact rock has been collected over the years (see Lama & Vutukuri, 1978). A complete review of all this data is, however, beyond the scope of this current study where the focus was on low temperature (< 100° C) creep of hard rock. The creep behaviour of brittle crystalline rock consists of three phases namely a primary (transient), secondary (steady-state) and tertiary creep phase (Lama & Vutukuri, 1978). Dusseault & Fordham (1993) suggested that hard rocks such as granite, gneiss and dolomite, which exhibit tertiary creep leading to rupture, probably do not experience true steady-state creep. The apparent steady-state phase should be seen as a transition between primary and tertiary creep. Unlike salt and ice, no mechanisms for true steady-state creep exist in these materials. Although the rate of creep in general is influenced by temperature, humidity and chemical environments, a temperature variation from 20° C to 100° C does not affect the creep of hard rock significantly (Pusch, 1993, Dusseault & Fordham, 1993). Of significance is that the creep

process can lead to delayed failure even though the stresses are below the short term laboratory strength. The primary and secondary creep phases have been investigated in detail and various empirical laws are used to describe this behaviour (Robertson; 1964; Pusch, 1993; Dusseault & Fordham, 1993). Tertiary creep of rock has not been investigated in the same detail as the other two phases and there is currently no acceptable fundamental equation to describe this phase. Most empirical equations are based on power or exponential laws and most predictions are based on site-specific measurements (Dusseault & Fordham, 1993). Although Carter & Kirby (1978) made a detailed study of transient creep of crystalline rocks, this focused mostly on high temperature (200° C to 600° C) creep and is not directly relevant to mining excavations in these rocks. The dominant mechanism of creep in crystalline rock has been shown to be the development and growth of microfractures (Kranz, 1979). The concept of stress-corrosion has been used to explain this phenomenon (Lama & Vutukuri, 1978; Atkinson, 1987). The tertiary creep stage is generally attributed to increased microfracture formation and coalescence leading to macroscopic failure. Kranz & Scholtz (1977) emphasized that a critical dilatant volume increase may be necessary to produce a tertiary creep stage by coalescence of microcracks at an associated critical crack density.

In the past a number of studies of time-dependent discontinuity behaviour have been related to the investigation of earthquake mechanisms and have focused on time-dependent friction (Dieterich, 1978). Other studies (Crawford & Curran, 1981) investigated the rate-dependent behaviour of rock discontinuities to displacement controlled boundary conditions. Although indirectly related to the time-dependent behaviour, these tests give no information about the creep behaviour under constant stress conditions. Only a limited number of studies investigated the creep behaviour of discontinuities. Wawersik (1974) conducted triaxial creep tests on cylindrical samples of Westerly granite with an artificially induced tension fracture inclined at 30° relative to the direction of greatest compression. An important observation made is that rock specimens containing discontinuities are much weaker and compliant than intact specimens. Solberg et al. (1978) investigated the time-dependent deformation of Westerly granite specimens containing a sawcut separated by crushed Westerly granite fault gouge. Results indicated that the displacement rate across the discontinuity decayed to a constant rate after several hours. If the differential stress was high enough, accelerated creep was observed leading to sudden violent slip. Schwartz & Kolluru (1984) investigated the influence of stress level on the creep of unfilled rock discontinuities. Uniaxial creep tests were conducted on synthetic samples consisting of gypsum plaster that contained inclined discontinuities. The results indicated that the ratio of the applied shear stress to the peak shear strength was the critical factor governing discontinuity creep: the higher this ratio, the more pronounced is the creep effect. The creep also appears to depend on the absolute stress level across the discontinuity. Bowden & Curran (1984) suggested that discontinuity creep can account for a significant proportion of the total deformation of a rock mass and investigated the creep behaviour of discontinuities in shale. A single surface bi-directional direct shear machine with a specimen size of 200 mm × 300 mm was used for the tests. The important conclusion drawn from the study is that the shear creep rate is non-linearly proportional to the shear stress ratio (applied shear stress/shear strength). The creep rate is small for small shear stress ratios and very large for large shear stress ratios. For shear stress ratios > 0,9, the creep rate is very sensitive to the shear stress ratio. At high values of shear stress ratios, time-dependent displacements are significant and may amount to centimetres in a matter of hours.

2.2.3 Explicit models for microfracture processes

The proper analysis of energy change and deformation mechanisms in mining operations requires a basic understanding of the failure processes occurring in the rock surrounding the underground workings. This is necessary to distinguish between failure processes that are slow in the sense of occurring over a period of hours, days or longer and failure which occurs rapidly and which is associated with sudden fault slip or bursting of excavation walls or pillars. Enquiry into the nature of failure immediately demands an understanding of the rock fabric and the mechanisms controlling damage localization and rock disintegration. In addition to this, it is

necessary to define the level of detail of the fundamental failure processes being studied. At the finest level interatomic breakage processes must be considered (Abraham et. al. 1994, Marder & Gross 1995). In the present research it is recognized that rock is an inhomogeneous and particulate material and it is assumed that basic failure processes are controlled by stress distributions at the grain scale (millimetres or fractions of a millimetre). This implies that grain and matrix inhomogeneities, pre-existing cracks, pores and inclusions play a basic role in initiating macro fracture localizations in rock. The explicit treatment of all these processes is impractical and equivalent structures have to be devised to describe the basic material properties. Fracture growth is simulated by considering the interaction of randomly placed flaws and the sequential initiation of further fracturing from the basic flaw population. The approach is distinct from continuum treatments of failure and also admits concepts of randomness and statistical mechanics into the treatment of rock failure. This philosophical concept is more fruitful than an adherence to deterministic modelling practices.

To construct explicit models of interacting microcracks it is convenient to employ small strain dislocation densities to represent the cracks (Cleary 1976, Napier 1990). It is further assumed that loading rates are sufficiently slow that elastodynamic stress waves do not play a significant role in the fracture growth processes. Then, the displacements and stresses induced by microcracks can be calculated from the displacement discontinuity formulation as shown in Sellers & Napier, 1997.

The simulation of microfracture processes is effected by specifying random assemblies of cracks which may be interconnected. For example, a given region of interest can be covered by a set of Voronoi polygons or Delaunay triangles (Napier & Peirce, 1995). A subset of the edges of these polygons are selected and designated as pre-existing flaws with assigned strength and friction sliding properties. A specified load increment is applied and the mutual interaction (sliding or opening) between the existing cracks is solved by an iterative scheme. At this point stresses are evaluated at each collocation point within elements which are assigned to the, as yet, unmobilized cracks. Following this evaluation, one or more elements are selected for mobilization according to a postulated priority and the entire problem is re-solved. (For example, elements having a specified degree of overstress outside the defined strength could be selected). In this manner, successive growth increments are evaluated leading to the evolution of an overall pattern of fracturing. The solution at each stage is found by means of an accelerated Jacobi iterative scheme. This procedure offers certain advantages over distinct element methods in that explicit block lists are not required and crack surface contact conditions are easily resolved at each collocation point (Jaswon & Symm, 1985).

Numerical experiments in which a sequence of incremental displacements were applied to the surface of a rectangular block to simulate compression tests have been performed to study the fracture mechanisms induced in random Voronoi and Delaunay tessellation patterns (Napier & Pierce, 1995, Napier et al., 1996). A distributed fracture pattern is observed where all the overstressed elements are permitted to activate simultaneously. The application of an incremental, weakest link rule for fracture selection causes a fracture pattern to form which is initially similar to a shear band, but then becomes distributed as loading progresses (Napier et al, 1996). In contrast, observations of compression test specimens suggest that microscopic fractures are initially randomly distributed (Krantz, 1983). As the sample is compressed new microcracks form in the direction of maximum compression and finally combine into a macroscopic shear band (Hallbauer et al , 1973).

The results of triaxial compression tests (Stavropoulou, 1979) and triaxial extension tests (Briggs & Vieler, 1984) on quartzite rocks from the South African gold mines have demonstrated that the strength, deformation and failure mode depend strongly on the ratio of quartz grains to matrix material. Thus, siliceous quartzites which contain more than 90 per cent quartz, with welded grain boundaries, are stronger and more brittle than rocks which consist of quartz grains surrounded by weaker argillaceous matrix material.

2.2.4 Modelling of fracture zone behaviour

Elastic modelling of mine excavations has been successfully implemented in two and three dimensional boundary element programs such as DIGS (Napier, 1990) and MINSIM (Napier & Stephansson, 1987). Correlation of observed stope closures with numerical results can be obtained if the damage due to the fracture zone is represented by reducing the Young's modulus of the rock mass by about 40 per cent to 50 per cent (Gürtunca & Adams, 1991). Regions of high stress and hence potential failure can be indicated using the Excess Shear Stress concept, but the elastic models cannot include the stress re-distribution associated with the development of the fracture zone as mining progresses (Legge & Spottiswoode, 1987).

The numerical modelling techniques based on the assumption of elastic rock behaviour are useful for overall mine planning, but their inability to predict the fracture direction and frequency is a shortcoming for the prediction of hangingwall conditions and design of support at the scale of a single excavation. The past few years have seen a number of advances towards this goal. Plasticity and ubiquitous joint models suggest that most deformation occurs at the stope face (Kuijpers & Napier, 1991) and do not predict the formation of fracture bands ahead of the stope, as observed in underground studies (Adams et al., 1981). Discrete element methods can cope with large numbers of blocks arising from a complex jointing pattern in a rock mass. The mining induced fracturing can be modelled as sets of initially welded discontinuities, at pre-defined angles, which activate ahead of the excavation as mining progresses (Lightfoot et al., 1994).

A considerable step towards the possibility of predicting the fracture directions was achieved using the concept of discrete fracture growth in the boundary element program DIGS (Napier, 1990). A mechanism for fracture initiation ahead of the face was postulated by allowing for activation of bedding planes ahead of the stope face (Napier & Hildyard, 1992). The success of the discrete fracture growth models has been limited by the need to choose the position of the seed points from which the fractures initiate and the computational effort required for searching for each crack direction at each crack increment.

A solution to this problem has been proposed (Napier & Peirce, 1995) in which the region of interest is covered by a random pattern, or tessellation, of potential fractures. Tessellation models have been applied in studies of micro-mechanics of fracture in laboratory tests (Sellers & Napier, 1997) as well as mine models with the stope modelled as a single slit (Malan & Napier, 1997).

2.2.5 Modelling of time-dependent rock mass behaviour

To include failure processes in rheological models, slider elements (also called St. Venant elements) are typically added to the elastic and viscous elements of viscoelasticity. These slider elements have a specified failure strength and are immobilised below this strength. Commonly a viscous element is placed in parallel with the slider to control the strain rate if the slider is loaded above its failure strength. This is the so-called Bingham unit. Various combinations of elastic, viscous and St. Venant elements have been used by researchers to simulate particular time-dependent problems. Gioda (1982) and Gioda & Cividini (1996) used a Kelvin viscoelastic model in series with a Bingham unit to represent primary and secondary closure in squeezing tunnels. Tertiary movements can be considered by providing suitable laws relating the values of the mechanical parameters (such as viscosity) to the irreversible part of the time-dependent strain. These rheological models are particularly suited for implementation in the finite element method. Other examples of the use of these rheological models can be found in Akagi et al. (1984), Song (1993), Lee et al. (1995), Euverte et al. (1994) and Sagawa et al. (1995).

Nawrocki (1995) developed a one-dimensional semi-analytical solution for the time-dependent behaviour of a coal seam. A Bingham type of material model was assumed. This study was initiated to investigate the rate of face advance on rockburst occurrence. The analysis showed

that rapid ore extraction produces zones of high stress concentrations close to the longwall face. This situation is deemed to be hazardous as it increases the likelihood of rockbursting.

Since Perzyna (1966) proposed the general concept of elasto-viscoplasticity, a number of workers have applied this theory to geological materials. Elastovisco-plasticity is essentially a modification of classical plasticity theory through the introduction of a time-rate rule in which the yield function and plastic potential function of classical plasticity are incorporated. In comparison with viscoelasticy, a viscoplastic material shows viscous behaviour in the plastic region only. Desai & Zhang (1987) used this theory together with a generalised yield function to characterise the viscoplastic behaviour of sand and rock salt. Sepehr & Stimpson (1988) used Perzyna's theory as a basis to develop a time-dependent finite element model to understand the time-dependent closure of excavations and seismicity in the potash mines in Saskatchewan. For a rheological analysis of tunnel excavations, Swoboda et al. (1987) developed a coupled finite element/boundary element approach to analyse the interaction of the rock with the viscoelastic properties of the shotcrete. The rock was assumed to behave in an elasto-viscoplastic fashion.

Fakhimi (1992) and Fakhimi & Fairhurst (1994) proposed a visco-elastoplastic constitutive model to simulate the time-dependent behaviour of rock. The model consists of an elasto-plastic Mohr-Coulomb model in series with a linear viscous unit. This model was implemented in an explicit finite difference code. A typical solution cycle would be to do an elasto-plastic analysis during which real time is frozen. After an equilibrium point is reached, the linear viscous unit is used to determine additional creep strain components for a specified period of real time. Control is then passed back to the elasto-plastic analysis to obtain a new equilibrium and the process is repeated. Although this model appeared successful in imitating the behaviour of uniaxial and triaxial tests and the stand-up time of excavations, the time-dependent behaviour of the model is independent of the failure processes. The entire material (including the far-field) also behaves in a viscous manner. This model is therefore not applicable to the conceptual model of deep excavations in hard rock (Figure 2.4.5.1) where the time-dependency is a direct consequence of the failure processes and the solid rock behaves essentially elastically.

2.2.6 Models to simulate the creep behaviour of discontinuities

Several workers (Tan & Kang, 1980; Schwartz & Kolluru, 1984) emphasised the role that discontinuities might play in the time-dependent behaviour of excavations. Realistic modelling of time-dependent rock behaviour therefore needs to simulate the rheological behaviour of discontinuities and the interaction between these discontinuities. Curran & Crawford (1980) and Crawford & Curran (1983) suggested that creep deformation along discontinuities may be appreciable, especially at loads near the peak strength. They developed a numerical technique based on the displacement discontinuity method to model time-dependent rock behaviour. Owing to a lack of experimental evidence on discontinuity creep behaviour, a simple three-parameter solid viscoelastic model was used. Numerical experiments showed that discontinuity creep is only important when discontinuity surfaces are relatively free to move. Samtani et al. (1996) developed a viscoplastic interface model for use in finite element programs. Interface elements in finite element programs can however cause numerical problems through ill-conditioning of the stiffness matrix and high stress gradients in the interface elements (Day & Potts, 1994). Further difficulties are experienced in generating multiple discontinuities in finite element meshes. These problems are not encountered in boundary element programs, although the number of elements is usually restricted by the amount of computer memory available.

2.2.7 Inclusion of multiple material zones in the boundary element method

The orebodies of the Witwatersrand Basin are associated with sedimentary and minor volcanic rocks predominantly. Generally, an orebody can be considered as a layered system composed of formations with different material properties (e.g. Schweitzer & Johnson, 1997). For example, the Ventersdorp Contact Reef (VCR), the overlying lava, and the underlying quartzite form a typical three-layer system. Assembling appropriate numerical techniques, capable of representing the fracture zone of a stope in a layered system, is essential to an understanding of the potential mechanism for material instability in relation to hanging wall and footwall with different properties.

Boundary element models are widely used for computing stresses and displacements around underground excavations. Most of these models assume the rock mass to be a homogeneous, isotropic, linearly elastic solid, although inhomogeneity and anisotropy can also be handled by the boundary element method (Banerjee & Butterfield, 1981, Crouch & Starfield, 1983, Napier & Ozbay, 1993). In particular, superposition schemes can be adopted to develop the displacement discontinuity method for multi-layered elastic media (Shou, 1997), using the analytical solution to the problem of a displacement discontinuity element within bonded half-planes (Frasier & Rongved, 1957, Crouch & Starfield, 1983, Pan, et al., 1998). The advantages of this approach are that, firstly, it is not necessary to introduce elements at the interface and, secondly, this method can easily be extended to three dimensions.

Problems involving layers of finite thickness are more difficult to treat as the closed form fundamental solution for the boundary element is difficult to derive. The fundamental solution for a multi-layered medium can be derived using the Fourier Transformation method, but the solution contains improper integrals which must be calculated numerically (Sneddon, 1951, Bufler, 1971, Chen, 1971, Wardle, 1980, Small & Booker, 1984, Benitez & Rosakis, 1987, Shou, 1994).

2.3 Methodology

The first section of the report deals with the development of the techniques and numerical tools required to advance the understanding of rock fracture processes and to be able to capture that knowledge in the form of numerical modelling programs that can be applied to solve practical problems. This methodology sets out the development of the research and describes the steps taken to be able to have a set of tools available to apply to the investigation of strategies to reduce fall of ground accidents and rockburst occurrences. These applications are then described in Section 4 of the report.

An aim of the first output of the research was to investigate the fabric sensitive fracture processes in rock. Applications of the tessellation modelling method developed in the SIMRAC project GAP029 indicated that certain choices of tessellation patterns could be applied to represent the fracture processes in particular rock types. A series of triaxial extension tests were performed to study the fracture process under laboratory conditions that approximate the stresses ahead of a stope face. The major principal stresses are applied as confinement and the axial stress is reduced until the macroscopic failure surface is formed in the direction of the major principal stresses. The comparison of a number of different rock types will lead to the identification of the most important parameters that distinguish the response of the different rock types.

The ultimate goal of the fracture studies is to represent the fracture growth processes in two and three dimensions. As the fracturing is a three dimensional process, occurring within the opaque test samples, it is difficult to characterize the whole fracture process. A twofold approach to solving the problem was taken by firstly considering sections through the sample, and secondly

analyzing the surface of the final fracture planes. Each method on its own has limitations on the amount of evidence that can be assembled regarding the nature of three dimensional fracture mechanisms, but seen together can provide a clear picture of the initiation, growth and interaction of the microcracks that make up the macroscopic fractures.

The study of time-dependent behaviour has been identified as being needed to determine the conditions associated with the transition from stable deformation to rockbursts. The first part of this study investigated the laboratory creep of intact rock samples from the mining industry under uniaxial conditions to determine the time-dependent parameters for relevant South African rock types. The rheological properties of discontinuities may also play an important role in the overall rock mass behaviour and so the second part of this study focussed on the shear creep of discontinuities.

All the creep experiments on intact rock specimens were conducted using the CSIR creep testing machine using deadweights and cantilevers to maintain a desired constant load on the specimen. For tests where the load was incrementally increased in steps, each new stress level was attained by adding additional weights. This machine is housed in a climate controlled laboratory with the temperature maintained at 22° C and the humidity at 50 per cent. For the shear creep tests, equipment was developed from an existing Wykeham Farrance shear box normally used for shear tests on soil. The upper and lower halves of the box were designed to give unrestricted access to the two sides of the specimen. This allowed for the mounting of four vertical LVDTs (linear variable differential transformers) and two horizontal LVDTs, in special machined attachments, directly to the sample. As there is no shear stress applied to these attachments, they will not creep relative to the rock surface. The six LVDTs can be used to resolve the complete three-dimensional spatial movement. As the range of the horizontal LVDTs was quite small, another horizontal LVDT with larger range was used outside the box to measure any large scale shear displacement.

The search for a numerical method to model fracture formation around deep level gold mine excavations led to the development of the DIGS (Discontinuity Interaction and Growth Simulation) boundary element code to simulate the incremental growth of fractures. However, the need to develop constitutive models of basic failure processes resulted in the adoption of a tessellation approach to simulate grain interaction and breakage during the SIMRAC project GAP029. The method involves representing the grain boundaries in a region of rock by a triangulation of potential fractures, called a tessellation. These elements activate when the failure strength is reached, and depending on a set of rules governing the sequence of fracture activation. The experience of applying the method led to a new interpretation of the tessellation approach that considers the elements in the tessellation as potential fracture paths. In the proposed method, some elements are considered to be weak flaws and all others may only fracture in tension. The tessellation is not directly associated with the exact rock fabric, but was adapted to include through grain and around grain fractures as a means of modelling the fabric dependence of fracturing in quartzitic rocks. Then, studies of the effect of material microstructure on the macroscopic behaviour of rock were undertaken using a variety of tessellations to investigate the effect of the micro-failure activation laws, the constitutive relations on the cracks and the effect of flaws. Simulations of laboratory tests were performed to investigate whether the sliding flaw - tension crack approach can represent experimentally observed macroscopic failure modes such as splitting in uniaxial compression, shear band formation in biaxial compression, localised failure in extension as well as the development of fractures in non-uniform stress states e.g. pillar failure and core disking.

The practical application of the tessellation method to stope scale problems, depended on the creation of a suitable tessellation and the computer memory available to solve the problem. The multipole method had been developed to reduce the memory requirements, but there was no means of selecting the optimal multipole parameters. A method for selecting the parameters has been developed and is described in the report. Utilities were developed to manipulate the tessellation constitutive rules to be able to describe different geological environments. The techniques developed as outputs of this project are applied to different geological environments in Section 4.4.2 of this report.

The time-dependent behaviour of the fracture zone was identified as having a considerable effect on the stability of underground excavations. Continuum viscoelastic and viscoplastic models were developed to allow for direct simulation of the time-dependent fracture zone response. The viscoplastic approach was retained in preference to the viscoelastic method. The model is based on classical viscoplasticity, with a novel time-dependent cohesion weakening rule to simulate the time-dependent failure of the rock. The model was then applied to simulate the time-dependent development of the fracture zone around large excavations and the response of the rock mass to a mining step in a longwall stope.

Although the continuum viscoplastic model can simulate the time-dependent behaviour of the fracture zone, it cannot be used if the behaviour is dominated by major discontinuities such as the creep of bedding planes. A discontinuous formulation was developed for the incorporation of viscoplastic effects on random discontinuities which allows for the relaxation of the discontinuities according to a postulated law. Sudden stress drop or elastodynamic effects are approximated by allowing rapid cohesion loss (softening) to be accommodated in the solution scheme but no attempt was made to include elastodynamic wave propagation effects in this current study. The most important aspect of the work is that explicit interaction between the mine openings and mobilized discontinuities are accounted for as an evolutionary time process. The model forms the basis for addressing problems such as varying the mining face advance rate, the effects of mining at greater depths, the desirability of continuous or punctuated mining cycles and questions relating to the rate of extraction of remnant areas and the expected recurrence of rockbursts and seismic energy release cycles.

The tessellation methods considered previously can only model the differences in the rock behaviour by assigning different strength parameters to the potential fractures. However, the orebodies of the Witwatersrand Basin can often comprise systems that are composed of formations with different material properties, e.g., the VCR (Ventersdorp Contact Reef), the overlying lava, and the underlying quartzite form a typical three-layer system. To account for variations in the elastic properties, a superposition scheme was adopted to develop the displacement discontinuity method for multi-layered elastic media. Typical gold mine stoping problems were then analyzed to apply the model and suggestions are given based on the numerical results.

All previous models of the fracture zone have been two-dimensional. A three-dimensional version of the DIGS code (3DIGS) has been designed and coded as part of the GAP332 project. Volumetric lumping and equivalent crack schemes were developed to allow reasonable sized problems to be solved. The program data structure has been designed to allow for the future implementation of multiple material regions. The 3DIGS program currently uses constant variation, polygonal shaped, displacement discontinuity elements and includes logic to allow time-dependent viscoplastic slip on designated elements. Future versions will include so called direct boundary elements for solid body and cavity problems. The code has been tested with preliminary studies of micro-mechanical 3D failure processes, seismic diffusion problems and the selection of optimal mine layout sequences.

2.4 Results

2.4.1 Experimental and numerical observations of the effect of rock fabric on fracture processes

2.4.1.1 Extension testing of different rock types

The Witwatersrand basin in South Africa contains the majority of the local gold reserves and is the site of the deepest mines in the country. The geology of the basin has been presented in

detail elsewhere (e.g. Myers et al., 1990, Schweitzer & Johnson, 1997) but for the purposes of the present rock mechanics studies, can be considered as consisting of quartzite and shale layers for several kilometres above the basement rocks. One of these layers forms the lower series of gold bearing reefs, known as the Carbon Leader Reef. This reef tends to be immediately overlain by a layer of highly siliceous quartzite. The upper or Ventersdorp Contact Reef is overlain by extensive lava flows. The lava is termed hard or soft depending on the content of tuffaceous material (Winter, 1994). The excavation procedures at the mining depths of up to four thousand metres, result in considerable fracturing of the surrounding rock mass. Underground observations (e.g. Berlenbach & Schweitzer, 1997, Quaye & Guler, 1998) suggest that the various rock types react in different ways, altering the pattern of fracturing and hence the rock mass conditions around the mining stopes.

The stress states around the mine openings range from the initially highly compressive virgin stress state with vertical stresses of more than 60 MPa and horizontal stresses ranging from 0,3 to 0,8 times the vertical stress. The arching action of the transfer of vertical stress around an extending opening causes a significant increase in the vertical stress. Simultaneously, the presence of the opening reduces the horizontal stress. These stress changes can be represented in the laboratory using the extension test procedure. A unique test machine was developed by the former Chamber of Mines Research Laboratories in which a 25 mm diameter cylindrical sample, 75 mm long, is loaded to a selected hydrostatic stress state and then the axial stress is reduced until the sample fails. The device has been constructed to withstand extremely high confining pressures, representative of the major principal stress ahead of a deep gold mine stope.

The 25 mm diameter cylinders were jacketed with rubber and had epoxy seals applied round the end contacts with the platens to prevent the hydraulic confining fluids penetrating to the specimen. The specimens were loaded hydrostatically (the axial stress and hydraulic confining stress were maintained equal to each other) up to a high stress (600 MPa) and then unloaded gradually along the cylinder axial direction to induce fracturing. After failure, the axial stress ($\sigma 3$) was again increased until it equalled the confining stress, after which the specimen was unloaded hydrostatically. The specimens fractured as a result of the extension strain in the axial direction, while the applied stress remained compressive in all directions. The macro-fracture directions tend to be perpendicular to the direction of the least compressive principal stress ($\sigma 3$) (Jaeger & Cook, 1969).

A series of triaxial tests was carried out on examples of different rock types associated with the hangingwall and footwall strata of deep mines. Three siliceous quartzites: Timeball Hill, Orange Grove and Black Reef, were selected and compared with the more argillaceous Elsburg quartzite. These were contrasted with hard (Alberton) lava and two types of soft (Westonaria) lava. In most cases, the specimens were obtained from surface to reduce the possibility of pre-existing microcracks that would obscure the test induce a cracking. The results of the tests are best presented graphically deviatoric stress against deviatoric strain. The deviatoric stress is calculated by subtracting the confinement from the axial stress. Some typical deviatoric stress - deviatoric strain results are shown in Figure 2.4.1.1 for four different types of quartzites. Subtracting 600 MPa from the ultimate stress values demonstrates that most of the samples failed whilst in a state of overall compression. This is significantly different to the conventional view of fracture, e.g. Olsen & Pollard (1991), that requires a state of tension, or internal hydrostatic pressure, for fracture to occur.

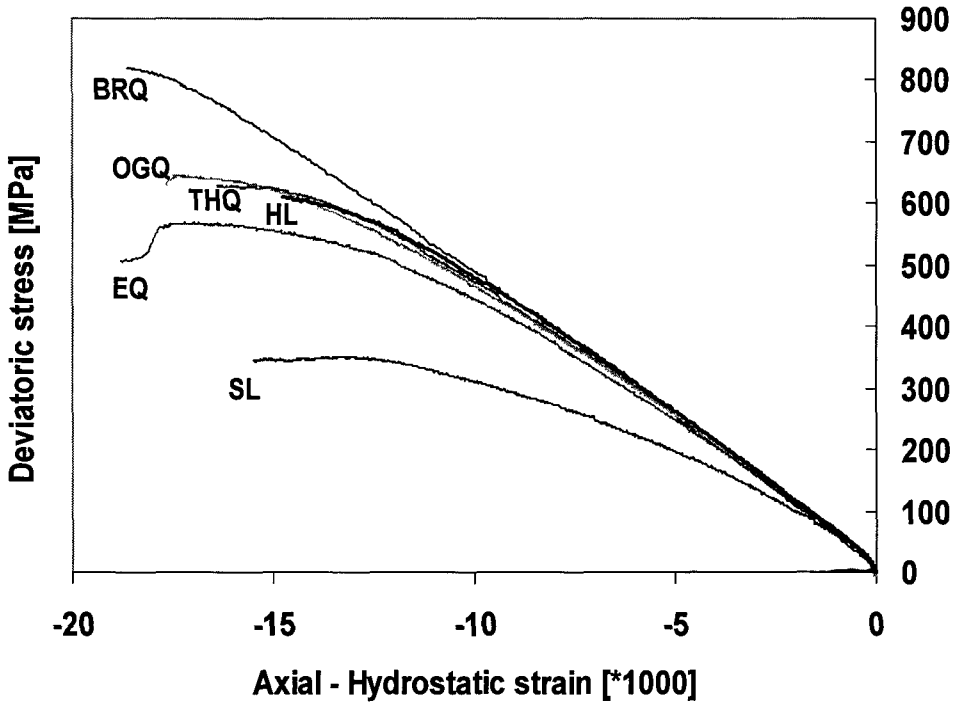

Figure 2.4.1.1 Comparison of extension test on six different rock types. (BRQ: Black Reef quarzite, OGQ: Orange Grove quartzite, THQ: Timeball Hill quartzite, HL: hard (Alberton) lava, EQ: Elsburg quartzite, SL: soft (Westonaria) lava.

Further details of the tests are provided in Appendix 2.1. Most of the quartzites have a very similar initial modulus, however the change in the stress - strain curve appears to be related to the rock fabric. The Orange Grove and Timeball Hill quartzites are finer grained, and show a very similar response. The Black Reef quartzite is a fine grained arenaceous material that is susceptible to cleavage due to its tectonic history (McCarthy, 1986). This probably accounts for the considerable strength variations observed in the tests (see Appendix 2.1). The Elsburg quartzite is weakend by the presence of chlorite on the grain boundaries, and exhibits a more ductile response. The brittle, fine grained quartzites fail at very small angles to the major principal stress. The largest being 10° in one Orange Grove quartzite sample. However, the Elsburg quartzite fails at about 25° to the major principal stress. The friction angle obtained from triaxial tests is 36°, which implies a Mohr-Coulomb localization angle (45° - $\varphi/2$) of 26°, very close to the measured values. The stonger quartzites have friction angles in the region of 62°, implying that the localization angle is about 14°, higher than observed in the extension tests. Thus, the material response must change from extension cracking in the direction of the major principal stress to shear localization as the material becomes more ductile. For a given stress state, with two different rock types, it may be expected that the fracture directions could be considerably different. Thus, there can be differences in the fracture pattern between, for example, the strong quartzite hangingwall and the weaker, argillaceous footwall in the Carbon Leader stopes.

The hard lava samples show a generally consistent initial response, and ultimate strength. There is considerable difference in the response of different types of lava. The failure planes of the hard lava samples were oriented in the direction of the major principal stress. An intermediate lava failed at 20° to the major stress. The stress - strain curve of the softest lava tested, shown in Figure 2.4.1.1, indicates that the material has passed the brittle-ductile transition and exhibits lower strength and a perfectly plastic response after failure. The rock failed on a series of slip lines, shown in Figure 2.4.1.2, as expected for a ductile material. This is confirmed by the slip plane angles of 45°, implying a friction angle of 0°, as associated with plastic flow. These mineralogy-dependent rock behaviours have important implications for the response of the rock in VCR stopes, and may explain the anomalous fracturing observed in soft

lava stopes (Guler & Quaye, 1998). If the stresses ahead of the face are sufficient to cause the soft lava to exceed the brittle-ductile transition it may be expected that the hangingwall would consist of a multitude of slip planes and may unravel when exposed.

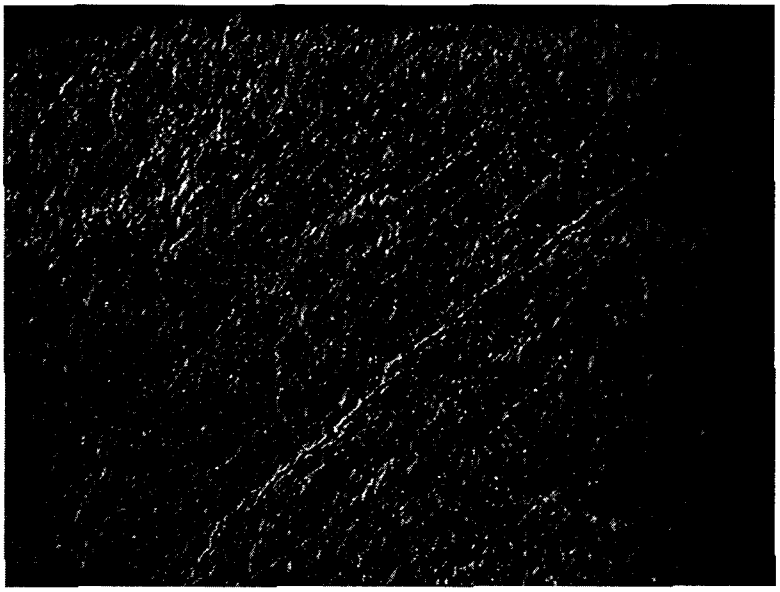

Figure 2.4.1.2 Side view of a soft lava extension test sample, showing slip planes.

2.4.1.2 Fracture nucleation and growth mechanisms in siliceous quartzites

In all the extension tests of highly siliceous rocks, performed for this study, and previously by Briggs & Vieler (1984), there is a very marked concentration or localization of microfracturing in a zone adjacent to the ultimate rupture plane. Evidence that might help in understanding the reason for this fracture localization effect was sought from a series of fractographic studies of thin sections and fracture surfaces. A detailed description of the results is given in Turner (1996) and Turner (1998). A summary of the findings is provided here.

A number of features can be inferred to be the initiation points for the microfractures. Because the proportion of the fracture within the slide thickness is limited, the fracture initiation point may not always be visible. Features such as dislocations that are fracture initiation points in many materials cannot be observed with a petrographic microscope. Initiation mechanisms observed in the study include: micaceous grains, apices on the micaceous material on grain boundaries and mica-veneered joints, quartz grains, micaceous layers oriented obliquely to the maximum compressive stress that allow sliding, lamination planes within micaceous granules that are parallel with the maximum compressive stress direction, bubble cavities, small nondescript granules on grain boundaries, irregularities on grain boundaries and heavy-mineral grains.

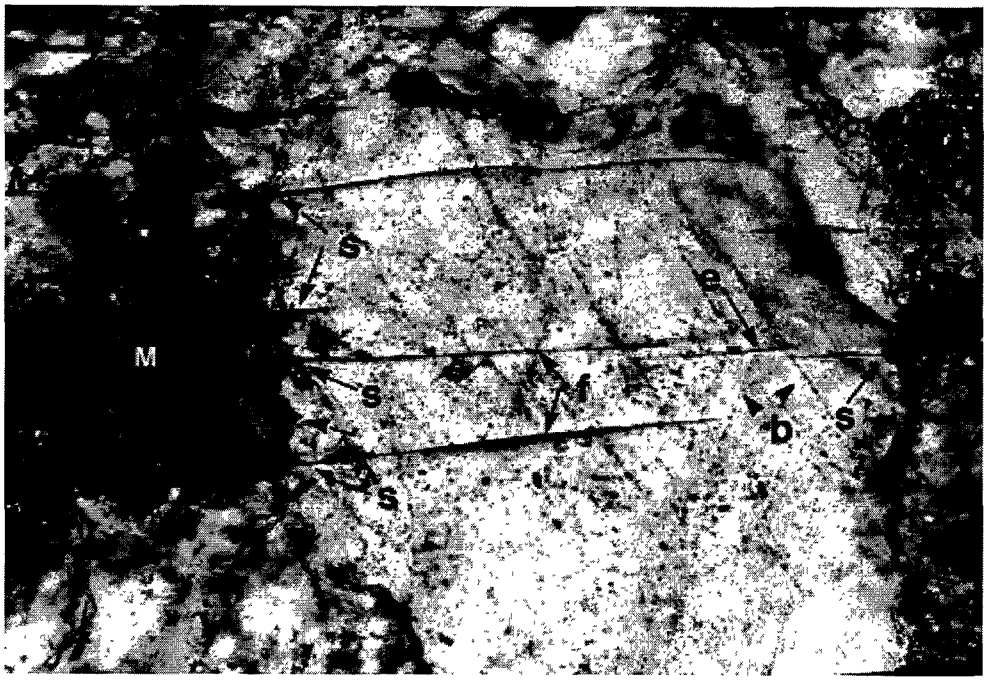

Figure 2.4.1.3 Photograph of a grain from a quartzite tested in triaxial extension. Several parallel microfractures occur within the grain. They are not parallel with the bubble trains (b). (X 100, plane polarised light).

The fracture sections away from the immediate vicinity of the major fracture/rupture plane through the specimen, appear to be nearly straight. Some slightly curved traces are to be seen amongst the numerous, closely spaced fractures that occur close to the rupture plane. Individual visible microfractures range in length from a few tens of microns, traversing a small fraction of a grain, or longer, traversing part of a grain, a whole grain or several grains. The zone of fracture localization near the rupture plane seems to be the location of most of the longer multi-grain fractures

In a few instances a minor multiple stepping of the fracture profile, by an amplitude of about 0,5 μm, could be seen. The surface fractography of the failure plane shows that many of such steps are those between the segments of the fracture surface that are delineated by the hackle lines or rib marks. In some other cases they may be cleavage steps. The growth of brittle fractures, as curved, and, sometimes lobed fronts, is common, at both the macro and the micro level, as found in materials such as polymers. Bifurcation (branching) of the microfractures is rare and seems only to occur within the fracture concentrations near the rupture zone. Where the micaceous protrusions in the quartz are platy and at a relatively small angle to the plane normal to the least compressive stress, the fractures are sometimes seen to follow this direction initially before curving to align with the least compressive stress. Similarly, they may occasionally follow the slightly irregular mica-veneered suture along a quartz grain boundary for a short distance before aligning with the normal to the least compressive stress within the quartz. There is a tendency, when following the irregular suture, to cut across the asperities. Occasionally, a fracture will emerge from its initiation point at an angle oblique to the plane normal to the overall least compressive stress, and then turn rapidly into such a plane. Such oblique angle initiations can usually be considered to be kinked-curved (wing) cracks due to slip on the micaceous planes.

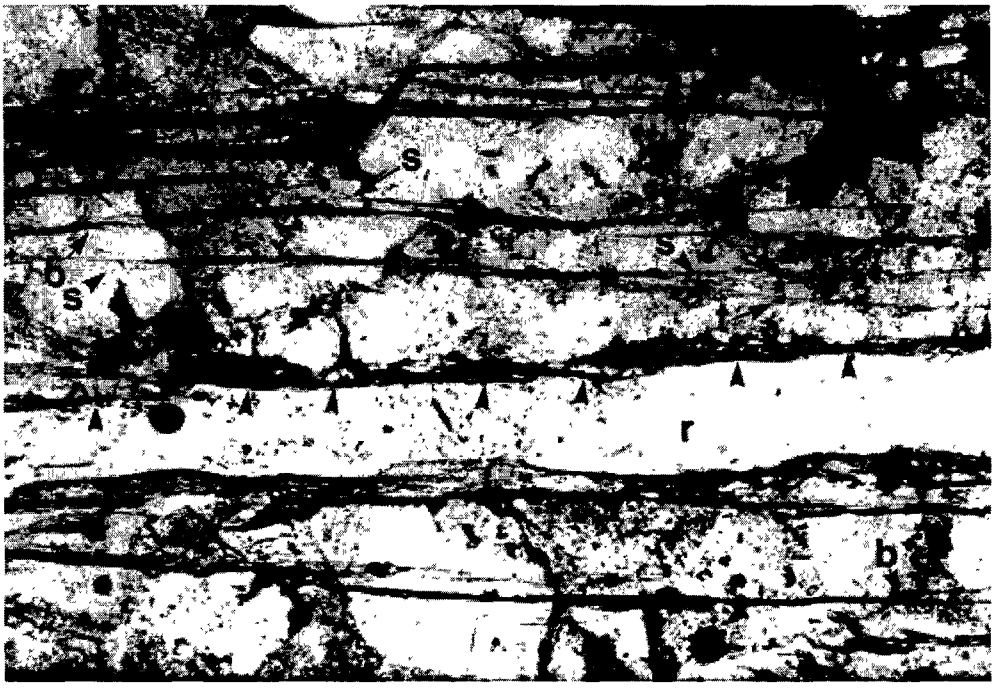

Figure 2.4.1.4 Fractures close to the rupture plane; (r) is in the resin filling the rupture. Despite the damage along the rupture it is apparent that the rupture plane is a concatenation of en echelon fracture pairs and side-stepping fractures (arrows indicate several of the component fractures). Several of these fractures are longish inter-granular fractures which are slightly curved and cross some of the mica-veneered grain boundaries. The ends of several of the fractures splay out (s) or bifurcate (b) while others have stepped (t) shadows (X 50, plane polarised light).

Even in these highly siliceous quartzites, in which a large number of the grains are welded together in a quartz continuum, individual microfractures are short. Their lengths range from part of a grain diameter, to a grain diameter and never more than a few grains in length. What is observed is that, shortly before the termination by pinching out of a fracture, a second fracture commonly appears parallel to and a short distance away from the first. The fractures overlap, forming an en echelon fracture pair (marked in Figure 2.4.1.3). En echelon fracture pairs may be isolated or pairing may be repeated at the remote ends of the members of the pair. The process is commonly repetitive, and elongated sequences or associations of en echelon fracture pairs are frequent.

While there generally seems to be no bridging link between the fractures of en echelon fracture pairs, there are also quite often one or more straight short bridging fractures. These bridging fractures may be more or less parallel with each other within a grain. This may indicate that they occur on one of the weakly developed cleavages of quartz. Their orientation relative to the en echelon fracture pairs ranges mostly from orthogonal to about 60°. Bridging may also occur along the more weakly cohesive micaceous veneer on a grain boundary. Gradual convergence between en echelon fracture pairs is rare. The normal mode of fracture growth in the fracturing of triaxial extension test specimens is definitely that the fractures remain straight and parallel to each other.

Because of the indeterminacy of the actual fracture growth direction it is often not possible to be sure if the truncation of a fracture represents a fracture initiation or termination point. Micaceous material on grain boundaries seems to be the most common visible cause of fracture termination. Although prior fractures are rare, fractures normal to σ_3 will terminate against these pre-existing fractures. Where the fractures terminate, the common offsetting or jogging of the fracture in the next grain causes a stepping of the fracture surface. The overall fracture can be

considered to be a sequence or concatenation of en echelon or stepping fracture pairs. The long fractures extending right through the specimen, the rupture, are clusters of such sequences or concatenations (see e.g. Figure 2.4.1.4). The fracture separation of en echelon fracture pairs is mostly small, ranging down to 2 μm with most (about 70 per cent) less than 22 μm. Overlap lengths range down to 5 μm with 60 per cent of overlaps being less than 160 μm.

A common feature of all the specimens of highly siliceous quartzite is the high density of microfractures in a zone adjacent to the rupture plane (Figure 2.4.1.4). As well as grains with multiple fractures, there are several linear concatenations of en echelon fracture pairs, of which one or more may be continuous through the width of the specimen. Elsewhere through the specimen, it is common for even an isolated grain to have more than one fracture in it (Figure 2.4.1.3). Single fractures in a grain are much less common. Within the zone of fracture localization where the specimen rupture occurs, it is common to see twisting and bifurcation or branching of the fractures (Figure 2.4.1.4).

It seems that, once a fairly major concatenation of microfractures has occurred, the stress field adjacent to such a concatenation is modified to favour the formation of further fractures. Possibly there is a local reduction in confinement close to the fractures that is due to the presence of the break in the continuity of the rock. This lower confinement allows fractures to form more readily in this zone immediately adjacent to the initial fracture. This would have a multiplying effect, allowing many fractures to form.

The features, such as the curving and stepping of the fracture planes and the branching of the fractures, seem to be indicative of a change in mode of fracture growth. The branching suggests high velocity unstable fracture growth, while the curvature and stepped/hackled nature of the tips of the fractures suggest a relaxation of the previously very dominant effect of the applied least compressive stress on fracture orientation. This is also thought likely to be due to a local reduction of the least compressive stress by the presence of the fractures. The greater lengths of individual fractures and greater frequency of multi-grain fractures, seem also to be significant.

On the much larger scale of geological joints, this feature of fracture localization manifests itself as the common occurrence of joints as localized swarms. This phenomenon was described by Dyer (1983). In joint zones hundreds of metres long and spaced 20 to 45 m apart, joints occurred, in the 0,5-2 m zones, as en echelon clusters with some parallel joints running side by side for tens of metres. The fracturing developed ahead of deep level tabular stopes has also been found to be concentrated into zones (Adams, Jager & Roering, 1981). There seems to be a likelihood that the mechanism controlling these large scale fracture localizations is similar to that causing the localization in extension test microfractures.

2.4.1.3 Surface fractography of the major fracture through siliceous quartzite specimens

The nature of the growth and the growth directions of the fractures and their growth relationships, relative to each other, can be interpreted using the surface fractographic features. The failure surfaces of a number of samples from the test series of Briggs & Vieler (1984) and the other tests, described in Section 2.4.1.1, were observed in reflected light under the microscope to identify the surface features associated with fracture growth in siliceous quartzites. A detailed presentation of the studies is given in Turner (1998). The transparency and bi-refringence of the quartz grains interfered with interpretation due to the presence of visible, but sub-surface, fractures. The problem was overcome by coating the surfaces with gold as palladium, as is the practice in scanning electron microscopy. The patterns of river lines, or hackle lines, and the arcuate rib marks are the most prominent and useful features. The overwhelming majority of the microfractures can be seen to have grown from the perimeters of the grains, confirming the observations made on thin sections. The features from which the microfractures nucleated, can commonly be identified despite the gold coating; mostly these are

inter-granular micaceous grains which are identifiable from their laminar texture. There are occasional fractures present that have nucleated from some feature within the grain but, from the surface view only, it has not been possible to identify what these features are.

The grains are so well welded that there is no grain-boundary fracture. (The fracture planes do not follow the curved route round the grains through the relatively weak matrix, such as can be seen in the quartz arenites with a higher proportion of micaceous matrix material). Nevertheless, most of the fractures stop at the edges of the grains. The single fractures through many of the grains traverse the grain from their nucleation points to the further margins of the grain, fanning out laterally to cleave the whole grain. Thus, the overall fracture is an almost coplanar composite of the microfractures through individual grains. It can be seen that the apparently very smooth planar fracture plane is, in fact, a series of en echelon surfaces, as shown in Figure 2.4.1.5. The steps between these surfaces in Figure 2.4.1.5 are on two scales, an almost grain by grain scale with an overlying coarser scale.

In the specimens with the regular series of en echelon surfaces, the growth was in the same direction, normal to the step line, for most of the grains on that step level. There was also some growth left or right parallel to the step line. In some of the other grains the growth spreads left or right, parallel to the step lines. Some fracture growth was initially away from the step line and curved towards being parallel with the step lines. A few fractures grew perpendicular to the step lines, but in a direction counter to the overall growth. The less common growth is parallel to the step lines. The growth direction across the step, on the next en echelon surface up or down, tends to be in the same overall direction. While such regularity of growth direction occurs fairly frequently, there are also regions of the surface on which the growth direction on adjacent grains is irregular.

On some parts of the surfaces, the microfractures occur as patches of apparently related fractures. There is no way of knowing which grains fractured first, but it can commonly be inferred that a particular group of grains fractured more or less sequentially; the overall fracture growing forward with a head-to-tail array of grain fractures. Such a sequence of fracturing of the grains is evident in Fig. 2.4.1.5. The dominant growth direction (large arrow) is reflected in the similar growth directions of individual microfractures (small arrows). Growth backwards, contrary to the general overall growth direction, also occurs on occasional grains.

a

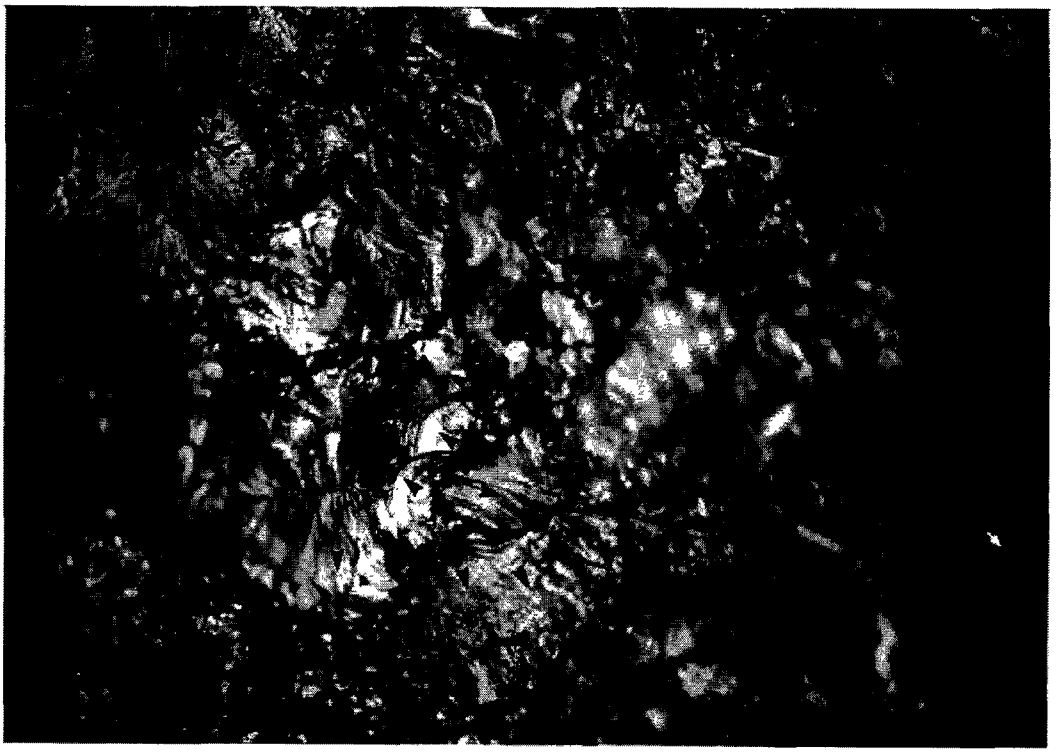

b:

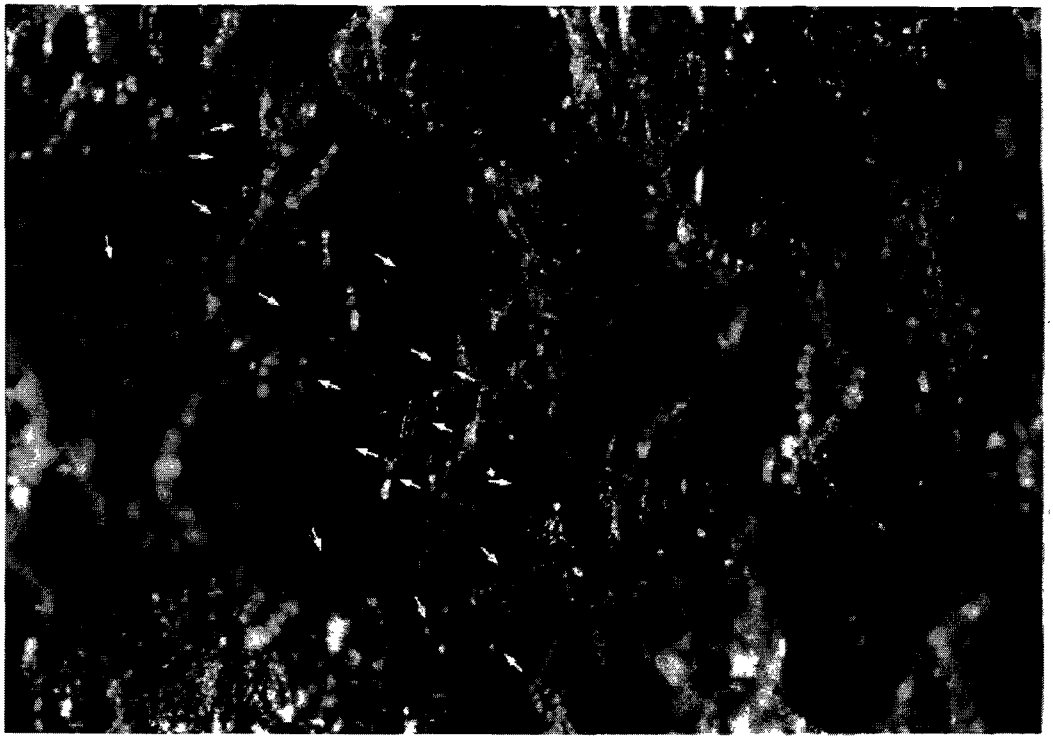

Figure 2.4.1.5 View of the surface of a fracture from an extension test. It can be seen that, for the part of the field in focus, the major fracture growth is diagonally from bottom right to top centre. The growth in the opposite direction is on the small fracture surfaces (X 100) a: illuminated with incident reflected light b: illuminated with oblique light.

These patches of fracture growth coalesce with other patches in the overall fracture surface. The dominant growth direction is not necessarily the same in adjacent patches. The coalescence is achieved by the lateral growth from both patches towards one another.

Usually there is a small step between the levels of these adjacent patches of fracturing: it is necessary to focus up or down to view them. They are not as coplanar as are the microfractures within the patches, as they are the more irregular en echelon surfaces mentioned above.

2.4.1.4 Numerical modelling of the growth of fractures in an extension stress state

Prediction of the response of the rock mass, in particular the hangingwall, is an important objective of the research towards improving the safety of mine workers. Any model of the overall rock mass behaviour at a specific site should incorporate the fracture mechanisms appropriate to the relevant rock types. Observations of the initiation and growth of micro-scale fractures have been obtained from micro-mechanical studies of fracture surfaces and thin sections from laboratory experiments on a range of quartzites (Briggs & Vieler, 1984, Turner, 1998). These studies posed questions as to the ability of available numerical techniques to model the rock type specific fracture patterns. Thus, it was necessary to determine whether the currently available numerical methods for predicting fracture growth could confirm the conclusions regarding the effect of crack interactions on the crack growth and localization processes reached from the experimental observations. This study seeks to address these questions and proposes solutions for extrapolating the numerical modelling on a microscopic scale to enable the numerical simulation of the fracture processes around a stope face.

The growth of fractures under tension has been considered in a number of studies. For example, Olsen & Pollard (1991) consider the tension cracks to extend when the stress intensity factor exceeds the fracture toughness. The stress intensity factor is calculated based on an approximation of the weight function. In the boundary element program DIGS, the crack growth is controlled by the tensile strength of the material around the crack. The crack direction is determined as being perpendicular to the direction of the most tensile principle stress measured a fixed distance ahead of the crack tip. This corresponds to the well-known maximum tensile stress criterion. A suitably located crack element is included when the stress at a distance ahead of the current crack tip exceeds the specified tensile strength. In a uniform stress state with a single far-field tensile stress, a single crack will extend in a straight line perpendicular to the tensile stress direction. This stress state is equivalent to a crack growing with an internal pressure of the same magnitude as the tensile stress. When a number of seed points are placed in the material, the cracks initially extend perpendicular to the tensile field stress, but then interact as the crack tips approach. In this model, the cracks deviate away from each other as the two tips approach, then change direction and approach each other. This characteristic deviation of the crack path was also observed by Olsen & Pollard (1989), when there was a significant difference in the principal stresses. As the principal stress difference decreases, the cracks become straighter and interact less. This can provide a diagnostic for field or microscopic observations to determine if a crack grew in a pure tension field.

As expected, no cracks are observed to grow under the action of a compressive stress field. The introduction of a stress raiser does however introduce tensile cracks, even in the highly compressive stress field of 600 MPa major principal compressive stress and a 10 MPa minor principal stress. The sliding surface flaw shown in Figure 2.4.1.6a, exhibits the well-studied wing cracks (e.g. Lehner & Kachanov, 1996) extending from each tip of the flaw in the direction of the major principal stress (horizontal in Figure 2.4.1.6). The cracks in the numerical model initiate at an angle of 45°, which is much less than the angle of 70,4° calculated in theory (e.g. Lehner & Kachanov, 1996). The reduced angle is due to the fact that the stress field is evaluated at a fixed distance around the crack tip and also depends on the shape function used in the displacement discontinuity formulation. The discrepancy will reduce as the element size in the wing crack increases. The wing cracks grow towards the direction of the principle stress and then terminate. The introduction of a diamond shaped hole with stress free boundaries causes tension cracks at the tips of the stress raiser, in the direction of the major stress. Thus, the size

and shape of the stress raiser and the specified tension strength are found to determine the length of the cracks.

A group of flaws stacked in a line perpendicular to the major principle stress demonstrates the effect that the interaction of the wing cracks may have on the length of tension cracks within the material. The wing cracks extend to different lengths to form a diamond shape that is slightly asymmetrical as shown in Figure 2.4.1.6d. When a crack approaches from the right, the longest cracks begin to extend. Thus, the set of cracks acts as a diamond shaped stress raiser, similar to those shown in Figure 2.4.1.6b, at a larger scale than the original sliding flaw stress raisers. In contrast, the crack growing towards the right, away from the influence of the approaching crack extends a short distance and then stops. The slider to the right does not experience any interactions and extend significantly. This study illustrates the importance of considering crack interaction on a number of different scales.

The inclusion of larger stress raisers alters the growth patterns considerably. In this case, the boundaries of a grain are included to investigate the effect on the growth of the wing cracks from a sliding flaw (see Figure 2.4.1.7). The boundaries included in the analysis are based, approximately, on the example of a grain in a siliceous quartzite (Figure 2.4.1.3). The grain is welded to neighbouring grains along the top and bottom, and surrounded by micaceous material along the two sides. The boundaries are modelled by displacement discontinuity elements that are permitted to interpenetrate a certain amount to simulate a softer material on the boundary. A friction angle of 30° is specified on the elements once closure occurs. A small triangular stress raiser is included on the left-hand boundary to investigate the effect of a non-smooth boundary.

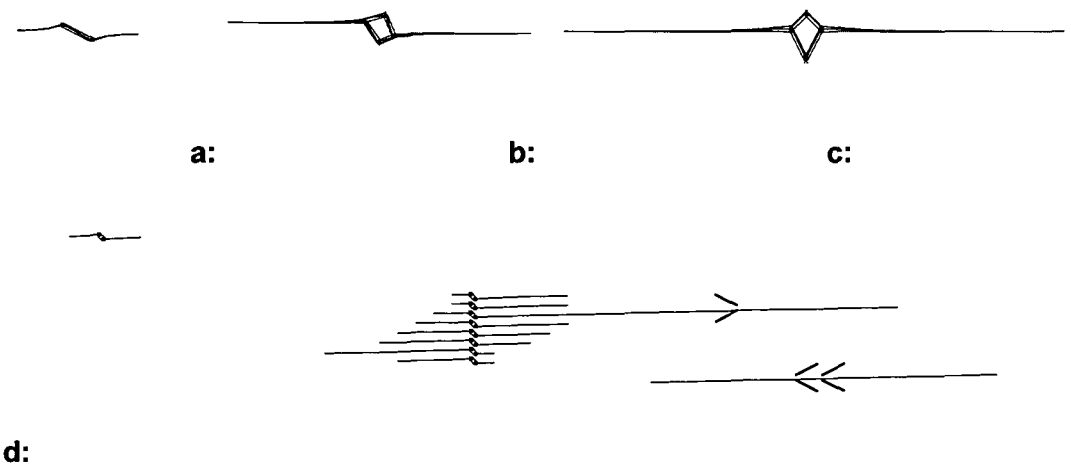

Figure 2.4.1.6 Tension crack initiation from flaws under a compressive stress field (600 MPa in the horizontal direction and 10 MPa in the vertical direction) a: sliding flaw, b: small diamond, c: larger diamond d: diamond shaped array of cracks initiated from line of sliding flaws, then acting as a flaw on a larger scale as crack approaches from right.

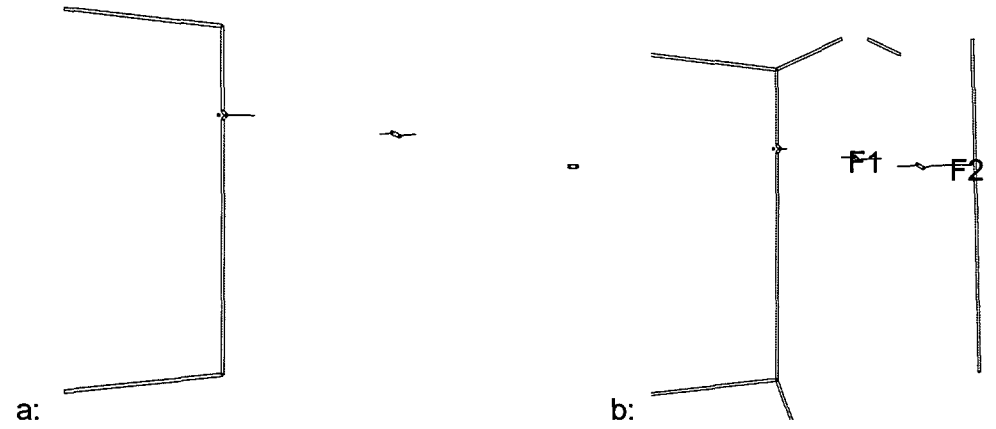

Figure 2.4.1.7 DIGS modelling of a single quartzite grain, as shown in Figure 2.4.1.3. a: left hand boundary only b: all boundaries.

The central flaw, marked F1 in Figure 2.4.1.7b, induces wing cracks that are similar in length to the crack in the uniform stress field. The flaw placed on the right, marked F2 in Figure 2.4.1.7b, exhibits a very different behaviour. The wingcrack growing towards the centre of the grain stops after a short length, but the right hand wing crack extends until it reaches the right hand boundary; increasing the distance of the boundary from the flaw increases the wing crack length. Thus, the wing crack extends into a region of tension.

The induced stresses surrounding the flaws can be observed by calculating the difference in the stresses between two growth increments. The tensile stresses induced by the interaction of two wing cracks are shown in Figure 2.4.1.8a. The initial induced tensile stresses are perpendicular to the direction of major compression. As the cracks extend, the zones of induced tension extend outwards from the crack tip. The greatest area of tensile stress extends between the approaching wing crack tips. The induced tension on the outer sides of the cracks is limited in extent. At some stage the zone of induced tension extends between the two wing cracks; this tensile stress would activate smaller flaws in tension and produce the stepped fracture surfaces depicted in Figure 2.4.1.5.

Taking the difference in the stresses between the first and the sixth growth steps indicates the change in the stress state and suggests the reasons for the termination of crack growth. As shown in Figure 2.4.1.8b, the overall stress state is reduced in the zone between the cracks, as evidenced by the extensive regions of induced tension (reduced compression) stress. The lighter stress vectors in Figure 2.4.1.8b indicate the induced compression. These vectors are directed along the original flaw towards the crack tip. This shows that the compressive stress has increased in the line of the flaw. The compressive stresses are able to clamp the tips of the wing cracks, preventing further growth.

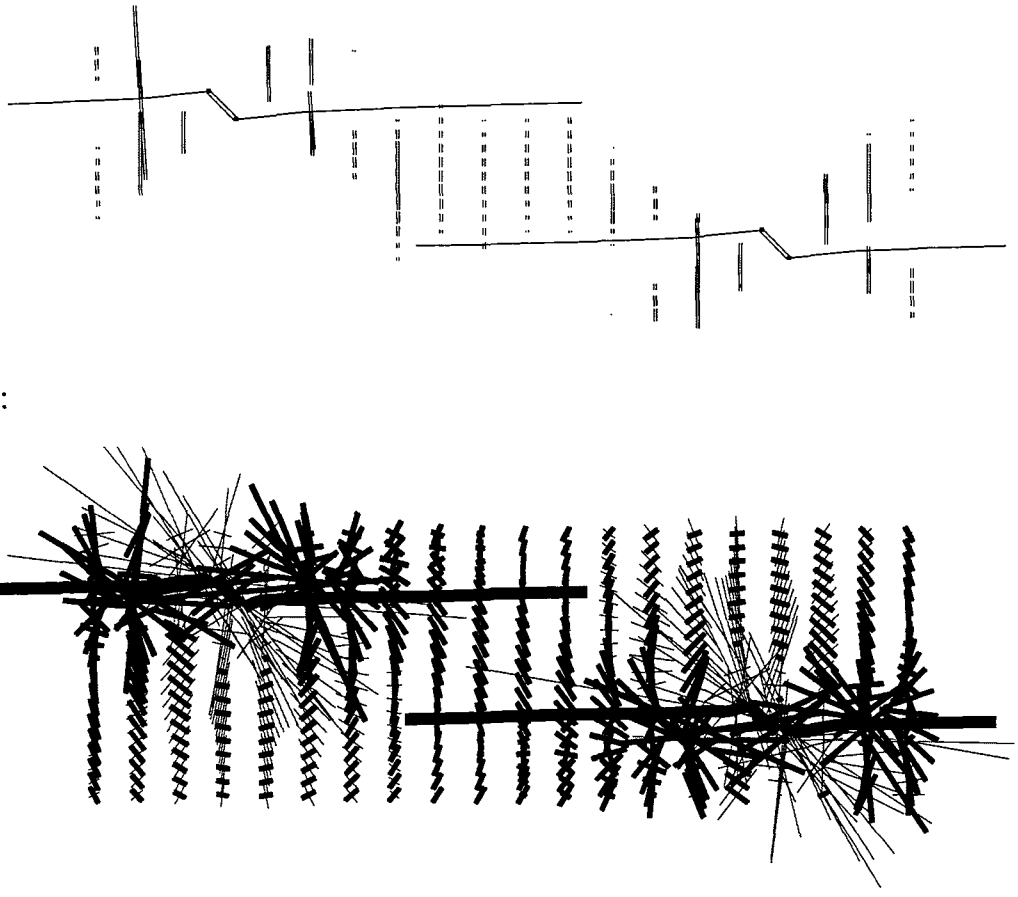

a:

b:

Figure 2.4.1.8 Induced stresses caused by interacting microcracks. a: zone of induced tensile stress (double lines are tensile stresses) b: difference in stresses between first and current step (light lines indicate compression and dark lines tension).

This study of microfractures seems to indicate that, while initial fractures are nucleated at widely scattered points through the specimen, the development of longer fractures is as a result of the association of distributed microfractures as concatenations of en echelon fracture pairs and arrays. One, or more, of these concatenations may extend through the specimen as a rupture plane. The standard DIGS models are able to model correctly the initiation and growth of such fractures. In a general model, it becomes difficult to insert specific flaws or seed points, because the position of fractures must be decided beforehand. Thus, cracks that may initiate as a result of stress field interactions will not be included. For this reason, the tessellation method was developed to remove the requirement of user input from the selection of fracture sites.

2.4.2 Laboratory studies of the physics of time-dependent deformation mechanisms

2.4.2.1 Introduction

Slow time-dependent deformation of the rock may cause a gradual non-violent reduction of stress concentrations and hence diminish the danger of rockbursts. The study of time-dependent rock deformation and strength degradation is required to determine the conditions associated with the transition from stable deformation to rockbursts. Although hard rock is not usually associated with large creep deformation, closure data collected from the excavations of

the deep South African gold mines (described in Section 4.4.3) illustrates significant time-dependent behaviour. As low porosity hard rock usually does not display significant steady-state creep, a laboratory testing programme was conducted in order to understand the underground behaviour better. As no published data is available on the creep of South African hard rocks, the first part of this study investigated the laboratory creep of intact rock samples from the mining industry under uniaxial conditions. This work was not intended to be an exhaustive study of the creep behaviour of all the different rock types found in South African gold mines, but to quantify the typical strain rates that could arise when subjecting some of these rocks to constant applied stresses. As the underground observations cannot be explained by the creep of intact rock alone, it is generally accepted that the time-dependent behaviour of hard rock on a mine scale is dominated by other mechanisms. As the rheological properties of discontinuities may play an important role, the second part of this study focussed on the shear creep of discontinuities.

2.4.2.2 Creep of intact rock specimens under uniaxial loading conditions

As a detailed overview of the testing programme is given in Malan (1998), this section will focus only on the most important findings. The typical laboratory creep behaviour of rock is illustrated in Figure 2.4.2.1 to define the various creep phases after load application. In the study, Ventersdorp lava and different types of quartzite where tested. The properties of these rocks are given in Table 2.4.2.1. The tests were conducted on the CSIR creep testing machine that uses deadweight loading and cantilevers to maintain a desired constant load on the specimen. The test methodology consisted of loading the same specimen to different stress levels by starting at a low value and increasing the stress in steps, allowing a certain time interval for creep. The advantage of this approach is that the creep strain may be monitored for an identical material at different stress levels and each specimen will be tested to failure within a reasonable period of time. In the deadweight loading machine, the successive stress levels are attained by simply adding further weights.

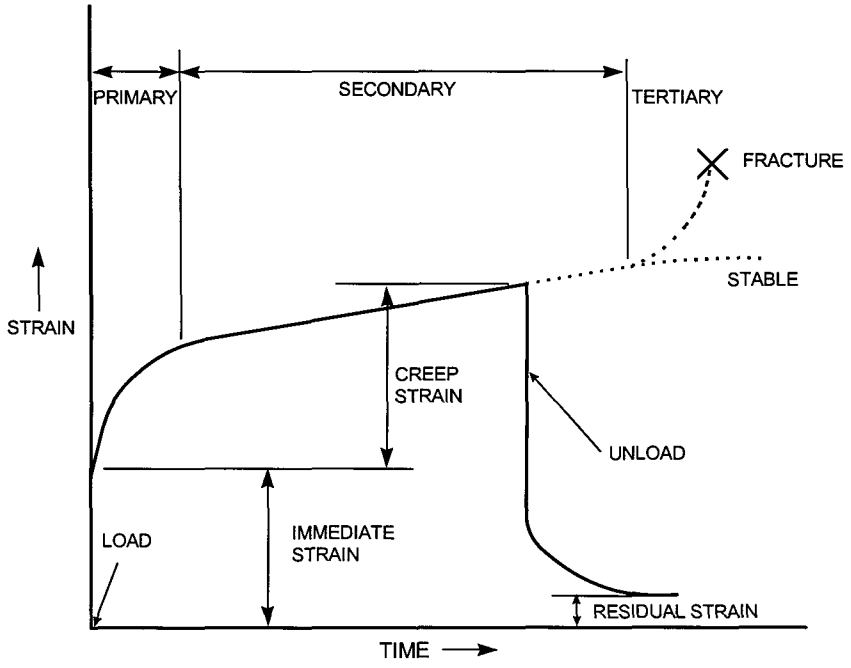

Figure 2.4.2.1 Typical creep behaviour of a rock specimen subjected to a constant load. The secondary creep phase is also called the steady-state creep phase.

Table 2.4.2.1 Average values of elastic and strength properties of the rocks analysed in this study. The number of samples indicates the number of tests conducted to calculate these average values and not the number of creep tests. The abbreviations are: UCS - Uniaxial compressive strength, E - Young's modulus, ν - Poisson's ratio.

Rock Type	*Location*	*UCS (MPa)*	*E (GPa)*	ν	*Number tested*
Argillaceous quartzite	Lorraine Mine	100	63	0,18	2
Ventersdorp lava	Western Deep Levels Mine	436	88	0,26	5
Quartzite	Western Deep Levels Mine	237	79	0,13	10
Argillaceous quartzite	Hartebeestfontein Mine	142	72	0,26	1

As an example of typical results obtained, the complete strain-time record for the lava specimen is given in Figure 2.4.2.2. Note that each loading step was preceded by a partial unloading. This procedure allowed for the monitoring of any changes in the deformation modulus after the specimen had been subjected to a creep phase. The incremental creep strain for each creep stage is given in Figure 2.4.2.3. Primary and secondary creep phases are visible. Similar creep profiles were obtained for the other rock types, but the quartzites failed at lower stresses and attained much higher creep rates at lower stresses than the lava. These results are given in Malan (1998).

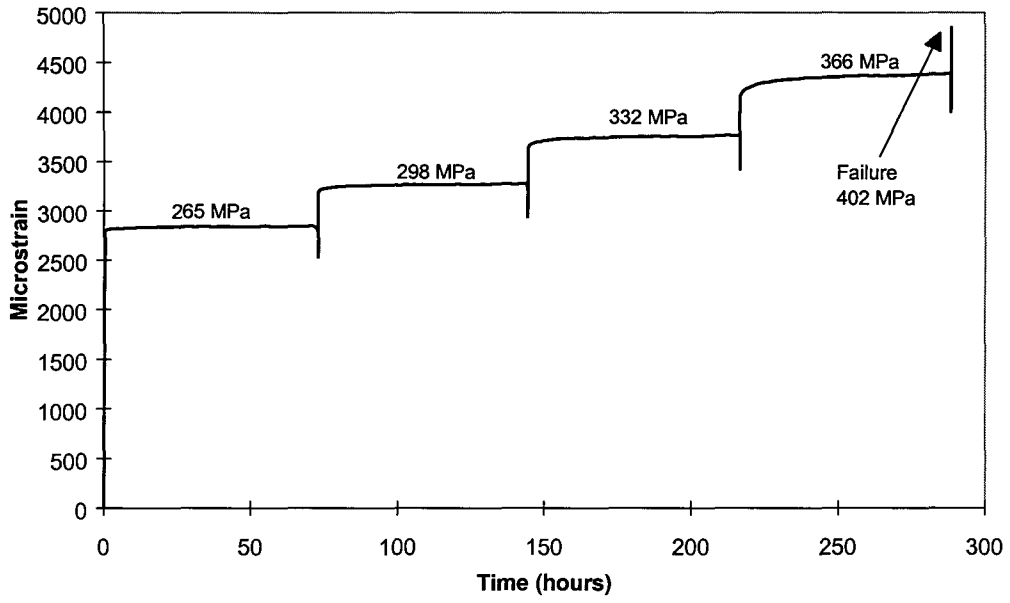

Figure 2.4.2.2 Complete strain-time record for the lava sample from Western Deep Levels Mine. The constant stress level for each creep stage is indicated on the figure.

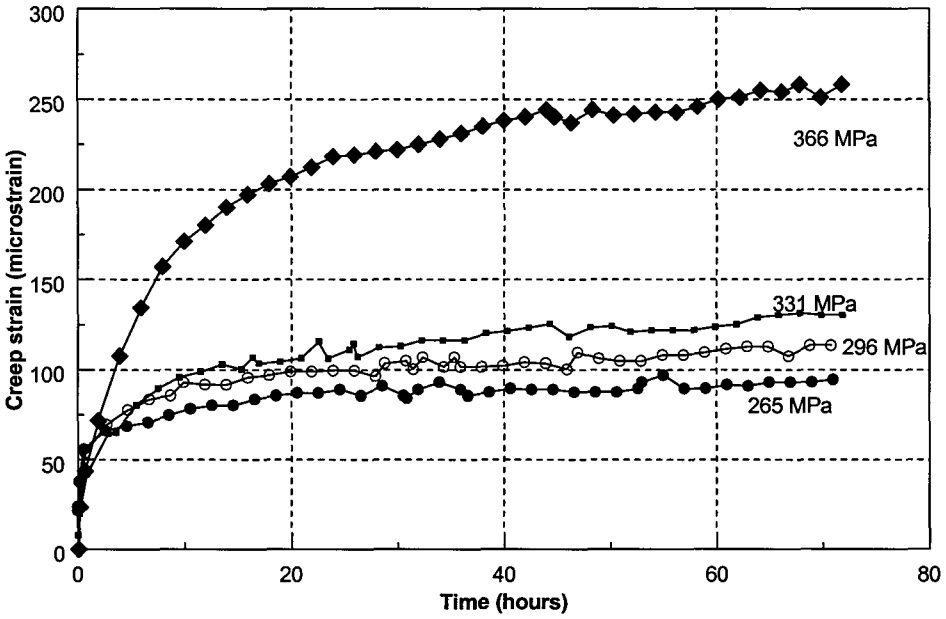

Figure 2.4.2.3 Incremental creep curves for the four stages of the test in Figure 2.4.2.2.

From this study it appears that for the lava and quartzite specimens, the rate of steady-state creep depends strongly on stress level. Figure 2.4.2.4 illustrates the steady-state creep rates for the different rock types at various stress levels. For all specimens, higher stresses lead to higher creep rates.

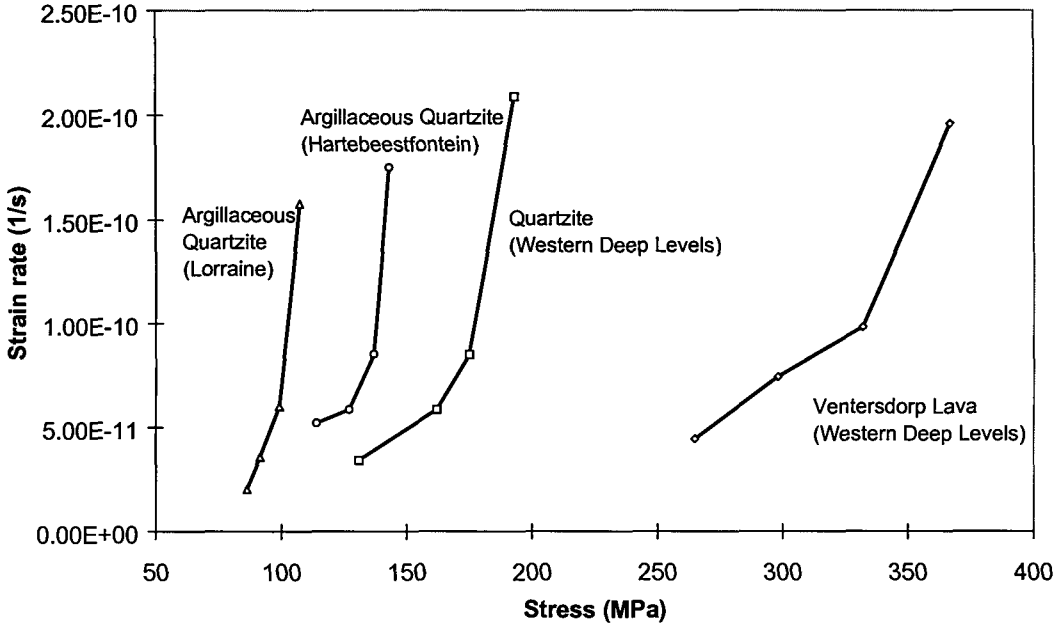

Figure 2.4.2.4 Effect of stress on the steady-state creep rate of different hard rocks in the South African gold mining industry.

When normalising the data from Figure 2.4.2.4 with respect to the uniaxial compressive strength (UCS) of the particular sample, it appears that the actual strain rate is determined by the ratio of the applied stress σ to UCS and independent of material type or absolute stress values. This is shown in Figure 2.4.2.5. For the rock surrounding a stope at a particular depth, quartzites with the lower uniaxial compressive strengths will have a higher σ/UCS ratio than lava. From Figure 2.4.2.5 the creep rate of the quartzite will therefore be higher. High creep rates will lead to creep failure in a shorter period. It is therefore postulated that mining in quartzite host rock as opposed to lava at a particular depth may lead to a more stable fracture zone extending further away from the stope. At the boundary between fractured and unfractured rock, the intact rock will undergo secondary creep leading to the time-dependent formation of new fractures. This creep process zone may extend further into the rock for quartzite. As stable fracturing dissipates stored energy, this behaviour may be advantageous in reducing violent rockbursts. Mining of the Ventersdorp Contact Reef (lava hangingwall, quartzite footwall) in areas where the lava is particularly hard can be difficult owing to the rolling nature of the reef. In areas where the reef rolls into the footwall, the mining is sometimes slow to follow, resulting in mining taking place entirely in the lava. The stable formation of the fracture zone might be disrupted leading to face bursting. This phenomenon has been observed at mines in the Carletonville area. Other factors such as the increased stoping width may however also play a role and should be investigated further.

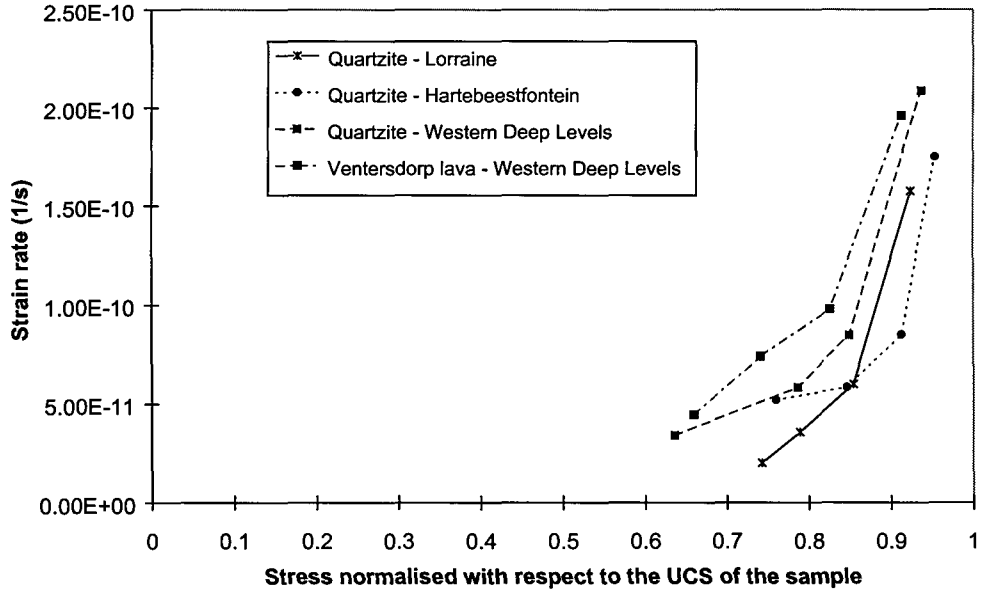

Figure 2.4.2.5 The steady-state creep rate of hard rock as a function of the σ/UCS ratio.

The dependency of the steady-state creep rate on stress can be described with a stress power law. This is shown in Malan (1998). It is also worthwhile to note that the primary and secondary creep phase of these rock samples can be simulated with a Burgers viscoelastic model. The viscosity parameters in this model are however not fundamental material constants but functions of stress. This is also described in Malan (1998).

2.4.2.3 Shear creep of discontinuities under laboratory conditions

The shear equipment and methodology developed in this study to test the creep behaviour of discontinuities in hard rock is described in Malan (1998). After the appropriate normal stress

was applied to the sample, the shear stress was increased in a stepwise fashion with a period of 24 or 48 hours between load increases. This was continued until the shear strength of the discontinuity was exceeded. Three different discontinuity types were tested namely a) discontinuities with gouge infilling, b) extensile fractures in lava from Western Deep Levels Mine and c) quartzite bedding planes from Hartebeestfontein Mine.

a) Discontinuities with gouge infilling

Tests were conducted on discontinuities containing gouge infilling as these were expected to have a high creep rate and to play a prominent role underground. Artificial gouge, used for the initial tests, was obtained by crushing quartzite from Western Deep Levels Mine. Gouge was also collected from the bedding planes in the argillaceous quartzite rock at Hartebeestfontein Mine and similar results to those for the artificial material were obtained. The quartzite from Western Deep Levels Mine was used to prepare two blocks containing a sawcut discontinuity for mounting in the shear box. This discontinuity was filled with the gouge material for testing.

The shear creep behaviour of the discontinuity with gouge infilling is illustrated in Figure 2.4.2.6. The last creep phase (for a shear stress of 0,517 MPa) is not plotted on this graph as the small displacement transducers (see Malan, 1998) were out of range. The sample eventually failed at a shear stress of 0,533 MPa giving a friction angle of 28°. Of interest is that a cumulative shear creep displacement of 1,8 mm was recorded for this sample before failure. Tests indicated that the rate of steady-state creep increased linearly as a function of the gouge thickness. The normal displacement for this test is given in Figure 2.4.2.7. A convention of dilation being positive and compaction being negative is assumed. The negative displacement in Figure 2.4.2.7 therefore indicates a reduction in the width of the gouge layer. The initial reduction is significant compared to the subsequent steps and reflects the compaction due to the application of the normal load. It appears that a further increase in the shear stress leads to further compaction even though the normal stress remains constant.

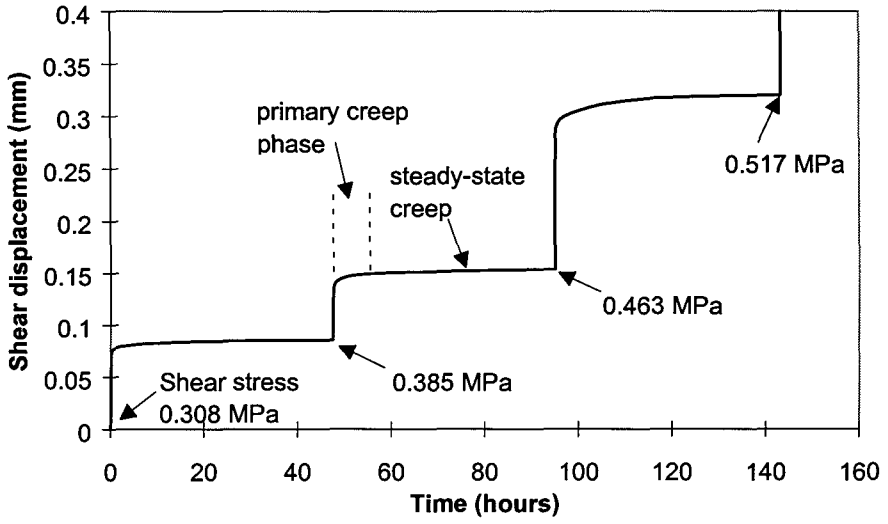

Figure 2.4.2.6 Typical shear creep behaviour of the sawcut discontinuity with gouge infilling and a stepwise increase in shear stress. The normal stress remained constant at 1 MPa. The gouge thickness was 2 mm and the ambient humidity was controlled at 50 per cent.

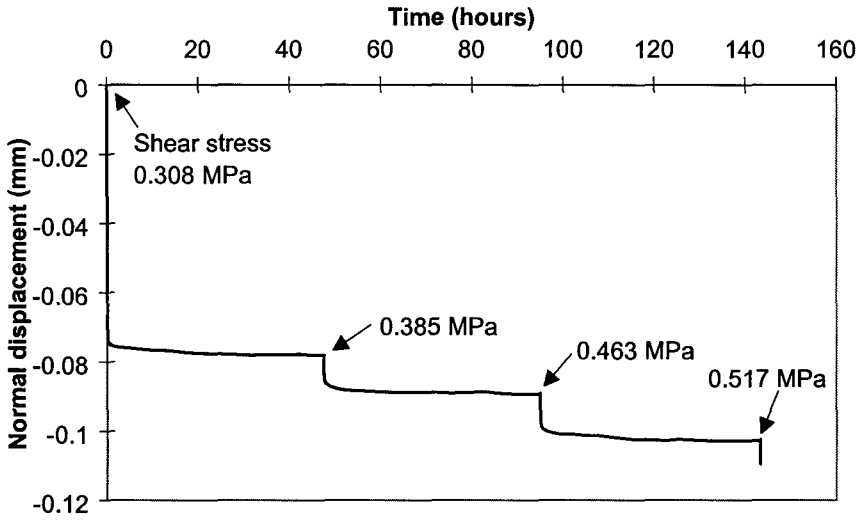

Figure 2.4.2.7 Normal displacement accompanying the shear displacement in Figure 2.4.2.6.

Figure 2.4.2.8 illustrates the incremental shear displacement of a further test for the different shear load increments and a normal stress of 0,5 MPa. Note that the magnitude of the instantaneous response is very prominent and increases with the shear stress to shear strength (τ/τ_S) ratio. The steady-state creep rate also increases with the shear stress magnitude. This is illustrated in Figure 2.4.2.9.

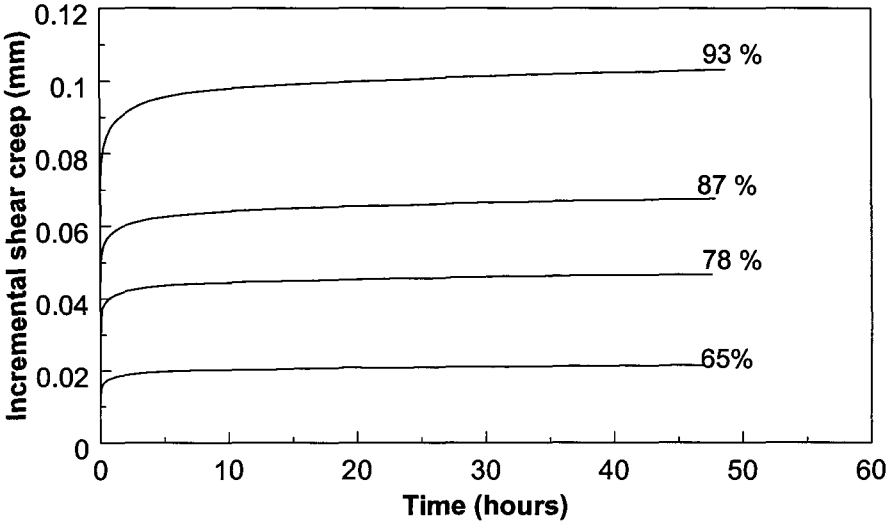

Figure 2.4.2.8 The effect of shear stress magnitude on the creep behaviour for a gouge-filled discontinuity. The percentages indicate the magnitude of the shear stress relative to the shear strength (0,276 MPa). The normal stress was 0,5 MPa and the gouge thickness 2 mm.

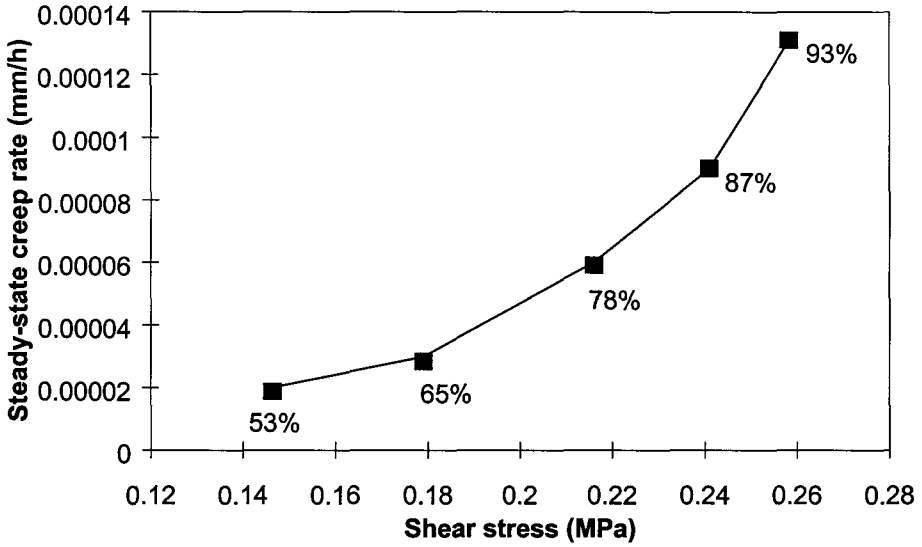

Figure 2.4.2.9 The effect of shear stress magnitude on the steady-state creep rate for a gouge-filled discontinuity. The percentages indicate the magnitude of the shear stress relative to the shear strength (0,276 MPa). The normal stress was 0,5 MPa and the gouge thickness 2 mm.

The dependence of the steady-state shear creep rate on the applied (τ/τ_S) ratio can be described by a power law as described in Malan (1998). For tests with normal loads of 1 MPa and 1,5 MPa, behaviour similar to that illustrated in Figures 2.4.2.8 and 2.4.2.9 was observed (Malan, 1998). It was, however, noted that the magnitudes of primary phase and steady-state creep rate are not only a function of the (τ/τ_S) ratio, but also of the absolute value of shear and normal stress. For a 1,5 MPa normal load, the steady-state creep rate at a (τ/τ_S) ratio of 0,93 was more than three times larger than that of the 0,5 MPa normal load test.

b) Creep of extensile fractures in lava

The results for discontinuities with infilling were compared with the creep of mining induced extensile fractures in lava (collected at Western Deep Levels Mine). The two opposing surfaces of the fracture were closely matched and were not subjected to any previous shear. The normal load was 1 MPa. Figure 2.4.2.10 illustrates the shear creep behaviour of a typical sample. The sample eventually failed at a shear stress of 1,66 MPa giving a peak friction angle of 59°. Although some creep behaviour is visible in the last increments before failure, it should be noted that the magnitude of this creep is negligible compared to some of the discontinuities with gouge infilling. From Figure 2.4.2.10 the total creep displacement before failure was 10 μm while for a typical gouge-filled discontinuity, the total creep movement can amount to more than 1 mm.

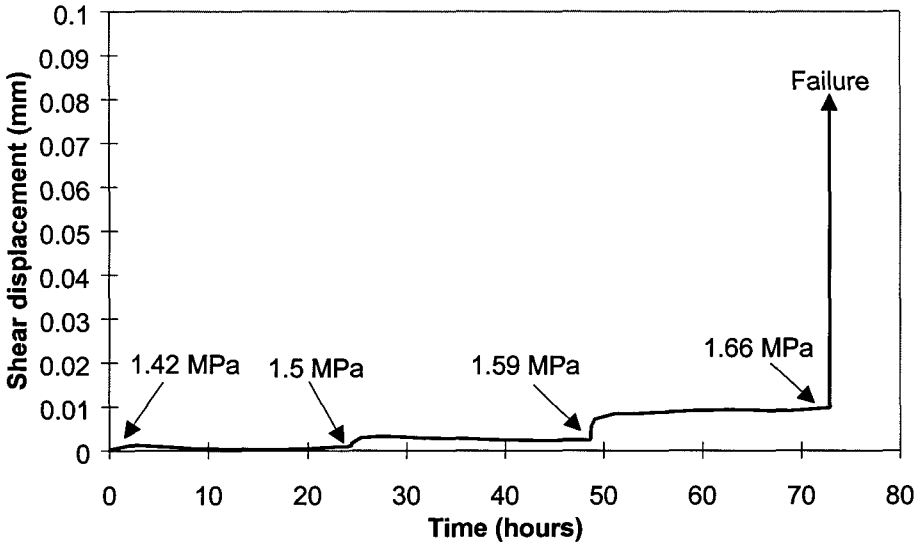

Figure 2.4.2.10 Shear creep behaviour of a mining-induced extensile fracture in lava for a stepwise increase in shear stress. The normal stress was 1 MPa. The sample was tested at the ambient humidity of 50 per cent.

c) Creep of bedding planes in quartzite

The bedding plane samples were obtained from No. 6 Shaft, Hartebeestfontein Mine with diamond core drilling parallel to the bedding planes in the MB2 quartzites. The core containing the discontinuities was cut to suitable lengths and cast in resin to allow mounting in the shear box. The surface of this particular bedding plane was coated with a micaceous layer and it did not show any signs of significant previous shear deformation. Similar to the tests with the thick gouge infilling, a constant normal load of 1 MPa was applied to these bedding plane specimens. The shear load was periodically increased, but also maintained at a constant value between these increases. Figure 2.4.2.11 illustrates typical creep behaviour. The creep for the last loading stage (0,38 MPa) is given in Figure 2.4.2.12. Note the very high creep rates. In comparison, the creep rates for lava specimens were so low that the total accumulated creep for these specimens never exceeded 0,06 mm, even when tested wet. It also became evident that for natural discontinuities such as bedding planes, the creep behaviour is very dependent on the previous sliding history. As the interlocking asperities are worn down, the creep rate increases. For these discontinuities, the creep behaviour is not as deterministic as for the specimens with thick uniform gouge layers, and random jumps may occur in the displacement.

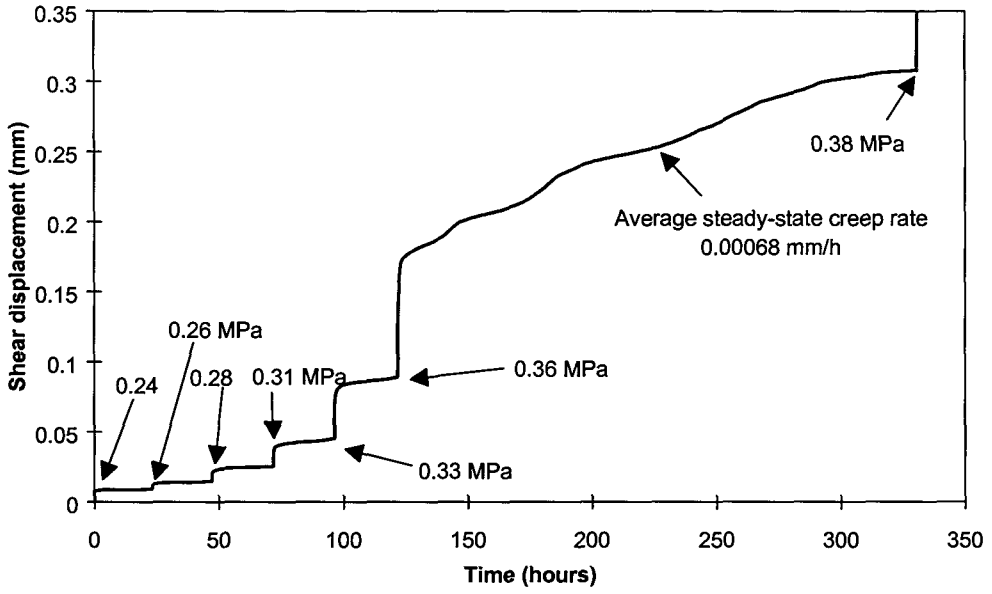

Figure 2.4.2.11 Shear creep of a bedding plane sample tested at 100 per cent humidity. The normal load was 1 MPa.

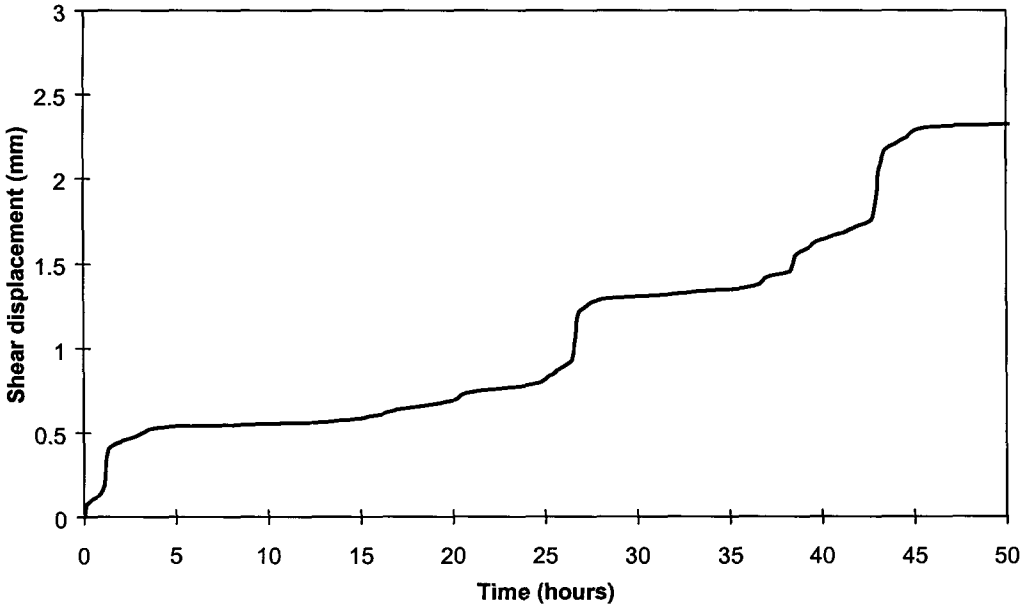

Figure 2.4.2.12 Shear creep of the last stage for the specimen in Figure 2.4.2.11 (a shear stress of 0,38 MPa). The specimen failed at 0,41 MPa giving a friction angle of 22°.

2.4.2.4 Summary

This study investigated the laboratory creep of intact rock and shear creep of discontinuities. It was found that the intact hard rocks of the South African gold mines undergo measurable room temperature creep under uniaxial loading conditions with primary, secondary and tertiary creep phases visible. When loading samples uniaxially to above 90 per cent of their failure strength, steady-state creep rates of typically $7{,}5\times10^{-11}$ s^{-1} to 2×10^{-10} s^{-1} are observed. These values were measured for different quartzites and lava specimens. It should, however, be noted that the

uniaxial compressive strength of the lava is significantly higher than that of the quartzites, requiring a much higher applied stress to obtain a load above 90 per cent of the failure strength. For a stope at a particular depth, quartzite host rock will therefore be more prone to creep with a non-violent dissipation of energy than the more competent lava, when subjected to the same stress levels. The strain rate in the steady-state creep phase is strongly dependent on stress magnitude for both quartzite and lava and increases with increasing stress. This can be successfully modelled with a stress power law.

For the shear creep of discontinuities, it was found that discontinuities in hard rock with gouge infilling can undergo significant shear creep. This creep behaviour is characterised by a prominent instantaneous response after shear load increments followed by a primary and steady-state creep phase. The steady-state creep rate increases as the shear stress to shear strength ratio is increased and can be modelled with a power law. This creep rate is also affected by the gouge thickness and the absolute values of shear and normal stress. The creep of bedding planes in quartzite is also significant and can be as high as 2,5 mm in two days if loaded above 90 per cent of its failure strength. The creep rate is dependent on the previous sliding history. For these specimens the creep behaviour is also not as deterministic as for the specimens with thick uniform gouge layers. Random creep-induced jumps may occur in the displacement.

In comparison to gouge-filled discontinuities and the bedding planes, the creep behaviour of extensile fractures in lava is negligible. This may be a contributing factor to the time-dependent closure rate of the VCR (hard lava) being so low compared to some areas of the Vaal Reef (see Section 4.4.3).

2.4.3 The sliding flaw - tension crack concept

2.4.3.1 Concept

A new concept has been proposed to model material which has a range of strengths on the microscale. In particular, the concept is being evaluated for modelling the interaction of inter- and intra-granular fracture in quartzites. Observations from extension tests on quartzites carried out by Briggs & Vieler (1984) and compression tests by Stravropoulou (1982), suggest that the relative proportions of inter- and intra-granular fracturing and the ultimate failure mode depends on the percentage of quartz in the material. Thus, siliceous quartzites which contain more than 90 per cent quartz, with welded grain boundaries, are stronger and more brittle than rocks which consist of quartz grains surrounded by weaker argillaceous matrix material. Argillaceous rocks (with lower quartz contents) exhibit relatively more inter-granular fracturing due to the higher percentage of weak matrix material. Fracture paths occur preferentially on weaker grain boundaries and the extent of this type of fracturing will depend on the proportion of matrix material to grain material.

The tessellation procedure was therefore modified in an attempt to simulate a rock material consisting of quartz grains with some welded grain boundaries and other intergrain spaces filled with weaker, plastic, material. The objective was to determine whether the fracture pattern and stress-strain response would depend on the flaw density, and whether the response of different rock types could be predicted by altering the tessellation of the material parameters.

A percentage of the boundaries of the Voronoi tessellation polygons are specified to be displacement discontinuity elements that can slide or open, in parallel, whenever the failure criterion is exceeded. These elements are given a lower cohesion and tensile strength to simulate the weak matrix material. The constitutive relation is specified to retain some residual cohesion after activation to simulate plastic flow on an interface. The corners of the Voronoi polygons are joined to the centroid of the polygon and the elements in these positions are only allowed to activate in tension and then to experience softening after activation.

2.4.3.2 Modelling of laboratory test samples

Models of a variety of laboratory tests were developed in order to test the ability of the method to represent fracture under any stress path. The numerical samples have a rectangular shape, are 20mm long and 10mn wide, and are tessellated with about 1000 Voronoi polygons. The tests are analysed in plane strain conditions. A portion of the Voronoi grain boundaries are considered to be weaker material, see for example Figure 2.4.3.1a.

A Mohr-Coulomb strength criterion, with tensile cut-off, is specified on each potential fracture site. The properties are given in Table 2.4.3.1. The residual cohesion on the flaws and intergranular sites is set equal to the initial cohesion to simulate ductile flow. The intragranular sites have a high initial cohesion, which is reduced to zero on activation to simulate brittle fracture.

In the compression simulations, the sample is loaded by displacement increments applied to one end of the sample. In confined tests, the required confinement was applied as a stress boundary condition to the longer sides of the sample. In the extension tests, the sample was initially loaded to a hydrostatic state by applying 600 MPa stress in the axial and lateral directions. The axial stress was subsequently reduced in increments to simulate extension loading.

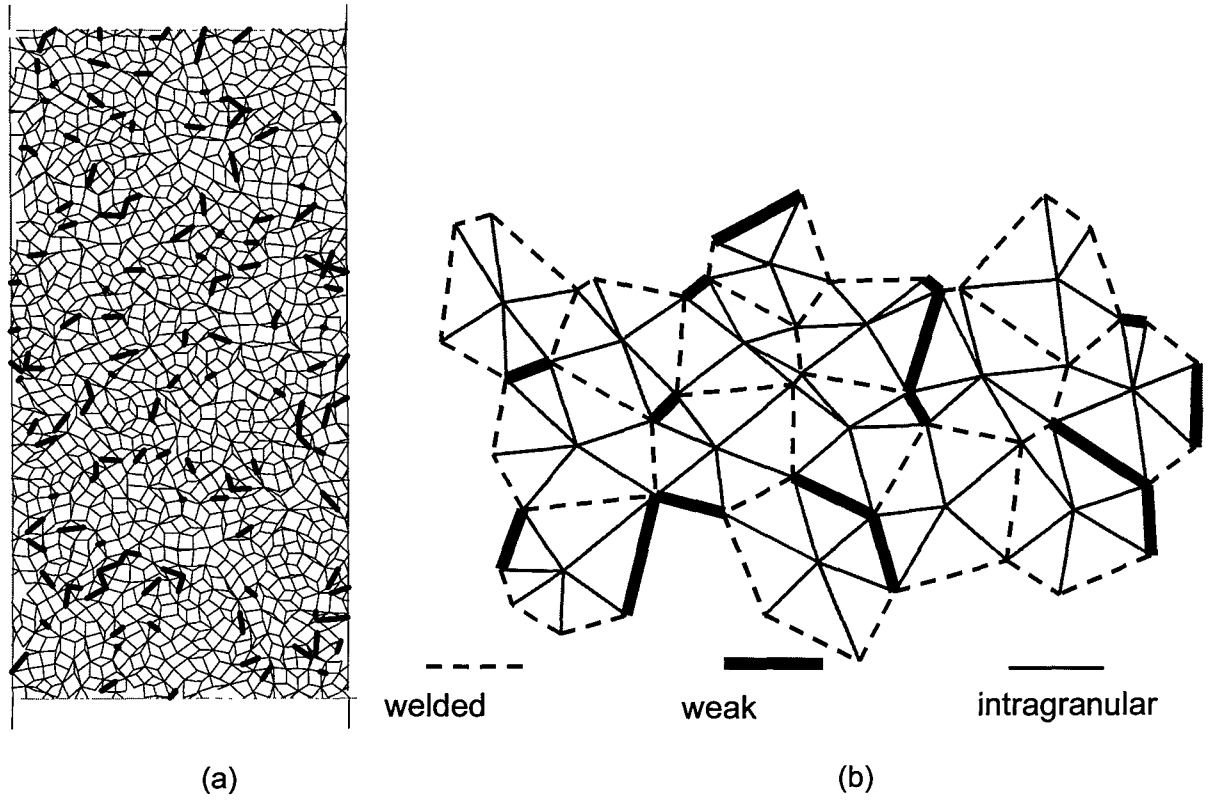

Figure 2.4.3.1 a: A typical tessellation used in the explicit fracture modelling (flaws are shown as dark lines) b: detail of Voronoi tessellation with welded boundaries, weaker intergranular flaws and intragranular fractures.

Table 2.4.3.1 Constitutive properties specified for the different types of site.

Site Type	Cohesion C_o (MPa)	Residual Cohesion C_m (MPa)	Friction angle ϕ	Residual friction ϕ_m	Dilation ψ_m	Tension cut-off (MPa)
intragrain	100	0	45°	30°	0	10
intergrain	40	40	45°	30°	10°	10
flaw	5	1	45°	30°	10°	1

2.4.3.3 Fracture patterns in compression

Typical fracture patterns for the biaxial compression tests are shown in Figures 2.4.3.2a to d. Each active flaw acts in a similar fashion to the sliding crack model (e.g. Horii & Nemat Nasser, 1986). Sliding on active flaws induces tensile stresses on some of the intragranular fractures. Activation of the most highly overstressed intragranular fracture leads to a further redistribution of stress and a sequence of fracturing is initiated. The ultimate fracture pattern depends on the density and the distribution of flaws and on the confining pressure. In unconfined compression, as shown in Figures 2.4.3.2a and 2.4.3.2b, the activated intragrain sites are generally aligned with the direction of maximum compression, suggesting an axial splitting mode of failure. Application of confinement to the sample leads to a diagonal zone of en echelon fractures, generally aligned with the maximum compression, as shown in Figure 2.4.3.2c. Multiple shear bands form in the samples confined to 50 MPa. The fracture patterns compare well with patterns observed in plane strain tests on quartzite (Yumlu & Ozbay, 1995).

Studies were undertaken to find a parameter to characterise the deformation within the sample and to determine whether a particular crack pattern had in fact induced localization in a sample. A modification of the multipole influence calculation technique is considered by calculating the equivalent plastic strains on a grid over the sample. The localized nature of deformation in a sample can be quantified by consideration of the corresponding contours of the second invariant of the deviatoric inelastic strain I_{2D}. This measure is able to highlight the predominant failure mode. A study of Figure 2.4.3.3a shows that the sample with 20 per cent flaws exhibits shear banding. In contrast, even though the fracture pattern of the sample with 4 per cent flaws (Figure 2.4.3.2b) suggests the formation of a shear zone, the I_{2D} contours show that the failure mode is axial splitting. The change in the I_{2D} contours for sample with 4 per cent flaws from Figure 2.4.3.3b to Figure 2.4.3.3c when the sample was confined at 10 MPa indicates that the addition of confinement leads to a transition from axial splitting to shear banding, as expected from laboratory tests.

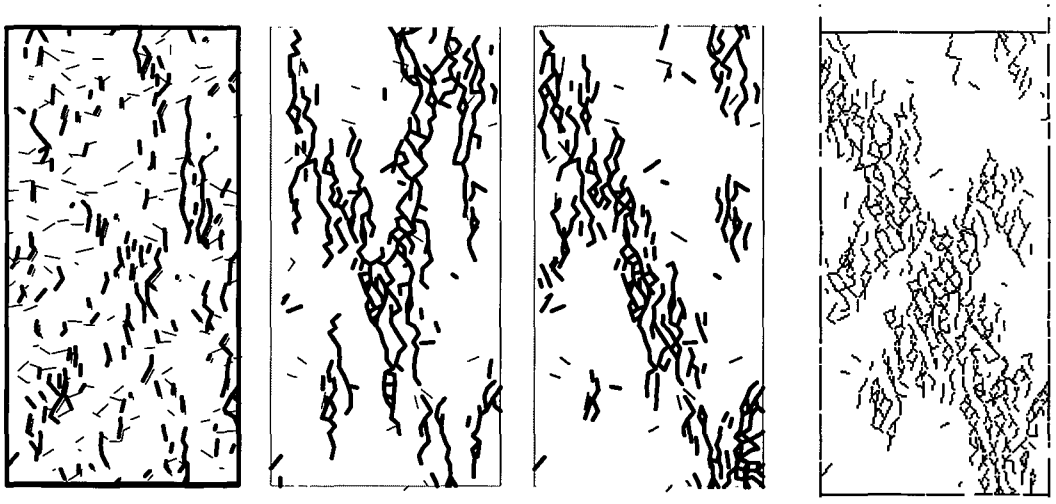

a: b: c: d:

Figure 2.4.3.2 Typical fracture patterns in compression a: tessellation with flaws, b: unconfined with 20 per cent flaws, c: unconfined with 4 per cent flaws, d: confined (10MPa) with 4 per cent flaws, e: confined (50MPa) with 4 per cent flaws.

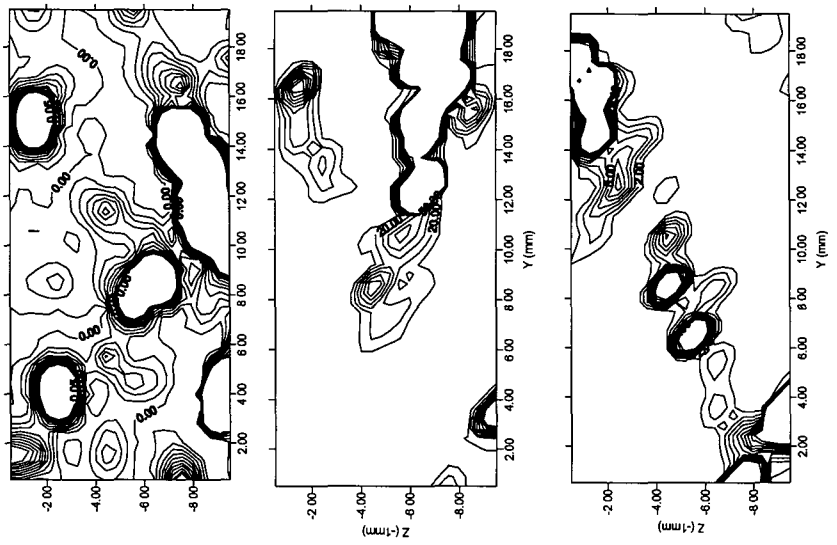

a: b: c:

Figure 2.4.3.3 Typical contours of I2d of inelastic strain in compression a: unconfined with 20 per cent flaws, b: unconfined with 4 per cent flaws, c: confined (10MPa) with 4 per cent flaws.

2.4.3.4 Effect of fracture activation rule

It was of interest to investigate whether the localization of deformation had been caused by the weakest link activation rule which allows potential sites to sustain stress above the strength envelope. The fracture patterns resulting from the parallel activation mode exhibit shear band formation instead of the axial splitting mode found in the sequential activation. Under incremental activation, the first cracks to grow alter the stress field and tend to activate nearby fractures. Other sites, further from the active region, experience stress states above the failure envelope. If time-dependent properties were provided, the material would continue to fail with time. Under parallel activation, no sites are allowed to be overstressed and therefore all failure is forced to occur simultaneously. This suggests that the incremental and parallel activation schemes may be seen as the extremes of rate dependent and rate independent loading respectively.

2.4.3.5 Influence of tessellation geometry

An important question with the tessellation approach is whether the fracture pattern depends on the tessellation mesh. Two examples of unconfined compression test simulations with different tessellations are shown in Figure 2.4.3.4, and can be compared with the pattern in Figure 2.4.3.2b. Changing the mesh tends to change the specific fracture pattern, but does not alter the tendency for axial splitting in unconfined tests and shear band formation with increasing confinement. The effect of a tessellation density has not been investigated systematically. Particular analyses indicate that fractures tend to be more strongly localized as the tessellation density is increased.

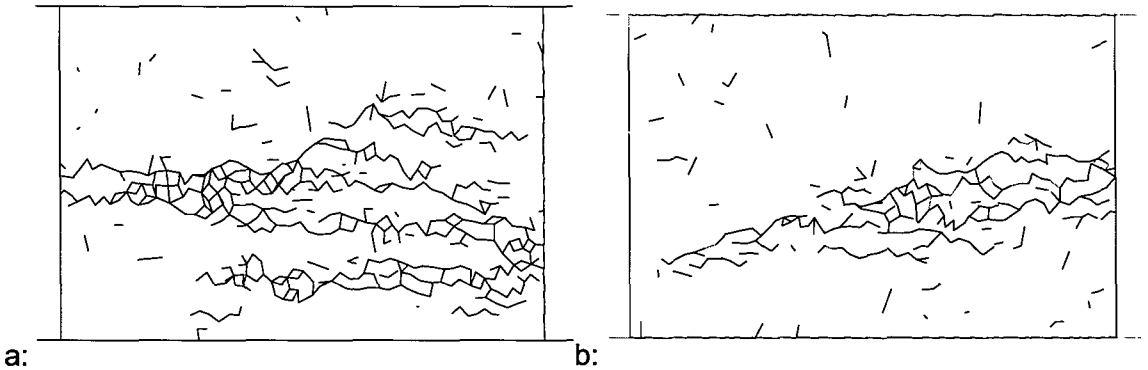

Figure 2.4.3.4 Effect of tessellation and flaw position on fracture pattern a: unconfined compression of old tessellation with new set of 4 per cent flaws, b: unconfined compression of new tessellation with 4 per cent flaws.

It seems that triangular tessellations such as the Delaunay or the Voronoi with intragranular sites, are required to permit axial splitting failure since they provide a sufficient number of potential fracture paths. The Voronoi polygons constrain the fracture paths to the boundaries of the rounded elements and exhibit more diffuse failure as would be expected in a loosely bonded material such as sandstone and not in quartzite with its partially welded grain structure.

Varying the tensile strength of the intragranular flaws suggested that significant differences in tensile strength are required to alter the activation sequence in the sample.

2.4.3.6 Fracture patterns in other stress paths

To investigate the effect of the tessellation when the stress path is changed, triaxial extension simulations were performed on the samples. These correspond nominally to the experiments described in Section 2.4.1.1. An equal pressure of 600 MPa was first applied to each side of the sample and then the axial stress was reduced in stages. The failure patterns (e.g. Figure 2.4.3.5a) are similar for all samples in which intragranular fracturing is permitted and compared well with the schematic diagram of fractures in a test on a 70 per cent quartzite specimen (Briggs & Vieler, 1984) shown in Figure 2.4.3.5b. The position of the final localized zone is confirmed by the contours of I2d given in Figure 2.4.3.5c, and varies across the sample depending on the distribution of flaws, and the confinement as was observed in the experiments. The sample in which no intragrain fractures are permitted exhibited intense fracturing in the direction of maximum compression, see Figure 2.4.3.5d. This failure mode is somewhat different to the conjugate shear bands, consisting of multiple slip planes formed at an angle to the major principal stress, observed (Briggs & Vieler, 1984) in the highly argillaceous rocks, with each grain surrounded by matrix material, that this particular tessellation is designed to represent. The tessellation provides a good representation of the relatively siliceous quartzites and the hard lavas in which failure is dominated by the linking of intragranular fractures, but is less successful for very argillaeous quartzites and soft lavas (e.g. Figure 2.4.1.2) where failure occurs due to plastic flow on a number of slip planes.

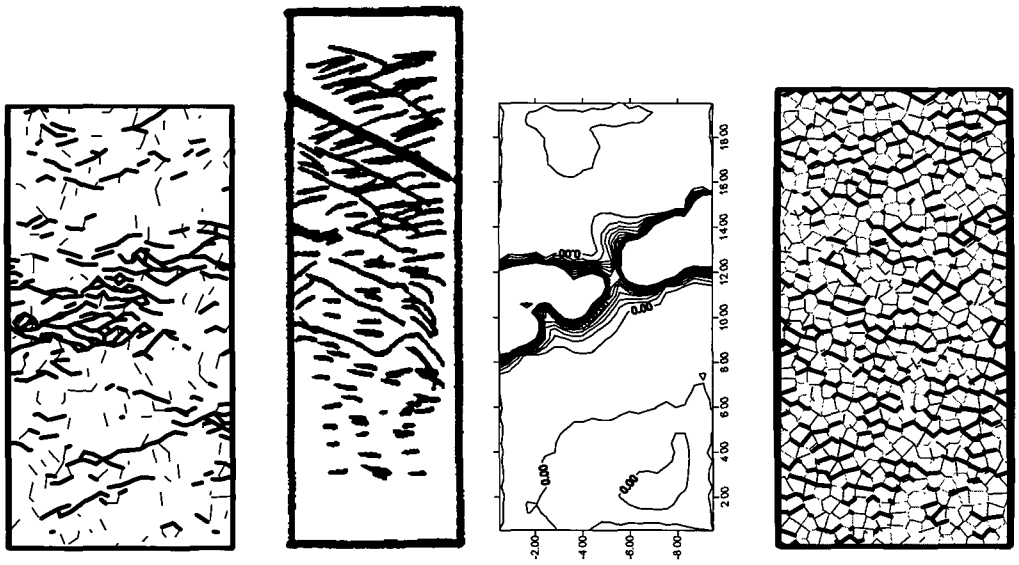

Figure 2.4.3.5 Typical extension test results a: fracture pattern with 20 per cent flaws, b: observed pattern (Briggs and Vieler, 1984) c: contours of inelastic strain d: no intragranular fracturing permitted.

In the extension tests, the failure is associated with a single failure surface, at the point where the fractures localize. In order to determine whether this is due to the length of the sample, a test was performed on a 5:1 length to diameter ratio sample. The fracture pattern, shown in Figure 2.4.3.6a, also shows a single failure zone. Thus, the repeating pattern of fractures underground must be formed by a mechanism that cannot be replicated in the simple extension test situation.

The question arises as to whether the extension test is representative of the fracture processes underground and so the test was modified to simulate a coring operation in a borehole. The boundary conditions of the sample in Figure 2.4.3.6a were changed to simulate the loading due to core drilling. The most realistic simulation considers the rock to be solid prior to the

overcoring and so a Coulomb friction law was specified on the boundaries. In this case (see Figure 2.4.3.6b), fractures only grow in the unloaded region. A core disc forms as observed underground in highly stressed rock. Further steps were impossible due to numerical instabilities. The fractures are much more localized than in the extension test and the fracture resembles the core disking phenomenon.

There are two ways of comparing the fracture patterns with those observed underground. Firstly, the extension type fractures of the face can be identified with the microcracks in the numerical or laboratory sample. Then, the small scale sample will represent a few metres of rock ahead of the face. The localized failure zones will represent the periodic shear failure zones observed underground (Adams et al., 1984) and can give some insight into the way that the mining induced fractures will interact and localize in a rockburst event, for a particular rock type. Secondly, the failure in the small scale sample can be considered to be representative of the process of formation of a single mining induced fracture in the rock surrounding the excavation. In this case, the sample represents a smaller region of rock and the failure angle may relate to the dip of the fracturing underground. The stress loading on the axis of the sample also does not represent the stiffness of the underground rock mass, which is able to alter the applied stresses in response to the dilation of the fractured rock, and cannot then provide information regarding the spacing of the mining induced fracturing.

These analyses suggest that the concept of tessellation with flaws and intragranular fracture paths can be applied to model underground situations where the fracture paths are controlled by stress gradients, as well as predicting the wide localized zone characteristic of the uniform stress state in an extension test. Calibration of the tessellation models is envisaged in order to investigate the development of the fracture zone around stopes in different geotechnical environments.

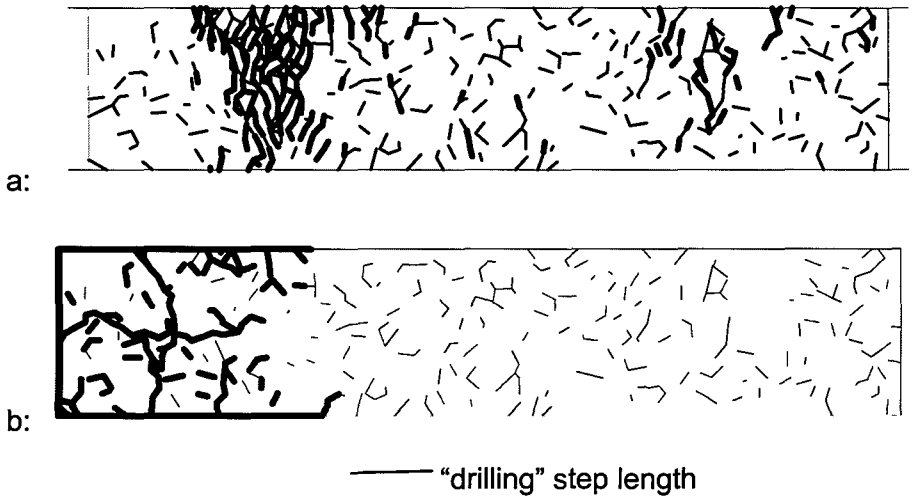

Figure 2.4.3.6 Fracture patterns in 5:1 sample. a: Extension test confined to 600 MPa b: overcoring in borehole (60 MPa in-situ stress in plane of axis and 30 MPa perpendicular) with edges that can sustain shear stress until overcored.

2.4.3.7 Comparison with damage models

In an effort to compare the numerical experiments with physical experiments, a number of macroscopic measures such as the stress, the strain and the crack density can be calculated during post processing of the DIGS results. The average strain and the average stress within the closed boundary of a test specimen, of area A, can be determined from formule presented in Appendix 2.1. A quantitative measure of the state of fracturing is obtained from the second order crack density tensor (Kachanov,1993). The inelastic strain components have been calculated on a 20x10 regular grid covering the region of interest. The second invariant of the deviatoric part of the inelastic strain provides a measure of the shear deformation in a grid cell and can indicate the positions of localized zones of deformation in the sample.

The macroscopic stress - strain curves for the three uniaxial compression tests are shown in Figure 2.4.3.7a. At each displacement increment, prior to localization, activation of fracturing results in non-linear hardening of the stress - strain response. The degree of nonlinearity depends on the density of flaws. The samples with intragranular fracturing exhibit softening once localization is initiated which continues until the computer memory constraints are exceeded. The sample with intergrain fracturing exhibits the most nonlinearity and numerical instability can occur due to the block rotation effects. A similar dependence of the strength and deformation on the density of flaws is shown in the stress strain response of the extension tests in Figure 2.4.3.7b. A sample without flaws fails due to sliding on the intragranular fractures when the stress state exceeds the Mohr-Coulomb failure criterion.

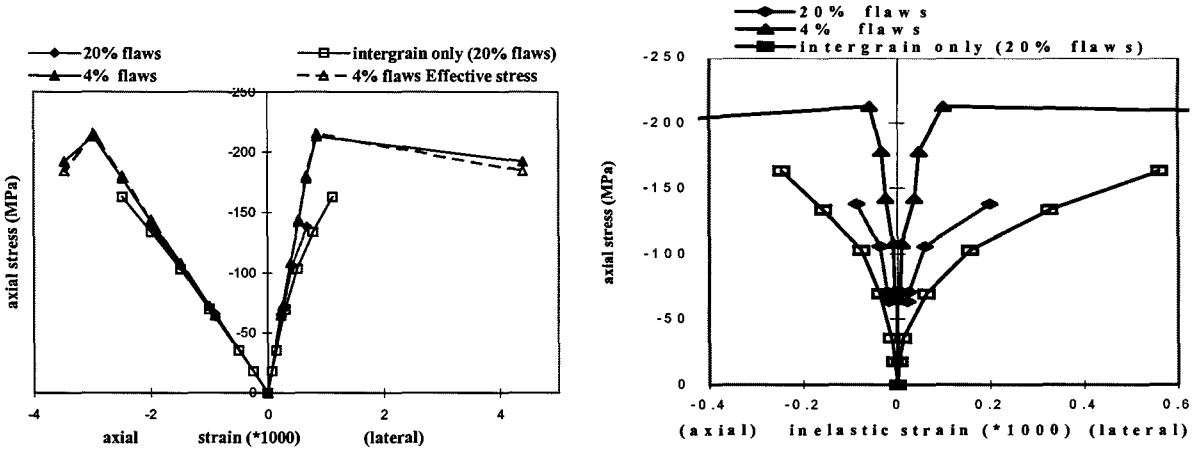

Figure 2.4.3.7 a: Average stress - average strain curves and b: average stress - inelastic strain.

Graphs of the stress - inelastic strain response for three uniaxial compression tests are shown in Figure 2.4.3.7b and demonstrate that most of the deformation occurs in the lateral direction as observed in experiments (Stavropoulou, 1979). The relationship between the crack pattern and the inelastic strain can be determined by comparing the angle of the principal direction of the crack density tensor with those of the inelastic strain tensor. The overall crack angle decreases with increasing axial strain whereas the principal directions of the inelastic strain remain constant. The intragrain fractures are shown to be directed within 1° of the loading axis and yet the direction of the principal inelastic strain is initially 12° and decreases with loading. This occurs because the crack density tensor takes no account of shear deformation (Kachanov, 1993) and should not be used as a basis for modelling the damage in rock under compression (Krajcinovic, 1989).

In these simulations, the effective stress is only higher than the overall stress during the hardening portion of the stress - strain curve, see for example the case with 4 per cent flaws in Figure 2.4.3.7a. After softening has occurred, the effective stress is found to be lower than the overall stress. In addition, the nonlinearity of effective stress - strain curves confirms doubts as to the applicability of the effective stress assumption in conventional continuum damage models (Krajcinovic, 1989) under general states of stress (Baste & Audion, 1991). Any damage model for rocks under compression should therefore combine the damage due to sliding on pre-existing flaws (Gambarrotta et al., 1993) and the opening of extension cracks (Kachanov, 1982, Sellers, 1994). The micromechanical interactions can be included on a macroscale in a continuum damage model by a proper implementation of the damage as being driven by micro plasticity in the effective stress space (Andriuex et al., 1986, Sellers & Scheele, 1997).

2.4.4 A methodology for the simulation of large scale fracture zones in two dimensions

2.4.4.1 Application of the DIGS discrete fracture growth method

The numerical code DIGS is based on the displacement discontinuity formulation of the boundary element method in which a set of fictitious cracks or dislocations in an elastic body, are used to represent the jump in the displacement field across each fracture (Napier 1990). The displacement discontinuity method can be extended to the modelling of fracture growth as a pseudo-static process if each crack tip is advanced incrementally in a direction that maximises a specified growth criterion (Napier 1990). Two basic modes of fracture in brittle rock are distinguished, namely extension, or cleavage, fracturing and shear fracturing (Napier & Hildyard 1992, Napier et al. 1997). The origin of fractures (seed position), fracture growth rule and material properties are defined for each anticipated crack. Growth is accomplished by searching around the available seed points or crack tips at a fixed distance with a given angular increment. For extension fractures the growth angle is chosen to be the direction of the major (compressive) principal stress. Numerical instabilities may be reduced by preventing crack intersections. In certain cases, this does not significantly alter the fracture pattern.

In the standard displacement discontinuity formulation of the boundary element method, the amount of memory (in words) required to store the direct influence kernels is given by

$$M_D = 4N_c^2 N^2 \qquad (2.4.4.1)$$

where Nc is the number of collocation points (for linear elements, Nc=2). The memory requirements increase with the square of number of elements. This can limit the effectiveness of the standard solution method, as insufficient fractures can be solved to permit modelling of the extensive fracture zone which develops at realistic stope lengths. Fractures are activated in the model when the induced stresses on crack segments exceed the Mohr-Coulomb failure criterion. In the incremental activation procedure, the crack site with the stress state furthest outside the failure criterion is activated. The problem is then solved and the activation procedure is repeated until all sites are within the failure envelope.

2.4.4.2 Tessellation models and the multipole method

The problems of pre-selection of fracture initiation sites and the computational effort required for modelling discrete fracture growth are compounded by the possibility of numerical instabilities arising from the linking of cracks at small angles, and the insertion of very small elements at crack intersection points. These shortcomings led to the development of the tessellation approach in which the region of interest is covered by a random tessellation of inactive elements (Napier et al., 1995), as discussed in Section 2.4.3. Fractures are formed, in this method, when induced stresses on crack segments exceed a specified failure criterion. The linking of preferentially aligned segments provides an approximation of a discrete fracture path. The segment lengths and angles of intersection are controlled by the choice of a particular tessellation pattern. Applying a Delaunay or Voronoi triangulation scheme can control the numerical instabilities arising from the intersections of cracks at small angles. The models of fracturing around stopes use tessellations based on the Delaunay triangulation scheme.

Memory limitations will affect the tessellation method if the standard solution technique is applied. A considerable saving in memory can be achieved by the application of the multipole method (Peirce & Napier, 1995). A grid of rectangular cells is defined to cover the irregular element mesh, see Figure 2.4.4.1. The multipole strain moments of all the elements within the cell are calculated about the centre point of the cell. The influences are transmitted between centre points of the cells using the Fast Fourier method (Peirce & Napier, 1995). The accuracy of the method can be improved by surrounding each cell by a pad region of two to four cells wide. The interactions of the elements within the pad region are resolved using the direct kernel influences. The amount of memory (words) for a grid of M multipoles can be estimated (Peirce & Napier, 1995) as

$$\begin{aligned} M_m = & \left[4(n_p+2)+\tfrac{3}{2}(n_p+1)(n_p+2)\right]M^{3/2}+5 \\ & +4(n_p+2)(n_l-n_{cl}+1)^2 \\ & +4IN_c^2 n_l^2 N^2 / M, \end{aligned} \qquad (2.4.4.2)$$

where n_p is the order of multipole (usually n_p=5), n_l is the total width of the pad region and n_{cl} is the width of the receiving multipole cluster, as shown in Figure 2.4.4.1. The number of multipole grids $M=2n_y n_z$, and n_y and n_z are the number of grids in the y and z directions, respectively. Two conflicting processes affect memory usage, as shown in Figure 2.4.4.2. Obviously, the influence transmission is more effective as the number of elements per cell increases. However, this implies that there are more elements in each pad region and more memory is required for direct storage of the element influences.

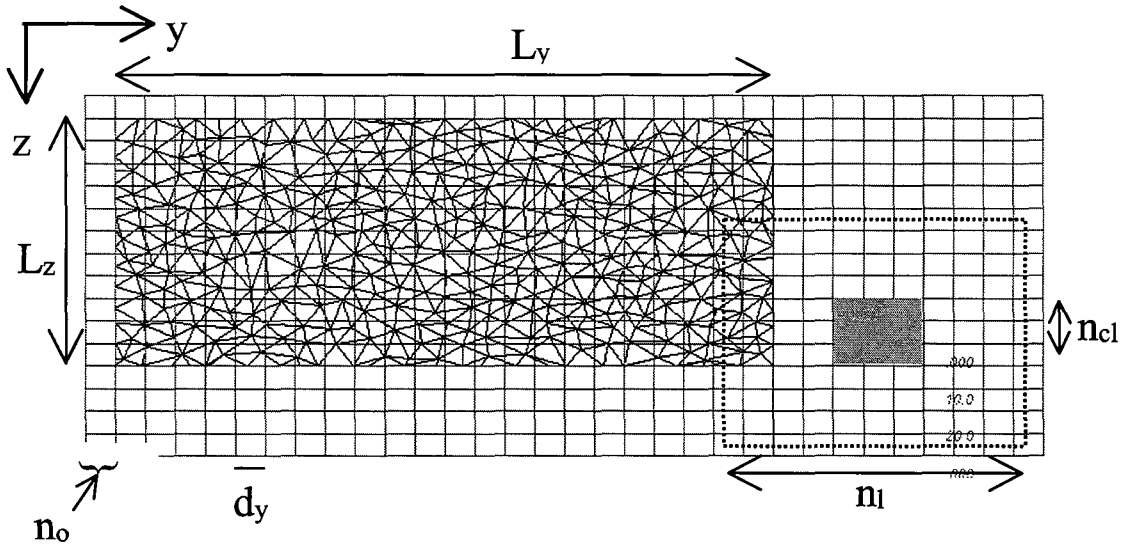

Figure 2.4.4.1 Multipole grid superimposed on a Delaunay tessellation consisting of 1683 elements within a rectangular region.

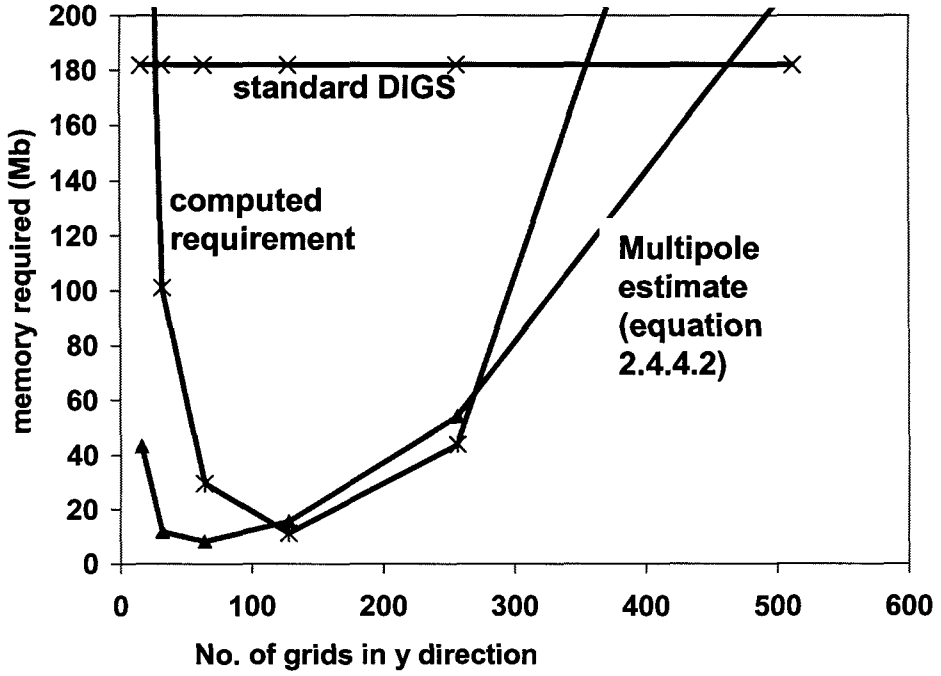

Figure 2.4.4.2 Comparison of estimated and computed multipole memory requirements with memory required for standard formulation, using the tessellation shown in Figure 2.4.4.1.

2.4.4.3 A procedure for the selection of the multipole grid size

The development of the multipole method as part of the SIMRAC project GAP029 highlighted that the choice of the multipole grid size required a certain amount of experimentation, but that an incorrect choice could reduce significantly the effectiveness of memory allocation. The multipole grid must cover all potential elements otherwise the influence of the external elements is transmitted directly to every other element, thus taking up significant amounts of memory. A correct choice can, however, use as little as 10 per cent of the memory for the standard method, see Figure 2.4.4.2.

Such a position was unacceptable for a method that would require regular application. A major output of the work for project GAP332, has been the development of a consistent procedure for construction of tessellations and the selection of the multipole grid size. The method is described below. All figure dimensions relate to Figure 2.4.4.1.

1. Determine tessellation region dimensions L_y, and L_z
2. Select desired average triangle side length L_s
3. Calculate the expected maximum number of random points $N_{max} = L_y * L_z / L_s * L_s$
4. Tessellate the region using the Delaunay algorithm
5. Calculate the mean element length Lm
6. Divide each element, k, until the element length $L_k < L_m$
7. Set multipole grid spacing $d_y = d_z = L_m$
8. Select number of MP grids:

$$n_y = 2^{(\text{int}[\log_2((L_y/d_y)+2n_o)]+1)} \qquad (2.4.4.3)$$

$$n_z = 2^{(\text{int}[\log_2((L_z/d_z)+2n_o)]+1)}$$

9. where int is the next highest integer and n_o is the minimum number of cells surrounding the tessellated region.

10. An estimate of the number of elements, before subdivision, is given by

$$\text{Nest} = [(3Ly/Ls+1)\ Lz/Ls + Ly/Ls\ ]/2 \qquad (2.4.4.4)$$

11. The rectangular borders of the tessellated region are excluded to ensure the randomness of the fracture activation.

The number of elements that can be solved with a given average triangulation size is still limited for a given size of computer memory. If all the elements are immediately included in the solution, the size of the tessellated region and the multipole grid must be carefully selected. The only alternative for saving memory is to reduce the size of the pad region, resulting in lower accuracy of the solution. However, when modelling the progressive excavation of a tabular stope, it is possible to include only crack elements in the solution once they have activated.

2.4.4.4 Setting up models of tabular mining with finite stope widths

The classical application of the boundary element method to mining analyses considers the stope to be a displacement discontinuity of zero width in an infinite elastic medium. Maximum closure on the stope elements is limited to the stoping width (Napier & Stephansson, 1987). However, underground observations suggest that fracturing of the reef ahead of the stope plays an important part in the development of the fracture zone (Adams et al., 1981) and so the inclusion of a stope with a finite width in the model is important. A mining procedure was developed where both the hangingwall and footwall are modelled by displacement discontinuity elements, and are connected by elements representing successive face positions. The elements are initially fixed with no displacement discontinuity. In each mining step, the boundary conditions on the elements defining the excavation are changed to a state of zero shear and

normal stress. The closure of the hangingwall elements is limited to the stope width. Any active or potential elements existing within the new block are removed, to prevent numerical instabilities associated with rigid body motions of separate blocks within the mined out region.

The multipole method considers the moments of the elements about the grid points and has been found to be more efficient and accurate in the presence of stress gradients. Thus, any given problem is solved initially with a length of hangingwall displacement discontinuity elements, to introduce a stress gradient into the uniform, virgin stress state, before the tessellation of potential crack sites is included in the analysis. This procedure has been proved to be stable for at least 30 mining steps, with the problem solved to within a stress tolerance of 1 MPa, but the fracture pattern is not unique and depends on the stress tolerance applied.

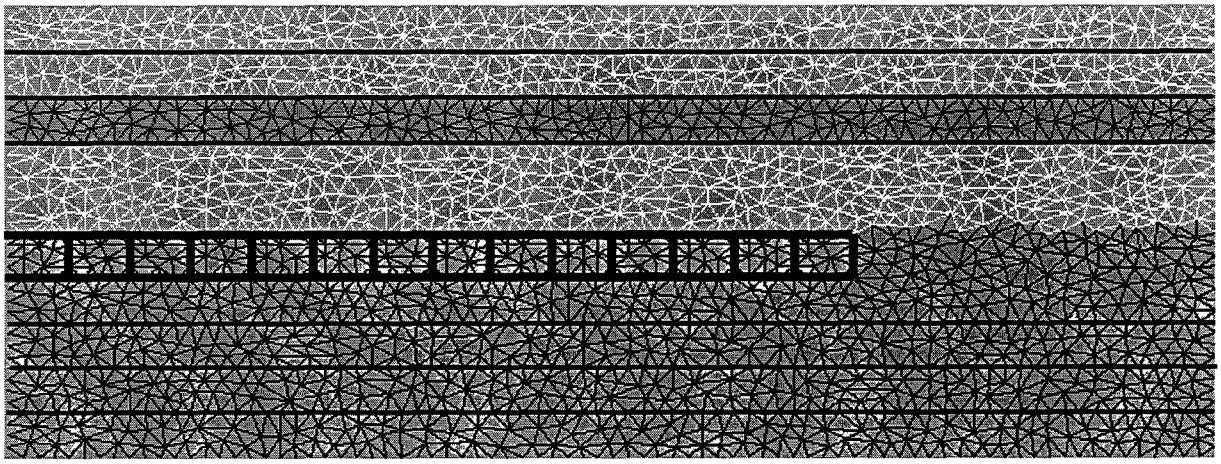

Figure 2.4.4.3 Tessellation of a Carbon Leader stope with a finite width.

The logic of the tessellation and multipole parameter selection has been implemented into a prototype computer program to enable automated mesh development. The program permits the input of finite or zero width stopes, with different mining sequences. Joint sets and bedding planes can be included if they do not intersect one another, or the mining. The program incorporates the random bedding plane models described in Section 4.4.3. Utilities are available to provide statistics of the potential fractures and to alter or remove their constitutive codes in rectangular regions or a series of strips to simulate different geological conditions. The data files can be changed automatically to permit time-dependent response.

2.4.4.5 Selection of the fracture activation rule

The choice of the way in which the fractures are allowed to activate can alter the appearance of the fracture zone. Three schemes have been developed to permit sequential activation of elements (Sellers & Napier, 1997).

(i) The first method involves an incremental activation procedure, in which the crack having a stress state, which is furthest outside the nominal failure envelope, is activated and the problem is solved again. This sequence of crack activation and solution cycles continues until there are no more elements with stress states outside the failure envelope. This method is called the incremental activation rule

(ii) The second method is a parallel activation procedure and all elements, which are outside the failure envelope, are activated simultaneously. The problem is solved and the next mining step is made. This method is called the parallel activation rule

(iii) Thirdly, the parallel activation sequence is extended so that once the first set of fractures has been activated, and the solution determined, the stress is redistributed into the unfractured regions, and may cause failure of another set of fractures. This process continues a number of times before the fracture pattern stabilizes. This method is called the iterated parallel activation rule

The Mohr-Coulomb failure criterion is applied to each element, the shear and normal stress being calculated in the local co-ordinate system of the element. The element activates when the driving shear traction T_y exceeds the shear resistance according to

$$|T_s| = S_o - \tan\phi_o T_n \qquad (2.4.4.5)$$

where S_o is the cohesion, ϕ_o, is the friction angle, T_S is the shear stress and T_n is the normal traction. Alternatively, failure occurs when the normal stress exceeds the tensile strength cut-off, as shown in Figure 2.4.4.4. After activation, the element is assigned the specified mobilized friction angle ϕ_m, dilation angle ψ_m, and cohesion S_m such that

$$|T_s| = S_m - \tan\phi_m T_n \qquad \text{and } D_n = -\tan\psi_m |D_s| \qquad (2.4.4.6)$$

where D_{sn} and D_y are the normal and tangential displacement discontinuities.

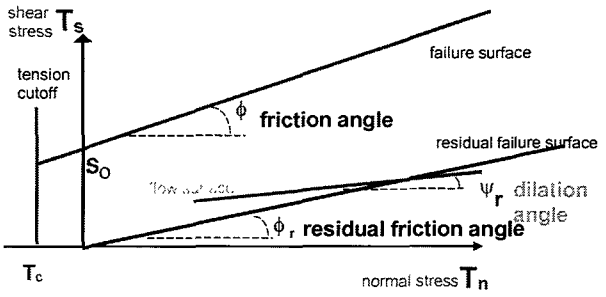

Figure 2.4.4.4 Mohr-Coulomb failure criterion with tension cut-off.

The studies of the effect of the different activation rules were performed using a single tessellation geometry, which is an idealization of the geological environment surrounding a Carbon Leader stope. The different strength rocks are represented by choosing different values of cohesion. A 2 m wide layer of a strong rock, corresponding to the siliceous hangingwall quartzites overlies the reef. A 1 m layer of weak rock overlies the hangingwall layer and is delimited by two parting planes with a low friction angle $\varphi = 5^o$ and $\varphi_m = 2^o$, representing the Greenbar shale. The reef and the rest of the hangingwall have the same properties as the hangingwall beam. The footwall is modelled as an intermediate strength material. All other parting planes have $\varphi = 10^o$ and $\varphi_m = 5^o$.

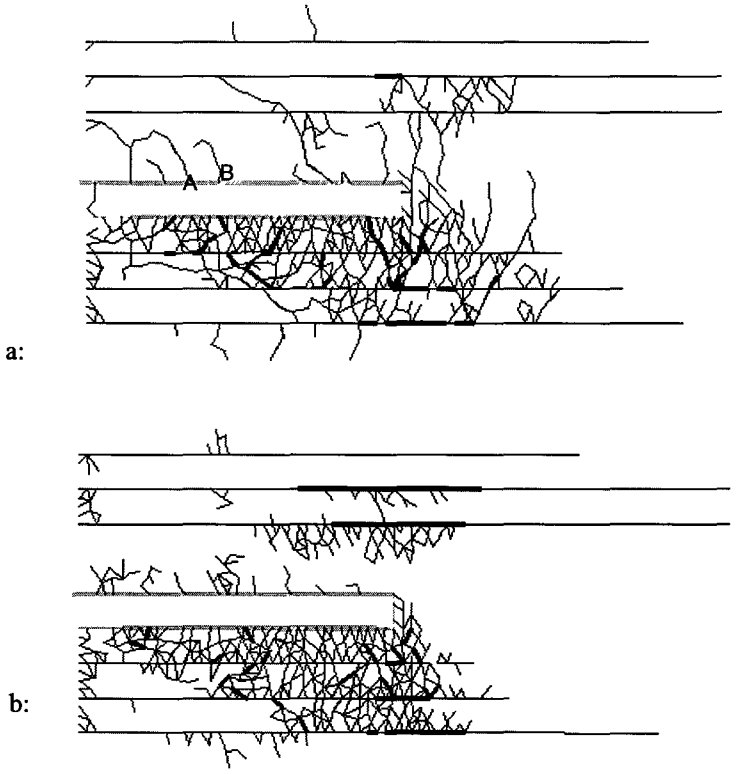

Figure 2.4.4.5 Influence of activation rule on the fracture pattern. a: Incremental activation, b: Parallel activation.

A comparison of the fracture patterns after ten mining steps of 1m per step with the incremental and parallel activation rules is shown in Figure 2.4.4.5a and Figure 2.4.4.5b, respectively. The incremental activation procedure (Figure 2.4.4.5a) requires a long solution time, as the problem must be solved after every fracture activation increment. As the stope length increases, this can require hundreds of solutions per mining step. Fortunately, the addition of a single element does not alter the equilibrium significantly and each solution converges in a few iterations. The parallel activation rule requires only one solution per mining step, but leads to a substantially different fracture pattern, as shown in Figure 2.4.4.5b. The fractures generally occur in the same regions around the stope as in the case of incremental activation. However, the fracturing is more diffuse and occurs in larger zones of activated elements. The fractures in the hangingwall do not extend across the entire beam. Few fractures form ahead of the face. An analysis with residual cohesion on the activated fractures resulted in slightly more distinct fracture zones but did not cause fractures to form ahead of the face.

2.4.4.6 Super elements

This section sets out some background concepts concerning the potential implementation of a computation method that will be generally applicable to both 2-D (DIGS) and 3D (MINSIM and 3-D fracture growth models, 3DIGS). The technique has the potential to enhance substantially the size of problems that can currently be solved and the speed with which the solution can be achieved using boundary element (BE) methods. One of the essential ingredients in an efficient boundary element program such as MINAP, DIGS, VOLSIM, MINSIM, MAP3D is some efficient means to communicate the effect that one boundary element has on every other boundary element. Once a BE model has been set up (i.e. once the geometry has been defined by the user) the computational task that takes the most time is the process of solving for the unknown displacement discontinuity (DD) values. This involves solving a large system of simultaneous equations. For example, a typical MINSIM run involves solving 12288 simultaneous equations

for 12288 unknowns. Typically, because of the large storage requirements of direct solution procedures, iterative methods are used to solve these large systems of equations. Iterative methods essentially involve taking an initial guess and then communicating the effects of the trial solution to all the other elements in the problem and then using this information to make a better guess. The process is repeated until the corrections become insignificant. In each such guess-correction cycle, called an iteration, the effect of each element has to be communicated to every other element. This can be an extremely expensive process if there are a large number of elements; for example the MINSIM model with 12288 elements would involve more than 150 million of these cross influences that need to be calculated. The way that MINSIM addresses this formidable computational task is to exploit the property of an elastic medium whereby elements that are far apart exert very little influence on one another. One approach would be to ignore these remote effects - but then to pay the price of the inaccuracies in the model solution. The approach adopted in MINSIM is to average these remote effects by communicating the effects of four neighbouring square elements by a single square element four times the size whose DD value is the average of the four component elements. This process is called lumping.

The problem with this form of lumping is that it is only really viable when the original model involves elements that are located on a regular grid - such as the planar MINSIM models in which the excavations are modelled by square elements all having the same size. This type of lumping becomes difficult if one needs to model problems in which the elements do not occur in such a regular form - for example a DIGS model with a random tessellation to represent the granularity of quartzite, or even a MINSIM model with multiple reefs that are inclined with respect to one another. In order to be able to address this problem in DIGS, a so-called multipole (MP) algorithm DIGSMP was developed to enable the influences of elements of arbitrary sizes and orientations to be calculated very efficiently. Using this new algorithm problems involving up to 15 000 elements have been modelled. Without the multipole method, the problems would be restricted to 1 500 elements using the same hardware. One of the major problems with the algorithm implemented in DIGSMP is that the method does not extend easily to 3D problems. Another disadvantage of the DIGSMP algorithm is that one cannot easily provide the user with the choice of reducing the size of error being made in the multipole approximation at the expense of more computer time. Some efforts to automate the choice of appropriate multipole parameters are described in Section 2.4.4.2

The idea behind the superelement algorithm, much like lumping, is to use some form of construct (circles in 2D and spheres in 3D) to communicate the remote influences more efficiently. The influences of the DD elements within a superelement will be communicated to side by calculating the displacements that the individual DD elements exert on the boundary of the superelement. Once the boundary displacements of all the DD elements within a superelement have been determined, they are used to communicate the effects of the external elements. The algorithm is most efficiently applied by forming a hierarchy of superelements in which the larger superelements contain a number of smaller superelements, and which are in turn contained in even larger superelements. The displacements on the boundary of the receiving superelements are then communicated to the smaller superelements that they contain, until, at the finest level, the displacements along the boundaries of the finest superelement are communicated to stresses or displacements at the remote receiving elements.

The proposed superelement approach provides an opportunity to increase the modelling capability of current BE algorithms both in terms of the size of the problems that can be solved and the speed with which the solution can be achieved. The attractive feature of the proposed algorithm is that extension from 2D to 3D is seen to be relatively straightforward in addition to providing the user with a wider range of parameter options and the possibility of arbitrary accuracy. It is anticipated that this new algorithm could be an important component in 2D and 3D fracture growth models (DIGS and 3D DIGS), seismic diffusion studies using viscoelasticity, body-force elastodynamic models, as well as developing improved solution procedures for general multiple reef MINSIM models. At present, it has been considered that the concept of the "superelement" construct should only be implemented once the three dimensional fracture

simulator 3DIGS has reached a sufficiently advanced stage of development where actual fracture processes can be reproduced by the code.

2.4.5 A continuum viscoplastic model of the fracture zone

2.4.5.1 Introduction

Linear viscoelastic theory is commonly used to simulate the time-dependent behaviour of rock. Although it is not possible to simulate rock failure and inelastic movements, even recent publications can be found where this theory is used (Pan & Dong, 1991; Yang et al, 1996). Work done for this project (Malan, 1998) however indicated that there are some subtle problems associated with the use of viscoelastic theory to simulate the time-dependent behaviour of tabular excavations in hard rock. These problems arise from the special tabular geometry of the excavations and are not readily apparent when applying the theory to circular tunnels. It is evident for the deep tabular excavations that the time-dependent failure processes in the rock play a prominent role in the time-dependent behaviour of these excavations. It appears as if the significant time-dependent effects are confined to the fracture envelope surrounding the excavations. The far-field rock mass behaviour has been shown to be adequately represented by elastic theory (Ryder & Officer, 1964). An idealisation of this concept is given in Figure 2.4.5.1. Note that the actual shape of the fracture envelope is not necessarily as depicted in the figure.

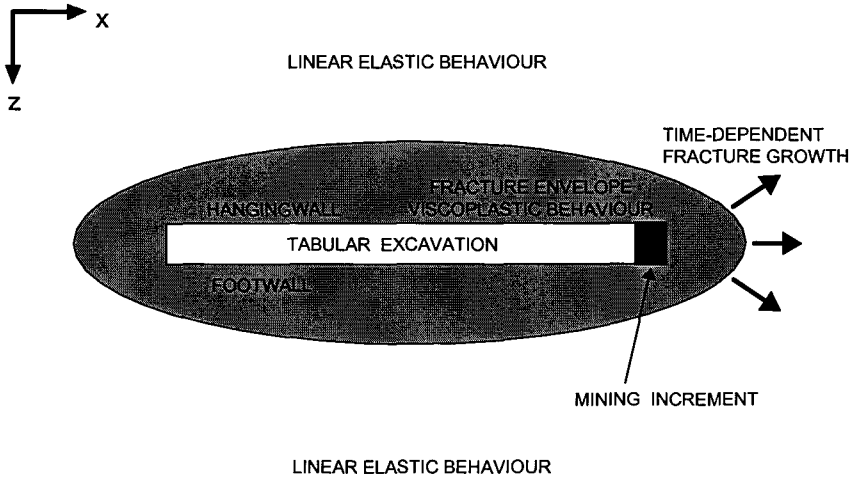

Figure 2.4.5.1 Conceptualization of the fracture zone surrounding tabular excavations (section view) and time-dependent extension of this zone following a mining increment.

2.4.5.2 Elasto-viscoplastic formulation

For this study, classical elasto-viscoplasticity as defined by Perzyna (1966) was used as a basis for the formulation of a time-dependent fracture zone model. Figure 2.4.5.2 shows the rheological analogue of the developed model. The strength of the slider is controlled by a novel time-dependent weakening rule as described below. Similarly to elastoplastic theory, the concepts of yield function and flow rule also apply. However, in viscoplasticity theory, stresses above the yield surface are permissible.

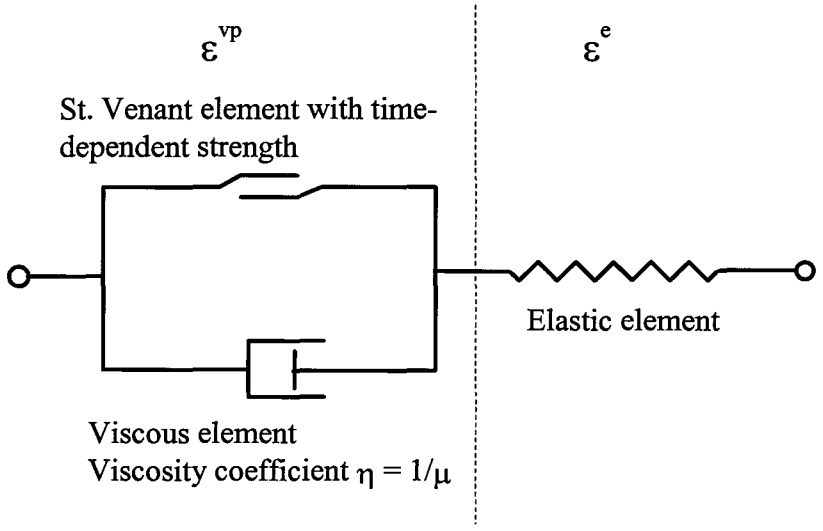

Figure 2.4.5.2 Representation of the developed elasto-viscoplastic model.

a) Yield surface

A time-dependent Mohr-Coulomb shear yield function is assumed and is given by

$$f_s(t) = \sigma_1 - \sigma_3 N_{\phi c} + 2C_c\sqrt{N_{\phi c}} \qquad (2.4.5.1)$$

and

$$N_{\phi c} = \frac{1+\sin\phi_c}{1-\sin\phi_c} \qquad (2.4.5.2)$$

where ϕ_c is the current value of friction angle, C_c is the current value of cohesion, σ_1 is the major principle stress and $\sigma_1 < \sigma_2 < \sigma_3$ for a convention of negative compressive stresses. Equation (2.4.5.1) is a function of time t owing to a time-dependent reduction in the value of the cohesion C_c once the rock fails. This is explained below.

Shear failure takes place for $f_s(t) \le 0$. For $f_s(t) > 0$, the rock behaves elastically. The cohesion C_c and friction angle ϕ_c will assume peak values C_p and ϕ_p for intact rock. Therefore, the shear yield function $f_s(t)$ is not a function of time for intact rock. For intact rock, equation (2.4.5.2) becomes

$$N_{\phi p} = \frac{1+\sin\phi_p}{1-\sin\phi_p} \tag{2.4.5.3}$$

Once the particular volume of rock starts failing, the friction angle assumes a residual value ϕ_r and the cohesion gradually decays to a residual value C_r. This cohesion softening process is simulated as a time-dependent process which is described later. This is also depicted in Figure 2.4.5.3.

b) Flow rule

If shear failure is detected, the viscoplastic strain rate $\dot{\varepsilon}_i^{vp}$ is given by

$$\dot{\varepsilon}_i^{vp} = \mu\langle f_s(t)\rangle \frac{\partial g_s}{\partial \sigma_i} \qquad \text{for} \quad i = 1, 2, 3 \tag{2.4.5.4}$$

where μ is the fluidity parameter and

$$\begin{aligned} \langle f_s(t)\rangle &= f_s(t) \quad \text{for} \quad f_s(t) \le 0 \\ \langle f_s(t)\rangle &= 0 \qquad \text{for} \quad f_s(t) > 0 \end{aligned} \tag{2.4.5.5}$$

A non-associated flow rule is used (Vermeer & De Borst, 1984) where the plastic potential function is given by

$$g_s = \sigma_1 - \sigma_3 N_\psi + 2C_c\sqrt{N_\psi} \tag{2.4.5.6}$$

with

$$N_\psi = \frac{1+\sin\psi}{1-\sin\psi} \tag{2.4.5.7}$$

and ψ is the dilation angle. From equation (2.4.5.4) it follows that in the model the strain rate of the failed rock is proportional to the excess stress above the yield surface.

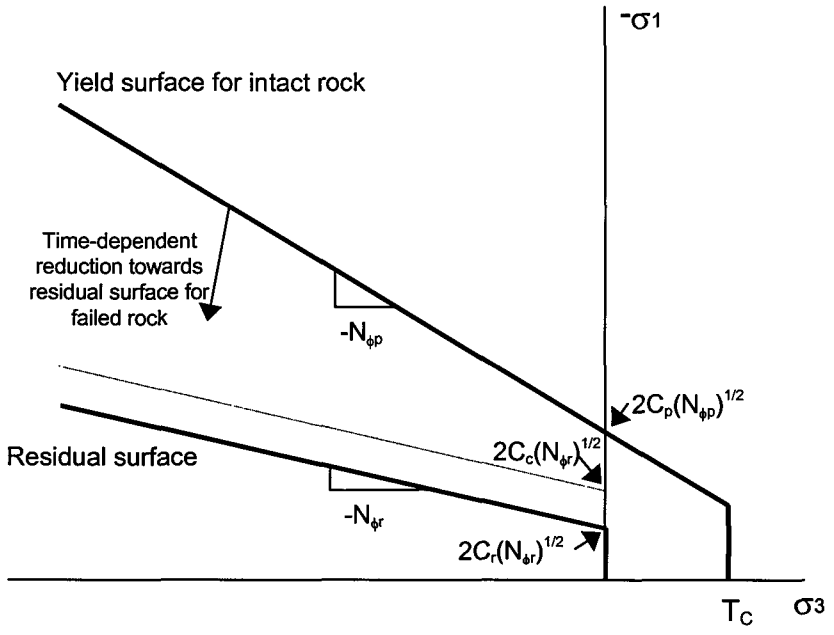

Figure 2.4.5.3 The evolution of the yield surface for intact rock to the eventual residual surface for failed rock. Note that compressive stresses are negative and that on the vertical axis the negative of the major principal stress is plotted to turn the figure upright. $N_{\phi r}$ ***is defined in equation (2.4.5.10).*** T_C ***is the tensile strength of intact rock.***

c) Time-dependent strength

A constitutive description of time-dependent rock behaviour should include the effect of strength degradation with time and/or deformation. Experimental evidence (Kranz et al., 1982) indicated that rock under load shows a decrease in strength with time. Fakhimi & Fairhurst (1994) modelled the time-dependent degradation of material strength by exponential friction and cohesion decay functions. Aydan et al. (1996) simulated the time-dependent behaviour of squeezing rocks as the degradation of strength properties as a function of time by utilising information obtained from creep tests.

Observations of time-dependent fracturing ahead of tabular stopes and in some haulages in the South African gold mines show that the rock becomes progressively more fractured with time resulting in the gradual loss of cohesive strength in a particular volume of rock. This loss of strength will be modelled by assuming that the rate of cohesion reduction is proportional to the excess stress above the residual target surface.

$$\dot{C}_c = k_c \langle f_{res} \rangle \tag{2.4.5.8}$$

where k_c is the cohesion decay factor and

$$f_{res} = \sigma_1 - \sigma_3 N_{\phi r} + 2C_r \sqrt{N_{\phi r}} \tag{2.4.5.9}$$

$$N_{\phi r} = \frac{1+\sin\phi_r}{1-\sin\phi_r} \tag{2.4.5.10}$$

is the residual target surface. The principle embodied in Equation (2.4.5.8) is based on laboratory observations (described in Section 2.4.2) that if rock specimens are loaded close to the uniaxial strength, the creep rate and eventual creep failure occur faster than for a low stress. For a particular volume of rock under high stress, creep fractures will therefore form more rapidly, resulting in a faster loss of cohesion in the rock than for low stress.

The model developed above was implemented in a creep version of the computer program FLAC (Itasca, 1993) using the built-in FISH language. Any other suitable finite difference or finite element code could however be used. FLAC is an explicit finite difference code developed for geotechnical engineering applications. The two-dimensional version of the code was used in this study. FISH is a programming language embedded within FLAC enabling the user to define new variables, functions and constitutive models. The creep version of FLAC gives access and control over a timestep that represents real time. Malan (1998) gives some detail regarding this implementation in FLAC.

2.4.5.3 Simulating the closure behaviour of tabular excavations

The model described above was used to successfully simulate the time-dependent increase in the extent of the fracture zone around squeezing tunnels at Hartebeestfontein Mine (Malan, 1998). Soon after development of the tunnel, the failed zone covered those areas where the stresses exceeded the failure strength of the intact rock ($f_s(t) \leq 0$). Time-dependent processes lead to a gradual loss of residual strength in the fractured rock, transferring stress to the unfailed rock. This then also becomes fractured resulting in a time-dependent increase in the extent of the fracture zone. Depending on the chosen model properties, an equilibrium position is eventually reached with no further growth in the fracture zone.

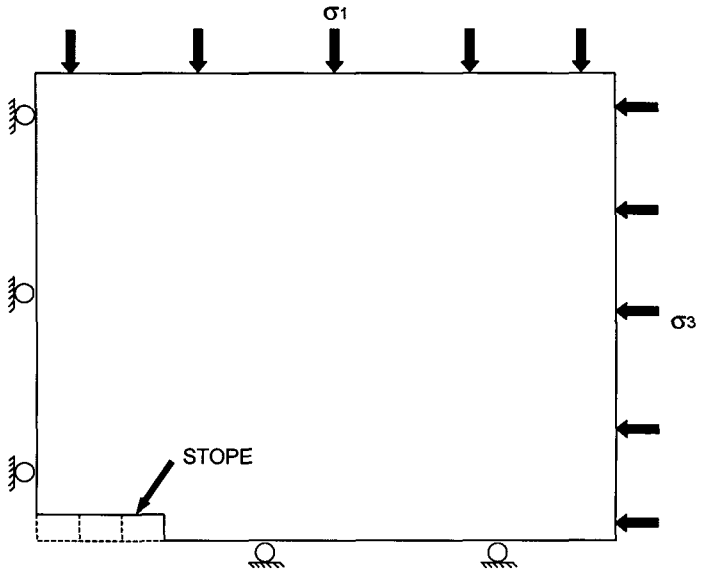

Figure 2.4.5.4 Geometry and boundary conditions used for simulating tabular excavations (not drawn to scale).

To investigate the applicability of the model for simulating time-dependent stope closure, the incremental mining of a panel was investigated. Figure 2.4.5.4 illustrates the geometry used. The size of the finite difference mesh was 100 × 80 elements, appropriately graded to ensure that the boundaries were sufficiently far away from the stope. The size of the elements in the area of the stope was 0,2 m while the size of each mining increment was 1 m. Quarter

symmetry was used to save on the number of elements. The stoping width was 1 m although only 0,5 m is shown in Figure 2.4.5.4 due to the imposed symmetry. Although the model appeared successful in replicating the closure behaviour as explained below, very large computer run-times were recorded. The explicit solution scheme of FLAC requires a small timestep to ensure stability. To simulate a mining step, the relevant material zones were removed instantaneously. Following a large instantaneous stress change (for example after a mining increment), the timestep must be very small. Only as a new equilibrium state is approached, can the timestep be progressively enlarged. The run-time for ten mining increments in the simulation of Figure 2.4.5.4 with weak rock properties can easily exceed 72 hours on a 200 MHz Pentium computer. This currently prohibits the simulation and calibration of incremental stope behaviour if the span is large. For the illustrative stope problems, a low number of mining increments was used with high field stresses to obtain the required high stresses ahead of the face.

To investigate the simulated closure behaviour of a tabular excavation, eight increments were mined (giving a total span of 16 m) using the properties given in Table 2.4.5.1. Typical closure results are given in Figure 2.4.5.5 as a function of time after mining the eighth increment. For the two distances from the face, behaviour similar to that noted for the experimental results of the Ventersdorp Contact Reef is obtained. The incremental jump after blasting is reduced as the distance to face increases. Furthermore, the closure rate of the steady-state phase also decreases into the back area. These results are encouraging as this behaviour cannot be simulated with a viscoelastic model as explained in Malan (1998). The viscoplastic model approximates the time-dependent failure processes and therefore gives the correct closure response for the Ventersdorp Contact Reef. No attempt was made to simulate the Vaal Reef as the behaviour of this reef is dominated by the bedding plane movements. The finite difference mesh is not suitable for the inclusion of multiple discontinuities to simulate these parallel bedding planes. To simulate the time-dependent behaviour within an assembly of explicit discontinuities, a discontinuum viscoplastic model suitable for implementation in a boundary element code was developed (see Section 2.4.6).

Table 2.4.5.1 Properties used for the incremental mining of the tabular stope to obtain the results in Figure 2.4.5.5.

Parameter	**Value**
Vertical stress, σ_v	90 MPa
Horizontal stress, σ_h	45 MPa
Bulk modulus, K	38,9 GPa
Shear modulus, G	29,2 GPa
Density of the rock, ρ	2700 kg/m^3
Cohesion of intact rock, C_P	22 MPa
Friction angle (Both peak, ϕ_P, and residual, ϕ_R)	30°
Residual cohesion, C_r	10 MPa
Cohesion decay, k_C	0,005 h^{-1}
Dilation angle, ψ	0°
Fluidity coefficient, μ	1×10^{-10} Pa^{-1}.h^{-1}

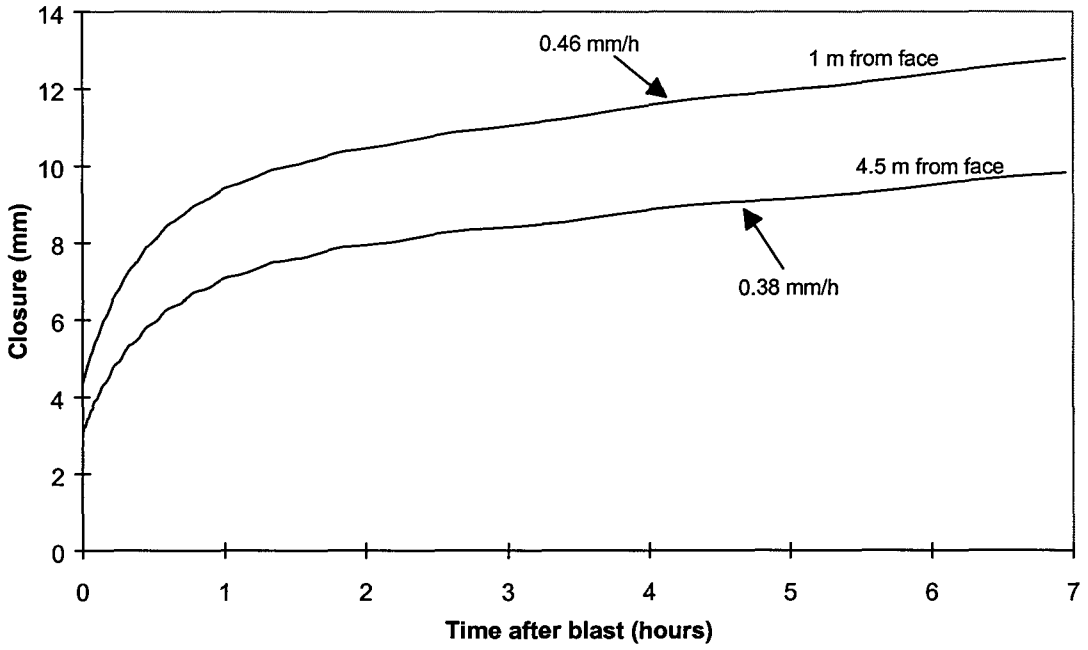

Figure 2.4.5.5 Simulated time-dependent closure. The distances were the original distances to face before mining the increment. The steady-state closure rate was calculated between 2 hours and the end of the data set. Note that although only the first 7 hours after the mining increment is plotted, the time period between each step was 24 hours.

In the example above, arbitrary model parameters were used to illustrate the closure profiles. Owing to the success of this model in simulating the time-dependent fracture process, it is desirable to calibrate these parameters using underground closure data. The two-dimensional plain strain version of FLAC was used and therefore only geometries where these assumptions can be made are appropriate. As the results obtained from viscoplasticity theory are path dependent, the entire stope span cannot be simulated in one mining increment. Data was therefore needed where the span of the stope was small. Closure data collected by Kersten (1995) at Hartebeestfontein Mine in 1965 was used. The geometry was such that a two-dimensional plane strain approximation could be made. The instrumented panel was situated at a depth of 1850 m with a span of 20 m. The actual stress conditions and rock parameters are not known accurately and therefore the objective of this simulation was not exact parameter calibration, but an attempt to replicate the observed profiles. The closure fitting process was very arduous as ten mining increments (using symmetry) had to be executed. It was found that the path dependence and slow run times made it very difficult to achieve the desired final closure by making small changes in the parameter values before the first increment. In spite of these problems, it should be noted that the closure behaviour of the viscoplastic model gives similar trends to that of the underground measurements. Figure 2.4.5.6 shows the experimental data and numerical results for a fluidity coefficient of $1x10^{-10}$ $Pa^{-1}h^{-1}$ and a cohesion decay rate of 0,005 h^{-1}. Other parameters used were bulk modulus = 38,8 GPa, shear modulus = 29 GPa, cohesion = 22 MPa, residual cohesion = 15 MPa and friction angle (peak and residual) = 30°. In the model the stope was mined incrementally to the required span using 1 m increments.

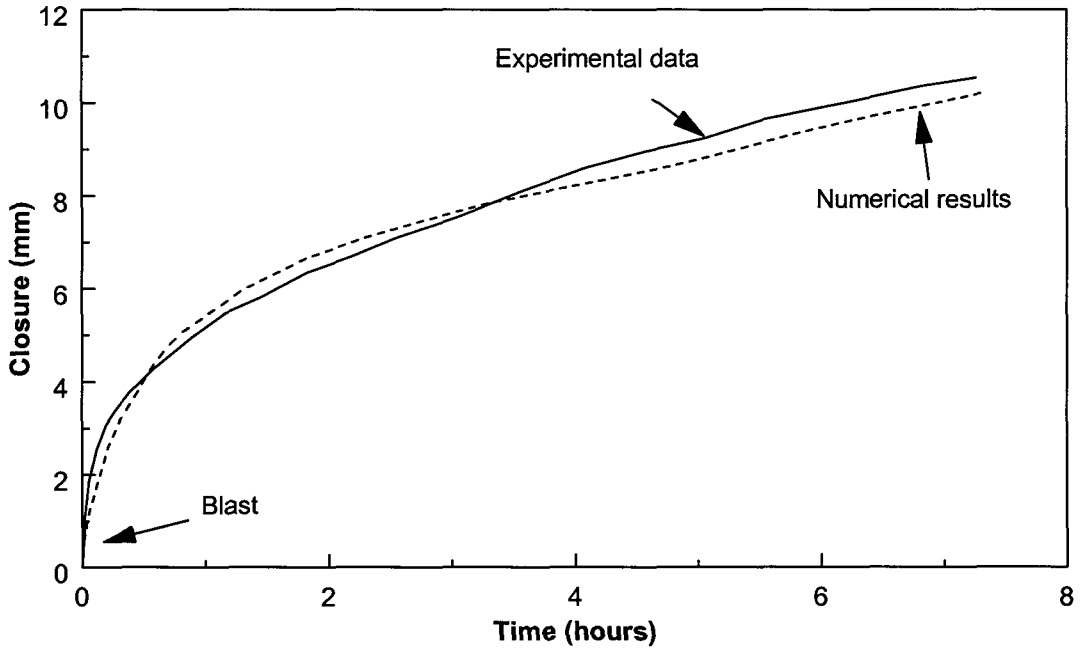

Figure 2.4.5.6 Experimental and simulated stope closure after blasting.

2.4.5.4 Summary

To allow for direct simulation of the time-dependent fracture zone behaviour, a continuum viscoplastic model was developed. The model is based on classical viscoplasticity, with a novel time-dependent cohesion weakening rule to simulate the time-dependent failure of the rock. A Mohr-Coulomb failure law and a non-associated flow-rule were assumed. For an excavation in this material, the failure zone soon after development, covers those areas where the stress exceeded the failure strength of the rock. The time-dependent processes lead to a gradual transfer of stress to the unfailed rock. This also becomes fractured, leading to a time-dependent growth of the fracture zone. The process continues until an equilibrium position is attained. This model has proved to be successful in simulating the time-dependent closure behaviour of tabular excavations, giving both the instantaneous response at blasting time and the primary and steady-state closure phases.

2.4.6 Explicit modelling of time-dependent fracture formation using a viscoplastic displacement discontinuity model

2.4.6.1 Introduction

Although the continuum viscoplastic model described in Section 2.4.5 can simulate the time-dependent behaviour of the fracture zone, it cannot be used if the behaviour is dominated by major discontinuities such as the creep of bedding planes. For these cases, a discontinuous formulation is required. Furthermore, to account for time-dependent seismic recurrence effects and to link these effects mechanistically to mining activity, it is necessary to represent in an explicit manner the rheological deformations that take place in the rock mass over periods of hours, days or weeks as well as rapid elastodynamic excitations. This section describes a framework developed for the incorporation of viscoplastic effects on random discontinuities which allows for the relaxation of the discontinuities according to a postulated law. Sudden

stress drop or elastodynamic effects are approximated by allowing rapid cohesion loss (softening) to be accommodated in the solution scheme but no attempt was made to include elastodynamic wave propagation effects in this current study. The most important aspect of the work is that explicit interaction between the mine openings and mobilized discontinuities is accounted for as an evolutionary time process. This allows realistic questions concerning practical mining problems to be addressed. Specifically, it becomes possible to investigate problems such as the consequences of varying the mining face advance rate, the effects of mining at greater depths, the desirability of continuous or punctuated mining cycles and questions relating to the rate of extraction of remnant areas and the expected recurrence of rockbursts and seismic energy release cycles. It is demonstrated that realistic seismic energy release and stope closure trends can be simulated using a random mesh of potential discontinuity sites surrounding a tabular mining excavation. The justification for employing a random mesh representation is based on some success in modelling physical experiments of brittle rock failure (Section 4.4.1) as well as the realistic replication of fracture patterns near mine openings (Section 4.4.2). Although a simple time-dependent slip rule is used, it can easily be adapted within the developed framework to simulate behaviour appropriate to different discontinuities types.

2.4.6.2 Formulation of the viscoplastic displacement discontinuity model

In the present development, it is postulated that the intact rock material behaves in an essentially elastic manner and that all inelastic behaviour, including viscoplastic effects, is controlled by the presence of multiple interacting discontinuities. In this approach, explicit slip is modelled as a time-dependent (but not elastodynamic) process and progressive redistribution of stress can occur near the edges of mine openings both as a function of time and in response to changes to the size of the openings.

Solution procedure

A complete mathematical description of the solution procedure is given in Appendix 2.1. It is assumed that all elements are designated as "elastic" (non-viscous) or as "viscoplastic". Figure 2.4.6.1 gives a flow chart explaining the time-dependent solution scheme. An iteration procedure to estimate new discontinuity values for the non-viscous elements is nested inside the time-stepping loop.

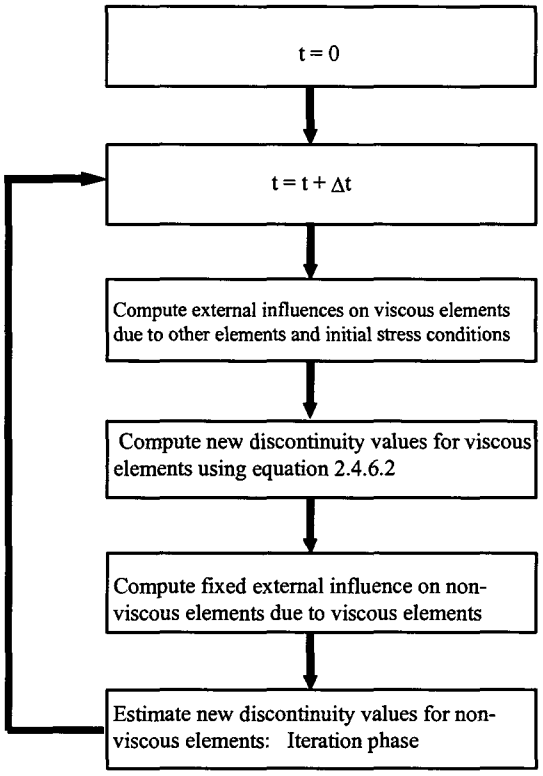

Figure 2.4.6.1 Time-stepping solution scheme.

Viscoplastic relaxation and timestep bounds

In order to resolve the viscoplastic relaxation step in Figure 2.4.6.1, it is necessary to assume a specific functional dependence of the slip rate on the current stress state. Each slip element is assumed to be in quasi-static equilibrium at each instant in time, with the rate of slip being a function of the stress state and the resistance to slip. Specifically, define the resistance to slip, ρ to be given by

$$\rho = S_0 - \tan\phi T_n \quad ; \quad T_n < 0 \tag{2.4.6.1}$$

where S_0 and ϕ are the residual cohesion and friction angle parameters as shown in Figure 2.4.6.2. T_n is the normal (clamping) traction acting on the discontinuity.

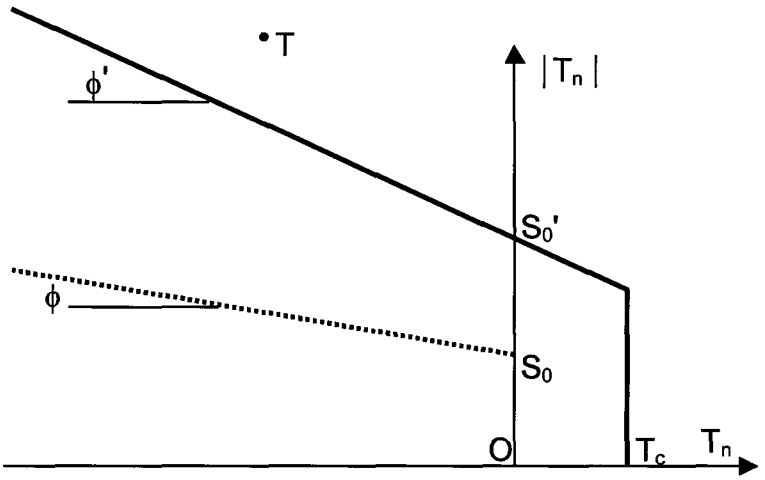

Figure 2.4.6.2 Mohr-Coulomb diagram illustrating the peak and residual values of friction angle and cohesion. T_y and T_z are the shear and normal tractions acting on the discontinuity. A convention of compressive stresses being negative is assumed.

The excess driving shear stress, τ_e, is defined to be

$$\tau_e = |T_s| - \rho \tag{2.4.6.2}$$

where T_s is the shear traction acting on the discontinuity. It is now postulated that the rate of slip is proportional to the driving shear stress τ_e. Specifically,

$$\frac{dD_s}{dt} = e\kappa\tau_e \tag{2.4.6.3}$$

where e is a slip direction indicator and D_s is the shear displacement discontinuity component. The variable κ is defined to be a parameter playing a similar role to the fluidity parameter of classical viscoplasticity theory (see Section 2.4.5). This parameter will be designated as the surface fluidity having units of $m/(Pa \cdot s)$. By writing Equation (2.4.6.3) in incremental form, the new value of D_s after each time step $\Delta t = t_i - t_{i-1}$, can be estimated as

$$D_s^{t_i} \approx D_s^{t_{i-1}} + e\kappa\tau_e\Delta t \tag{2.4.6.4}$$

2.4.6.3 Estimation of seismic energy release

In the analysis of mining or earthquake problems it is convenient to define the gravitational body forces and far-field tectonic forces as "loading" forces. In the course of mining or fault slip, the earth is deformed and the loading forces perform work. Let the incremental work done by the loading forces during a given time interval be ΔW_L. In the particular case of an elastic body, conservation of energy requires that

$$\Delta W_L = \Delta U + \Delta W_A \tag{2.4.6.5}$$

where ΔU is the change in internal strain energy and ΔW_A represents kinetic energy changes and energy dissipated by frictional sliding on discontinuities or consumed in creating new discontinuity surfaces. Consider in particular the transition between two states *p* and *t* which are

associated with equilibrated stress and displacement fields at each point in the body. In each case the body force field components remain the same. Appendix 2.2 illustrates how the work done by the loading forces, ΔW_L, is calculated in the developed displacement discontinuity framework for a transition from state *p* to state *t*. The crucial assumption is made that the equilibrated states *p* and *t* can be sufficiently well approximated using the static solution procedure. Having identified two equilibrium states of the system, it is possible to compute the incremental work done by the loading forces ΔW_L and the change in the strain energy ΔU. Since the two states *p* and *t* are computed using a quasi-static solution procedure, there will generally be an unaccounted gap ΔW_A between ΔW_L and ΔU. By conservation of energy, ΔW_A must be assumed to comprise both kinetic energy and other dissipated energy. ΔW_A can be loosely termed released energy. If some estimate can be made of the energy that is dissipated by frictional sliding during the transition from state *p* to state *t*, it is possible to infer the maximum level of kinetic energy that could exist in the body during the transition. The kinetic energy is itself assumed to be dissipated by unspecified material damping and radiation mechanisms. The validity of this approximation rests on the assumption that elastodynamic stress waves do not give rise to significant additional fracture formation and that there is little overshoot in computing the final discontinuity values. The difference, ΔW_A, between ΔW_L and ΔU then provides a measure of the released energy which arises in the transition from state *p* to state *t*. The level of kinetic or seismic energy, ΔW_S, that arises during the transition from state *p* to state *t* can be expressed as

$$\Delta W_S = \Delta W_A - \Delta W_D \tag{2.4.6.6}$$

where ΔW_D is the energy dissipated by frictional sliding or by the creation of new fracture surfaces. In the specific examples considered in this study, it is assumed that the dissipated energy is predominantly frictional. A complete mathematical description of how these terms are calculated in the developed program can be found in Appendix 2.2.

2.4.6.4 Examples and applications

Strain softening and creep acceleration

As a first example, the viscoplastic response of an isolated straight crack in an infinite medium was considered. Results (Appendix 2.2) indicated that the simple slip law, represented by Equation (2.4.6.3), predicts a monotonically decreasing rate of slip as the equilibrium condition $\tau_e = 0$ is approached. To replicate the behaviour of granular materials such as rock or concrete, suppose that a population of pre-existing flaws is represented as a random assembly of sliding cracks. If the initial flaw population is sufficiently dilute, then cohesionless cracks which are suitably oriented can be expected to have a response similar to that of the isolated crack described above, when a load is suddenly applied to the material. The overall deformation of a sample of the material would be expected to follow primary creep behaviour (see Section 2.4.2) until sufficient slip on the mobilized flaws causes additional fracturing to occur. The progressive mobilization of fracturing may then result in a phase of secondary creep where the deformation is proportional to the loading time. As small fractures coalesce to form larger structures, it can be expected that accelerated deformation will occur leading eventually to a tertiary creep phase and collapse of the sample.

This sequence can, in fact, be reproduced by the random population of sliding flaws displayed in a rectangular region of width *L* and length 2*L*,as shown in Figure 2.4.6.3. Approximately one tenth of the flaws, depicted by heavy lines in Figure 2.4.6.3, are assumed to be weak and to have no cohesion or tensile strength. The remaining flaws are assumed to be strong and to have a uniform strength. Specific material properties of the weak and strong flaws are given in

Table 2.4.6.1. The flaws in this case were generated using a Delaunay tessellation scheme and the flaw size statistics quoted in Table 2.4.6.1 are relative to the dimension *L* of the sample.

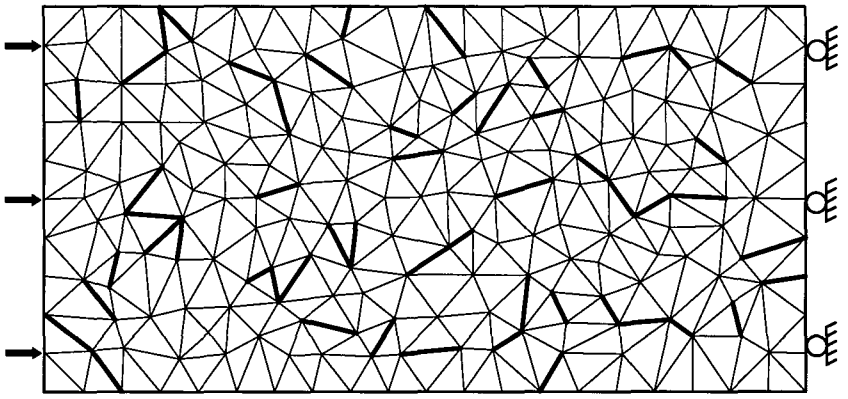

Figure 2.4.6.3 Random population of flaws. The highlighted flaws are assumed to have no cohesion or tensile strength.

Table 2.4.6.1 Sample flaw population properties.

PROPERTY	WEAK FLAWS	STRONG FLAWS
Cohesion, $S_o^{'}$ (MPa)	0	25
Friction, $\phi^{'}$ (degrees)	30	45
Tensile strength, T_c (MPa)	0	10
Mobilized cohesion, S_o (MPa)	0	0
Mobilized friction, ϕ (degrees)	30	30
Mean flaw length (normalized)	0,120	0,116
Standard deviation (normalized)	0,028	0,273
Minimum length (normalized)	0,072	0,070
Maximum length (normalized)	0,178	0,202
Total length (normalized)	6,352	55,75

It is now assumed that a load of 50 MPa (i.e. $2S_o^{'}$) is applied to the left hand side of the sample and that the right hand side is rigidly restrained by a frictionless platen. It should be noted that the applied load is approximately 41 per cent of the uniaxial strength corresponding to the material properties of the strong flaws (Table 2.4.6.1). The fluidity parameter κ is chosen to be 2×10^{-5} in an appropriate set of units and the time step size is set equal to 0,1 time units. The average strain component in the sample, parallel to the applied load, is shown as a function of time in Figure 2.4.6.4 as well as the fraction of the total flaw length mobilized at each point in time. Before time 5, the strain increases at a decreasing rate which is similar to a primary creep phase. The length of mobilized flaws is also seen to increase slowly during this period. The duration of this period is governed by the weak flaw density and by the fluidity κ. Between time

5 and time 14, the strain rate is observed to increase almost linearly with time, corresponding to an increased rate of mobilization of flaws. However, the rate of change of the flaw length falls off after time 10 indicating that the deformation occurs mainly by sliding on existing flaws between times 10 and 14. A sudden jump in the strain rate is observed between times 14 and 15 and this is followed by a generally accelerated deformation rate similar to a tertiary creep phase. The relatively abrupt increase in the strain rate between times 14 and 15 corresponds to an axial crack forming through the whole length of the sample as shown in Figure 2.4.6.5. Accelerated flaw length mobilization is observed after time 17.

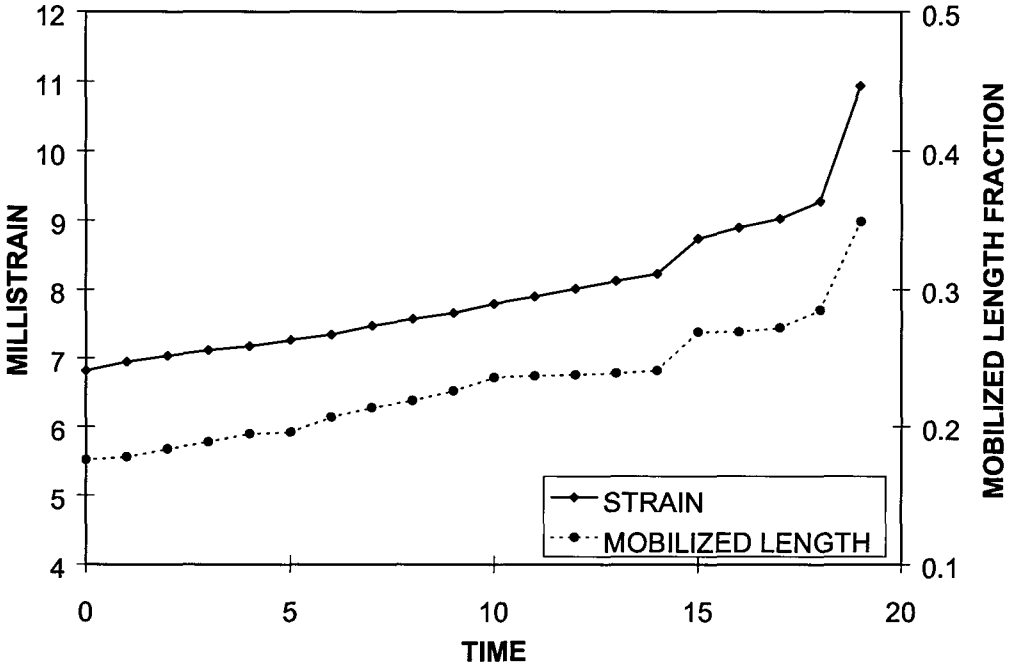

Figure 2.4.6.4 Response of the sample to a sudden application of load.

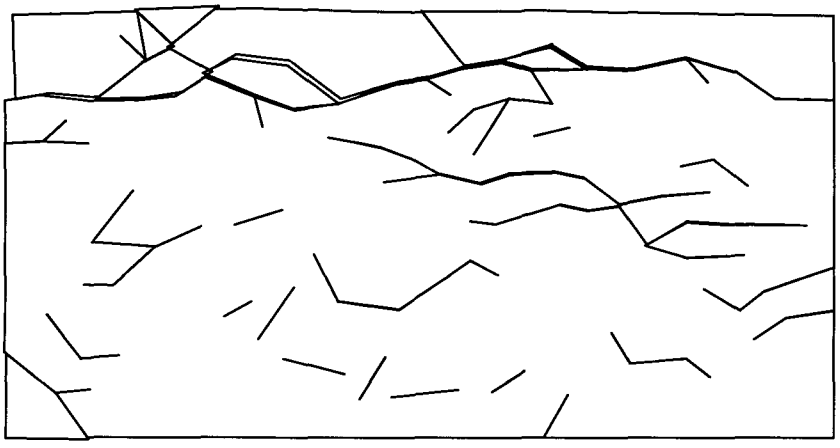

Figure 2.4.6.5 Formation of axial crack parallel to the loading direction between times 14 and 15.

The example shown here demonstrates that plausible material behaviour can be simulated with a simple viscoplastic relaxation law. At the same time, the assumed material fabric, represented in this case by a random mesh of sliding cracks, plays a central role in controlling the overall strain response and the detailed damage mechanisms.

Application to deep level mining problems in brittle rock

In order to investigate the applicability of this model to simulate the time-dependent behaviour of tabular stopes, the initial extraction of a parallel sided panel is considered. The opening is approximated as a crack, with interpenetrating faces, embedded in a random mesh of potential discontinuity segments. The strength properties of each segment and the statistics of the random mesh are given in Table 2.4.6.2. Representative *in situ* rock properties were used with the surface fluidity κ determined by back-analysis of the measured underground time-dependent closure. The opening is created incrementally in a series of mining steps and each segment of the random mesh is tested for failure at designated time step intervals. The seismic energy changes that occur in each time step are computed using the procedure outlined above. In this example, no geological features such as parting planes, parallel to the tabular opening, or faults are considered. The inclusion of these features is, however, accommodated directly by the solution procedure if necessary.

Table 2.4.6.2 Properties of discontinuity strength and random mesh statistics used for the stope models.

PROPERTY	MINING SIMULATION
Cohesion, $S_o^{'}$ (MPa)	25
Friction, $\phi^{'}$ (degrees)	45
Tensile strength, T_c (MPa)	5
Mobilized coh, S_o (MPa)	0
Mobilized frn, ϕ (degrees)	30
Mean segment length (m)	1,119
Std. deviation (m)	0,272
Min. segment length (m)	0,605
Max. segment length (m)	2,073
Total length (m)	2594
Surface Fluidity, κ, ($MPa^{-1}.h^{-1}.m$)	$1x10^{-5}$
Time step size, Δt, (hours)	0,1
Young's modulus (MPa)	70000
Poisson's ratio	0,2
Vertical stress (MPa)	60 and 100
Horizontal stress (MPa)	30 and 100

An important consequence of the numerical viscoplastic discontinuity behaviour is that the additional fracturing caused by a sudden increase in stress occurs in a time-dependent fashion.

After a mining increment, the existing discontinuities surrounding the stope are subjected to an increase in mining induced stress. Those discontinuities subjected to stresses above the target yield surface, relax causing a transfer of stress to the solid rock at the edge of the fracture zone. New fractures then form in these positions as a time-dependent process. For the example above, the increase in cumulative fracture length as a function of time after a blast is illustrated in Figure 2.4.6.6. It should be emphasised that there are no changes in the excavation dimension during this time period. Similarly to Adams & Jager's (1980) observations, the majority of new fractures form within a short period after the blast and the rate of fracturing then diminishes until the next blast. For comparison with the numerical results, the cumulative seismicity after production blasting at an experimental site in the Blyvooruitzicht Gold Mine is also plotted in Figure 2.4.6.6. A description of the site can be found in Kullmann *et al.* (1996). It is clear from Figure 2.4.6.6 that a similar trend is observed for the seismicity. Events with magnitude greater than -1,5 were used. The seismicity following 304 production blasts was added, or stacked, for Figure 2.4.6.6. All recorded events within five minutes of the start of the face blast were excluded because face blasting took approximately five minutes and most events within this time appeared to be face blasts.

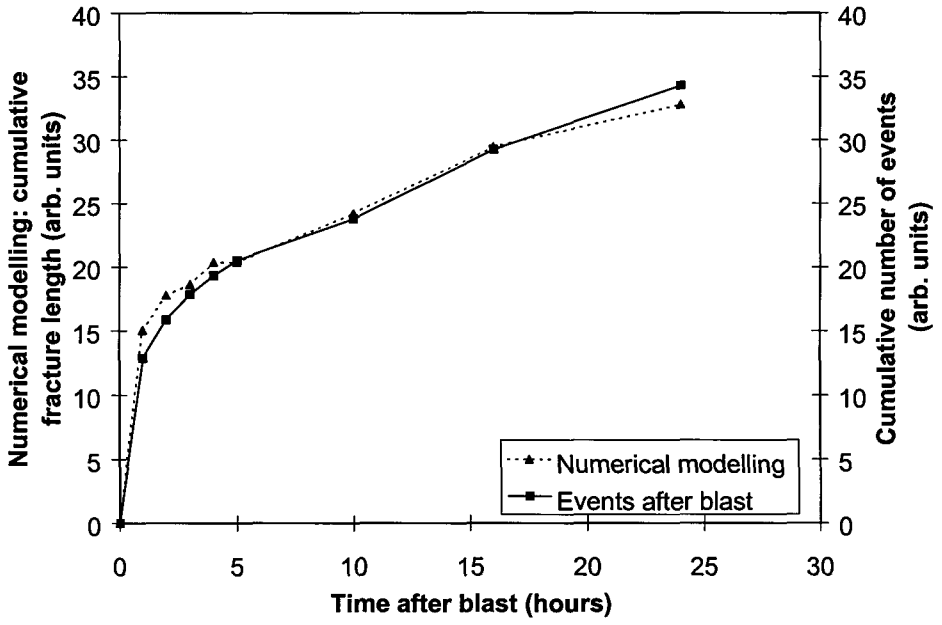

Figure 2.4.6.6 Cumulative fracture length after blasting. The rate of seismicity after blasts is also plotted showing similar trends.

In the numerical simulation, the time-dependent fracture process results in stope closure profiles similar to those observed underground. Typical numerical and experimental closure profiles measured after blasting (t=0), are plotted in Figure 2.4.6.7 showing similar trends. The experimental closure data was also obtained from the experimental site at the Blyvooruitzicht Gold Mine. Figure 2.4.6.8 shows the incremental seismic energy release within each time step as mining proceeds at an advance rate of 1m/day. The release pattern is contrasted for two mining depths of nominally 2200 m (60 MPa) and 3700 m (100 MPa) respectively. It is clear that most seismic energy is released immediately after each sudden advance of the mining face. Additional seismic activity is seen to occur at a generally decreasing rate before the next face advance step. This corresponds qualitatively to the very well known pattern of seismic activity that is observed in deep level gold mines between each blast cycle. Figure 2.4.6.8 also indicates that greater levels of seismic activity occur at the greater depth. In some cases, secondary peaks can be observed between face advance cycles. It is also of interest to note that following an initial trend of increasing energy release peaks in the first seven days,

successive peak values become more random. The corresponding mobilized fracture length in each time step is shown in Figure 2.4.6.9 for the two mining depths. The successive peak values are more irregular than the energy release peaks. It can be seen from Figure 2.4.6.9 that more fractures are mobilized at the increased depth. More extensive simulation studies are required to determine the fracture extent for a wide span stope once total closure of the mined region occurs. Further examples of the use of this code can be seen in Section 4.4.4 and Malan (1998).

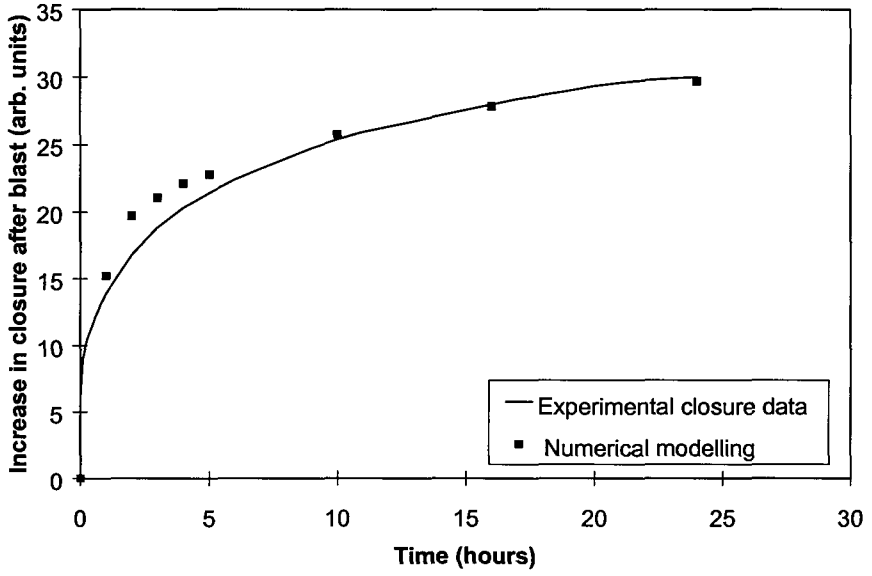

Figure 2.4.6.7 Experimental and numerical stope closure after blasting.

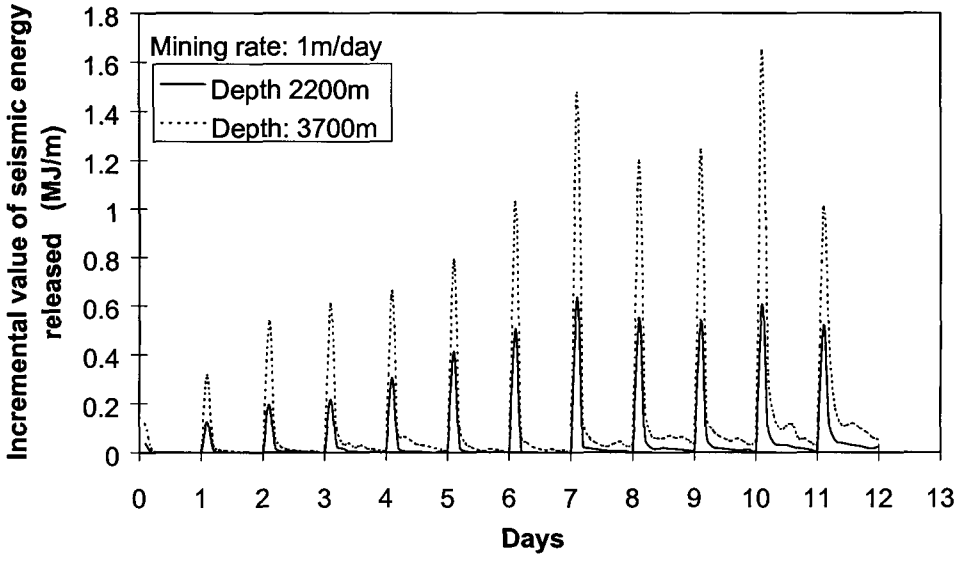

Figure 2.4.6.8 Incremental seismic energy release.

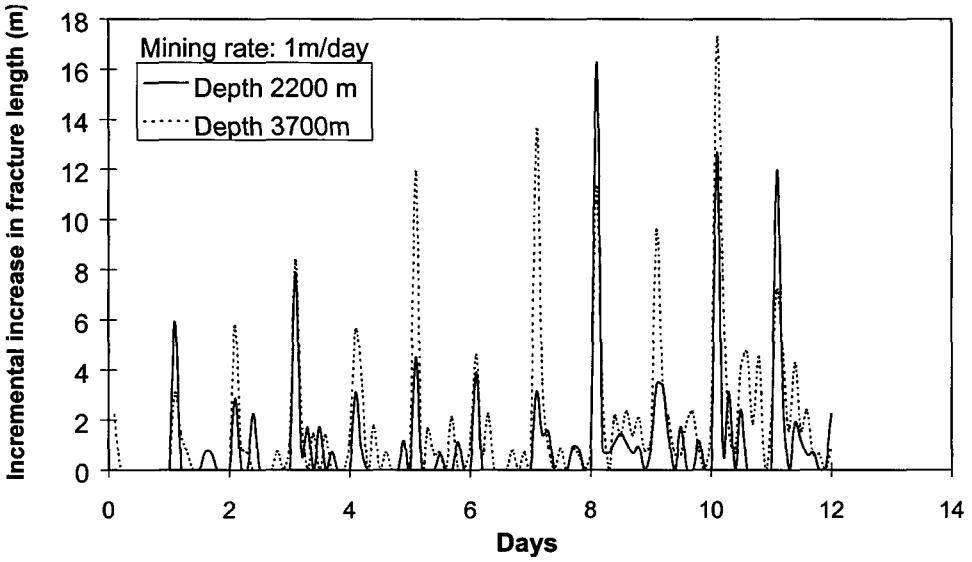

Figure 2.4.6.9 Incremental mobilized fracture length.

2.4.6.5 Summary

A framework has been presented for the solution of interacting crack assemblies in which a discontinuum viscoplastic formulation is used to control the rate of slip on individual cracks. It is shown that this approach is able to reproduce intricate material behaviour such as primary, secondary and tertiary creep effects when the rock fabric is represented by a set of interacting cracks which are specified on a random mesh. When applied to mining problems, favourable agreement is found between observed numbers of seismic events following actual face advances and the cumulative length of fractures that are mobilized in a simulated stope panel embedded in a random mesh of discontinuities. In addition, the numerically computed time-dependent closure, at a given point in the stope panel, follows the same qualitative trend as the actual observations of the stope closure.

2.4.7 The inclusion of layered elastic materials in the boundary element formulation

2.4.7.1 Development of the method

A three-layered elastic region, with Young's modulus E_1, E_2, and E_3, can be obtained by the superposition of two sets of bonded half-plane regions and an infinite plane. This is accomplished by the superposition of two sets of bonded half-plane solutions with elastic modulus sets (E_2, E_3) and (E_1, E_2), respectively, and subtracting a supplementary infinite domain solution, as shown in Figure 2.4.7.1. The complete solution can be written as:

$$u_i = (u_i)_{[A]} + (u_i)_{[B]} - (u_i)_{[C]}$$

$$\sigma_{ij} = (\sigma_{ij})_{[A]} + (\sigma_{ij})_{[B]} - (\sigma_{ij})_{[C]} \qquad (2.4.7.1)$$

where subscript [A] represents the bonded half-planes with parameters (E_2 , ν_2) and (E_3 , ν_3), [B] represents the bonded half-planes with parameters (E_1 , ν_1) and (E_2 , ν_2), and [C] represents the infinite plane with parameters (E_2 , ν_2). For completeness, the derivation of the fundamental solution is given in Appendix 2.3.

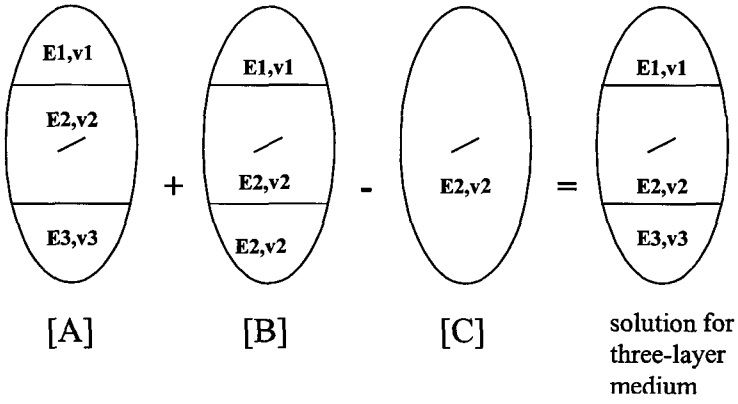

Figure 2.4.7.1 The superposition scheme to achieve solution for a three-layer medium.

Based on this superposition scheme, a two-dimensional constant strength displacement discontinuity model was developed, verified and applied (Shou, 1994). This scheme has been extended to include linear variation displacement discontinuity elements and has been coupled it to the existing numerical model DIGS (Napier, 1990) to form a special layer version of the code called DIGSL.

2.4.7.2 Study of the influence of the elastic material contrast

The problem of stoping on the Ventersdorp Contact Reef (VCR), which can be considered as a three-layered system, is systematically analysed with DIGSL. According to Roberts (1996),, and Schweitzer & Johnson (1997), the combination of rock types in the hangingwall and footwall results in different rock mass behaviour, which can be identified by different fracture orientations and intensities around the stopes. Three major rock type combinations and the associated fracture populations were observed. These were (1) the hard lava/VCR/quartzite type (Deelkraal, WDL, Leeudoorn), (2) the soft lava/VCR/quartzite type (Kloof, WAGM), and (3) the soft lava/VCR/Jeppestown shale type (East Driefontein). The material properties and observed fracture populations are given in Table 2.4.7.1 and Figure 2.4.7.2.

Table 2.4.7.1 Material properties of formations associated with the different types of Ventersdorp Contact Reef

Type	**I (Deelkraal)**		**II (Kloof)**		**III (East Driefontein)**	
Formation	**HW**	**FW**	**HW**	**FW**	**HW**	**FW**
	hard lava	**quartzite**	**soft lava**	**quartzite**	**soft lava**	**shale**
Young's modulus (GPa)	72,35	63,55	60,83	82,77	66,99	61,01
Poisson's ratio	0,21	0,14	0,27	0,11	0,22	0,25
Cohesion (MPa)	73	49	28	22	29	40
Friction angle	35	34	14,5	27	34	28
Tension cut-off (MPa)	7,3	4,9	2,8	2,2	10,7	13,5
Dilation	10	10	8,6	8,8	10	10

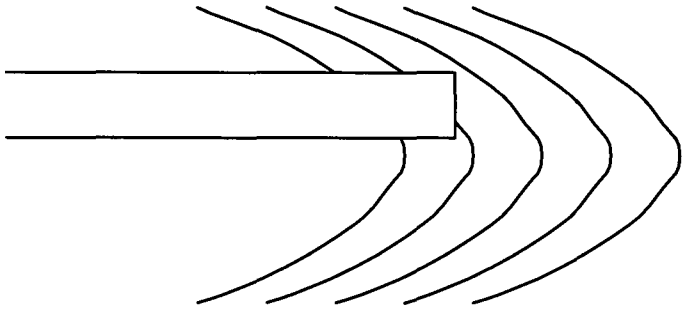

(a) type I (e.g. Deelkraal)

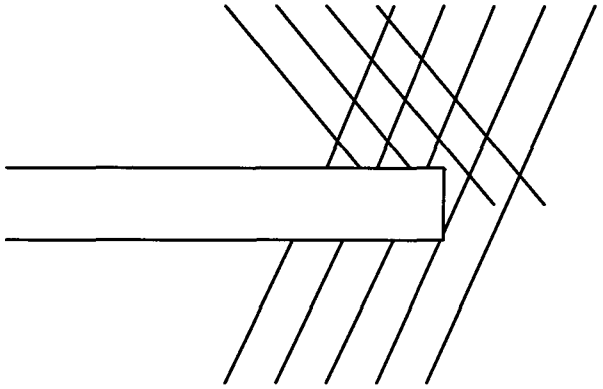

(b) type II (e.g. Kloof)

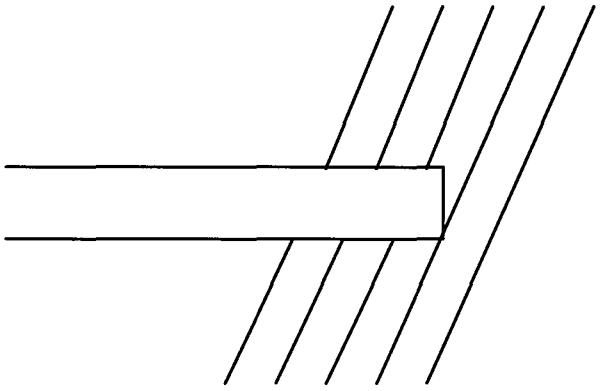

(c) type III (e.g. East Driefontein)

Figure 2.4.7.2 The mining induced fracture patterns observed in different geotechnical areas.

The fracture patterns of the three typical VCR combinations are modelled using a random Delaunay mesh comprising 2000 segments and having an average segment length of 0,5m. The initial vertical and horizontal stress is taken as 54 MPa and 27 MPa, corresponding to a depth of approximately 2000 m, and the thickness of the VCR is taken as 2m. Although the influence of the material contrast on the stress distribution is not very marked due to the mildness of the contrast, it appears that the three different layers can make a significant difference to fracture patterns (see Figure 2.4.7.3), which show some similarity to those from *in situ* observations. For the hard lava/VCR/quartzite combination, there are lower angle fractures dipping toward the face in the hangingwall and higher angle fractures dipping away from the face in the footwall. The inflection point of the fracture pattern appears to be in the footwall. For

the soft lava/VCR/quartzite type, there are two sets of fractures in the hanging wall and only one major fracture set in the footwall, which may somehow explain the weakness of the hangingwall in the real case. For the soft lava/VCR/Jeppestown shale combination, there are two major sets of fractures, one in the hanging wall and one in the footwall, the inflection point of the fracture sets is located in the hanging wall.

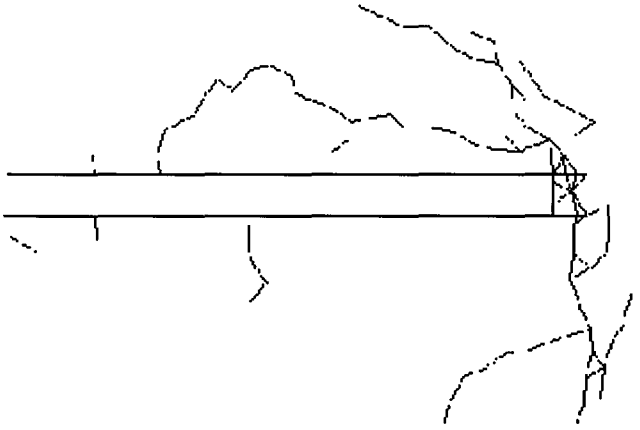

(a) type I (e.g. Deelkraal)

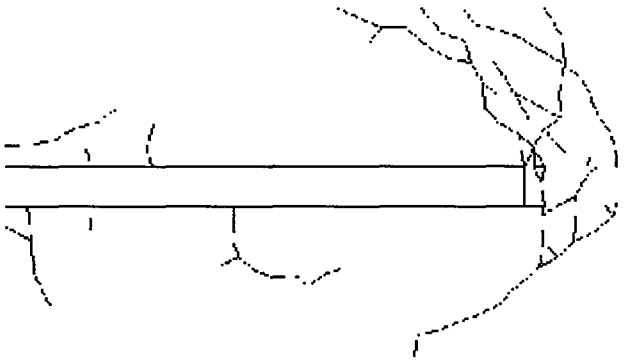

(b) type II (e.g. Kloof)

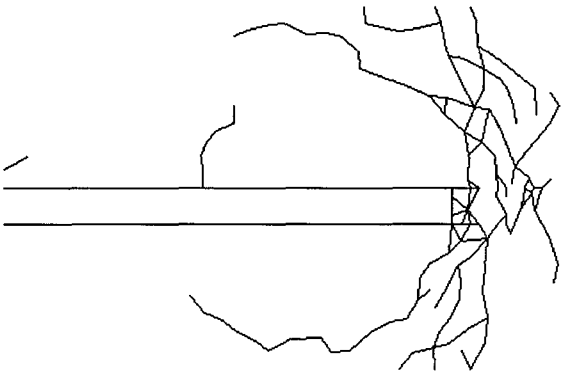

(c) type III (e.g. East Driefontein)

Figure 2.4.7.3 The fracture pattern near the VCR stoping from the numerical simulation.

2.4.7.3 Study of stoping through a dyke

A stope approaching a dyke, with different material properties from the host rock, may trigger slip along the interface or may induce stress concentrations within the dyke leading to seismic activity related to rockbursts. An example problem of a stope approaching and penetrating a dyke (see Figure 2.4.7.4) with properties given in Table 2.4.7.2 is analysed using DIGSL. In order to understand the behaviour of the interface before and after the stope penetrates the interface, the strain energy density distribution was computed for different mining stages. The strain energy density distribution in Figure 2.4.7.5(a) -(d) shows the concentration always at the mining face, and a release of energy along the interface after the mining face reaches the interface.

Table 2.4.7.2 Input data for the example of stoping through a dyke

Property	**Value**
E (host rock)	78 GPa
ν (host rock)	0,21
E (dyke)	120 GPa
ν (dyke)	0,38
σ_v (vertical in situ stress)	54 MPa
σ_h (horizontal in situ stress)	27 MPa (i.e. k=0,5)
t (width of dyke)	5 m
d (step I distance from the mining face to dyke)	5 m
θ (angle between the stope and interface)	90°

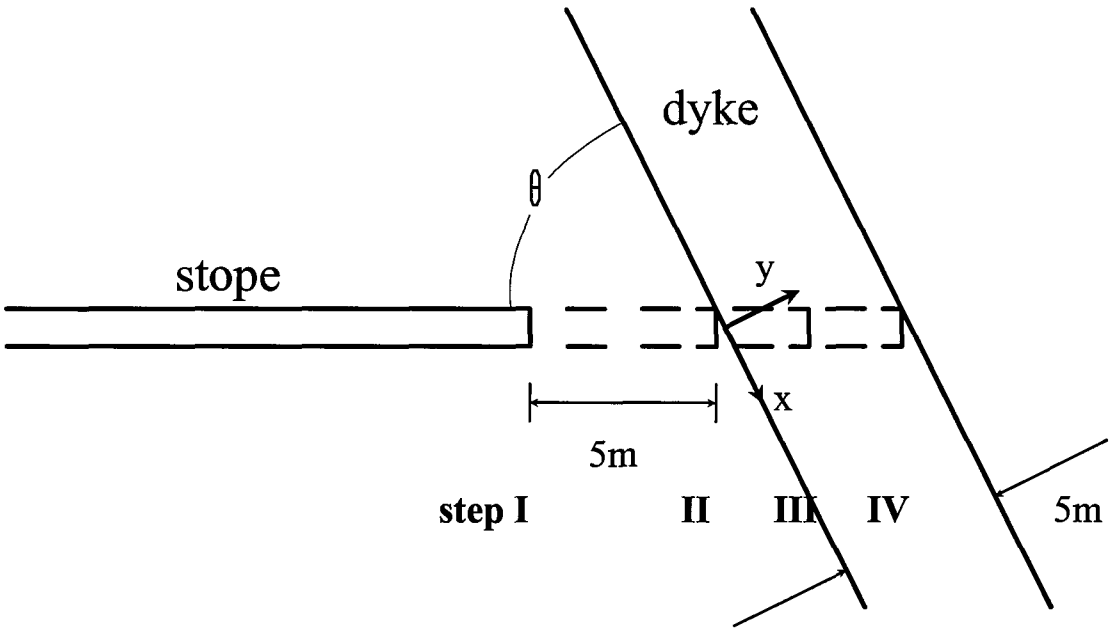

Figure 2.4.7.4 Problem of a stope penetrating through a dyke.

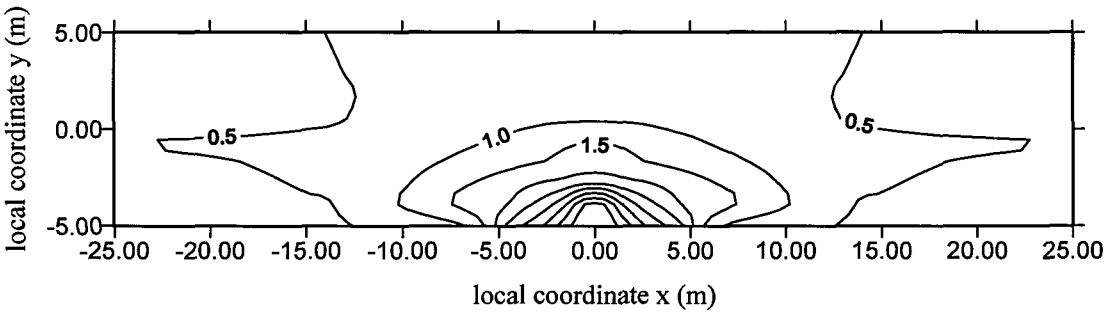

(a) mining face at (0;-5)---5m away from the dyke

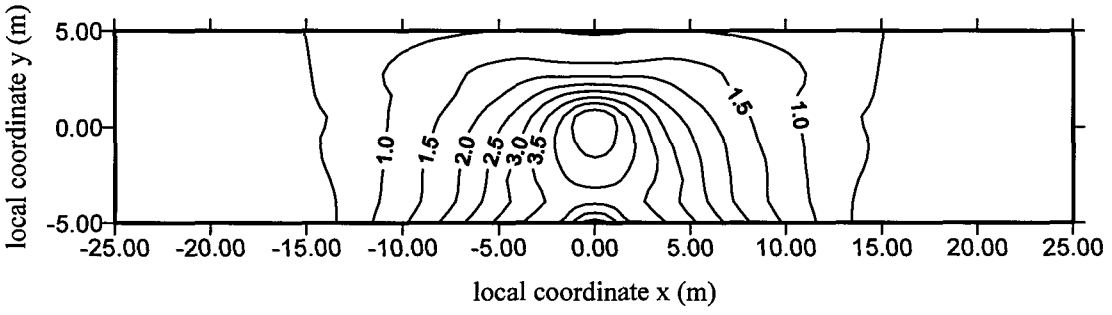

(b) mining face at (0;0)---at the surface of the dyke

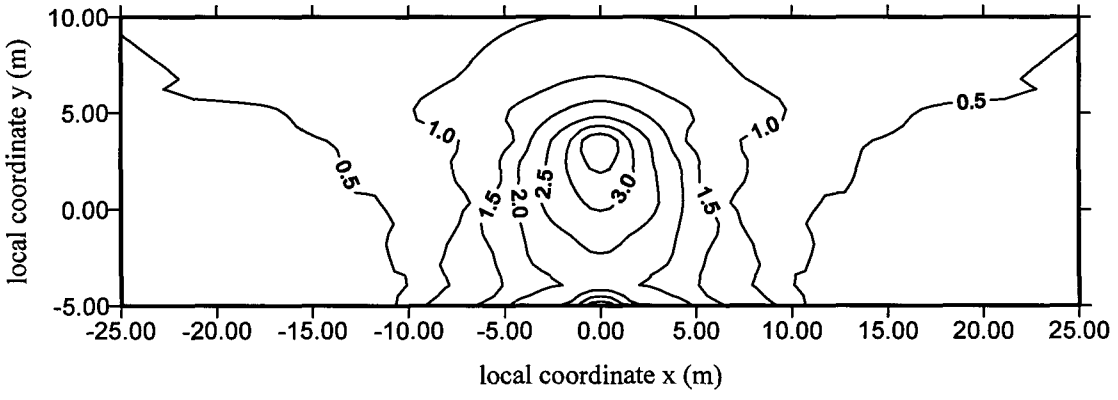

(c) mining face at (0;2,5)---2,5m penetrating into the dyke

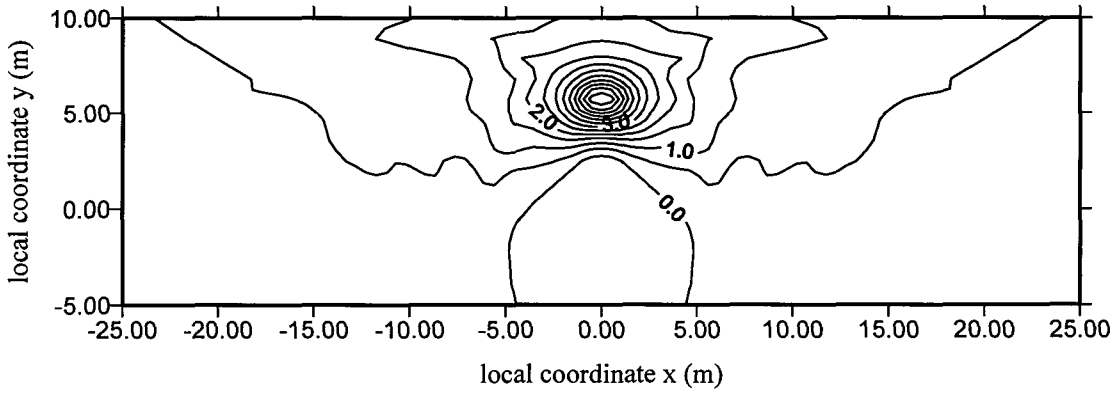

(d) mining face at (0;5)---penetrating through the dyke

Figure 2.4.7.5 The distribution of strain energy density for a stope approaching a dyke.

2.4.7.4 Study of the effect of mining face advance length

The length of the mining face advance may be an important factor in controlling the stability of the fracture zone around the stope. In the previous section, the stope excavation was simulated in one step, however the stoping sequence must be modelled in sequential steps to understand the influence of mining face advance on the fracture zone behaviour. A series of mining simulations were analysed for the two VCR material contrast settings described in Section 2.4.7.3. The effect of the distance of face advance distance was compared using three analyses, by excavating the span in three, five or ten steps, respectively. The results of the analyses for type I (hard lava) and type II (soft lava) are presented in Figure 2.4.7.6 and 2.4.7.7. The results suggest that the fracture patterns are similar for each face advance length. The shorter face advance may lead to more fractures, which suggests more damage (rock falls) and support difficulties. Less fractures are mobilized for the long face advance, which suggests a higher rockburst potential as the energy released per unit length of fracture is higher.

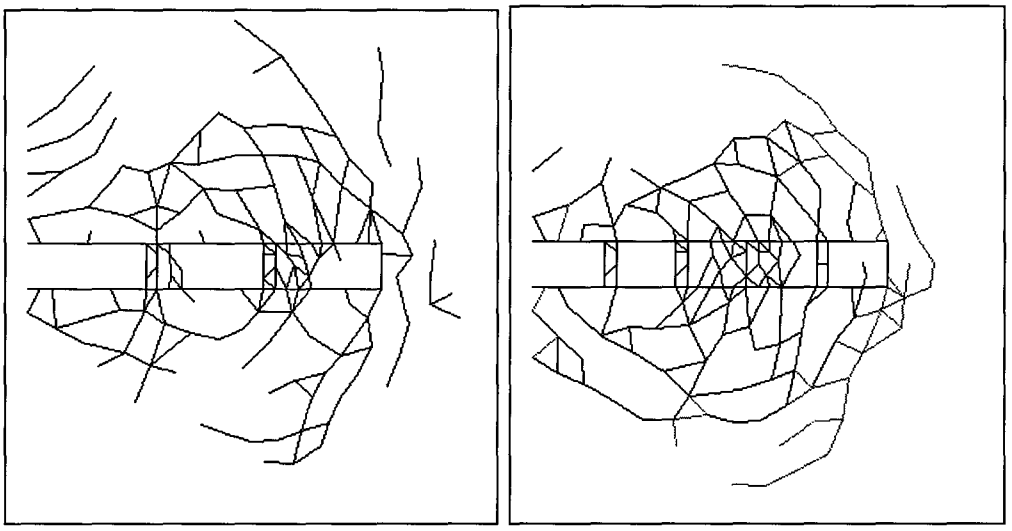

a: b:

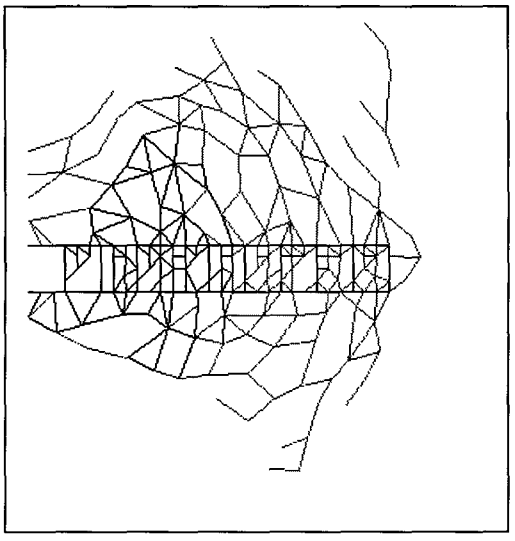

c:

Figure 2.4.7.6 The influence of mining rate on the fracture patterns - for type I (hard lava) VCR a: stoping in three steps b: stoping in five steps c: stoping in ten steps.

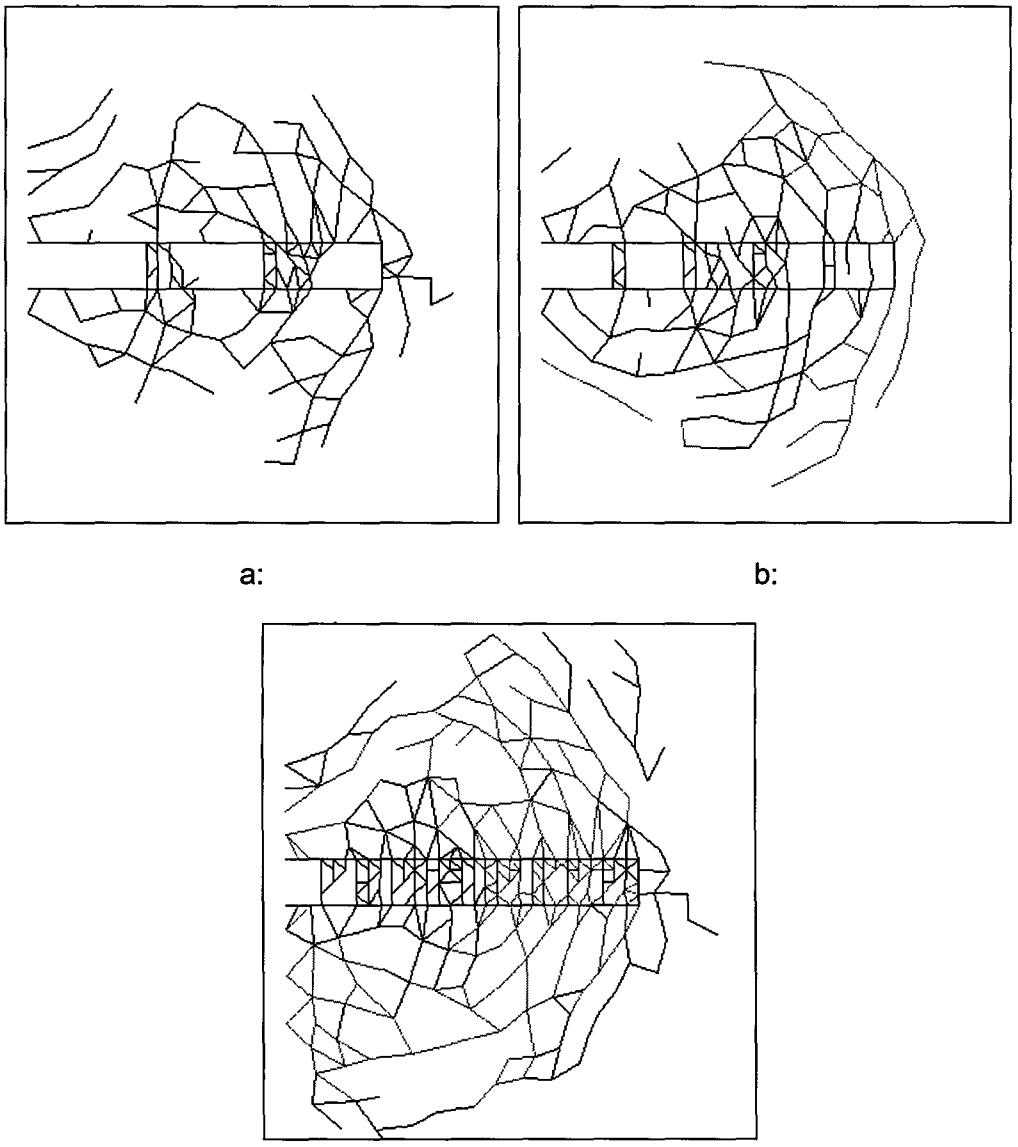

Figure 2.4.7.7 The influence of mining rate on the fracture patterns - for type II (soft lava) VCR. a: stoping in three steps b: stoping in five steps c: stoping in ten steps.

The inclusion of layered elastic materials in the boundary element formulation was accomplished by a superposition scheme. The model is capable of systems comprising three layers. The procedure can be extended to treat problems with more than three layers as well as the analysis of three dimensional problems.

2.4.8 Three-dimensional modelling of fracture processes and mining sequence automation

The design and coding of a three dimensional version of the DIGS code (3DIGS) has proceeded as part of the GAP332 project. The system utilizes a volumetric lumping scheme to allow large scale problems to be analysed. The program data structure has been designed to allow for the future implementation of multiple material regions. The 3DIGS program currently uses constant variation, polygonal shaped, displacement discontinuity elements and includes logic to allow time-dependent viscoplastic slip on designated elements. Future versions will include so called direct boundary elements for solid body and cavity problems. Potential applications of the code will be to studies of micro-mechanical 3D failure processes, seismic diffusion problems and the selection of optimal extraction rate and mine layout sequences.

An equivalent crack concept has been introduced to reduce run times in solving large scale interacting crack growth problems. Initial testing of this scheme has indicated that the method works reasonably well but can lead to errors in the estimation of remote stresses of the order of ten per cent when set to run at the maximum possible speed. A sacrifice in the speed by a factor of about nine, allows the error to be reduced to approximately one per cent. In order to improve this situation an investigation of numerical integration schemes for influence kernel computation has also been undertaken. The numerical scheme shows good correlation with the analytical scheme for inter-element distances of about two element diameters. In addition, the numerical approach allows the potential treatment of both higher order variation of the crack discontinuity shape and the introduction of curvilinear elements if required.

Some successful tests of the 3DIGS code on fracture growth near a lead-lag face geometry have been carried out. Other tests involving single reef or stope-reef intersection problems have also been completed. However, the simulation of the failure of a cubic shaped block filled with triangular elements, arranged on the faces of contiguous tetrahedra, gave rise to numerical instabilities. It appears that these instabilities are caused by the strongly singular behaviour of acutely angled piecewise constant elements used in the current version of the code. As noted previously, a higher order scheme is being developed to address this problem. An outline of the lumping scheme techniques together with some preliminary applications is given in the next sections. In addition, some indication of the potential use of the code for the selection of optimized mining sequence policies is given.

2.4.8.1 Large scale three-dimensional problems

For mine design purposes it is very desirable to represent stress transfer and seismic recurrence effects as a definite mechanistic (though not necessarily deterministic) process which can be analysed numerically in routine mine design studies. One of the major challenges in reaching this goal is the ability to model large scale damage, recognizing that fracturing occurs on a multiplicity of length scales. The essence of the problem therefore is not merely to implement efficient numerical solution procedures for large systems of equations but, in addition, to be able to represent the self-organizing fracture coalescence processes on many scales. A number of attempts to address these goals have been made using renormalization solution concepts (Madden 1987, Allegre et. al. 1995, Main 1995) based on concepts of critical phenomena in physics (Wilson 1979). The present section presents some initial steps towards the formulation of a general solution scheme. This incorporates time-dependent stress relaxation effects in a three dimensional model and also allows hierarchical failure processes to be modelled by approximating the inelastic strain in a given region as a special set of appropriately aligned crack elements. Failure is represented by means of discontinuity elements at all hierarchical levels, enabling fracture coalescence and clustering to be manifested at all scales.

Cracks are modelled conveniently by means of small strain dislocations or so-called displacement discontinuities (Crouch & Starfield 1983). The displacement discontinuity vector is

defined at point Q of a crack surface by the jump in the displacement vector $u_i(Q)$ across the surface. In the case of a discontinuity across a flat surface A, it is convenient to define a local coordinate axis system where the discontinuity falls in the x-y plane and the z-axis is perpendicular to the discontinuity. If the discontinuity vector $D=[D_x,D_y,D_z]^T$ is constant over the surface A, the stress tensor components τ_{ij} at a field point P in the local axis system are given by

$$T = KD \tag{2.4.8.1}$$

where $T=[\tau_{xx},\tau_{yy},\tau_{zz},\tau_{yz},\tau_{zx},\tau_{xy}]^T$ and where the components of the influence matrix *K* are expressed in terms of the derivatives of the Newtonian potential integral over the surface of the discontinuity. Details of the influence function components are given in the final SIMRAC report for project GAP029 (Napier et. al. 1995). When the field point P is chosen at a specific point P_0 inside the polygon A, the local traction vector components T_x, T_y, T_z at point P_0 can be written in the condensed form

$$\begin{bmatrix} T_x \\ T_y \\ T_z \end{bmatrix} = \begin{bmatrix} K_{xx} & K_{xy} & 0 \\ K_{yx} & K_{yy} & 0 \\ 0 & 0 & K_{zz} \end{bmatrix} \begin{bmatrix} D_x \\ D_y \\ D_z \end{bmatrix} + \begin{bmatrix} E_x \\ E_y \\ E_z \end{bmatrix} \tag{2.4.8.2}$$

where $[E_x \quad E_y \quad E_z]^T$ is the external influence due to the primitive stress field and other mobilized discontinuities. Equation (2.4.8.2) can be used as the nucleus of an iterative scheme to solve the mutual interaction between an assembly of discontinuity elements A^i (Ryder & Napier 1985). This scheme can be extended to allow for the time-dependent relaxation of a set of discontinuity elements if it is postulated that the rate of shear slip is proportional to the net shear stress acting at point P_0. In particular, assume that

$$dD_s / dt = \kappa(\tau - \tau_r)^\beta \tag{2.4.8.3}$$

where $D_s = \sqrt{D_x^2 + D_y^2}$ is the total slip and κ and β are parameters controlling the slip rate. The resultant shear stress τ and shear resistance τ_r are given by

$$\tau = \sqrt{T_x^2 + T_y^2} \tag{2.4.8.4}$$

$$\tau_r = S_0 - \mu T_z \tag{2.4.8.5}$$

respectively, where S_0 is a residual cohesion and μ is the coefficient of friction controlling the resistance to slip. These parameters can also be considered to be functions of time, slip rate and of the local stress state but there is at present very little data available to support any specific assumptions concerning the potential form of these relationships. It should be noted that in Equation (2.4.8.5), T_z is assumed to be negative when compressive. Equation (2.4.8.3) can be written in discrete form as

$$\Delta D_s = \kappa(\tau - \tau_r)^\beta \Delta t \tag{2.4.8.6}$$

where Δt is a suitably small time step. The slip components are chosen to be in a direction $[D_x^0, D_y^0]^T$ which tends to reduce the shear stress to zero. Specifically, once ΔD_s is determined from Equation (2.4.8.6), D_x and D_y are given by

$$\begin{bmatrix} D_x \\ D_y \end{bmatrix} = \gamma \begin{bmatrix} D_x^0 \\ D_y^0 \end{bmatrix} \tag{2.4.8.7}$$

where $$\begin{bmatrix} D_x^0 \\ D_y^0 \end{bmatrix} = -\begin{bmatrix} K_{xx} & K_{xy} \\ K_{yx} & K_{yy} \end{bmatrix}^{-1} \begin{bmatrix} E_x \\ E_y \end{bmatrix} \tag{2.4.8.8}$$

and $$\gamma = \Delta D_s / \sqrt{(D_x^0)^2 + (D_y^0)^2} \tag{2.4.8.9}$$

Consider now a problem comprising N interacting displacement discontinuity elements. In order to evaluate the total traction vector T^i at point P_0^i of element i it is necessary to compute the sum

$$T^i = \sum_{j=1}^{N} K^{ij} D^j + V^i \tag{2.4.8.10}$$

where K^{ij} represents the influence at receiving point P_0^i due to sending element j as given by Equation (2.4.8.1) with a suitable stress rotation to the local receiving element coordinate system. V^i is the primitive stress state at point P_0^i. Designate the computational effort required to compute one of the entries in the sum of Equation (2.4.8.10) as a basic influence computation. Consequently, the total number of influence computations required for the evaluation of the traction vector at all receiving elements is equal to

$$I_B = N^2 \tag{2.4.8.11}$$

In order to reduce this computational effort, it is assumed that the problem space is partitioned into a number of cubic cells such that each cell forms one of eight equal sized members of a parent cell and itself contains eight daughter cells (an "octree" structure). Suppose that the side length of each finest level cell is L_F , then the size L_n of a cell at a given level n is given by

$$L_n = 2^{n-1} L_F \quad ; \; n \geq 1 \tag{2.4.8.12}$$

The representative cell volume increases by a factor of eight for each unit increase in n ($L_{n+1}^3 = 8L_n^3$). It is further assumed that at the finest level the cells are located in fixed spatial positions and have unique address indices (i,j,k). In particular, the cell (1,1,1) is assumed to occupy the cube $0 \leq x < L_F$, $0 \leq y < L_F$, $0 \leq z < L_F$. The index address of any cell at any level can be determined uniquely by the following recurrence relations.

$$i_{L+1} = \lfloor i_L + 1 \rfloor / 2 \quad \text{if} \quad i_L \geq 0$$

$$i_{L+1} = -\lfloor |i_L| \rfloor / 2 \quad \text{if} \quad i_L < 0 \tag{2.4.8.13}$$

It should be noted that schemes similar to the hierarchical process described here, termed lumping, have been used previously for the solution of three dimensional cavity problems (Deist & Georgiadis, 1976) and for the solution of large scale tabular mining problems (Ryder & Napier, 1985).

Consider now a solution strategy where the stress influences at all elements in a finest level cell (level 1) are computed directly from sending elements within a specified inner region surrounding the cell. Outside this inner region and inside a specified outer region, the stress

influence is computed at R designated interpolation points surrounding the receiving cell by using a fixed number S of equivalent discontinuity elements which are specified in each sending cell. Let the overall problem dimension be D and suppose that the average element density is ρ. The total number of elements N is therefore given by

$$N = \rho D^3 \tag{2.4.8.14}$$

The number of finest level cells is

$$N_F = (D / L_F)^3 \tag{2.4.8.15}$$

The receiving cell A is surrounded by a cubic region of fine cells whose side is defined as a multiple of the cell size, L_F, and an outer cube whose side is the same multiple of the parent cell size, $2L_F$. It should be noted that the inner ring falls on the grid system of cell A and the outer ring falls on the grid system of the parent cell A_P. The sizes of the inner and outer regions, h and H respectively, are determined by defining a cell gap parameter g such that

$$h = (2g+1)L_F \quad \text{and} \quad H = 2h \tag{2.4.8.16}$$

Hence, the total number of direct influences on elements within the inner rings of all finest level cells is given by

I_D = (Number of elements in each fine cell)

X (Number of elements in inner ring)

X (Number of fine cells)

Using the parameter definitions this can be expressed as

$$I_D = (\rho L_F^3)(\rho h^3) N_F \text{ , whence,}$$

$$I_D = (2g+1)^3 N^2 (L_F / D)^3 \tag{2.4.8.17}$$

The total number of indirect influences from cells in the region between the inner and outer rings is given by

I_F = (Number of influences per sending cell)

X (Number of sending cells)

X (Number of receiving points per cell)

X (Number of receiving cells)

This can be shown to be equal to

$$I_F = 7SR(2g+1)^3 (D / L_F)^3 \tag{2.4.8.18}$$

The total number of influences, $I_D + I_F$, is therefore

$$I_T = (2g+1)^3 [N^2 (L_F / D)^3 + 7SR(D / L_F)^3] \tag{2.4.8.19}$$

It can be seen from Equation (2.4.8.19) that there is a tradeoff between the number of direct influences, which decreases as L_F is decreased, and the number of cell influences which increases as L_F is decreased. The optimum choice of D/L_F is given by

$$(D / L_F)^* = (N^2 / 7SR)^{1/6} \tag{2.4.8.20}$$

and the corresponding minimum number of influence computations is given by

$$I_T^* = 2(2g+1)^3 \sqrt{7SR}\, N \tag{2.4.8.21}$$

The most significant point of Equation (2.4.8.21) is that the total computational effort is now proportional to N rather than to N^2. (This conclusion is still valid if all the remaining coarse level cells, above the first level, are considered). Furthermore, the breakeven number of elements, N_c, for the hierarchical scheme to be more efficient than direct evaluation of influences, is such that $I_T^* < N^2$. Consequently, the hierarchical scheme is more efficient if

$$N > N_c = 2(2g+1)^3 \sqrt{7SR} \tag{2.4.8.22}$$

In the particular case when g=1, S=3 and R=27, N_c=1286.

A crucial aspect of achieving the computational performance demonstrated for the hierarchical solution scheme, is that the number, S, of equivalent discontinuities used in each sending cell should be fixed. It is also desirable for the chosen set of equivalent cracks to provide a physical representation of the coalesced fracture structure which arises from the fine level elements in a given cell. It is proposed that a suitable equivalent crack set can be constructed using three orthogonal, rectangular shaped, discontinuity elements that are centred on the approximate centre of gravity of the mobilized fine level elements in the cell. The orientations of the three representative cracks are assumed to be aligned with the principal directions of the crack density tensor in the designated volume. Following Kachanov 1993, define the components of the crack density tensor α_{rs} by

$$\alpha_{rs} = (1/V)\sum_k (A_k / \pi)^{3/2} n_r^k n_s^k \tag{2.4.8.23}$$

where the sum is over all elements k within the volume V. A_k is the area of the k^{th} crack and n_i^k are the components of the normal to the k^{th} crack. Let the principal direction vectors of the crack density tensor be designated by X^1, X^2, X^3 respectively. The average strain due to all cracks in the volume V is

$$< \varepsilon_{ij} >= \frac{1}{2V} \int_A [D_i(Q) n_j(Q) + D_j(Q) n_i(Q)] dS_Q$$

or, in approximate form

$$< \varepsilon_{ij} > \approx \frac{1}{2V} \sum_k A_k [D_i^k n_j^k + D_j^k n_i^k] \tag{2.4.8.24}$$

where k is again summed over the crack elements falling in V and D_i^k, n_i^k designate the components of the discontinuity vector and normal vector for the k^{th} crack, rotated to the principal axis system of the crack density tensor. Assume now that for the three equivalent cracks,

$$\frac{1}{2}\sum_{k=1}^{3} A_k[\hat{D}_i^k X_j^k + \hat{D}_j^k X_i^k] =< \varepsilon_{ij} > \qquad (2.4.8.25)$$

Equation (2.4.8.25) represents a system of six equations (due to the symmetry of the strain tensor) in the nine unknown displacement discontinuity components $\hat{D}_i^k$ of the equivalent cracks. If it is assumed that $\hat{D}_i^k = \hat{D}_k^i$, Equation (2.4.8.25) is satisfied provided

$$\hat{D}_i^j = 2 < \varepsilon_{ij} > /(A_i + A_j) \qquad (2.4.8.26)$$

The areas A_i of each equivalent crack are assumed to be given by the sum of the projections of all the cracks in the representative volume onto the planes normal to each principal direction of the crack density tensor. The effectiveness of this scheme for the assignment of equivalent crack sets was tested by considering two cases. In the first case a square plane of side 100m is covered by a set of 50 random Delaunay triangular elements. The plane is assumed to be parallel to the x-axis of the global coordinate system and inclined at 70 degrees to the x-y plane. The crack elements on the plane are allowed to slip in response to a compressive stress field of 600 MPa applied in the z-direction. The resultant stress field is evaluated at particular points along a line in the y-direction, starting at the point x=50, y=50, z=50. The values of two selected components τ_{yy} and τ_{yz} are plotted as solid lines in Figure 2.4.8.1. The values corresponding to the equivalent crack set are plotted as broken lines in Figure 2.4.8.1. If it is assumed that the original set of 50 crack elements is located in a cell occupying the region with diagonally opposite vertices (-50,-50,-50) to (50,50,50) then L_F = 100 and the effective position of the inner boundary of the first level influence cell is at y = 150. It can be seen from Figure 2.4.8.1 that the agreement between the equivalent set of cracks and the actual stress components is excellent for values of y beyond the inner boundary.

In the second case, the vertices of the triangles used in the first test were perturbed randomly in the normal direction to the nominal plane to form an irregular surface. The system was solved again with the external field stress of 600 MPa parallel to the z-axis. The values of the two stress components are compared to the equivalent crack set in Figure 2.4.8.2, again showing excellent agreement beyond the inner boundary. The good agreement also holds if the exact and equivalent discontinuity schemes are compared for the component u_y of the displacement vector as shown Figure 2.4.8.3, for both the smooth and irregular surfaces.

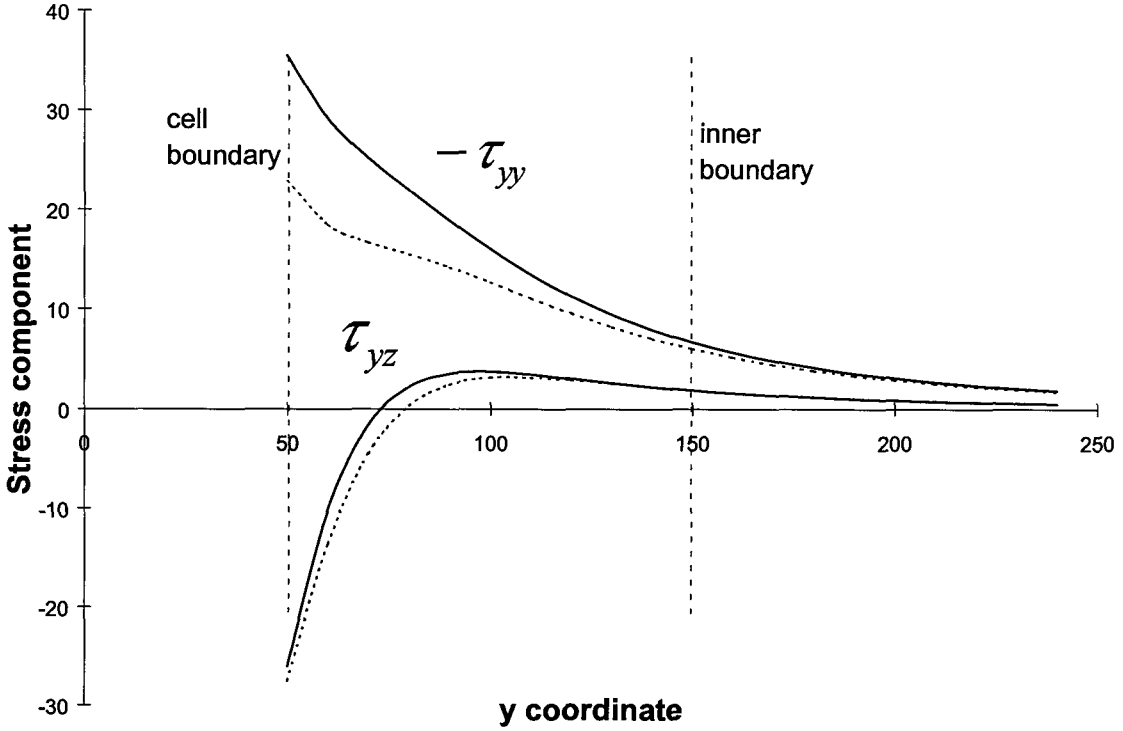

Figure 2.4.8.1 Comparison of stresses, generated by a set of 50 crack elements (solid lines) on a plane, to the stresses due to an equivalent single crack (broken lines).

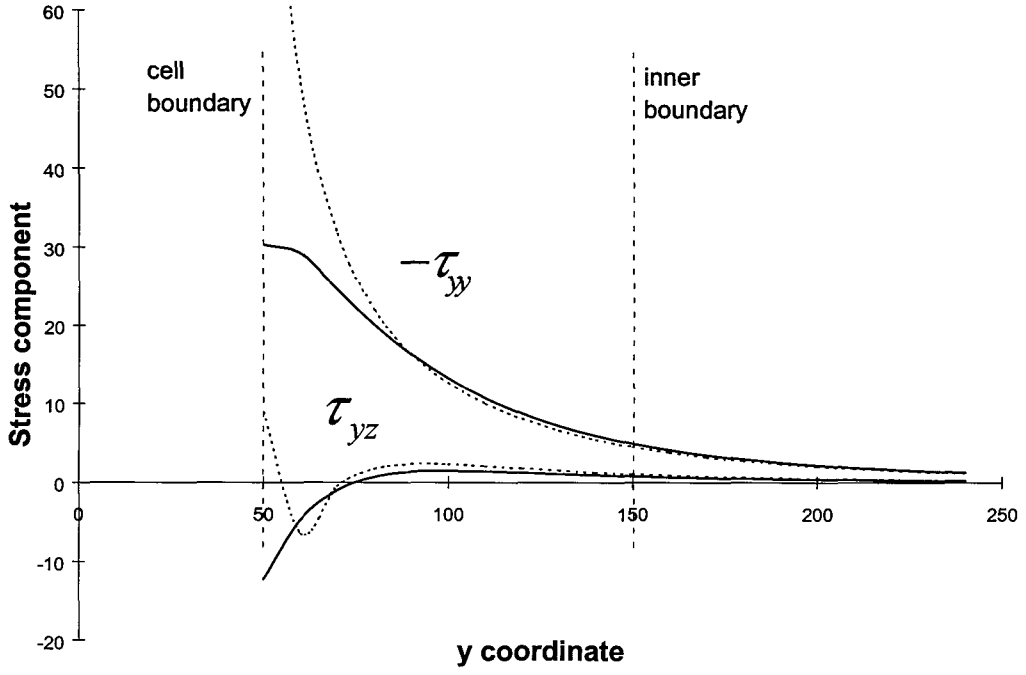

Figure 2.4.8.2 Comparison of stresses generated by a set of 50 crack elements, irregularly perturbed about a nominal plane (solid lines), to the stresses due to an equivalent set of three cracks (broken lines).

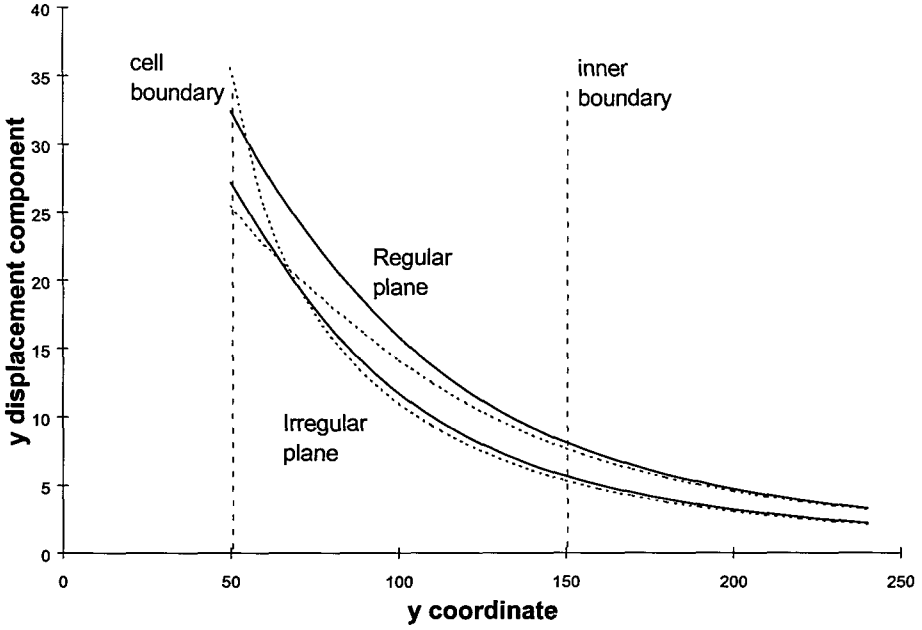

Figure 2.4.8.3 Comparison between the exact (solid lines) and equivalent discontinuity sets (broken lines) for the displacement component u_y.

The hierarchical solution scheme described here, together with the slip relaxation model can be applied to the analysis of time-dependent seismic energy release near deep level mining excavations and the analysis of rate of mining policies. Full-scale trials of the scheme have not yet been carried out. Important future investigations will address the mechanisms of stress accumulation on fault planes and the processes of stress transfer and diffusion in the rock mass as a function of the mining rate. The hierarchical equivalent crack solution scheme offers a first step in representing fracture clustering and localization processes on multiple length scales. The proposed solution method opens some exciting possibilities for the analysis of multi-scale, three-dimensional damage modelling and time-dependent stress transfer processes in deep level mines.

2.4.8.2 Automation of mining sequence selection

A particular application of the 3DIGS code is to evaluate optimum mine layout extraction sequences. In conventional MINSIM runs, this is carried out by solving the closure and ride distributions associated with a number of proposed extraction scenarios and then choosing the best sequence according to several mine evaluation criteria. These criteria include the energy release rate concept (ERR) and other measures of mining hazard such as the so-called excess shear stress" (ESS). It may be of some assistance to the mine planner if the best extraction sequences could be selected automatically according to some sensible overall objective function. For example, it may be considered appropriate to determine the mining sequence such that the maximum energy release arising in any one mining step never exceeds a given level or is required to be as small as possible. Some thought will show that it is not obvious how such a sequence should be chosen, even in apparently simple situations. This can be illustrated by noting that for a particular block of ground that is to be extracted in N mining increments there are N factorial extraction sequences that could in fact be chosen. When $N=10$ this reduces to approximately 3,6 million alternatives. For practical problems where N may range from a hundred steps to several thousand steps, it is not feasible to solve the problem by direct combinatorial evaluation of all possible sequences. However, in certain special cases it is possible to deduce the optimal solution directly. For a single parallel sided mining panel in a uniform stress field, it can be shown that if the panel is extracted on one or both sides, the energy release rate increases in proportion to the span of the panel. Furthermore, it can be shown by numerical or analytical calculations that when a pillar inside the panel is extracted, the

energy release is always greater than if the same area is extracted from one of the abutments. Consequently, for a single panel, the optimal extraction sequence which ensures that the maximum energy release in any one step is as small as possible, is to extend the span uniformly on one or both sides from a specified starting point. It must be emphasized that this conclusion might have to be revised if off reef fracturing is explicitly modelled. In a similar manner, it is possible to show that the energy release from mining the corner elements of a square region will be less than if the mid-side of each edge is mined. The optimal mining policy, satisfying the objective of yielding a minimum of the maximum energy release in any step and which preserves the overall square shape, is then to mine symmetrically from the centre of each side towards the corners.

It is also of interest to evaluate the mining sequences that arise when certain local extraction policies are followed. Consider two extreme cases of tabular mining. In the first case, suppose that each mining block is selected according to the rule that the block must be adjacent to an existing mined block and that the average normal stress acting on the block should be a minimum. Let this policy be designated as SMIN. The results of applying this policy to a rectangular tabular region are illustrated in Figures 2.4.8.4a and 2.4.8.4b, which show the resulting mining pattern after 120 and 200 mining steps respectively. The starting block is marked in each case. From this apparently desirable local policy, it is apparent that the mining proceeds in a way which requires a self-avoiding extraction path. Clearly though, the ultimate mining pattern, as shown in Figure 2.4.8.4b, results in a number of scattered remnants which can be expected to behave in a hazardous manner when mined. The detailed mining sequence is strongly dependent on the starting position of mining relative to the boundaries of the overall extraction region. This is seen in Figure 2.4.8.5 where the starting point is centrally located with respect to the overall region.

A second local mining policy, designated as SMAX, is to select each successive mining block according to the requirement that the selected block is subjected to the maximum normal stress of all the candidate blocks. In this case the more coherent mining pattern, shown in Figure 2.4.8.6, is seen to evolve. It is interesting to note that the local SMAX mining policy will actually result in a mining pattern that is very similar to the global objective which requires the maximum energy release arising in any mining step to be as small as possible. Again, it must be noted that inelastic effects related to fracture zone deformation or large scale fault slip will, in general, modify the optimal extraction sequence.

It is suggested that the 3DIGS framework can be used to evaluate proposed mining policies automatically and that explicit off-reef deformations may also be included in these evaluations. A detailed exploration of these possibilities has not been carried out. It would also be of interest to combine the automatic mining sequence selection with a simulation of off-reef seismic activity as proposed by Salamon, 1993. In this case, off-reef seismic activity is generated by the mining induced stress field which sweeps through a volume of postulated randomly sized and positioned flaws as the mining progresses. The implications of selecting a mining policy such as SMAX can be tested against the expected seismic activity and modified if necessary.

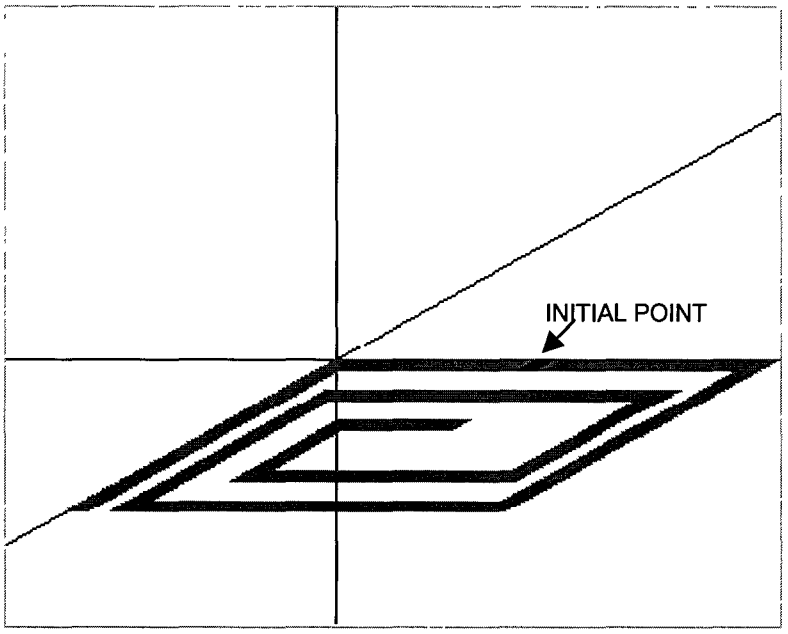

(a)

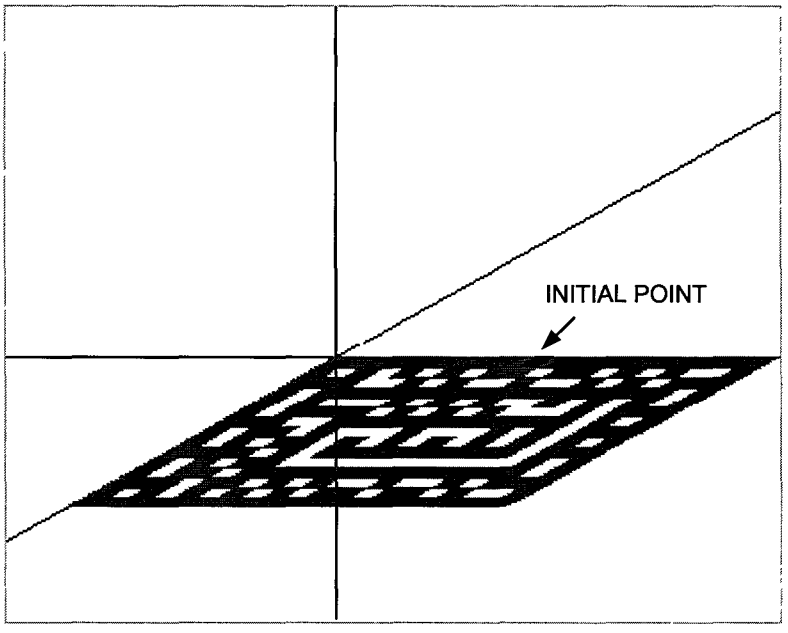

(b)

Figure 2.4.8.4 Automatic mining by selecting blocks having a minimum average stress. (a) 120 steps, (b) 200 steps.

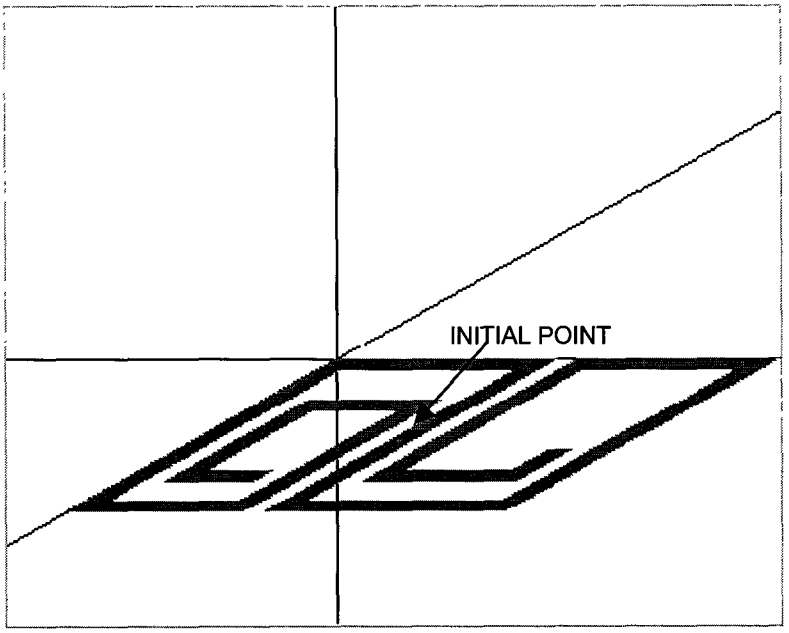

Figure 2.4.8.5 Automatic mining by selecting blocks having a minimum average stress: central starting point.

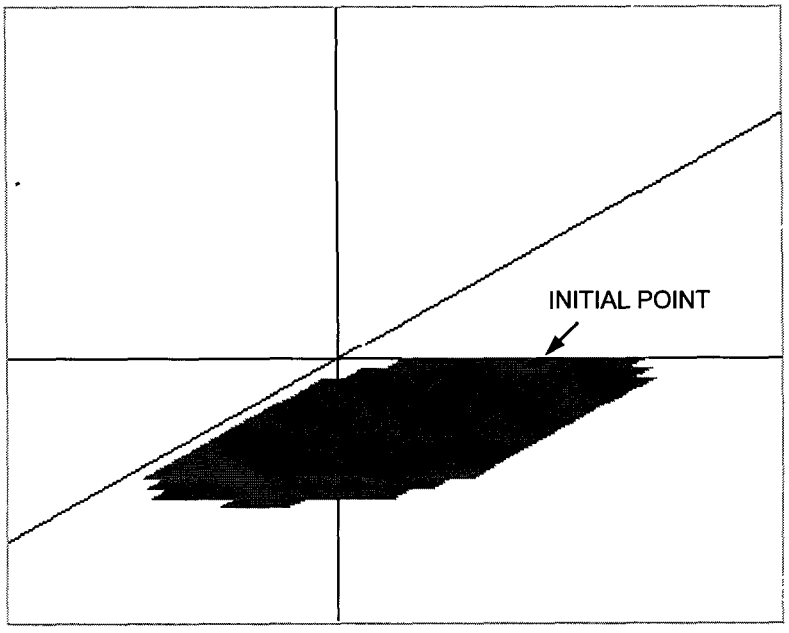

Figure 2.4.8.6 Automatic mining by selecting blocks having a maximum average stress.

2.5 Conclusions

The work presented in this section represents a significant advance in the understanding of fracture processes in hard rock. Considerable advances have been made to the numerical modelling programs that were developed as part of GAP029, and new methods have been implemented.

The study of microfractures in rock samples tested in laboratory triaxial extension experiments has provided a wealth of information regarding the nucleation, growth and coalescence of fractures. The consideration of thin sections of the sample as well as the surface fractography has resulted in a full three dimensional picture of fracture growth. Fracture surfaces that appear to grow in one direction have many component microfractures, some even growing towards the expanding fracture front. Numerical modelling of a two-dimensional section through the samples using the standard DIGS displacement discontinuity program has proved that the numerical techniques are able to capture the nucleation from flaws and the effect of larger scale stress re-distributions by grain boundaries. Further verification studies are presented in Section 4 of the report.

The coalescence of the fractures depends on a complicated process whereby tensile stresses produced ahead of growing fractures initiate other fractures and lead to a localized failure surface on a larger scale. In certain cases, the compressive stress regions induced by the flaws, perpendicular to the initiated fractures, can halt the growth of other fractures. Thus, the presence of flaws can both induce and inhibit fracture growth and the final fracture density will depend on the flaw density, and hence the rock fabric. The observation of these features from surface fractography provides a basis for the development of three dimensional modelling programmes, and also enables forensic studies of fractures that will assist in identifying the origin of fractures that have caused, or arisen from, rockfalls and rockbursts.

The tessellation approach to modelling, developed in project GAP029, was a major advance in the modelling of rock fracture processes. This allows the fracture pattern to develop with the minimum input from the program user as opposed to the standard DIGS method that requires the user to pre-select the fracture initiation sites. A new fracture activation concept has been developed to apply in the tessellation models that includes only the sliding resistance and tensile strength that can be considered to be fundamental parameters of the rock. Flaws, with only a sliding resistance, placed randomly throughout the mesh, induce local zones of tension, and initiate potential tensile fractures. The method can model the transition from axial splitting to localized shear failure and finally multiple shear band formation with increasing confining pressure, that is observed in laboratory tests. The method is able to respond to different stress paths, e.g. the extension test, and correctly predict the fracture pattern. The method can be expanded into three dimensions, and can be applied within the context of 3D boundary element analysis methods that have been developed and implemented as part of this project. The 3D program 3DIGS is still in an early stage of development, but the results from the fracture studies will provide excellent data with which to verify the numerical outputs.

The tessellation method has been applied in the modelling of stope scale problems. The multipole method developed in project GAP029 is applied to obtain memory savings that permit the analysis of an order of magnitude more elements, than are allowed in the standard boundary element formulation. The stope scale problems highlighted the need for a more systematic approach to the selection of the multipole parameters to optimize the memory saving. A scheme that produces a saving that is close to optimal was developed and included in a prototype user interface to facilitate the building of models. Studies of the fracture zone behaviour predicted by the models and the comparisons with underground observations are presented in the final section of this report.

The time-dependent behaviour of the rock mass has been identified as an important factor controlling the closure of stopes and the potential for face bursting. Laboratory studies of the

uniaxial creep of intact rock samples indicated that the hard rocks of the South African gold mines exhibit measurable creep strains and follow the characteristic primary, secondary and tertiary creep phases. For a particular stress level, the creep rate of the quartzites were found to be higher than that of hard lavas. If, however, the different samples are loaded to 90% of their respective failure strengths (which is much higher for the lava), the creep rates are approximately similar. The dependence of the strain rate on the stress level can be modelled successfully with a power law. Discontinuities exhibit an instantaneous response to shear stress followed by primary creep and then a steady state response. Extension fractures in lava exhibit negligible creep compared to bedding planes or gouge filled discontinuities, which may be a reason for the low time-dependent closure rates in VCR (hard lava) stopes, compared to stopes in layered rock, such as the Carbon Leader and Vaal Reefs.

A continuum viscoplastic model, based on the Mohr-Coulomb failure criterion, was developed to allow simulation of the time-dependent fracture zone behaviour. The model includes a novel time-dependent cohesion weakening rule to simulate time-dependent failure. The model predicts that regions around an excavation with high stresses, exceeding the failure state, will fail first and followed by a gradual transfer of stress to the unfailed rock until an equilibrium state is attained. The instantaneous response to blasting, and subsequent primary and steady state closure phases observed in tabular stopes can be well represented.

A shortcoming of the continuum approach is the inability to consider the creep response of specific discontinuities. The framework for a discontinuum viscoplastic model was developed in order to control the rate of slip on individual fractures, partings or other discontinuities. The rock fabric is represented by a random mesh of interacting discontinuities that interact and reproduce the primary, secondary and tertiary creep response of the overall rock mass. The method is applied in Section 4 to the modelling of stopes and the investigation of the rate of mining on energy release.

The methods developed so far, have considered only the strength properties of the rock, and neglected the differences in elastic material properties. A three layer method, based on superposition schemes, has been developed and implemented in a version of the DIGS code. The model has been applied to the modelling of fracture zone development on different reefs and has demonstrated that the effect of the geology on the fracture pattern is significant.

The extension of the modelling capabilities to three dimensions has been initiated with the development of the framework for a three-dimensional boundary element programme 3DIGS. A lumping scheme for far-filed influence computations has been introduced to enable large scale problems to be analysed. The influences of small cracks are represented as an equivalent crack set to effect efficient influence transmission. The method provides an initial step for dealing with the interaction of fractures over a range of physical scales. A preliminary application to the mining of a lead-lag stope has been considered.

A particular application of the 3DIGS code is to evaluate the optimum choice of a number of possible mining sequences. Such sequences can be generated with the next increment to be mined determined by a pre-selected criterion such as minimum normal stress in the block to be mined. The optimal mining sequence can be evaluated by permitting the program to select mining blocks automatically according to the preset criteria. This work is at an early stage and no firm conclusion can be drawn, other than that the optimum overall mining policy does not necessarily result from the policy that seems best at a local mining step point of view. The implications of this work need to be considered further, but have great potential for mining strategy evaluation and selection.

2.6 References

Andriuex, S. Bamberger, Y. & Marigo, J. 1986. Un modèle de matériau microfissuré pour les bétons et les roches, *J Theoret. Appl. Mech.* 5, 471-513.

Abraham, F.F., Brodbeck, D., Rafey, R.A. & Rudge, W.E. 1994. *Phys. Rev. Lett.* 73, 272-275.

Adams, G. R. & Jager, A. J. & Roering, C. 1981. Investigation of rock fractures around deep-level gold mine stopes, *22nd US Symposium on Rock Mechanics*, MIT, 213-218.

Adams, G.R. & Jager, A.J. 1980. Petroscopic observations of rock fracturing ahead of stope faces in deep-level gold mines. *J. S. Afr. Inst. Min. Metall.*, 44, 204-209.

Akagi, T., Ichikawa, Y., Kuroda, H. & Kawamoto, T. 1984. A non-linear rheological analysis of deeply located tunnels. *Int. J. Num. Anal. Meth. Geomech.*, 8, 457-471.

Allegre, C.J., Le Mouel, J.L., Chau, H.D. & Norteau, C. 1995. Scaling organization fracture tectonics (SOFT) and earthquake mechanism. *Phys. Earth Planet. Inter.*, 92, 215-233.

Aydan, Ö., Akagi, T. & Kawamoto, T. 1996. The squeezing potential of rock around tunnels: Theory and prediction with examples taken from Japan. *Rock Mech. Rock Engng.*, 29, 125-143.

Bahat, D. 1996. *Tectonofractography.* Springer-Verlag, Berlin.

Ball, M J.. Landini, D.J. & Bradt, R.C. 1984. Fracture mist region in a soda-lime-silica float glass. In *Fractography of ceramic and metal failures.* Mecholsky and Powell (eds.), ASTM STP 827, Philadelphia, 110-120.

Banerjee, P.K. & Butterfield, R. 1981. *Boundary Element Methods in Engineering Science.* McGraw-Hill, London.

Baste, S. & Audoin, B. 1991. On internal variables in anisotropic damage. *Eur. J. Mech., A/Solids,* 10, 587-606.

Benitez, F. G. & Rosakis, A. J. 1987. Three-dimensional elastostatics of a layer and a layered medium. *J. Elasticity,* 18, 3-50.

Berlenbach, J. & Schweitzer, J, 1997 Rock mass behaviour as predicted by DIGS: Performance evaluation considering underground observations, *CSIR internal report*

Berry, J.P. 1964. Fracture of polymeric glasses, in *Fracture processes in polymeric solids*, Rosen (ed.), Wiley and Sons, NY, 37-92.

Bieniawski, Z.T. 1967. Mechanism of brittle fracture of rock, Part II - Experimental studies. *I. J. Rock Mech. and Mining Sci.*, 4, 407-423.

Bowden, R.K. & Curran, J.H. 1984. Time-dependent behaviour of joints in shale. In: *Proc. 25th Symp. Rock Mech.*, 320-327.

Briggs, D. J. & Vieler, J.D.S. 1984. *Microfracture studies of quartzite in triaxial extension.* COMRO (now Miningtek, CSIR, South Africa) Internal Research Report 12/84.

Briggs, D.J. 1983. *Mechanical properties of quartzites and associated rock-types*, Chamber of Mines of South Africa Internal Report 13/83.

Brummer, R.K. & Rorke, A.J. 1984. *Mining induced fracturing around deep gold mines stopes*, Chamber of Mines of South Africa Internal Report 38/84.

Bufler, H. 1971. Theory of elasticity of a multilayered medium. *J. Elasticity,* 1, 125-143.

Carter, N.L. & Kirby, S.H. 1978. Transient creep and semi-brittle behaviour of crystalline rocks. *Pure Applied Geophysics*, 116, 807-839.

Chen, W. T. 1971. Computation of stresses and displacements in a layered elastic medium. *Int. J. Engng. Sci.,* 9, 775-800.

Chen, W.T. 1971. Computation of stresses and displacements in a layered elastic medium. *Int. J. Engng. Sci.,* 9, 775-800.

Cleary, M.P. 1976. Continuously distributed dislocation model for shear bands in softening materials. *Int J. Numer Meth. Eng.* 10, 679-672.

Cooke, M.L. & Pollard, D.D., 1996 Fracture propagation paths under mixed mode loading within rectangular blocks of polymethyl methacryalate. *J. Geophys. Res.*,101 3387-3400.

Crawford A.M. & Curran J.H. 1981. Rate-dependent behaviour of rock joints: Black quartz syenite. *Proc. Int. Symp. Weak Rock*, Balkema, Rotterdam, 291-296.

Crawford A.M. & Curran J.H. 1983. A displacement discontinuity approach to modelling the creep behaviour of rock and its discontinuities. *Int. J. Num. Anal. Meth. Geomech.*, 7, 245-268.

Crouch, S.I. & Starfield, A.M. 1983. *Boundary element methods in solid mechanics.* George Allen & Unwin, London.

Curran J.H. & Crawford A.M. 1980. Comparative study of creep in rock and its discontinuities. *Proc. 21st Symp Rock Mech.,* Rolla, 596-603.

Day, R. A. & Potts, D. M. 1994. Zero thickness interface elements - numerical stability and application. *Int. J. Num. Anal. Meth. Geomech.*, 18, 689-708.

Deist, F.H. & Georgiadis, E. 1976. *A computer system for three-dimensional elastic analysis using a boundary element approach.* Unpublished COMRO Research Report No: 43/76.

Desai, C.S. & Zhang, D. 1987. Viscoplastic model for geologic materials with generalised flow rule. *Int. J. Num. Anal. Meth. Geomech.,* 11, 603-620.

Dey, T.N. & Wang, C.Y. 1981. Some mechanisms of microcrack growth and interaction in compressive rock failure. *I. J. Rock Mech. and Mining Sci.*, 18, 199-209.

Dieterich, J.H. 1978. Time-dependent friction and the mechanics of stick slip. In *Rock friction and earthquake prediction,* Byerlee and Wyss (eds.), 791-806.

Dusseault, M.B. & Fordham, C.J. 1993. Time-dependent behavior of rocks. In *Comprehensive rock engineering*, vol. 3, Hudson (ed.), Pergamon Press, London, 119-149.

Dyer, J.R. 1983. *Jointing in sandstones, Arches National Park, Utah*, Ph.D. dissertation, Stanford University, Stanford, Calif.

Dyskin, A. V. & Germanovich L.N. 1995. A model of fault propagation in rocks under compression. *Rock Mechanics*, Daemen and Schultz (eds) Balkema, Rotterdam.

Euverte, C., Allemandou, X. & Dusseault, M.B. 1994. Simulation of openings in visco-elastoplastic media using a discrete element method. In*Computer Methods and Advances in Geomechanics*, Siriwardane and Zaman (eds.), Balkema, Rotterdam, 809-814.

Fairhurst, C. & Cook, N.G.W., 1996 The phenomonen of rock splitting parallel to the direction of maximum compression in the neighbouthood of a surface. *Proc. 1 Congr. Int Soc Rock Mech*, Lisbon, 1,687-692.

Fakhimi, A.A. 1992. *The influence of time-dependent deformation of rock on the stability of underground excavations*. PhD thesis, University of Minnesota.

Fakhimi, A.A. & Fairhurst, C. 1994. A model for the time-dependent behavior of rock. *Int. J. Rock Mech. Min. Sci.,* 31, 117-126.

Frasier, J.T. & Rongved, L. 1957. Force in the plane of two joined semi-infinite plates. *J. Appl. Mech.,* 24, 129-174.

Frechette, V.D. 1998. Failure analysis of glass and ceramics, In *Failure analysis : Techniques and applications, Chapter 8, Failure analysis of non- metallics and bio-materials.* ASM International guide, Introductory view from Internet : http;//www.asm-intl.org/www-asm.

Gambarotta, L. & Lagomarisino, S 1993. A microcrack damage model for brittle materials. *Int. J. Solids Structures,* 25, 803-833.

Gay, N.C., Jager, A.C., Ryder, J.A. & Spottiswoode, S.M. 1995. Rock engineering strategies to meet the safety and productivity needs of the South African mining industry. 21st century. J. S. Afr. Inst. Min. Metall., 115-135.

Gioda, G. 1982. On the non-linear 'squeezing" effects around circular tunnels. *Int. J. Num. Anal. Meth. Geomech.,* 6, 21-46.

Gioda, G. & Cividini, A. 1996. Numerical methods for the analysis of tunnel performance in squeezing rocks. *Rock Mech. Rock Engng.,* 29, 171-193.

Gürtunca, R.G. & Adams, D.J. 1991. Determination of the in situ modulus of the rock mass by the use of backfill measurements. *J.S. Afr. Inst. Min. Metall.* 91, 81-88.

Hallbauer, D.K., Wagner, H. & Cook, N.G.W. 1973. Some observations concerning the microscopic and mechanical behaviour of quartzite specimens in stiff, triaxial compression tests. *Int. J. Rock Mech. Min. Sci.*, 10, 713-726.

Handley, M.F. 1996. The constitutive behaviour of a simple granular model as determined from numerical experiment. *Proceedings of the Second North American Rock Mechanics Symposium*, Balkema, Rotterdam.

Hoek, E. & Bieniawski, Z.T. 1965. Brittle fracture propagation in rock under compression, International Journal of Fracture Mechanics, 1, 137

Horii, H. & Nemat-Nasser, S. 1985. Compression-induced microcrack growth in brittle solids: axial splitting and shear failure. *J. Geophys. Res.,* 90, 3105-3125.

Hull, D.(1995), The effect of mixed mode I/III on crack evolution in brittle solids. International Journal of Fracture. 70, 59-79

Itasca. 1993. FLAC - Fast Lagrangian Analysis of Continua: User's Manual.

Jaeger, J.C. & Cook, N.G.W. 1969. Fundamentals of Rock Mechanics, Chapman and Hall, London.

Jaswon, M.A. & Symm G.T. 1977. Integral methods in potential theory and elastostatics, Academic Press, London

Kachanov, M. 1993. Elastic solids with many cracks and related problems. In *Advances in Applied Mechanics,* Hutchinson and Wu (eds.), 30, 259-445.

Kemeny, J.M. & Cook, N.G.W. 1987. Crack models for the failure of rock under compression, *Proceedings of 2nd International Conference on Constitutive laws for Engineering Materials: Theory and Applications.*, 2, 879-887, Tucson.

Kies, J.A., Sullivan, A.M. & Irwin, G.R. 1950. Interpretation of fracture markings, *Journal of Applied Physics,* 21, 716-720

Krajcinovic, D. 1989. Damage mechanics. *Mechanics of Materials,* 8, 117-197.

Kranz, R.L. 1979. Crack growth and development during creep of barre granite. *Int. J. Rock Mech. Min. Sci.,* 16, 23-35.

Kranz, R.L. 1979. Crack-crack and crack-pore interactions in stressed granite. *Int. J. Rock Mech. Min. Sci.*, 16, 37-47.

Kranz, R.L. 1983. Microcracks in rocks: a review. *Tectonophysics*, 100, 449-480.

Kranz, R.L. & Scholtz, C. 1977. Critical dilatant volume of rocks at the onset of tertiary creep. *J. Geophys. Res.*, 82, 4893-4898.

Kranz, R.L., Harris, W.J. & Carter, N.L. 1982. Static fatigue of granite at 200° C. *Geophys. Res. Lett.*, 9, 1-4.

Kuijpers, J.S. & Napier, J.A.L. 1991. The effect of loading history on stress generation due to inelastic deformation around deep-level tabular stopes, *J. S. Afr. Inst. Min. Metall.,* 91,183-194.

Kullman, D.H., Stewart, R.D. & Grodner, M. 1996. A pillar preconditioning experiment on a deep-level South African gold mine, In: *Proc. 2nd North Am. Rock Mech. Symp*: NARMS '96, Aubertin, et. al. (eds.), Montreal, 375-380.

Lama, R.D. & Vutukuri, V.S. 1978. *Handbook on mechanical properties of rocks - Testing techniques and results - Volume III.* Trans Tech Publications, Germany, 209-320.

Lee, C., Lee, Y. & Cho, T. 1995. Numerical simulation for the underground excavation-support sequence in the visco-plastic jointed rock mass. In: Fujii (ed.) *Proc. 8th Int. Cong. Rock Mech.,* ISRM, Balkema, Rotterdam, 619-621.

Legge, N.B. 1986. *Rock deformation in the vicinity of deep gold mine stopes and its relation to fracture,* Chamber of Mines of South Africa Internal Report 14/86.

Legge, N.B. & Spottiswoode, S.M. 1987. Fracturing and microseismicity of a deep gold mind stope in the pre-remnant & remnant stages of mining, IRSM 6th Int. *Congr. Rock Mech. Montreal*, 1071-1077.

Lehner S. & Kachanov, M. 1996 On modelling of winged cracks forming under compression. *Int J. Fracture*. 77,R69-R75.

Lemaitre, J. 1987. Formulation and identification of damage kinetic constitutive equations, *Continuum damage mechanics*, Springer-Verlag, Wien, 37-90.

Levengood, W.C. 1958. Effect of origin flaw characteristics on glass strength. *Journal of Applied Physics*, 29, 820-826.

Lightfoot, N., Leach, A.R. & Kullman, D.H. 1994. A conceptual model of a hard rock, deep level, tabular ore body. *1st North American Rock Mechanics Symposium*. Balkema, Rotterdam.

Lockner, D.A. Moore, D.E. & Reches, Z. 1992 Microcrack interaction leading to shear fracture *Rock mechanics*, Tillerson and Wawersik (eds), Balkema , Rotterdam.

Madden, T.R. 1983. Microcrack connectivity in rocks: A renormalization group approach to the critical phenomena of conduction and failure in crystalline rocks. *J. Geophys. Res.,* 88, 585-592.

Main, I.G. 1995. Earthquakes and critical phenomena: Implications for probabilistic seismic hazard analysis. *Bull. Seismol. Soc. Am.,* 85, 1299-1308.

Malan, D.F. 1998. An investigation into the identification and modelling of time-dependent behaviour of deep level excavations in hard rock. *PhD Thesis*, University of the Witwatersrand, Johannesburg.

Malan, D.F. & Napier, J.A.L. 1997. Viscoplastic Discontinuum Model of Time-Dependent Fracture & Seismicity, Submitted to *Int. J. Rock Mech. Min. Sci.*

Marder, M. & Gross, S. 1995. Origin of crack tip instabilities. *J. Mech. Phys. Solids.*, 43, 1-48.

Martin, R.J.M. & Durham, W.B. 1975. Mechanisms of Crack Growth in Quartz, *Journal of Geophysical Research*, 80, 35, 4837-4844.

McCarthy, T.S., 1994 The tectono-sedimentary evolution of the Witwatersrand basin with special reference to its influence on the occurrence and character of the Ventersdorp contact reef. *S Afr. J. Geol.* 97, 247-259

Myer L.R., Kemeny, J.M., Zheng, Z., Suarez, I.R., Ewy (2), R.T. & Cook, N.G.W. 1992. Extensile cracking in porous rock under differential compressive stress, In "Micromechanical modelling of quasi-brittle materials behaviour" edited by Victor C Li, ASME Book No AMR1 18 Applied Mechanics Review 45, no P, August Nemat-Nasser, S. and Horii, H. (1982), Compression-induced non-planar crack extension with application to splitting, exfoliation and rockburst. Journal of Geophysical Research, 87, 6805-6821.

Myers, R.E., McCarthy, T.S., & Stanistreest, I.G., 1990, A tectono-sedimentary reconstruction of the development and evolution of the Witwatersrand basin with particular emphasis on the central rand group. *S Afr. J. Geol.* 93, 180-201

Napier, J.A.L. 1990. Modelling of fracturing near deep level mine excavations using a displacement discontinuity approach. In H.P. Rossmanith(ed*), Mechanics of jointed and faulted rock*: 709-715. Rotterdam: Balkema.

Napier, J.A.L. & Hildyard, M.W., 1992, Simulation of fracture growth around openings in highly stressed, brittle rock, J. S. Afr. Inst. Min. Metall. 92 pp. 159-168.

Napier, J.A.L. & Malan, D.F. 1997. A Viscoplastic Discontinuum Model of Time-dependent Fracture and Seismicity Effects in Brittle Rock. *Int. J. Rock Mech. & Mining Sci.*, 34, 1075-1089.

Napier, J.A.L. & Ozbay, M.U. 1993. Application of the displacement discontinuity method to the modelling of crack growth around openings in layered media. *Assessment and Prevention of Failure Phenomena in Rock Engineering*, Pasamehmetoglu, et al. (eds.), Balkema, Rotterdam, 947-956.

Napier, J.A.L. & Peirce, A.P. 1995. Simulation of extensive fracture formation and interaction in brittle materials. In *Mechanics of Jointed and Faulted Rock - MJFR –2,* Rossmanith (ed.*),* Balkema, Rotterdam, 63-74.

Napier, J.A.L. & Stephansson, S.J. 1987. Analysis of deep level mine design problems using the MINSIM-D Boundary element program, *Proc. 20th Symp on application of computers and mathematics in the mineral industries*, SAIMM, Johannesburg, 3-19.

Napier, J.A.L., Daehnke, A., Hildyard, M.W., Kuijpers, J.S., Malan, D.F., Sellers, E.J. & Turner, P.A.T. 1996. Quantification of stope fracture zone behaviour in deep level gold mines, *J. SAIMM.*

Napier, J.A.L., Hildyard, M.W., Kuijpers, J.S., Daehnke, A., Sellers, E.J., Malan, D.F., Siebrits, E., Ozbay, M.U., Dede, T. & Turner, P.A. 1995. *Develop a quantitative understanding of rock mass behaviour near excavations in deep mines.* SIMRAC Final Project Report, Project GAP029.

Nawrocki, P.A. 1995. One-dimensional semi-analytical solution for time-dependent behaviour of a seam. *Int. J. Num. Anal. Meth. Geomech.*, 19, 59-74.

Nemat Nasser S., & Horii H. 1982 Compression induced non-planar crack extension with application to splitting, exfoliation and rockburst. *J. Geophys Res,* 87 6805-6821

Olson, J. E. & Pollard, D. D. 1991. The initiation and growth of en echelon veins. Journal of Structural Geology, 13, 595-608.

Olson, J.E. 1993. Joint pattern development: Effects of sub-critical crack growth and mechanical interaction. *Journal of Geophysical Research*, 98, B7, 12251-12265.

Pan, E., Amadei, B. & Kim, Y.I. 1998. 2-D BEM analysis of anisotropic half-plane problems-application to rock mechanics. *Int. J. Rock Mech. Min. Sci.,* 35, 69-74.

Pan, Y.W. & Dong, J.J. 1991. Time-dependent tunnel convergence - I. Formulation of the model. *Int. J. Rock Mech. Min. Sci.,* 28, 469-475.

Peirce, A. P. & Napier, J.A.L, 1995. A spectral multipole method for efficient solution of large-scale boundary element models in elastostatics, Int. J. Num. Methods Eng. 38, 4009-4034.

Perzyna, P. 1966. Fundamental problems in viscoplasticity. *Adv. Appl. Mech.*, 9, 243-377.

Pusch, R. 1993. Mechanisms and consequences of creep in crystalline rock. In *Comprehensive rock engineering*, vol. 1, Hudson (ed.), Pergamon Press, London, 227-241.

Quaye, G.B., & Guler, G., 1998, The importance of both geological structures and mining induced stress fractures on the hangingwall stability in deep mines. *J.SAIMM*, 98, 157-162

Raffield, M. P., James, J.V., Humphreys, I. & Issacs, A. 1993. Model input parameter selection through instrumentation and back analysis of large excavation failure, *Innovative Mine Design for the 21st Century,* Bawden and Archibald (eds.), Balkema, London, 641-652.

Ravi-Chandar, K. & Knauss, W.G. 1984. An experimental investigation into dynamic fracture: 4. On the interaction of stress waves with propagating cracks. *International Journal of Fracture*, 26, 189-200.

Renshaw, C.E., & Pollard, D.D 1994 Numerical simulation of fracture set formation: A fracture mechanics model consistent with experimental observations *J. Geophys. Res.* 99, 9359-9372.

Roberts, M. K. C., et. al. 1996. *Improved support design by an increased understanding of the rock mass behaviour around the Ventersdorp Contact Reef.* SIMRAC report, GAP 102.

Robertson, E.C. 1964. Viscoelasticity of Rocks. In *State of stress in the earth's crust. Proc. Int. Conf.,* Judd (ed.) Santa Monica, California, 181-233.

Ryder, J.A. & Napier, J.A.L. 1985. Error analysis and design of a large-scale tabular mining stress analyser. In *Proceedings 5th international conference on numerical methods in geomechanics,* Nagoya, 1549-1555.

Ryder, J.A. & Officer, N.C. 1964. An elastic analysis of strata movement observed in the vicinity of inclined excavations. *J. S. Afr. Inst. Min. Metall.*, 64, 219.

Sagawa, Y., Yamatomi, J. & Mogi, G. 1995. A rheology model for non-linear and time-dependent behaviour of rocks. In *Proc. 8th Int. Cong. Rock Mech. ISRM*, Fujii (ed.) Balkema, Rotterdam, 311-314.

Salamon, M.D.G. 1993. Some applications of geomechanical modelling in rockburst and related research. Keynote address: *Rockbursts and Seismicity in Mines*, Young(ed.), Balkema, Rotterdam, 297-309.

Samtani, N.C., Desai, C. S. & Vulliet, L. 1996. An interface model to describe viscoplastic behaviour. Int. *J. Num. Anal. Meth. Geomech.*, 20, 231-252.

Schwartz, C.W. & Kolluru, S. 1984. The influence of stress level on the creep of unfilled rock joints. In *Proc. 25th Symp. Rock Mech.*, 333-340.

Schweitzer, J. K. & Johnson, R. A. 1996. Geotechnical classification of deep and ultra-deep Witwatersrand mining areas, *Mineralium Deposita,* 32, 335-348.

Sellers, E. & Napier, J. 1997. A comparative investigation of micro-flaw models for the simulation of brittle fracture in rock. *J. Comp. Mechanics*, to be published.

Sellers, E.J. 1994. *An anisotropic damage model for rock*, PhD. thesis, University of Cape Town.

Sepehr, K. & Stimpson, B. 1988. Potash mining and seismicity: A time-dependent finite element model. *Int. J. Rock Mech. Min. Sci & Geomech. Abstr.*, 25, 383-392.

Shou, K. 1994. Boundary element method for stress analysis of multi-layered elastic media. *J. Chinese Ins. Engrs.,* 17, 805-814.

Shou, K. 1997. A Two-Dimensional Displacement Discontinuity Method for Multi-Layered Elastic Media. *NYROCK'97.*

Simmons, G. & Richter, D. 1976. Microcracks in rocks. In The Physics and Chemistry of Minerals and Rocks, Strens (ed.), Wiley & Sons, London, 107-137.

Small, J.C. & Booker, J.R. 1984. Finite layer analysis of layered elastic materials using a flexibility approach. Part I - strip loading. *Int. J. Numer. Methods Engng.,* 20, 1025-1037.

Sneddon, I.N. 1951. *Fourier Transforms.* McGraw-Hill, New York.

Solberg, P.H., Lockner, D.A., Summers, R.S., Weeks, J.D. & Byerlee, J.D. 1978. Experimental fault creep under constant differential stress and high confining pressure. In *19th US Symp. Rock Mech.*, Kim(ed.), Stateline, Nevada, 118-121.

Song, D. 1993. Non-linear viscoplastic creep of rock surrounding an underground excavation. *Int. J. Rock Mech. Min. Sci. & Geomech. Abstr.,* 30, 653-658.

Squelch A. P., 1990, *Horizontal stresses in the face area hangingwall of backfilled and conventional stopes at Vaal Reefs*, Chamber of Mines of South Africa Internal Report R16/80.

Stavropoulou, V. 1982. *Constitutive laws for brittle rocks*, PhD. Thesis, University of the Witwatersrand, Johannesburg.

Swoboda, G., Mertz, W. & Beer, G. 1987. Rheological analysis of tunnel excavations by means of coupled finite element (FEM)-boundary element (BEM) analysis. *Int. J. Num. Anal. Methods. Geomech.*, 11, 115-129.

Tan, T. & Kang, W. 1980. Locked in stresses, creep and dilatancy of rocks, and constitutive equations. *Rock Mech.*, 13, 5-22.

Vermeer, P.A. & De Borst, R. 1984. Non-associated plasticity for soils, concrete and rock. *Heron,* 29, 5-62.

Wardle, L.J. 1980. *Stress Analysis of Multi-Layered Anisotropic Elastic Systems Subject to Rectangular Loads.* CSIRO Aus. Div. Appl. Geomech. Tech. Paper No.33.

Wawersik, W.R. 1974. Time-dependent behaviour of rock in compression. In: Advances in Rock Mechanics. *Proc. 3rd Congr. Int. Soc. Rock Mech.*, Denver, Colorado, 357-363.

Willemse, E.J.M. & Pollard, D.D., 1998 On the orientation and patterns of wing cracks and solution surfaces at the tips of a sliding flaw or fault. *J. Geophys. Res.,* 103, 2427-2438.

Wilson, K.G. 1979. Problems in physics with many scales of length. *Scientific American*, 241, 140-157.

Winter H. de la R., 1994, The Ventersdorp contact reef in relation to the Witwatersrand Basin and overlying Ventersdorp volcanic rocks. *S Afr. J. Geol,* 97, 260-278

Wollock, I. & Newman, S.B. 1964. Fracture topography. In *Fracture processes in polymeric solids*, Rosen (ed.), Wiley and Sons, NY.

Yang, L., Zhang, K. & Wang, Y. 1996. Back analysis of initial rock stresses and time-dependent parameters. *Int. J. Rock Mech. Min. Sci & Geomech. Abstr.*, 33, 641-645.

Yumlu M. & Ozbay M.U. 1995. A study of the behaviour of brittle rocks under plane strain and triaxial loading conditions. *Int J. Rock Mech Min Sci*, 32,725-733.

Zheng, Z. 1991. Observations of microcracking and pore collapse in limestone using liquid metal porosimetry, *Proceedings Eighth Engineering Conference,* Columbus, Ohio, 1046-1050.

3 Stress wave and dynamic fracture propagation in rock

3.1 Introduction

Within the field of rock mechanics, an important sub-category is the study of transient processes such as stress wave and dynamic fracture propagation. The theory of rock dynamics has been advanced considerably this century in the fields of seismology and earthquake engineering, leading to further understanding of wave propagation effects along free surfaces and along the interfaces between different material layers in the crust of the earth. Within the mining context, research in this field has been spurred in the last three decades particularly by the technical difficulties of deep level mining operations and the associated occurrence of seismicity and rockbursts. Although the research effort has accelerated over the past decade, rockbursts and rockfalls continue to be the single largest cause contributing towards the toll of injuries and fatalities suffered by the workforce during mining operations.

An important general aspect of rock dynamics is the interaction of stress waves with geological or mining induced discontinuities and fractures. Knowledge of this field is necessary to assess the propensity for wave trapping and energy channeling in geological strata surrounding mining excavations. Furthermore, this gives valuable insight towards understanding the performance of blasting, percussion drilling and the development of non-explosive rock breaking equipment such as impacting and ripping tools.

It is of interest to consider the following specific aspects of rock dynamics, which have to be assessed by the engineer engaged in mining design and operations:

- *Mining Induced Seismicity:* Mining through highly stressed rock in deep level mines is often accompanied by considerable seismic activity. High geological and mining induced stresses can lead to sudden movements on existing discontinuities such as faults or on geological inhomogeneities such as intrusive dyke structures. The resulting seismic waves interact with mining excavations leading to loss of stability with falls of ground or with dynamic formation of new fractures and the explosive failure of brittle rock.

- *Blasting:* In hard rock mining, the most common technique of excavating rock is in the form of blasting. Knowledge of this process is of importance in order to understand mechanisms governing the following aspects of blasting:

    (i) Stress Waves: Blast induced stress waves can induce strong dynamic loading and may in turn trigger further movements on faults and other pre-existing planes of weakness. These triggered movements may lead to rockfalls and damage to the excavations.

    (ii) Fracturing: In general, the primary purpose of blasting is the efficient fragmentation of rock. Understanding of the fracturing mechanisms is of importance to break the rock into fragments of the required size, and to limit unwanted blast damage in terms of additional fracturing, which can have an unpredictable effect on the subsequent stability of the excavation.

    In certain cases the blasting operations are supplemented by additional charges located ahead of, for example, the stope face. The purpose of the additional charges is to pre-condition the rock in order to reduce the probability

of uncontrolled face bursting. Any attempt to implement and understand the consequences of such control strategies requires knowledge of blast driven dynamic fracture propagation in highly stressed rock.

From the foregoing examples, it is evident that there is a need to quantify and to gain insights into the fundamental mechanisms governing rock dynamics in terms of stress wave interactions with discontinuities ranging in scale from microcracks to mining excavations, as well as important phenomena governing the rock mass stability such as stress wave and blast induced fracturing.

In many cases a definite gap is perceived between the theory and application of rock dynamics. This work attempts to reduce this gap by ensuring the results are relevant in practice, and emphasising the practical implications of the knowledge gained. The work addresses stress wave propagation and the interaction with discontinuities, as well as dynamic fracturing due to stress wave loading and blasting. More specifically, the main objectives can be classified according to the following categories, which are illustrated for a deep level mining application in Figure 3.1.1:

- **Stress Wave Interactions with Rock Mass Discontinuities:** Various types of rock joints and fractures, and the associated interface conditions, are analysed and their stress wave reflection and transmission characteristics are quantified.

- **Stress Wave Interactions with Tabular Mining Excavations:** The transient wave field due to wave interactions with mine excavations is investigated, and the mechanisms of energy channeling and fracturing due to the superposition of reflected, refracted and diffracted waves are studied.

- **Blasting:** The process of rock blasting is examined, where consideration is given to (i) blast induced stress waves and their proclivity for promoting fracturing in the borehole vicinity, and (ii) fractures driven by combustion gases.

Progress towards understanding the mechanisms governing dynamic processes has been impeded by the inherently complex nature of transient phenomena. In many cases the existing knowledge of rock dynamics is based on empirical results and field studies, particularly in the area of rock blasting. Some of the difficulties associated with analytical, numerical and experimental approaches in studying dynamic phenomena are outline below:

- *Analytical:* The time-dependence results in mathematical models are more complicated than the equivalent static models. Indeed, the analysis of dynamic fracture and the interaction of stress waves ranks among the most difficult problems of the theory of elasticity, and analytical solutions are available for only a few very basic problems.

- *Numerical:* The limitations associated with analytical models have prompted the use of numerical techniques such as finite difference, finite element, discrete element and boundary element methods. These techniques have been proven to be extremely powerful, particularly so when investigating stress wave interactions with excavations of complex shape and modelling dynamic fracture propagation. However, limitations exist regarding the accuracy and validity of the numerical results, and care needs to be exercised when interpreting numerically generated data.

  In addition, numerical simulations of transient phenomena are computationally expensive. To obtain accurate and stable solutions, the numerical simulation consists of many (typically numbering between 100 and 10 000) time increments, and the complete problem is solved after each increment. Furthermore, in order to simulate the propagation of a smooth stress pulse, with limited numerically induced spurious oscillations, the spatial domain needs to be discretised by a large number of elements; significantly more elements than would be required for the accurate solution of the equivalent static problem. The many time steps,

coupled with the requirements of a finely discretised spatial mesh, requires powerful computers and/or long run times to model accurately the dynamic behaviour of structures. Numerical programs which can simulate dynamic fracturing have only been developed comparatively recently, and involve additional complexities in terms of satisfying fracture criteria, iteration techniques and re-meshing algorithms.

- *Experimental:* From an experimental point of view, the time-dependence requires that many accurate sequential measurements of highly variable quantities of interest must be made in an extremely short time period in a way that does not interfere with the stress wave and fracture propagation. High speed photography coupled with dynamic photoelasticity has proven to be a valuable tool to record transient phenomena and further understand their mechanisms.

The results are based on analytical and numerical, as well as experimental investigations. A recurring theme throughout this work is the verification of numerical and analytical results by means of controlled laboratory experiments. This is considered an important aspect of the investigation and ensures accurate, relevant and meaningful results. Purely analytical or numerical investigations of complex phenomena such as dynamic fracturing, while being suitable for the purposes of parametric studies, lose value when not tested and checked by means of comparisons with experimental data.

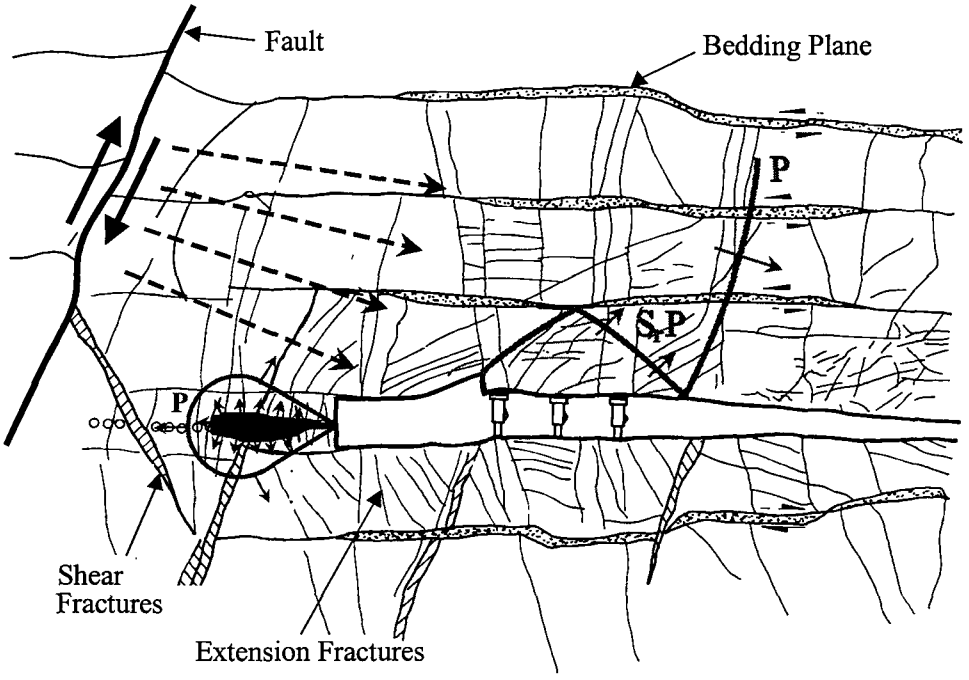

Figure 3.1.1 Stress wave propagation and dynamic fracturing in a deep level mining operation.

3.2 Literature survey

The aim of the present section is to review briefly previous work and basic theoretical concepts which are used to examine the dynamic behaviour of rock. The overview is structured in three parts, namely:

- elastodynamic wave interactions with discontinuities,
- dynamic fracture mechanics, and
- blast induced fracturing.

3.2.1 Elastodynamic wave interactions with discontinuities

Upon stress wave interaction with discontinuities, incident energy is reflected and refracted (transmitted). Over the past century many analytical, numerical and experimental studies have been conducted to determine the characteristics of reflected and refracted waves. Knott (1899) and Zoeppritz (1919) were amongst the first to study by analytical means the reflection and transmission of plane waves. Further studies by Koefoed (1962) investigated the reflection and transmission amplitude coefficients due to incident *P*-waves, whereas Costain et al. (1963) investigated amplitude coefficients and energy ratios for incident *SV*-waves. Tooley et al. (1965) calculated the energy flux ratios of a plane *P*-wave at a planar interface between two half-spaces. In essence, these studies solved analytical equations to calculate the stress and energy amplitudes of reflected and refracted waves due to incident waves interacting with welded bimaterial interfaces, i.e. a perfectly bonded joint across which both tractions and displacements are continuous.

3.2.1.1 Wave interactions with discontinuities: Analytical and numerical work

Wave interactions with non-welded interfaces were investigated, amongst others, by Mindlin (1960), and Kendall and Tabor (1971). Schoenberg (1980) studied wave propagation across an interface with slip linearly related to the stress traction, which is continuous across the discontinuity, i.e. an interface incorporating an elastic spring (hereafter referred to as the displacement discontinuity model). He calculated reflection and transmission coefficients for harmonic plane waves. It was shown that the coefficients are dependent on the frequency of the incident wave. In further studies Schoenberg (1983) calculated the reflection coefficients for incident waves propagating through a homogeneous medium with multiple, equally spaced, parallel interfaces, where the interfaces were permitted to slip.

Recent analytical studies were conducted by, amongst others, Borejko et al. (1992) to investigate wave interactions in wedge-shaped and constant thickness layers, and Rossmanith et al. (1994) to investigate the time evolution of damage at a bimaterial interface under the action of *P*- and *S*-waves. Hirose (1994) used time domain boundary integral equations to investigate a pre-opened crack subjected to a normally incident *P*-wave, a pre-stressed crack loaded by normally incident *P*- and *S*-waves and a frictional crack subjected to an obliquely incident *P*-wave. Watanabe (1995) applied the Cagniard technique to investigate reflected and transmitted waves interacting with an interface with normal and shear stiffness. Gu et al. (1996) used the displacement discontinuity method to investigate the amplitude of fracture induced waves, which showed that the resulting waves are controlled by fracture stiffness, frequency and the Poisson's ratio of the medium. Fourney and Dick (1995) examined the propagation of stress waves across filled and open joints. Some of their results were explained analytically by Simha (1996).

3.2.1.2 Wave interactions with discontinuities: Experimental work

Experimental studies of wave interactions with interfaces are summarised by Kolsky (1963). Split-Hopkinson bar arrangements and techniques have been particularly useful to record reflected and transmitted pulses for one dimensional problems. Two-dimensional wave interaction problems can advantageously be studied utilising the combination of photoelasticity and high speed cinematography. Numerous dynamic photoelastic studies in wave propagation have been published (Rossmanith and Knasmillner, 1990; Daehnke et al., 1996), and interface problems have been studied by Rossmanith and Fourney (1982).

In an experimental study, Blair (1989) used Schoenberg's (1980) theory to determine the stiffness of a joint contained within a granite block by means of the seismic pulse assessment. The paper demonstrates the potential of the seismic pulse technique for the measurement of fractures opening at depth in rock where it is difficult to obtain direct displacement measurements. Pyrak-Nolte et al. (1990a, 1990b) used laboratory experiments to investigate longitudinal and shear wave transmission across natural fractures, and successfully correlated the experimental findings with analytical results for discontinuities with normal and shear stiffness. An experimental study conducted by Suarez-Rivera et al. (1992) investigated the transmission of *S*-waves across thin liquid films, and analytical calculations based on Schoenberg's (1980) displacement discontinuity interface model gave results which compared well with the experimental data. Myer et al. (1995) conducted experimental work and used an analytical displacement discontinuity model to investigate the scattering and transmission of incident *P*-waves by multiple voids positioned in the plane of the fracture. The tests showed that the effects of fractures can be treated independently until fracture spacing approaches the size of the voids within the fractures, and the potential applicability of the approach for detection and characterisation of fractures is demonstrated.

The above mentioned studies represent only a fraction of the work dealing with wave interactions with discontinuities. However, in spite of the large amount of literature dealing with this subject, no single publication gives amplitude coefficients (i.e. the amplitude ratios of the reflected or refracted waves versus the incident waves) for a wide variety of interface conditions. Furthermore, a disadvantageous situation prevails as different authors give reflection and transmission coefficients for different physical quantities. The coefficients may be defined for potentials, displacement, velocity, stress and energy. Some authors (Graff, 1975; Kolsky, 1963; Miklowitz, 1978) give only amplitude coefficients of the potential function, a quantity, which is difficult to interpret physically, whilst other texts give stress (Rinehart, 1975), energy (Miklowitz, 1978), displacement (Achenbach, 1973) or velocity (Rinehart, 1975) coefficients.

In practical work the blasting engineer generally makes use of stress reflection and transmission coefficients to gain insight into the stress wave driven rock fragmentation in the borehole vicinity. The seismologist, on the other hand, makes use of geophones to measure the rock acceleration under the action of seismic waves, and, upon integration, obtains the velocity and displacement amplitudes. Hence, in a typical application, the seismologist would make use of displacement coefficients to determine the influence of rock mass discontinuities on seismic waves. Energy coefficients are useful to investigate, for example, the effect of energy channeling in rock layers. It is evident that various disciplines make use of different types of reflection and refraction coefficients.

3.2.2 Dynamic fracture mechanics

A detailed literature survey is given in Daehnke (1997) to address (i) fundamental dynamic fracture mechanics concepts, (ii) analytical treatment of specific crack problems, (iii) numerical work and (iv) experimental work. These represent the main avenues of research into dynamic fracturing over the last five decades.

This overview is necessary to appreciate the capabilities of analytical fracturing models, and to recognise the development and current state of the art of numerical models. Historical and topical experimental investigations are reviewed to assess past applications of experimental data and gain insight into techniques, which are suitable to investigate mechanisms governing dynamic fracturing.

It is found that the basis of the most important and relevant analytical work was conducted in the 1960's and 1970's. During this time various mathematical models of crack propagation problems were formulated, and give valuable insights into the crack tip behaviour of rapidly propagating cracks. Particularly noteworthy is the work by Broberg (1960), Kostrov (1964a, 1966) and Freund (1972a, 1972b, 1973 and 1974). Some of their results characterising the crack tip stress intensity factor are applied in subsequent work.

With the advent of computing power, numerical methods have become increasingly successful in simulating dynamic fracturing problems. Finite element methods, particularly, have been shown since the early work by Kobayashi et al. (1976, 1977b) and Nishioka et al. (1981, 1982, 1983) to be one of the most suitable techniques to model dynamic fracturing. Finite element methods are continually improved and recent developments (e.g. Swenson et al., 1988, 1990 and Munjiza et al.,1992, 1995) have resulted in sophisticated codes capable of complex and detailed simulations.

Experimental methods have played an important role in dynamic fracture mechanics since the early 1950's. To this day they form the cornerstone of many studies dealing with dynamic fracture concepts, and are particularly suitable to assess and check the validity of numerical simulations. It is of interest to note that the majority of experimental investigations continue to be conducted using polymeric materials such as PMMA, often in conjunction with high speed photography. These materials offer advantages in terms of, for example, consistent and known material properties, transparency, ease of specimen fabrication, etc., whilst qualitatively showing evidence of fracture behaviour similar to that of brittle rock.

3.2.3 Blast induced fracturing

This review dealing with the science of rock blasting is representative of selected publications which are considered to have led to significant new insights in these time. The review is not meant to be a comprehensive nor an exhaustive overview of blasting in general, but only lists investigations dealing with fundamental mechanisms of blast induced fracturing, with particular emphasis on the role of stress wave versus gas pressure induced fracturing.

Although drilling and blasting have been the principal methods of excavating hard rock for over a century, the fundamentals of the processes of explosive rock breaking have only been investigated comparatively recently. The science of the explosives themselves, and their detonative characteristics, was well established in the 1950's; Cook (1958) covers the state of the art at the time of the science of high explosives, reporting on empirical observations as well as mathematical models describing the detonation process of explosives. The explosive – rock interaction process was subjected to detailed investigations only at the end of the 1960's.

Due to the complexity and multiple parameters and mechanisms associated with blasting, past development in this area has relied heavily on experimental observations. Few analytical studies

have been conducted and numerical modelling has, with the advent of increased computing power, been used only comparatively recently to simulate blasting mechanisms. In this literature review the following topics dealing with blasting mechanisms have been identified:

- experimental investigations
  - stress wave versus gas driven fracturing
  - the role of discontinuities
- analytical investigations
- numerical investigations
- gas driven fracturing

Past and current developments in each of these topics are addressed below.

3.2.3.1 Experimental investigations: Stress wave versus gas driven fracturing

One of the first detailed studies dealing with rock blasting was completed by Kutter (1967). He investigated the role of stress waves and gas pressure in the fracture process of an underground explosion in rock. To this end he considered the action of the explosively generated stress wave in the rock separately from that of the expanding combustion gases. Based on experimental observations, he found that the main role of the stress wave is to generate a densely radially fractured zone around the borehole. The subsequent gas pressure, exerted against the walls of a highly fractured cavity, generates a quasi-static stress field, which was modelled as a pressurised cylindrical equivalent cavity, with radius equal to that of the crack tips. It was found that the quasi-static stresses cause further extension of the radial cracks, where the longest cracks would extend first, and extension of two diametrically opposed radial cracks would be favoured. At the time Kutter (1967) did not consider gas flow and penetration into the radial cracks.

Since the 1950's laboratory experiments involving high speed photography and polymers such as PMMA and Homalite-100 have been used extensively to investigate mechanisms of dynamic fracture. By 1970 high speed photography was effectively employed to investigate specifically blast induced fracture propagation. Persson (1970) used high speed photography in conjunction with scale-model blasts performed in blocks of glass and acrylic to observe the evolution of fractures from charged boreholes. He found two predominant crack systems: radial cracks initiated near the borehole, or spalling cracks initiated as tensile fractures caused by the reflected stress wave. Work by Persson et al. (1970) illustrated the basic difference between bench and crater blasting.

Further laboratory tests were done by Kutter and Fairhurst (1971) in an attempt to clarify the respective roles of stress waves and gas pressure in the fragmentation. They investigated the problem theoretically and experimentally and found that, based on post-blast observations[1] in PMMA and rock discs, the fracture pattern generated by the stress wave is that of a dense, radially fractured zone in the immediate borehole vicinity, followed by a ring of wider spaced radial cracks. The diameter of the fractured zone was theoretically computed to be approximately six hole diameters for a spherical charge and nine hole diameters for a cylindrical charge. It is in this expanded or equivalent cavity (first introduced by Kutter, 1967) that the gas

[1] In this study high speed photography was not utilised.

pressure becomes active, rather than the original borehole. The investigation demonstrated that high-pressure gases play a considerably more important role than had generally been anticipated and admitted. However, the role of the gas pressure alone would not be very effective. The borehole needs to be pre-conditioned, i.e. the pre-cracking and effective widening of the cavity by the emitted stress waves makes it possible for the expanding gases to be fully utilised in rock fragmentation. Furthermore, it was found that cracks have a preferential growth orientation in the direction of maximum principal stress of superimposed stress fields, and cracks pointing towards the free surface are longer than cracks pointing away from it. Finally, the important conclusion was made that, at high loading rates, the fracture pattern in plexiglas appears to be practically identical to that in rock. Only the scale, i.e. the length of the cracks, was found to differ.

Using laboratory models, Hagan and Just (1974) investigated various parameters such as explosive properties, rock properties, blast geometry and initiation sequences, and evaluated the effect of these parameters on the mechanics of fracturing. Although they did not derive mathematical models describing fracturing mechanisms, their work is useful in terms of recommendations and conclusions applicable to actual field blasting operations. They also note the difficulty of extrapolating information gained from small-scale laboratory tests to full-scale field operations.

The effect of gas pressure on the fracture process was investigated more closely by Dally et al. (1975). With the aid of dynamic photoelasticity they investigated two Homalite-100 models, one where the combustion gases were vented, and one where they were contained by a special sealing device. The contained charge produced cracks which were larger by a factor of seven compared with those produced by the vented charge, thereby illustrating the importance of gas pressurisation as a fracture driving mechanism. In further studies (Fourney and Dally, 1975) fracture propagation due to gas penetration was investigated using split and ligamented tubes lining the borehole walls. Similar studies by Dally and Fourney (1976, 1977) achieved fracture plane control by using longitudinally grooved boreholes; they illustrated the technique of propagating a limited number of cracks considerable distances by the gas pressurisation mechanism only. Wave and fracture propagation in the immediate borehole vicinity was investigated by Dally et al. (1976) using Homalite-100 plates and a high speed CS camera. Further studies were conducted by Fourney et al. (1981, 1983) to investigate fracture propagation from notched, fluid-filled boreholes in PMMA blocks. They found that notched boreholes enhance fracture propagation distances significantly. Although fluid-filled boreholes result in initiation at lower pressures, the resulting fractures appear to arrest more quickly than fractures driven from air filled boreholes.

Post-blast investigations of the fractography of pre-split fractures in PMMA models were conducted by Carrasco and Saperstein (1977). They found that when boreholes are spaced less than a critical distance apart, crack initiation occurs at the midpoint between holes and is probably due to stress wave superposition. At distances greater than this critical distance, the cracks initiate at the boreholes and are probably due to the wedging action of gas expansion. In the observed models, the critical distance was less than the optimum calculated for efficient explosive use.

Bhandari (1979) conducted experimental studies by small scale blasting carried out in bench shaped blocks of cement-mortar and granite, with the objective of explaining the role of stress waves and gas energy. He recognised the importance of both the stress wave and gas action, however he emphasised that the role of the stress waves particularly is poorly understood and that further work is necessary to appreciate fully the manner in which stress waves participate.

McHugh (1983) assessed the relative importance of internal gas pressurisation versus stress wave induced fracturing. Simple calculations were performed to estimate an upper bound on crack length resulting solely from gas pressurisation. The calculations indicated that the gas pressure could increase the crack length by a factor of 10-100 (no confining pressure) or 3-25 (with 7 MPa confining pressure); these results were in agreement with laboratory experiments in

PMMA. Explosives residue was observed on the blast induced fractures, indicating that the combustion gases penetrated up to the tips of the cracks.

Explosive stem induced fracturing was investigated by Young et al. (1986). They used a downhole camera and showed the absence of any vertical fracturing before explosive treatment, and well-developed fractures after blasting. These vertical fractures developed despite the fact that *in situ* stresses favoured horizontal fracturing.

The effects of stemming on crater blasting were investigated by Simha et al. (1987), and they found that even when stemming was not used, little difference was observed in the resulting craters that were formed. From this they reached the conclusion that cratering is largely stress wave controlled. Further work by Wang et al. (1990) conducted in PMMA models lead to enhanced crater blasting efficiency. Using a circumferential groove in the borehole at the location where crater initiation is desired was shown to increase the volume of material removed by a factor of as much as six.

Stagg and Nutting (1987) used reduced-scale tests on dolomite benches to investigate the influence of blast delay time on rock fragmentation. They found that the finest fragmentation occurred at blasthole delay intervals of 3 to 60 milliseconds per metre of burden. In this range stress wave induced strains interacted with longer lasting gas pressure strains from earlier holes. Shorter delays resulted in coarser fragmentation, where breakage approached pre-split conditions with a major fracture between blastholes. Coarser fragmentation also resulted from long delays (>60 milliseconds per metre), with explosive charges acting independently.

Small-scale blasting experiments were conducted in acrylone and rock by Dojcar et al. (1996). From the experimental data they derived empirically based equations for calculating the parameters of controlled blasting, i.e. the burden and the spacing of the boreholes, and the charge weight.

3.2.3.2 Experimental investigations: The role of discontinuities

Two quotes are cited here to emphasise the importance of the interference of discontinuities in the rock mass and the fracture process in blasting: "*It must be strongly emphasised that the influence of the structural characteristics of a rock mass may often overshadow the influence of the mechanical and physical properties of the rock*" (Gnirk and Pfleider, 1967), and "*Blasting pattern and techniques should be adjusted to minimise detrimental geologic effects and maximise beneficial geologic effects*" (Pugliese, 1973). Since then numerous studies have been conducted by various authors to gain insights and understanding of the effects of rock mass discontinuities.

The effect of pre-existing discontinuities (such as joints, fissures, bedding planes and hard bands) on blast induced fractures was investigated by a number of studies in the early 1980's. Hagan (1980) gave a general discussion of the effects of these discontinuities, whereas Singh et al. (1980) specifically investigated the influence of orientation of jointing on fragmentation. The latter study involved blasting bench-shaped laboratory models fabricated from sandstone, and it was found that the effect of the orientation of jointing on the average mass of fragments was significant, with vertically jointed models yielding a higher mass of broken fragments.

Worsey et al. (1981, 1984) conducted tests in polyester resin as well as rock and concrete to investigate qualitatively the interaction of blast induced cracks with pre-existing joints. They found that the dominant cracks may cross successive discontinuities at approximately right angles.

Further work on blasting in discontinuous rock was conducted by Ismail and Gozon (1987), who conducted small-scale blasting experiments in rock. They found that the borehole should be perpendicular to the discontinuities in order to maximise the utilisation of the explosive energy.

A synopsis of possible mechanisms of joint interference with blast induced fractures is given by Kutter and Kulozik (1990). Based on plate experiments in PMMA and rock they found that, contrary to the conclusion reached by Ismail and Gozon (1987), blastholes should be oriented parallel to the pre-dominant joint sets to achieve a minimum joint intersection with the blastholes.

Chakraborty et al. (1994) used model blasts and field investigations to determine the effects of rock mass quality and joint orientation on tunnel blasting. They found that deeper boreholes are required in formations with joint planes perpendicular to the hole axis, however the number of blastholes should be greater when the joints are parallel to the blast hole axis.

From these partly conflicting results it is evident that the extremely complicated problem of blast induced fractures interacting with discontinuities requires further work to improve understanding of the interaction of blast induced fractures with rock joints and pre-existing fractures surrounding stopes and tunnels.

3.2.3.3 Analytical investigations

Due to the inherently complex nature of the blast process, only a few purely analytical investigations have been conducted. Of these the following are particularly noteworthy.

Clark (1967) studied specifically the blast induced stress wave and, using a viscoelastic[2] model and analytical solutions for plane and spherical waves, attempted to correlate mathematical and empirical data. He noted that at the time no suitable mathematical model had been developed to describe blast induced stress waves in rock.

Cherepanov (1973) presented a general mathematical model of the process of fracture of solids by explosion. His model is based on the assumption that, similar to the Griffith criterion, the necessary minimum quantity of elastic energy liberated in brittle fracture per unit mass is a constant of the material. This constant, which is similar in the physical sense to the specific surface energy, needs to be determined by means of experiments with explosives.

Further work based on fracture mechanics was conducted by Ouchterlony (1974). He considered explicit radial cracks extending from a borehole (static analysis) and calculated stress intensity factors due to loading of the borehole wall and crack surfaces by gas pressure. The work showed that the critical gas pressure for crack growth increases with an increasing number of cracks, and the circular borehole no longer influences the crack tip stresses outside a near-zone of 2-3 hole radii. Furthermore the presence of short cracks does not influence the crack tip stresses of longer ones when the crack length ratio is larger than 2-3, and in the presence of long cracks, shorter cracks tend to arrest. A uniform growth of all cracks in a radial crack system was found to be virtually impossible. An important conclusion was that the crack lengths obtained in rock blasting are strongly influenced by the extent of gas penetration (ten-fold to hundred-fold increase in their length), i.e. the equivalent cavity analysis by Kutter (1967) would predict shorter cracks and might represent an incomplete model.

---

[2] Further work dealing with non-linear material behaviour in the immediate borehole vicinity was conducted by Larson (1982) using small-scale laboratory experiments on geologic materials.

3.2.3.4 Numerical investigations

Numerical simulations are increasingly used to model the blasting process. Particularly in the last decade, numerous numerical models have been developed and applied to gain valuable new information. Numerical simulations will no doubt play an increasingly important role in the future.

Heuze et al. (1990) illustrated the power and suitability of discrete element modelling (two-dimensional) to describe and simulate the interaction of a large number of rock blocks and their dynamics through large motions and dislocations due to near surface and underground explosions. An initial force-time history was applied radially to the blocks immediately surrounding the borehole cavity. Their preliminary analysis provided results, which are quantitatively similar to those observed in the field. However, they emphasised that the discrete element method at the time was in its infancy, and substantial further work was required to improve the modelling.

Taylor and Preece (1989) developed a two-dimensional distinct element code in which the elements were disks derived from the cross-section of spheres, mainly for modelling the motion associated with blasting layered rock masses. The code was subsequently developed to employ a porosity based gas flow model (Preece, 1993; Preece et al., 1994).

Finite element methods were used in two-dimensional models by Szuladzinski (1993), and Swoboda and Li (1993) to investigate, in the former case, the elastic response of the rock medium to explosive borehole pressure and, in the latter study, blast loading of a tunnel, where special interface elements were used to model rock joints.

McKenzie et al. (1995) used numerical modelling to optimise the designs of blasts to create final walls in large open pit mines. Their numerical model provided damage maps based on the peak particle velocity (PPV), where the PPV was determined by sequentially pressurising a spatial distribution of spherical cavities. This model is described further in Section 3.4.3.2, and it will be shown that it can only be used to obtain approximate PPV's when the velocity of detonation of the explosive is significantly faster than the *P*-wave speed in the material.

Using the MSC/NSTRAN finite element code Ghosh and Daemen (1995) modelled the two-dimensional crack extension due to gas pressure, where the extent of gas penetration is fixed and assumed apriori. It is found that tensile stresses which develop between the first order radial cracks could generate second order cracks which fragment the rock between the radial cracks. They also point out that the pressurisation of radial cracks is essential to propagate them for longer distances; pressurisation of the borehole alone leads to significantly reduced crack length.

Toper (1995) analysed numerical two-dimensional models using the quasi-static boundary element code DIGS. He assumed the gas pressure to extend uniformly to the crack tips and investigated the interaction of cracks propagating from a borehole with each other and with pre-existing discontinuities. Qualitatively the DIGS simulations showed some degree of similarity with field observations.

Yang et al. (1996) proposed a simple constitutive model for blast damage resulting from impulsive loading from stress waves. In the model they assume that brittle failure of rock during blasting is controlled by extensional strain. The model was implemented in a dynamic finite element code (ABAQUS/Explicit) and, by comparisons with field observations, the model was calibrated by reproducing the observed crater shape. Discrepancies were noted to occur due to the omission of the gas penetration effects in the model. The authors noted that, to their knowledge, no current blast damage model combined the contributions of shock and gas energy.

Cundall et al. (1996) and Potyondy et al. (1996) used the discrete element method (PFC) to simulate the effects of explosive loading on rockfill. They demonstrated the suitability of distinct element methods to model the motion and interaction of individual rock blocks. In addition to

modelling the stress wave, they also modelled the gas/rock interaction. The development of a discrete, gas-filled fracture network of interconnected, penny shaped crack reservoirs is modelled explicitly, with fracture, flow and pressure distributions evolving dynamically during the simulation.

An explicit finite/discrete element method was used by Minchinton and Lynch (1997) to model dynamically the stress field development, crack generation and crack growth as well as the motion and stacking of the rock fragments. They modelled the rock failure due to both stress wave action and due to gas flow, which is treated (similarly to Cundall et al., 1996) by coupling the discrete element porosity field to a finite volume gas flow model. Several examples are discussed which show significant differences between blasting with stemming to contain the gases in the blastholes, and without stemming.

Summarising, it is recognised that the numerical simulations by Cundall et al. (1996) and Minchinton and Lynch (1997) currently represent the state of the art in modelling the coupled stress wave – gas interaction process during blasting. While recognising the superlative research effort of these authors, these codes need to be further developed to incorporate a more complete gas flow model, particularly a model taking into account non-isothermal gas flow. Both codes currently neglect heat transfer from the hot combustion gases to the surrounding rock mass, and in the following sections it will be shown that thermal effects play an important role and significantly affect fracture propagation speeds and the final fracture extent. Neither of the codes has not yet been developed and applied to solve true three-dimensional blasting problems.

3.2.3.5 Gas driven fracturing

It will be shown that it is reasonable to model the gas driven fracturing process separately from the earlier stress wave propagation phase. Hence, in this literature review gas driven fracturing is treated separately, although in many cases the studies mentioned below employed experimental, analytical and numerical aspects.

The process of hydraulic and gas induced fracturing has found widespread geotechnical applications. Early work was driven by the petroleum industry, with one of the first comprehensive analyses conducted by Hubbert and Willis (1957). They investigated the mechanics of hydraulic fracturing to generate underground fractures with suitable extent, orientation and distribution in order to improve the flow rate of oil and/or gas from low permeability rock, thereby stimulating oil and gas wells. Since then research in this general area has mushroomed, and useful reviews are given by Cleary (1982) and Mendelsohn (1984 a, b).

Hydraulic fractures are propagated at pressures that are slightly higher than the *in situ* stress. Pumping times that are of the order of hundreds of seconds, typically produce only a single fracture whose orientation is aligned with the *in situ* stresses. To extend multiple fractures radially from the wellbore, propellants or explosives are used and the fractures are driven by high pressure combustion gases. Initial studies of gas pressure induced fracturing (Bligh, 1974; Coursen, 1979; Warpinski et al., 1979) gained insights into fracturing mechanisms using quasi-static approaches. They typically assumed a uniform gas pressure distribution along the fracture and estimated fracture extent based on the total gas volume liberated by the propellant/explosive versus the post-blast fracture volume.

The analysis of gas driven fracturing is considerably more complicated than the analysis of hydraulic fracturing due to the fact that (i) the compressible nature of gases needs to be taken into account and (ii) non-uniform gas temperatures exist along the length of the fracture. This increases the complexity of the governing equations.

Nilson (1981) investigated the problem of wedge shaped gas-driven fractures. His problem formulation was novel at the time as it modelled the dynamic gas flow in addition to the gas-solid coupling by including the temporal wall divergence in the flow analysis. He assumed a constant driving pressure and isothermal gas flow, and solved the problem by separation of the time and position variables, followed by numerical integration of the resulting ordinary differential equations. The main findings of this analysis are that the flow accelerates through a sequence of self-similar laminar and turbulent regimes, and that a strong vacuum can exist at the tip of the fracture, i.e. the driving gases do not necessarily penetrate up to the fracture tip. A numerical procedure for solving the governing equations by means of a straining coordinate system, which moves with the fracture, was developed and tested by Nilson and Griffiths (1983).

The numerical procedure was further elaborated (Nilson, 1986) to include seepage losses, as well as convection and conduction heat transfer from the hot combustion gases to the surrounding medium. The numerical method was used in a parameter study (Nilson et al., 1985) and reasonably good correlation with observed field results was noted.

Further analytical work applying similarity analyses of energy transport in gas-driven fractures was conducted by Nilson and Griffiths (1986). Various thermal models were considered, and local values of gas pressure, temperature and speed were computed. Similarity analyses were also used to investigate the flow of gases or liquids along an isolated fracture in a permeable medium, i.e. taking account of seepage losses (Nilson and Morrison, 1986; Nilson, 1988). A hybrid analytical/numerical method was used to investigate specifically the heat transfer in a gas-driven fracture (Griffiths et al., 1986).

At this stage it was generally recognised that the work done by Nilson and his co-workers represented the most complete model for gas driven fracture propagation. Schatz[3] et al. (1987) incorporated gas flow based on Nilson's work in a boundary element program to model fracture propagation and curvature in a pre-stressed medium. They compared their numerical results with post-blast observations of laboratory tests and found favourable correlation. It was found that fractures curve less than previously thought and that ultimately fracture length is controlled by gas volume loss, leakage to adjacent rock and thermal quenching. Roberts and Swenson (1988) used Nilson's gas flow approach in conjunction with the dynamic finite element program CRACKER (Swenson, 1985) to investigate gas-driven fracture propagation.

Heuze et al. (1990) also implemented Nilson's (1986) approach to gas-driven fractures in a finite element code. They modelled dynamic gas flow in conjunction with a quasi-static finite element analysis to investigate the interaction of gas-driven fractures with pre-existing discontinuities such as joints, bed interfaces and lens boundaries. However, their work did not consider losses due to convective and conductive heat transfer from the high temperature combustion gases to the host material. These heat losses significantly affect the fracturing speed and extent.

Schatz (1993) extended Nilson's formulation of gas driven fractures to include the motion of the gas in the borehole and provided a method of approximately predicting the number of fractures emanating from a borehole. He hypothesised that a limiting maximum fracture velocity exists and assumed that this was one half of the shear wave velocity. Then, when a calculation predicts tip velocities that exceed this velocity restriction, another fracture is added to the fracture count. This continues until the maximum fracture velocity does not exceed the specified limit.

Further approaches to gas driven fracture modelling are given by Paine and Please (1994) and Petitjean and Coust (1994). In both cases they verified their solutions by means of comparisons with existing analytical solutions provided by Nilson (1988).

---

[3] Summarised in a paper by Christianson et al. (1988).

3.2.3.6 Summary

This section has given a literature review of the most relevant studies dealing with blasting mechanisms. The overview is structured according to previous experimental, analytical and numerical investigations, as well as work dealing with gas driven fracturing. These categories are briefly summarised below:

Experimental Investigations: Due to the complexities and large number of poorly defined parameters associated with field studies, laboratory experiments have played an important role in understanding fundamental mechanisms pertaining to blast induced fracturing. Polymeric materials, particularly in the form of PMMA, have been used extensively and offer multiple advantages (ease of manufacturing, cost, well defined material properties, transparency, etc.), whilst exhibiting fracturing mechanisms which agree closely to those observed in brittle rock.

Analytical Investigations: Due to the complex interaction of multiple processes, only comparatively few analytical studies, which are directly applicable to blasting, have been conducted. Particularly noteworthy of these is the work based on fracture mechanics by Ouchterlony (1974), which remains important and relevant in many practical applications.

Numerical Investigations: With the further development of numerical methods and increasing computing power, numerical investigations of blasting processes have made significant contributions, particularly since the mid 1990's. While recognising the completeness of some of these models, in terms of modelling the complete blasting process from the detonation of the explosive to the formation of the muck pile, important mechanisms (e.g. heat transfer) are not taken into account, or are not modelled in sufficient detail.

Gas Driven Fracturing: Gas driven fractures are important, as they are the predominant fracture type propagating the furthest distances. The work by Nilson (1981, 1986, 1988) resulted in the most complete gas driven fracturing model incorporating thermal quenching and seepage losses. In this study, the gas driven fracturing model originally formulated by Nilson (1986) is further developed and applied to investigate parameters governing the final fracture extent in rock.

3.3 Methodology

Optical methods are especially suited for the observation and measurement of transient phenomena such as wave propagation and dynamic fracturing. These methods are fast and inertia free, do not disturb the process under observation and allow a simultaneous recording of stress wave and crack propagation over an extended area. Using sequential recordings or cinematographic techniques, temporal variations can be detected. The principal experimental methods applicable in dynamic stress analysis which are considered here are, therefore, optical methods.

3.3.1 Photoelastic method

Many transparent non-crystalline materials that are optically isotropic when stress free become temporarily bi-refringent when stressed. This effect normally persists while the loads are maintained, but vanishes almost instantaneously when they are removed. The phenomenon of bi-refringence (also known as double refraction) occurs when a ray of light entering a medium is split into two components, which in general are transmitted through the medium in different directions. The refractive index and velocity of transmission are therefore different for the two rays. Bi-refringence was first observed by Sir David Brewster in 1816 and is the physical characteristic on which the science of photoelasticity is based.

3.3.2 High speed photography

Since Tuzi (1928) initiated research in the field of dynamic photoelasticity, there has been a continuous development of new and improved high speed photographic systems. In dynamic photoelasticity the isochromatic fringes associated with stress waves propagate at speeds of a few km/s. A suitable high speed recording system, which provides full-field, high resolution photographs, is required to record the transient fringe patterns. While many different electro-optical systems have been developed and effectively employed to record dynamic fringe patterns, the multiple spark camera is particularly well-suited for investigations of dynamic stress wave and fracture propagation. This type of camera was used in the present study to investigate stress wave interactions with discontinuities and dynamic fracturing. The specific camera used for this study was developed by the Fracture and Photomechanics Laboratory of the Vienna University of Technology.A brief overview of the multiple spark gap camera follows.

The multiple spark gap camera was originally developed by Cranz and Schardin (1929), and is henceforth referred to as the Cranz-Schardin (CS) camera. A complete description of the CS camera system has been given by Riley and Dally (1969); an overview is given here describing the three basic subsystems comprising a CS camera. These are: (i) the spark-gap assembly, (ii) the optical bench and (iii) the control synchronisation circuit.

The Spark Gap Assembly

A near-square array of p x q[4] spark gaps is energised by a bank of capacitors charged to ≈15 kV. The capacitors are sequentially discharged through the spark gaps, thereby providing a time-sequenced series of short-duration high intensity light flashes, which are used to illuminate the specimen. The flash pulse duration is in the range of 400-500 nenoseconds, where the exposure time is measured at 1/3 of the peak intensity. The framing rate f at which the capacitors are discharged can be controlled by varying the inductance L for a given capacitor setting C: $f = \sqrt{2}/(\pi L C)$. Framing rates vary between 20 000 and 800 000 frames per second, and the inter-frame time can be varied individually from spark to spark.

The Optical Bench

The configuration of the optical bench associated with a CS camera is given in Figure 3.3.2.1. The optical bench performs three main functions, which include light polarisation, separation of the images and magnification. The light is polarised by passing through two circular polarisers between the two field lenses. The images of the sequential snapshots of the dynamic event are separated by the geometric positioning of the spark gaps, field lenses and camera lenses. Images are formed on a sheet of stationary film. The magnification of the optical system depends on the choice of field lenses; however, a magnification ratio of 0,1 is common, which results in an image of 35 – 50 mm in diameter for relatively large field lenses of 350 – 500 mm diameter.

The Synchronisation Circuit

In dynamic photoelastic applications involving propagating stress waves, event times normally range from about 50 μs to 300 μs. In this brief interval the model is dynamically stressed, the

[4] For the present study a CS camera with an array of p = 4 and q = 6 was used.

exposure of the first image is delayed by a selected delay period, and then p x q frames are recorded at discrete time intervals. These functions are initiated and controlled on the microsecond time scale, and synchronised by a number of sequenced electronic circuits.

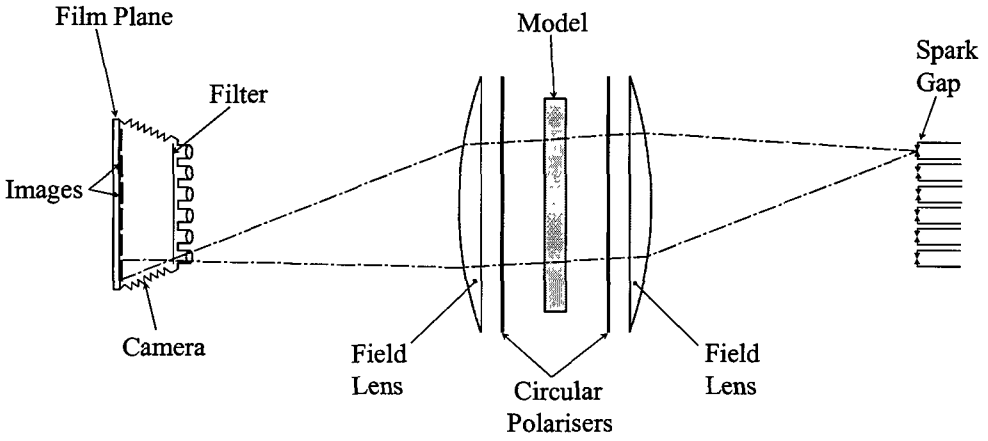

Figure 3.3.2.1 Components of a typical Cranz-Schardin multiple-spark gap camera.

3.4 Results

3.4.1 Stress wave interactions with rock joints

Stress waves interacting with stopes are significantly influenced by pre-existing discontinuities such as bedding planes and rock joints surrounding the mining excavation. The aim of the work is to advance the understanding of stress wave interactions with pre-existing discontinuities, and to quantify amplitudes of waves born during the interaction process with various interface types.

Upon stress wave interaction with discontinuities, incident energy is reflected and refracted (transmitted). The resulting reflected and refracted waves affect the dynamic behaviour of the rock mass and can lead to dynamic stress concentrations, energy channeling and stress wave superposition, which can cause the rock to fracture and/or lead to loss of rock mass stability. Hence, in order to gain insights into the mechanisms associated with dynamic processes, such as blasting, percussion drilling and seismicity, knowledge of the amplitudes of the reflected and refracted waves is of importance.

3.4.1.1 Analytical models

The objective of this work is to supply a detailed and comprehensive set of curves giving stress, energy and displacement coefficients for reflected and refracted waves due to the interaction of incident *P-, SV-* and *SH*-waves with a range of interface conditions. In addition to covering the well-known wave interactions with standard discontinuities, such as the free boundary and welded interface, some new interface conditions are analysed, e.g. interfaces with friction and

shear strength, interfaces with normal and shear stiffness related to measurable rock properties, as well as undulating and dissipative joints. The study acts as a reference for the rock engineer, seismologist, geophysicist and blasting engineer, and assists in further understanding stress wave interactions with rock mass discontinuities. Full details of the amplitude coefficients, as well as mathematical derivations and example problems illustrating the applicability of the coefficients to actual wave propagation problems, are given in Daehnke (1997).

Reflection and refraction coefficients, defined as the ratio of the reflected/refracted wave amplitude versus the incident amplitude, are determined analytically by using the local (at the interface) stress, velocity and displacement components of the incident, reflected and refracted plane waves to satisfy the boundary conditions at the discontinuity (Figure 3.4.1.1). Stress, energy, velocity and displacement coefficients are calculated for incident *P-, SV-* and *SH*-waves at angles of incidence ranging from 0° to 90°.

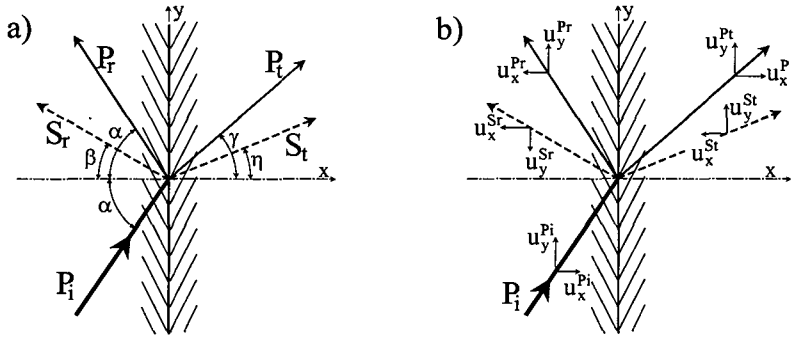

Figure 3.4.1.1 Displacement components of incident, reflected and refracted waves at a discontinuity.

A list of the types of discontinuity interface conditions that have been analysed is given. Also included is a brief review of the findings of the new interface types that have been investigated.

Free Boundary: Incident *P-* and *S*-waves interacting with a free boundary are reflected in the form of two additional waves, a reflected *P*-wave, and a reflected *S*-wave. The stress, energy and displacement/velocity amplitudes of the reflected waves depend only on the angle of incidence and Poisson's ratio.

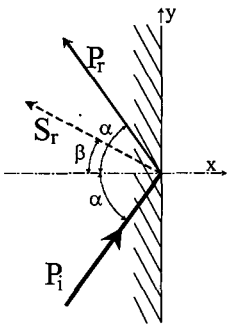

Perfectly Bonded Interface: Incident waves interacting with a perfectly bonded joint between two media generate two additional waves upon reflection, and two additional waves upon transmission. The amplitudes of the reflected and transmitted waves depend on the angle of wave incidence, Poisson's ratio and the acoustic impedance mismatch ratio (*n*) between the two materials (Miklowitz, 1978). Energy is conserved at the discontinuity. However, for $n > 1$ and certain angles of incidence, the stress amplitude of the transmitted wave exceeds the corresponding amplitude of the incident wave.

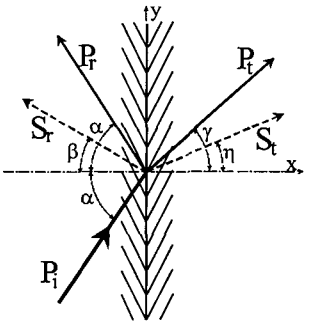

Non-Cohesive Frictionless Interface: This interface type acts as a wave filter and only compressive stress waves are transmitted. Tensile waves open the joint, and all incident tensile energy is reflected.

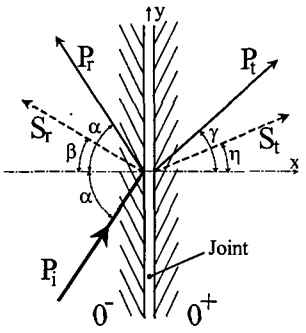

Non-Cohesive Frictional Interface: In the case of a frictional interface the amplitudes of the reflected and transmitted waves depend on the angle of wave incidence, Poisson's ratio, the acoustic impedance mismatch ratio and the coefficient of friction between the joint surfaces. During the slip process energy is dissipated; curves detailing the maximum energy dissipation versus angle of wave incidence and coefficient of friction are given in Daehnke (1997).

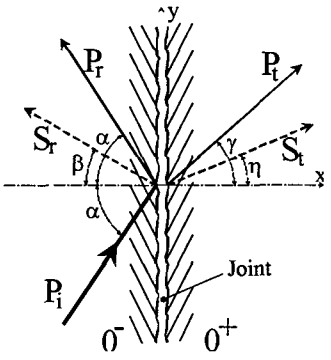

Cohesive Frictional Interface: Rock joints can contain narrow bands of filler material, which lend the joint normal and shear strength. Curves are given of the joint failure envelope (i.e. transition from intact to broken joint) versus internal friction, cohesive strength and angle of incidence for incident *P*- and *S*-waves.

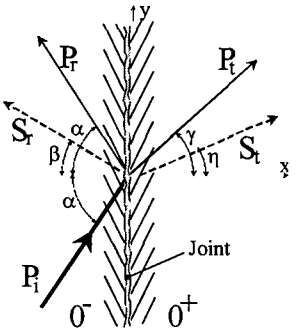

Interface with Equal Normal and Shear Stiffness: Joints displaying normal and shear stiffness can be modelled by interface conditions relating the normal and tangential displacement to the normal and shear stresses acting at the joint surfaces, respectively. It is shown that the amplitudes of the reflected and transmitted waves depend on the frequency of the incident wave. Low frequency waves are more readily transmitted, whereas a higher portion of the energy of high frequency waves is reflected.

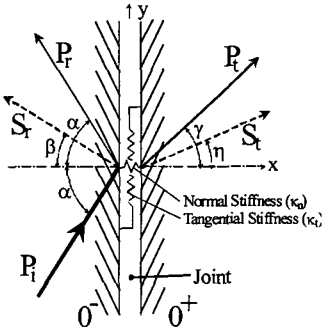

Interface with Stiffness Values Related to Actual Joint Properties: Empirical data is used to relate the normal and tangential joint stiffness to measurable rock properties. The joint stiffness can then be expressed as a function of the normal stress acting on the rock joint (e.g. see Figure 3.4.1.2). The amplitudes of reflected and transmitted waves are given for joint examples in dolerite, limestone and sandstone, and it is shown (for these joint types) that at a frequency of f = 100 Hz most of the incident energy is transmitted. At f = 2000 Hz the amplitudes of the waves reflected by the joint are approximately the same as the amplitudes of waves reflected by a free boundary, i.e. the transmitted energy is negligible compared with the reflected energy.

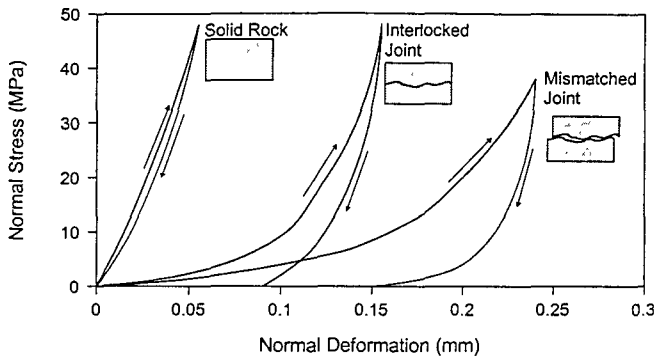

Figure 3.4.1.2 Normal stress versus deformation of various interface types.

Pre-Stressed Joints: It is shown that the reflection and transmission characteristics of rock joints are significantly influenced by the degree of joint pre-stress. Even at comparatively low pre-existing compressive stresses, significantly more energy is transmitted compared with unloaded joints. The implications of joint pre-stress are important in deep-level mining and for numerical modelling of stress wave propagation through fractured rock mass.

Undulating Joints: Interlocked, smoothly undulating joints can be modelled by cross-coupling the terms in the stiffness matrix. Generally, the stress amplitude of the reflected waves increases with increasing cross-coupling, whilst the amplitudes of the transmitted waves are reduced. A further unique effect of the cross-coupling is the generation of mode converted reflected and transmitted waves at normal wave incidence.

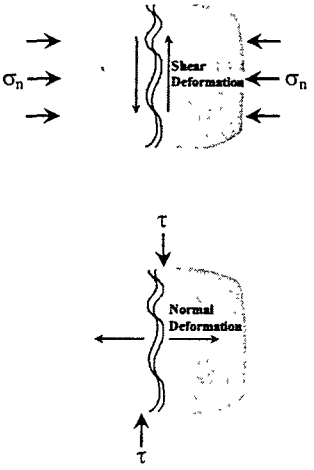

Dissipative Joints: The generalised Kelvin model is suitable to investigate the dynamic behaviour of interfaces modelling fluid filled joints, as well as discontinuities containing comparatively soft material. The reflection and transmission characteristics of this model are dependent on the joint stiffness, viscosity and the frequency of the incident wave. With increasing stiffness and viscosity, the amplitude of the reflected waves decreases, while more energy is transmitted. Increasing wave frequency results in more energy being reflected, and a reduced portion is transmitted. For the Kelvin model analysed here, a maximum of 25 per cent of the energy can be dissipated during wave passage across the interface. It is shown that the energy dissipation is relatively insensitive to the angle of wave incidence. Values of wave frequency, joint stiffness and damping are given at which maximum dissipation occurs. Knowledge of this parameter window (at which maximum energy is absorbed) is important to assess the interface integrity during passage of seismic and blast induced stress waves.

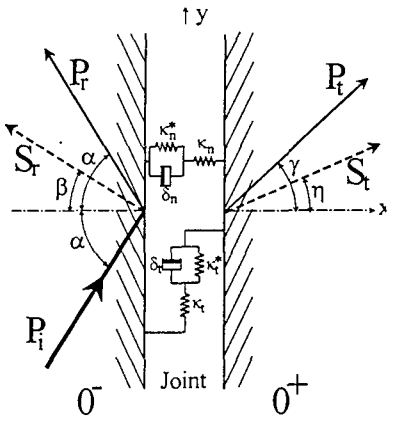

In summary, the characteristics of reflected and transmitted waves born during the interaction of incident stress waves with rock mass discontinuities are governed by a large number of parameters. This work has been published in two papers and represents the most comprehensive analysis of reflection and transmission coefficients for a wide variety of joint configurations and material parameters. The most important advances in the understanding of wave interactions with discontinuities have been made in the following areas:

- In this work the joint stiffness model is further developed to incorporate non-linear normal and tangential interface stiffness, where the relations governing the stiffness are based on actual joint properties. For typical joints analysed here, stress waves with a frequency of 100 Hz are predominantly transmitted, whereas at a comparatively high frequency of 2000 Hz most of the incident energy is reflected. Previously, although reflection and transmission coefficients were available for constant stiffness interface models, the coefficients were not related to actual joint properties and no lower – higher end frequency limits were established. The method developed here can be used to establish the reflection – transmission characteristics for any joint type, provided the interface surface properties have been determined by means of field or laboratory testing.

- An essential aspect of studies dealing with joint – wave interactions is the influence of joint pre-stress. This effect has previously been neglected. Based on actual interface properties, it is shown in this work that at even comparatively low levels of pre-stress, the joint reflection and transmission characteristics are altered significantly. With increasing pre-stress more energy is transmitted across the joint, and the amplitude of reflected waves is reduced. These results have important implications in deep-level mining applications and numerical simulations of wave propagation through fractured rock.

- The generalised Kelvin model is used to investigate the dynamic behaviour of fluid filled joints. The reflection and transmission as well as energy dissipation characteristics of this model are quantified, and are found to depend on the joint stiffness, viscosity and wave frequency.

- Further novel work dealing with joint – wave interactions examines energy dissipation at frictional joints, failure envelopes for joints with cohesive filler materials, undulating joints and the influence of wave amplitudes.

3.4.1.2 Numerical models

Numerical models are an important component in this research. An important aspect is that there is ultimately a need to represent generalised fracturing in dynamic models, which is not possible in the conventional WAVE code which has been extensively used in this work. Developments covered in this section are concerned with improvements in representing fractures and the fracture zone.

Alternative meshes

Trial runs were made on alternative meshes using the computer programs UDEC and ELFEN. These both use triangular elements and represent general orientations of fractures by allowing deformations in the mesh structure. This generalization requires far greater storage for each element (e.g. the positions of each node), leading to very limited model size compared to codes such as WAVE. A simple problem was used to test this approach to implementing an angled crack. The model consisted of a horizontal crack loaded normally with a low frequency pulse, a horizontal open crack and a receiving point below the crack (Figure 3.4.1.3a). The model was

rotated at 45° (Figure 3.4.1.3b) and the results compared within ELFEN and UDEC. The case for ELFEN is also shown in Figure 3.4.1.3, with (c) showing the mesh, and (d) comparing waveforms between the horizontal and 45° cases. The waveforms for the 45° case are similar to the horizontal case, indicating that the mesh deformations due to the angled crack introduce little error for this model.

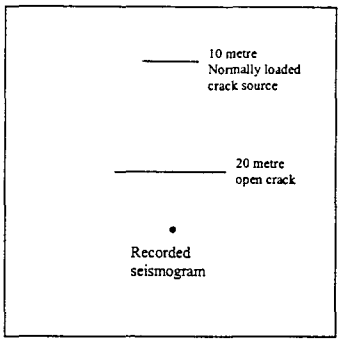

(a) Model geometry for horizontal cracks

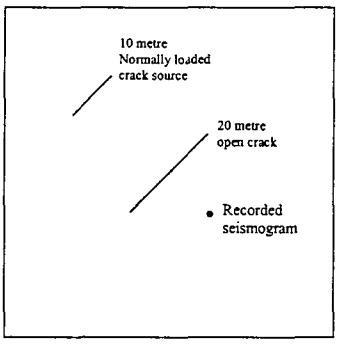

(b) Model geometry for 45° cracks

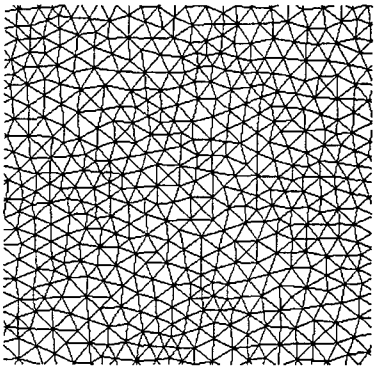

(c) Portion of ELFEN grid (45° model)

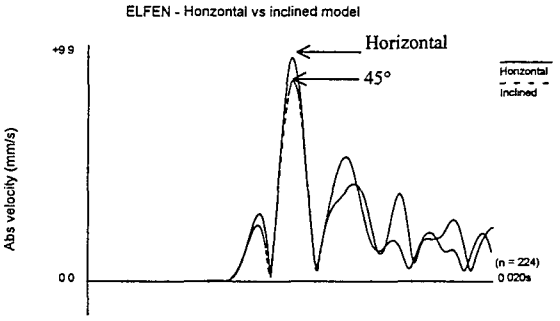

(d) ELFEN: Waveforms of absolute velocity for horizontal and 45° crack models

Figure 3.4.1.3 An equivalent horizontal and 45 ' crack model in ELFEN.

Equivalent medium angular cracks

An approach to representing general orientations of fracturing that is currently popular in seismic literature, is to represent a discrete fracture by an equivalent anisotropic material. Equations were developed (Coates and Schoenberg, 1995) for a discrete crack with linear normal and shear stiffnesses. The resulting stiffness matrix in the crack coordinate system was then rotated into a stiffness matrix for the grid coordinate system, and implemented in a staggered finite difference mesh, with encouraging results reported.

This approach was implemented and tested using WAVE. Results were accurate for very high stiffness cracks, but deteriorated for low stiffness cracks. In the limit, a zero-stiffness angled crack, fully transmits waves. This appears not to be an error in the implementation, but a necessary consequence - the tangential stiffness is non-zero, and therefore all components of the stiffness matrix in the grid-coordinate system are non-zero. This would prevent the method from being used to represent open cracks and hence also the opening/ closing contact behaviour which has previously been shown to be important. The approach is nevertheless convenient, and further progress in the literature should be monitored. However, the above would seem to indicate that the use of single-sided differencing with explicit crack surfaces, cannot be avoided.

Explicit angular cracks

An effort was made to develop angular cracks in a regular staggered finite difference mesh (i.e. WAVE). A limited breakthrough was achieved through the solution of a 45° angled crack (or potentially any single angle of crack according to the element aspect ratio). A solution for a fully general orientation remains elusive.

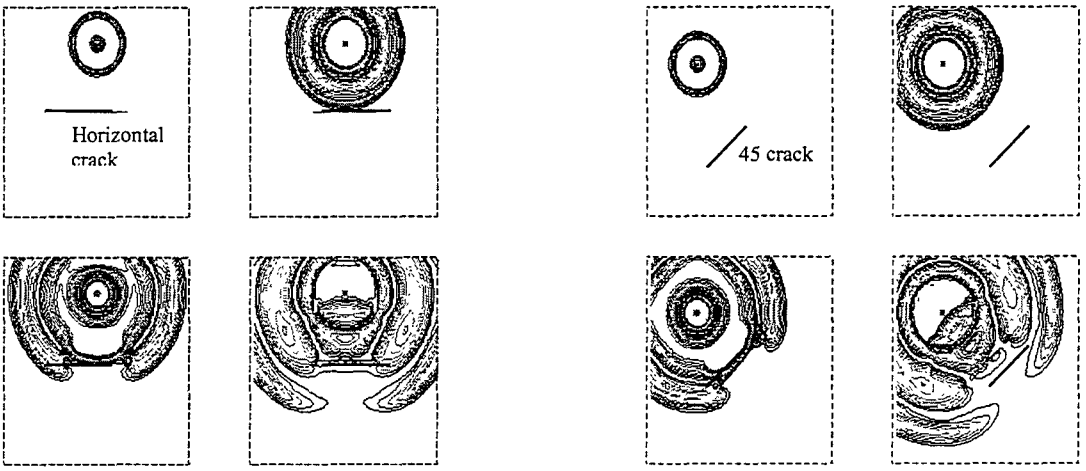

(a) horizontal open crack

(b) 45° open crack

Figure 3.4.1.4 Snapshots of velocity showing wave propagation about an open crack, comparing a horizontal crack in WAVE with a 45° crack.

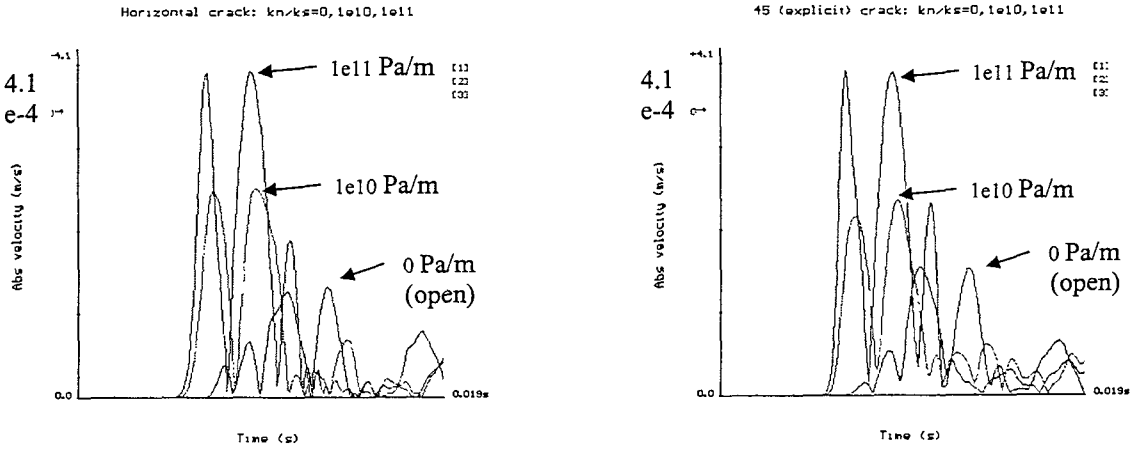

(a) Waveforms of absolute velocity for a horizontal crack for three different crack stiffnesses

(b) Waveforms of absolute velocity for a 45° crack for three different crack stiffnesses

Figure 3.4.1.5 Comparison of a horizontal crack with a 45° crack, showing waveforms for wave propagation about a crack for three different crack stiffnesses (0, 10 and 100 GPa/m).

In developing an explicit crack solution, it appears necessary for the crack to pass through two grid-points in the element. The approach used is to represent the orientation of the crack accurately, while approximating the position such that it passes through the nearest grid-point (without distorting the mesh). The justification here is that one should be dealing with wavelengths much larger than one element length.

The approach follows the development (Cundall, 1992) of equations for a horizontal crack, through the hypothesis of fictitious grid-points which can be eliminated with equations based on the crack constraints (normal and shear stresses continuous and related to the normal and shear discontinuities). The complication in the general case is that the crack boundary conditions are not in the grid-coordinate system, requiring tensor rotations. These require knowledge of the full tensor, which is not generally known in the staggered mesh. Other complications compared to the grid-aligned crack, are that more fictitious grid-points are required, and all components of the stress tensor are double-valued in the grid-coordinate system. The position has been reached where there is an explicit solution, provided that the tangential strain rates for the upper and lower surfaces at the σ_{11} and σ_{12} grid-points can be expressed in terms of known and fictitious velocities. A suitable expression has been found when the crack angle is 45° at both the normal and shear stress positions. (This is for a square element, a rectangular element would allow other angles). No general expression is available as yet.

Figure 3.4.1.4 shows the wave patterns from a point source interacting with a horizontal open crack, compared to the equivalent case of an open crack aligned at 45° to the grid, which shows similar behaviour. Figure 3.4.1.5 shows the waveforms at a point below the crack for three different crack stiffnesses (0, 10 and 100 GPa/m) for the horizontal and 45° crack, all of which compare well.

The formulation is such that non-linear slip and opening/ closing contact behaviour could be readily implemented. Use of a rectangular element would allow other crack angles to be studied (in isolation). The 135° (-45°) case, linking of horizontal and angled cracks, and crack tip conditions would need to be developed, and this may be non-trivial. Extension to three-dimensions has not yet been considered, and is potentially complex. The above general approach looks more readily implementable in a grid whose stress components are coincident. The suitability of the approximation of the crack position, and effectiveness of the method, could be tested out in such a grid.

Practical numerical dispersion expression

Owing to the need for more general fracturing, alternative grid schemes to the staggered mesh are being considered. One of the important issues for such grids is the accuracy in terms of numerical dispersion. A numerical approach for calculating dispersion curves has been developed. This is intended as an improved way to quantify different grid schemes, and may be a suitable way to evaluate the effects of a non-uniform grid on the accuracy of wave propagation. This is an important issue as the dynamic modelling of the fracture zone will probably require non-uniform meshes. The approach is shown for a uniform WAVE mesh. A plane wave is passed through the mesh and spatial waveforms are recorded at two points in time (Figure 3.4.1.6a). For a plane wave the phase velocity should be given by:

$$c(w) = \frac{1}{wt}\left[-\left(\phi - \phi_0\right) + i\ Ln\left(\frac{A}{A_0}\right)\right] \qquad (3.4.1.1)$$

(where $A(\omega)e^{i\phi(\omega)}$ and $A_0(\omega)e^{i\phi_0(\omega)}$ are Fourier Transforms of the spatial waveforms, A is the amplitude spectrum, 'ϕ' the phase spectrum, and subscript '0' indicates the earliest waveform). This yields the dispersion curves in Figure 3.4.1.6b for the second and fourth order WAVE scheme, confirming the improved accuracy of a fourth order scheme. Results have been found

to be fairly consistent for different grid sizes and test sources. The appropriateness of applying this to a non-uniform mesh has not been established.

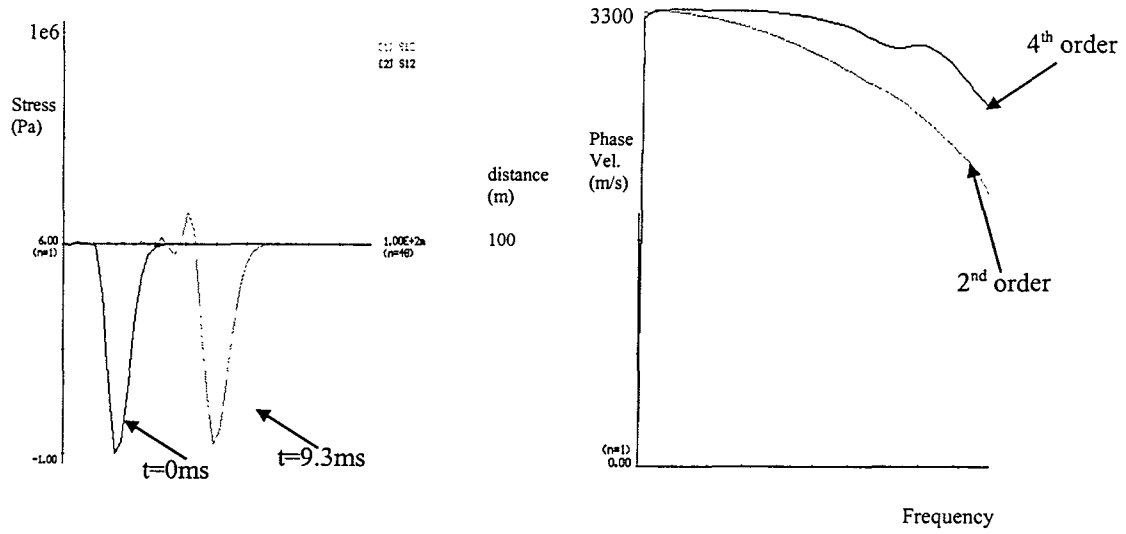

(a): Spatial waveforms at times (i) t=0 (ii) t=9,3 milliseconds

(b): Measured phase velocity vs. frequency for (i) 2nd (ii) 4th order schemes

Figure 3.4.1.6 Dispersion curve calculation and comparison for 2nd and 4th order WAVE schemes

Stress dependent crack stiffness

This was found to be important to the modelling of cracks under load (see Section 3.4.1.3). A hyperbolic joint stiffness relation can be represented as

$$u_n = \frac{a\sigma_n}{1+b\sigma_n}, \qquad (3.4.1.2)$$

where u_n = normal closure, and σ_n = normal stress, and a and b are constants. This relationship was implemented by calculating the local crack stiffness (k_n) at a point every time cycle using the expression

$$k_n = \frac{\delta\sigma_n}{\delta u_n} = \frac{a}{(a-bu_n)^2} \qquad (3.4.1.3)$$

Conclusions

A range of possibilities have been considered for representing the fracture zone in dynamic models. Novel developments were made in WAVE which extend its capability to model fracturing. However, implementing general fracturing in the staggered WAVE mesh would appear to be limited, and costly. In conjunction with Prof. P. Cundall extensive thought has been given as to how best to deal with general fracturing and other features in dynamic models. His recommendation was to investigate changing the grid scheme in WAVE to one which is more flexible but equally efficient. Schemes were proposed both for quadrilateral and for triangular elements. Both schemes can be made very efficient for areas of regular elements,

but can more readily represent fracturing than the current gridding scheme in WAVE. Triangular elements would have greater flexibility for fracturing, but the quadrilateral elements seem to be more readily extendible to higher order accuracy which has advantages for wave propagation studies.

3.4.1.3 Modelling experiments of waves through multiple interfaces

Appropriate models of fracturing need to be found which exhibit correct behaviour of fractured rock under seismic loading. A displacement discontinuity has been widely used as an explicit model of a crack. In this work the capability of a displacement discontinuity to model cracks from the point of view of wave propagation was investigated. Numerical models of discrete fractures were compared with waveforms recorded in experiments passing seismic waves through multiple aligned fractures. Significant departure of the numerical from the experimental results was noted for wave propagation across fractures. It was shown that a modification made to this model may account for these differences, without the need for a fundamentally different model.

Original Experiments

Schoenberg (1980) developed expressions for wave transmission across a displacement discontinuity. Pyrak-Nolte et al (1990a) compared theoretical expressions with experimental measurements, and showed that the wave interaction with a single natural fracture was well represented over a wide range of frequencies by an infinite displacement discontinuity (coupled by linear stiffness springs). The justification assumes that the wavelength is much larger than the distance between asperity contacts. Later work (Pyrak-Nolte et al., 1990b), extended this to an approximate expression for transmission through multiple parallel interfaces. These analytical expressions were compared with experiments of multiple parallel steel plates, showing that such a representation of the interface can account for frequency dependence in group velocities and amplitudes as found in the experiments. This paper also showed that the frequency dependence does not occur if an equivalent linear transversely isotropic material is used to model the multiple fractures. The displacement discontinuity model of a crack is shown in Figure 3.4.1.7.

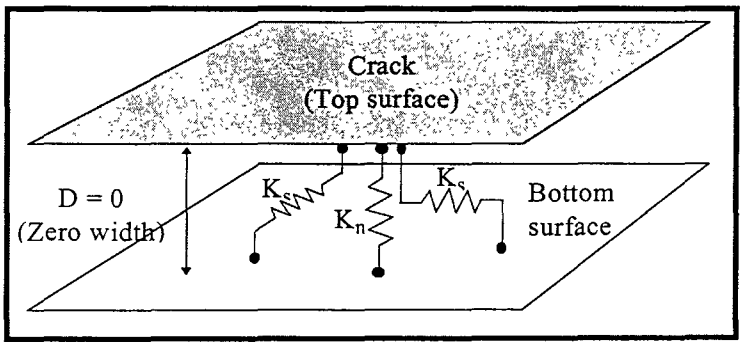

Figure 3.4.1.7 Displacement discontinuity model of a crack. (two surfaces with zero separation, connected by linear normal and shear stiffnesses K_n and Ks, relating stress and strain such that $\sigma_n = K_n u_n$, and $\sigma_s = K_s u_s$).

These experiments (Pyrak-Nolte et al., 1990b), consisted of 31 mild steel plates approximately 3 mm thick, stacked to form a cube of side 90 mm. To simulate the surfaces of fractures, the steel plates were sandblasted before being stacked. The block was biaxially loaded - one load clamping the plates and a second equal load parallel to the plates. The results presented are for a 30 kN (3,7 MPa) load. As a control, a solid cylinder of 99 mm height and 102 mm diameter was also tested. Seismic transducers for transmission and reception were loaded in series with the block (Figure 3.4.1.8). Each transducer had both compressional and shear wave piezzo-electric elements. These were excited in either compression or in shear with a 1 kV spike of 0,3 μs duration, and the response recorded for different orientations of the layered block.

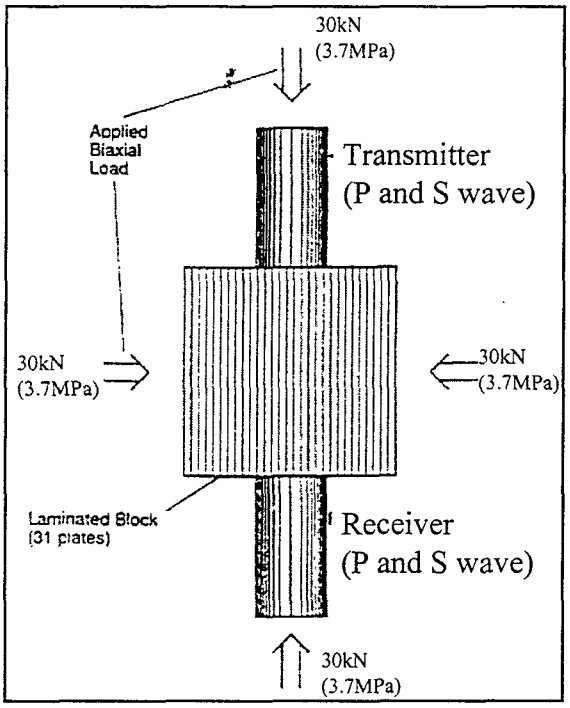

Figure 3.4.1.8 Sketch of experimental system used in the steel plate experiments (from Pyrak-Nolte et al, 1990b).

Numerical Model

The experiment was modelled in three dimensions using WAVE (Figure 3.4.1.9). A three-dimensional model was necessary, as the experiments were not plane strain, and most experiments were not axisymmetric. (Plane strain modelling was used in the initial tests, but the results differed considerably from the 3D modelling). The interfaces between the steel plates were modelled with displacement discontinuities with linear stiffnesses of k_n=6e13 Pa/m and k_s=2e13 Pa/m (no failure allowed). The source excitation was applied uniformly over a square of side 22 mm. The boundary conditions and source shape are not clearly available from the experimental data. The approach taken was to use the control (unfractured) case to establish a suitable source and then to use this in the fractured models. The results obtained required large models. For the shear wave experiments more than three million grid zones were required - at lower grid resolutions, the waveforms were not recognisable.

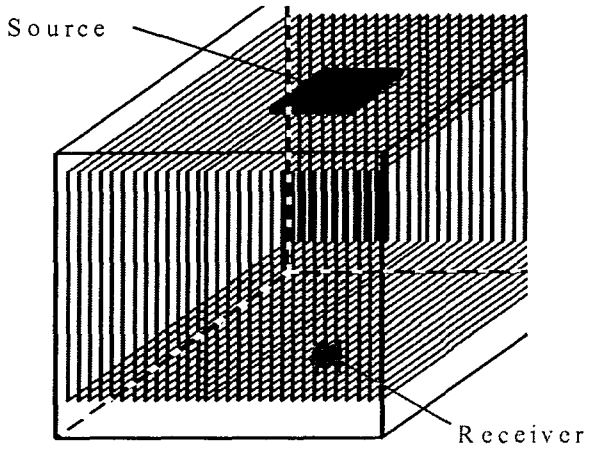

Figure 3.4.1.9 Sketch of 3D WAVE model with displacement discontinuities representing interfaces between the steel plates.

Source Inversion

The source waveform was determined for the control (solid cylinder) experiment, and then this source was applied to the fractured models (Figure 3.4.1.10). The source was determined by applying an arbitrary test pulse (I_t) to the solid cylinder and obtaining the response (O_t). Defining O_{Exp} as the observed (experimental) response, and I_{Exp} as the unknown source, it can be shown by taking Fourier transforms that

$$I_{Exp}(\omega) = \frac{O_{Exp}(\omega)}{O_{Tst}(\omega)} I_{Tst}(\omega) \qquad (3.4.1.4)$$

Apply an arbitrary test source (I_t) to the model of the solid cylinder experiment, giving the response (O_t). Taking Fourier Transforms of the experimental response (O_{Exp}), the test source, and the test response, a source (I_{exp}) can be found which produces the correct response in the solid model.

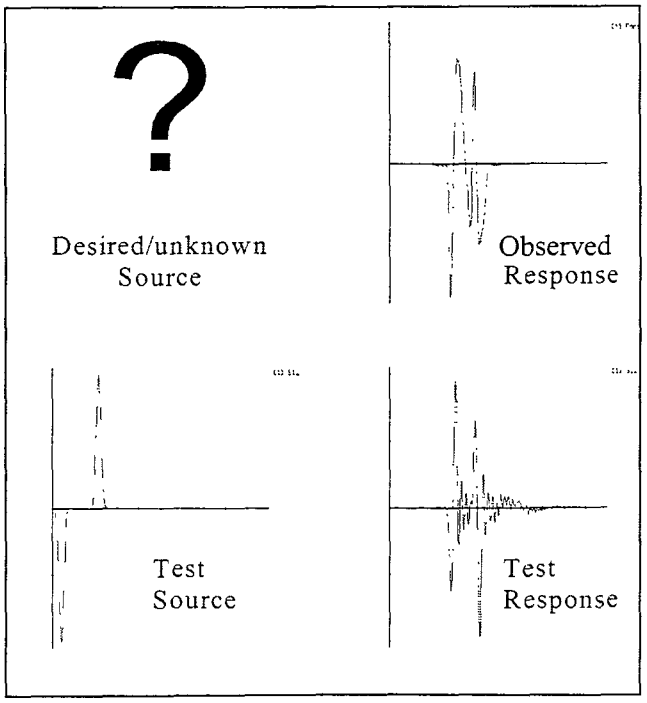

Figure 3.4.1.10 Procedure followed to invert for the shear source.

Applying formula 3.4.1.4 and taking the inverse Fourier transform gave the source in Figure 3.4.1.11a. Similarly, a *P*-wave source was found which would best reproduce the experimental result for *P*-waves through the solid cylinder (Figure 3.4.1.11b).

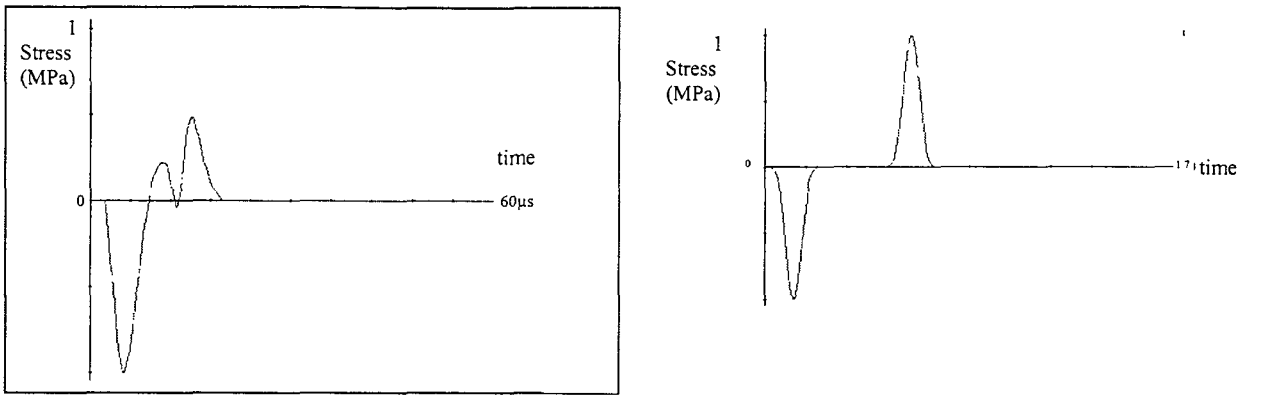

(a) Shear wave source-shape (b) P-wave source-shape

Figure 3.4.1.11 Source-shapes used in models of the P- and S- wave experiments.

P-wave Results

These results are given in Figure 3.4.1.12. There are three cases for *P*-wave propagation - solid cylinder, horizontal fractures (wave propagation across fractures) and vertical fractures (wave propagation parallel to fractures). In all cases the numerical results match well in terms of wave shape and arrival time. The effect on wave propagation parallel to the fractures is a slight delay in arrival, decrease in frequency, slight amplification and increased duration (Note that the later arrival in the unfractured case is due to the sample being approximately ten per cent longer). The effect on the propagation transverse to the fractures is a marked decrease in frequency, delay in arrival, attenuation and increased duration. The attenuation in the WAVE model is significantly less than the experiment (in the experiment the wave is attenuated to nearly 1/20 of the input, whereas the wave in the WAVE model is attenuated to 1/3 of the input). The full (modelled) waveforms are shown in Figure 3.4.1.13, showing that the fractures affect the durations of the oscillations significantly. (The full measured waveforms are not available for comparison).

An attempt was made to match the attenuation in wave propagation transverse to the fractures, by changing the crack normal and shear stiffnesses. Table 3.4.1.1 shows the trends noted for increasing normal and shear stiffness, over a small range of values. From the table, increasing the shear stiffness decreases the amplitude of the wave propagation transverse to the fractures, without greatly affecting other waveforms or characteristics. However, this effect is not sufficient to account for a six-fold difference in attenuation. This appears to indicate a different mechanism which is not present in the numerical model.

Table 3.4.1.1 Effect of crack stiffness on the frequency, arrival time and amplitude of P-waves

	Propagation transverse to fractures			Propagation parallel to fractures		
	Frequency	Arrival	Amplitude	Frequency	Arrival	Amplitude
>Kn	>>	<<	>	>~	>~	X
>Ks	~	X	<	~	>~	X

(Symbols used: X: no measurable effect; ~: approximately no effect;
>~: very slight increasing trend; <~: very slight decreasing trend)

(a) Solid Cylinder

(Unfractured, Control experiment)

(b) Horizontal Fractures

Wave propagation across (transverse to) the fractures

(c) Vertical Fractures

Wave propagation parallel to fractures.

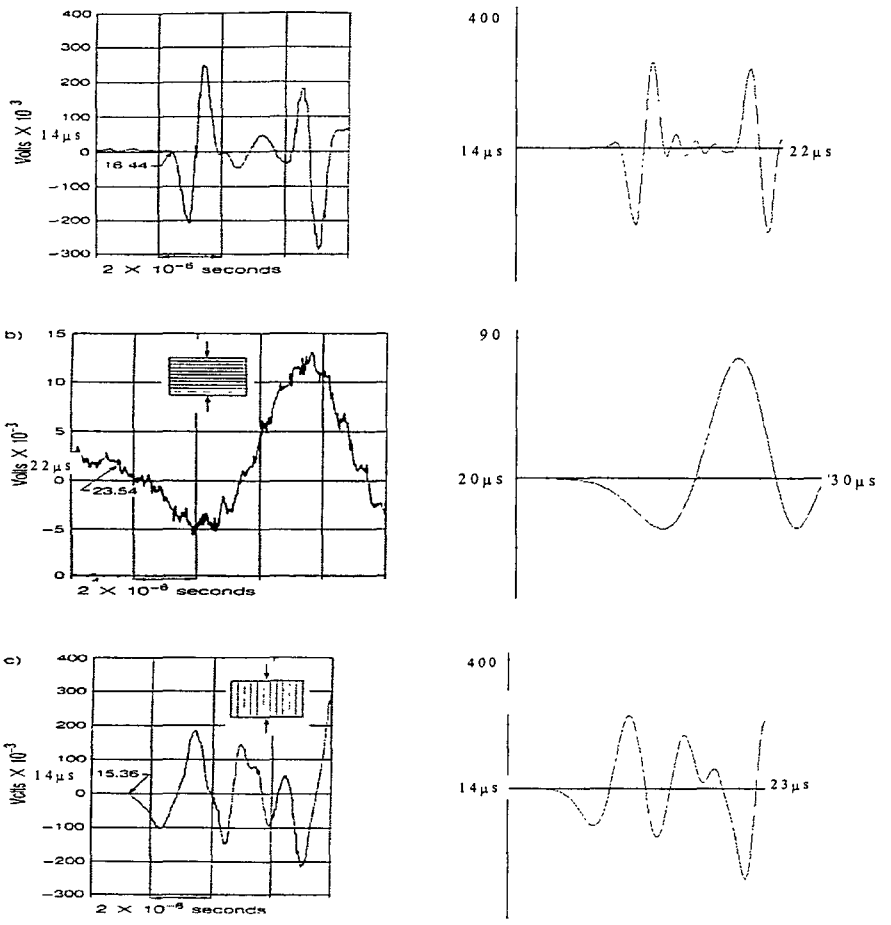

Experimental Waveforms (from Pyrak-Nolte et al., 1990)

Modelled Waveforms (WAVE)

Figure 3.4.1.12 P-wave comparisons for experimental and modelled waveforms.

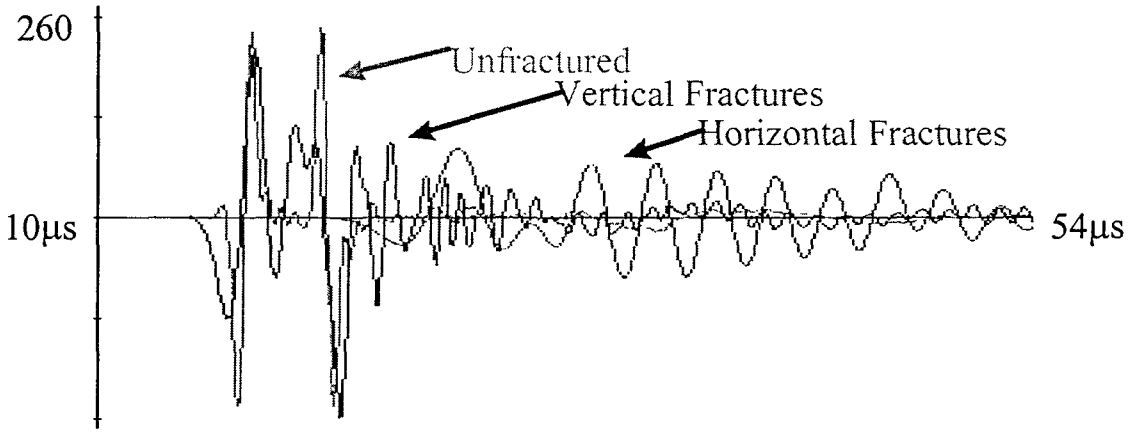

Figure 3.4.1.13 Full modelled P-wave responses for three experiments, showing some of the effects of fracturing on amplitude, frequency and delayed arrival.

(a) Solid Cylinder

(Unfractured, Control experiment)

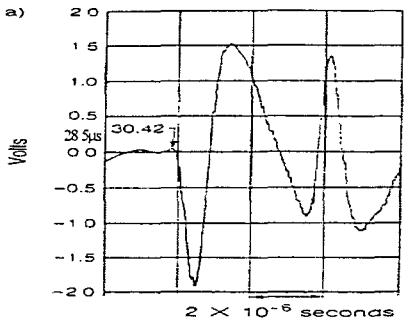

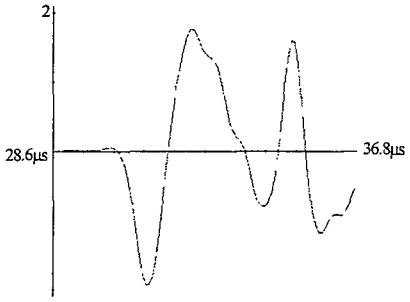

(b) Horizontal Fractures

Wave propagation across (transverse to) the fractures

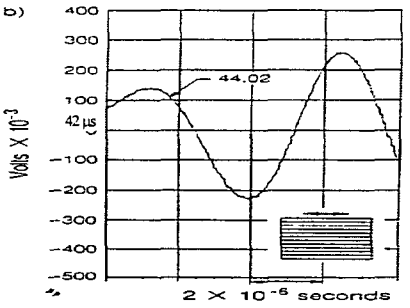

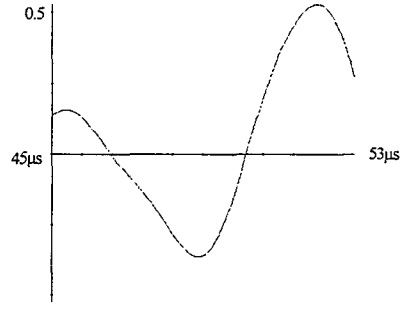

(c) Vertical Fractures

(Polarised, shear excitation parallel to fractures)

Wave propagation parallel to fractures.

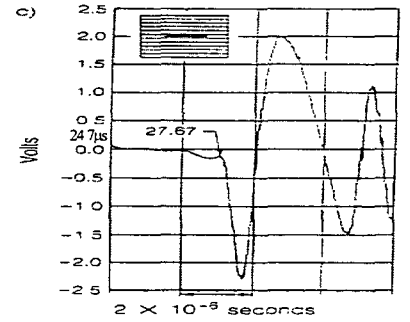

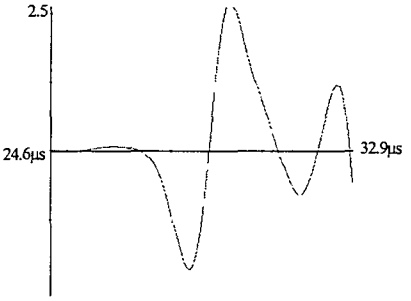

(d) Vertical Fractures

(Polarised, shear excitation perpendicular to fractures)

Wave propagation parallel to fractures.

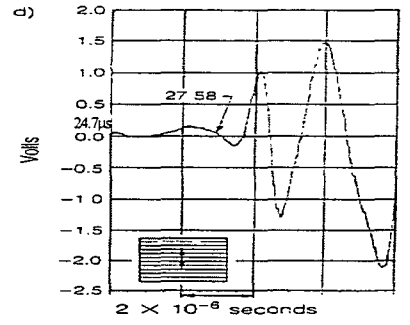

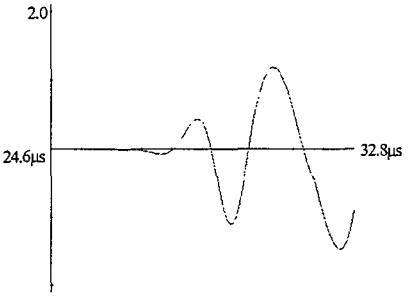

Experimental Waveforms (from Pyrak-Nolte et al., 1990)

Modelled Waveforms (WAVE)

Figure 3.4.1.14 Shear-wave comparisons for experimental and modelled waveforms for the different fracture orientations.

S-wave Results

The four modelled results are compared with the measured responses in Figure 3.4.1.14 with the same scale and time duration. There are two cases for shear wave propagation parallel to the cracks - one where the excitation is parallel to the cracks (3.4.1.14c), the other where the excitation is transverse to the cracks (3.4.1.14d). Once again the modelled wave shapes match well. For propagation parallel to the fractures, there is little effect on frequency and arrival time, and there is slight amplification. For propagation transverse to the fractures there is significant attenuation (~6 times), decrease in frequency and delay in arrival (~13 μs). In the model the delay is much later (~21 μs) and the attenuation less (~3 times). No study on the effects of different crack stiffness was attempted. It is expected but not proved, that choice of a more suitable stiffness would account more readily for the discrepancy in arrival, rather than the attenuation.

Discrepancies between modelled and measured waveforms

Overall there is a remarkable correspondence in wave shapes between the model results and the experimental observations for both *P* and *S* waves. Results for models of propagation parallel to the cracks were extremely close to that of the experiment. Results for models of propagation across the fractures showed the same effects as the experiment on wavelength, attenuation and arrival times. However the degree of these effects was significantly underestimated by the model. Figure 3.4.1.15 compares the modelled and measured *P*-waveforms on the same scale, illustrating this discrepancy in amplitude (i.e. amplitude in the model is about six times that of the experiment). Such a large discrepancy raises some doubt about the ability of the spring model to represent wave propagation through the fracture zone around excavations.

(a) Experiment

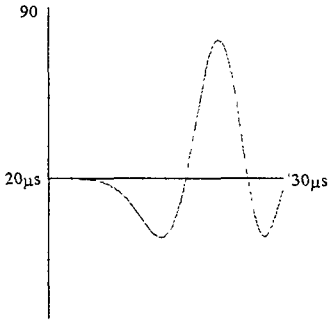

(b) Model (uniform crack stiffness)

Figure 3.4.1.15 Comparison of experimental and modelled waveforms for P-wave propagation across multiple horizontal fractures shown on approximately the same scale, indicating the discrepancy in amplitude. (The modelled amplitude is significantly larger than the observed amplitude).

It is important to establish whether these differences in amplitude (attenuation) indicate a need to introduce some further dissipative mechanism that may remove mechanical energy from the system - this requires a fundamental alteration of the assumed crack model. Alternatively, the next results indicate that greater attenuation in the experiment could be caused by a non-uniform stress field, and that models of cracks may need to incorporate stress-dependence.

Non-uniform stress-field

The vertical load in the experiment was applied over only one ninth of the block face area but the horizontal load was applied over the full face area, leading to a non-uniform vertical stress but an approximately uniform horizontal stress. Fracture stiffness is related to the compression of a crack and hence can be expected to vary across the cracks if the stress distribution is non-uniform. Figure 3.4.1.16 shows the cross-sectional variation of the stress normal to the cracks for the cases of horizontal and vertical cracks. The normal stress for the experiments with horizontal cracks is significantly non-uniform and the resulting variation in fracture stiffness may be expected to have an influence on wave propagation. This may account for greater attenuation in the horizontal crack experiments, with little effect in the vertical crack experiments.

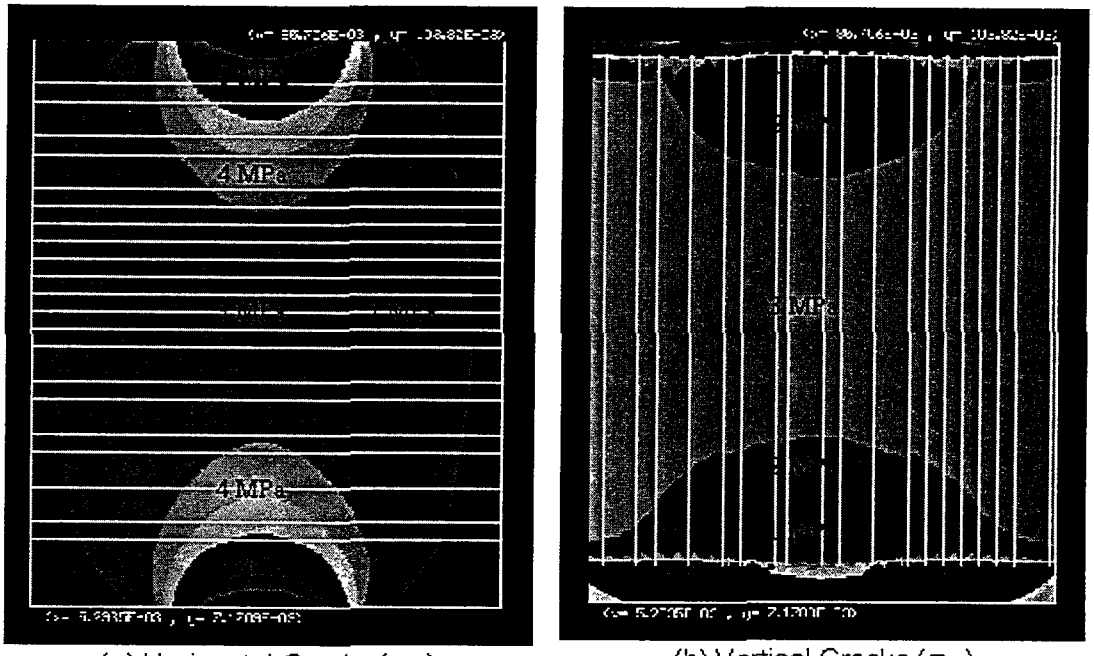

(a) Horizontal Cracks (σ_{22}) (b) Vertical Cracks (σ_{11})

Figure 3.4.1.16 Cross-sectional variation in crack normal stress (stress variation in the experiments with horizontal fractures, indicates that it may be dependent on the stress state)

Stress-dependent fracture stiffness displacement discontinuity model

To test this hypothesis the stress-dependence of fracture stiffness was incorporated into the model, using a hyperbolic joint stiffness relation (Bandis, Lumsden and Barton, 1983; Curran and Goodluck, 1993).

$$u_n = \frac{a\sigma_n}{1+b\sigma_n}, a = \frac{1}{k_{ni}}, b = \frac{a}{u_{n(\max)}} \qquad (3.4.1.5)$$

where u_n = normal closure; $u_{n(max)}$= maximum closure; σ_n = normal stress; k_{ni} = Stiffness at σ_n = 0MPa.

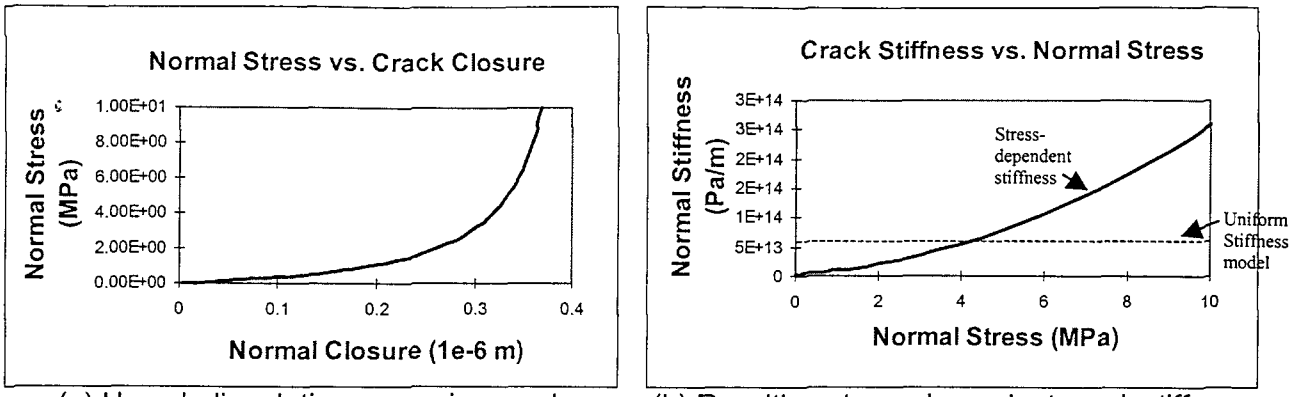

(a) Hyperbolic relation governing crack deformation

(b) Resulting stress-dependent crack stiffness

Figure 3.4.1.17 Crack-stiffness relation applied in WAVE model.

Values of a = 3,5e-13 and b = 8,5e-7 were used, giving a crack normal stiffness of 6e13 MPa/m for a normal stress of 4,2 MPa. (This was the fracture stiffness used in the uniform crack stiffness model). Figure 3.4.1.17a shows how this relation leads to a hyperbolic relationship between normal stress and crack closure. Figure 3.4.1.17b is the resulting function for a stress-dependent crack stiffness.

Applying this model to the representation of a crack slightly alters the stress distribution in the model. Figure 3.4.1.18 shows the altered cross-sectional variation of the stress normal to the cracks for the case of horizontal cracks, compared with that of Figure 3.4.1.16a.

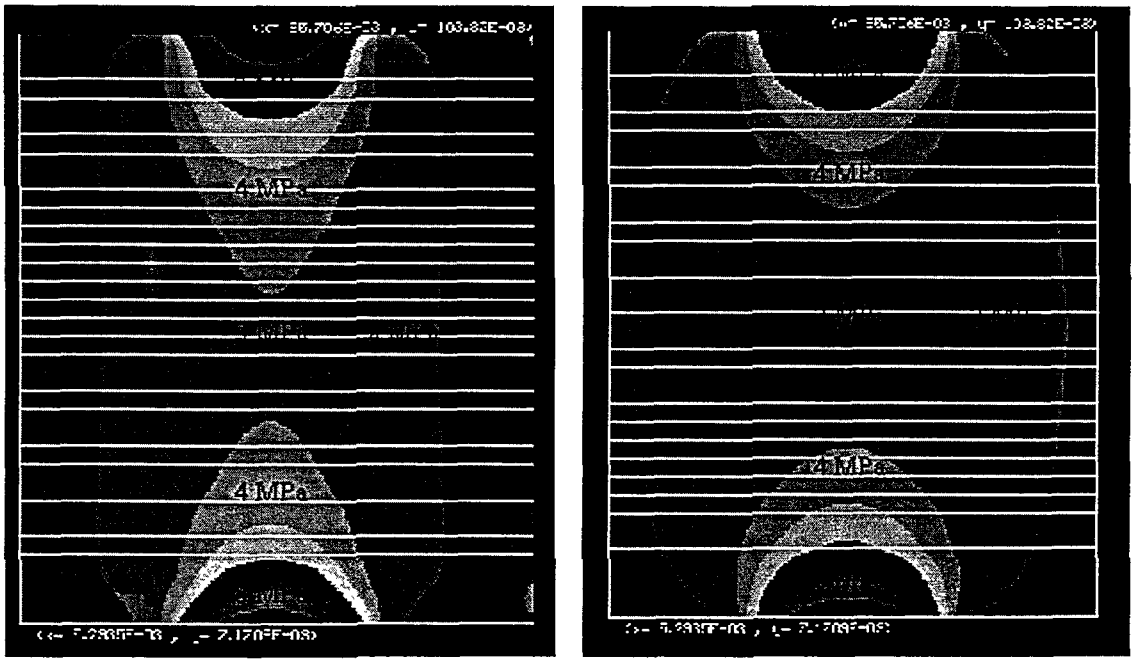

(a) Stress-dependent crack stiffness

(b) Uniform crack stiffness

Figure 3.4.1.18 Modified normal stress (σ_{22}) distribution for horizontal cracks, due to the stress-dependent crack stiffness.

(a)

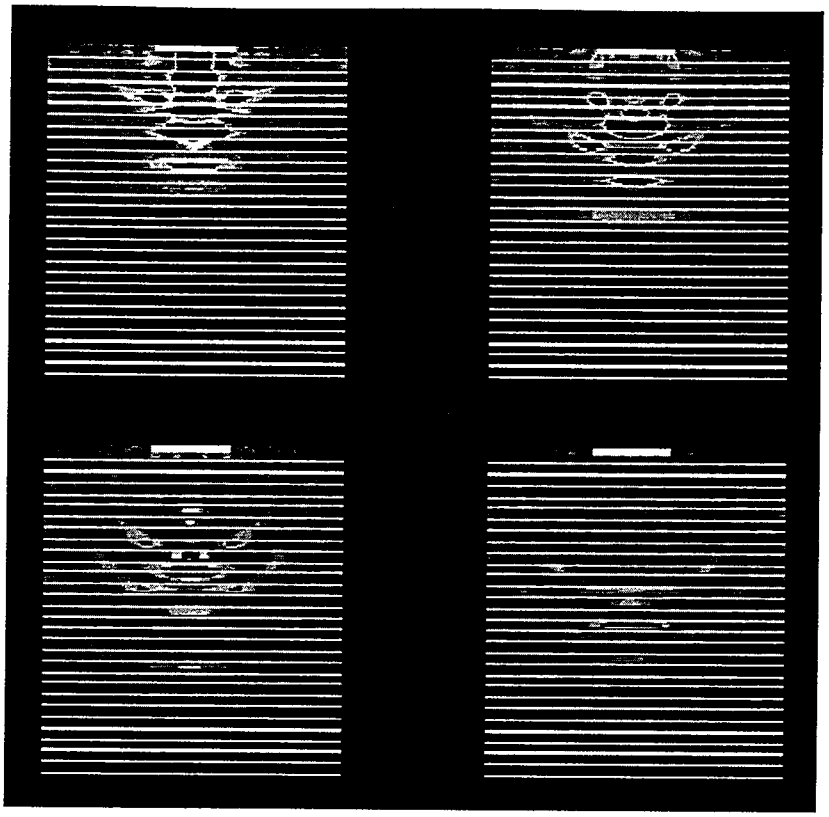

(b)

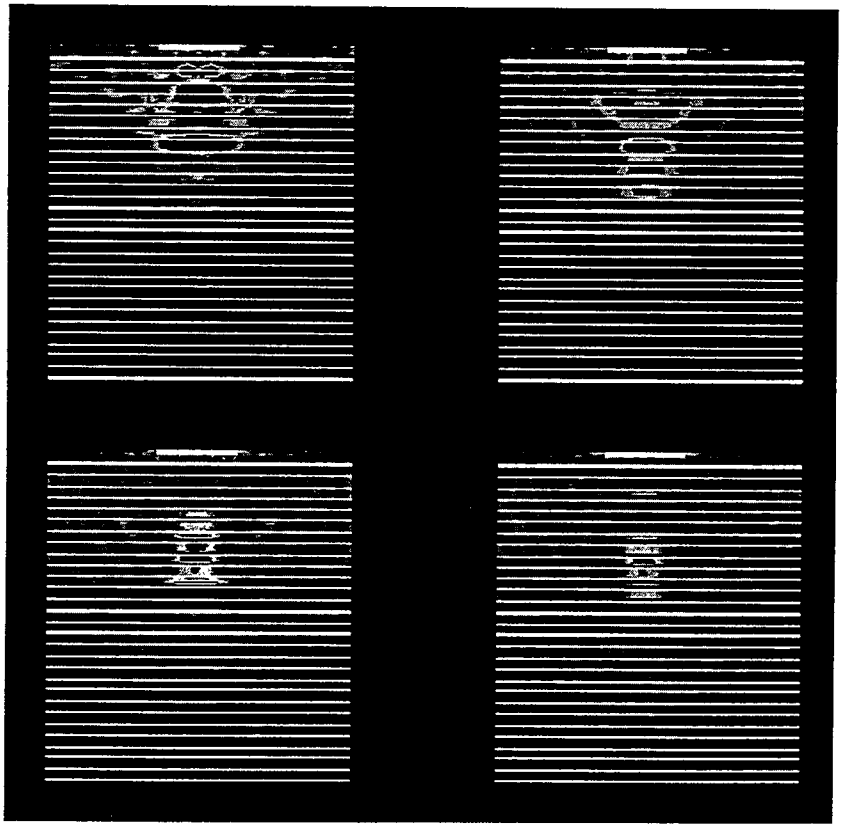

Figure 3.4.1.19 Snapshots of wave propagation for (a) uniform stiffness cracks, and (b) stress-dependent stiffness cracks.

Comparisons with experiment and uniform stiffness model

Having equilibrated the system yielding a static stress state and fracture stiffness distribution, *P*-waves were then passed through the models. Figure 3.4.1.19 compares snapshots of waves passed through the model with a uniform fracture stiffness with that of the stress-dependent fracture stiffness. The stress-dependent fracture stiffness leads to faster propagation through the centre of the model, and ultimately to greater scattering and dispersion of the wave.

Figure 3.4.1.20 compares the actual seismograms from the two models with the experiment. The amplitude in the stress-dependent model is only fifty percent greater than that of the experiment, compared to the uniform stiffness model in which the amplitude is five hundred per cent greater than the experiment. The arrival time and wavelength is also improved in this model.

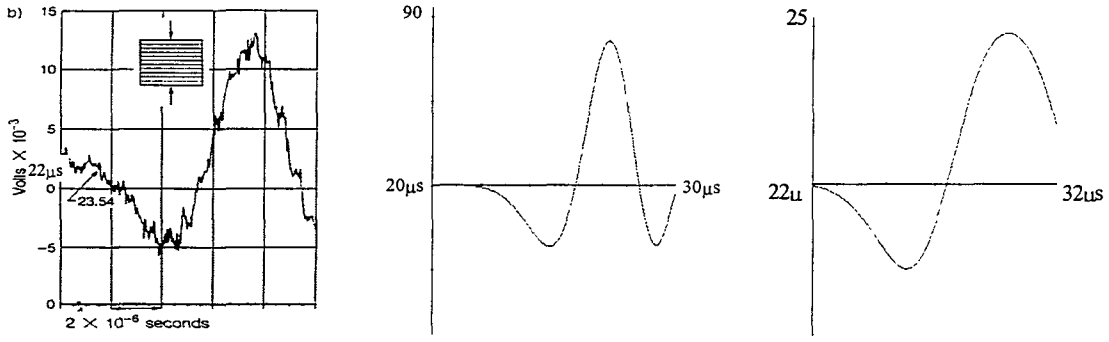

(a) Experiment (b) Uniform fracture stiffness (c) Stress-dependent fracture stiffness

Figure 3.4.1.20 Comparison of waveforms for P-wave propagation across (horizontal) cracks.

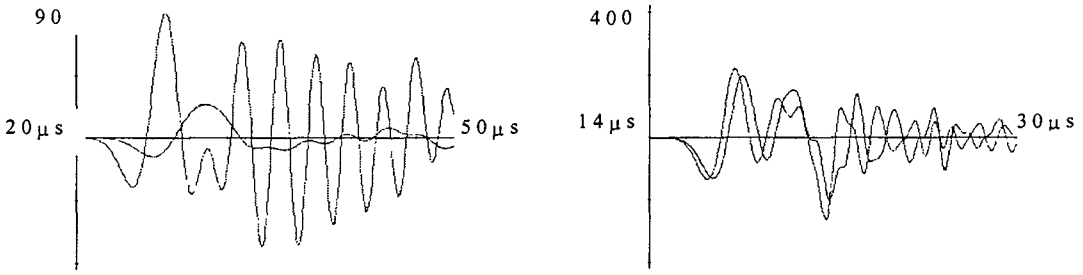

(a) Horizontal fractures (b) Vertical fractures

Figure 3.4.1.21 Comparison of full waveforms for the P-wave responses for the two models (constant vs. stress-dependent stiffness).

Figure 3.4.1.21 compares the full waveforms for the *P*-wave responses for the two models (constant vs. stress-dependent stiffness). The stress has little influence in the vertical fracture case, which explains why the uniform stiffness model matches the experiment in this case only.

Conclusions

This work has shown that modelling wave interaction with displacement discontinuities appears to capture much of the physics observed in experiments with real joints and, by inference, with fracturing. The important conclusion however is that in a non-uniform stress field, modelling wave propagation through fractures without a stress-dependent fracture stiffness may be inaccurate. This could be particularly important in models of wave propagation around excavations where the stress state is not uniform. Further work needs to establish whether this effect is important for the typical range of wavelengths interacting with such excavations. Only the errors in the *P*-wave transmission have been accounted for in this model, and the effect on shear wave transmission still needs to be evaluated. Another aspect is how this model will behave for large amplitude waves where non-linear behaviour is to be expected. (i.e. the fracture stiffness changes during passage of the wave, and hence the fractures respond differently for different wave amplitudes).

3.4.1.4 Representation of stope fracture zone

The experiments and models developed in section 3.4.1.3 involve wave interaction with joints in general. We are more specifically interested in wave interaction with the fracture zone of stopes, and in particular the waves and frequencies associated with damaging rockbursts. A number of questions need to be addressed to evaluate how such results relate to the stope fracture zone.

(i) The experiments have very high frequency (~250 kHz), high fracture stiffness and small spacing (~3 mm). What frequencies, spacings and stiffnesses produce similar effects on the stope scale, and are these realistic?
(ii) In the experiments, there is little amplification but significant attenuation - yet high particle motions are expected in the fracture zone.
(iii) There is a fully compressive stress state in the experiment. One would at least expect low fracture stiffnesses in the fracture zone, but also non-linear behaviour. Is the model still appropriate?
(iv) The experiments contained parallel fractures only - the behaviour with intersecting fractures and blocky material was not established.
(v) Could the experiments have been modelled with an alternative to an explicit crack representation (equivalent materials)?

Points (iii) and (iv) can only be investigated with further experiments. A simple two-dimensional stope model with different representations of the fracture zone, was used to consider points (I), (ii) and (v). In particular the influence of wave frequency and fracture stiffness on the attenuation and amplification of particle motions was investigated, as well as an alternative to explicit fracture representation, through a continuum model.

Figure 3.4.1.22 (a-d) contains four model geometries. (a) is the basic unfractured stope geometry - a 50 m stope, 5 m shear source 20 m ahead of the stope face, and recording positions in the stope hangingwall. (b) shows a zoomed portion of the second model with horizontal (stope parallel) fractures of 2 m spacing - represented by linear stiffness displacement discontinuities as for the experiment. (c) is the explicit case with vertical fractures also with 2 m spacing, while (d) is the model where the fracture zone is represented by an equivalent volumetric material - in this case a transversely isotropic model calculated to be equivalent to the horizontal fracture case.

In the stope models, the fracture spacing was 2 m, and pulse widths of 1 milliseconds, 4 milliseconds and 10 milliseconds were used (loosely corresponding to frequencies of 1 kHz, 250 Hz and 100 Hz). The shear experiment had a pulse width of ~2 μs and a fracture spacing of 3 mm, translating into the mid-range of the stope models). Crack stiffness was allowed to range from k_n=2e10, k_s=1e10, down to k_n=4e9, k_s=2e9 Pa/m.

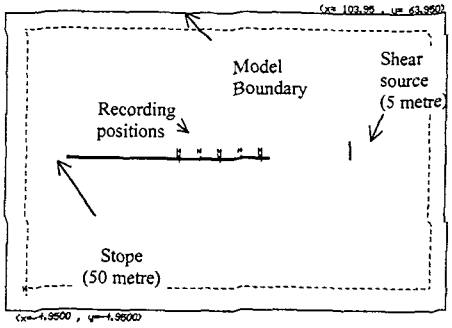

(a) Full unfractured stope model

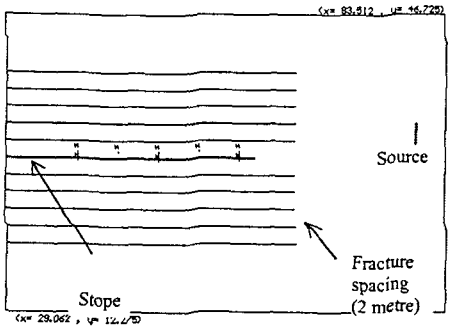

(b) Zoomed portion of model with fracture zone represented by horizontal fractures

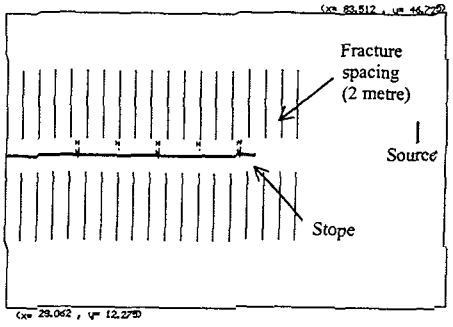

(c) Zoomed portion of model with fracture zone represented by vertical fractures

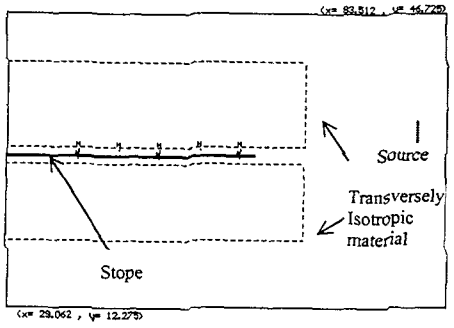

(d) Zoomed portion of model with fracture zone represented by a transversely isotropic material (equivalent to horizontal fracturing)

Figure 3.4.1.22 Simple 2D stope models with different fracture zone representations.

Figure 3.4.1.23 examines the effect of source frequency for a 2 metre fracture spacing. For a high frequency source (a, ~1 kHz), the fractures cause attenuation in the hangingwall motions (as in experiments of Section 3.4.1.3) while for lower frequencies (b, ~100 Hz), the fractures cause amplification. Figure 3.4.1.24 looks at the effect of reduced fracture stiffness for the case of horizontal fractures. For the high frequency source (a), the reduced stiffness increases the attenuation significantly. For the low frequency source (b), the reduced stiffness increases the amplification significantly. (Not shown here is that for even lower stiffness, attenuation again dominates).

The above shows that representation of explicit fractures in the model can account for both amplification and attenuation in stope motions, depending on the frequency and fracture spacing, and on the fracture stiffness.

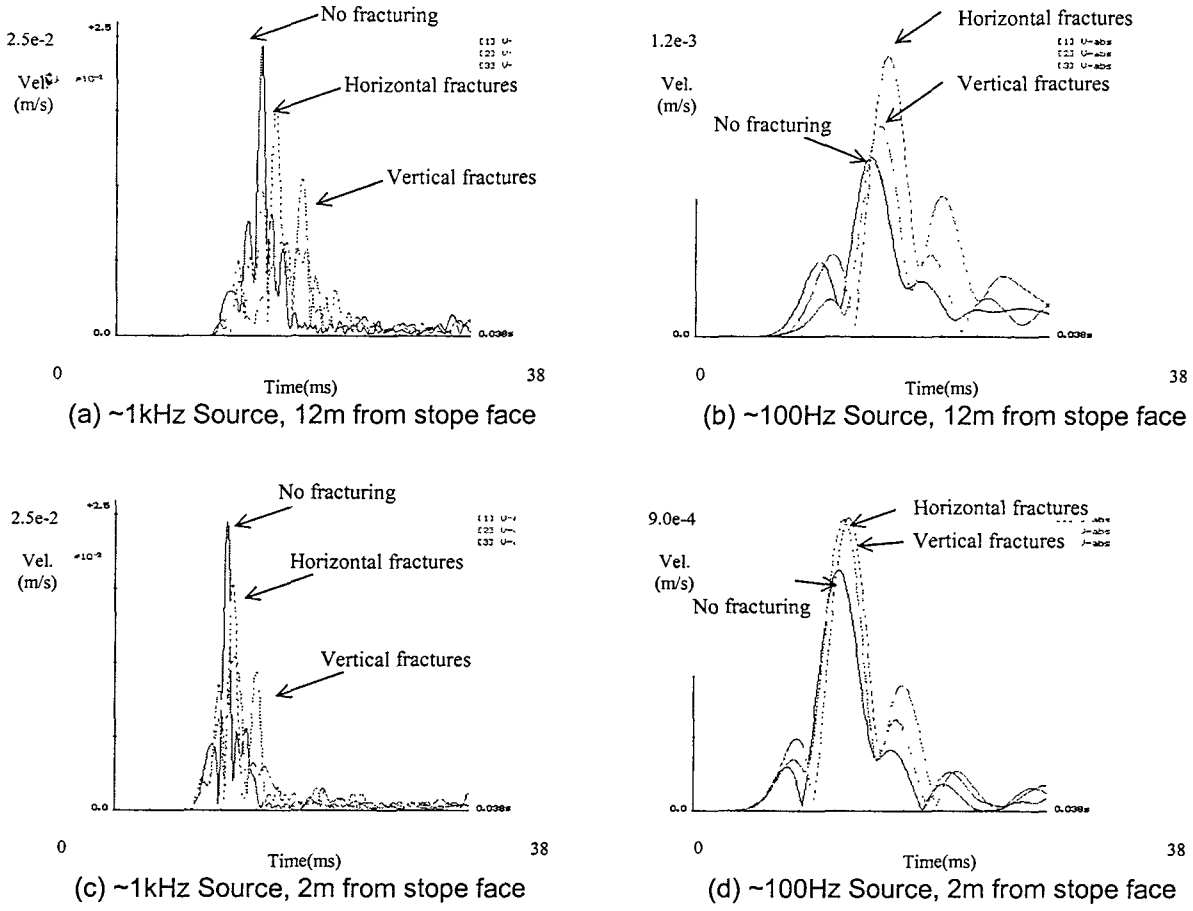

Figure 3.4.1.23 Effect of source frequency. Hanging wall velocities at 12 metres and at 2 metres from the face, for cases of no fractures, horizontal fractures and vertical fractures, and comparing two different source frequencies. (Fracture stiffness is constant; k_n=2e10, k_s=1e10).

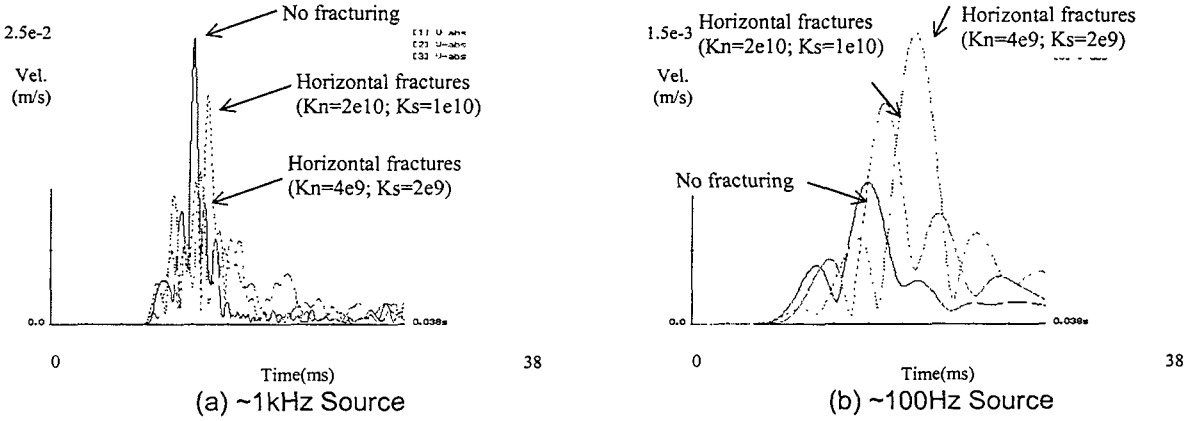

Figure 3.4.1.24 Effect of fracture stiffness at different frequencies. Hanging wall velocities at 12 metres from the face with varying crack stiffness, and for different source frequencies.

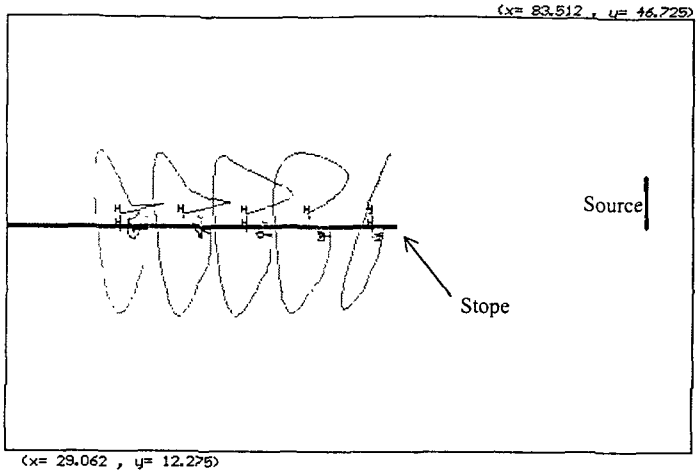

(a) Stope Model

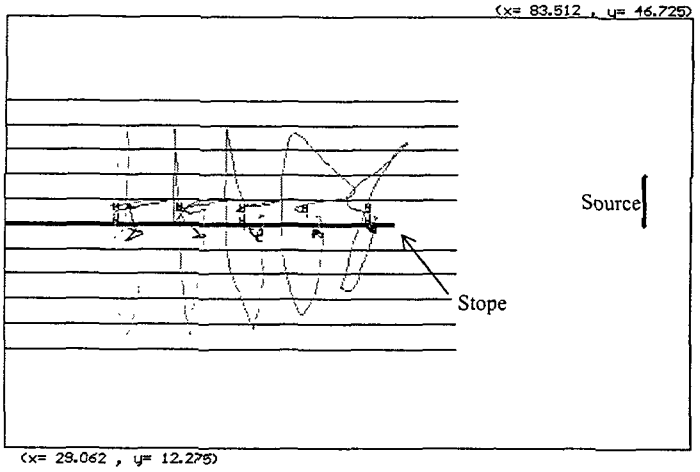

(b) Fracture zone represented by horizontal fractures

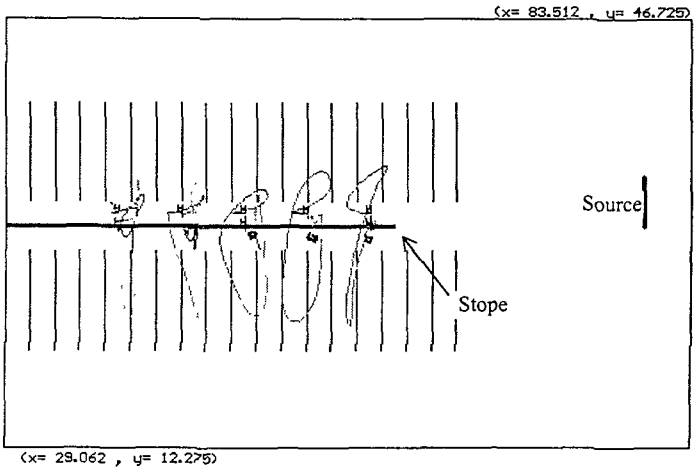

(c) Fracture zone represented by vertical fractures

Figure 3.4.1.25 Influence of fractures on trajectories. Hangingwall trajectories compared for cases of no fractures, horizontal fractures and vertical fractures, for 1kHz source.

An interesting effect is also shown in Figure 3.4.1.25, where the trajectories of points in the unfractured hangingwall (a) are modified to be predominately vertical, both for horizontal fractures (b) and for vertical fractures (c). The trajectories shown are exaggerations of the particle motion at a point in the rock, tracing the displacement path that would be followed. Realistic representation of not just amplitude, but actual particle motion could be important to issues such as support, so that the influence of fracturing on trajectories is important.

One approach to representing fractured rock, is to replace the fracturing by an equivalent medium. In particular, a number of papers in the literature have shown that fracturing in a single direction can be replaced by an equivalent medium with transversely isotropic behaviour, provided that the fracture spacing is much smaller than the wavelength. The approach to calculating this equivalent medium, used by Coates and Schoenberg (1995), was implemented in WAVE for two-dimensions. This calculates a stiffness matrix from, the surrounding medium, the given fracture stiffness and the fracture density, defined here as the total length of fractures per unit area.

Material parameters were chosen to correspond to the case of horizontal fracturing, with a spacing of two metres. The results are compared with the explicit horizontal Fracture models (displacement discontinuities) at different points along the hangingwall in figure 3.4.1.26 (a and b), for the case of low frequency and high stiffness. The waveforms are nearly equivalent to those from the model with explicit fractures. However, in cases of either low stiffness (Figure 3.4.1.27a) or high frequency (Figure 3.4.1.27b), the transversely isotropic representation is unsuitable. (Note however that the first arrivals still match well, but the rest of the waveform and amplitudes differ considerably). The need for high stiffness cracks would appear to limit the application of a transversely isotropic model to wave propagation in the fracture zone.

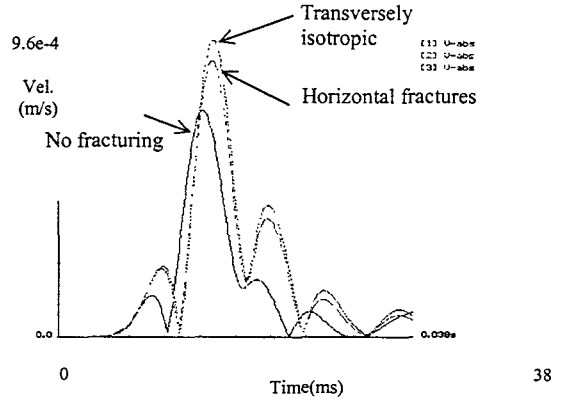

(a) Low frequency, High fracture stiffness (100Hz source, k_n=2e10, k_s=1e10, 2 metres from stope face)

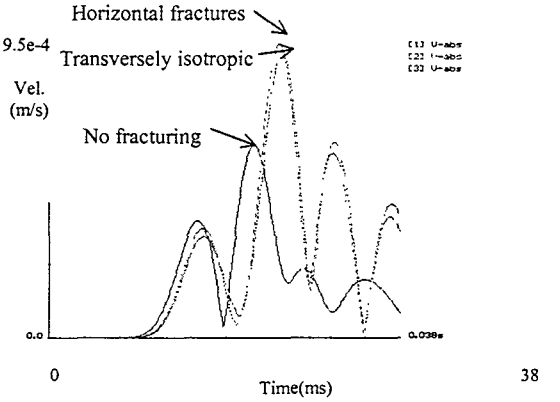

(b) Low frequency, High fracture stiffness (100Hz source, k_n=2e10, k_s=1e10, 22 metres from stope face)

Figure 3.4.1.26 Comparison of equivalent transversely isotropic medium with explicit horizontal fractures, showing near equivalence if the source frequency is low and the fracture stiffness is high.

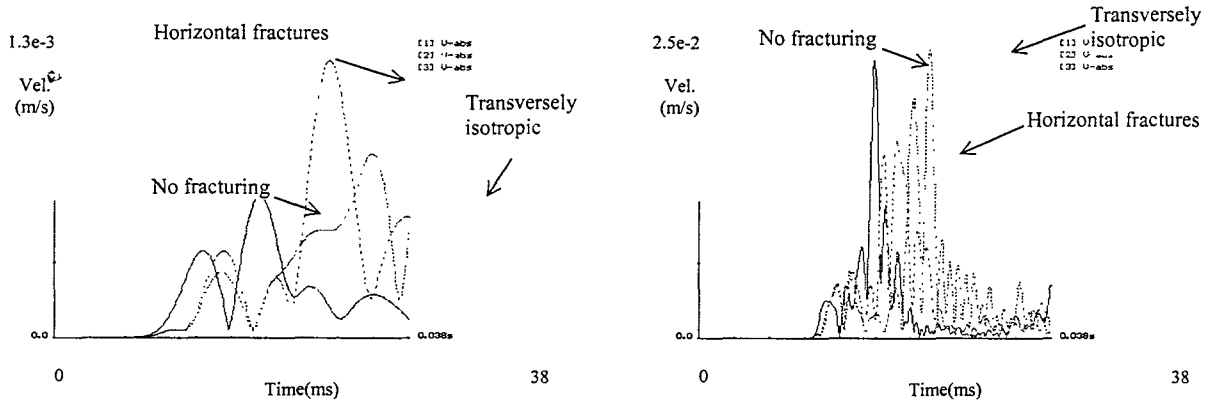

(a) Decreased stiffness
(100Hz source, k_n=4e9, k_s=2e9,
22 metres from stope face)

(b) Increased frequency
(1KHz source, k_n=2e10, k_s=1e10,
22 metres from stope face)

Figure 3.4.1.27 Comparison of Equivalent Transversely Isotropic Medium with explicit horizontal fractures, showing departure for higher source frequencies or lower fracture stiffness.

Summary

In searching for a suitable numerical representation for the fracture zone, the validation of explicit cracks is especially important - not only for direct use as a model of the fracture zone, but also to create data against which other equivalent models can be tested. The modelling showed that displacement discontinuities could be applied to model the stope fracture zone, and would produce attenuation or amplification of motions depending on the frequency of the source and the fracture stiffness. Only the linear fracture stiffness model was examined and further work is required to take the conclusion from Section 3.4.1.3, and examine whether stress-dependent fracture stiffness has a significant influence on modelling wave motions in the fracture zone. Finally, an equivalent transversely isotropic model was tested and found to correspond to an explicit fracture representation for high stiffness cracks, but to differ from the explicit crack model for low stiffness cracks.

3.4.2 Stress wave interactions with mining excavations

In deep level mining, the most severe mining hazard is in the form of seismic stress waves interacting with stopes. The stress waves can propagate fractures in the stope vicinity resulting in rock mass instabilities which endanger mining personnel and disrupt mining operations. In a study by Heunis (1980), rockburst and rockfall related accidents were found to account for approximately 40 per cent of the total mining related fatalities. Therefore, to continue mining at increasing depths, an understanding of mechanisms pertaining to stress wave induced instabilities and dynamic fracturing is of paramount importance.

The objectives are to investigate stress wave interactions with mining excavations, and to identify possible mechanisms leading to high transient stresses, which could initiate fracturing and rock mass instabilities.

The investigation makes use of dynamic photoelastic experiments to visualise transient stress fields and dynamically propagated fractures. The laboratory experiments are back-analysed by numerical simulations, and the numerical codes are checked and verified in terms of their accuracy and modelling capabilities. The numerical programs are then further applied to investigate additional parameters, which could influence the rock mass stability.

3.4.2.1 Enabling model developments

Numerical models have been important tools in this research, and a number of numerical developments have been necessary during this period. These have primarily been evolutionary developments to the program WAVE needed to improve models of wave interaction with mining excavations. These have been made either to generalise the capabilities of the program, to extend different models to give more physical behaviour, or to increase efficiency and viable model sizes.

Graded static mesh and internal absorbing boundary

Many dynamic models require an *in situ* static stress solution, either for initiating a slip source, or for the behaviour of fractures in the model for correct wave-fracture interaction. For dynamic accuracy and efficiency, the element size in WAVE has always been kept constant. This however leads to limitations in model resolution when stress fields around stopes are required. A rule of thumb in 2D (although over-conservative) is for the model size to be eight times the stope span vertically, and six times the stope span horizontally. This leads to undesirably large element sizes in the dynamic area of interest which is particularly limiting for three-dimensional work requiring a static solution (e.g. 3D back-analyses).

A graded mesh for establishing a background static solution was therefore implemented in WAVE. Zones are of constant size inside the dynamic area of interest, but are then increased exponentially toward the static boundary. Absorbing boundary conditions are enforced around the constant mesh, so that the changes in mesh size do not degrade the dynamic accuracy through reflections. The exponential increase in mesh size allows a very efficient implementation of the static mesh equations, with no memory overhead, and virtually no speed overhead - element sizes and node positions do not need to be stored or calculated. (There is however some overhead, as a 2D mesh is divided into nine regions, which are each dealt with slightly differently. The static solution also converges more slowly than the same number of gridpoints in a constant mesh - this is because the model covers a larger area and the

boundaries are further away).

There are two phases to the solution. During the static phase, the entire mesh is switched on, and the outermost static boundary (applied stress and absorbing conditions) is operative, with the internal dynamic boundary switched off. On switching to the dynamic phase, the existing stresses on the internal boundary become locked in, and are applied as fixed stresses together with an absorbing boundary condition at the internal boundary. The static mesh is switched out (not updated). Note that motions during the dynamic phase are assumed not to affect the locked-in boundary stresses, so that fault slip for example should still not be allowed to occur too close to the dynamic boundary. The applied boundary stresses are only updated during the next static solution phase.

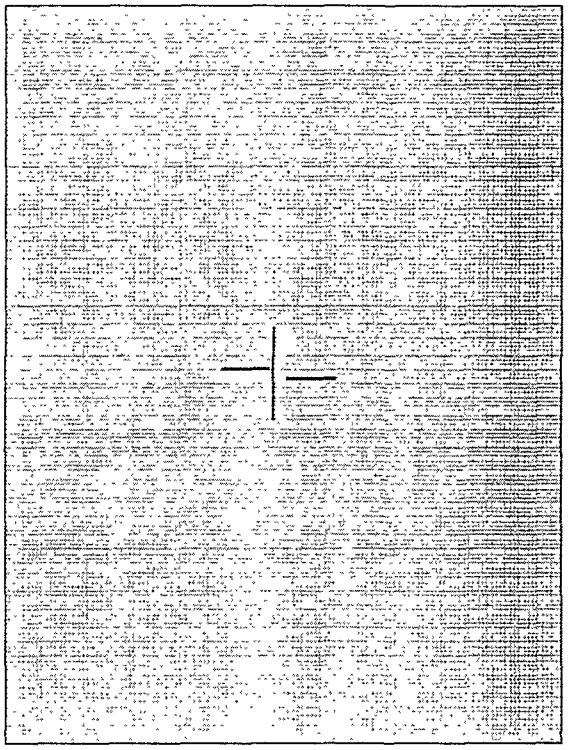

(a) Mesh with 160x120 constant sized elements covering an area of 1600 m by 1200 m.

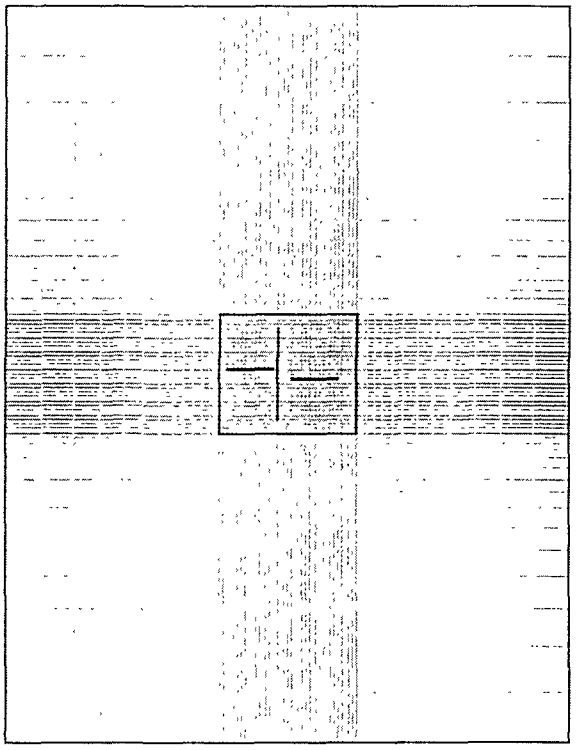

(b): Mesh with 56x56 non-uniform elements (internal constant element mesh of 30x26 elements), covering an area of 1600 m by 1200 m.

Figure 3.4.2.1 Stope-fault model for a constant-element mesh and graded mesh.

A 2D stope-fault model with a throw of 20 metres and span of 100 metres was used to illustrate the problem and test the distorted mesh. The *in situ* stress in the model is first solved assuming a depth of 3000 metres. The fault is then allowed to slip, assuming a friction angle of 30 degrees, cohesion of 4 Mpa, and a slip-weakening law. Using a mesh size of 10 metres, the dynamic area of interest comprises about 30 x 24 zones. A model with 160x120 uniform mesh zones was used as the base case for comparison (Figure 3.4.2.1), with boundary stresses applied to an overall region size of 1200 metres by 1600 metres. Figure 3.4.2.2 a and b compare this base case with smaller constant-sized meshes with closer boundaries. Waveforms received in the stope are significantly different. This is due to differences in the static stress state and hence ESS on the fault. Figure 3.4.2.2c shows that a non-uniform static mesh of 56x56 elements produces dynamic waveforms very close to that of the much larger mesh. The graded mesh has only been implemented for 2D models. It is in many ways even

more necessary for three-dimensional models, which are generally more limited in resolution.

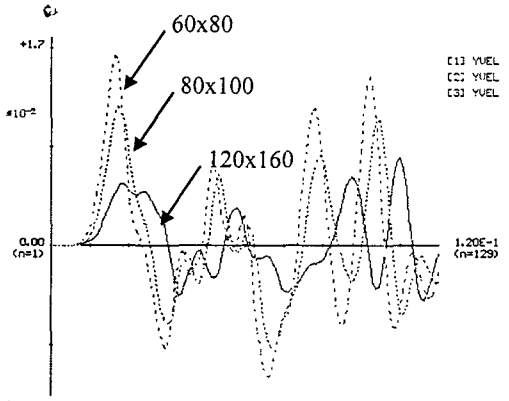

(a) Constant element size, with different static boundary positions (i) 120x160 elements; (ii) 60x80 elements; (iii) 80x100 elements

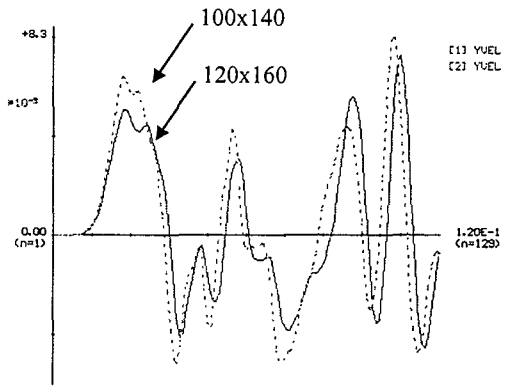

(b) Constant element size, with different static boundary positions (i) 120x160 elements; (ii) 100x140 elements

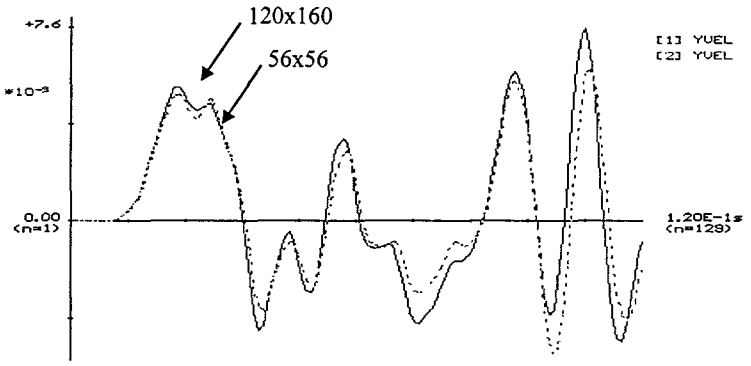

(c) Comparison of constant element mesh, with mesh with graded static area, with boundaries at equal distances, (i) 120x160 elements, constant element size; (ii) 56x56 elements, (Dynamic mesh of 30x26 elements of constant size, rest is a non-uniform mesh)

Figure 3.4.2.2 Comparisons of stope waveforms for different positions of applied boundary stresses. A grid of 120x160 constant-size elements (1200 m x 1600 m) is used as the base case for comparison.

"Linked" stopes

This was added to provide an approximate representation of non-orthogonal features. A linked stope links two points via a stepped series of connecting stope or fault segments. This has been used to simulate a dipping stope and also angled faults (although it is not suitable for active fault slip), where errors associated with the spurious corners have been acceptable for the application.

Angled sources

Although dilitational and shear sources are available, often a source is required with a given orientation (for example a 75° source was needed for the calibration blast in Section 3.4.2.4, or for studies of different angles of wave incidence on features). Such useful studies are not strictly possible using WAVE. Attempts have been made to develop an approximate angled source. This would take the form of a forced source, where a dilational or shear stress loading can be applied over an area in the mesh at any angle. This would allow any ESS distribution to be applied as a stress drop, allowing some studies of events from angled faults.

Two approaches are currently available which allow a source angle and stress tensor to be specified. The first simply distributes the correct components of load to points in the mesh. Unfortunately, except for a 45° angle (or any single angle according to the element aspect ratio), this leads to some spurious waves and asymmetry in the radiation patterns. It is however similar to the original source implementation. (This approach was used in Section 3.4.2.2 to model propagation from angled faults based on the static solution of ESS).

A second approach is to use a superimposition of point sources. The load at a point is superimposed on the existing state of a cell, which is influenced by the rest of the mesh. This leads to a source with similar radiation patterns for all orientations. Figure 3.4.2.3(a) compares the radiation pattern and Figure 3.4.2.3(b) the velocity waveforms for different source angles.

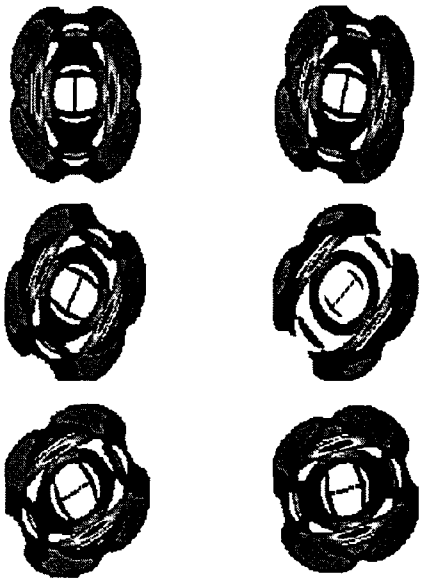

(a) Radiation patterns

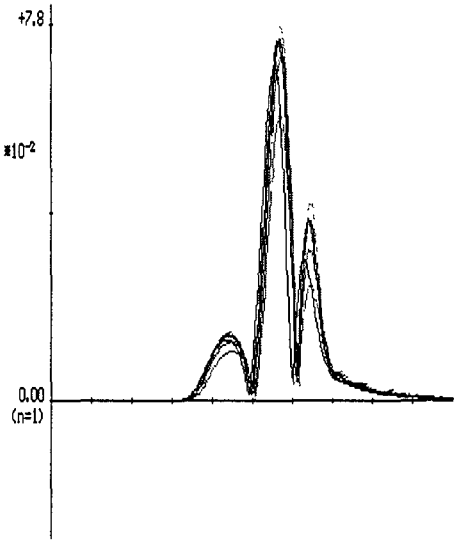

(b) Velocity Waveforms

Figure 3.4.2.3 Radiation patterns and velocity waveforms from the 'superimposed' angled source, for angles of 90°, 75°, 60°, 45°, 30° and 15°

Unfortunately the user does not have complete control over the amplitude, wavelength and waveshape of the superpositional source. This means that the actual goal of being able to apply an ESS distribution as a stress drop on a fault plane has not yet been realised. In applications to date, test runs are used to calibrate the source to the correct stress drop required to imitate a known source. It was found that the superpositional source can have a similar radiation pattern to a conventional source, if the correct amplitude and period are determined.

The above methods are not ideal, but do provide a means to model dynamic response to a slip event on an angled fault. This would enrich the range of possible investigations in project areas

applying dynamic models, particularly where parametric studies of wave incidence angle or fault orientation are useful. It would be particularly desirable to have this feature for three-dimensional models.

Tunnels in three-dimensions

Tunnels have previously only been implemented in 2D in WAVE. A three-dimensional volume excavation (contrasted with planar stope excavations) was required (e.g. Section 3.4.2.5). This was done by allowing stope intersections, with the free surfaces combining to form an enclosed volume. Only a single case of intersection has been developed (a stope in the x-z plane intersects a stope in the y-z plane), allowing tunnels with an axis in the z direction to be modelled. This has not been fully tested, but encouraging agreement was noted between a 2D plane strain model and its 3D counterpart.

Other important developments have been:

- *linear transversely isotropic material* (e.g. used in Section 3.4.1.4)
- *propagating source*, used in Section 3.4.2.5 for a propagating blast source, but also applicable to fault sources.

Conclusions

A number of generalisations have been made to WAVE increasing its scope of application. Developments such as the separate graded static mesh in WAVE, and source models, are important features for any code being used for elastodynamic studies. Regarding general orientations of sources in WAVE, similar conclusions were reached to the conclusions on representing generalised fracturing in Section 3.4.1.2 - i.e. an alternative grid scheme may be required.

3.4.2.2 Elastodynamic wave interactions with stopes

The material in this section was covered in the final report of GAP 032 in 1995. It is, however, included here in an abbreviated format, as it forms the basis of the new work reported in Section 3.4.2.3.

Dynamic photoelasticity is used for visualising the complex interaction process between elastic waves and geometrical discontinuities, which are in the form of open slots. The photoelastic experiments are back-analysed by the dynamic finite difference program WAVE, and the code is assessed in terms of its accuracy and modelling capabilities.

The open slots have aspect ratios that are similar to tabular mining excavations (stopes) in deep level gold mines. Three model geometries are investigated:

(i) a stope situated in a homogeneous medium,

(ii) a stope surrounded by fracture softened material, where the interface (representing a parting plane) between the softened and bulk material is bonded, and

(iii) a stope situated within a softened material, with a non-cohesive material interface.

Prominent waves resulting from the diffraction, refraction and reflection of incident waves, as well as dynamic stress intensification at the stope face, stope back area and along the hangingwall skin are analysed (Daehnke et al., 1995, 1996 a, b).

The gold excavated in South African deep level mines occurs typically in tabular ore deposits. Narrow stopes give access to the reef, and the coupling between the mining excavations and the geological stresses leads to stress concentrations in the stope vicinity. These high stresses generate under quasi-static conditions so-called mining induced fractures, which can be broadly classified into two types: shear fractures, which penetrate up to 6 m into the hanging- and foot-wall, and shorter extension fractures.

Bedding or parting planes are near stope-parallel geological features, which are planes of weakness offering little or no cohesion. Figure 3.4.2.4 gives a schematic of a stope and some geological and mining induce features, namely bedding planes (1), shear fractures (2) and extension fractures (3).

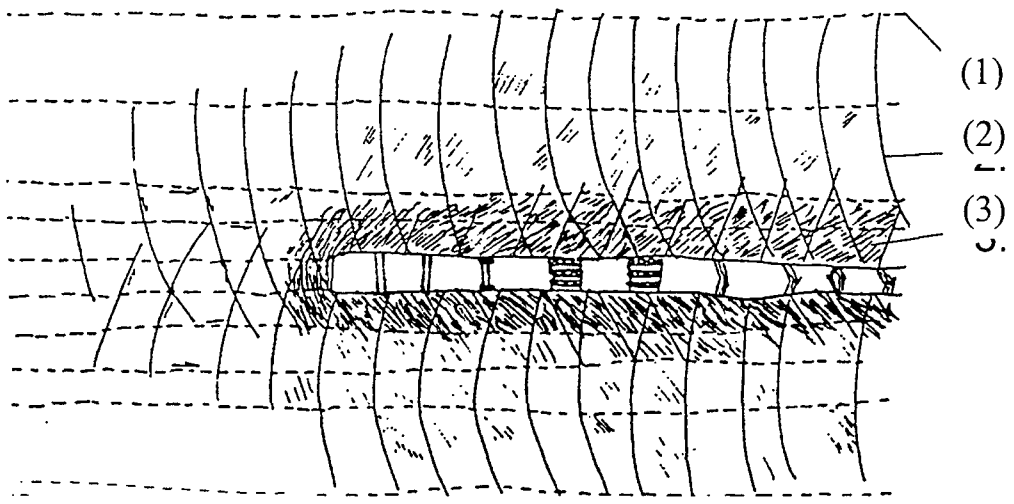

Figure 3.4.2.4 Typical stope and surrounding geological and mining induced rock mass discontinuities (Adams et al., 1981).

Planes of weakness of geological (faults or the interface between intrusive dyke structures and the rock massif) or mining induced (shear fractures) origin are loaded in shear by mining induced stresses, and sudden rupture can occur. The resulting seismic waves interact with mining excavations, in some cases triggering rockbursts and rockfalls.

Theoretical aspects of wave propagation and the interaction of stress waves with discontinuities such as cracks and the interface between two dissimilar media have been investigated in numerous studies. Amongst them Achenbach (1973), Borejko et al. (1992), Brekhovskikh (1960), Fokkema (1981) and Rinehart (1975) have concentrated on the geophysical aspects of wave interaction with geometrical discontinuities.

In spite of the comparatively large number of available theoretical analyses, it is difficult to obtain quantitative information of wave interaction in terms of stress magnitudes of real wave pulses. Of the few experimental analyses that have been conducted, dynamic photoelasticity has been used successfully in two-dimensional models (Rossmanith and Fourney, 1982; Rossmanith and Knasmillner, 1983). The photoelastic technique offers full-field visualisation and information is obtained about instantaneous wave location and stress wave amplitude distribution over the entire region of interest and allows qualitative and quantitative interpretation of the complicated behaviour associated with stress wave interaction with discontinuities.

Experimental Procedure

Dynamic photoelasticity, in conjunction with high speed photography, is used to analyse the interaction between stress waves and an open slot, representing a stope in a deep level mine. To represent a stope, a horizontal slot is cut into a 6 mm thick plate of bi-refringent material. Two types of bi-refringent materials are used, namely (i) Makrolon and (ii) Araldite B, where the former has a lower acoustic impedance compared with the latter. The heavily fractured and thus softer rock in the immediate stope vicinity is represented by the softer Makrolon, whereas the comparatively competent rock mass is represented by the stiffer Araldite B. The interface between the Makrolon and Araldite B is either glued or left unglued, thereby representing either a cohesive or non-cohesive parting plane, respectively. The three model geometries (A, B and C) are shown in Figure 3.4.2.5.

All three models were cut to a rectangular shape with the length of the horizontal side equal to 410 mm and the vertical side 365 mm. A 5 mm wide, 150 mm long horizontal slot was cut into

the centre of each model. A 4 mm diameter hole was drilled 50 mm to the left hand side and 75 mm above the centreline of the stope, and this hole was packed with PETN (pentaerythritol tetranitrate) explosive.

Model A was constructed from Araldite B only and was used to investigate the stress wave interaction with the stope in a homogeneous medium. Model B included a 45 mm wide Makrolon layer in the model centre, and the interface between the Makrolon and the Araldite was bonded with UHU Plus Endfest 300 epoxy glue and allowed to set for 24 hours. Model C consists of the same components as Model B, however the interface between Araldite B and Makrolon was not bonded.

To represent the geological stresses at depth, the models were placed in a rigid frame and the boundaries loaded by hydraulic jacks to 2,4 MPa in the vertical direction and 1,3 MPa in the horizontal direction, giving a ratio of the horizontal versus vertical stresses of approximately 0,5. These were the maximum loads the models could sustain without becoming unstable and buckling.

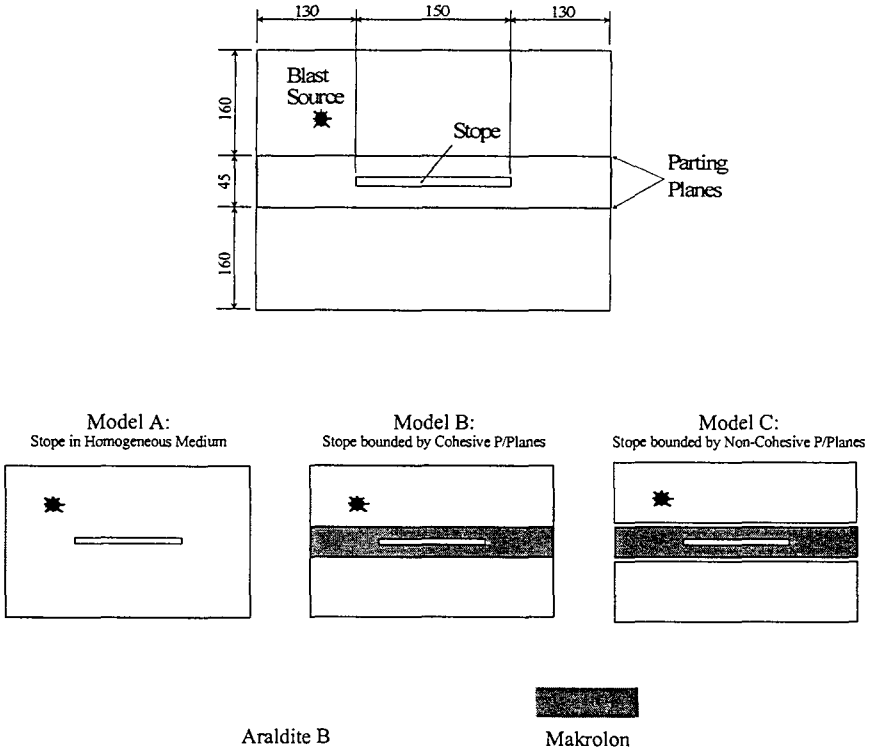

Figure 3.4.2.5 Schematics of the three model geometries used in the photoelastic experiments (dimensions are given in mm).

Mining induced seismicity is usually associated with shear type events. However, no experimental technique exists currently to generate pure shear type events in photoelastic models. In this study, stress waves are initiated by a point blast source, located in the hangingwall so that the blast induced wavesed travel through the fractured hangingwall rock and interacted with the stope.

Stress waves were initiated by detonating 50 mg of PETN. This explosive type is suitable for the dynamic loading of photoelastic models because the resultant stress pulse has a short rise time (± 5 μs) with a mean pulse period of 15 μs. The explosive is packed in a 4 mm diameter borehole, and a pressure containment device prevents immediate combustion gas venting. The detonation is triggered by a 2 kV DC voltage pulse.

Upon detonation of the explosive, the isochromatic[1] fringe patterns associated with the ensuing stress waves can be visualised (using circularly polarised monochromatic light) due to the optical interference of the bi-refringent material. The order of interference, N, is related to the state of stress in the model by the stress-optic equation, $\sigma_1 - \sigma_2 = Nf_\sigma / h$, where σ_1 and σ_2 are the principal stresses, f_σ is the material fringe value and h is the model thickness.

A Cranz-Schardin (1929) camera is used to record the dynamic fringe patterns; an overview of this camera type is given in Section 3.3.2. The camera is triggered by detonation of the explosive and the exposure of the first negative occurs after a selected delay period. Twenty-four frames are recorded at discrete times during the dynamic event at a framing rate of 220 000 frames per second. A short exposure time of 200 nenoseconds is necessary to record sharp photographic images of moving fringe patterns.

Experimental Results

When investigating wave propagation in a two-dimensional plane, four wave types need to be considered. The (i) longitudinal wave propagates at a velocity almost twice that of the (ii) transverse wave. The absence of normal and shear tractions at the free boundary gives rise to additional stress waves: surface (iii) Rayleigh waves and (iv) von Schmidt waves.

The interaction of waves with geometric discontinuities results in complicated wave patterns due to the superposition of incident, diffracted, reflected and refracted waves. In order to identify the various wave types the following notation is adopted: longitudinal, transverse, von Schmidt and Rayleigh waves are referred to as *P*, *S*, *V* and *R* waves respectively. Reflected waves are labelled with subscript *r*, refracted (transmitted) waves are given the subscript *t* and diffracted waves are described by subscript *d*. Waves reflected by the stope are given the additional subscript *s*.

The leading black line of a stress wave is of fringe order $N = 0{,}5$. Due to the slope of the wave stress profile, this line does not represent the true wave front, which is positioned just ahead of the first half-order fringe. As the slope of the stress profile is different for the various wave types, and also depends on the extent to which the wave has attenuated, it is difficult to estimate the exact position of the wave front. For this reason the positions of the theoretical waves are demarcated by their maxima and not by their wave fronts.

Stope in a Homogeneous Medium (Model A)

After applying the pre-load, Model A was loaded explosively and the resulting dynamic fringe patterns were recorded by the exposure of 24 photographs. Here, three photographs, taken at 64 μs, 94 μs and 139 μs after charge detonation, are reproduced in Figure 3.4.2.6 to illustrate the wave-stope interaction.

In the first photograph of Figure 3.4.2.6, taken 64 μs after charge detonation, the incident *P*-wave has just interacted with the left-hand-side slot tip, resulting in a comparatively strong stress concentration, which can be identified by the pseudo-caustic at the bottom left hand corner. The pseudo-caustic is formed by nesting of fringes beyond the resolution power of the high speed photographic system. The incident *P*-wave is reflected by the slot and, due to mode conversion, most of the incident energy is reflected in the form of a shear wave ($S_{sr}P$). The isochromatic contours on the right-hand-side slot end are static contours due to the pre-stress loads applied to the model.

[1] An isochromatic contour is a line of constant maximum shear stress.

The second photograph was exposed 94 μs after charge detonation. The incident *P*-wave has propagated 60 per cent along the slot surface and has attenuated to a maximum fringe value of 7; however at the point of reflection at the slot the fringe number increases to 11. During reflection at the slot, most of the incident *P*-wave energy is mode-converted to a prominent shear wave (S_{sr} *P*). Effects such as fringe islands and the bending of fringes indicate the presence of diffracted *P*- (P_d *P*) and *S*- (S_d *P*) waves. The characteristic wave shape of the Rayleigh wave is apparent in the foot-wall and five fringe lines can be discerned in the subsurface peak. Fringes indicating a von Schmidt wave at $\beta_V = \arcsin(c_S/c_P) = 35^\circ$ to the slot between P_d *P* and S_d *P* can be identified.

The final photograph presented in this sequence was taken at 139 μs after loading the model dynamically. The incident *P*-wave has propagated beyond the stope, and the prominent S_{sr} *P*, created due to mode conversion, is visible above the slot. Isochromatic contours due to the diffraction of the incident *P*-wave are apparent at the right-hand-slot side, and a pseudo-caustic indicates a comparatively high stress concentration at the upper slot corner. The Rayleigh wave is by now well developed and has propagated 60 per cent along the slot length.

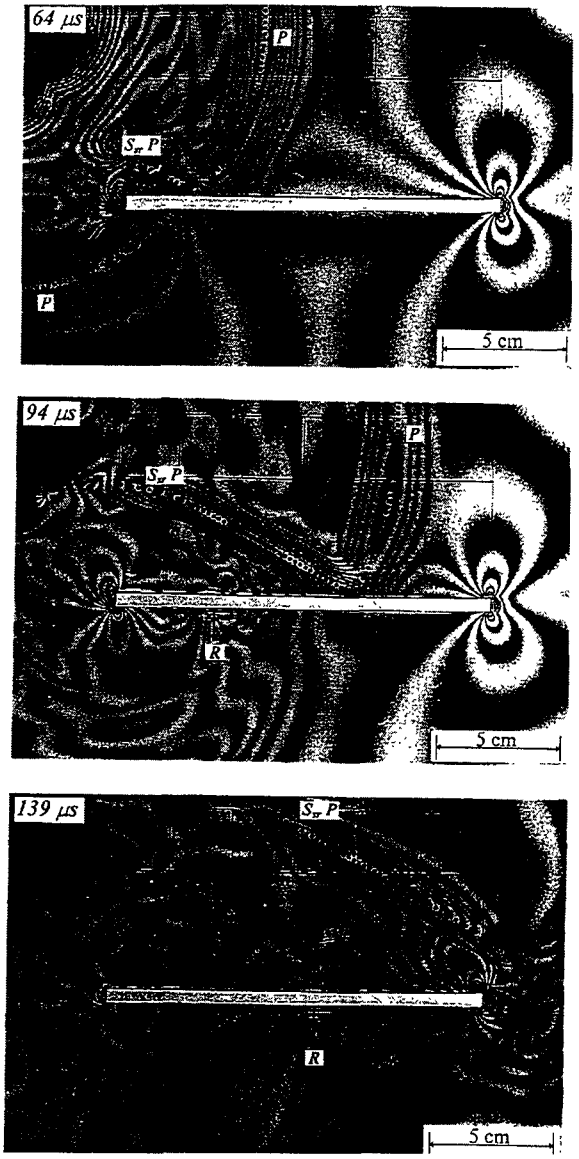

Figure 3.4.2.6 Stope in homogeneous medium: Isochromatic contours at three time intervals.

Stope Bounded by Cohesive Parting Planes (Model B)

Figure 3.4.2.7 shows three snapshots in time of Model B, i.e. a stope in a softened layer bounded by cohesive parting planes. From the three photographs it is apparent that most of the incident *P*-wave energy is refracted in the form of a *P*-wave (P_t *P*) across the Araldite B – Makrolon interface, and the energy of the refracted *P*-wave is converted to a shear wave (S_{sr} P_t *P*) as reflection occurs at the slot surface. Due to the slight acoustical impedance mismatch between Araldite B and Makrolon, $(\rho c_P)^{\text{Araldite B}} = 1{,}14 \times (\rho c_P)^{\text{Makrolon}}$, only slight bending of the *P*- and *S*-waves occurs as the waves propagate from one medium to the next. The epoxy bond between the two bi-refringent material types is not broken by the tensile components of the stress waves, and fringe lines progress smoothly from one material into the next. The characteristic isochromatic fringe patterns of Rayleigh waves propagating along the hanging- and foot-wall surfaces can easily be recognised.

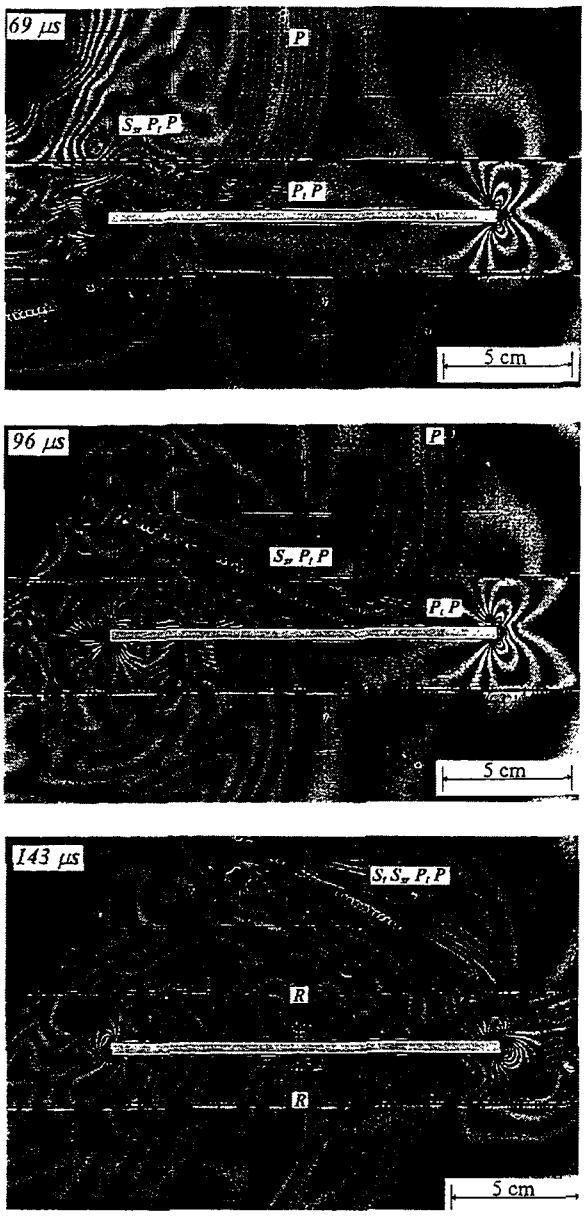

Figure 3.4.2.7 Stope bounded by cohesive p/planes: Isochromatic contours at three time intervals.

Stope Bounded by Non-Cohesive Parting Planes (Model C)

The frames chosen to describe wave interactions in Model C were exposed 64 μs, 94 μs and 130 μs after detonation (Figure 3.4.2.8). As the incident *P*-wave interacts with the non-cohesive parting plane, the incident energy is partitioned into reflected and refracted *P*- and *S*-waves. Traces of all four wave types are visible in the photographs, however the most prominent are the $S_r P$ and $P_t P$ waves. The formation of a strong shear wave ($S_{sr} P_t P$) due to the reflection of the transmitted *P*-wave ($P_t P$) is visible. The $S_{sr} P_t P$ wave is reflected at the Araldite B – Makrolon interface and the energy is re-directed back towards the stope in the form of a $S_r S_{sr} P_t P$ and $P_r S_{sr} P_t P$ wave.

To summarise, the non-cohesive parting plane traps energy within the hangingwall beam in the form of reflected shear waves. This is contrary to the wave field observed in Model B, where incident energy transmitted across the cohesive parting plane is reflected by the stope and re-transmitted back across the cohesive interface into the bulk material.

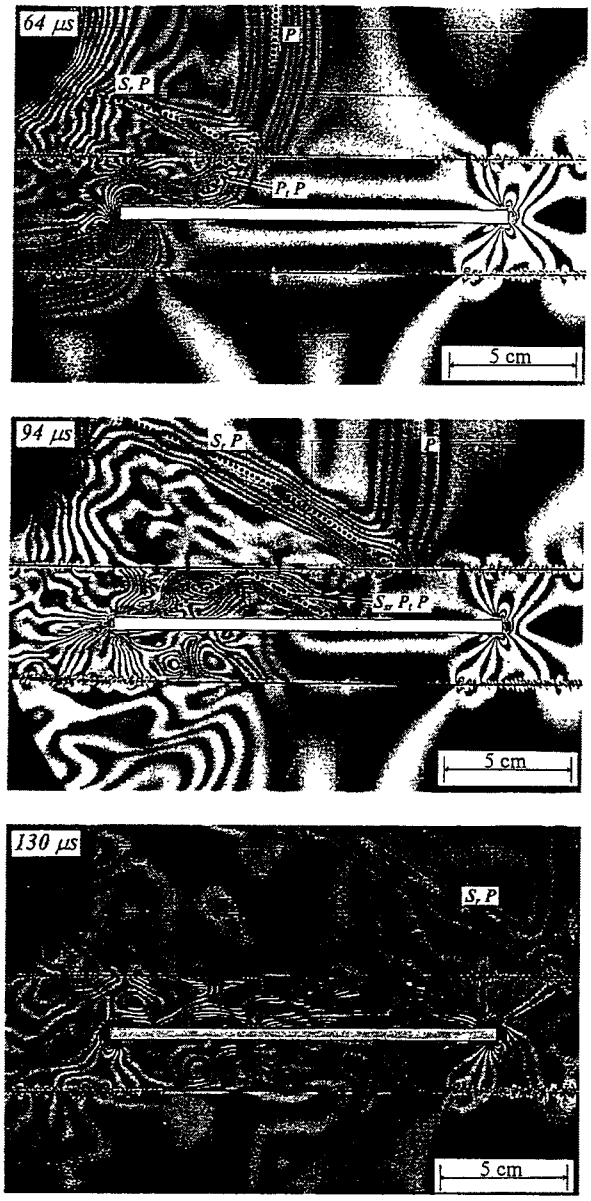

Figure 3.4.2.8 Stope bounded by non-cohesive p/planes: Isochromatic contours at three time intervals.

Numerical Analysis Procedure

The dynamic finite difference program WAVE was used to back-analyse the photoelastic experiments. WAVE is a program that models wave propagation in either a two- or three-dimensional elastic medium. Second order interlaced finite difference equations are used on an orthogonal grid with uniform grid spacing. WAVE has the ability to model grid-aligned dislocations which can represent cracks and planes of weakness, as well as incorporating various material properties.

The WAVE analyses were completed in two steps: during Step 1, the stress field was applied to the model, and the program cycled until the velocities in the finite difference mesh were low enough (<1 per cent of the peak particle velocities generated by blast waves), to approximate equilibrium. In Step 2, a point blast source generated stress waves which interacted with the slot and discontinuities. Steps 1 and 2 were superimposed in order to obtain the total elastodynamic behaviour.

The WAVE blast source was tailored such that the resulting far-field stress pulse approximated the stress amplitude, pulse period and pulse shape of the stress wave propagating through the photoelastic models.

The two-dimensional WAVE models were analysed in plane strain, whereas the photoelastic models are assumed to represent plane stress. The material properties used by the numerical analyses were determined by adjusting the material properties of Araldite B and Makrolon from a plane stress application to plane strain (Bishop, 1953).

The non-cohesive interfaces were modelled with zero cohesion and with interface friction angles ranging from 0° to 30°. Waves refracted and reflected by interfaces modelled with a 10° friction angle proved to correlate closest with the wave field observed in the experiment.

The numerical models were discretised with a mesh consisting of 400 x 360 elements (element dimension: 1 mm x 1 mm), and the models were analysed on a 50 MHz 486 computer. Step 1 required approximately eight to ten hours of run time, whereas to model the blast waves propagating across the area of interest (Step 2) required approximately thirty CPU minutes.

Correlating Photoelastic and Numerical Results

In this section the numerical back-analyses are compared to the experimental results, and the finite difference code WAVE is assessed in terms of its accuracy, modelling capabilities and suitability for analysing elastodynamic problems. Models A, B and C were back-analysed, and for each case isochromatic fringes are compared at a time instance of 94, 95 and 94 μs after charge activation, respectively. To identify some of the weaker waves which cannot be identified directly in the photoelastic patterns, each of the figures describing photoelastic fringes is accompanied by a diagram showing the theoretical wave pattern at that time instant. In these diagrams, longitudinal waves are indicated by solid lines, shear waves by dashed lines and von Schmidt waves by dash-dot-dash lines.

Model A – Experimental versus Numerical Comparison

Figure 3.4.2.9 gives the theoretical wave pattern as well as the experimentally observed and numerically calculated isochromatic fringes of Model A, 94 μs after charge activation. It is evident that the WAVE analysis compares favourably with the photoelastic results and isochromatic contours indicating the $S_{sr}P$ wave, diffracted *P*- (P_d *P*) and *S*- (S_d *P*) waves, Rayleigh (*R*) and von Schmidt (*V*) can be identified.

Model B – Experimental versus Numerical Comparison

The experimental – numerical comparison for a stope bounded by cohesive parting planes is given by Figure 3.4.2.10 for a time instance of 94 μs after detonation. Numerous wave types can be identified with the help of the theoretical wave diagram, and qualitatively the numerically generated isochromatic fringes compare closely with the experimental data. In both cases most of the incident energy is refracted (transmitted) across the welded Araldite B – Makrolon interface; this energy is then reflected by the hangingwall surface and re-transmitted back into the bulk material (Araldite B).

Model C – Experimental versus Numerical Comparison

The isochromatic contours calculated by WAVE and the experimental observations 94 μs after source activation for Model C are displayed in Figure 3.4.2.11. Prominent wave types consistent with the photoelastic results are a strong shear wave reflected by the material interface ($S_r P$), the reflection of the transmitted *P*-wave at the stope ($S_{sr} P_t P$), and the high density of reflected waves within the material layer immediately above the slot. By comparing the fringe patterns, it is evident that the isochromatic contours calculated by the numerical analysis correlate closely to the actual contours observed in the photoelastic experiments.

Model A: Stope in a homogeneous medium.

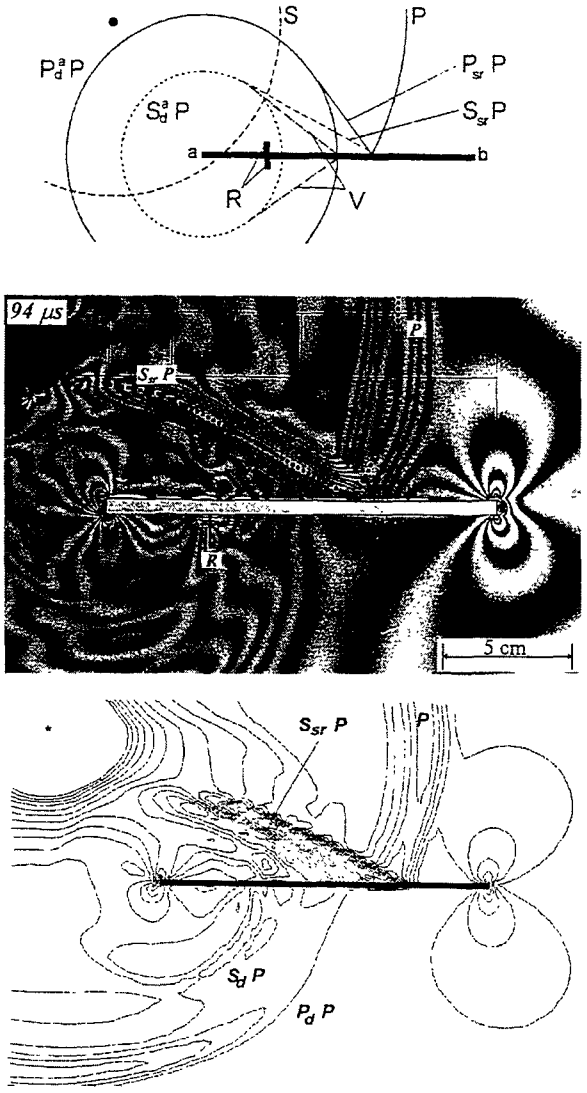

Figure 3.4.2.9 Wave field 94 μs after charge activation: theoretical wave field (top), isochromatic fringes observed in the experiment (middle) and fringes calculated numerically (bottom).

Model B: Stope bounded by cohesive parting planes.

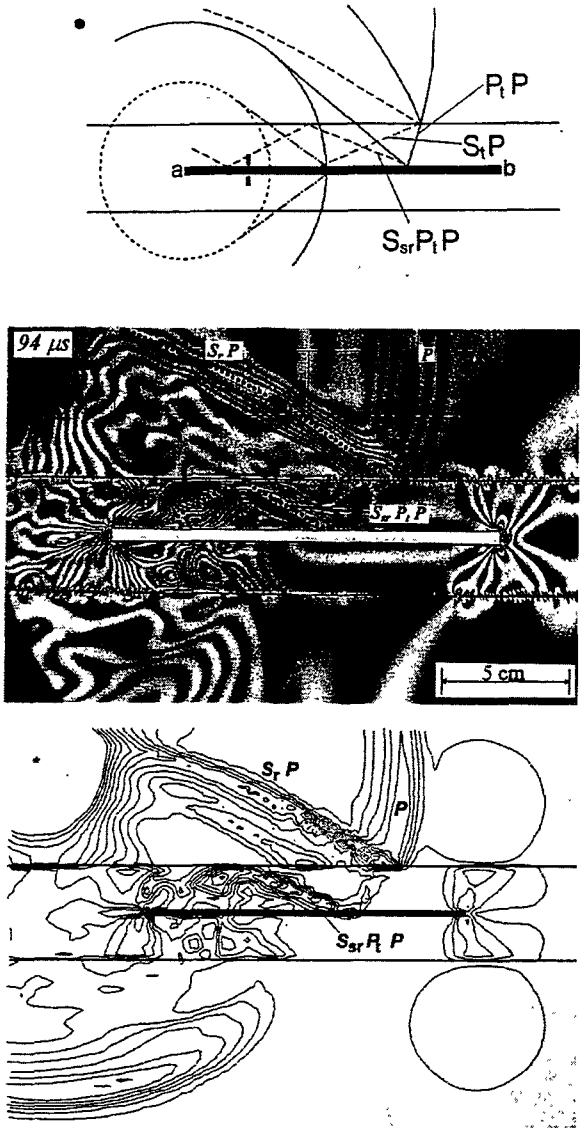

Figure 3.4.2.10 Wave field 94 μs after charge activation: theoretical wave field (top), isochromatic fringes observed in the experiment (middle) and fringes calculated numerically (bottom).

Model C: Stope bounded by non-cohesive parting planes.

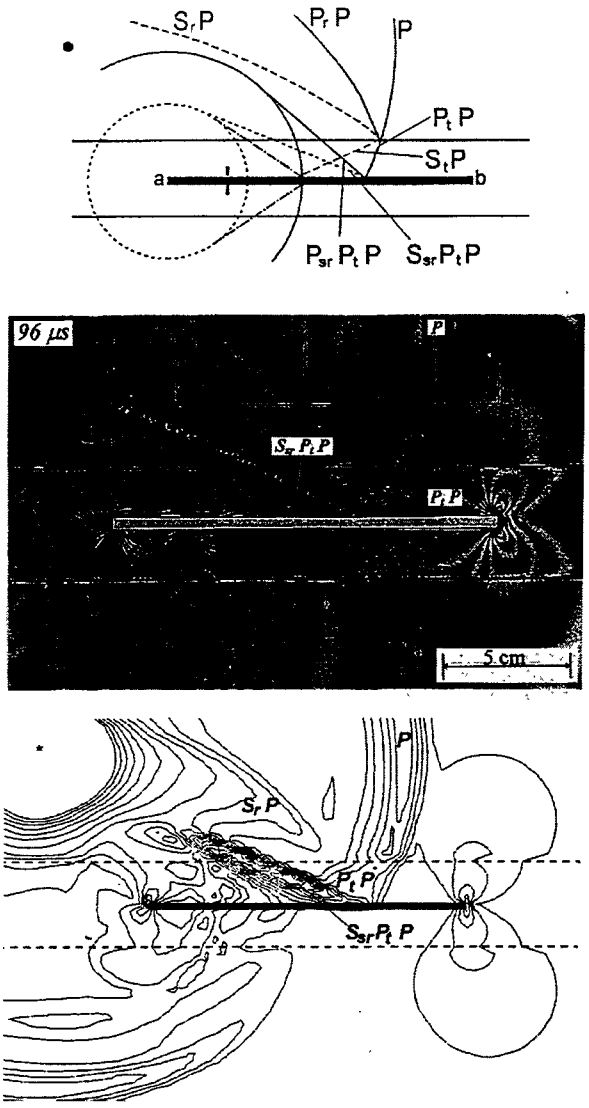

Figure 3.4.2.11 Wave field 96 μs after charge activation: theoretical wave field (top), isochromatic fringes observed in the experiment (middle) and fringes calculated numerically (bottom).

Summary

Dynamic photoelasticity is a useful experimental technique for visualising complex stope-wave interactions and for obtaining quantitative information in terms of stress magnitudes of real wave pulses. The experimental technique is one of the few means available to judge the quality of numerical simulations of dynamic behaviour. The dynamic finite difference program WAVE has been proven to model accurately the diffraction, refraction and reflection of stress waves in a homogeneous medium and the interaction of waves across cohesive and non-cohesive interfaces separating two material types.

The experimental and numerical work described here has demonstrated that parting planes reflect a portion of the incident energy and thus shield the stope. A cohesive parting plane allows stress waves reflected by the stope to re-enter the surrounding material. However, a non-

cohesive parting plane traps energy within the hangingwall beam, thereby negating any shielding benefits associated with parting planes.

This work is limited by the simplified and idealised nature of the model geometries analysed. The results of further investigations are given in the following section, where dynamic photoelasticity is used to investigate the wave interactions in more complicated model geometries incorporating discontinuities representing shear fractures.

3.4.2.3 Fracturing due to wave interactions with stopes

In the previous section the photoelastic technique was used to investigate the interaction of an incident *P*-wave with a stope; the focus here was on the distribution of wave energy in the stope vicinity and identifying potentially hazardous zones subjected to high dynamic stresses.

In this section further experiments investigate the interaction of an incident *S*-wave with a stope surrounded by six pre-existing cracks. In this series of experiments the dynamic stresses propagated by the stress waves are of sufficient magnitude to re-mobilise and propagate the pre-existing cracks, and the emphasis of the work is on identifying wave types and mechanisms leading to fracture initiation and propagation (Daehnke et al., 1996b, 1997). The objectives of the work are to conduct controlled photodynamic laboratory experiments, and to verify numerical models by back-analysis of the experimental observations using the dynamic finite-discrete element program ELFEN (Munjiza et al., 1995), which can model dynamic fracture propagation in two dimensions. ELFEN is subsequently used to investigate parameters and mechanisms governing dynamic fracturing in the stope vicinity due to loading by *P*- and *S*-waves.

Mining through highly stressed rock in deep level mines is often accompanied by considerable seismic activity. High geological and mining induced stresses can lead to the sudden rock failure, and the resulting seismic waves interact with mining excavations. The resulting loss of stability may lead to rockbursts, with large scale falls of ground, or with dynamic formation of new fractures and explosive failure of brittle rock.

Experimental procedure

Dynamic photoelasticity, in conjunction with high speed photography, is used to analyse the interaction between stress waves and an open slot, where the slot represents a stope in a deep level mine. The Cranz-Schardin camera (described in Section 3.3.2) was used to record the dynamic fringe patterns. Twenty-four frames were recorded at discrete times during the dynamic event at a framing rate of between 150 000 and 220 000 frames per second. The plane models were cut from 10 mm thick Araldite B plates, and using circularly polarised mono-chromatic light, optical interference of the bi-refringent material produces isochromatic fringe patterns.

To represent mining induced shear fractures, which typically occur in deep level mines, discontinuities in the form of near-vertical cracks extending from the stope were propagated quasi-statically prior to the blast loading. The models were placed in a rigid frame and the boundaries loaded by hydraulic jacks to 1,5 MPa in the vertical direction and 0,8 MPa in the horizontal direction, giving a ratio of the horizontal versus vertical stresses of approximately 0,5. These were the maximum loads the plate models could sustain without becoming unstable and buckling.

Currently in dynamic photoelasticity no suitable experimental method exists to generate a pure shear wave. Here a point blast source, using lead azide as explosive, was detonated on the

model boundary and in addition to a *P*-wave, a strong *S*-wave was created. Figure 3.4.2.12 indicates the isochromatic contours associated with the principal stress waves due to a simulated detonation at the model edge. Also shown are the stope and the six pre-existing cracks surrounding the excavation. The stress wave field was calculated by making use of the dynamic finite difference computer program called SWIFD (Rossmanith and Uenishi, 1996).

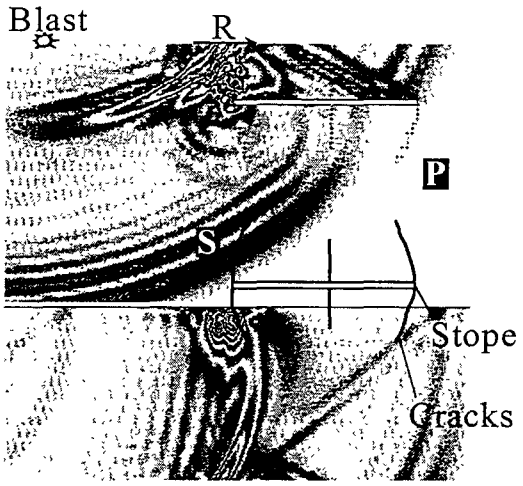

Figure 3.4.2.12 Stress waves, due to a blast source on the model boundary, interacting with a stope and pre-existing cracks.

Numerical Analysis Procedure

In this study the finite-discrete element program ELFEN (Munjiza et al., 1995) is used to back-analyse the photodynamic experiments. ELFEN uses constant strain elements to discretise the spatial domain and an explicit time integration in the form of the standard central difference scheme. After a critical state of stress is reached, an element can separate into two or more discrete elements. Remeshing is performed when breakage occurs, and the time step is appropriately reduced to ensure a stable solution path. A Rankine plasticity model is used to detect the spread and direction of localisation zones along which cracks will open. A local bilinear material model (Figure 3.4.2.13) is adopted which depends on the tensile material strength limit, σ_t, and the fracture energy release rate in tension, G_f, and the local control length, $h_i = \sqrt{A_i}$, where A_i is the area associated with the integration point considered. The fracture energy G_f is assumed to control only the post peak process, i.e. after the strength limit σ_t has been reached.

The Rankine plasticity model is assumed to be isotropic, i.e. the accumulated effective plastic strain is monitored in the principal direction only. If, after the strength limit is reached, a full breakage does not occur, the effective plastic strain is treated as a scalar state variable for the next state of deformation, which will be valid for any new rotated principal direction. If at this stage the element is totally unloaded, and thereafter re-loaded, the initial material response is treated as elastic.

At the stage when the strength of the material at the element Gauss-point is reduced to zero, a crack is assumed to open. The direction of the crack coincides with the direction of the largest principal plastic stretch.

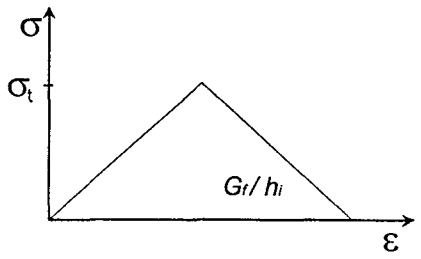

Figure 3.4.2.13 Bilinear material model used by ELFEN.

The pre-existing cracks surrounding the stope were modelled with interface elements, which allowed opening, but no interpenetration. A coefficient of friction of 0,1 was assumed at the interface elements.

The numerical analyses were conducted in two stages:

(i) the model was slowly pre-stressed to an initial equilibrium state,

(ii) the model was then loaded dynamically by a simulated blast loading at the model boundary.

The material properties used for the numerical simulation are those corresponding to Araldite B (Wolf, 1976) and quartzite (Lama, 1978).

Experimental and Numerical Results

The results of the following three experiments are reported:

(i) waves incident at 45° to a stope in a homogeneous medium,

(ii) waves incident at 45° to a stope bounded by non-cohesive parting planes, and

(iii) waves incident at 90° to a stope in a homogeneous medium.

The sequence of photographs taken by the Cranz-Schardin camera show instants in time of the isochromatic contours associated with the stress waves. Longitudinal and shear waves are labelled by *P* and *S*, respectively, and waves reflected by the stope are labelled with subscript *sr*, whereas waves reflected by the pre-existing cracks are given the subscript *cr*. The positions of *P*-waves are shown by solid lines, *S*-waves are indicated by dashed lines and the direction of shear is given for incident and stope reflected *S*-waves.

Waves incident at 45° to a stope in a homogeneous medium

In the first experiment the incident waves propagate at an angle of $\pm 45°$ relative to the stope, where the stope is situated in a homogeneous medium (Figure 3.4.2.14). Prior to the dynamic loading, six cracks were propagated quasi-statically from the stope into the hangingwall and footwall. This experiment is back-analysed by an ELFEN numerical analysis, and isochromatic fringe patterns and dynamically propagated fractures are compared.

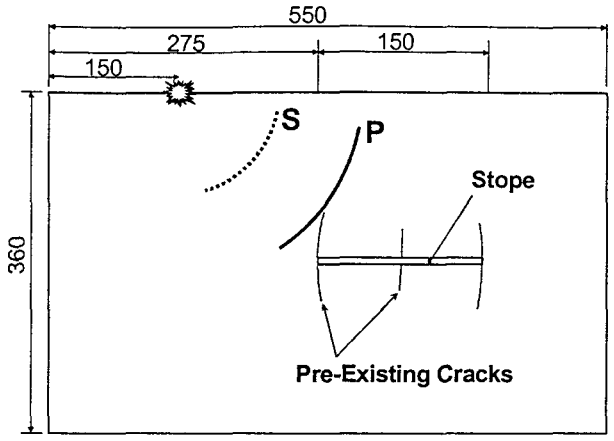

Figure 3.4.2.14 Geometry of model used to investigate incident P- and S-waves propagating at ≈45° relative to the stope (dimensions are in mm).

Isochromatic fringes of stress waves interacting with a stope in a homogeneous medium surrounded by the six pre-existing cracks are shown in Figures 3.4.2.15 a) and b), giving two photographs 169 μs and 276 μs after charge detonation, respectively.

Figure 3.4.2.15 a) shows a comparatively weak *P*-wave which has propagated to the right-hand-side stope end, followed by a stronger *S*-wave which is about to interact with the pre-existing left-hand-side upper crack. Other prominent wave types are a $S_{sr}P$ wave due to reflection and mode conversion of the incident *P*-wave, and a shear wave due to the reflection of the incident *P*-wave at the left-hand-side stope cracks ($S_{cr}P$). Due to loading by the dynamic stresses propagated in the incident (*S*) and stope reflected ($S_{sr}P$) shear waves, the top left-hand crack is under mixed-mode loading This is evident from the crack tip fringe loops. The crack reflected shear wave ($S_{cr}P$) is interacting with the bottom left-hand crack and the characteristic fringe loops at the crack tip indicate predominantly mode II loading. At this stage no crack re-initiation and dynamic propagation due to stress wave loading has occurred.

In Figure 3.4.2.15 b) the incident *S*-wave has propagated seventy per cent along the upper surface of the stope. The $S_{sr}S$ wave generated by the reflection of the incident *S*-wave is interacting with the top left-hand crack, which has re-initiated and is propagating under mode I loading at approximately 250 m/s. During fracture initiation, the sudden unloading of the material in the immediate fracture tip vicinity generates a longitudinal and shear wave, and traces of these waves are visible and labelled by P_{ini} and S_{ini}, respectively.

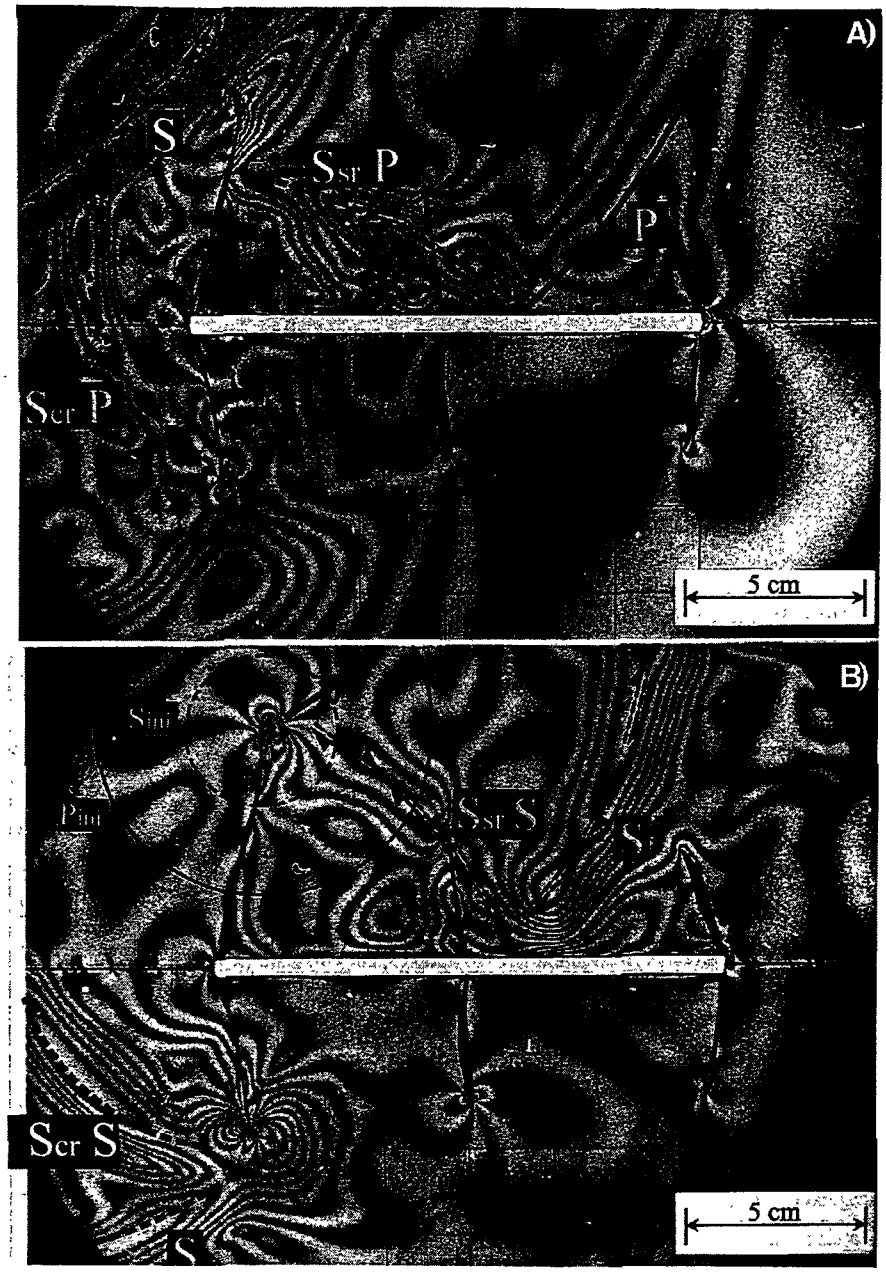

Figure 3.4.2.15 a) and b) Experimentally observed wave field 169 and 276 μs after charge detonation.

ELFEN was used to back-analyse the experimental results shown in Figures 3.4.2.15 a) and b). Figures 3.4.2.16 a) and b) show the numerically generated isochromatic contours at time instances of 166 μs and 271 μs after charge activation, respectively. By comparing Figures 3.4.2.16 to Figures 3.4.2.15 (at the respective time instances), it is apparent that the numerical results correlate reasonably well with the experimental observations. The same wave type (S_{sr} *S*) initiates fracturing at approximately the same time instant, and fracture propagation rates and the final fracture extent correlate closely.

To summarise, the photoelastic and numerical results indicate that, for the angle of wave incidence analysed in this experiment, fractures initiate and propagate due to loading by the stope-reflected shear wave (S_{sr} *S*), and are less likely to grow when loaded by the incident *S*-wave. Due to the polarity of the shear stresses propagated by the S_{sr} *S* wave, the fracture extends towards the top right-hand-side, approximately normal to the front of the S_{sr} S wave.

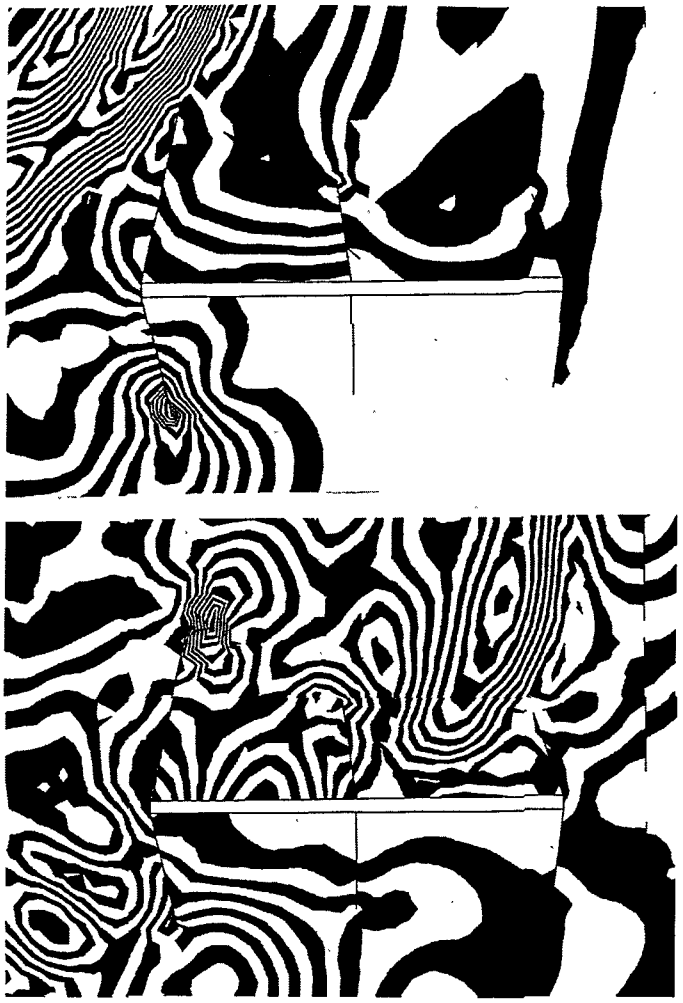

Figure 3.4.2.16 a) and b) Numerically calculated fracturing by means of element splitting and isochromatic wave field 166 and 271 μs after charge detonation.

Waves incident at 45° to a stope bounded by non-cohesive parting planes

An experiment was conducted to investigate the interaction of waves at 45° to a stope bounded by non-cohesive parting planes (detailed results are given in Daehnke (1997)). The model geometry is identical to the previous case of a stope in a homogeneous medium, with the addition of non-cohesive parting planes situated 25 mm (a quarter of the stope length) above and below the stope centreline.

As in the case of an unshielded stope, fracture propagation occurs owing to loading by the reflected shear wave, and the top left-hand-side fracture at the time instance shown in Daehnke (1997) is propagating at a rate of 400 m/s. Unlike in the case of an incident *P*-wave (see Section 3.4.2.2), most of the energy of an incident *S*-wave is reflected by non-cohesive parting planes due to the incident angle exceeding the critical angle of reflection (β_{crit}), and the stope is effectively shielded. Zones of high stresses occur at the parting plane and the material in the immediate stope vicinity is subjected to significantly lower stresses.

Waves incident at 90° to a stope in a homogeneous medium

The geometry of the model used to investigate waves propagating at 90° towards the stope is shown in Figure 3.4.2.17.

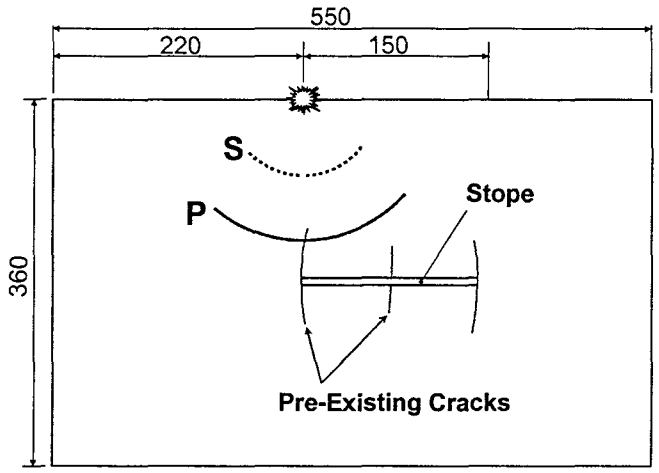

Figure 3.4.2.17 Model geometry used to investigate normal wave incidence (dimensions are in mm).

In this model fractures initiate from the left-hand-side and middle cracks above the stope and propagate under strong mode I loading induced by the tensile $P_{sr}P$ wave. No fracture propagation due to the loading of the incident *S*-wave occurred, however propagation of the top, left-hand fracture is re-initiated by the reflected $S_{sr}S$. As observed previously, fractures propagate due to loading by reflected waves, as opposed to incident waves.

Experimentally observed and numerically calculated fringe patterns compare well, and in both the experimental and numerical results the top left-hand and centre fracture initiate and propagate due to loading by the $P_{sr}P$ wave (the tensile *P*-wave generated by the stope reflected incident compressive *P*-wave). The top left-hand fracture re-initiates due to loading by the $S_{sr}S$ wave (the hangingwall surface reflected *S*-wave). Again, fracture propagation occurs due to loading by reflected waves.

Back analysis of the laboratory experiments and the correlation found between the numerical and experimental results have shown that ELFEN can accurately model the mechanisms leading to fracture initiation and propagation.

Mechanisms and parameters governing dynamic fracturing

The finite-discrete element program ELFEN was used to investigate the interaction of incident planar *P*- and *S*-waves with a slot in a homogeneous medium. The slot, representing a stope, is surrounded by material that can fracture according to a tensile failure criterion, where the tensile limit is set at 10 MPa. The aim of the numerical modelling is to investigate mechanisms and parameters influencing stress wave induced dynamic fracturing. Pre-existing static stresses would influence and complicate the overall fracturing significantly; hence, to interpret and understand mechanisms governing stress wave induced fracturing, the numerical analyses discussed here model dynamic fracturing in an initially stress-free medium. Further numerical models taking into account pre-existing compressive stresses are recommended. In the numerical models presented here, it was not possible to model fracturing under the influence of pre-existing stresses due to numerical instabilities associated with the fracturing algorithm.

A summary of the parameters investigated and their influence on fracturing in the stope vicinity follows.

P- versus S-wave loading

Figure 3.4.2.18 a) shows maximum shear stress contours associated with a 45° incident compressive *P*-wave interacting with a 50 m slot in an initially stress free medium. The incident *P*-wave is reflected by the hangingwall surface, and in addition to a reflected *P*-wave ($P_{sr}P$), the incident energy is mode-converted and a prominent *S*-wave ($S_{sr}P$) is generated. Hangingwall fracturing coincides with loading by the reflected waves. Previously (Daehnke and Hildyard, 1997), it was shown that fracturing occurs due to the stress field created by the superposition of the tensile reflected *P*-wave ($P_{sr}P$) and the reflected *S*-wave ($S_{sr}P$). The tensile stress associated with this field is near vertical, and this leads to the predominance of horizontal fracturing observed in the model. The final fracture network after the stress waves have propagated beyond the stope is shown in Figure 3.4.2.18 b).

In the case of a 45° incident *S*-wave (Figure 3.4.2.19 a and b), the incident wave is totally reflected by the hangingwall surface and no mode conversion occurs, i.e. the only reflected wave is in the form of a $S_{sr}S$ wave. In rock, total reflection occurs for angles of incidence exceeding approximately 30°. Further analysis of the dynamic stress field indicates that there is a tensile *P*-wave ($P_d S$) caused by the diffraction of the incident *S*-wave at the left-hand-side stope edge. The wavelength is such that the faster $P_d S$ wave does not separate completely from the reflected $S_{sr}S$ wave until the far end of the stope. The maximum tensile limit is reached during the interaction between the $P_d S$ and $S_{sr}S$ waves. As is the case with an incident *P*-wave, the tensile stress field is approximately vertical. As a consequence, the fracture network observed due to loading by a 45° incident *S*-wave is similar to the network created by an incident *P*-wave. In both cases fracturing is associated with stresses propagated by stope reflected *S*-waves ($S_{sr}S$ and $S_{sr}P$ for incident *S*- and *P*-waves, respectively) interacting with other tensile *P*-waves.

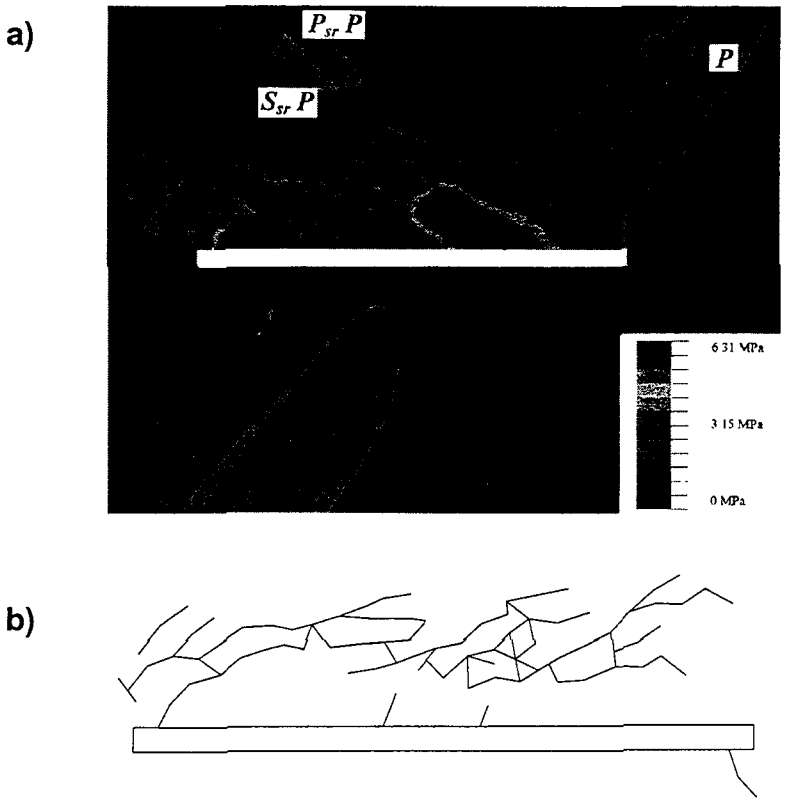

Figure 3.4.2.18 a) Isochromatic wave field due to a 45° incident P-wave interacting with a stope (top), and b) final fracture network (bottom).

a)

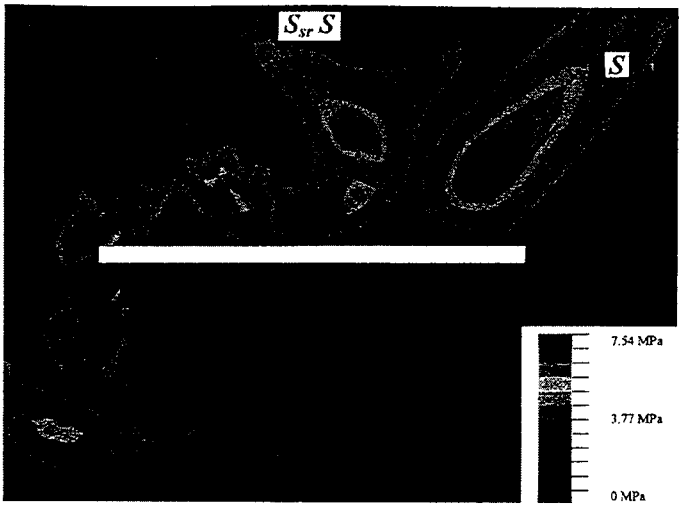

b)

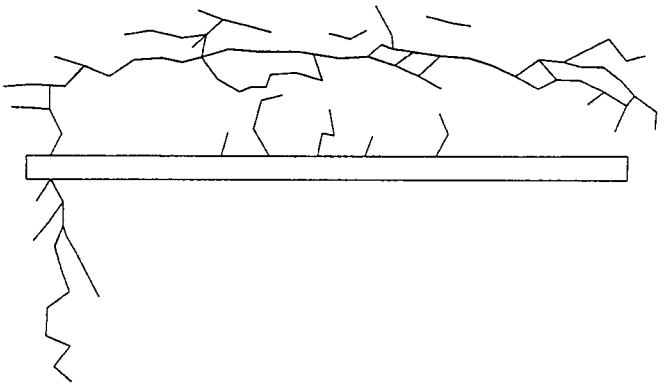

Figure 3.4.2.19 a) Isochromatic wave field due to a 45° incident S-wave interacting with a stope (top), and b) final fracture network (bottom).

S-wave polarity

In deep level tabular mining layouts, positive excess shear stress (Napier, 1987) lobes intersecting steeply dipping planes of weakness, such as faults, can lead to sudden fault rupture. The sense of slip affects the direction of shear of the incident *S*-wave, and is shown here to influence significantly the resulting fracture network. The fracture network due to incident shear waves with two different shear polarisations interacting with a slot in an unstressed medium are indicated in Figures 3.4.2.20 a) and b), where the shear sense is indicated within each diagram. It is evident that far less fracturing occurs in the stope vicinity during interaction of an S-wave with polarisation indicated in Figure 3.4.2.20 b), as compared with the reversed shear polarisation (Figure 3.4.2.20 a).

Both senses of shear have a prominent reflected *S*- (S_{sr} *S*) wave. In case a) however, diffraction at the stope edge causes a tensile P_d *S* wave, and the interaction of this and the S_{sr} *S* waves results in a tensile stress field aligned approximately vertical and causing extensive near stope-parallel fracturing. In case b), the diffraction at the left-hand-side stope edge causes a compressive P_d *S* wave and the magnitude of the tensile stress field is reduced, resulting in far less fracturing.

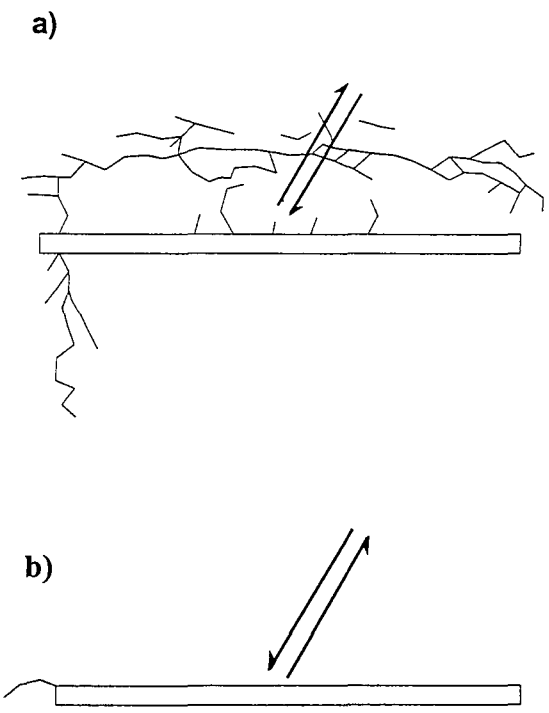

Figure 3.4.2.20 Shear polarity and fracturing due to: a) Incident S-wave with wave front motion towards, and b) incident S-wave with wave front motion away from the stope.

Analysis of the static stress state (Daehnke and Hildyard, 1997) using the boundary element program DIGS (Napier, 1990) shows that, except for very near events, the most likely direction of mining induced fault slip is such that the relative ground movement is upwards on the stope side of the fault. Figure 3.4.2.21 b) shows the relation between direction of shear, pillar distance and fault angle, where these parameters are defined as shown in Figure 3.4.2.21 a).

It is evident that, for stope-fault distances of more than 10 metres, slip is likely to occur for fault angles less than 75° with a sense of shear corresponding to the case shown in Figure 3.4.2.20 b). For distances more than 10 metres, slip is likely on fault angles greater than 75° with a sense of shear corresponding to the case portrayed in Figure 3.4.2.20 a). This result was based on a horizontal stope of 100 m span, with vertical compressive stress of 81 MPa and horizontal stress of 40,5 MPa, corresponding to an approximate depth of 3000 m and k-ratio of 0,5.

a)

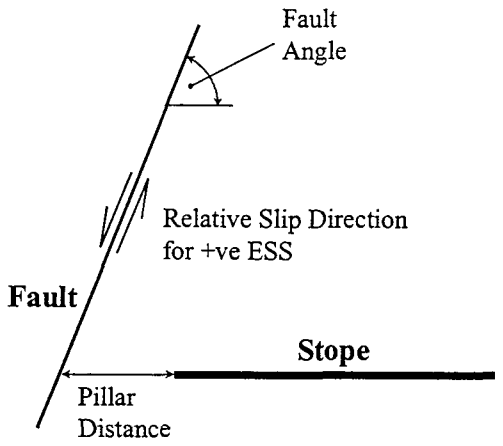

b)

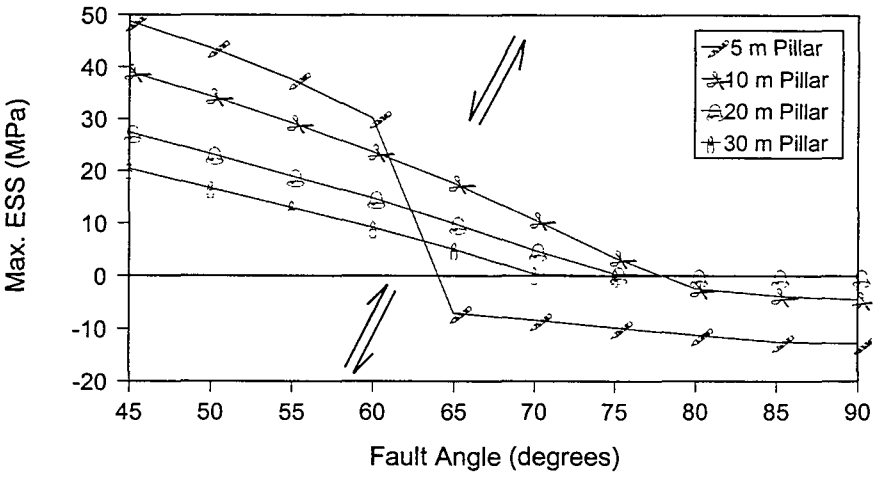

Figure 3.4.2.21 a) Stope-fault geometry and definition of pillar distance. b) Maximum excess shear stress (ESS) for different fault angles and pillar widths (Daehnke and Hildyard, 1997).

Angle of Wave Incidence

Numerical analyses were conducted to investigate fracturing due to incident *P*-waves at angles of incidence of 22,5°, 45°, 67,5° and 90° relative to the long axis of a slot in an unstressed medium.

- For *P*-waves it is found that, at angles of incidence between 0° and 25°, negligible fracturing occurs in the stope vicinity (Figure 3.4.2.22 a).
- At 45° and 67,5°, part of the incident *P*-wave is reflected as a *S*- ($S_{sr}P$) wave, and part as a tensile *P*- ($P_{sr}P$) wave. Stope-parallel fracturing occurs due to a combination of both reflected *P*- and *S*-waves (Figure 3.4.2.22 b and c).
- At a 90° angle of incidence, the compressive incident *P*-wave is stope reflected as a tensile $P_{sr}P$ wave, which initiates extensive stope-parallel fracturing (Figure 3.4.2.22 d).

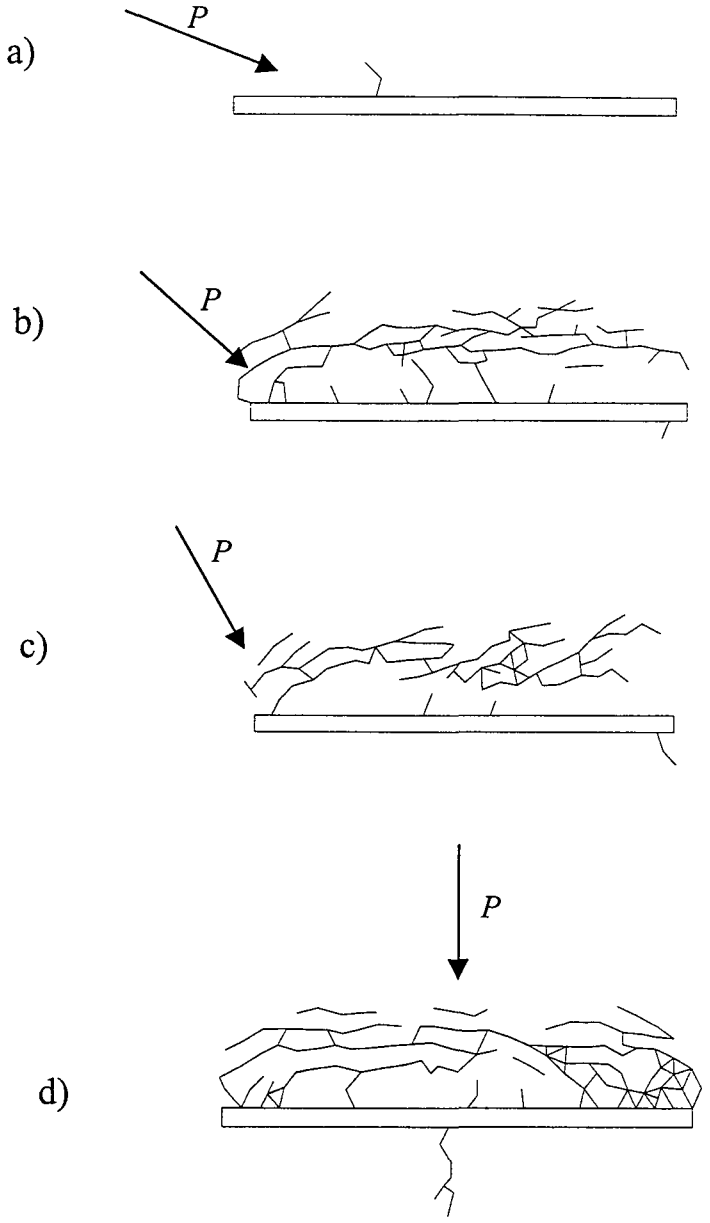

Figure 3.4.2.22 Fractures due to a) 22.5°, b) 45°, c) 67.5° and d) 90° P-wave incidence (the arrow labelled P indicates the wave ray direction).

Stope support

To illustrate the effect of support stiffness on wave interaction and fracture formation, the results of two numerical analyses are presented. In Figure 3.4.2.23 a) a model is shown with stiff stope support, where the support stiffness is equal to the surrounding rock mass (e.g. pillars). As is evident, most of the wave energy is transmitted across the stope, and the stress amplitudes of the reflected waves are low, thereby resulting in little fracturing. In Figure 3.4.2.23 b) the modulus of the support elements is 300 MPa (e.g. timber packs), and in this case the support is too soft to transmit significant incident energy across the stope. Extensive fracturing occurs in the hangingwall due to a prominent $S_{sr}P$ wave created by mode-conversion of the incident *P*-wave.

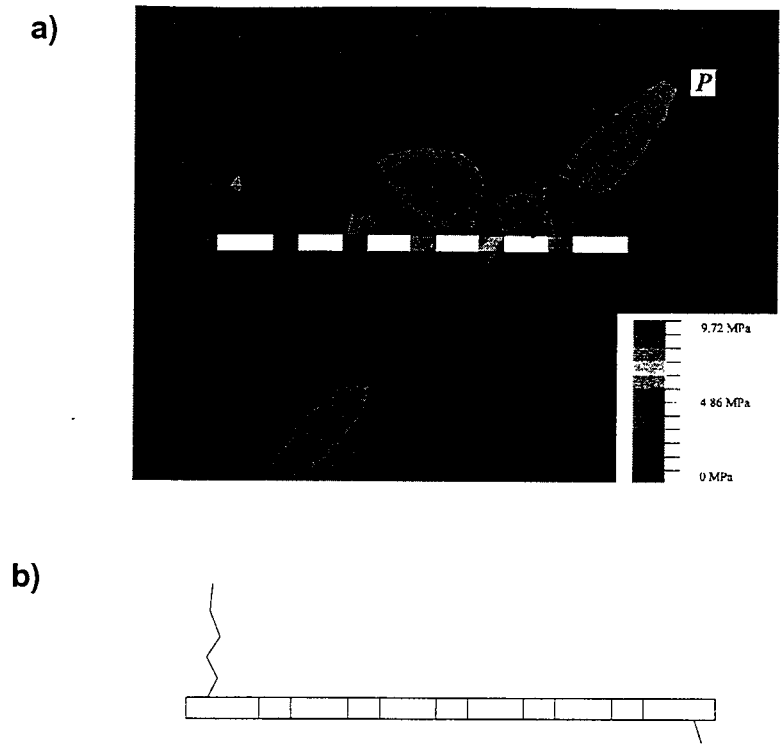

Figure 3.4.2.23 a) Isochromatic wave field (top) and final fracture network (bottom) for stope supported by stiff support (e.g. pillars).

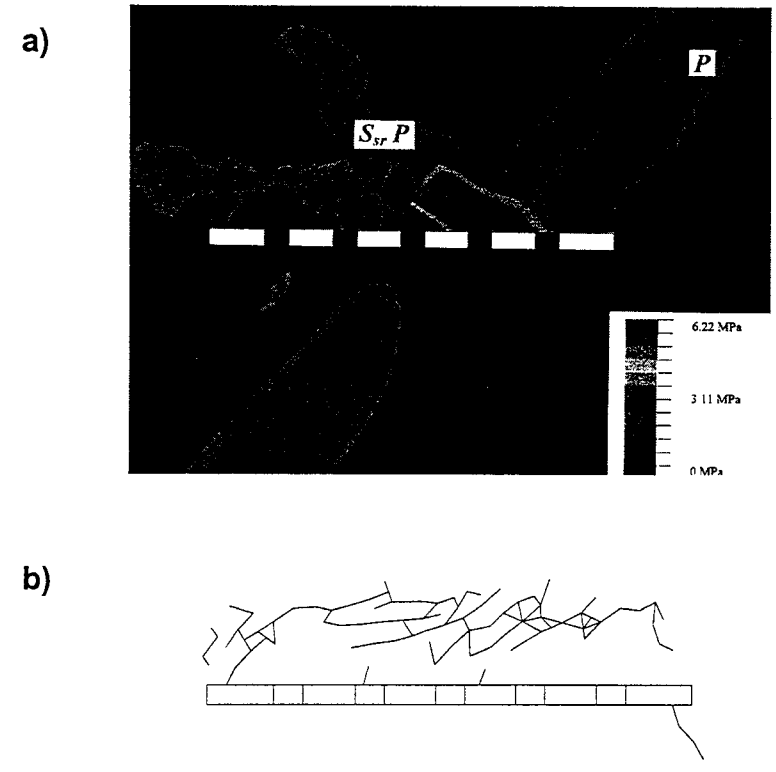

Figure 3.4.2.23 b) Isochromatic wave field (top) and final fracture network (bottom) for stope supported by soft support (e.g. timber packs).

In addition to support stiffness, the amplitude of the reflected waves depends on the frequency of the incident waves and on the pillar spacing. Further work is required to establish a relationship between support stiffness and spacing as well as wave frequency, and to determine the stress amplitude, and hence potential for fracturing, of stope-reflected stress waves.

Wave Amplitude

Various numerical analyses were conducted to determine the effect of stress wave amplitude on the degree of fracturing in the stope vicinity. Incident compressive *P*-waves with equal wavelengths of 15 m and amplitudes of 10; 12.5; 15 and 20 MPa were modelled, resulting in the fracture networks of Figure 3.4.2.24. In all cases the tensile rock strength was assumed to be 10 MPa.

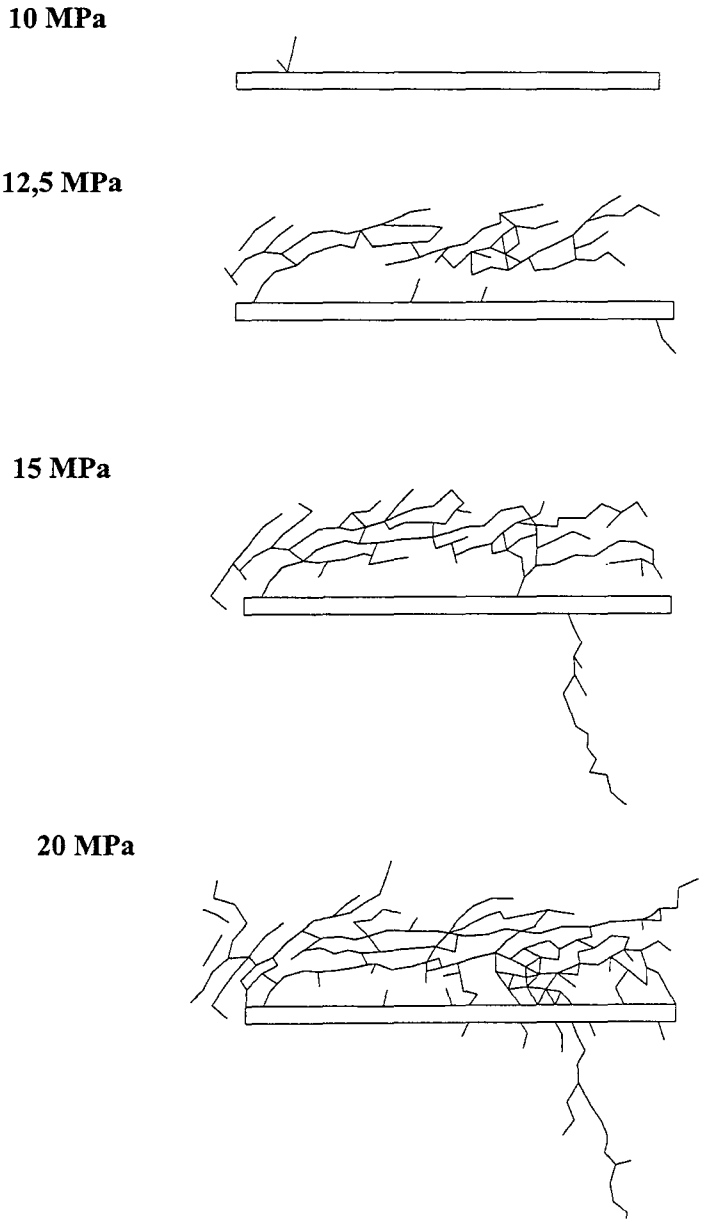

Figure 3.4.2.24 Fracturing in the stope vicinity with incident P-wave amplitudes of 10; 12.5; 15 and 20 MPa, respectively.

Previously (Daehnke and Hildyard, 1997) the tensile stresses associated with the 10 MPa and 15 MPa case were related to dynamic stresses initiated by sudden fault slip in deep level mines. Using dynamic numerical analyses, it was shown that induced fault slip resulting in a seismic event of magnitude M_L = 1,84 generated dynamic tensile stresses corresponding to the 10 MPa case investigated here. An event of magnitude M_L = 1,98 corresponds approximately to the 15 MPa case investigated. Hence, the theoretical wave amplitudes used in the numerical ELFEN analyses are realistic wave amplitudes corresponding to actual seismic events typically occurring in deep level mines.

Summary

Two-dimensional photoelastic experiments were conducted to investigate stress wave driven fracture propagation in thin plates. The experiments were back-analysed using the finite element program ELFEN, and good correlation was observed between the numerical and experimental results. ELFEN was used as well to study the interaction of *P*- and *S*-waves with stopes. The investigation has illustrated possible mechanisms which may lead to fracturing in the stope vicinity:

- In both cases of incident *P*- and *S*-waves, fracturing is primarily associated with the waves generated by reflection of the incident waves at the stope surface.
- Extensive stope parallel fracturing is observed at angles of incidence between 45° and 70°. The fracturing occurs due to $S_{sr}P$ and $S_{sr}S$ waves generated during the reflection of incident *P*- and *S*-waves, respectively.
- The shear wave polarity is shown to significantly influence the resulting fracture network, and a *S*-wave with wave front motion directed towards the stope induces more extensive fracturing than the case of a *S*-wave of opposite polarity.
- The stope support stiffness affects the extent of fracturing. Stiffer support (e.g. pillars) transmits more energy across the stope, and hence, compared with softer support, the amount of fracturing in the stope vicinity is reduced.

This investigation has illustrated some mechanisms and parameters, which affect stress wave driven fracturing in the stope vicinity. Fracturing is governed by many more parameters, and further numerical studies need to be conducted to investigate, for example, the influence of pre-existing discontinuities such as parting planes and joints, as well as the influence of pre-existing compressive stresses.

3.4.2.4 Modelling of mine seismic events

Blyvooruitzicht preconditioning site

A back-analysis of a set of seismic events at the Blyvooruitzicht preconditioning site was made using WAVE models. Good seismic records were available over a three year period, and interpretations of seismic traces suggest a slip mechanism on near-vertical joints lying more or less parallel to the breast mining faces. The geometry of the site is sufficiently simple for reasonably accurate representation in WAVE. In this study it was not possible to obtain a model whose waveforms correspond in detail with the measured waveforms. However an approximate model was found where certain waveform features such as arrival times, first motions and amplitudes could be matched for a selected event. The match could then provide some indication of the slip mechanism for the event. Using the model, the effects of different stope spans on waveforms were studied, allowing conclusions to be drawn about the state of stope closure. The details of this work are covered in a paper by Handley et al. (1996).

Description of the model

The layout of the Blyvooruitzicht preconditioning site is shown in Figure 3.4.2.25a. It involves the extraction of a strike-stabilising pillar, which can be seismically hazardous. More than 180,000 events have been recorded at the site since the mini-network was installed. The geometry lends itself to analysis with WAVE, in which faults and stopes are required to be aligned to the orthogonal elements that make up the finite difference mesh.

In previous modelling of actual mining events (Tinucci and Spearing, 1993, Siebrits et al., 1995), a close correspondence between synthetic and observed seismograms was not obtained. In this work therefore the primary goal was not to obtain good fits in seismograms, but rather to develop ideas at the expense of capturing all the features of the seismograms. The model used was kept as simple as possible to reduce analysis times to a minimum, and the number of evaluated alternatives to a maximum. The size of the WAVE model was chosen to be a 320 by 320 by 320 metre cubic volume aligned parallel to reef dip, and discretised into 8 by 8 by 8 metre cubic zones, i.e. 64000 zones. The 8 metre grid zone size limited the frequencies that could be modelled to about 100 Hz.

The Carbon Leader Reef at the site dips to the south at 25 degrees; a plan view of the model, as it appears on the reef horizon is shown in Figure 3.4.2.25b. The geophone positions as shown are projected onto the reef plane, and are approximate as they can only be located to the nearest eight metre cell. The vertical component of each geophone in the model is perpendicular to the reef plane, in contrast to the geophones at site which have plumb vertical components. For strict correspondence therefore, seismic trace components should have been rotated to give consistency between the model co-ordinate system and the measurement co-ordinate systems.

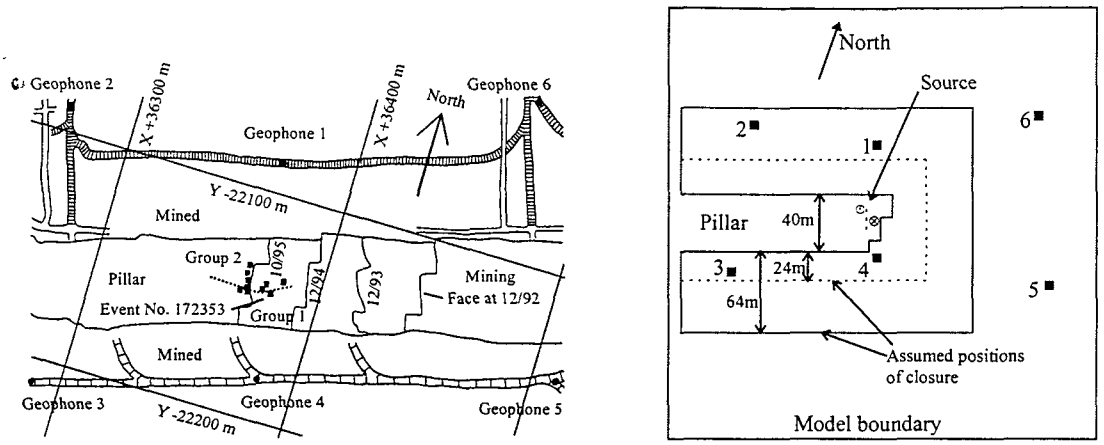

(a) Plan of Mining Site

(b) Plan View of WAVE Model on Reef Plane

Figure 3.4.2.25 Geometry for Blyvooruitzicht backanalysis.

Source model

Nine seismic events with a local magnitude varying from 0.0 to 0.8 took place ahead of the breast mining faces between 3 February and 26 August 1995. These events are indicated in Figure 3.4.2.25a and were selected as comparators for the WAVE model. These events took place within about 20 metres of the reef elevation, and within 20 metres ahead of the face position at the time of there ocurrence (Figure 3.4.2.25a), which suggests that the seismic mechanism could only have been one of shear. The events were amongst the largest to have occurred at the site, and were selected because their frequency content tended to be lower, thereby better matching the frequency limitations imposed by a coarse model. All the events chosen were located with errors of three metres and less, and could be divided into hangingwall and footwall groups based on location.

The source was assumed to be a 16 by 16 metre square area, 8 metres ahead of the breast panels. The source behaviour in both cases was assumed to be a shear stress applied over the whole source area simultaneously, growing to 5 MPa in 10 milliseconds, after which it remained constant. The sense of the shear stress was such that it would result in stope closure behind the breast faces in the pillar, typical of the real situation underground, where stope closure has been found to accompany seismic events. Such closure usually contains a vertical component - direct closure - plus a ride component in which the hangingwall moves updip in relation to the footwall. Both these components were included in equal measure in the shear representation of the source plane.

Correlation of model results with measurements

Initial comparisons were based on all nine events with the purpose of eliminating those events that did not conform to the model that was developed. For simplicity, the comparisons were made only with the vertical trace components and limited to the following features :

- *P*-wave onset times for all geophones;
- direction of first motion in both velocity and displacement traces;
- net displacement values after the seismic event;
- trace amplitudes.

The factors governing the arrivals are the geometry of the situation, including the relative

positions of the geophones and source, and the wave transmission velocities in the rock. Material parameters used for seismic event location at the site (Table 3.4.2.1) were not optimal for the model. This is not surprising as these values combine all the rock mass properties and other site effects into a single set of averaged values. With a low velocity layer (Table 3.4.2.2) above and below the stope, better comparisons of arrival times as well as order of arrival were obtained. This was used to represent intense mining induced fracturing which has been found to exist for about 10 metres above and below stopes in deep mines.

Table 3.4.2.1 Rock properties from seismic system (Stewart, 1995)

Property (units)	Value
C_p (m/s)	5860
C_s (m/s)	3748
K (Gpa)	42,1
G (Gpa)	37,9
n	0,15
Density (kg/m^3)	2700

Table 3.4.2.2 Modified rock properties assigned to the model

Material Property	<8m above and below stope	>8m above and below stope
C_p (m/s)	5000	6500
C_s (m/s)	2041	3980
K (Gpa)	52,5	57,0
G (Gpa)	11,2	42,8
n	0,4	0,2
Density (kg/m^3)	2700	2700

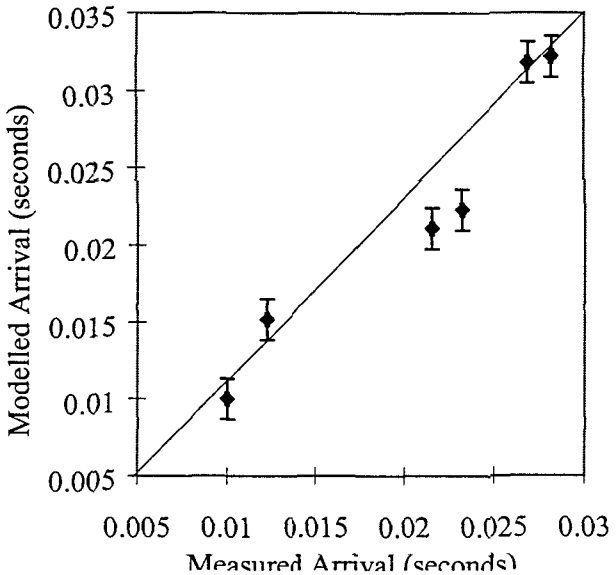

Figure 3.4.2.26 Comparative plot of arrival times for source model no. 1.

A plot of measured arrival times versus model arrival times for source-1 events is given in Figure 3.4.2.26. The error bars are based on model grid size, source size, and sampling time increment of the geophones (0,1 millisecond). Perfect agreement between arrival times would lie on the diagonal. As shown, only four of the measurements include the diagonal in their error bars. The agreement shown was obtained after many trial and error runs of the model. Analysis of events with the second source model was stopped at this stage due to poor correlation with arrivals.

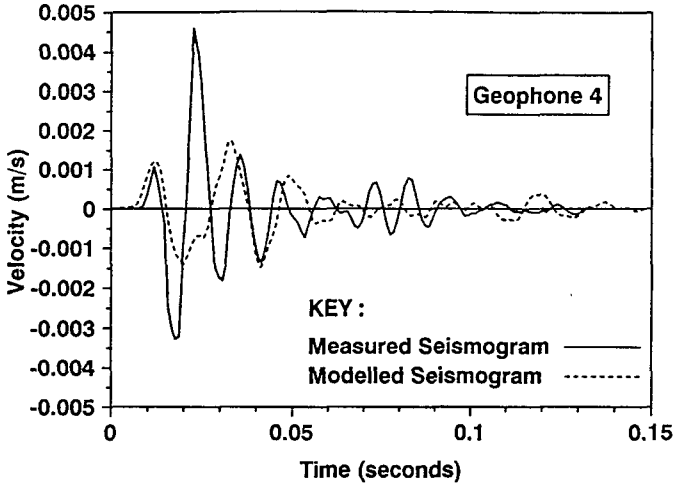

Figure 3.4.2.27 Comparison of velocity seismograms.

A comparison between the measured and model velocity traces is given in Figure 3.4.2.27 for the same event and geophone. The figure shows that there is reasonable correspondence between the arrival times and the first motions, after which correspondence is poor, and a more sophisticated source model and material model would be required to improve this.

One event provided reasonable agreement with model traces for first motions for all the geophones. This was Event No. 172353 which showed similar sense first motions for three of the four geophones, (nos. 4, 5 and 6) while Geophone No. 1 showed an opposite first motion. Comparisons of first motions in displacements appear in Figures 3.4.2.28 (a,c,e) below. First motion comparisons were limited to the *direction* of motion only, the form was ignored. Unfortunately two geophones (Nos. 2 and 3) were unserviceable when this event was recorded by the network. The fact that only one event approximately fits this source model, highlights how complex each event is and how variable the source mechanism can be. This event was then used for all further analysis.

Effect of stopes on seismograms

The model was used to determine the effect of open stopes on seismograms, with the purpose of estimating the span of open stope surrounding the pillar. This has significance in estimating the average pillar stress and therefore the potential seismic hazard.

Three models were analysed, assuming no stope around the pillar; open stopes spanning 24 metres on all sides of the pillar; open stopes spanning 64 metres on all sides of the pillar (see Figure 3.4.2.28b). The displacement traces from the event were used to make the comparisons and the estimates. Figures 3.4.2.28 (a,c,e) compare the measured displacement traces for geophones 1, 4 and 6, with the modelled traces corresponding to an open stope span of 24 metres.

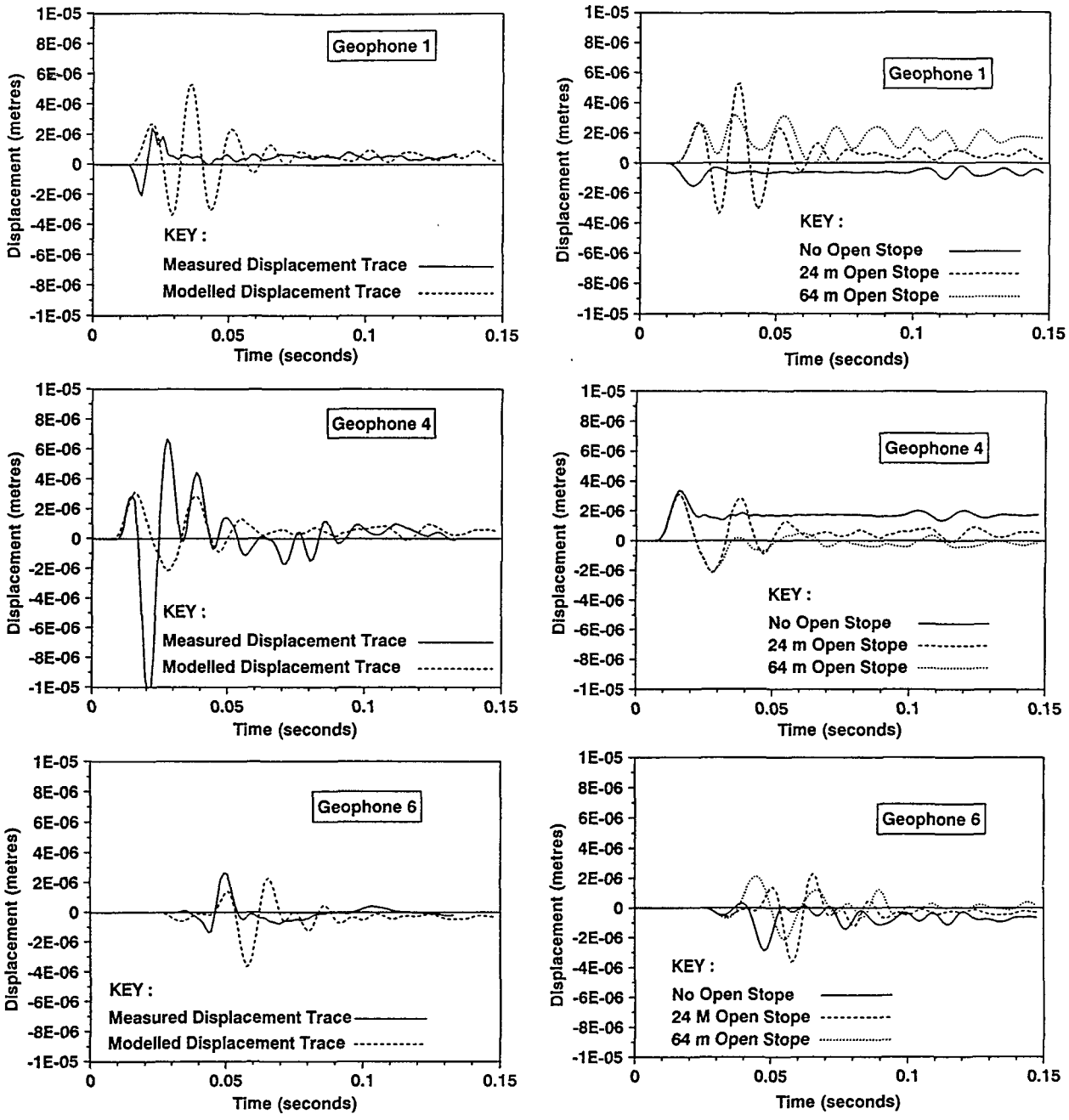

Figure 3.4.2.28 Comparison of measured and modelled displacement traces (a,c,e), and comparison of model displacement traces for different stope spans (b,d,f), for geophones 1,4 and 6.

The model displacement plots for all three stope spans are shown for geophones 1,4 and 6 in Figures 3.4.2.28 (b,d,f). Comparing final displacements with those measured, the 24 metre span trace gives the best agreement with the measured trace for geophone 1 (Figure 3.4.2.28b). For geophones 4 and 6 it appears that open stope spans are closer to about 60 metres (Figures 3.4.2.28d,f). It is therefore concluded from this data, and from underground observation, that full stope closure occurs between 20 and 60 metres from the pillar, which would result in significant stress relief in the pillar itself when compared with that calculated from an elastic analysis.

Although correspondence between seismic traces was generally poor, several simple measures showed reasonable correspondence, such as *P*-wave arrival times, arrival sequence at the geophones, and first motions. These measures indicate that seismic events can at least be modelled approximately, and that meaningful results can be obtained from the model. In particular some estimates of stope closure around the pillar were possible, indicating that on average the stope is open to at least 20 metres from the pillar, partially open between 20 and 60 metres, and closed beyond 60 metres from the pillar. Elastic analyses suggest that the average stress for the pillar is 350 MPa, which would be reduced to approximately 160 MPa if total closure took place between 20 and 60 metres away.

Western Deeps event

Preliminary modelling of a mine seismic event at Western Deeps was performed using WAVE. The event was modelled some time ago with ABAQUS (Siebrits et al, 1995). There are a number of motivations for modelling this event. Firstly, improvements in the models now allow further insights, and general inferences can be made on what is missing from existing models for effective back-analysis. WAVE could not be used at the time as it did not support features such as three-dimensional stope layouts. Theoretically WAVE should offer better dynamic detail, at the expense of geometric detail, and the first phase of comparing a rough model with the original approach was completed. The mine layout is given in Figure 3.4.2.29.

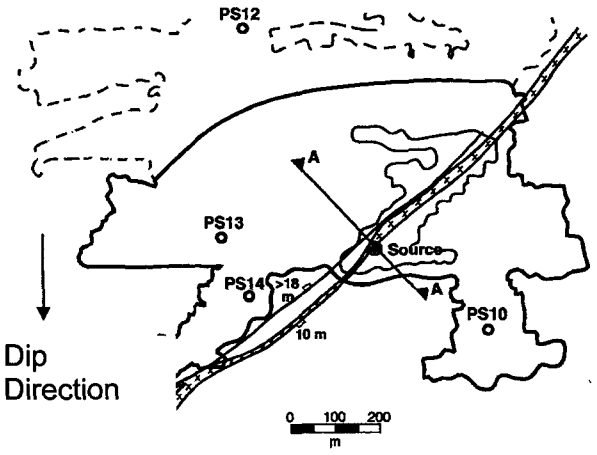

Figure 3.4.2.29 Mine plan showing stope layout, fault/ dyke, source location and position of geophones.

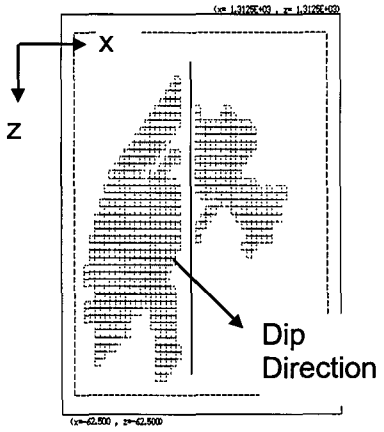

Figure 3.4.2.30 Mine layout as modelled in WAVE.

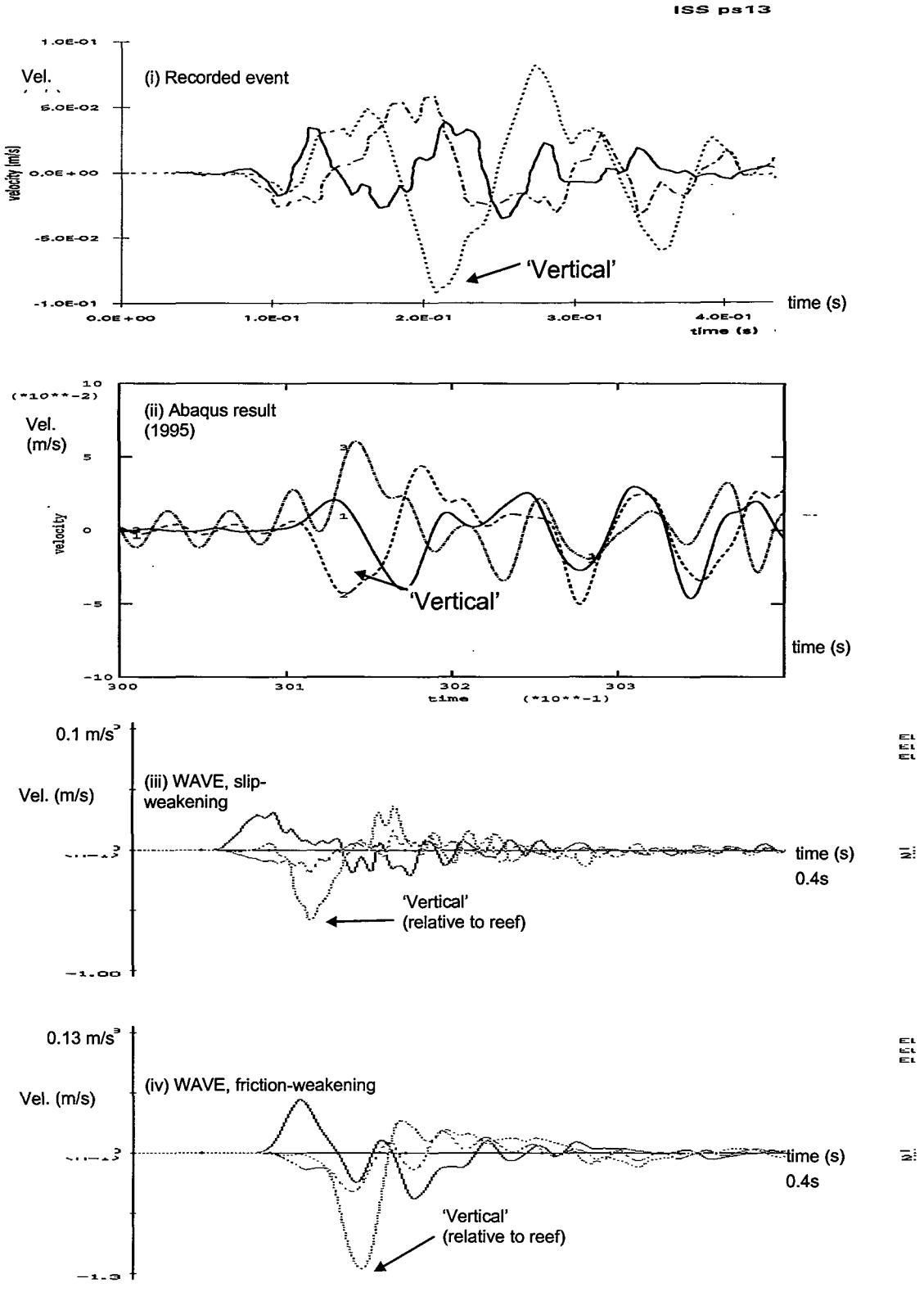

Figure 3.4.2.31 Waveforms at geophone #13 (i) Recorded (ii) Previous ABAQUS result (iii) WAVE: slip-weakening (iv) WAVE: friction-weakening.

In WAVE both the reef plane and fault plane have to be grid-aligned. An *in situ* stress field of Sxx=-35 MPa, Syy=-70 MPa, Szz=-35 MPa is assumed. The model co-ordinate system was rotated about the x-axis by the dip angle of 20 degrees, and then about the y axis (x_2) by 43 degrees, to align the fault. The applied stress state was then: Sxx=-37,2 MPa, Syy=-66,0 MPa,

Szz=-36,9 MPa, Sxy=8,2 MPa, Syz=-7,7 MPa, Szx=2,0 MPa. A coarse model of 50x50x50 fourth order elements was used, covering an area of 1,2km x 1,2km x 1,2 km. This is comparable to the size and resolution of the original modelling. The WAVE model is shown in Figure 3.4.2.30

The original source model was a friction-weakening model, where the fault friction was reduced over 50 milliseconds, from 60 to 15 degrees. This source was again modelled along with a slip-weakening source model with a friction angle of 15 degrees, cohesion of 8MPa and a slip-weakening displacement of one millimetre (the slip distance required to reduce the cohesion linearly to zero).

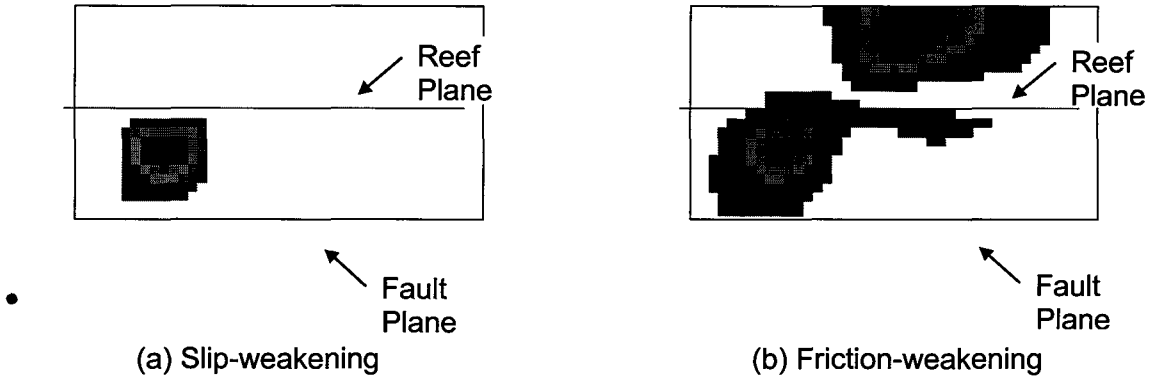

(a) Slip-weakening (b) Friction-weakening

Figure 3.4.2.32 Contours of final slip on the fault for two different stress-driven sources.

Figure 3.4.2.32 compares final slip profiles for the two source types. It is interesting that while velocities recorded at geophones were similar for the two source models, the area of slip was much greater and more widespread in the friction-weakening case. Velocity waveforms for one geophone for each of the two source types are compared with the recorded and previously modelled waveforms in figure 3.4.2.31. Waveforms have not been rotated into the correct co-ordinates. The waveforms do capture a higher frequency content, but do not correspond closer than earlier modelling.

One of the common conclusions from these back-analyses is that the source mechanism has a great influence on the seismograms. It is difficult to have confidence in correspondence between modelled velocity distributions and wave motions in the stopes, and that of the actual event as there are two coupled problems, namely, source complexity and site complexity. Ideally data is required where the source is well-understood or controlled, to decouple this unknown from the investigation.

3.4.2.5 Models of the tunnel rockburst/ blasting experiment

In models of mine seismic events discrepancies between modelled and measured waveforms have been large (Section 3.4.2.4). This has highlighted the need for more controlled field data that can be used to improve the capability of models to represent wave motions around underground excavations. In developing models of wave motions about excavations, we need data where the source uncertainty is decoupled from the problem. The source needs to be well known not only in location and orientation, but also in its detailed loading history in time and space. An artificial rockburst experiment has been performed as part of project GAP 530 with a well-defined blast source. The purpose was to create a controlled seismic event which could be extensively monitored, and to induce and observe damage in a nearby tunnel.

Description of experiment

The experiment was performed at a site where blast holes could be drilled parallel to a tunnel at approximately five metres from the tunnel. Five blast holes were used to emulate a seismic event, by generating stress waves incident on the tunnel, with gas driven fracturing limited to as small a volume as possible. Three eight-channel seismic arrays were installed on the various tunnel faces and at various distances along the tunnel (ranging from 10 to 30 m from the blast). Three accelerometers were installed close to where the maximum motion and damage was expected. Surveys of the fracturing were made before and after the blast, and the blast was captured on high speed video to study rock ejection.

Source Model

A source was required which would model stress waves emanating from a propagating blast in a borehole, to a distance many times larger than the borehole radius. (In the experiment, the borehole charge lengths were from 4 to 7 m and the borehole diameter was 0,1 m. The tunnel was 5 m away, and geophones were located up to 25 m ahead of the blast). A three-dimensional numerical model with this volume of interest, required as coarse as possible a representation of the source to be developed. i.e. it would be pointless to model the borehole in any detail, and ideally the source diameter should require just a single element.

A propagating blast source is modelled in Section 3.4.3.2 by applying a moving radial load to the surface of a borehole. This work uses two-dimensional numerical models with axisymmetry, and considers the resulting stresses close to the borehole surface. Interesting results are that shear waves are developed due to the non-uniform loading of the surface, and that for a velocity of detonation (VOD) less than the *P*-wave speed (Cp), the shear wave is dominant.

In three-dimensions it is undesirable to model the borehole directly, for reasons of efficiency as already stated. A single-element diameter volumetric representation of this propagating force on the surface of a borehole was developed. The model more strictly represents a force applied to the sides of a square borehole (due to the cubic mesh structure), which propagates with time along the axis of the borehole.

An important phase was to evaluate if indeed a single element wide volumetric model could represent this conceptual model of a propagating force along a borehole. Kouzniak (1998) has developed an analytic solution for this model, for the case where VOD is greater than the *P*-wave speed of the surrounding material. (No analytical solution exists at present for the case of Cs < VOD < Cp). Comparisons have been made of the numerical and analytical models for loading functions (in time) which were analytically tractable - namely, a triangular load and a smooth step load. These were for the case of VOD = 2,24 Cp. The radial stress at 2, 80 and 100 borehole radii (measured from the centre of the borehole) are shown in Figures 3.4.2.33 and

3.4.2.34 for the two different load functions respectively. The result applies in a dimensionless manner, but the actual parameters used in the numerical model were VOD=12000 m/s; E=70 GPa; ν=0,2; ρ=2700 kg/m^2; Cp=5367 m/s; Cs=3287 m/s; $Diam_{bh}$= 0,05 m. It was found that the square borehole is equivalent to a circular borehole with a radius of 1,27 times the square element length. (This results from the need for an equal area over which the force is applied). The numerical waveform corresponds very accurately to the analytic result - except for known numerical dispersion at high frequencies, which could be removed using smaller element sizes. Although this result is only for the case of VOD > Cp, the assumption is made that the numerical model is an accurate representation of the conceptual model for all values of VOD.

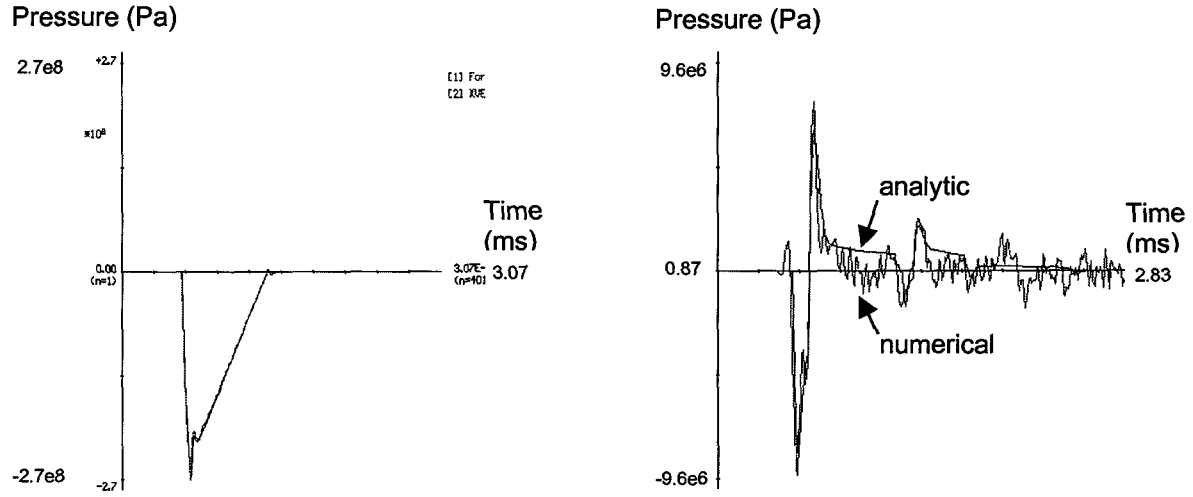

(a) Radial Stress at 0,2 m
(2 radii, from centre of the borehole)

(b) Radial Stress at 4,0 m
(80 radii, from centre of the borehole)

Figure 3.4.2.33 Comparison of a coarse single element borehole numerical solution with the analytical solution for a propagating triangular load along the borehole wall (VOD = 2.24 Cp).

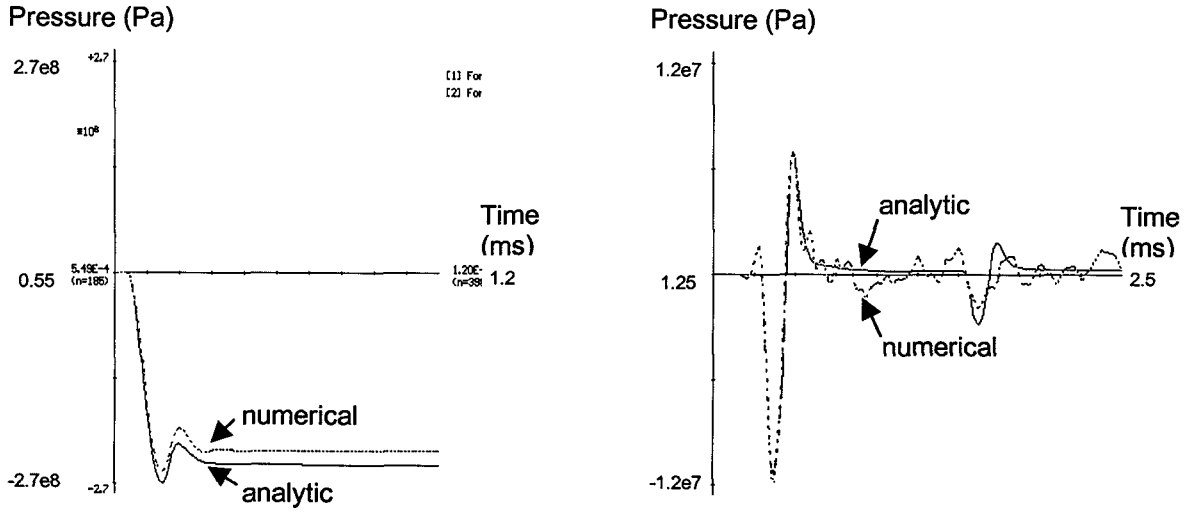

(a) Radial Stress at 0.2m
(2 radii, from centre of the borehole)

(b) Radial Stress at 5.0m
(100 radii, from centre of the borehole)

Figure 3.4.2.34 Comparison of a coarse single element borehole numerical solution with the analytical solution for a propagating smoothed step load along the borehole wall (VOD = 2.24 Cp).

Forward modelling of the experiment using this source model

An approximate representation of the tunnel experiment was made in the program WAVE. A 3D cavity was not available, so solid gaps were left between the free surfaces of the different faces of the tunnel. Forward numerical modelling was used to aid in the design of the experiment, to give insight into which measurements are likely to be the most useful, and the positions where recordings should be made. The following questions were identified:

- Can the experiment be tailored to simulate waves emanating from a rockburst event?
- Where is the expected position of maximum damage?
- How quickly do the motions die off with distance along the tunnel?
- How much relative damage can be expected on the other walls of the tunnel?

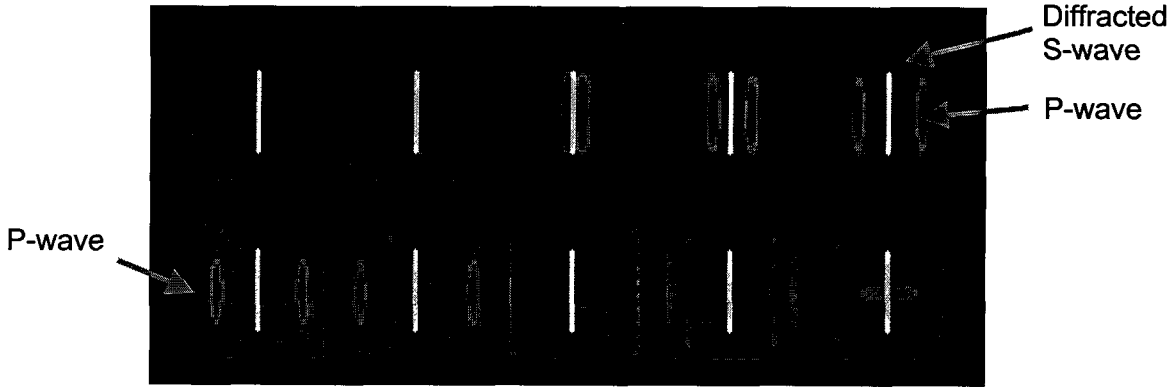

Figure 3.4.2.35 Source radiation pattern for a pressure applied at the same time throughout the borehole in an infinite medium. (This is equivalent to an infinite velocity of detonation (VOD)).

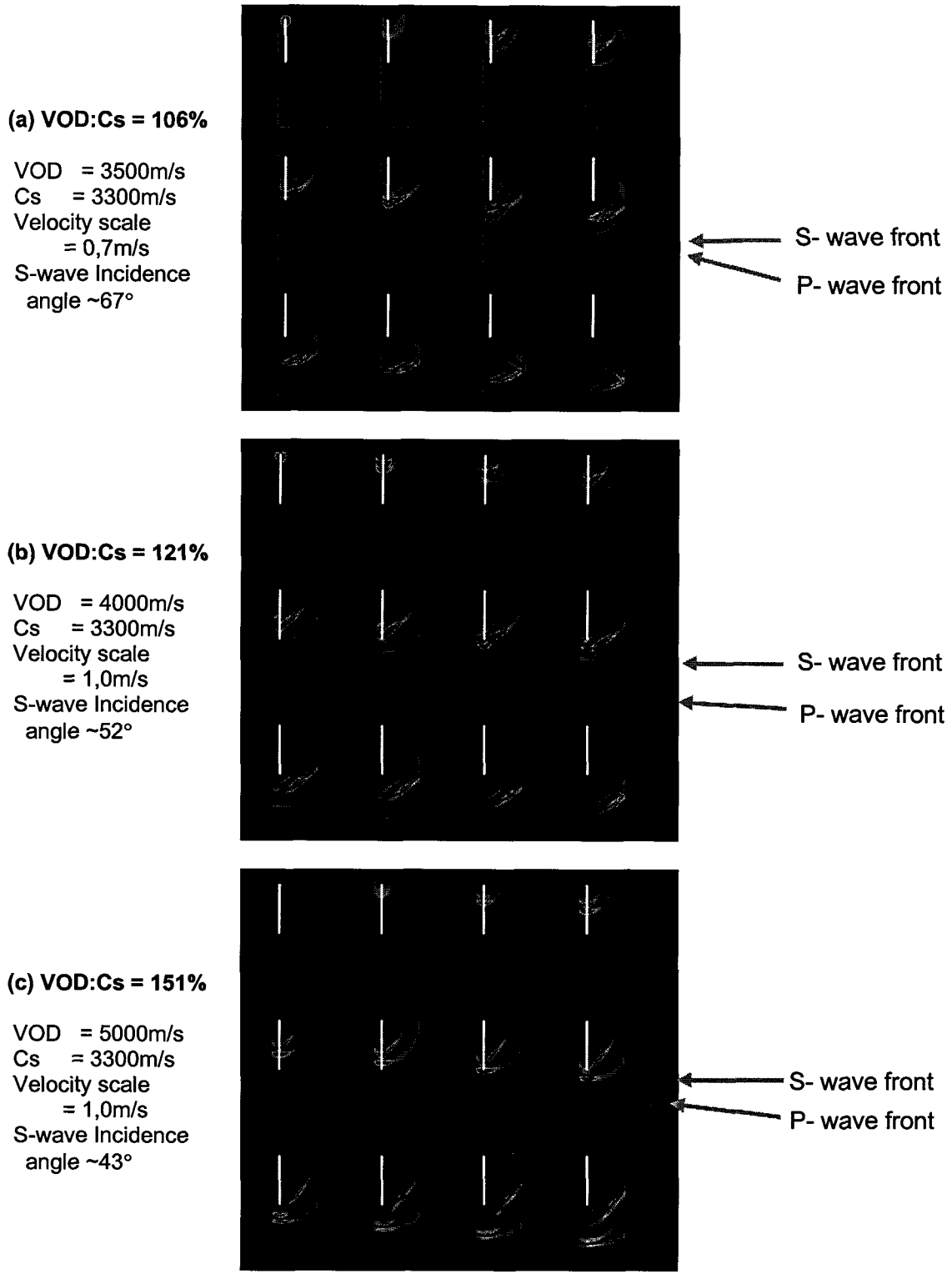

Figure 3.4.2.36 Sequences of velocity snapshots showing wave propagation from a propagating blast. Comparisons are shown for different velocities of detonation, showing that the VOD:Cs ratio affects the angles of incidence and relative content of P- and S- waves

Figure 3.4.2.35 shows the wave radiation pattern from a borehole blast where the pressure rises simultaneously throughout the borehole (this is equivalent to an infinite VOD). In this case, predominately *P*-wave energy is radiated, except for shear waves diffracted from the ends of the borehole. Figure 3.4.2.36 shows models of the experiment with wave radiation patterns for a propagating blast, comparing three different source VODs. This shows the emergence of a clear

shear wave, and that the *P*-wave becomes very small for VODs close to the shear wave speed. This is due to *P*-wave energy propagating faster than new energy is released. The first conclusion was that by keeping the VOD sufficiently low (greater than but close to the shear wave speed Cs), the blast could be tailored to produce a large incident shear wave which was considered to correspond best to a rockburst event.

Results also indicated that the actual position of the maximum velocity experienced at the tunnel is not directly opposite the blast, but at some distance ahead of the blast depending on the VOD. This can be explained from Figure 3.4.2.36 where the angle of the *P*- and *S*- waves generated is dependent on the VOD:Cs ratio, and waves first strike the tunnel at some distance ahead of the blast. This leads to the situation in Figure 3.4.2.37 where the position of maximum velocity (on the near tunnel wall) depends on the VOD:Cs ratio.

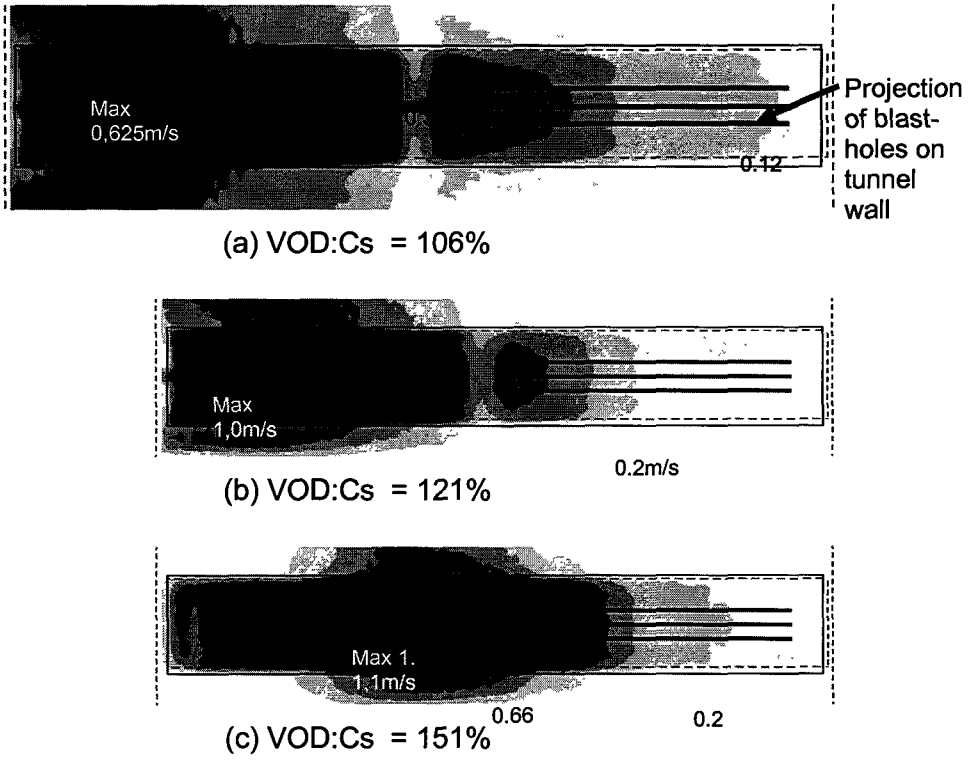

Figure 3.4.2.37 Maximum velocities at near tunnel wall and for 3 different VOD:Cs ratios, indicating how this ratio affects the position of maximum velocity. The model has 3 blastholes with simultaneous ignition. These are six metres from the tunnel and parallel to the tunnel. Rise-time to maximum pressure is 200 μs.

The maximum particle velocity on the tunnel sidewall was found to depend on the following:

- The maximum borehole pressure; this is the assumed maximum pressure reached at the walls of the borehole. The maximum velocity in the models is linearly related to this pressure.
- The rise-time of the pressure; this is the duration over which a point on the borehole wall moves from zero load to maximum load. The faster the rise time, the higher the resulting velocities. This also determines the wavelength of the incident waves.
- Delay between (the five) multiple blasts; the initial design involved a delay of at least 1ms between blasts (due to detonation error). The modelling showed that this was far too great a delay, for the blasts to behave as a single event i.e. velocities at the tunnel were greatly reduced if the blasts were not nearly simultaneous.

The following values were assumed as good estimates of these factors:
- maximum borehole pressure = 1 GPa
- rise time of pressure at a point = 200 μs
  (in space, maximum pressure is reached over approximately 12 borehole radii)
- simultaneous blasting (the detonation method in the experiment design was changed)

In general the modelling demonstrated that:
- Predominantly shear waves could be generated by controlling the VOD.
- The position of maximum damage depends on the VOD:Cs ratio of the blast, and the distance between the blast and the tunnel wall.
- The magnitude of the maximum velocity (at the tunnel wall) depends on the maximum borehole pressure, rise time of pressure at a point, simultaneity of the (5) blasts.
- Meaningful estimates were still required for the borehole pressure and rise-time of the source model.
- Estimates of motions on the other walls of the tunnel were considered unreliable, since there was not a continuous tunnel surface in this model.

Calibration

It was important to estimate parameters for the source model, and indeed to evaluate whether this source model is valid as a representation of the blast. Accelerograms recorded near a blast in solid rock were available from an earlier experiment. Attempts to model these with the chosen source model were not conclusive, and it became apparent that a calibration blast at the actual rockburst experimental site needed to be made. Other data was available to calibrate the model in terms of empirical expressions for far-field velocities due to a blast.

Three experiments were performed (Rorke, 1992) where acceleration data was collected at six positions close to a blast as part of the preconditioning (Lightfoot et al, 1996) research project. A 61 mm diameter, 1,95 m blast hole was detonated 4,75 m ahead of a tunnel, with propagation back toward the tunnel face. An array of accelerometers were mounted 3,7 m into the tunnel face (Figure 3.4.2.38).

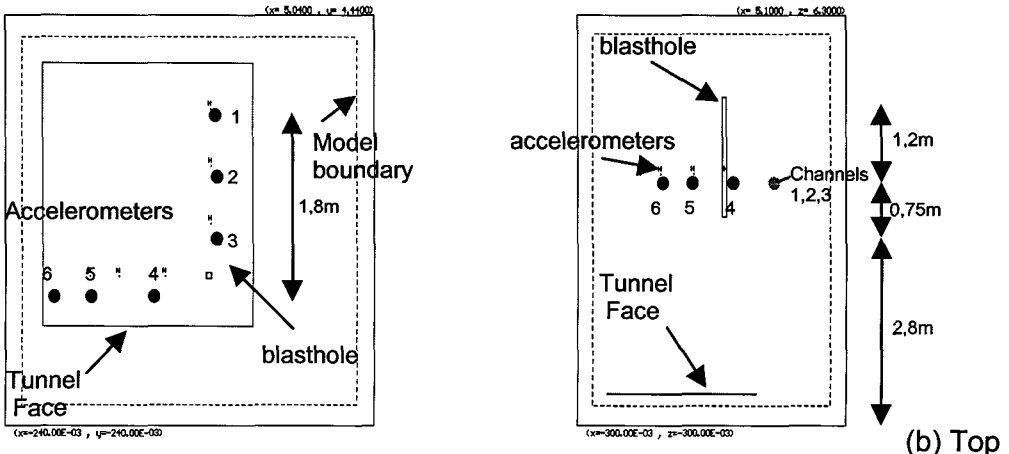

Figure 3.4.2.38 Geometry for model of the preconditioning experiment, showing positions of the blast hole, tunnel and accelerometer channels.

The physical parameters for the first experiment were, 6 kg Anfex, 1,95 m length, 0,06 m diameter, VOD=3760 m/s, with measurements at 0,6 m, 1,2 m, 1,8 m from the axis of the blast. The blast was modelled with the chosen source parameters of a peak borehole pressure of

1 GPa and a rise time of 200 μs, and then compared with the experimental waveforms (Figure 3.4.2.39). Note firstly that arrival times cannot be obtained from the experimental data - the delay in the experimental waveforms is due to the recordings being initiated before the blast. The measured amplitudes were between 20 and 60 times larger than the modelled amplitudes. The differences were similar when modelling the other two experiments. To increase the modelled amplitudes, the options were to increase the pressure, decrease the rise-time, soften the material properties, or increase the borehole radius. Making the peak pressure too high was considered aphysical, while the measured waveforms did not indicate a faster rise-time. Increasing the radius may have some validity in terms of intense fracturing in this region, and large strains.

If the physical borehole size of 0,06 m was used, a pressure of about 25 GPa would be required, and the fall-off with distance would be much faster than the experimental data. The borehole diameter, pressure, and rise-time were varied to obtain the best match. The strategy which provided the best match to the observations was: to match the rise time and pulse width, 0,1ms source rise time; to match the decay with distance 0.12m (2 times) diameter; to then match the velocity magnitudes, a pressure of 10 GPa. The comparison for just two accelerometer channels is shown in Figure 3.4.2.40 for this model.

It was clear from the above that more data was needed to derive a suitable blast source model. A calibration blast was made at the site. The physical parameters were: a 75 degree charge hole 1 metre from the tunnel wall, 0,65 m length, 0,037 m diameter, 0,6 kg charge mass, VOD = 4500m/s. The best match was found with a source rise-time of 0,8e-3 s, a diameter of 0.1 m (3 times the physical diameter), and a peak pressure of 9 GPa. The long rise time seems necessary because of surprisingly long pulse widths in the data - (this differs significantly from data from the preconditioning experiment, where pulse widths are much shorter). Comparisons for various geophones in the tunnel are shown. Geophones A2, A3 and A5 (Figure 3.4.2.41) are a triaxial set on the tunnel wall. Geophones C8, C3, C6 and C5 (Figure 3.4.2.42) are geophones normal to the tunnel wall at approximately 4 m intervals from the calibration blast. Geophones A6, A7 and A8 (Figure 3.4.2.43) are a triaxial set of geophones mounted 5 m into the tunnel wall (i.e. in solid rock) 0,2 m from at the calibration blast.

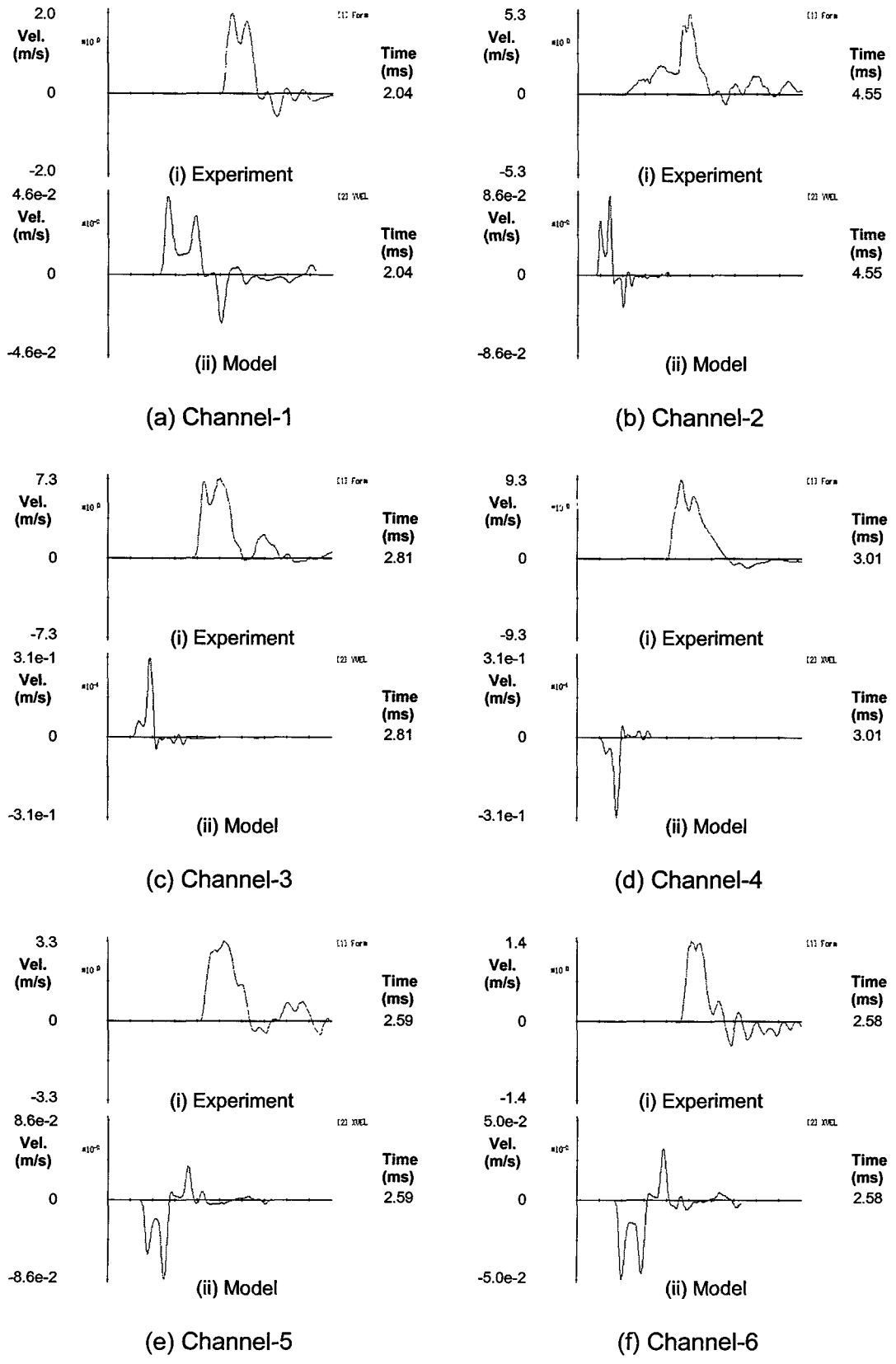

Figure 3.4.2.39 Comparisons of velocities from the preconditioning experiment (obtained by integrating accelerometer data), and the modelled velocities for a source of 1 GPa, 100 μs, step-shaped load and a 0,06m diameter borehole.

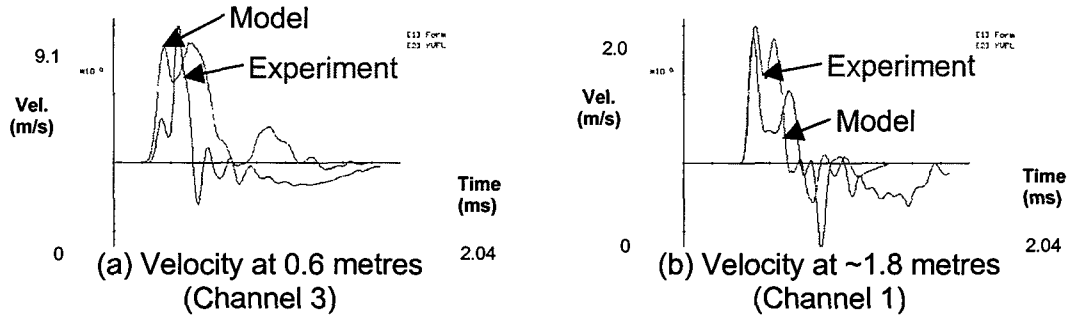

Figure 3.4.2.40 Comparison of velocities from experimental recordings in the preconditioning experiment for two channels with numerical waveforms, for modelled source #2 of 10 GPa, 100 μs, step-shaped load and a 0,12 m diameter borehole. (Experimental waveforms have been shifted to correspond with the arrival time in the model).

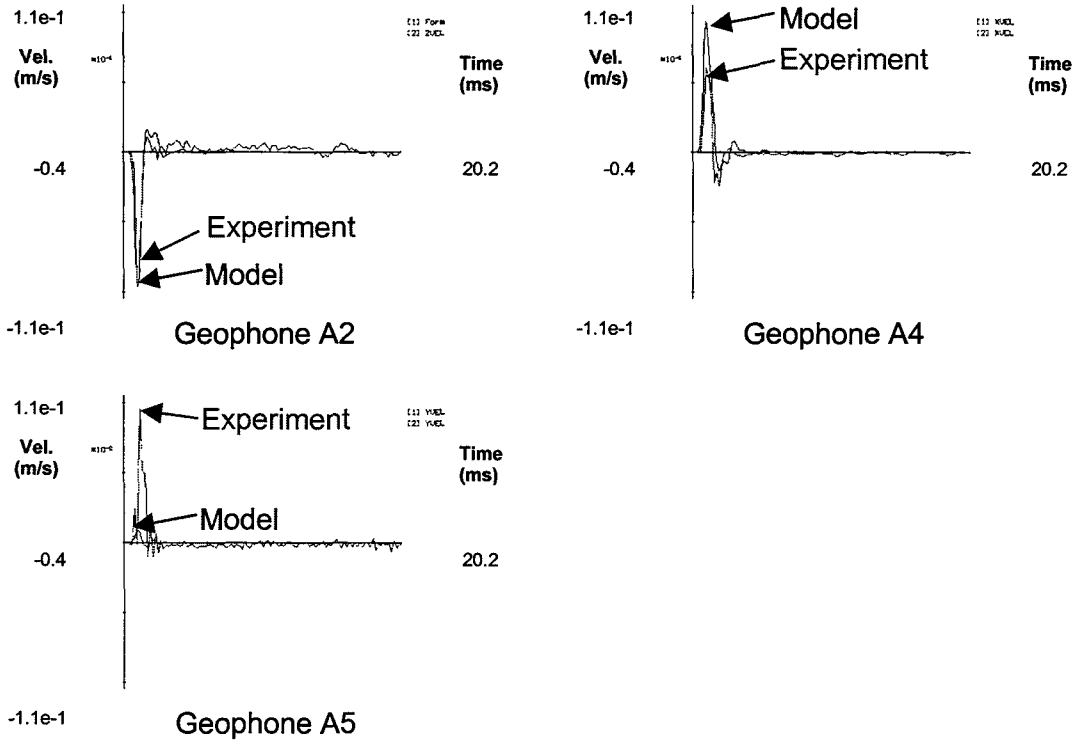

Figure 3.4.2.41 Comparison of modelled velocities with geophone recordings from the calibration blast, for the modelled source #3 of 9 GPa, 800 μs, step-shape load and a 0,1 m diameter borehole. The geophone recordings are a triaxial set on the tunnel wall, 1,7 m from the calibration blast.

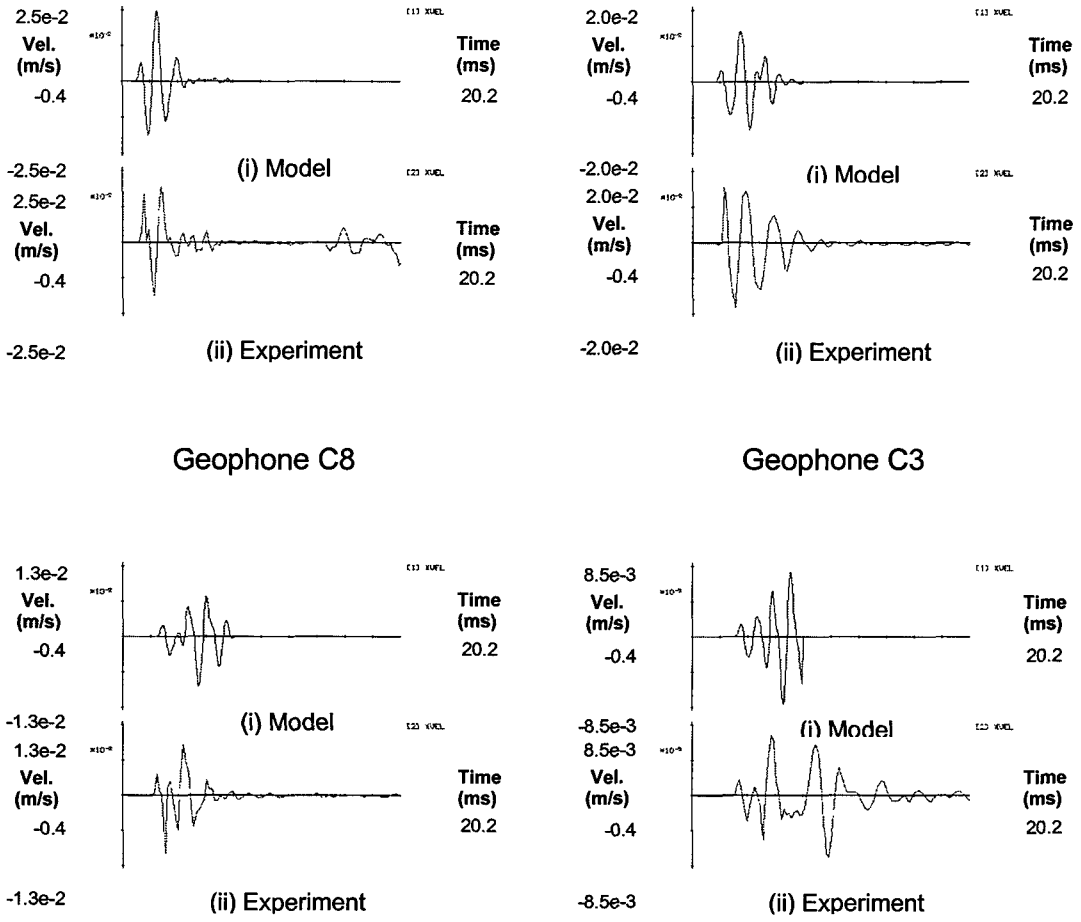

Figure 3.4.2.42 Comparison of model with geophone recordings from calibration blast, for modelled source #3 of 9 GPa, 800 μs rise-time, step-shaped load and a 0,1 m borehole diameter. Geophones C8, C3, C6 and C5 stretch in a line along the near tunnel wall, starting at 5,5 m from the blast and in approximately 4 m intervals. Motion is normal to the tunnel wall.

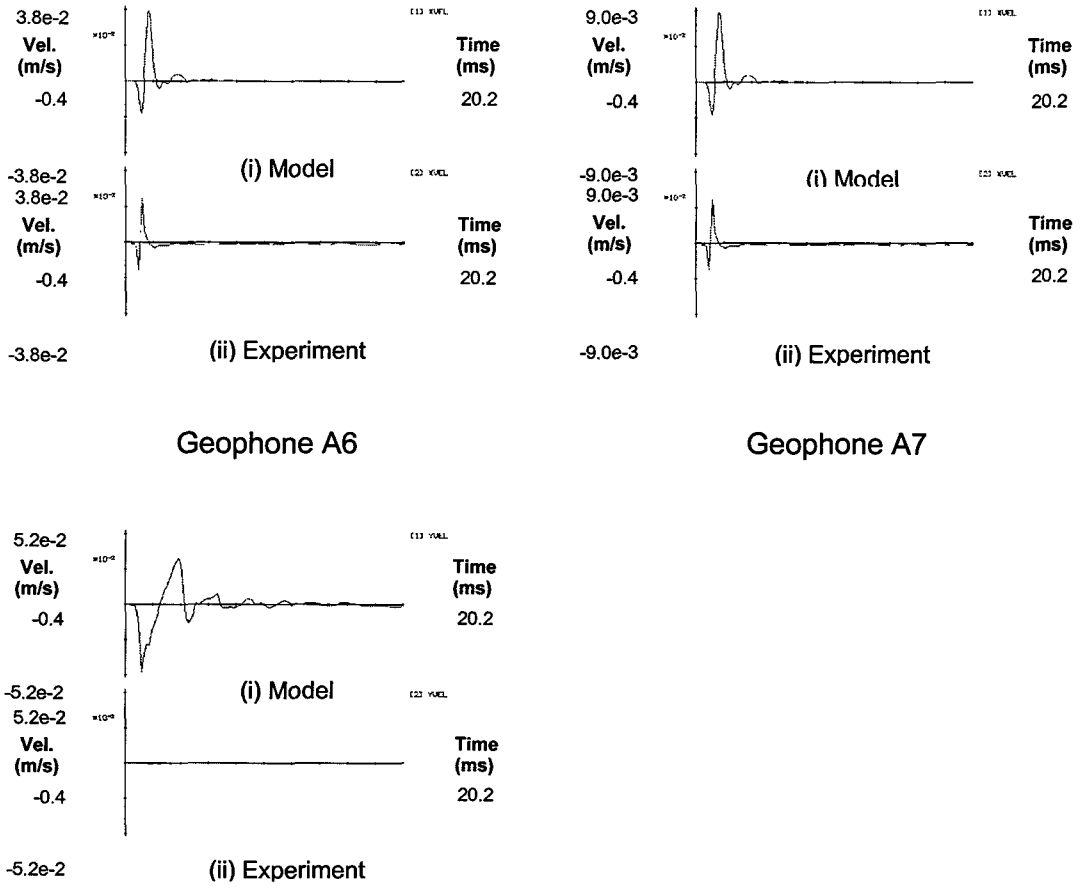

Figure 3.4.2.43 Comparison of model with geophone recordings from the calibration blast, for modelled source #3 of 9 GPa, 800 μs rise-time, step-shaped load and a 0,1 m diameter borehole. Geophones A6, A7 and A8 are a trixial components mounted 5 m into the tunnel wall in solid rock, 1,5 m ahead of the calibration blast

Pre-blast Modelling

Although neither was ideal, two distinctly different source models were suggested from the different calibration methods. These were applied in a model of the final blast design to document predictions before the actual blast. From the blast experiments source #1 for models of the main blast was inferred as:

- 0,1 ms rise time
- diameter = 0,2 m (2x real source)
- peak pressure = 10 GPa

The results for this source seemed to be unrealistically large; for example the maximum tunnel velocity due to a single blast-hole is 13 m/s. The high frequency in the experimental data appears to die out much faster than in this model. Maximum velocity is from about 3 m ahead of the blast. From the calibration blast, source #3 for models of the main blast was inferred as:

- 0,8 ms rise time
- diameter = 0,3 m (3x real source)
- peak pressure = 9 GPa

This produced more realistic maximum tunnel velocities (3 m/s from a single 8 m blast hole). A surprising result is that the maximum is no longer ahead of the blast (Figure 3.4.2.44). This

seems to be due to the very long pulse width of the source. Although based on the calibration data, it seems to be an unrealistically slow rise-time and pulse-length. If the rise-time is reduced, the maximum tunnel velocity shifts ahead of the blast again.

Modelled and recorded waveforms at the geophone positions at approximately 4 m intervals along the tunnel wall are shown in Figure 3.4.2.45. Experimental waveforms begin before the blast, so these have been shifted into approximately the same time window as the model. In the case of the experiment the maximum occurs in the initial *P*-wave pulse and there is virtually no *S*-wave, while for the model the maximum occurs later due to arrival of the shear wave. The maximum amplitudes are similar which indicates that the load pressure is too high in the source model, since the model was for a single blast hole.

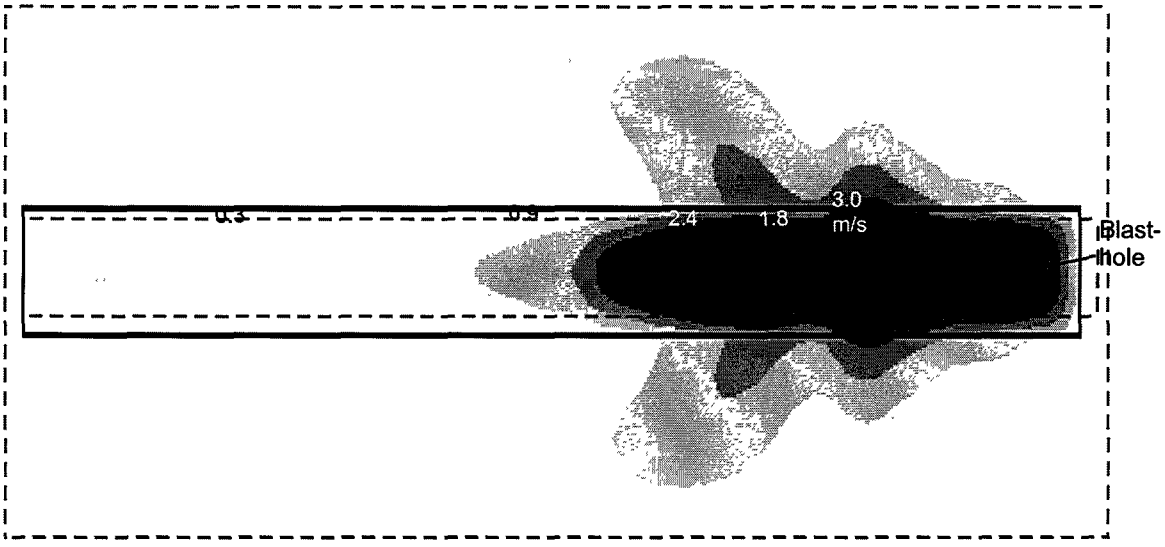

Figure 3.4.2.44 Maximum velocity on the near tunnel wall for pre-blast model source #3, 9 GPa, 800 μs, step-shaped load and a 0,3 m borehole diameter, with a single 8 m blasthole

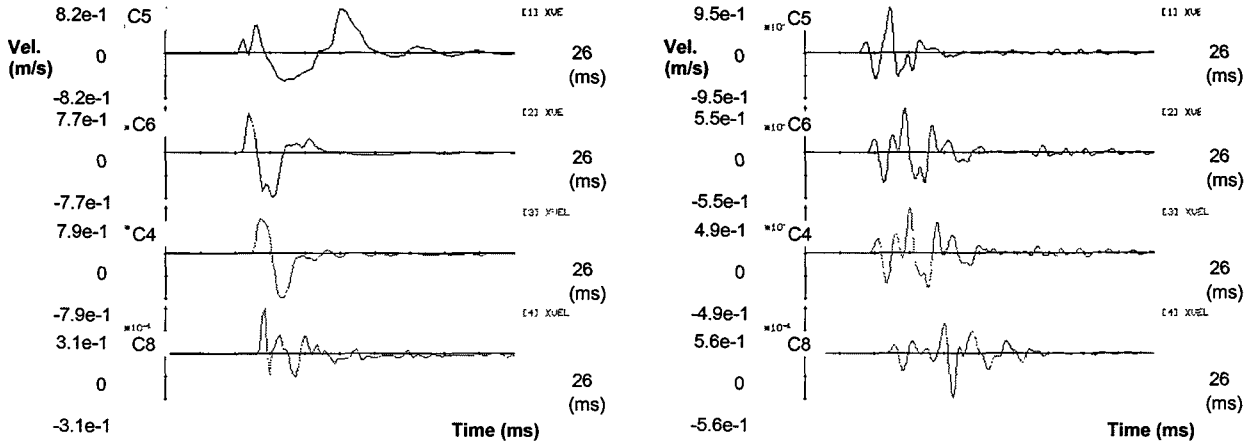

(a) Velocity recordings (m/s) from final blast

(b) Velocities (m/s) from pre-blast model, source #3

Figure 3.4.2.45 Comparison of the pre-blast model velocities for source #3 with the final blast measurements for geophones C5, C6, C4 and C8 starting at 7 m ahead of the blast, and at approximately 4 m intervals along the tunnel wall

Post-blast Modelling

A large amount of data has been gathered from the experiment and has been analysed in project GAP 530. Most of this has still to be considered from a modelling back-analysis perspective. The validity of the source model has not been established, since the predicted large shear wave is not present in the experiment. Two aspects are being investigated to produce waves which better correspond to the experiment: work on a true tunnel cavity implementation (in case spurious waves are due to the approximate numerical implementation), and alteration of the source model or parameters which may reduce the *S*-wave and increase the *P*-wave content.

Nevertheless, a model was run using the final blast positions, sizes, synchronisation, and recordings at all geophone positions. The source was reduced to 0,2 m diameter (two times the real diameter), and the pressure to 1 GPa, with a 0,8 ms rise time. Figure 3.4.2.46 compares modelled and recorded waveforms for geophone positions along the tunnel wall at approximately 4 m intervals. It is encouraging that velocities approaching the recorded values are obtained without the extremely high borehole pressures suggested by the calibration modelling. However, once again the experiment does not have a dominant shear wave, whereas the shear component is much greater than the *P*-wave component in the model. The modelled velocity profile along the tunnel near wall is shown in Figure 3.4.2.47.

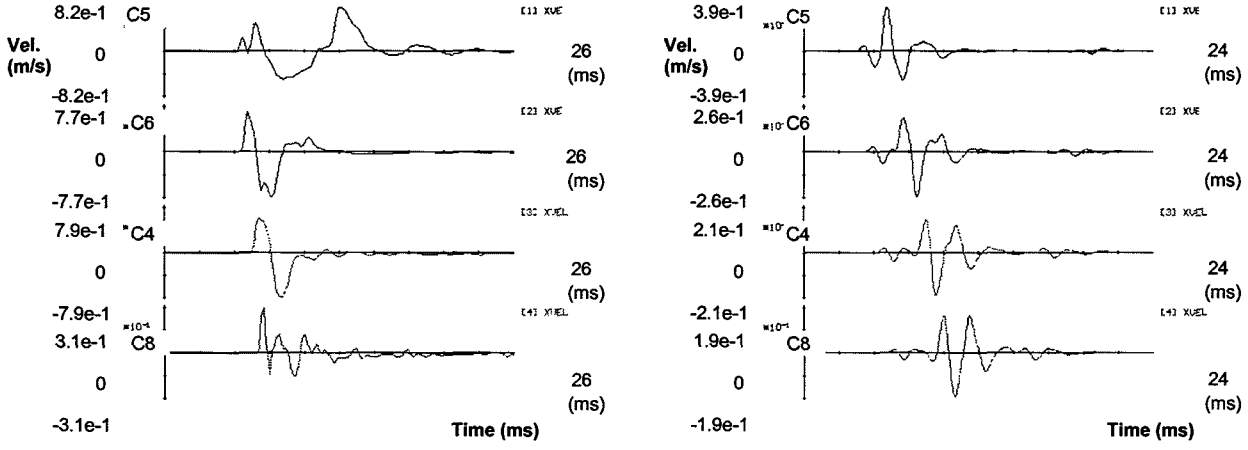

(a) Velocity recordings (m/s) from final blast

(b) Velocities (m/s), post-blast model source #4

Figure 3.4.2.46 Comparison of post-blast model for source #4 with final blast measurements for geophones C5, C6, C4 and C8 starting at 7 m ahead of the blast, and at approximately 4 m intervals along the tunnel wall. (Modelled source #4 of 1 GPa, 800 μs rise-time, step-shaped load and a 0,2 m borehole diameter).

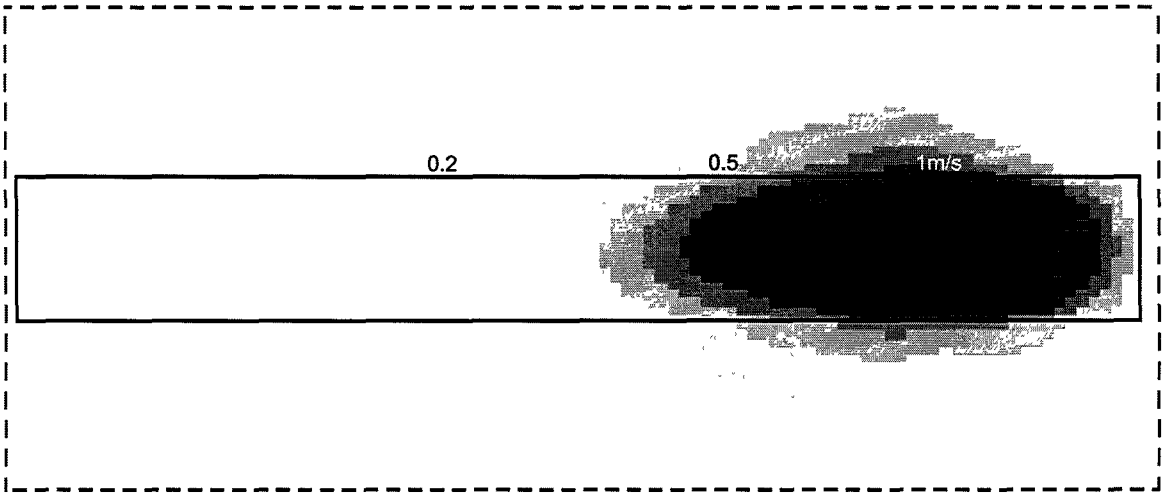

Figure 3.4.2.47 Maximum velocities at near tunnel wall for the post-blast model source #4. Maximum velocity for a blast pressure of 1 GPa is much lower than that recorded. Position of maximum velocity is now opposite the blast holes, due to the relatively long wavelength, and synchronisation of the blasts.

Conclusions

Encouraging results were obtained in the development of an equivalent source representation to a set of blast holes. Realistic parameters for rise-time, borehole radius and borehole pressure produce velocities which are much lower than velocities from available data. Nevertheless altering the source produced some encouraging waveform correspondence with the calibration data. The back-analysis of the main experiment is still in progress. However, the lack of a strong shear wave in the measurements of the final blast may indicate that the source model is not valid. One of the anticipated advantages of modelling data from a controlled experiment is a detailed knowledge of the source so that the source uncertainty is decoupled from the investigation, allowing focus on the interaction with the excavation surface. So far this goal has not been realised. An accurate source model needs to be developed for the modelling phase to be useful, possibly requiring further experiments measuring waveforms from blasts in solid rock.

3.4.3 Blast induced fracturing

Knowledge of blast induced fractures is important to ensure efficient rock fragmentation and post-blast rock mass stability. Although drilling and blasting have been the principal methods of excavating hard rock for over a century, the fundamentals of the processes of explosive rock breaking have only been investigated comparatively recently. Most knowledge regarding blasting practices is based on field observations and empirical data, and relatively little is knownabout the fundamental mechanisms governing the interactions between the explosives and the rock mass, and ensuing fracture propagation.

The aim of this investigation is to re-examine and gain new knowledge of the mechanisms leading to rock fragmentation by explosives. These mechanisms are investigated by means of controlled laboratory experiments and mathematical modelling of the blast process. Particular attention is paid to the interaction between the detonating explosive and the rock, and the ensuing gas driven fracture propagation. The main findings of this work are reported according to (i) experimental investigation, (ii) borehole breakdown and stress wave propagation, and (iii) gas driven fracturing.

3.4.3.1 Experimental investigation

The interaction of rock mass and detonating explosives is a complicated process involving non-linear material behaviour, dynamic fracturing and gas dynamics in terms of hot combustion gases streaming into propagating fractures. These processes occur over an extremely short time scale, and typically the detonation of the explosive and full borehole pressurisation occurs within a time range of a few microseconds to a few milliseconds. The subsequent extension of radial fractures due to gas pressurisation occurs during a slightly longer time period which lasts up to a few hundred milliseconds. It is difficult to assess these short-term processes quantitatively in such a manner that does not interfere with the processes themselves. High speed photography is a suitable technique to gain information about blasting processes, particularly in conjunction with transparent materials (polymers or glasses) as the spatial evolution of the stress wave[1] and blast induced fractures can be photographed at discrete time intervals.

A further advantage of using glasses or polymers in blasting experiments is their homogeneous and consistent structure. In many cases rock samples are not repeatable and the rock structure is complicated by natural discontinuities such as inclusions, joints, cracks and planes of weakness. This significantly increases the difficulties associated with blasting experiments aimed at studying fundamental fracturing mechanisms.

In laboratory experiments Kutter and Fairhurst (1971) compared blast induced fracture patterns in laboratory models fabricated from PMMA with patterns in equivalent models constructed from homogeneous monolithic blocks of rock. They found that the fracture patterns in PMMA appeared to be practically identical with those in hard rock without joints, and only the scale, i.e. the length of the cracks, differed. As the objective of this investigation is to understand the underlying mechanisms governing dynamic fracture, PMMA was chosen as a suitable material to study fracture mechanisms which also apply to low-porosity brittle rock encountered, for example, in deep level mines.

In this work controlled three-dimensional laboratory experiments are conducted in transparent PMMA and, by means of high speed photographic techniques, the evolution of blast fractures is recorded. This yields a qualitative (fracture structure), as well as a quantitative (fracture surface

[1] Stress waves can be visualised due to the temporary bi-refringent nature of most glasses and polymers.

area and propagation rates versus time after detonation) description of a blast model with known input parameters.

A Cranz-Schardin camera (see Section 3.3.2) provides 24 frames photographed at discrete time intervals at a framing rate of approximately 50 000 frames per second. The experiments were conducted in transparent PMMA cubes (250 x 250 x 240 mm^3), thus allowing full-field visualisation of the fracture evolution. The use of circularly polarised monochromatic light, in conjunction with the bi-refringent material property of PMMA, permits the recording of isochromatic fringe patterns of the propagating stress waves. Thus the exact fracture front and stress wave position in time is recorded for further assessment of the fracture growth mechanisms.

As the detonation gases play a vital role during the fracture evolution, two-dimensional plate models (Daehnke et al., 1995), which would vent the gases as the fractures propagate through the plate, are not suitable for investigating blast induced fracturing. Thus, three-dimensional cube type PMMA models are used and the amount of explosive is restricted, such that (i) the fractures do not propagate to the cube sides and vent their gases, and (ii) the effect of the stress waves reflected by the cube boundaries and interacting with the propagating gas-driven fractures is small.

The PMMA cubes were manufactured by stacking eight 30 mm thick 250 x 250 mm PMMA plates and bonding adjacent plates with liquid PMMA. The liquid PMMA was cured for thirty-six hours before dynamic loading. The resulting PMMA cube is homogeneous, and the effect of the bonded interfaces on fractures propagating across them was found to be insignificant. A number of experiments were conducted to determine the consistency of the PMMA, borehole geometry and explosive, and a high degree of repeatability of the experiments was established.

The aims of the experiments were twofold:

(i) to gain qualitative insights into the resulting fracture structure of particular charge configurations,

(ii) to gain quantitative information in terms of fracture extent versus time (thereby obtaining fracture velocity) under controlled laboratory conditions with known input parameters, these data were then used to back-analyse and verify numerical models.

A total of 13 cube-type experiments were conducted and the noteworthy experiments, which will be presented here, are:

(i) penny shaped crack

(ii) sealed charge

(iii) stemmed charge

(iv) stemmed charge intersecting a plane of weakness

(v) stemmed charge in an uni-axial stress field.

(vi) line charge

Experiments (i) and (ii) are used as calibration and back-analysis experiments, i.e. they are used to verify analytical and numerical methods to model the gas flow in propagating fractures, whereas the line charge (experiment vi) is used to investigate stress wave induced fracturing in the immediate borehole vicinity. A brief summary is given of each experiment.

(i) Penny Shaped Crack: A novel experiment was designed to propagate a planar penny shaped crack. The purpose of the experiment is to investigate gas driven fracturing and the

experimental data is subsequently back-analysed by an analytical/numerical model simulating dynamic fracturing due to gas pressurisation (Section 3.4.3.3). Photographs of the propagating penny shaped crack show a lag between the gas and crack front (Figure 3.4.3.1). This phenomenon has previously been theoretically predicted, however this is the first physical evidence of the vacuum behind the propagating crack tip.

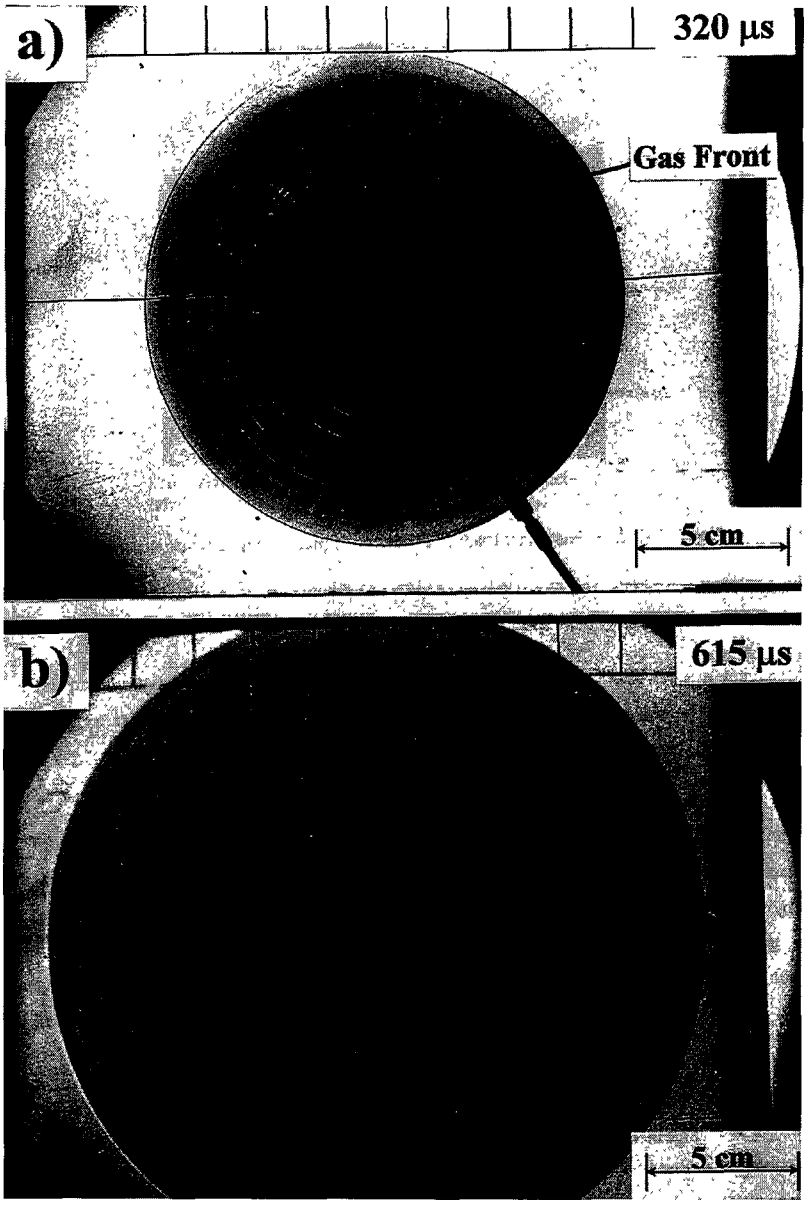

Figure 3.4.3.1 Propagating penny-shaped crack showing lag between the gas and crack front.

(ii) Sealed Charge: Upon detonation of a sealed charge in a short cylindrical cavity, two prominent conical cracks propagate from the ends of the cylindrical cavity. Data from this experiment is used subsequently during numerical back-analyses in order to verify a computational technique to model gas driven conical cracks (Section 3.4.3.3). Practical applications of sealed explosives are, for example, the underground detonation of nuclear charges.

(iii) Stemmed Charge: Detonation of a stemmed charge results in wedge or axi-radial shaped fractures propagating radially along the borehole length. A comparatively small conical crack extends from the blind end of the borehole. The stemmed borehole represents the most common charge configuration in mining operations and wedge or axi-radial fractures are the predominant fracture type observed in praxis.

(iv) Stemmed Charge Intersecting a Plane of Weakness: When a charge intersects a plane of weakness, interface delamination is likely. In the experiment conducted here the fracture direction was not influenced by the interface, but the fractures did not propagate across the interface. Combustion gases pressurised the weak layer, which delaminated at approximately the same rate as the fracture propagation speed.

(v) Stemmed Charge in Uni-Axial Stress Field: In underground mining, blast induced fracturing is influenced by the pre-existing stress field. Here it is shown that fractures originally propagating radially from the borehole are reoriented and subsequently propagate in the direction of the maximum principal stress.

(vi) Line Charge: Two line charge experiments were conducted to investigate fracturing resulting from the progressive detonation of a column charge. Fractures are observed to extend radially and along the length of the borehole, and comparatively small conical fractures form at the borehole ends. Upon inspection of the stress wave driven fracturing in the immediate borehole vicinity, fracture kinking is apparent between two and four borehole radii. Mechanisms leading to the fracture kinking are accounted for by investigating the maximum tensile stresses of the transient stress field due to charge detonation (Section 3.4.3.2).

3.4.3.2 Borehole breakdown and stress wave propagation

The detonation of an explosive charge in a borehole liberates combustion gases, which expand and suddenly pressurise the borehole cavity. As a result, the immediate vicinity of the borehole is highly strained and this can lead to borehole breakdown in terms of fracture initiation and propagation.

Most authors distinguish between three annular zones surrounding the borehole: (i) an innermost zone in the immediate borehole vicinity, (ii) a transitional zone with short dense cracks, and (iii) an outer elastic zone with long radial cracks. Numerous experimental and theoretical studies of blasting in different materials have been conducted over many decades. In the literature one finds highly conflicting interpretations of the fracture pattern evolution in borehole blasting, particularly regarding the interpretation of material behaviour within the innermost zone, with some authors finding a crush zone around the borehole and others reporting a smooth zone with an uncertain history of material behaviour (Rossmanith et al., 1997).

In the case of shock wave propagation in metals, Davis and Calvit (1963) identify an innermost zone around the hole in which the material behaves in a fluid-like manner and where no cracks whatsoever are visible. In the transition zone, short tensile and shear cracks were found with some of these cracks penetrating into the outer zone. Similar results were obtained by Persson et al. (1970) when blasting laboratory scaled models fabricated from PMMA cubes. The blasting behaviour of polymers, glass and rock, studied in several papers by Fourney et al. (1983), Kutter and Fairhurst (1971), Liu and Katsabanis (1993), Rossmanith (1978), Singh and Sarma (1983), Swoboda and Li (1983) and others, reveals a highly crushed zone around the borehole instead of a fluidised regime characterised by the complete absence of cracks and damage.

A simplified quasi-static fracture mechanics approach gives insight into borehole pressures required to activate flaws in the borehole wall and initiate fracturing (see Appendix 3). It is shown that (i) pressures are unlikely to exceed 400 MPa, (ii) wedge (axi-radial) shaped fractures are more likely to propagate than penny shaped fractures, and (iii) a higher borehole pressure is

required in order to activate an increasing number of flaws (Daehnke, 1997). Influences of these effects have been observed and confirmed in field and laboratory blasting investigations.

Knowledge of blast induced stress waves is of importance to understand the fracture processes, which typically occur in the immediate borehole vicinity and which extend for approximately three to ten borehole radii. In the literature, inconsistencies prevail regarding the explosive induced transient stress field, and most previous studies erroneously assume spherical or cylindrical wave expansion, or the stacked sphere approach when modelling wave expansion from progressively detonating column charges. Here, it is shown that the velocity of detonation has a significant influence on the resulting stress waves. Simplified models result in a dynamic stress field which differs substantially compared with that calculated by the more complete model incorporating the effect of the velocity of detonation (VOD). The quantitative description of stress waves due to column blasting given in this section has not been available previously.

The principal findings of the three charge configurations investigated here are as follows:

Spherical and Cylindrical Charges

Dynamic tensile stresses are of importance, as these are likely to govern the extent and direction of stress wave driven fractures. In this study it was shown that, for both the spherical and cylindrical wave expansion, the radial and tangential stress components at the borehole wall are initially both compressive; this would lead to crushing of the borehole walls. Beyond the crush zone radial cracks extend due to high tensile tangential stresses. Maximum tensile radial stresses occur at approximately four to five borehole radii. However, compared with the amplitude of the maximum tensile tangential stress component, the tensile radial component is small ($\pm$ 5 per cent of the maximum tensile tangential stress). Further details of the analyses are given in Appendix 3.

Progressively Detonating Column Charge

Numerical simulations are conducted to analyse the transient stress field due to progressively detonating column charges. The numerical analyses are verified by means of comparisons with existing analytical solutions. Various analyses are conducted to investigate the effects of (i) borehole pressure profile, (ii) velocity of detonation, and (iii) borehole discontinuities.

The *pressure profile* acting along the borehole walls is shown to have a comparatively small influence on the dynamic stress field, and important characteristics of the dynamic minor principal stress components, which would influence fracturing in the borehole vicinity, remain similar for a range of pressure profiles. The profile has important implications regarding fracturing due to the static stress field induced by borehole pressurisation and gas pressurisation of cracks.

The *velocity of detonation* (*VOD*) is one of the most important parameters governing blast induced dynamic stress waves. At supersonic detonation velocities (i.e. $VOD > c_P$) two Mach cones associated with *P*- and *S*-waves form (Figure 3.4.3.2 a). Initially the maximum tensile stress (minor principal stress) acts in a tangential direction, i.e. radial fracturing is promoted. At a distance of approximately three borehole radii the maximum tensile stress (now propagated within the *S*-wave cone) is associated with the formerly axial stress, which, when resolving for principal stresses, is rotated by approximately 25°. Hence fracture reorientation (kinking) can be expected; fracture kinking has been observed in laboratory experiments.

At a transonic *VOD* (i.e. $c_P > VOD > c_S$) the *P*-wave dispersion rate exceeds the energy input into the system, and hence the *P*-wave amplitude is negligible compared to the amplitude of the *S*-wave cone (Figure 3.4.3.2 b).

Rayleigh type surface waves are created when the *VOD* corresponds approximately to the shear wave speed (Figure 3.4.3.2 c). The Rayleigh waves have a strong leading tensile stress component and hence would promote fractures oriented normal to the borehole axis. At subsonic detonation velocities (i.e. $c_S > VOD$) the borehole is effectively pressurised quasi-statically, and dynamic stresses are low in magnitude.

A *borehole discontinuity* in the form of a free surface intersecting the borehole orthogonally results in wave reflection. High tensile stresses are associated with the reflection point and fracturing is likely to occur in the immediate vicinity of the interface (spalling).

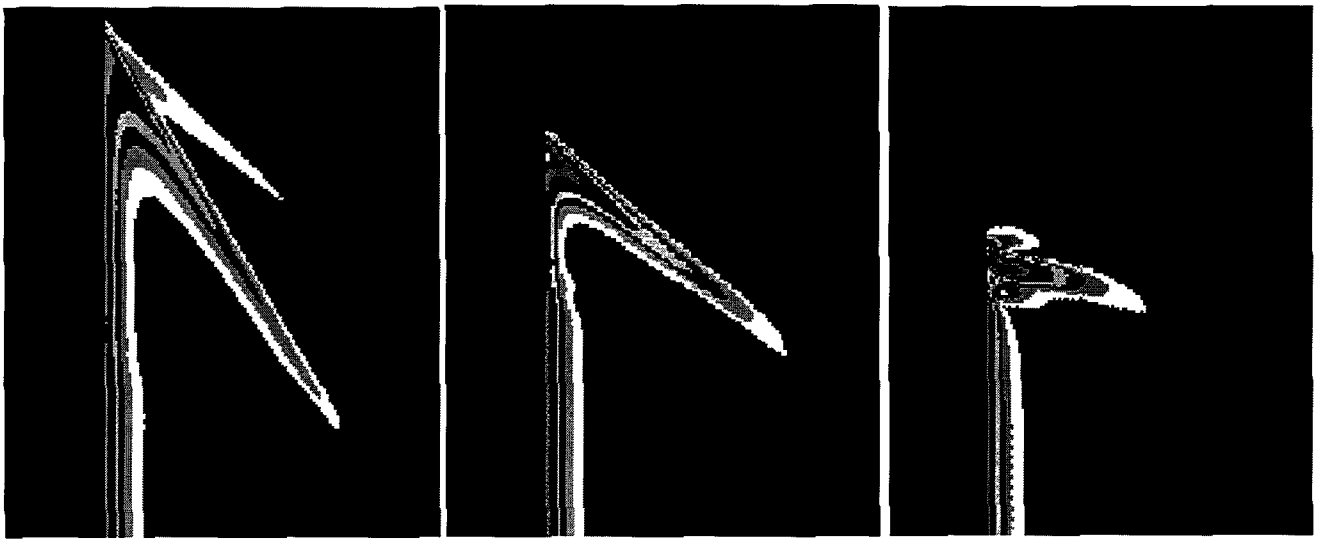

a) b) c)

Figure 3.4.3.2 P- and S-wave Mach cones represented by contours of constant maximum shear stress (isochromatics) associated with a) supersonic, b) transonic and c) subsonic velocity of detonation.

3.4.3.3 Gas driven fracturing

In Section 3.2.3.5 the investigations representing the most significant developments and progress in understanding gas driven fracture propagation were reviewed. Some of these studies, particularly those coupling the dynamic gas flow analysis with numerical codes based on finite element and boundary element methods, deal with highly complicated and advanced phenomena such as fracture propagation in a non-uniform stress field, or fracture interactions with pre-existing discontinuities. However, the present investigation has shown that numerous fundamental mechanisms pertaining to gas driven fracture propagation remain poorly understood. The objectives of this study are to investigate some of the fundamental mechanisms in more detail, with particular reference to the following issues:

- *Model Verification:* In previous studies, the mathematical models simulating dynamic gas driven fractures were verified by comparisons with post-blast observations of laboratory tests (Schatz et al., 1987) or field observations (Nilson et al., 1985). The laboratory or field tests were generally conducted in a geological material, which increases the complexity and uncertainty of the verification process due to poorly understood material properties. Here, the mathematical models are verified by means of comparisons to controlled laboratory experiments using PMMA cubes. The dynamic material properties of PMMA are well

documented and, furthermore, the transparent nature of PMMA, in conjunction with high speed photography, allows the fracture propagation process, as well as the gas flow within the fracture to be photographed. A sequence of snapshots yields valuable information of fracture velocity versus time and facilitates rigorous comparisons of theory and practice.

- *Heat Transfer:* The effects of heat transfer from the hot combustion gases to the host medium have been considered in numerous papers (Nilson et al., 1985; Nilson, 1986; Nilson and Griffiths, 1986), however, very little is known about the influence of various thermal models when modelling actual blasting in rock. A number of recent publications (Heuze et al. 1990; Cundall et al., 1996; Minchinton and Lynch, 1997), while representing the state of the art in blast modelling and contributing significantly towards understanding blasting mechanisms, assume isothermal gas flow and neglect heat losses. It will be shown that heat losses affect the fracture extent significantly and that thermal quenching needs to be incorporated in numerical analyses of blast induced fracturing.

- *Dynamic Fracture Mechanics:* Most studies pertaining to gas driven fracturing use a stress intensity factor fracture criterion. Generally the stress intensity factor is assumed to remain constant at increasing fracture speed. Broberg (1960), Kostrov (1964) and Freund (1972), amongst others, showed that as the fracture speed increases, the stress intensity factor is reduced, and as a consequence fracture growth is inhibited. An objective of the work presented here is to illustrate the effect of including dynamic fracture mechanics in the form of a velocity dependent stress intensity factor.

- *Dynamic Material Properties:* It is a well-known fact that, during rapid fracture, many materials exhibit higher fracture toughness as compared to their static toughness value. To the authors knowledge no previous studies dealing with gas driven fracturing considered the effect of dynamic material properties in the form of dynamic fracture toughness values. Unfortunately, practically no data exist regarding the dynamic fracture toughness of rock. However, dynamic toughness values have been measured for PMMA, and in the present study the effect of incorporating dynamic toughness values in PMMA laboratory models will be considered.

- *Application to Blasting:* Most previous work dealing with gas driven fracturing pertains to the petroleum industry in the form of wellbore stimulation using propellants. In this report, a procedure is proposed to relate the type and mass of the explosivefilling the borehole to the final fracture extent when blasting in hard, competent rock.

Comparisons between numerical and experimental results

A coupled solid, fluid and fracture mechanics analytical/numerical model is used to analyse gas driven fracture propagation. The model is novel in terms of incorporating dynamic material properties, quasi-dynamic fracture mechanics, as well as convectional and conduction heat transfer from hot combustion gases to the surrounding rock. Full details of the model and solution procedure are given in Daehnke (1997).

The analytical/numerical simulation is used to back-analyse the penny shaped crack experiment in order to verify the numerical procedure. This entails comparing the fracture radius and speed versus time as observed with the high speed camera in the experiment versus the numerical predictions. The crack propagation behaviour depends on the initial borehole conditions (temperature and pressure) which, in turn, depend on the type and amount of explosive used in the experiment.

The input to the numerical analysis consists of the initial borehole pressure and temperature, as well as the volume of combustion gases produced by the detonation of the $Pb N_6$ explosive charge. The pressure was measured in the plenum (see Figure 3.4.3.3) utilising a pressure

transducer. The temperature was estimated by means of a theoretical analysis of the gas flow from the spherical explosives cavity into the plenum. The amount of gas liberated by the complete detonation of 140 mg Pb N_6 (the mass of explosive used in the experiment) is taken as the mass fraction of nitrogen, i.e. 57 mg.

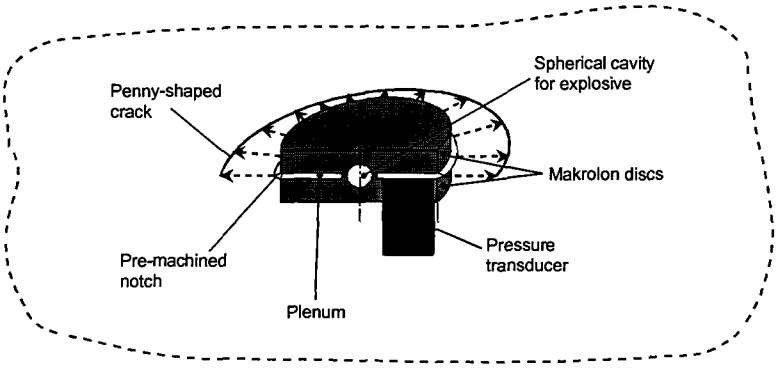

Figure 3.4.3.3 Details of experimental configuration.

A rapid response (rise time: 0,2μs) tourmaline pressure transducer was used to measure the gas pressure in the annular plenum cavity. The pressure transducer was manufactured by PCB Piezotronics Inc. (Buffalo, USA) and is suitable for investigating high pressure, short rise time blast waves. The pressure values monitored by a 10 MHz digital oscilloscope.

Figure 3.4.3.4 shows the pressure history as recorded by the transducer. The blast wave was first registered 37 μs after charge detonation (the time taken for the combustion gases to stream from the explosives cavity into the annular plenum chamber), and the peak pressure of 66 MPa occurs 128 μs after detonation; thereafter the pressure decreases. At a time of ± 300 μs the transducer ceased to record data.

For the back-analysis the dashed line indicated in Figure 3.4.3.4 shows the pressure versus time history. Section **A** of the curve represents the specified input pressure at the fracture inlet, i.e. this section of the pressure history was used as a fixed input to the numerical analysis. Section **B** represents the predicted pressure history as calculated by the numerical code, without any specified input borehole pressure.

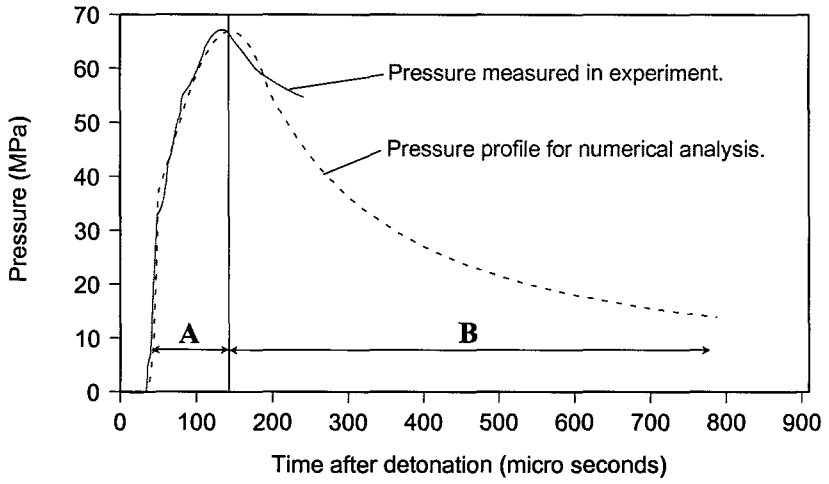

Figure 3.4.3.4 Pressure history measured in experiment and calculated numerically.

Figure 3.4.3.5 presents numerical and experimental data for the fracture speed and radius versus time after detonation. The crack speed is governed by the rate at which hot combustion gases penetrate the crack. As the crack propagates and is pressurised by combustion gases, the borehole pressure decreases. Due to increased flow resistance as the crack area increases and the divergent geometry of the penny shaped crack, the driving gas speed is reduced and the speed of fracture propagation decreases.

Generally, the analytical/numerical analysis correlates well with the fracture extent and speed observed in the experiment. The crack speed rapidly increases to a maximum of 230 m/s for the numerical and to a maximum of 195 m/s for the experimental results. Thereafter the speed decreases and crack arrest occurs at 900 μs as observed in the experiment. The numerically simulated crack growth continues for a longer time period and after 1000 μs the calculated fracture speed decreases rapidly to a negligible value. The curves representing crack radius versus time after detonation correlate closely, and the final fracture extent of 126 mm calculated by the numerical analysis agrees within ten per cent of the experimental observations.

In the experiment it was observed that, for most of the fracture propagation duration, the combustion gases lagged slightly (≈ five per cent of the total fracture length) behind the crack front. In the numerical analysis it was found that the gas front mostly coincided with the crack front.

Considering the many complexities of gas fracturing, the numerical and experimental results compare well. Although some discrepancies prevail, e.g. the numerically predicted fracture growth continues for a longer time period, implying that crack arrest mechanisms have not been accounted for in sufficient detail, the important features such as the final fracture extent and maximum fracture speed agree closely. A 10 per cent accuracy in terms of final fracture extent seems to indicate that the dominant mechanisms governing gas driven fracturing are modelled correctly.

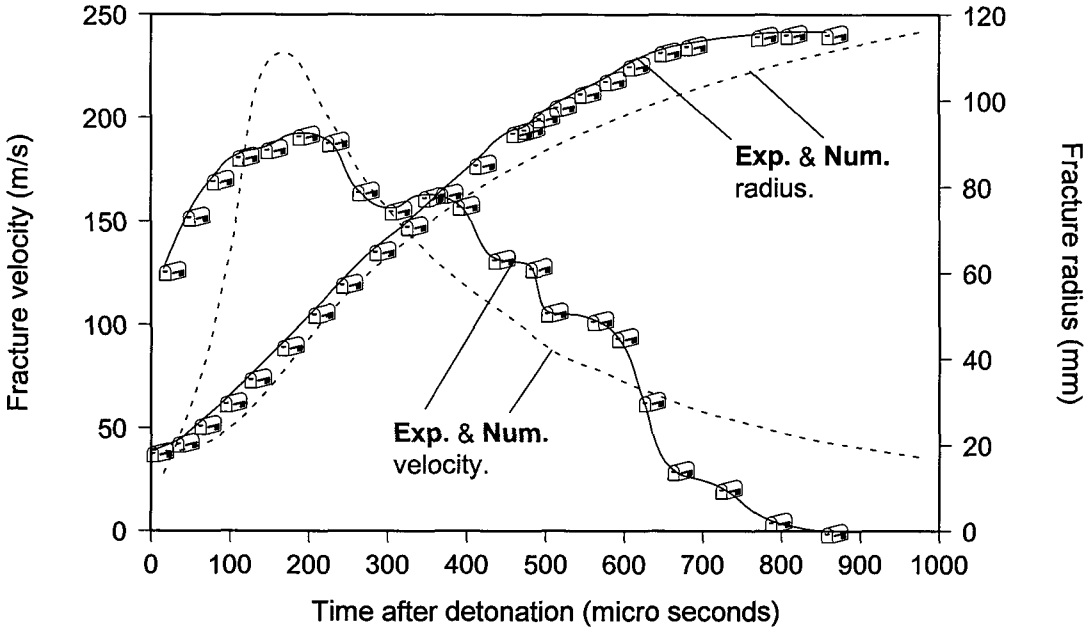

Figure 3.4.3.5 Experimental and numerical data relating fracture speed and radius to time after detonation.

Application to Estimate Fracture Extent in Rock

The combined analytical/numerical procedure used to simulate gas driven fracturing is applied to estimate the fracture extent in rock due to detonation of an explosive column charge. As noted earlier, stress waves associated with blasting result in intense and localised fracturing in the immediate borehole vicinity; high pressure combustion gases are the predominant driving mechanism for long radial fractures extending between 10 and 100 borehole radii. Here, a method is proposed to predict the lengths of the radial, gas driven fractures, where the results are applicable to blasting rock confined by a uniform stress field, e.g. blasting in deep level mines, wellbore stimulation in the gas and oil industry and rock pre-conditioning as is currently practised by some deep level hard rock mines in the USA, Canada and South Africa. A parametric study is conducted to investigate the influence of the following parameters on the final fracture lengths:

(i) initial borehole pressure,

(ii) initial borehole temperature,

(iii) *in situ* stress,

(iv) rock fracture toughness,

(v) number of radial fractures, and

(vi) gas seepage.

It is found that the final fracture extent is relatively insensitive to the initial borehole pressure, whereas fracture extent increases with higher temperatures. Increasing *in situ* stress, rock fracture toughness, number of fractures and gas-leakoff due to seepage all reduce the final fracture extent. For the parameters investigated, the influence of *in situ* stress has the greatest bearing on fracture extent, whilst in confined rock a wide range of fracture toughness values

results in a comparatively minor variation in fracture extent. Further quantitative results of the various parameters investigated are given in Daehnke (1997).

Various thermodynamic models are discussed, and it is shown that approximate models (e.g. adiabatic and isothermal gas flow) over-emphasise the fracture extent. To model combustion gas induced fracturing accurately, it is recommended that conductive and convective heat transfer effects need to be taken into account.

The analytical/numerical method is further developed to model gas driven conical cracks. By means of numerically determined correction factors for the crack opening displacements and stress intensity factors, the penny shaped crack is generalised to a 45-degree conical crack. The modified model is verified by back-analysing a laboratory experiment and good agreement between the numerical and experimental data is observed.

The extent of conical fractures propagating in a uniform compressive stress field in hard, competent rock is estimated and it is shown that, with increasing compressive stresses, fracture growth is inhibited. By approximating a 45-degree conical crack with a penny shaped crack the fracture extent is underestimated, and it is recognised that the conical geometry has a significant influence on fracture growth. Gas driven conical cracks had not been analysed previously.

3.5 CONCLUSIONS

Combined experimental and theoretical approaches are developed in this work to study various aspects of the dynamic behaviour of rock. Specifically, the interaction of stress waves with rock mass discontinuities and dynamic fracturing due to blasting are investigated. Full details of the work are given in Daehnke (1997). Theoretical concepts of elastodynamics and dynamic fracture mechanics are reviewed, and a comprehensive analysis of stress wave interaction with interfaces modelling various rock joint types is given. Important parameters and effects such as joint pre-stress, wave amplitude, non-linear interface conditions and energy dissipation are studied and discussed.

A brief overview is given of experimental methods and techniques, which are suitable to examine transient phenomena such as stress wave propagation and dynamic fracturing. These techniques are subsequently applied to investigate by experimental means wave interactions with mining excavations. The laboratory experiments are back-analysed by numerical simulations, and upon finding close correlation, the numerical programs are further applied to investigate parameters influencing rock mass instabilities and dynamic fracturing.

Blast induced fracturing is addressed by means of cube-type laboratory models to study the effect of charge geometry and the relative importance of stress wave versus gas driven fracturing. Analytical as well as numerical methods are applied to investigate the dynamic stress field radiated by a progressively detonating column charge. Gas driven fracturing is simulated by means of a hybrid analytical/numerical model, and mechanisms and parameters which govern the final gas driven fracture extent in rock are identified and discussed.

A brief overview of the findings of the main research topics, the advance in the state of the art, as well as recommendations for future work is given below. The three principal research topics are identified as follows and are dealt with separately:

1. wave interactions with rock joints,

2. wave interactions with mining excavations, and

3. blast induced fracturing.

3.5.1 Wave interactions with rock joints

Determining the nature of the interactions between stress waves and rock fractures/joints is an important area of research forming the basis of many rock dynamics problems. Notable progress has been made, particularly since the investigations of M. Schoenberg, who first investigated the comparatively simple interface stiffness model in detail. The validity of this model was further confirmed in later work by L.J. Pyrak-Nolte, N.G.W. Cook and L. Myer, and the stiffness model was successfully correlated to data obtained by means of reduced scale laboratory experiments. The interface stiffness model had, before the current study, not yet been applied in a general manner to actual rock joints, with stiffness related to measurable rock joint properties.

Principal findings

- In this work the joint stiffness model is further developed to incorporate non-linear normal and tangential interface stiffness, where the relations governing the stiffness are based on actual joint properties. For typical joints analysed here, stress waves with a frequency of $\pm$ 100 Hz are predominantly transmitted, whereas at a comparatively high frequency of $\pm$ 2000 Hz most of the incident energy is reflected.

- Previously, although reflection and transmission coefficients were available for constant stiffness interface models, the coefficients were not related to actual joint properties and no lower to higher end frequency limits were established. The method developed here can be used to establish the reflection – transmission characteristics for any joint type, provided the interface surface properties have been determined by means of field or laboratory testing.

- An essential aspect of studies dealing with joint – wave interactions is the influence of joint pre-stress. This effect has previously been neglected. Based on actual interface properties, it is shown in this work that at even comparatively low levels of pre-stress, the joint reflection and transmission characteristics are altered significantly. With increasing pre-stress, more energy is transmitted across the joint and the amplitude of reflected waves is reduced. These results have important implications in deep level mining applications and numerical simulations of wave propagation through fractured rock.

- The generalised Kelvin model is used to investigate the dynamic behaviour of fluid filled interfaces. The reflection and transmission as well as energy dissipation characteristics of this model are quantified, and are found to depend on the joint stiffness, viscosity and wave frequency.

- Further novel work dealing with joint – wave interactions examines energy dissipation at frictional joints, failure envelopes for joints with cohesive filler materials, undulating joints and the influence of wave amplitudes.

Recommendations for further work

Further studies are required to establish a hierarchy of joint types typically occurring in mines and quarry sites, and to determine their wave reflection and transmission characteristics. Typical amplitudes and frequencies of blast induced and seismic waves need to be ascertained by means of numerical simulations and field measurements, and the transmission and filtering attributes of certain types of joint sets, as well as multiple discontinuities, need to be quantified. In practice, neither the waves or joints will be necessarily planar or at steady state, and further work is required to model non-planar wave and joint problems.

3.5.2 Wave interactions with mining excavations

Seismic stress waves interacting with mining excavations are the most severe mining hazard associated with deep level mines. The complicated radiation field resulting from stope – wave interaction leads to stress wave superposition, which can result in rock mass instabilities. Here, numerical and photoelastic investigations are used to identify zones of high dynamic stress concentrations and parameters influencing stress wave driven fracturing in the vicinity of the stope.

Principal findings

- Dynamic photoelasticity is used to visualise the complex stope – wave interactions and, by means of back-analyses, the numerical codes WAVE and ELFEN are verified to be able to model stress wave interactions and dynamic fracturing.

- This work has demonstrated that parting planes in general are found to reflect a portion of the incident energy and thus shield the stope. However, non-cohesive parting planes trap energy within the hangingwall beam, and wave superposition associated with dense energy channeling gives rise to dynamic stress concentrations, which are likely to initiate fracturing and lead to rock mass instabilities.

- Numerical and experimental parametric studies are conducted to investigate stress wave driven fracturing in the stope vicinity. It is shown that fracturing occurs primarily due to reflected waves, and individual fractures are most likely to be oriented parallel to the free surface of the mining excavation. The polarity of incident shear waves affects the extent of fracturing significantly, and shear waves with wave front motion towards the excavation promote more extensive fracturing than incident *S*-waves with reversed polarity. Stiff stope support transmits a higher portion of energy across the stope; hence the amplitude of reflected waves is reduced, and less fracturing occurs. However, the stiffness that is required to reduce fracturing substantially must be approximately the same magnitude as the rock mass stiffness (e.g. pillars) and, comparatively, support in the form of timber packs is too soft to reduce fracturing to a significant extent.

Recommendations for further work

Further experimental work should be conducted to investigate stress wave channeling, wave superposition and the dynamic stability of a blocky hangingwall beam. Additional numerical work is required to establish the influence of further parameters such as rock strata, intrusive dyke structures, wave frequency, support spacing and pre-existing geological stresses.

3.5.3 Blast induced fracturing

An important aspect of rock dynamics is blast induced fracturing. The blasting process is investigated by means of laboratory experiments and mathematical modelling. Specific attention is given to blast induced stress waves and gas pressurisation mechanisms that drive comparatively few fractures for a distance of many borehole radii.

Principal findings

- Novel three-dimensional cube-type laboratory experiments were conducted in specimens fabricated from PMMA and dynamically loaded with explosives The resulting stress wave and fracture evolution was recorded by means of high speed photography. The experiments have provided new insights into the evolution of fracture systems due to detonation of various charge geometries.

- Photographs of the lag between the gas and crack front were obtained. This lag has previously been predicted theoretically, however this is the first direct physical evidence of the vacuum behind the propagating crack tip.

- The transient stress field due to the progressive detonation of a column charge is quantitatively studied by means of numerical analyses. It is shown that the shape of the pressure profile acting on the borehole walls has a relatively small influence on the dynamic stress field.

- When the velocity of detonation of the explosive exceeds the shear wave speed of the material, it is found that the maximum tensile stress initially acts in a tangential direction. At a distance of two to three borehole radii, the maximum tensile stress acts in an approximately axial direction and fracture re-orientation is likely. This fracture kinking has been observed in laboratory blasting experiments. At a detonation velocity below the Rayleigh wave speed of the material, the borehole is effectively pressurised quasi-statically, and the dynamic stresses are low in magnitude.

- Descriptions of blast induced fractures obtained under controlled conditions in the laboratory are valuable for developers of dynamic fracture codes to validate and check their results. Here, upon recognising that stress waves rapidly outpace the slower dynamic fractures and the majority of fracturing occurs due to pressurisation by detonation gases, a coupled solid, fluid and fracture mechanics numerical model is used to analyse the gas driven fracture propagation phase. The model is verified by back-analysing laboratory experiments, and good correlation between numerical and experimental data is observed. The analytical/numerical model is able to predict fracture propagation rates and the final fracture extent. The model gives insights into pressure profiles and gas velocities within fractures, incorporates dynamic material properties and quasi-dynamic fracture mechanics. Previously, a similar analysis was checked by limited post-blast data, and in this investigation a detailed verification is possible by correlating data obtained during the complete gas driven fracturing process.

- Using the analytical/numerical model, it is found that, for a given volume of gas, the fracture extent is similar for a wide range of initial peak borehole pressures. A method is proposed to estimate the final lengths of radial fractures for a given quantity of combustion gases, where the gas quantity is related to the explosive type and borehole diameter or charge mass. The method is applied in the form of a study to investigate various parameters governing the extent of blast induced fractures in confined rock. The influence of gas pressure, temperature, *in situ* stress, rock fracture toughness, number of fractures and gas leak-off due to seepage on the final fracture extent is illustrated. The study quantitatively assesses the effect of these parameters on fracture extent related to explosive type and amount.

Various thermodynamic models are assessed and the importance of incorporating heat transfer from the hot combustion gases to the surrounding rock is demonstrated.

The results given here have important practical implications for blasting in confined rock, well-bore stimulation and rock pre-conditioning as is currently practiced in some deep-level mines in South Africa, the USA and Canada.

- Gas driven conical cracks extend typically from the ends of cylindrical cavities containing sealed charges and have not been investigated in detail previously. Here, the combined analytical/numerical method is further enhanced to model gas driven conical cracks. Practical results are given to relate the final fracture extent of sealed charges, at various levels of *in situ* stress, to the type and amount of explosives.

Recommendations for further work

Blasting is a highly complicated process and the following aspects remain poorly understood.

- fracture curvature due to non-uniform stress fields,
- gas driven fractures intersecting discontinuities in the form of planes of weakness and voids,
- complicated three-dimensional fracture networks, and
- the interactions of fractures from adjacent boreholes,

These problems warrant further attention and need to be considered to ensure efficient fragmentation, post-blast rock mass stability and an engineered fracture zone in the stope face vicinity to facilitate the safe and efficient extraction of ore.

3.6 REFERENCES

Achenbach, J.D. 1973. *Wave Propagation in Elastic Solids.* North-Holland, Amsterdam.

Bandis, S.C., Lumsden, A.C. & Barton, N.R. 1983. Fundamentals of rock joint deformation, *Int. J. of Rock Mech.*, Vol 20 (6), pp 249-268.

Bhandari, S. 1979. On the role of stress waves and quasi-static gas pressure in rock fragmentation by blasting. *Acta Astronautica*, 6, pp. 365-383.

Bishop, R. E. D. 1953. On dynamical problems of plane stress and plane strain. *Quart. J. Mech. Appl. Math.,* 6, pp. 250-254.

Blair, D.P. 1989. Seismic pulse assessment of cracked and jointed rock. *Eng. Fracture Mechanics,* 3, pp. 1-9.

Bligh, T.P. 1974. Principles of breaking rock using high pressure gases. *Advances in Rock Mechanics, Proc. of the 3rd Congress of the Int. Soc. for Rock Mechanics,* Denver, Colorado, (II B), pp. 1421.

Borejko, P., Rossmanith, H.P. & Wei, Y.Z. 1992. Stress waves in layered rocks. *Acta Mechanica,* 92, pp. 175-181.

Brekhovskikh, L. M. 1960. *Waves in Layered Media.* Academic Press, New York.

Broberg, K.B. 1960. The propagation of a brittle crack. *Archiv f–r Fysik*, 18, pp. 159-192.

Carrasco, L.G. & Saperstein, L.W. 1977. Surface morphology of pre-split fractures in plexiglas models. *Int. J. Rock Mech. Min. Sci. & Geomech. Abstr.*, 14, pp. 261-275.

Chakraborty, A.K., Jethwa, J.L. & Paithankar, A.G. 1994. Effects of joint orientation and rock mass quality on tunnel blasting. *Engineering Geology*, 37, pp. 247-262.

Cherepanov, G.P. 1973. On the theory of fracture of a brittle body by explosion. *Brittle Materials and Glass*, pp. 145-154.

Christianson, M.C., Hart, R.D. & Schatz, J.F. 1988. Numerical analysis of multiple radial fracturing. *Key Questions in Rock Mechanics*, eds. P. Cundall et al., Balkema, Rotterdam, pp. 441-451.

Clark, G.B. 1967. Blasting and dynamic rock mechanics. *Proc. 8th Symp. on Rock Mechanics, University of Minnesota, Failure and Breakage of Rock*, ed. C. Fairhurst.

Cleary, M.P. 1982. Theory and Application of Hydraulic Fracturing Technology. *Lecture Presented at International Centre for Mechanical Sciences*, 4-10 July, Udine, Italy.

Coates, R.T. & Schoenberg, M. 1995. Finite-difference modelling of faults and fractures. *Geophysics,* V60 (5) Sep/Oct, pp 1514-1526.

Cook, M.A. 1958. *The Science of High Explosives.* Reinhold Publishing Corporation.

Costain, J.K., Cook, K.L. & Algermissen, S.T. 1963. Amplitude, energy and phase angles of plane SV waves and their application to earth crustal studies. *Bull. of the Seism. Soc. of America*, 53, pp. 1039-1074.

Coursen, D.L. 1979. Cavities and gas penetrations from blasts in stressed rock with flooded joints. *Acta Astronautica*, 6, pp. 341-363.

Cranz, C. & Schardin, H. 1929. Kinematographie auf ruhendem Film und mit extrem hoher Bildfrequenz. *Zeits. F. Physik*, 56, pp.147.

Cundall, P.A. 1992. 'Theoretical basis of the program WAVE'. *Unpublished internal report, COMRO (now Miningtek, CSIR, South Africa)*, pp. 1-12.

Cundall, P.A., Lorig, L.J. & Potyondy, D.O. 1996. Distinct-element models of explosion-induced failure of rock, including fragmentation and gas interaction. *Workshop on Explosion Effects in Granular Materials*, Oslo.

Curran & Goodluck, 1993. Modeling discontinuities in Numerical Analysis. In *Comprehensive Rock Engineering, ed. Hudson J.A.*, Vol 1, pp 447,448.

Daehnke, A. 1995. Comparisons between WAVE and seismological data. *J. South African Inst. of Mining and Metall.,* September, pp. 197-206.

Daehnke, A. 1997. Stress wave and fracture propagation in rock. Ph.D. thesis, Vienna University of Technology.

Daehnke, A., Napier, J.A.L., Knasmillner, R.E. & Rossmanith, H.P. 1995. Using dynamic photoelasticity to investigate stress waves interacting with stopes. *Proc. of the 2nd Int. Conf. on the Mechanics of Jointed and Faulted Rock*, ed. H.P. Rossmanith, Balkema, pp. 707-712.

Daehnke, A., Rossmanith, H.P. & Knasmillner, R.E. 1996a. Using dynamic photoelasticity to evaluate the influence of parting planes on stress waves interacting with stopes. *Int. J. Num. and Analyt. Methods in Geomech.*, 20, pp. 101-117.

Daehnke, A., Rossmanith, H.P. & Knasmillner, R.E. 1996b. Seismicity and stability in deep level gold mines. *Proc. Korea-Japan Joint Symp. on Rock Engineering*, Seoul, Korea, pp. 165-172.

Daehnke, A. & Hildyard, M.W. 1997. Dynamic fracture propagation due to stress waves interacting with stopes. *Proc. of the 1st Southern African Rock Mechanics Symposium*, Johannesburg, South Africa, pp. 97-108.

Dally, J.W., Fourney, W.L. & Holloway, D.C. 1975. Influence of containment of the borehole pressures on explosive induced fracture. *Int. J. Rock Mech. Min. Sci. & Geomech. Abstr.*, 12, pp. 5-12.

Dally, J. W. & Fourney, W.L. 1976. *Fracture Control in Construction Blasting*. Research Report, National Science Foundation, November 1976.

Dally, J.W., Fourney, W.L. & Holloway, D.C. 1977. Application of dynamic photoelasticity to excavation technology. *Recent Advances in Eng. Sciences*, 7, pp. 19-28.

Dojcar, O. 1996. Design methods for controlled blasting. *Trans. of the Inst. of Mining and Metallurgy*, A, pp. A166-A172.

Fokkema, J. T. 1981. Reflection and transmission of elastic waves by spatially periodic interface between two solids - Numerical results for the sinusoidal interface. *Wave Motion,* 3, pp. 33-48.

Fourney, W.L. & Dally, J.W. 1975. *Controlled Blasting using a Ligamented Tube as a Charge Containing Device*. Research Report, National Science Foundation, December 1975.

Fourney, W.L. & Dick, R.D. 1995. The utilization of explosive loading as a non-destructive evaluation tool in geologic materials. *Int. J. Solids Structures,* 32(17/18), pp. 2511-2522.

Fourney, W.L., Barker, D.B. & Holloway, D.C. 1981. Model studies of explosive well stimulation techniques. *Int. J. Rock Mech. Min. Sci. & Geomech. Abstr.*, 18, pp. 113-127.

Fourney, W.L., Barker, D.B. & Holloway, D.C. 1983. Model studies of explosive well stimulation using propellant charges. *Int. J. Rock Mech. Min. Sci. & Geomech. Abstr.*, 20, pp. 91-101.

Freund, L.B. 1972a. Crack propagation in an elastic solid subjected to general loading. I. Constant rate of extension. *J. of the Mechanics and Physics of Solids*, 20, pp. 129-140.

Freund, L.B. 1972b. Crack propagation in an elastic solid subjected to general loading. II. Nonuniform rate of extension. *J. of the Mechanics and Physics of Solids*, 20, pp. 141-152.

Freund, L.B. 1973. Crack propagation in an elastic solid subjected to general loading. III. Stress wave loading. *J. of the Mechanics and Physics of Solids*, 21, pp. 47-61.

Freund, L.B. 1974. Crack propagation in an elastic solid subjected to general loading. IV. Obliquely incident stress pulse. *J. of the Mechanics and Physics of Solids*, 22, pp. 137-146.

Ghosh, A. & Daemen, J.J.K. 1995. Rock fragmentation in bench blasting – a numerical study. In *Rock Mechanics*, eds. J.J.K. Daemen & R.A. Schultz, Balkema, Rotterdam, pp. 553-558.

Gnirk, P.F. & Pfleider, E.P. 1967. On the correlation between explosive crater formation and rock properties. *Proc. 9th U.S. Symposium on Rock Mechanics*, Colorado Schoolf of Mines, Golden, Colorado, AIME, pp. 321-345.

Graff, K.F. 1975. *Wave Motion in Elastic Solids*. Ohio State University Press.

Griffiths, S.K., Nilson, R.H. & Morrison, F.A. 1986. Hybrid analytical/numerical computation of heat transfer in a gas driven fracture. *J. of Heat Transfer*, 108, pp. 585-590.

Gu, B., Suarez-Rivera, R., Nihei, K.T. & Myer, L.R. 1996. Incidence of plane waves upon a fracture. *J. of Geophys. Research,* 101(B11), pp. 25337-25346.

Hagan, T.N. 1980. The effects of some structural properties of rock on the design and results of balsting. *Proc. of the 3rd Australia-New Zealand Conf. on Geomech.*, Wellington, New Zealand, pp. 205-213.

Hagan, T.N. & Just, G.D. 1974. Rock breakage by explosives – theory, practice and optimization. *Proc. of the 3rd Congress Int. Soc. Rock Mechanics,* Denver, Colorado, II, B, pp. 1349-1358.

Handley, M.F., Hildyard, M.W. & Spottiswoode, S.M. 1996. The influence of deep mine stopes on seismic waves. *Proceedings of the 2nd North American Rock Mechanics Symposium*, Montreal, pp. 499-506, 19-21 June 1996.

Heunis,R. 1980. The development of rock-burst control strategies for South African gold mines. *J. S. Afr. Inst. Min. Metall.,* 80, pp. 139-149.

Heuze, F.E., Shaffer, R.J., Ingraffea, A.R. & Nilson, R.H. 1990. Propagation of fluid-driven fractures in jointed rck. Part I – development and validation of methods of analysis. *Int. J. Rock Mech. Min. Sci. & Geomech. Abstr.*, 27(4), pp. 243-254.

Heuze, F.E., Walton, O.R., Maddix, D.M., Shaffer, R.J. & Butkovich, T.R. 1990. Analysis of explosions in hard rocks: the power of discrete element modelling. *Proc. of the Int. Symp. of the Mechanics of Jointed and Faulted Rock*, ed. H.P. Rossmanith, Balkema, Rotterdam, pp. 21-28.

Hirose, S. 1994. 2-D Scattering by a crack with contact-boundary conditions. *Wave Motion,* 19, pp. 37-49.

Hubbert, M.K. & Willis, D.G. 1957. Mechanics of hydraulic fracturing. *Trans, AIME*, 210, pp.153-168.

Ismail, M.A. & Gozon, J.S. 1987. Effects of discontinuities on fragmentation by blasting. *Int. J. of Surface Mining*, 1, pp. 21-25.

Kendall, K. & Tabor, D. 1971. An ultrasonic study of area of contact between stationary and sliding surfaces. *Proc. R. Soc. London,* 323, pp. 321-340.

Knott, C.G. 1899. Reflexion and refraction of elastic waves with seismological applications. *Philos. Mag.,* 48, pp. 64-97.

Kobayashi, A.S., Emery, A.F. & Mall, S. 1976. Dynamic finite element and dynamic photoelastic analyses of two fracturing Homalite-100 plates. *Experimental Mechanics*, 16(9), pp. 321-328.

Kobayashi, A.S., Emery, A.F. & Mall, S. 1977. Dynamic FE and dynamic photoelastic analyses of crack arrest in Homalite-100 plates. *Fast Fracture and Crack Arrest,* ASTM STP 627, eds. G.T. Hahn & M.F. Kanninen, American Society for Testing and Materials, pp. 95-108.

Koefoed, O. 1962. Reflection and transmission coefficients for plane longitudinal incident waves. *Geophys. Prosp.*, 10, pp. 304-351.

Kolsky, H. 1963. *Stress Waves in Solids.* Dover Publications, Inc., New York.

Kostrov, B.V. 1964. The axisymmetric problem of propagation of a tensile crack. *Applied Mathematics and Mechanics (PMM)*, 28, pp. 793-803.

Kostrov, B.V. 1966. Unsteady propagation of longitudinal shear cracks. *Applied Mathematics and Mechanics (PMM)*, 30, pp. 1241-1248.

Kouzniak N. (1998). Personal communication on 'Comparisons with the analytical propagating source model'. University of Vienna, Austria.

Kutter, H.K. 1967. The Interaction between Stress Wave and Gas Pressure in the Fracture Process of an Underground Explosion with Particular Application to Presplitting. Ph.D. Thesis, University of Minnesota.

Kutter, H.K. & Fairhurst, C. 1971. On the fracture process in blasting. *Int. J. Rock Mech. Min. Sci.*, 8, pp. 181-202.

Kutter, H.K. & Kulozik, R.G. 1990. Mechanics of blasting in a discontinuous mass. *Mechanics of Jointed and Faulted Rock*, ed. H.P. Rossmanith, Balkema, Rotterdam, pp. 295-304.

Lama, R.D. & Vutukuri, V.S. 1978. *Handbook on Mechanical Properties of Rocks.* Trans Tech Publications, Switzerland.

Larson, D.B. 1982. Explosive energy coupling in geologic materials. *Int. J. Rock Mech. Min. Sci. & Geomech. Abstr.*, 19, pp. 157-166.

Lightfoot, N., Kullmann, D.H., Toper, A.Z., Stewart, R.D., Grodner, M., Janse van Rensburg, A.L. & Longmore, P.J. 1996. Preconditioning to reduce the incidence of face bursts in highly stressed faces. *Mining Technology Division of CSIR, SIMRAC Final Report, Project GAP 030*

McHugh, S. 1983. Crack extension caused by internal gas pressure compared with extension caused by tensile stress. *Int. J. of Fracture*, 21, pp. 163-176.

McKenzie, C.K., Scherpenisse, C.R., Arriagada, J. & Jones, J.P. 1995. Application of computer assisted modelling to final wall blast design. *EXPLO'95*, AusIMM/ISEE Technical Paper.

Mendelsohn, D.A. 1984a. A review of hydraulic fracture modeling – part I: General concepts, 2D models, motivation for 3D modeling. *J. of Energy Resources Technology*, 106, pp. 369-376.

Mendelsohn, D.A. 1984b. A review of hydraulic fracture modeling – II: 3D modeling and vertical growth in layered rock. *J. of Energy Resources Technology*, 106, pp. 543-553.

Miklowitz, J. 1978. *Elastic Waves and Waveguides*. North-Holland Publishing Company, Amsterdam, New York, Oxford.

Minchinton, A. & Lynch, P.M. 1997. Fragmentation and heave modelling using a coupled discrete element gas flow code. *Int. J. for Blasting and Fragmentation*, 1, pp. 41-57.

Mindlin, R.D. 1960. *Waves and vibrations in isotropic elastic planes*. Structural Mechanics, ed. J.F. Goodier & W.F. Hoff, Pergamon, New York.

Munjiza, A. 1992. Discrete elements in transient dynamics of fracture media. Ph. D. Thesis, Department of Civil Engineering, University College of Swansea.

Munjiza, A., Owen, D.R.J. & Bicanic, N. 1995. A combined finite-discrete element method in transient dynamics of fracturing solids. *Engineering Computations,* 12, pp. 145-174.

Myer, L.R., Hopkins, D., Peterson, J.E. & Cook, N.G.W. 1995. Seismic wave propagation across multiple fractures. *Fractured and Jointed Rock Masses*, eds. L.R. Myer, N.G.W. Cook, R.E. Goodman & P. Tsang, Balkema, Rotterdam, pp. 105-109.

Napier, J.A.L. 1987. The application of excess shear stress to the design of mine layouts. *J. S. Afr. Inst. of Min. and Metall.*, 87, pp. 397-405.

Napier, J.A.L. 1990. Modelling of fracturing near deep level mine excavations using a displacement discontinuity approach. *Proc. of the Int. Symp. on Mechanics of Jointed and Faulted Rock*, ed. H.P. Rossmanith, Balkema, Rotterdam, pp. 709-715.

Napier, J.A.L., Hildyard, M.W., Kuijpers, J.S., Daehnke, A., Sellers, E.J., Malan, D.F., Siebrits, E., Ozbay, M.U., Dede, T. & Turner, P.A. 1995. Develop a quantitative understanding of rock mass behaviour near excavations in deep mines. *Unpublished SIMRAC Final project report (GAP029)*. December.

Nilson, R.H. 1981. Gas driven fracture propagation. *J. of Applied Mechanics*, 48, pp. 757-762.

Nilson, R.H. 1986. An integral method for predicting hydraulic fracture propagation driven by gases or liquids. *Int. J. for Numerical and Analytical Methods in Geomechanics*, 10, pp. 191-211.

Nilson, R.H. 1988. Similarity solutions for wedge shaped hydraulic fractures driven into a permeable medium by a constant inlet pressure. *Int. J. for Numerical and Analytical Methods in Geomechanics*, 12, pp. 477-495.

Nilson, R.H. & Griffiths, S.K. 1983. Numerical analysis of hydraulically-driven fractures. *Computer Methods in Applied Mechanics and Engineering*, 36, pp. 359-370.

Nilson, R.H. & Griffiths, S.K. 1986. Similarity analysis of energy transport in gas driven fractures. *Int. J. of Fracture*, 30, pp. 115-134.

Nilson, R.H. & Morrison, F.A. 1986. Transient gas or liquid flow along a preexisting or hydraulically-induced fracture in a permeable medium. *J. of Applied Mechanics*, 53, pp. 157-165.

Nilson, R.H., Proffer, W.J. & Duff, R.E. 1985. Modelling of gas driven fractures induced by propellant combustion within a borehole. *Int. J. Rock Mech. Min. Sci. & Geomech. Abstr.*, 22(1), pp. 3-19.

Nishioka, T. & Atluri, S.N. 1982. Numerical analysis of dynamic crack propagation: Generation and prediction studies. *Eng. Fracture Mechanics*, 16, pp. 303-332.

Nishioka, T. & Atluri, S.N. 1983. A numerical study of the use of path independent integrals in elasto-dynamic crack propagation. *Eng. Fracture Mechanics*, 18(1), pp. 23-33.

Nishioka, T., Stonesifer, R.B. & Atluri, S.N. 1981. An evaluation of several moving singularity finite element models for fast fracture analysis. *Eng. Fracture Mechanics*, 15(1-2), pp. 205-218.

Ouchterlony, F. 1974. Fracture mechanics applied to rock blasting. *Proc. of the 3rd Congress Int. Soc. Rock Mechanics*, Denver, Colorado, II, B, pp. 1377-1382.

Paine, A.S. & Please, C.P. 1994. An improved model of fracture propagation by gas during rock blasting – some analytical results. *Int. J. Rock Mech. Min. Sci. & Geomech. Abstr.*, 31(6), p. 699-706.

Persson, P.A. 1970. High-speed photography of scale-model rock blasting. *Proc. of the 9th Int. Congress on High-Speed Photography*, Denver, Colorado.

Persson, P.A., Lundborg, N. & Johansson, C.H. 1970. The basic mechanisms in rock blasting. *Proc. of the 2nd Congress on the Int. Soc. for Rock Mechanics*, 5-3, Belgrade.

Petitjean, L. & Coußt, B. 1994. Modeling of gas driven fracture propagation for oil and gas well stimulation. *Eurock'94*, Balkema Rotterdam, pp. 455-463.

Potyondy, D.O., Sarracino, R.S. & Cundall, P.A. 1996. Modeling of shock- and gas driven fractures induced by a blast using bonded assemblies of spherical particles. *Proc. of the 5th Int. Symp. on Rock Fragmentation by Blasting*, ed. B. Mohanty, Balkema, Rotterdam, Montreal, pp. 55-62.

Preece, D.S. 1993. Momentum transfer from flowing explosive gases to spherical particles during computer simulation of blasting induced rock motion. *9th Ann. Symp. on Explosives and Blasting Res.*, Society of Explosives Engineers, San Diego, CA, pp. 251-260.

Preece, D.S., Thorne, B.J., Baer, M.R. & Swegle, J.W. 1994. Computer simulation of rock blasting: a summary of work from 1987 through 1993. *Sandia National Laboratories Report,* SAND92-1027.

Pugliese, J.M. 1973. Some geologic structural influences in quarrying limestone and dolomite. *Engineering Geology Case History No.9, Geologic Factors in Rapid Excavation*, ed. H.J. Pincus, Geol. Soc. of America, Boulder, Colorado, pp. 11-16.

Pyrak-Nolte, L.J., Myer, L.R. & Cook, N.G.W. 1990a. Transmission of seismic waves across single natural fractures. *J. Geophys. Research,* 95(B6), pp. 8617-8638.

Pyrak-Nolte, L.J., Myer, L.R. & Cook, N.G.W. 1990b. Anisotropy in seismic velocities and amplitudes from multiple parallel fractures. *J. Geophys. Research,* 95(B7), pp. 11345-11358.

Riley, W.F. & Dally, J.W. 1969. Recording dynamic fringe patterns with a Cranz Schardin Camera. *Experimental Mechanics*, 9(8), pp. 27-33N.

Rinehart, J.S. 1975. *Stress Transients in Solids*. Hyper Dynamics, Santa Fe, New Mexico.

Roberts, J.M. & Swenson, D.V. 1988. A numerical model of gas driven dynamic fractures with an application to borehole stimulation. *ASME Int. Conf. on Computers in Engineering*, San Francisco, California.

Rorke A.J. 1992. Measurement of the direct effects of preconditioning blasts. Monitored results from the first test blast. Internal report, prepared for D. Adams, Feb 1992, COMRO, Ref R62/92.

Rossmanith, H. P. & Fourney, W. L. 1982a. Fracture initiation and stress wave diffraction at cracked interfaces in layered media. I. Brittle/brittle transition. *Rock Mech.,* 14, pp. 209-233.

Rossmanith, H.P. & Fourney, W.L. 1982b. Determination of crack-speed history and tip locations for cracks moving with nonuniform velocity. *Experimental Mechanics*, 22(3), pp. 111-116.

Rossmanith, H. P. & Knasmillner, R. E. 1983. Spallation, break-up and separation of layers by oblique stress-wave incidence. *1st Int. Symp. on Rock Fragmentation by Blasting,* Lulea, Sweden, pp. 149-168.

Rossmanith, H.P. & Knasmillner, R.E. 1990. Application of photomechanics to studies of fracture in jointed rock. *Proc. of the Int. Conf. on Mechanics of Jointed and Faulted Rock*, ed. H.P. Rossmanith, Balkema, Rotterdam, pp. 285-293.

Rossmanith, H.P., Groschupf, K., Knasmillner, R.E. & Uenishi, K. 1994. Numerical simulation of stress wave interaction with cracks in layered rock. *Rock Mechanics Models and Measurements Challenges from Industry. Proc. 1st North American Rock Mechanics Symp.*, eds. P. Nelson & S. Laubach, Balkema, Rotterdam, pp. 697-703.

Rossmanith, H.P. & Uenishi, K. 1996. PC software assisted teaching and learning of dynamic fracture and wave propagation phenomena. *Teaching and Education in Fracture and Fatigue*, ed. H.P. Rossmanith, Chapman & Hall, pp. 253-262.

Rossmanith, H.P., Uenishi, K. & Kouzniak, N. 1997. Blast wave propagation in discontinuous rock mass. *Int. J. for Blasting and Fragmentation*, 1(3/4), (in Press).

Schatz, J.F. 1993. Modeling and field example of the dynamic fracturing of rock with propellants. *Rock Fragmentation by Blasting*, ed. H.P. Rossmanith, Balkema, Rotterdam, pp. 413-418.

Schatz, J.F., Zeigler, B.J., Bellman, R.A., Hanson, J.M., Christianson, M.C. & Hart, R.D. 1987. *Prediction and Interpretation of Multiple Radial Fracture Stimulations.* SAIC Report to the Gas Research Inst., Contract No. 5084-213-1149.

Schoenberg, M. 1980. Elastic wave behaviour across linear slip interfaces. *J. Acoust. Soc. Am.*, 68(5), pp. 1516-1521.

Schoenberg, M. 1983. Reflection of elastic waves from periodically stratified media with interfacial slip. *Geophys. Prosp.*, 31, pp. 265-292.

Simha, K.R.Y. 1996. Effect of open joint on stress wave propagation. *Proc. of the 5th Int. Symp on Rock Fragmentation by Blasting – Fragblast-5*, ed. B. Mohanty, Balkema, Rotterdam, pp. 81-86.

Simha, K.R.Y., Fourney, W.L. & Dick, R.D. 1987. An investigation of the usefulness of stemming in crater blasting. *Proc. of the 2nd Int. Symp. on Rock Fragmentation by Blasting*, eds. W.L. Fourney & R.D. Dick, Keystone, Colorado, pp. 591-599.

Singh, D.P., Appa Rao, Y.V. & Saluja, S.S. 1980. A laboratory study of effects of joints on rock fragmentation. *Proc. of the 21st U.S. Symp. on Rock Mechanics*, Missouri, Rolla, pp. 400-409.

Stagg, M. S. & Nutting, M.J. 1987. Influence of blast delay time on rock fragmentation. *Proc. of the Int. Symp. on Surface Mine Blasting*, pp. 79-95.

Stewart R.D. 1995: Personal communication on rock mass properties at the mining site. CSIR Division of Mining Technology, December 1995.

Suarez-Rivera, F.R., Cook, N.G.W. & Myer, L.R. 1992. Study on the transmission of shear waves across thin liquid films and thin clay layers. *Rock Mechanics,* eds. Tillerson & Wawersik, Balkema, Rotterdam, pp. 937-946.

Swenson, D.V. 1985. *Modeling Mixed-Mode Crack Propagation using Finite Elements.* Dept. of Structural Engineering Report, Number 85-10, Cornell University, Ithaca, NY.

Swenson, D.V. & Ingraffea, A.R., 1988. Modeling mixed-mode dynamic crack propagation using finite elements: Theory and application. *Computational Mechanics*, 3, pp. 381-397.

Swenson, D.V. & Kaushik, N. 1990. Finite element analysis of edge cracking in plates. *Eng. Fracture Mechanics*, 37(3), pp. 641-652.

Swoboda, G. & Li, N. 1993. Numerical modelling of blast loading. *Proc. of the Int. Symp. on Rock Fragmentation by Blasting*, ed. H.P. Rossmanith, Balkema, Rotterdam, pp. 25-31.

Szuladzinski, G. 1993. Response of rock medium to explosive borehole pressure. *Proc. of the Int. Symp. on Rock Fragmentation by Blasting*, ed. H.P. Rossmanith, Balkema, Rotterdam, pp. 17-23.

Taylor, L.M. & Preece, D.S. 1989. DMC – a rigid body motion code for determining the interaction of multiple spherical particles. *Sandia Report.* SAND88-3482.

Tinucci J.P. and Spearing A.J.S. 1993: Strategies for clamping faults and dykes in high seismicity tabular mining conditions. In : Young (ed.) *Rockbursts and Seismicity in Mines*, AA Balkema, Rotterdam.

Tooley, R.D., Spencer, T.W. & Sagoci, H.F. 1965. Reflection and transmission of plane compressional waves. *Geophysics,* 4, pp. 552-570.

Toper, A.Z. 1995. Numerical modelling to investigate the effects of blasting in confined rock – simulation of a field study. *Rock Mechanics*, eds. J.J.K. Daemen & R.A. Schultz, Balkema, Rotterdam, pp. 541-546.

Tuzi, Z. 1928. Photographic and kinematographic study of photoelasticity. *J. Soc. Mech Eng.*, 31(136), pp. 334-339.

Wang, X.J., Fourney, W.L. & Dick, R.D. 1990. Model studies of optimised crater blasting. *Proc. of the Int. Symp. on Fragmentation due to Blasting*, Brisbane, pp. 137-142.

Warpinski, N.R., Schmidt, R.A. & Cooper, P.W. 1979. High-energy gas frac: multiple fracturing in a wellbore. *20th U.S. Symp. on Rock Mechanics*, Austin, Texas, pp. 143-153.

Watanabe, K. 1995. Reflection and refraction of impulsive elastic waves at a jointed interface. *MJFR-2, Mechanics of Jointed and Faulted Rock*, ed. H.P. Rossmanith, Balkema, Rotterdam, pp. 713-718.

Wells, A.A. & Post, D. 1958. The dynamic stress distribution surrounding a running crack – a photoelastic analysis. *Proc. of the SESA*, 16, pp. 69-92.

Wolf, H. 1976. *Spannungsoptik, Zweite Auflage.* Springer Verlag, Berlin-Heidelberg-New York.

Worsey, P.N. 1984. The effect of discontinuity orientation on the success of pre-split blasting. *Proc. of the 10th Conf. on Explosives and Blasting Technique*, Orlando, Florida, pp. 197-217.

Worsey, P.N., Farmer, I.W. & Matheson, G.D. 1981. The mechanics of pre-splitting in discontinuous rock. *Proc. of the 22nd U.S. Symp. on Rock Mechanics*, pp. 218-223.

Yang, R. Bawden, W.F. & Katsabanis, P.D. 1996. A new constitutive model for blast damage. *Int. J. Rock Mech. Min. Sci. & Geomech. Abstr.*, 33(3), pp. 245-254.

Young, C., Barker, D.B. & Clark, H.C. 1986. Field tests of the stem-induced explosive fracturing technique. *SPE Production Eng.*, pp. 266-274.

Zoeppritz, K. 1919. *Nach. d. K–nigl. Gesell. d. Wissen. z. G–ttingen, Math.-Phys.*, Berlin, pp. 66-84.

4 Model calibration and the investigation of mining rate strategies to reduce fall of ground accidents and rockburst occurrences

4.1 Introduction

An important aspect of excavation design is to control the incidence of fracturing to improve the stability of the opening. Low-angled fractures and other discontinuities can break the hangingwall into semi-detached keyblocks which enhance the possibility of falls of ground. Section 2 described the development of improved numerical methods to simulate the formation and behaviour of the fracture zone. These improved codes allow a more realistic determination of time-dependent deformation mechanisms and hold significant promise for the evaluation of different mining rate strategies. Improving the understanding of rock mass behaviour and developing better numerical models are, however, interactive processes and the two need to be continually checked and validated against one another. Physical information obtained in situ is preferred to facilitate this interaction but, in many cases, this is difficult to interpret because of the complexities involved in describing the rock mass structure and variations in the local stress state. Testing of models under controlled conditions in the laboratory offers a complementary option for the initial calibration and validation of numerical models and constitutive laws, and for studying the mechanisms of fracture initiation and growth. The initial part of this section focuses on the laboratory work carried out to validate the fracture zone models developed in Section 2. This work was supplemented by underground observations of fracturing around tabular excavations and the simulation of these processes with the fracture zone simulator.

An important feature of project GAP332 is the significant progress made in understanding the time-dependent behaviour of the rock mass. The use of continuous closure measurements to characterise this behaviour in underground stopes is described in this section. It is clear that continuous time-dependent closure profiles are a good indicator of the rock response to stress changes caused by blasting operations or seismicity. High stresses in the face area can cause sudden and, generally, unpredictable failure of the face. Methods are therefore needed to estimate the magnitude of stress in the fracture zone ahead of stope faces. Unfortunately traditional overcoring methods of stress measurements cannot be used successfully in the fracture zone. Studies described in this section indicated that time-dependent closure measurements can assist the determination of changing stress conditions near the face. The measuring of time-dependent closure in every panel might become an important data input to a "design-as-you-mine" strategy.

As the fracture zone behaves in a time-dependent fashion, one strategy which may be useful to control this zone is the rate of face advance. The speed of extraction combined with an appropriate viscous constitutive law should provide some guidance as to how to determine safe extraction rate policies and how to control the stability of the fracture zone. This was part of the motivation for developing the time-dependent models described in Sections 2.4.5 and 2.4.6. The application of these models to examine the effect of different rates of mining is described in this section.

Finally, the discontinuum viscoplastic model can be used to investigate questions concerning time to failure and if possible to predict future energy release or face stress buildup.

4.2 Literature survey

4.2.1 Laboratory experiments

Fracturing in physical models around highly stressed openings in rock and artificial material has been investigated by many researchers (e.g. Chen et al., 1992; Gay, 1973; Napier & Özbay, 1993). Gay (1976) tested blocks of quartzite and sandstone containing holes of circular or rectangular cross-sections in uniaxial and biaxial compression. The fractures developing around the holes resembled those seen in deep mines. In the literature, however, virtually no tests are described where triaxial compression was applied to the models. Germanovich et al (1994) have shown that under increasing applied load, a single 3D crack does not grow extensively and that interaction between adjacent cracks is responsible for their unstable growth. Dyskin et al. (1995) described three-dimensional crack propagation experiments showing that some fracture processes are difficult to explain using two-dimensional analyses.

4.2.2 Stope observations – Factors controlling rock mass behaviour

With the increase of depth in mining, geological parameters have an increasing influence on rock mass behaviour (e.g. Adams et al., 1981; Gay et al., 1984; Gay & Jager, 1986). A detailed overview of the relationship between stability of an excavation, mining layout and geological structures is provided by Schweitzer & Johnson (1997). Rock composition influences rock mass behaviour on a regional scale. For example, the different rock mass behaviour in the Klerksdorp area, compared to the Carletonville area has been attributed to the generally weaker (about 200 MPa uniaxial strength) quartzites associated with the Klerksdorp excavations (Roberts & Jager, 1991).

It has been shown that factors such as beam thickness, hangingwall stability, footwall lift and pillar and tunnel stability can also be related to the various kinds of bedding, (e.g. planar bedding, cross bedding) and sharp lithological contacts (Atkins & Keen, 1984; Gay & Jager, 1986; Jager & Turner, 1986). Where flow bands occur in volcanic rocks, they may result in parting planes which control rock mass behaviour, similar to bedding planes in quartzites.

Reef thickness may also affect seismicity, as the effects of seismicity are reduced with narrow stoping widths (Arnold et al., 1994). This has important implications, for example, where the orebody is rolling (McWha, 1994; Germs & Schweitzer, 1994).

Geological structures such as joints, faults and dykes play a strong role in rock mass behaviour. Berlenbach (1993) showed that fault structures may control the orientation of mining-induced fractures. Faults and dykes also control the epicentres of mining-induced seismicity (Van der Heever, 1982). Fault rocks are another parameter controlling fracture formation. A wide variety of Witwatersrand fault rocks with different compositions, textures and competencies is observed (Roering et al., 1991).

4.2.3 Time-dependent closure measurements

Analysis of the rock mass at depth requires some knowledge about the response of the rock to the progressive enlargement of the excavations. Limited techniques are available to characterise the *in situ* behaviour of the rock. Seismic data has been used extensively in an attempt to characterise the rock in the deep gold mines in South Africa (Legge & Spottiswoode, 1987; Mendecki, 1997). Another potential source of valuable data is the closure behaviour of excavations. Continuous time-dependent closure data is a good reflection of the localised rock

response and can provide important information which may be more difficult or even impossible to obtain with other methods. Unfortunately this source of data has been largely neglected in the South African industry since the early seventies. Although a large number of closure measurements have been recorded (Wiggill, 1965; Gürtunca et al., 1989; King et al. 1989; Güler, 1997), these measurements were usually at 24 hour intervals or longer between successive data points. Data collected by Walsh et al. (1977) at West Driefontein Mine had an interval of a week between measurements. All these measurements will be collectively termed *long period* measurements. The results from these measurements can be misleading as the closure curves are not only indicative of the true time-dependent behaviour of the rock but the complex result of a) enlargement of the excavation, b) the face moving away from the measurement position and c) the true time-dependent behaviour of the rock. As will be shown in Section 4.4.3, much of the useful information, especially after blasting, is lost with these long period measurements. In spite of this limitation, significant time-dependent rock behaviour was noted by several researchers. King et al. (1989) measured closure behaviour in two adjacent panels at Hartebeestfontein Mine. After blasting activity had stopped in one of the panels, the closure rate in this panel continued at a constant rate of 6 mm/day for 37 days. Only after this period did the rate gradually start to decrease. Mining however continued in the second panel (and probably in other nearby panels) and it is unclear what the effect of these geometrical changes was on the first panel. After mining stopped in the second panel, the closure rate in this panel persisted for thirteen days and then gradually declined. Closure data collected by Gürtunca (1989) in the Klerksdorp area to quantify the effect of backfill also exhibited significant time-dependent effects. Daily closure rates varied from panel to panel and were in some instances as high as 30 mm/day. The study showed that closure rates are significantly lower in backfilled panels than in partially filled panels.

The true time-dependent behaviour of the rock mass can be identified by closure measurements with instruments that record in a continuous fashion. The following observations and analyses of continuous closure measurements are described in the literature. Leeman (1958) used closure recorders to measure time-dependent closure profiles in a tabular stope at East Rand Proprietary Mines (E.R.P.M.). He noted that the rate of closure suddenly increases just after blasting time. This high rate of closure decreases within hours to give a gradual steady-state closure until the next blast occurs and the pattern is repeated. On Sundays no blasting took place and, as expected, no incremental jump is visible in the data. The rate of gradual steady-state closure was usually also a minimum on Sundays. Hodgson (1967) also measured time-dependent closure at E.R.P.M. His experimental technique differed slightly from that of Leeman (1958) as his convergence meters were anchored 15 m into the hangingwall and footwall. He stated that over a long period of time, convergence measured by these anchored instruments corresponded to the elastic displacements resulting from changes in layout geometry. A more detailed examination of the manner in which the convergence takes place indicated, however, that the closure is time-dependent. He explained the gradual steady-state closure as being caused by the time-dependent migration of the fracture zone ahead of the face resulting in the effective stope span becoming bigger. The first quantitative attempt to analyse time-dependent closure profiles of tabular stopes was made by McGarr (1971) using data from E.R.P.M. McGarr (1971) suggested that the relaxation time τ of the rock may be used as a parameter to describe the ability of the rock mass to form a fracture zone in response to the face advance. Certain values of τ might be associated with mines that are prone to rockbursts.

4.2.4 The effect of rate of mining

Very limited knowledge is available about the effect of rate of mining on seismicity and on the incidence of falls of ground. For the South African gold mining industry, Hodgson (1967) predicted that if the face advanced faster than the migration of the fracture zone, less energy would be released in a stable manner, thereby increasing the incidence of rockbursts. Cook et al. (1966) found from a statistical analysis of rockburst data that there is an increase in

rockbursts for a face advance rate of more than 4 m a month, for small abutments, to 8 m a month, for large abutments. This dependence of seismicity on rate of mining is also noted for coal mining operations. Linkov (1996) noted that in the Kizel coal mines, doubling the rate of coal cutting on a face from 0,27 m/min to 0,54 m/min resulted in a drastic increase in the incidence of rockbursts. Nawrocki (1995) found from a numerical study of a coal seam that rapid ore extraction produces zones of high stress concentrations close to the longwall face. This situation is deemed to be hazardous as it increases the likelihood of rockbursting.

With regards to falls of ground, it is well known in the gold mining industry that a deterioration of hangingwall conditions occurs for areas where the faces are left standing. Very slow face advance rates might possibly lead to an increase in the risk of falls of ground. Arnold (1993) noted that at Hartebeestfontein Mine, increased rates of face advance decreased the time-dependent loosening or unravelling of hangingwall blocks and improved hangingwall stability. It appears that hangingwall conditions and thus support requirements are favourably influenced by the achievement of a rapid rate of face advance.

McGarr (1971) investigated the stope closure rate throughout the week at E.R.P.M. The closure rate calculated during six-hour intervals is illustrated in Figure 4.2.1 with the values plotted in the centre of the given six-hour period. The data has been averaged over 30 weeks. The highest rate of closure occurs during the six-hour intervals that include periods of face advance. The rate of closure generally increases from Monday through Saturday, which suggests that during the week stress relaxation does not occur as fast as face advance. No blasting occurred on Sunday. After the last blasting period of the week on Saturday afternoon, the rate of closure diminishes considerably until the face advances again on Monday. If an additional blast was thus carried out on Sunday, this relaxation would not take place, thereby increasing the potential for violent energy release. Although this appears to be compelling evidence against mining operations on Sundays, it should be noted that these measurements were taken at E.R.P.M. and might not be applicable to other geotechnical environments.

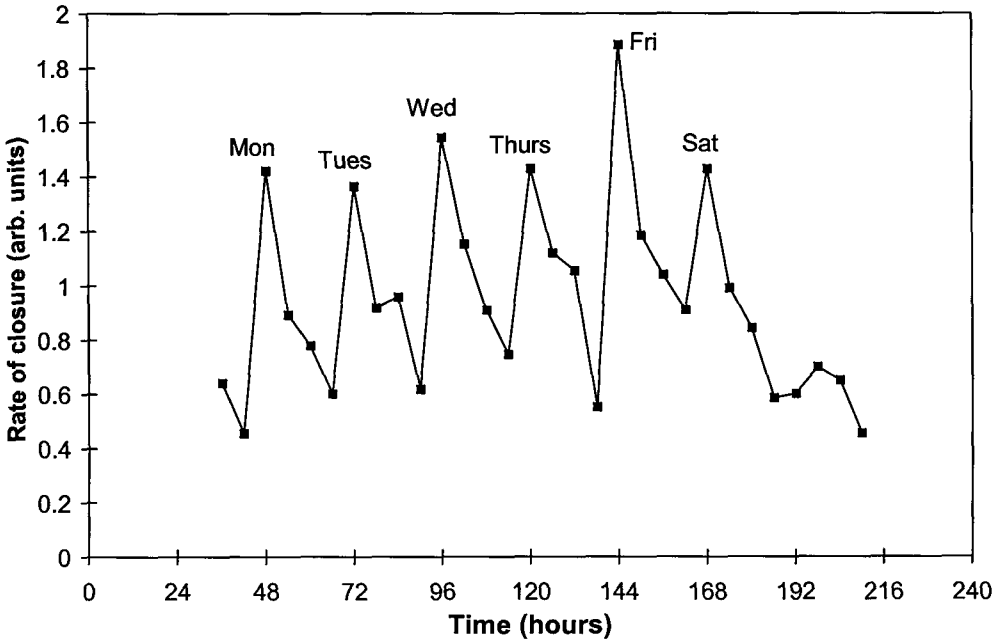

Figure 4.2.1 Rate of stope closure throughout the week at E.R.P.M. (after McGarr, 1971).

4.3 Methodology

The results described in Section 4.4 were obtained by a combination of laboratory experiments, underground observations, time-dependent closure measurements and numerical modelling. The methodology behind the numerical modelling is described in detail in Section 2 and the underground observations are self-explanatory. This sub-section will therefore only describe the laboratory equipment for the physical experiments and the instrumentation used for the closure measurements.

4.3.1 Laboratory equipment

4.3.1.1 The biaxial load cell

All the laboratory experiments described in this section were carried out using a biaxial load cell constructed from a steel ring with dimensions of 360 mm outer diameter, 160 mm inner diameter and a height of 120 mm (Figure 4.3.1). This load cell was mounted in the MTS 815 servo-controlled testing machine at the University of the Witwatersrand. The lateral confining stresses are provided by the two hydraulic pistons built into the steel ring. Curved spacers are used to convert the inner side to a square to accommodate cubic specimens. Additional prismatic spacers can be used to change the inner dimensions of the cell to accommodate different sizes of specimens which may be typically cubes with 70, 80, and 100 mm side lengths. The coefficient of friction of rock-steel contact is reduced to approximately 0,01 by applying stearic acid on all loaded surfaces of the specimen.

A centrifugal electric pump delivers hydraulic pressure to the two hydraulic pistons which, in turn, transmit the load onto the specimen. The maximum load that can be applied to the specimen is about 170 KN, which is equivalent to a lateral confinement of 27 MPa on the side of an 80 mm cubic block. An electronic gauge, which is placed between the cell and a needle valve mounted on the hydraulic fluid pipe, measures the pressure being delivered to each hydraulic piston. A pair of dial gauges is also mounted on the fluid pipe to allow visual observation the pressure. Two needle valves are placed before the gauges to lock the pressure at a desired level.

The 2800 kN actuator piston of the MTS compression testing machine is used to apply a vertical load on the specimen. The built-in LVDT measures the piston displacement. The vertical loading of the specimen is programmed on the MTS TestStar software which runs on a OS/2-based computer.

The cubic specimens used in the tests had a side length of 80 mm. All sides are machined perpendicular to within 0,01°. The blocks were cut either into one 80x80x80 or two 80x80x40 mm prismatic blocks with the lower half machined to create different load concentrating configurations.

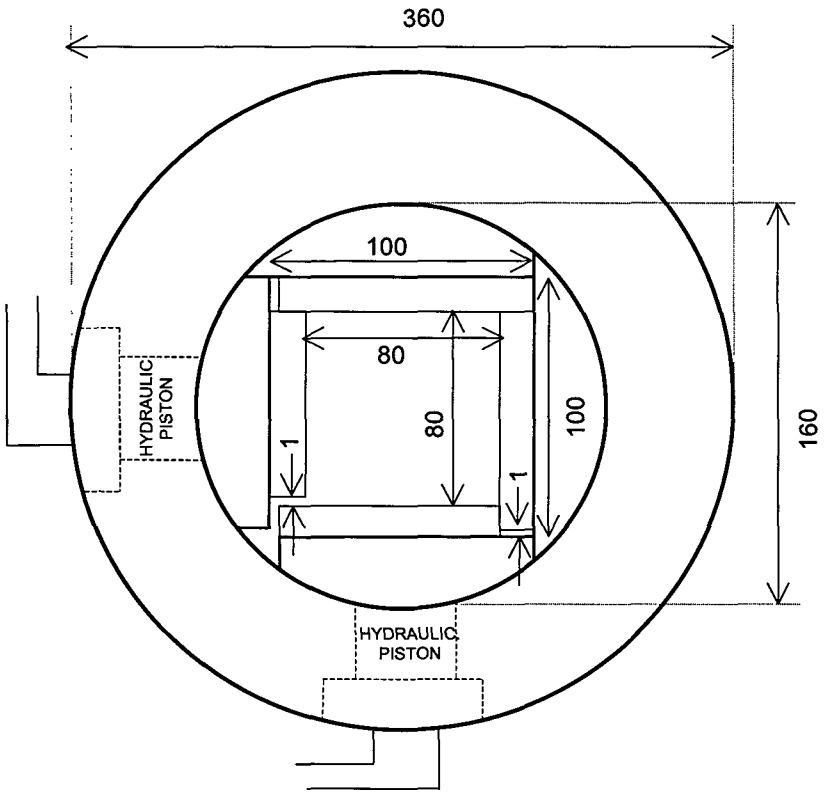

Figure 4.3.1 A schematic view of the biaxial cell used for the experiments (dimensions are in mm).

4.3.1.2 Data acquisition

The vertical displacement of the actuator piston and load applied are recorded by the MTS data acquisition system. An external data acquisition system is also used to record the vertical load from a load cell placed on the top platen. The pressure is measured by electronic pressure gauges and the horizontal displacements measured by cantilever gauges.

An acoustic emission system, which operates at a data acquisition rate of 4 MHz per channel, was used to record the location of fracturing in the specimen. Three-dimensional location of fracturing was achieved using nine sensors around the sample in the slots machined into the side platens. A one millimetre thick steel membrane separates the sensors from the specimen. The location calculations were done using a least squares algorithm.

The acoustic energy release mentioned in the following text and figures is a relative measure determined from integration of the uncalibrated amplitude - time curve and is not the absolute energy of the event. Energy release rate is the total amount of relative energy released in a time increment.

4.3.2 Closure measurements

For the underground studies, time-dependent closure data was collected using clockwork closure meters designed for the CSIR. Although an old mechanical design, this was still useful as a research tool as the meters were inexpensive, easy to install and intrinsically safe for use in mines. The mechanism of this instrument is illustrated in Figure 4.3.2

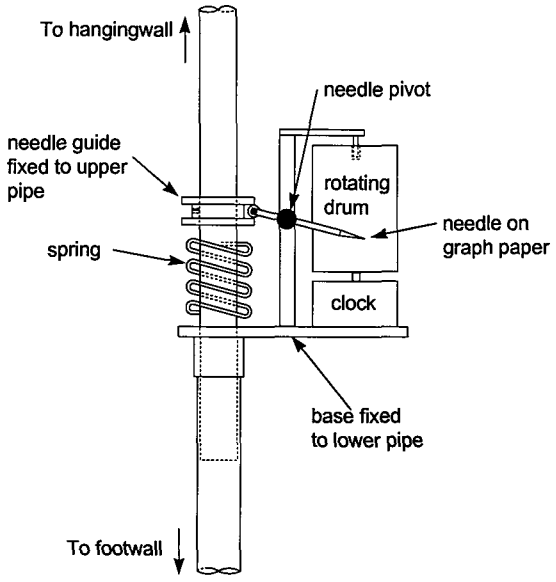

Figure 4.3.2 Mechanism of the clockwork closure meter used to collect time-dependent closure data.

From Figure 4.3.2 it can be seen that the instrument comprises two pipes, with the one pipe sliding inside the other against the pressure of a spring. The base of the instrument is fixed to the lower pipe with the needle being moved by a guide fixed to the upper pipe. The instrument is installed with the needle point close to the bottom of the graph paper on the drum. Stope closure moves the upper pipe further into the lower pipe with the needle point moving upwards on the paper. The clock rotates the drum once every seven days resulting in a continuous record of the closure over this period. The needle arm is designed with various possible pivot points to allow for different amplification factors of the closure magnitude. Unfortunately, this design is inherently flawed as instantaneous closure is recorded as an arc, thereby distorting the time axis. The data needs to be corrected before use and the approach developed by the author for these instruments is given in Malan (1998). An example of the raw data recorded on the graph paper is shown in Figure 4.3.3. Figure 4.3.4 illustrates the same data after it was digitised and corrected according to the developed procedure. Note that no attempt was made to smooth any of the closure data, although large digitisation intervals will have some smoothing effect. The typical digitisation interval used is illustrated in Figure 4.3.4.

When installing the instruments underground, it is important that the two pipes make contact with solid rock in the hangingwall and footwall. The top pipe was secured to the hangingwall using quick-setting putty. When installed close to the face, the instrument should be protected from blast damage. This was done by installing the meter behind one of the timber support packs.

In dipping stopes the instruments were installed normal to the plane of the reef to measure the closure component (see Figure 4.4.3.1 in Section 4.4.3). *Closure* refers to the relative hangingwall and footwall movement normal to the plane of the reef while *ride* is the component parallel to the reef plane. It should be noted that with time, a significant ride component will tilt the instrument resulting in a composite measurement. In the instrumented panels, the ride component was small (less than 3 mm/day in the panels at Western Deep Levels Mine; Toper, 1997) and this effect was ignored.

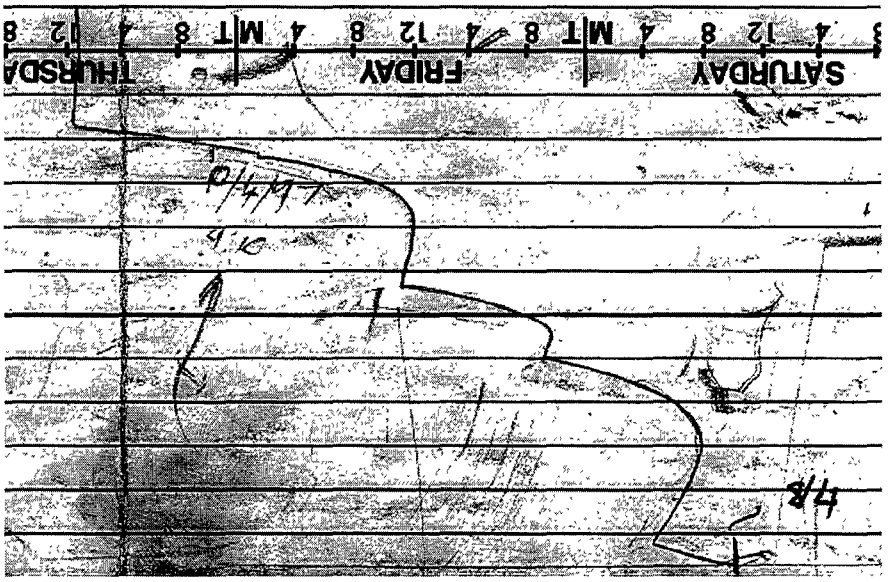

Figure 4.3.3 An example of continuous closure data recorded using the clockwork closure meter (see comments in the text above regarding the corrections needed). This figure only shows a small section of the graph paper sheet and is not printed to scale. (The horizontal grid lines are separated by a vertical distance of 5 mm.) Note that the horizontal axis represents time, which increases to the left. (The days printed on the paper indicate an increase of time to the right, but this is incorrect as the paper was mounted upside down on the drum.) The vertical axis represents closure magnitude which increases upwards. The pivoting needle arm resulted in the actual closure magnitude being multiplied by a factor of 1,86 on the graph paper.

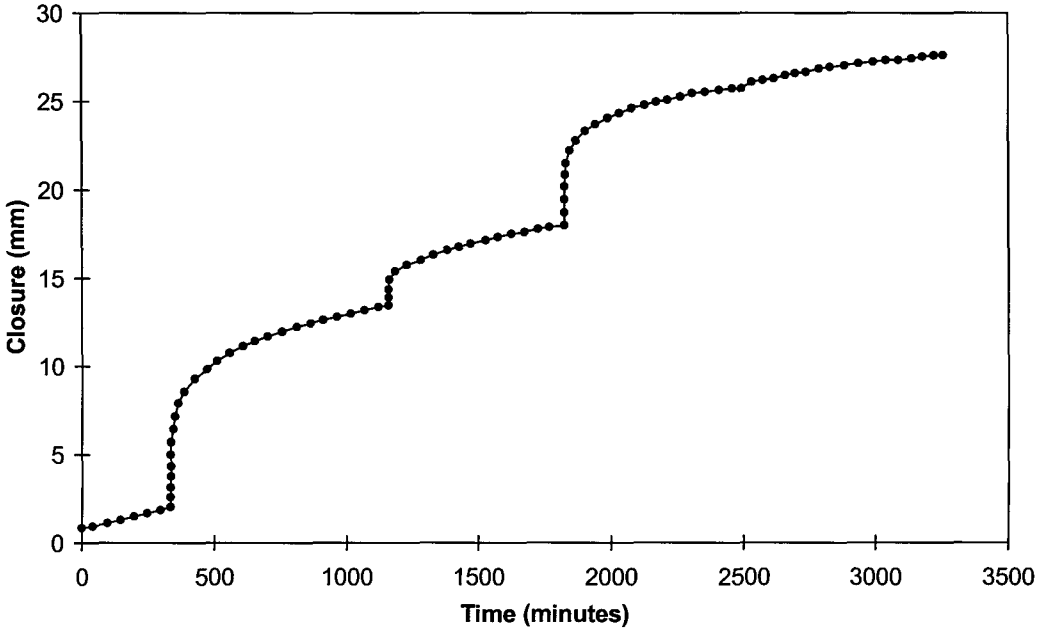

Figure 4.3.4 The corrected closure data for the measurements depicted in Figure 4.3.3. The data points give an indication of the digitisation interval used.

4.4 Results

4.4.1 Physical models

As described in Sections 2.4.3,2.4.4, and 2.4.8, computer programs based on the boundary element method have been developed to simulate mining-induced fracture patterns in two and three dimensions (Napier, 1990, Napier et al., 1998). These programs obviously require extensive verification to ensure that the numerical representations of fracture growth are representative of real situations. The approach used here is to simulate fracture growth in idealised laboratory tests where the loading is known and the fracture patterns can be studied in detail. This section of the report compares the results of physical experiments in cubic blocks of rock containing stope models with numerical simulations to determine whether the developed program can simulate the fracture patterns accurately.

4.4.1.1 Simulating stope experiments with discrete fracture growth in DIGS

The initial tests were conducted on blocks containing a slot to represent a tabular stope. The models were prepared from Elsburg quartzite and Black Reef quartzite. The properties of the rock types used for making the test samples are given in Table 4.4.1.1.The models were typically cubic blocks with a side length of 80 mm. Figure 4.4.1.1 shows a typical geometry used for the physical experiments.

Table 4.4.1.1 Properties of the rock types used for the tests.

Parameter	Elsburg Quartzite	Black Reef Quartzite	Norite
Uniaxial compressive strength	180 MPa	203 MPa	290 MPa
Elastic modulus	69,6 GPa	78 GPa	90 GPa
Poisson's ratio	0,2	0,17	0,28
p-wave velocity	5200 m/s	5500 m/s	

The fracture patterns observed from testing are shown in Figure 4.4.1.2a. The resulting fracture pattern is dependent on whether or not total closure occurs in the slot. The tests with total closure in the back area of the slot resulted in fractures forming ahead of the face of the slot. In the case where total closure did not occurr, the fractures grew backwards over the slot. It was attempted to simulate these fracture patterns using discrete fracture growth from seed points in the displacement discontinuity code DIGS (Napier and Hildyard, 1992). The fracture patterns produced by DIGS were dependent on the location of the seed points and the failure criterion used, but correctly predicted the change in fracture pattern as the slot width increased. The fracturing resulting from the extension failure criterion tended to develop backwards over the slot, as shown in Figure 4.4.1.2b, while fractures that developed according to the shear criteria propagated ahead of the stope (Figure 4.4.1.2c). Closure in the stope limits the extent of extension fracturing and also causes shallower angle shear fractures than for the case with no closure (see Appendix 4.1). Specification of some seed points with the extension failure criterion and others with the shear criterion results in a close agreement with the physical model, as can be seen by comparing Figures 4.4.1.2a and 4.4.1.2d. In the case with a wider slot (diagrams on the left in Figure 4.4.1.2), a shear fracture develops ahead of the face, and an extension fracture develops behind the face. The lack of symmetry in the physical model is due to slight

differences in the boundary conditions, or inhomogeneities in the rock, whereas the asymmetry in the model is due to the particular choice of seed positions. In the upper half of the model, the tensile fracture growing from the boundary intersects and terminates the shear crack growing from the slot. On close inspection, the shear cracks in the lower halves of the model are terminated by an array of extensile (or tensile) fractures, as predicted in the model. Thus, what appears to be a single fracture was formed in a combination of extension and shear fracture modes.

In the model with the narrower slot (diagrams on the right in Figure 4.4.1.2), the extension fracture is suppressed and the shear fracture dominates, as in the physical model. This comparison of the numerical modelling with actual fracture patterns in a highly non uniform stress field, suggests that the extension and shear criteria are both able to predict the relevant fracture directions and lengths. When suitable seed points are present, the DIGS model is able to simulate the complex interactions of the cracks. In general, the discrete fracture growth logic can simulate the complex fracture patterns observed in physical experiments and should therefore be able to represent fracturing on the larger scale of mine excavations. The final fracture patterns does, however, depend strongly on the placing of seed points in suitable positions within the model, and on the selection of the appropriate growth criterion. The tessellation approach (Napier et al., 1996) offers a means of removing the dependence on the user input and permits fracture interaction to occur as required by the changing stress state.

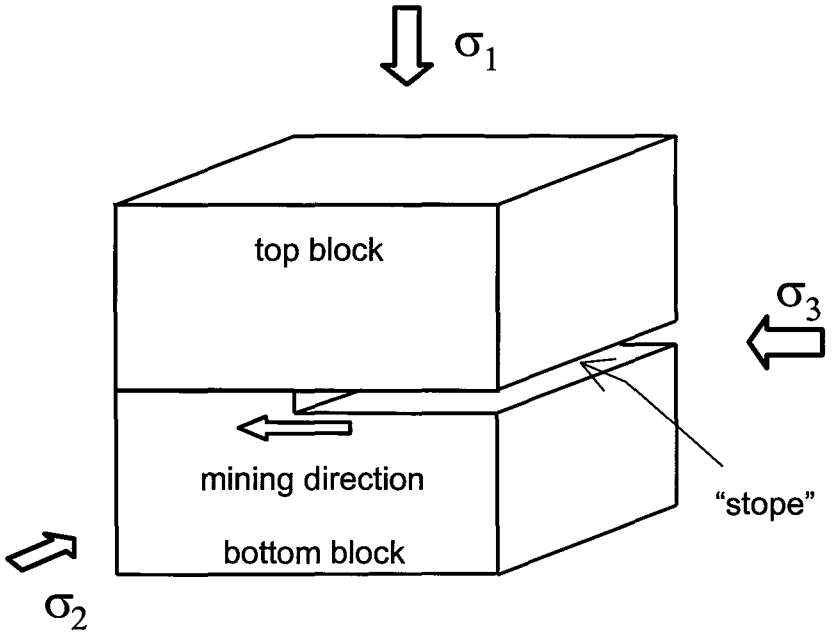

Figure 4.4.1.1 Geometry of a typical test specimen.

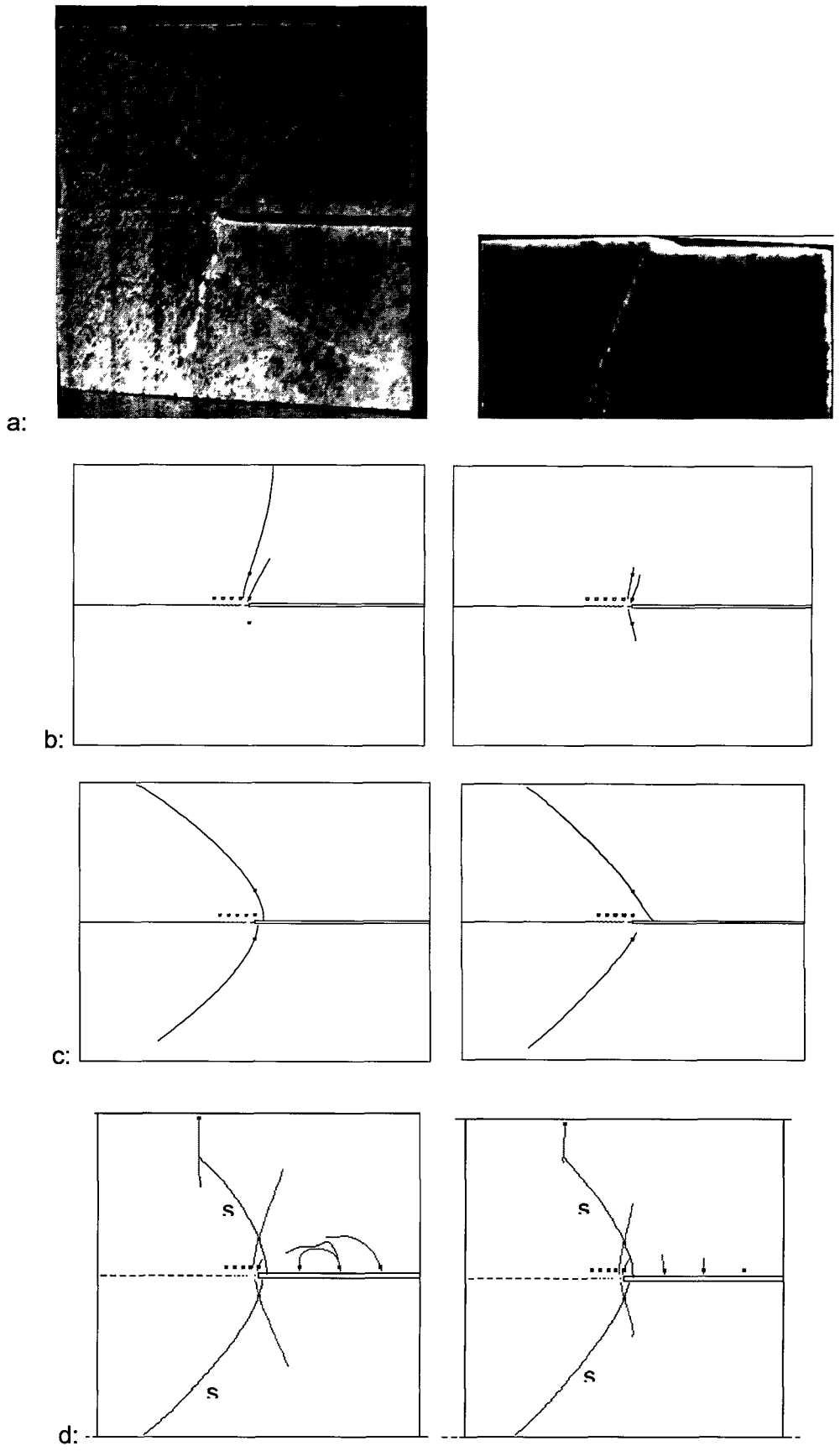

Figure 4.4.1.2 Results of stoping width experiments. a: physical models. b: extension failure criterion c: shear failure criterion d: both shear (s) and extension (all other fractures) criteria. Slot width is 2 mm in diagrams on the left and 0.2 mm in diagrams on the right.

The importance of considering the history of loading on the fracture pattern was investigated by sequential extension of the slot. As the slot could not be extended under load, the sample was loaded to a pre-selected stress, then unloaded and the slot was extended by 1 mm. The sequence of loading and unloading was continued for as much as 10 steps in some blocks. In one case, the top half of the sample contained a natural discontinuity, consisting of a welded joint with quartz infilling. This was used to investigate the influence of a pre-existing discontinuity on the fracture pattern around the slot. The test involved sequential enlargement of the slot towards this discontinuity. The fracture patterns obtained after the last mining step from the numerical and physical modelling experiments are shown in Figure 4.4.1.3. In the physical model, an initial shear fracture formed in the first load application and was directed ahead of the face. The uniform samples, and the lower half of the block with the discontinuity show similar behaviour. In these cases, the subsequent loading produced smaller, apparently extension mode, fractures that are angled in the opposite direction and intersect the initial shear fracture. As the slot is extended, the dip of these fractures increases until another, larger, shear fracture forms in front of the slot.

The physical and numerical models show similar fracture patterns, as shown in Figure 4.4.1.3. The numerical model shown in Figure 4.4.1.3 has only the shear criterion specified, but the introduction of both shear and extension fractures, at a much finer element size, allows the prediction of the observed sequence of shear and extension fractures. In the case with the discontinuity, a different fracture pattern is apparent in the hangingwall. The initial fracture was formed in much the same way as the homogeneous sample and terminated at the discontinuity. Observation of the tested sample showed evidence that the discontinuity had been activated as a new zone of intense microcracking associated with the joint. Activation of the discontinuity appears to have permitted the deformation of the rock mass towards the stope, required by the action of the boundary loads and averted the need for the initiation of the extension cracks. The second shear fracture develops at the same slot length as the second shear in the lower block, but is terminated by the active discontinuity. These tests provide information at two levels. Firstly, they confirm that the DIGS code is able to model the complicated history of fracturing, and the interactions with pre-existing discontinuities. Secondly, although the physical models do not represent scale models of tabular stopes, they do indicate that sequential excavation may produce a periodic pattern of large and small fracture events. If these prove to exist at the stope scale, the characterization of the nature of the periodicity, and the governing rock mass parameters may prove to be significant in predicting the onset of large seismic events. This would be of particular importance in mining remnant pillars, which would experience a similar loading pattern as the rock in front of the slot in these block tests.

Underground observations (e.g. Adams et al., 1981, Berlenbach & Schweitzer, 1996) and numerical modelling of tabular stope excavations (Napier & Hildyard, 1992, Sellers, 1997) have emphasised the importance of the parting planes, associated with the stratified rock mass, in the development of fractures ahead of, and surrounding, the stope face. To investigate the effect of the presence of parting planes on fracture formation, a sample was constructed from four stacked blocks resulting in two discontinuities located above and below the open slot. To ensure horizontal symmetry, two slots were machined from both the top and the bottom blocks to a depth of 0,25 mm to give an overall slot opening width of 0,5 mm. A sample without any discontinuities was also prepared and tested for comparison purposes. The specimens were prepared from Black Reef quartzite. The sample with the parting planes consisted of four 20 mm thick blocks. The friction angle on each interface was measured as 26°. Acoustic emission monitoring of the sample was performed to attempt to obtain an indication of the position and direction of fracture growth. This information is important to distinguish between fractures growing down from the partings and those growing up from the slot.

Figure 4.4.1.4a shows the located acoustic emission (AE) events in the sample without parting planes. In Figure 4.4.1.4a, the event symbols are scaled to the inverse of the time, so that earlier events have larger symbols. Early on in the test, a vertical fracture grew from the bottom of the sample towards the slot, and some distance ahead of the slot. The numerical models and fractographic observations confirm that this grew due to tension induced on the boundary as the

lower portion of the block acts as a cantilever and bends towards the slot. Numerical studies indicate that this occurs when the boundary conditions are relatively soft and the sample has a high Young's modulus. The events are clustered in the same regions as the observed fractures (see Appendix 4.1). The events in the centre of the sample correspond to the fractures, which curve into the hangingwall from the edge of the stope. A small cluster of events at the edge of the sample corresponds to a small horizontal fracture observed about half way up the edge of the upper block.

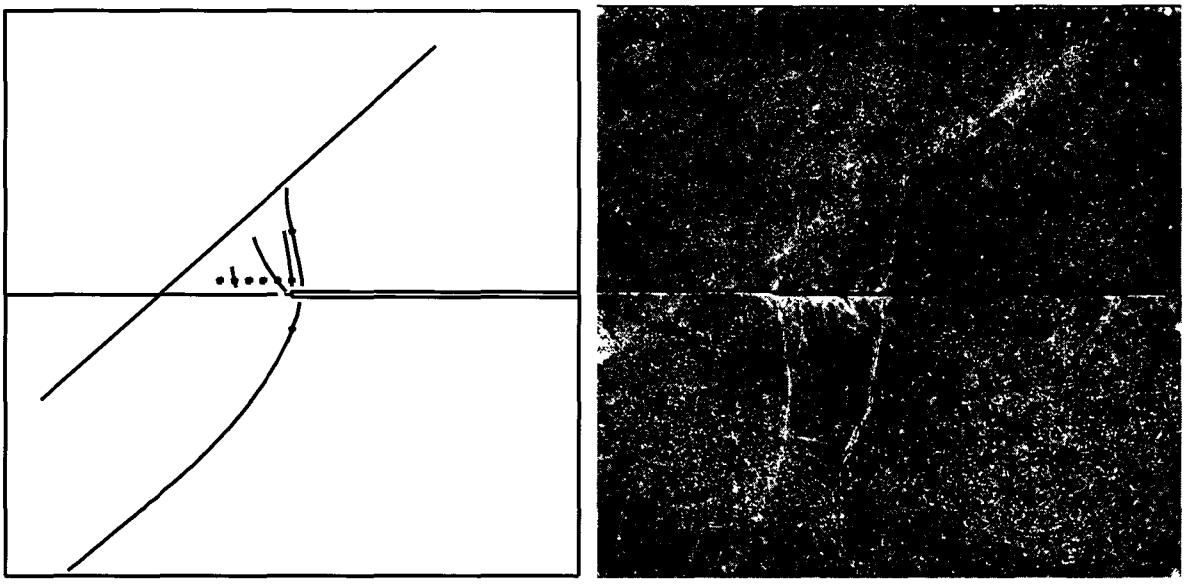

Figure 4.4.1.3 Final fracture patterns observed from numerical and physical modelling of the block with a natural discontinuity ("away from the stope" side).

Two steps were mined in the sample containing the parting planes and, in each step, the positions of the AE events correspond closely to the cracks observed (Figure 4.4.1.4b). In the first step, the vertical cracking is evident in the two footwall blocks, ahead of the stope. There is less AE activity in the immediate hangingwall block and the located events in the centre of the sample correspond to the angled crack extending from the slot tip. In the top block, two small clusters of events relate to the initiation of two small vertical fractures ahead of the face. These fractures are initiated from the parting plane as the plates cantilever in towards the open slot. In the second step, these vertical fractures ahead of the slot extended through the sample and the angled cracks in the hangingwall extended to connect the slot with the parting plane above, as shown by the AE events above the slot.

The fracture pattern obtained from the numerical simulation of the parting plane model is shown in Figure 4.4.1.5. A tension mode of failure was selected for the formation of the cracks from the designated seed points with zero tensile strength and a residual friction angle of 20°. In Figure 4.4.1.5, the fractures extend behind the advancing slot. The predicted crack angles are very close to those of the physical. The asymmetry of the numerical crack pattern is, once again, due to the choice of seed points. In this case, the selected seed points resulted in a fracture pattern that is very close to the observed pattern, but upside down i.e. in the numerical model the two angled cracks grew upwards whereas they grew downwards in the physical model. Again, the DIGS model predicts a fracture pattern that is very close to the observed one, but cannot exactly predict the observed pattern due to the specific distribution of flaws in the tested sample.

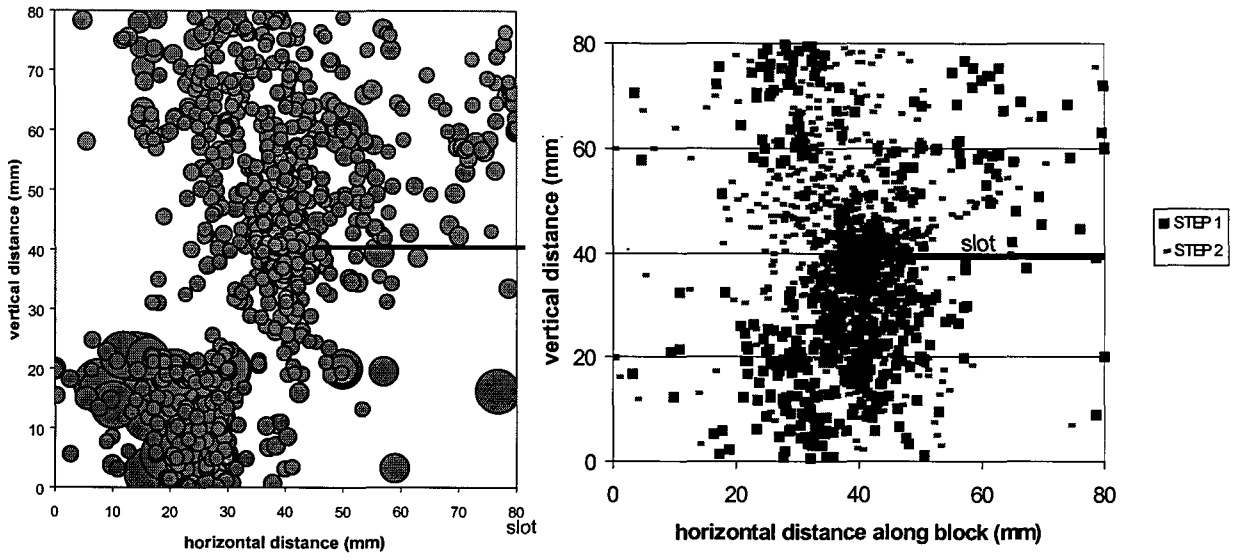

a: b:

Figure 4.4.1.4 Locations of acoustic emissions determined in physical models using Black Reef quartzite. a) sample without parting planes (with symbols scaled to "youth" i.e. earlier events have larger symbols), b) sample with parting planes.

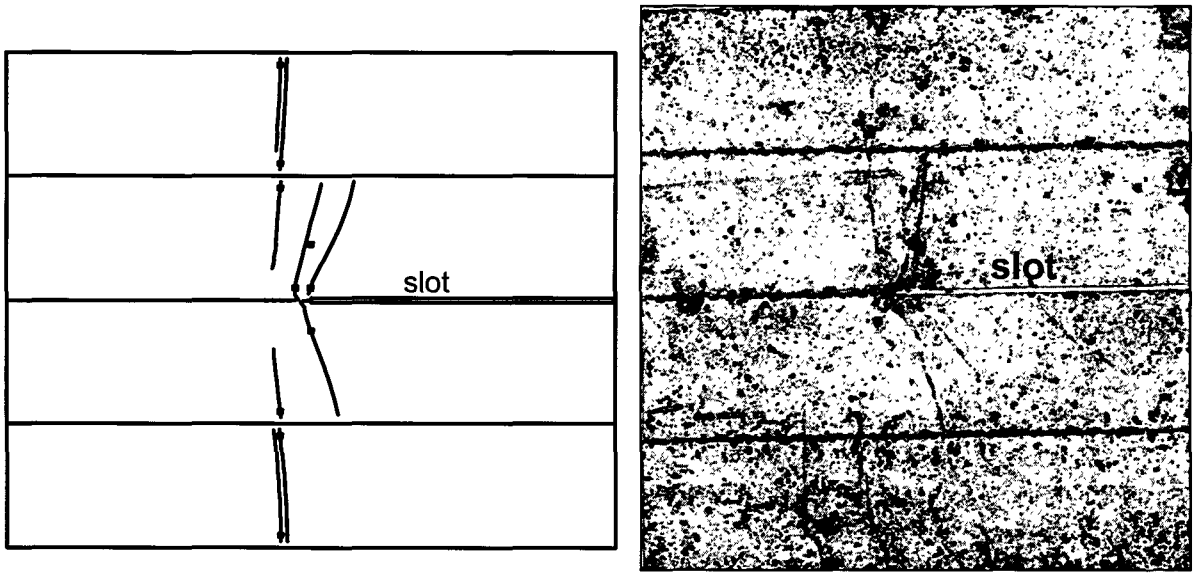

Figure 4.4.1.5 Comparison of the results from the numerical and physical modelling of parting planes in Black Reef quartzite. (Image inverted and photo-manipulated to enhance the fracture pattern)

These comparisons have been very valuable in confirming that the DIGS discrete fracture growth code can predict the fracturing arising from the complicated stress state surrounding a slot in a cube of rock. The physical and numercial modelling has confirmed that fractures are initiated at horizontal parting planes, as suggested by Napier & Hildyard (1992). It was also found that pre-existing discontinuities can alter the stress distribution within the sample, depending on the interface properties, and hence affect the fracture pattern. The three-dimensional acoustic emission location provides useful information regarding the sequence of fracture growth and the growth directions, which correlate well with the numerical simulations (see Appendix 4.1).

4.4.1.2 Simulating strip punch experiments with a tessellation approach in DIGS

The difficulty in modelling the failure processes in brittle materials is associated with making a suitable choice of building block which can be used to synthesize large scale patterns of failure. In the case of a continuum plasticity formulation it is necessary to postulate the flow rule for the basic continuum element and to calibrate the details of the flow rule parameters against suitable laboratory tests. An alternative approach is to assume that the fundamental composition of the rock fabric is in the form of interacting particles (Cundall,1989; Handley, 1996) or some generalised cellular structure (Wilson et. al.,1996). The approach followed here is to assume that the basic failure mechanism is a sliding crack. Failure is then modelled by tracking the successive mobilization of a random assembly of such cracks. This approach is described in detail in Section 2.4.3. The specific case where the cracks are associated with the arcs of a Delaunay triangulation is investigated. The model is applied to the problem of a loaded rectangular strip punch. The effect of allowing the cracks to initiate sequentially or simultaneously is investigated and the results are compared to the experimentally observed fracture patterns. The possibility of formulating a macro shear fracture growth rule that is equivalent to the detailed coalescence processes is examined.

The question arises, however, as to the applicability of the Delaunay tessellation when modelling fracturing in circumstances where the stress field is rapidly varying as is the case near the edge of a mining excavation or in the vicinity of a stabilizing pillar. Sellers (1997) has performed a number of simulations of fracturing near tabular shaped openings in layered and unlayered strata, using Delaunay tessellations to represent the fracture paths. In the cases studied, an encouraging qualitative agreement has been obtained between modelled and observed fracture patterns. A more quantitative test for the approach is afforded by strip punch experiments to examine the pattern of fracturing induced below a rigid rectangular punch applied to the surface of a cubic block (see Figure 4.4.1.6 and Appendix 4.2).

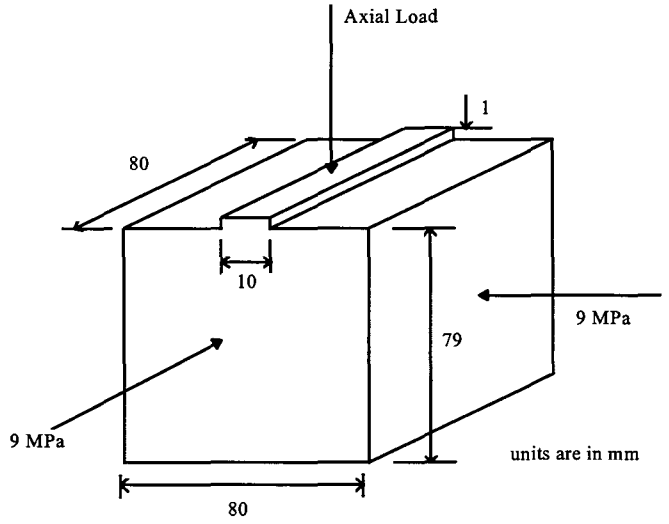

Figure 4.4.1.6 Dimensions of strip punch test specimen.

The cubic sample profile described in the previous section was modelled with a rectangular boundary comprising 320 plane strain displacement discontinuity boundary elements. The edge below the loading platen comprised ten elements. This edge was displaced uniformly in a series of eight loading steps such that the final displacement yielded an average stress of approximately 500 MPa on the punch. A sub-region of the sample, 30 mm wide and nominally 80 mm high, was selected below the punch and filled with a random mesh of Delaunay triangles. This resulted in a tessellation comprising 4444 segments with a total length of 6257,8 mm. The statistics of the mesh segments are given in Table 4.4.1.2.

Table 4.4.1.2 Class interval and other statistics of segments comprising the tessellation used in the punch loading problem.

Size interval (mm)	0,0-0,4	0,6	0,8	1,0	1,2	1,4	1,6	1,8	2,0	2,2	2,4	2,6	2,8	3,0
Number of Segments	0	0	18	508	898	902	847	664	367	181	44	13	2	0

A series of numerical simulations was carried out to investigate the effect of the growth strategy, parallel or incremental, and to examine the effect of the choice of the failure parameters, namely the peak and residual friction angle, the peak and residual cohesion and the tension cut-off on the fracture pattern in relation to the observed patterns shown in Figure 4.4.1.7a. The failure parameters chosen correspond to a material having a uniaxial compressive strength of 200 MPa and a tensile strength of 25 MPa. These are representative but not exact values for the quartzite specimens described previously. The Young's modulus and Poisson's ratio of the intact material were assumed to be 68 GPa and 0,19 respectively. Figure 4.4.1.7b illustrates the final fracture pattern obtained from the modelling using an incremental growth rule. Further results are given in Appendix 4.2.

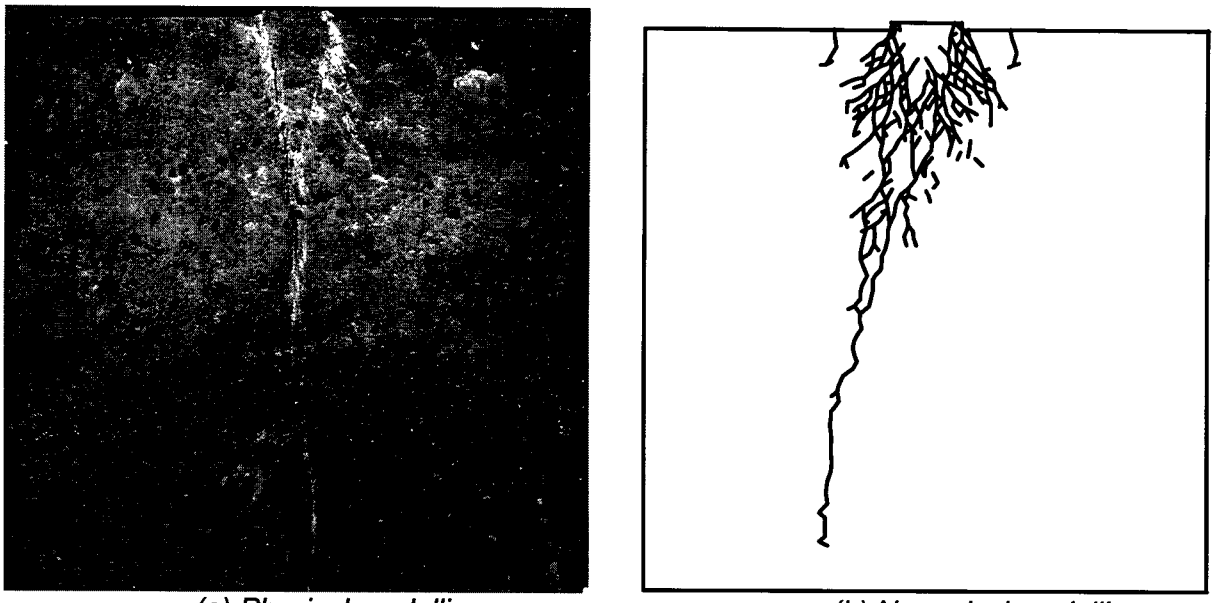

(a) Physical modelling *(b) Numerical modelling*

Figure 4.4.1.7 Strip punch experiments.

Encouraging agreement has been obtained between physical experiments and numerical simulations of fracture formation processes for these rectangular strip punch experiments (Figure 4.4.1.7). This suggests that some confidence can be placed in the use of a random mesh to represent complex failure processes near mine openings in hard rock. It is important to note that the failure pattern is best modelled by assuming that the fracture is initiated in a sequential manner by choosing the mesh segment that is most likely to fail in each step.

4.4.1.3 Simulating three dimensional fracture patterns around openings

Section 2.4.8 describes the development of a three dimensional fracture zone simulator (3DIGS). Some laboratory experiments were carried out both as a preliminary validation of this code and in order to address the fundamental question of three dimensional fracture initiation processes. It must be noted that the 3DIGS fracture growth simulator requires considerable

additional development and that the selection of suitable three dimensional tessellation structures has not been determined. The laboratory experiments were performed on cubical Elsburg quartzite samples with a machined lead-lag slot geometry shown in Figure 4.4.1.8. The final fracture pattern after loading is shown in Figure 4.4.1.9 (also see Appendix 4.3).

The initial attempt to model three dimensional fracture growth simulation showed that fractures initiate and propagate from the edges of the stress raising slot (Figure 4.4.1.10). Further results are given in Section 2.4.8 of this report. The tessellation approach (Napier at al., 1997) has been applied to model a two-dimensional section of the model. The resulting fracture pattern is shown in Figure 4.4.1.11. The upper half of the block experiences a series of fractures dipping above the slot, and an en echelon pattern of fracturing in the lower block. This fracture pattern provides a close representation of the fracturing, for example the Elsburg quartzite model shown in Figure 4.4.1.9a. Testing of more siliceous rock types leads to narrower fracture zones. These require a finer tessellation density to be used in the modelling.

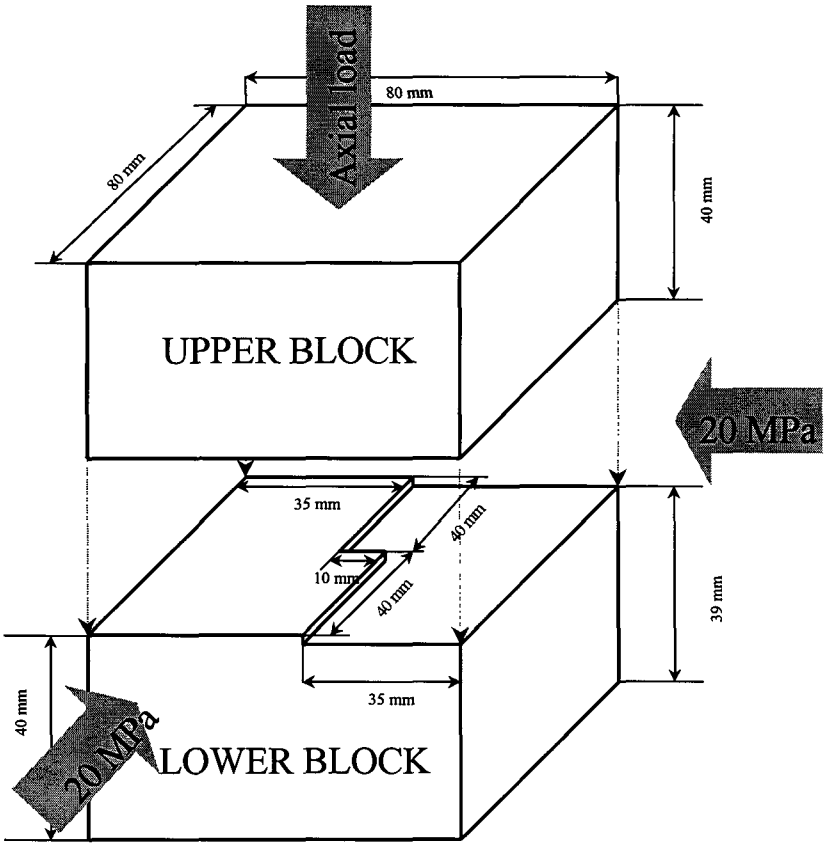

Figure 4.4.1.8 Layout and dimensions of sample used in lead-lag laboratory experiment.

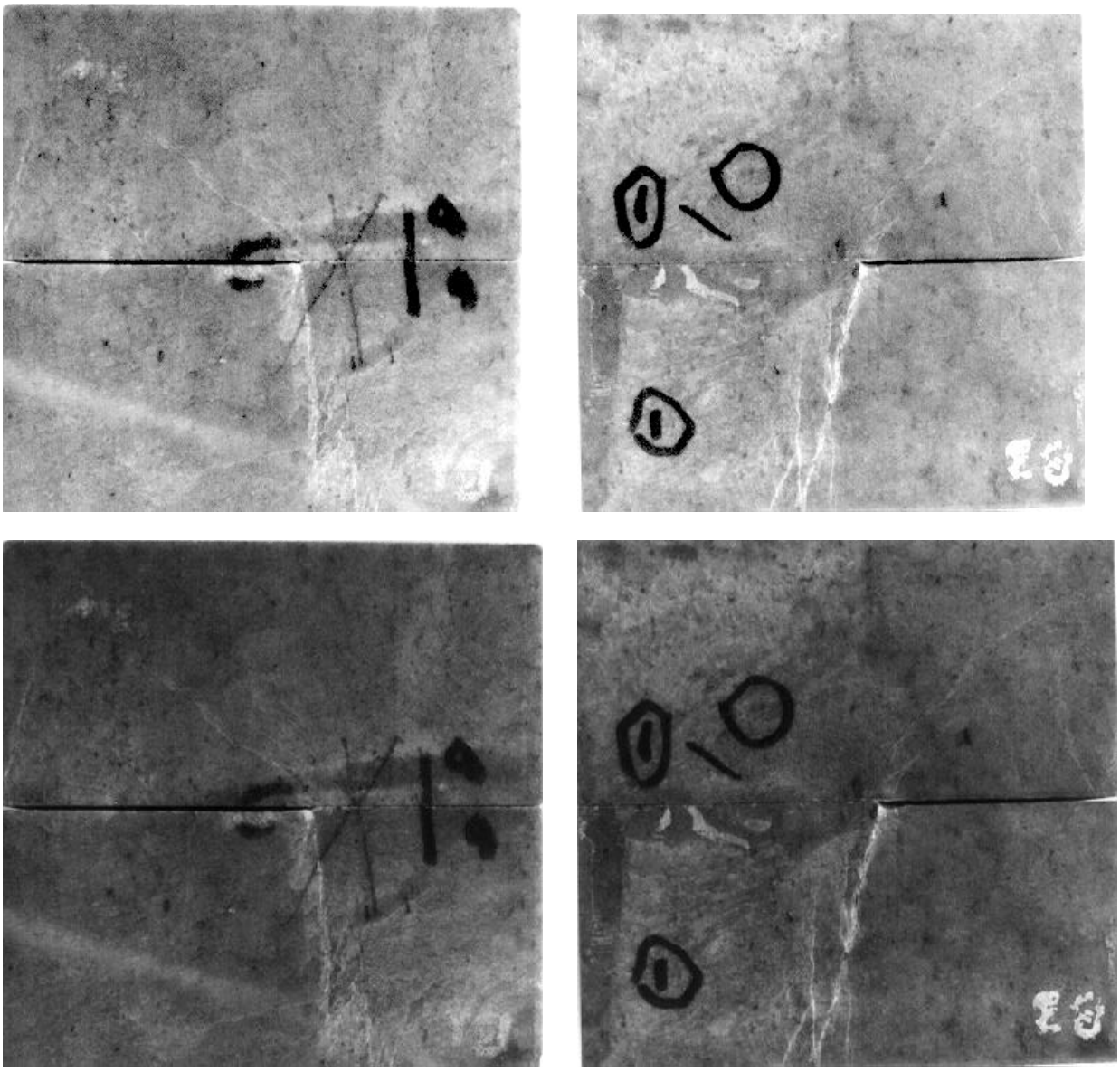

(a) (b)

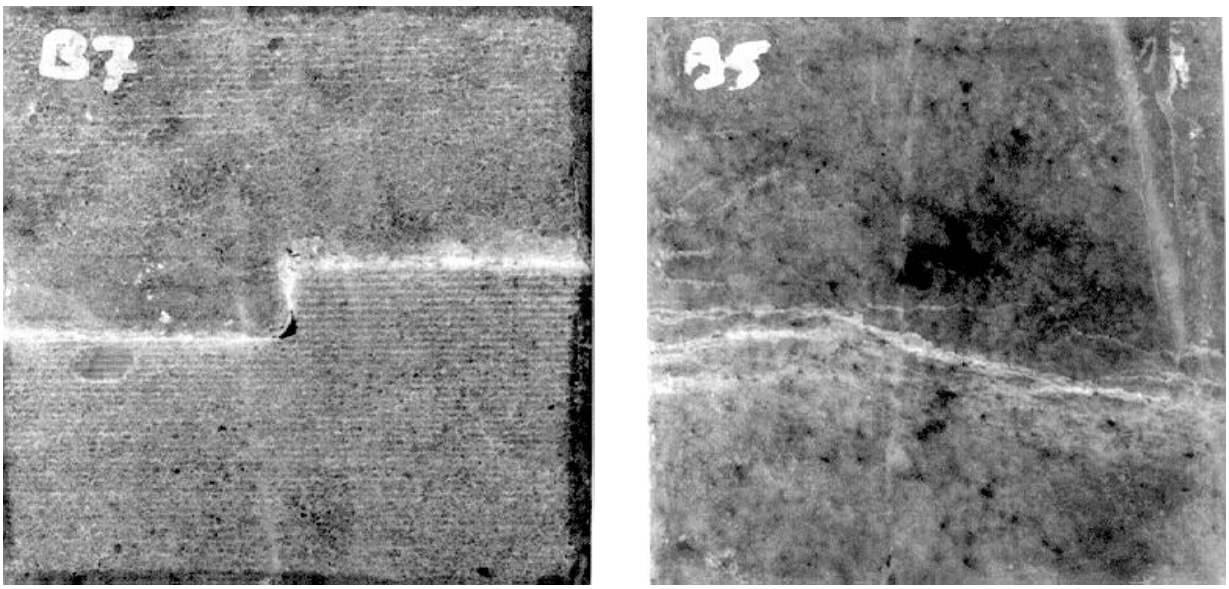

(c) (d)

Figure 4.4.1.9 Laboratory results of the lead-lag experiment (a) side view (b) side view, (c) view from the bottom and (d) top view of lower portion of the sample.

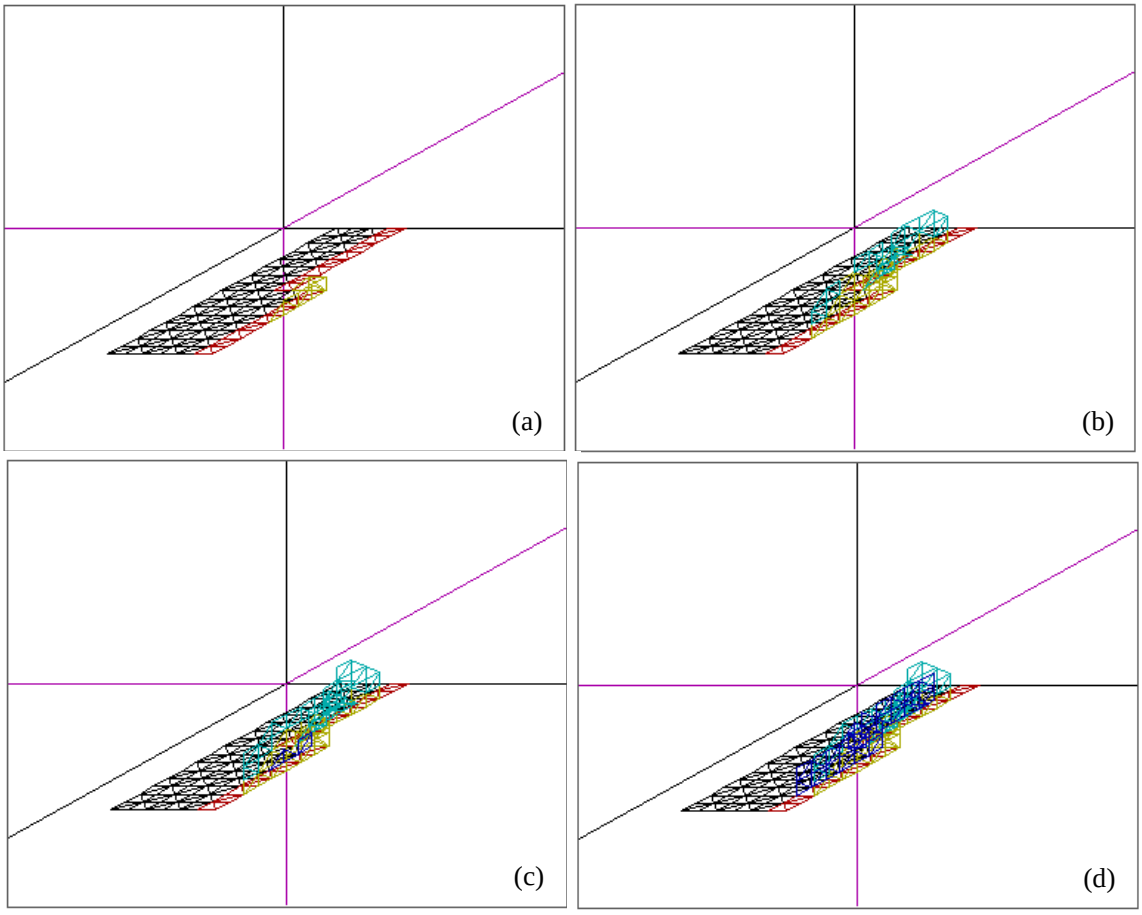

Figure 4.4.1.10 Simulated three dimensional fracture propagation at different stages of the mining using 3DIGS.

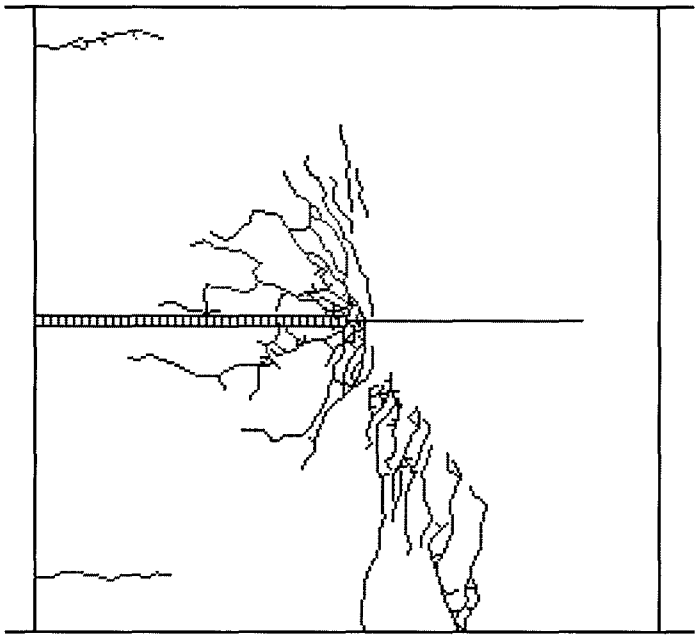

Figure 4.4.1.11 Simulated two-dimensional fracture pattern using tessellation method.

4.4.2 Stope observations and modelling

4.4.2.1 Introduction

Although the numerical simulation of the laboratory experiments has given encouraging results, it is vital that a fracture zone simulator should be able to reproduce actual stope fracture patterns and behaviour. Therefore, the laboratory studies was supplemented with underground observations. It is crucial for any of the rock engineering strategies proposed for safe and efficient mining of ultra deep orebodies to be able to predict the response of the rock mass to a planned mining layout (Gay et al., 1995). For example, the design of effective support systems depends on the fracture directions and spacing in the hangingwall, which in turn are influenced by the rock properties and the geological structures in a particular geotechnical area (Schweitzer & Johnson, 1997). The development of the fracture pattern around a stope and the seismicity associated with mining is also influenced by the primary geological structures, such as faults and dykes which are located in the vicinity of the stope (e.g. Legge & Spottiswoode, 1987). Monitoring of the seismicity can possibly identify potential hazards once mining has started, however the evaluation of alternative mining strategies requires the ability to simulate the development of the fracture zone around potential mining layouts in a given geological environment.

Detailed discussions of the relationships between the stability of an excavation or mining layout and geological structures are provided by Adams et al. (1981), Gay & Jager (1986) and others. An overview is given by Schweitzer & Johnson (1997) who divide geological parameters into two classes:

- Primary features: rock type, sedimentary structures (e.g. planar and cross beds), reef geometry (e.g. rolls), lithological contacts and flow bands.

- Secondary features: joints, extension gashes, faults, dykes, metamorphism.

The primary features can be modelled in the displacement discontinuity boundary element context by altering the strength of the potential fractures. Layering, bedding and rolls are best modelled with the tessellation approach (Section 2.4.3) by altering the strength properties of the potential discontinuity positions in the relevant regions. In the discrete growth mode, fracture properties are defined by the original seed position and do not change to represent different layers. In both methods, the secondary features are modelled explicitly as displacement discontinuity elements, with a Mohr-Coulomb failure criterion and post-failure properties.

A mining procedure was developed where the stope excavation is modelled as a slot. In each mining step, a rectangular block is removed to increase the span of the slot. The closure of the hangingwall elements is limited to the stope width. Any active or potential elements existing within the removed block are deactivated, to prevent numerical instabilities.

The tessellation method has been applied to the modelling of large scale mining simulations with a finite stope width, using the multipole method (Napier and Pierce, 1997, Sellers, 1997). The ability of the tessellation approach to model fracturing around stopes in various geotechnical environments is demonstrated and compared with examples of Carbon Leader stopes.

4.4.2.2 Underground study sites

Underground studies concentrated on Carbon Leader and Vaal Reef stopes in the Carletonville and Klerksdorp areas. These two reef horizons are economically important for future mining operations (Schweitzer & Johnson 1997). Detailed stratigraphic descriptions are provided in Berlenbach & Schweitzer, (1996). Observations were undertaken at Doornfontein, East Driefontein, Vaal Reefs and Western Deep Levels East mines. Site depths varied from 2000 m to 3400 m below surface (Berlenbach & Schweitzer, 1997).

4.4.2.3 Effect of rock type and bedding

The influence of some primary geological features, such as different rock types and the existence of bedding planes, is best investigated using the Carbon Leader reef. The Carbon Leader is a narrow conglomerate seam, with a maximum thickness of 45 cm, overlying a complex quartzite sequence with alternating incompetent and competent partings. The Carbon Leader is immediately overlain by a competent, medium- to coarse-grained siliceous quartzite, between 1,4 m and 4 m thick. The quartzite is overlain by the Green Bar, a 1,0 m to 2,5 m thick argillaceous unit. The transitions between these two lithologies are defined by pronounced parting planes with a low friction angle (peak friction angle, ϕ, is 5° and residual friction angle, ϕ_m, is 2°). The studies of fracture formation were performed using a tessellation geometry, which is an idealization of the geological environment surrounding a Carbon Leader stope. The different rock strengths are represented by specification of different values of cohesion. A 2 m wide layer of a strong rock, corresponding to the siliceous hangingwall quartzites overlies the reef. A 1 m layer of weak rock overlies the hangingwall layer and is delimited by two parting planes and represents the Greenbar shale. The reef and the rest of the hangingwall have the same properties as the hangingwall beam. The footwall is modelled as an intermediate strength material. All other parting planes have a peak friction angle, ϕ, of 10° and a residual friction angle, ϕ_m, of 5°.

Table 4.4.2.1 Material properties for Carbon Leader rocks calculated from laboratory tests (Briggs, 1983) with the UCS (uniaxial compressive strength) reduced for calculation of the in-situ cohesion

Rock type	UCS	lab cohesion	*In situ* cohesion		Friction angle		tensile strength
	MPa	MPa	MPa		initial	mob	MPa
Hangingwall Quartzite	320	52	18		52	30	5
Footwall Quartzite	200	52	18		43	25	5
Greenbar	180	52	18		32	20	5

A series of laboratory tests on the Carbon Leader hangingwall and footwall quartzites, and the Greenbar shale (Briggs, 1983) were analysed to obtain realistic material parameters (see Table 4.4.2.1). For the Mohr - Coulomb failure envelope, the cohesion S_o depends on the unconfined compression strength (UCS) and the friction angle ϕ (Jaeger & Cook, 1979) and is expressed as

$$S_o = \frac{UCS}{2\tan(45+\phi/2)} \qquad (4.4.2.1)$$

As shown in Table 4.4.2.1, the relative values of the UCS and the friction angle resulted in a similar value of cohesion for all three rock types. A number of test programs, using different types of rock, suggest a reduction in strength as the size of the sample increases (Martin, 1997). As a first approximation, the strength of the in situ rock is about 30% of the value obtained for small test specimens (e.g. Martin, 1997, Raffield et al., 1993). Thus, to simulate *in situ* properties in an analysis, the cohesion was reduced to 30% of the calculated laboratory strength.

The fracture patterns for the two cases of laboratory and in situ cohesion values are shown in Figure 4.4.2.1 for a span of 14 m. Both analyses demonstrate similar fracture patterns, although the low strength *in situ* properties result in considerably more fracturing ahead of the face. In the initial steps, the fracturing is mostly in the footwall. As the mining progresses, a sub-horizontal fracture develops in the hangingwall whilst the footwall continues to exhibit steeply dipping fracturing. Subsequently, fractures open in the lower footwall, sub-parallel to the bedding planes. As the span increases, fracturing extends ahead of the face.

In the analysis with lower cohesion, Figure 4.4.2.1a, an extensive zone of fracturing extends about 6 m ahead of the stope face. Immediately ahead of the face, open sub-vertical fractures are connected by inclined fractures, which exhibit shear, into a shear zone dipping away from the face. Further ahead of the face, a smaller shear zone dipping towards the face follows a region of unfractured rock. These possibly correspond to the shear zones reported from fracture mapping studies in Carbon Leader stopes (Adams et al., 1981; Brummer & Rorke, 1984) and shown in Figure 4.4.2.2. Details of the deformation and stress profiles are given in Appendix 4.4. Dilation is evident for about 6 m ahead of the stope face, and the deformation becomes compressive at, or just behind, the face. The different magnitudes of dilation indicate that the hangingwall moves further towards the stope than the reef and footwall leading to a ralative shear movement between the layers, as observed underground (Legge, 1986). The analysis with laboratory properties, Figure 4.4.2.1b, exhibits only 1 m of fracturing ahead of the face.

To consider the effect of fracturing, on the stress ahead of the face, stress distributions for a set of grid points in the middle of the reef layer are shown in Figure 4.2.2.3. About 20 m ahead of the face, the stress equals the initial virgin stress state. The stress increases to a maximum about 6 m ahead of the stope, just ahead of the fractured zone, and the maximum induced stress is about 30 MPa. The vertical stress decreases within the fractured zone, and is about

10 MPa within 2 m of the face. The analysis with less fracturing results in a maximum stress that is 22 per cent higher than the maximum in the highly fractured case and the position of the maximum stress is much closer to the face. The horizontal stress decreases more when there is less fracturing and thus, the ratio of maximum to minimum principal stresses will increase and bring the rock mass close to the failure state. This could imply a greater risk of face bursting. Thus, techniques such as preconditioning that increase the fracturing ahead of the face will relieve the face stresses. However, in this model, the closure is more than doubled in the presence of considerable fracturing ahead of the face, as shown in Figure 4.4.2.4. This is explored further in Section 4.4.3 in relation to the time-dependent development of the fracture zone.

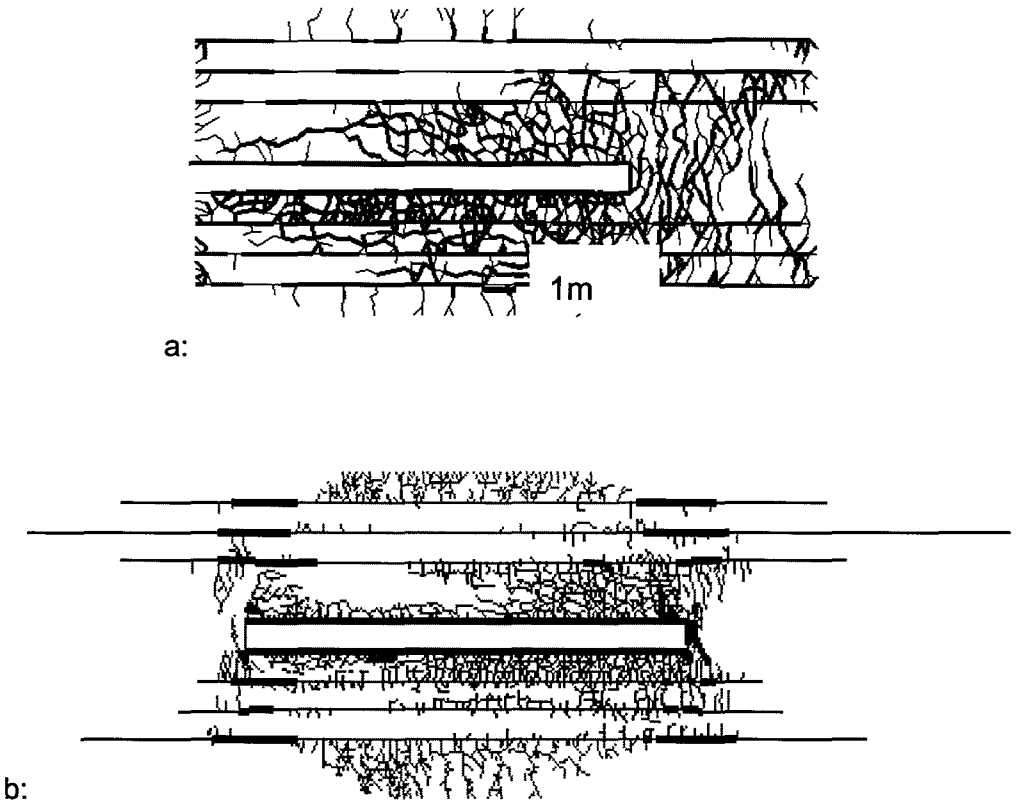

Figure 4.4.2.1 Predicted fracture pattern around Carbon Leader stope after 14 mining steps. a: in situ properties b: laboratory properties.

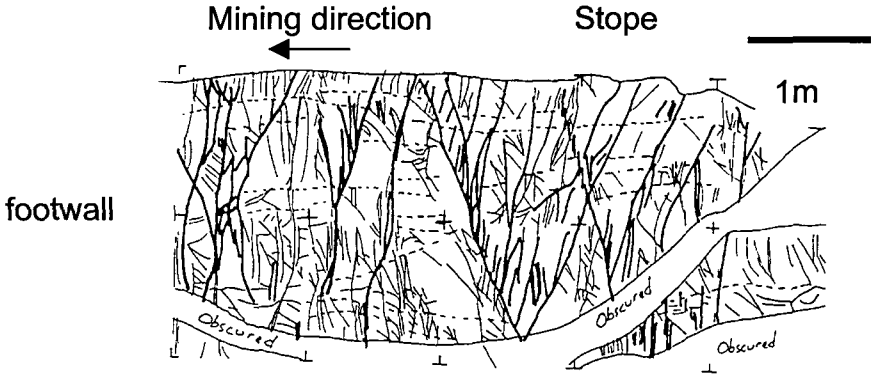

Figure 4.4.2.2 Fractures in the footwall of a Carbon leader stope, mapped from photographs (Brummer & Rorke, 1984).

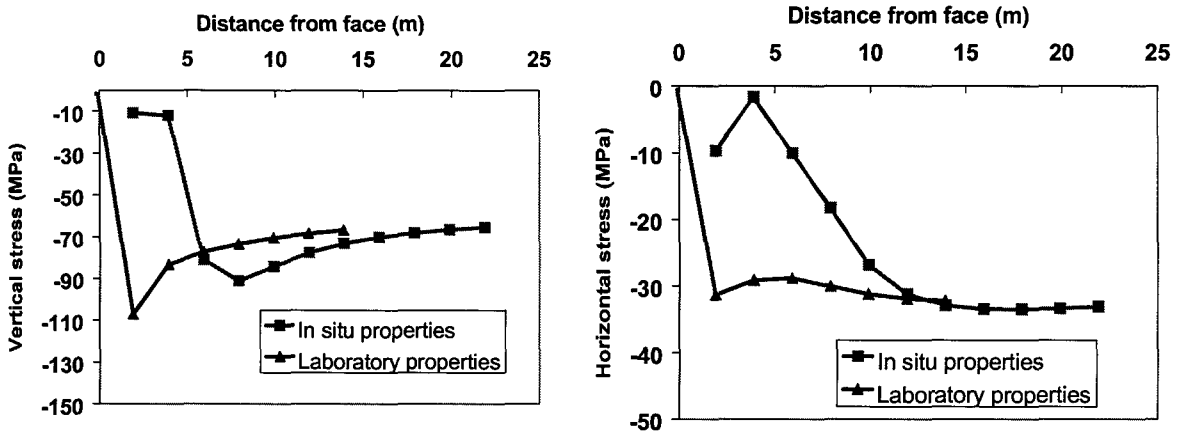

a) b)

Figure 4.4.2.3 Comparison of stress distribution ahead of face for stope models with laboratory and in situ material properties at a span of 14m. a) vertical stress b) horizontal stress.

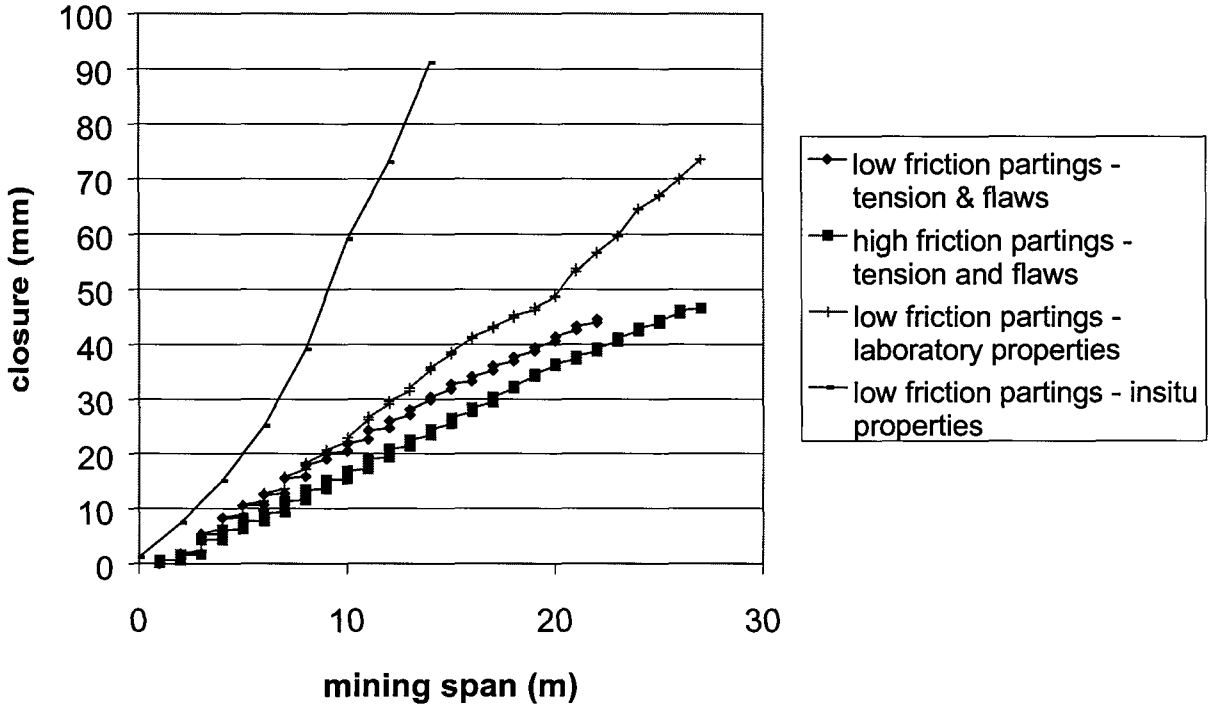

Figure 4.4.2.4 Increase in maximum closure due to a change in material properties, fracture activation criteria and parting plane friction.

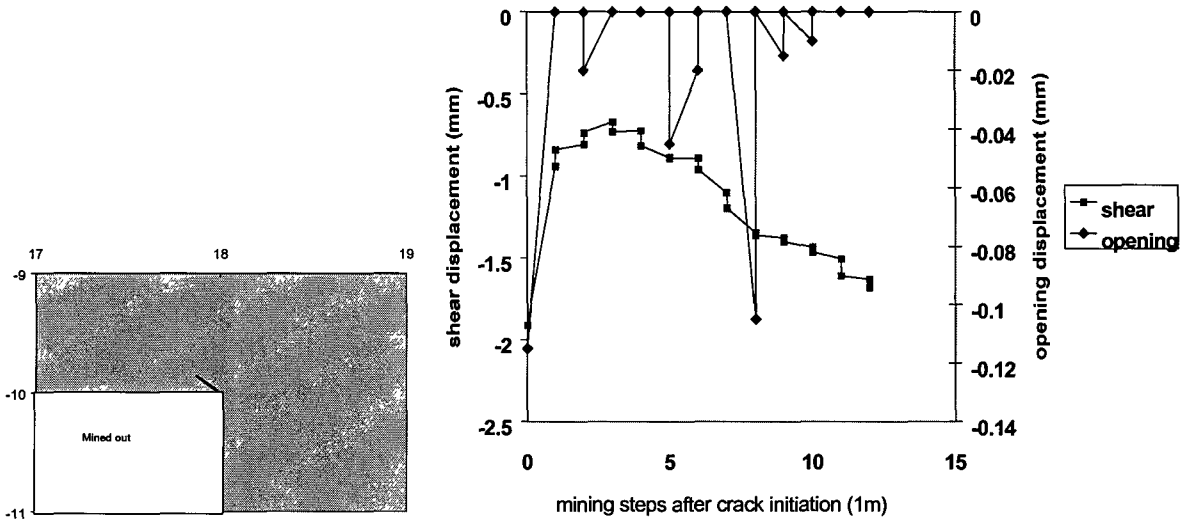

Figure 4.4.2.5 Comparison of opening and shear displacements on a crack in the hangingwall for a stope model with laboratory material properties. (Inset shows position of crack at activation at a span of 10m).

The rock mass response around the stope is thus highly controlled by the fracture zone. This response, in turn, affects the selection of support. It is therefore important to understand the behaviour of the fractures in the hangingwall. The shear and opening displacements for a single crack in the hangingwall of the model with laboratory material properties are shown in Figure 4.4.2.5. The crack activated at a span of 10 m and dips at 45° towards the face. It can be seen that the crack experiences several opening and closing phases as mining progresses.

4.4.2.4 Influence of parting planes

When the initial friction angle on the parting plane is high, φ = 30° and φ_m = 30°, corresponding in practice to lithological contact on the parting planes, the fracture zone is found to extend behind the stope face (Figure 4.4.2.6a). Slip on the partings is only evident, above and below the excavated region and the length of parting plane that has experienced slip decreases away from the stope horizon. The active fractures tend to be aligned in the vertical direction, especially in the immediate hangingwall and footwall. The fractures are observed to be continuous across the parting planes.

Reduction of the initial friction on the parting to φ = 5° and φ_m = 4°, suggesting a parting plane containing material with a low friction angle associated with the shale layer, causes the partings to activate ahead of the stope face. The magnitude of slip varies over the length of the parting and is greatest in the region of the stope face, as denoted by the thicker lines in Figure 4.4.2.6b. Fractures form at the surfaces of the parting planes closest to the stope. Thus, the rock between the partings acts as a set of cantilevered beams, which fail in tension at the point where the slip initiates, and the remaining beam is clamped ahead of the face. These positions of fracture activation due to slip on low friction parting planes correspond well with similar predictions using discrete fracture analyses (Napier & Hildyard, 1992).

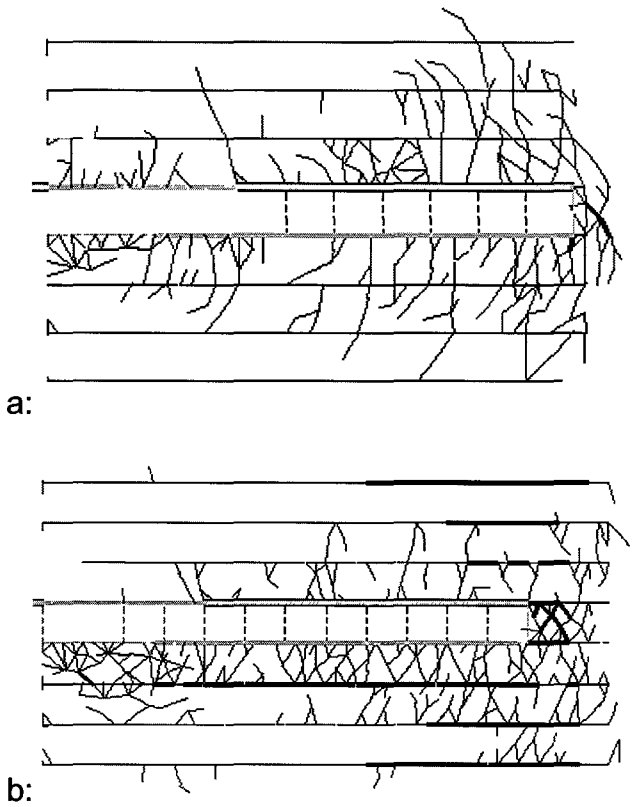

Figure 4.4.2.6 The effect of parting planes on the fracture pattern around a stope. a) high friction angles on parting planes with $\phi = \phi_m = 30^o$, b) low friction angle parting planes with $\phi = 5^o, \phi_m = 4^o$.

4.4.2.5 Inclusion of random parting planes

An apparent conflict arises between the requirement for low friction angles on the partings and laboratory test results (e.g. Malan, 1998) that indicate higher friction angles of about 30° for quartzite-quartzite interfaces. This can be resolved by explicitly including random variations in the amplitude and wavelength of the parting planes in the models, and specifying realistic friction angles of 30°. Underground observations suggest that the partings are related to the sedimentary structures such as cross bedding and flow structures in lava (Schweitzer & Johnson, 1997) and thus are seldom perfectly planar. This can be seen in the observations of Brummer & Rorke (1984), as shown in the dotted lines of Figure 4.4.2.2. The photograph of a stope hangingwall shown in Figure 4.4.2.7 confirms that the partings can have a wavelength of several metres and significant, and variable, amplitudes.

An equation was developed for a random parting plane, based on the sine wave function, and was applied to generate a tessellation representing a Carbon Leader stope. The wavelength selected for the partings is also random, but in the region of 5 m, and the amplitude is about 0,25 m. The fracture pattern produced is shown in Figure 4.4.2.8. The mining is towards the right, and both the active and passive faces indicate fracturing some distance ahead of the face. The fracture patterns ahead of the face have a similar pattern to rockburst fractures due to shear rupture observed underground. Figure 4.4.2.9 shows that the stope closure is strongly influenced by the way that the parting plane is characterized. The higher closure associated with the variable partings should enable the prediction of closure at realistic stope spans. Since there is no dilation specified on the partings, the additional closure is due to the wedging open of parting planes due to the explicitly included roughness.

The model clearly indicates that fractures form ahead of the face, even when the friction on the partings is realistic. The fractures form around the stope face at dip angles that are similar to observations, and exhibit zones of unfractured rock ahead of the stope. These zones may correspond to the periodic "hard patches" reported by Adams et al, 1981, and associated with the presence of irregular bedding planes (King et al., 1990). In the models, the amount of fracturing ahead of the face also varies for different mining spans. There are also differences in the fracture pattern, for the same span, if the face position is shifted relative to the parting planes.

Figure 4.4.2.7 Photograph of a Carbon leader stope showing the variation in the hangingwall parting plane amplitude

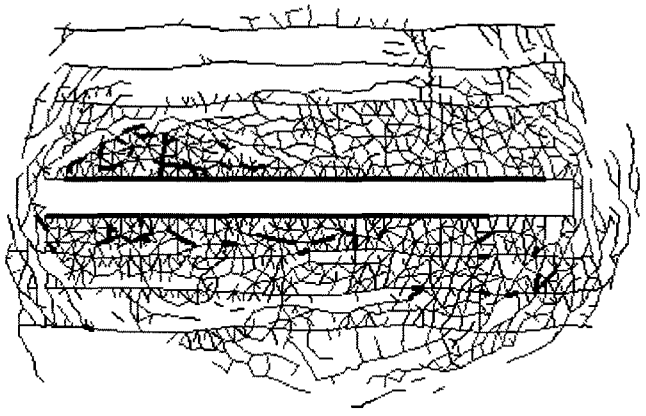

Figure 4.4.2.8 Fracture pattern predicted for stope with random amplitude parting planes with incremental analysis. Maximum amplitude of parting is 0,25 m and the wavelengths are approximately 5 m. Material properties are similar to those in Table 4.4.2.1, but with no tensile strength.

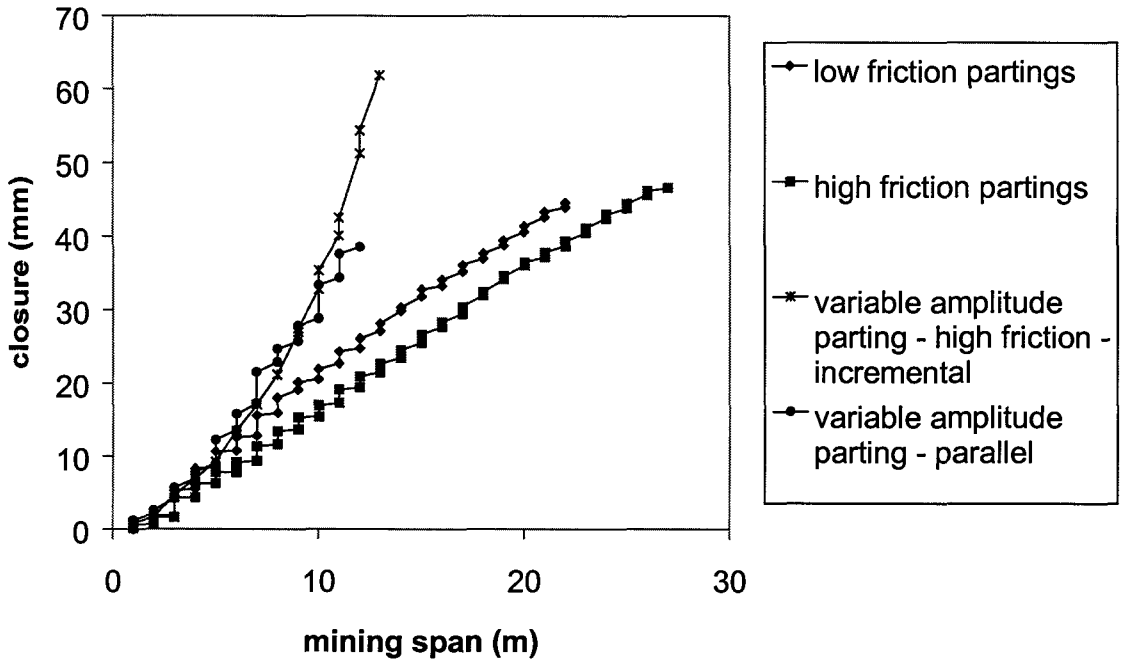

Figure 4.4.2.9 Increase in maximum closure due to changed parting plane friction, random amplitude partings and activation rule.

The addition of a tensile strength results in a similar pattern, as shown in Appendix 4.4, but there is less fracturing sub-parallel to the hangingwall and more fractures develop ahead of the face.

4.4.2.6 Effect of pre-existing joints

The dominant geological structures at the Doornfontein and Western Deep Levels sites were quartz filled extension gashes in the quartzite overlying the Carbon Leader. At Doornfontein, the strike of the extension gashes deviates by approximately 15° from the strike of the face and the average dip is 85° away from the face. Mining induced fractures are consistently parallel to the extension gashes i.e. opposite to conventional concepts of mining induced extension fracturing which suggest that the fractures dip towards the face (Adams et al. 1981). Similarly, fractures are parallel to extension gashes in the footwall quartzites. The relationship between fractures and extension gashes suggests that the gashes, and/or residual stresses, influenced fracture formation. At the Western Deep Levels site, the extension gashes and the associated mining induced fractures dip towards the face.

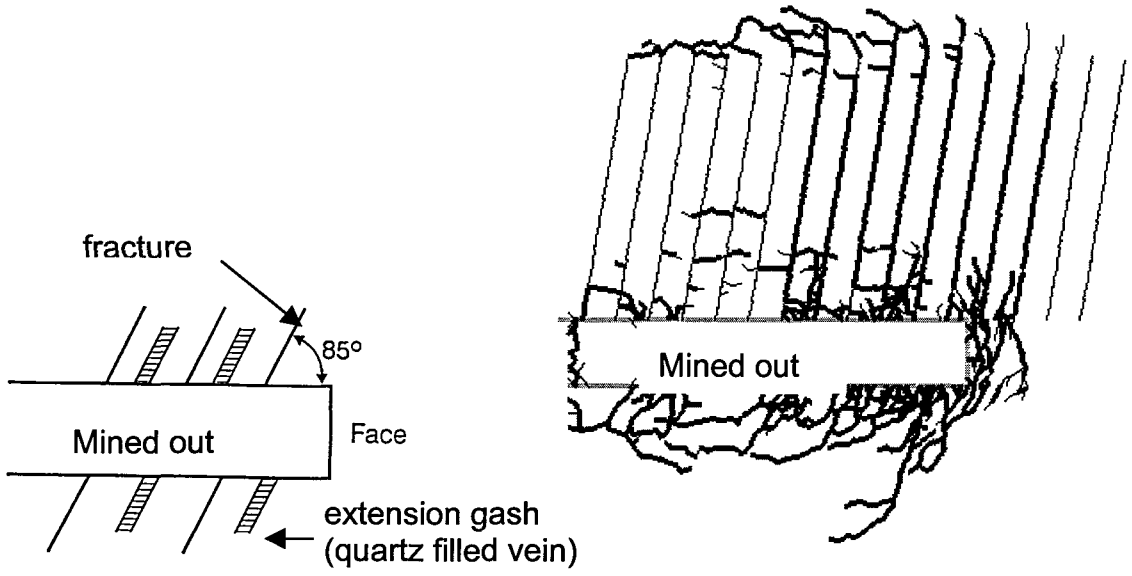

Figure 4.4.2.10 Activated fractures in a tessellation analysis of a stope with a set of steeply dipping, healed, joints/extension gashes in the hangingwall

A model was developed to investigate whether pre-existing joints, or extension gashes, set in the hangingwall and dipping at 80° away from the face with a spacing of 0,5 m, could induce extension fractures with the anomalous dip observed at Doornfontein. Due to memory limitations, each joint is assumed to extend only 4 m into the hangingwall. The footwall has no jointing for comparison. Each joint is 0,5 m apart and is assumed to have healed (i.e. be quartz filled) and is assigned an initial cohesion of 5 MPa. The friction angle is initially 20° and reduced to 15° upon activation. In this case, the average element size is 0,1 m. The *in situ* stress was 60 MPa in the vertical direction and 30 MPa in the horizontal direction.

As the mining progressed, the joints slightly ahead of the face failed by sliding. Fractures formed ahead of the face and extended into the hangingwall. The mining induced fractures in the hangingwall are observed to dip away from the face, sub-parallel to the jointing, as in the underground situation. Fracturing in the footwall is as expected for a uniform rock mass as the dip decreases with distance from the stope and finally becomes sub-horizontal within 1 m to 2 m of the face.

4.4.2.7 Effect of *in situ* stress

The underground observations suggested that mining in opposite directions resulted in distinctly different fracture patterns. The best example was found at the Vaal Reefs site. There, they form part of an alternating argillaceous and siliceous quartzite sequence (Berlenbach & Schweitzer 1996). Unconfined strengths range from 180 MPa to 250MPa.

In the hangingwall of the panel that was being mined in a westerly direction, fractures were found to dip between 70° and 80° towards the face. The spacing of fractures is of the order of cm-dm. The fractures are concentrated in a 80 cm thick quartzite beam and, apparently, do not extend across this parting plane. Shear fabrics (s-c fabrics) in argillaceous units within the reef horizon indicate a bedding-parallel movement towards the east (i.e. the hangingwall moved in the direction of the stope). This suggests that the in situ stress plunges to the east. Measurements of the stresses in the Klerksdorp district indicate that the major principal stress

may plunge either 60° to the east or 30° to the west (Gay et al. 1984). No stress measurements are available near the site itself.

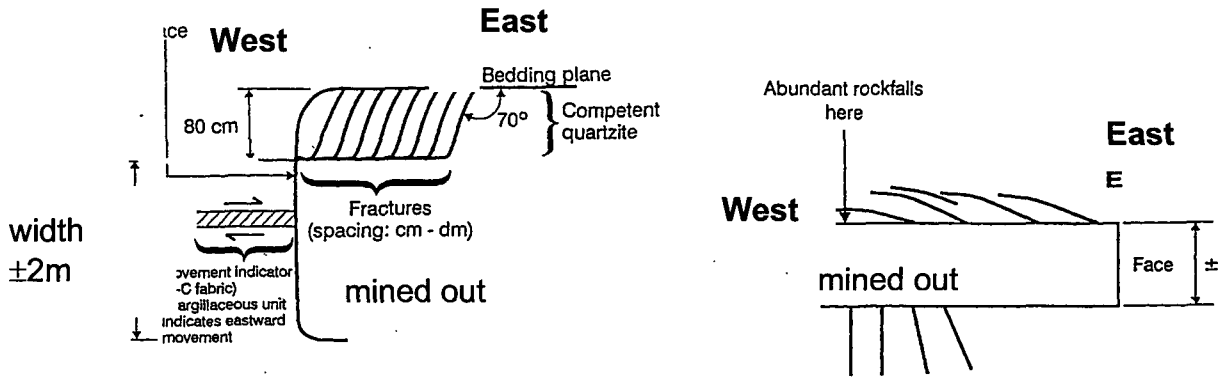

Figure 4.4.2.11 Schematics of fracture patterns observed at Vaal Reef site. A: Steeply dipping fractures when mining westwards b: Flatter dipping fractures when mining eastwards

Fractures in the hangingwall of the panel being mined to the east are sub-parallel to the bedding and result in highly unstable hangingwall conditions. However, fractures in the footwall are vertical to steeply dipping towards the face. A rockfall in this area, a week before the site investigation, indicated that the large, flat slabs of rock in the hangingwall were difficult to support and were a hazard to miners.

Tessellation and discrete growth models were set up with the direction of the major principal stress component plunging at 70° to the east. This is achieved by setting the vertical stress σ_v = 60 MPa, the horizontal stress σ_h = 12 MPa, and the shear stress σ_{vh} = ± 25 MPa. Thus, the k-ratio is reduced to 0,2. The tessellation models proved inconclusive as the initial shear stress activated significant regions of the tessellation and obscured the stope fracturing. These fracture zones would correspond to large-scale secondary faulting, which cannot be modelled as discrete discontinuities with the tessellation scheme, alone. In contrast, the discrete models were able to show that the fracture pattern depends on the mining direction. The prevention of crack intersections has permitted stable analyses for spans of more than 14 m. Thus, in Figure 4.4.2.12(west), most fractures dip at angles between 60° and 75° towards the face, whereas in Figure 4.4.2.12(east), the fractures dip at 30° to the face.

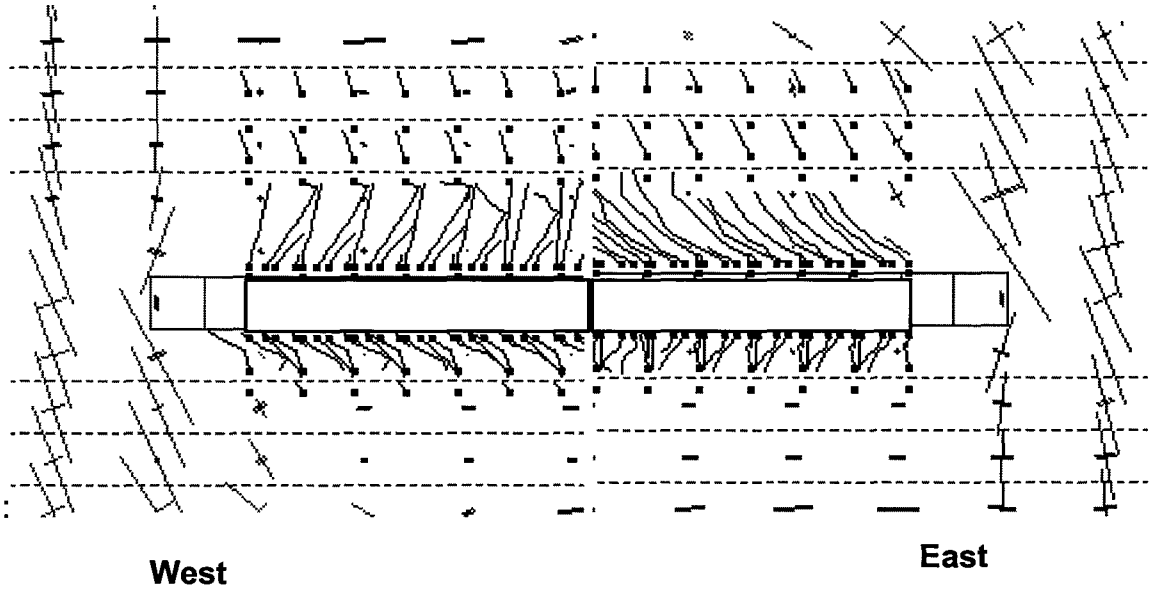

Figure 4.4.2.12 Fracture patterns, after 14 mining steps of 1m, from discrete fracture analysis with inclined major principal stress. a) steep dipping fractures when mining westwards b) shallow dipping fractures mining eastwards (single grey lines are compressive stresses double lines are tensile)

Consideration of a tessellation model with the *in situ* stress distribution having a vertical stress σ_v = 60 MPa, horizontal stress σ_h = 25 MPa, shear stress σ_{vh} = ± 12 MPa, maintains the ratio of major to minor principal stresses at 0,5. The k-ratio of 0,42 is higher than in the previous analysis. These tessellation models did indicate similar effects to the DIGS models shown in Figure 4.4.2.8. For low friction partings, the slip on the partings ahead of the face results in stress transfer some distance ahead of the face. The stress at the face rotates to become vertical and the effect of the inclined initial stress is not obvious. However, when the partings are assigned a friction angle of 40° a significant difference is obtained between dip angles in the two fracture patterns. The fracture patterns are shown in Appendix 4.4.

4.4.2.8 Time-dependent response of the rock mass and partings

The DIGS tessellation program was modified to permit the application of time-dependent material parameters on the rock mass and the partings (see Section 2.4.6). The program can also cater for the finite stope width models and so the Carbon Leader stope model with random parting planes, described in section 4.4.5, was used to investigate the effect of different surface creep relaxation (fluidity) parameters. The values of fluidity used in this study are shown for convenience and do not necessarily represent realistic parameters. The friction angle on the partings was reduced from 40° to 20°, and the tensile strength was set to zero, for this study.

The fracture pattern is shown in Figure 4.4.2.13. The zero tensile strength rock mass leads to significant fracturing above the open span. The lower friction angles allow some slip on the partings ahead of the face, which develops with time. The parallel activation rule is applied. In this case, a number of discrete fractures are observed in the hangingwall and footwall, ahead of the face, This is in strong contrast with the more diffuse fracture zones generally predicted with the parallel growth mode without time-dependent material properties. Thus, the addition of viscoplasticity leads to fracture patterns that are in between the diffuse fracture zones predicted by the parallel growth mode and the very discrete fractures of the incremental growth mode. The effect of the fluidity on the extent and density of fractures must still be investigated. The plot

of activated elements with time, Figure 2.4.14, shows that most fractures activate immediately after mining. There is a pattern of irregular peaks of fracture activation, as observed for the models with zero width stopes, as shown in Section 2.4.6.4. The numerical scheme exhibits path dependence and the response depends on the number of increments specified in the solution procedure. It must be accepted that each simulation run represents the outcome of a statistical experiment and will in general be different for different starting tessellation patterns. The analysis with 50 increments exhibits significantly higher energy release rates than the analysis with 10 increments, as shown in Figure 2.4.2.15.

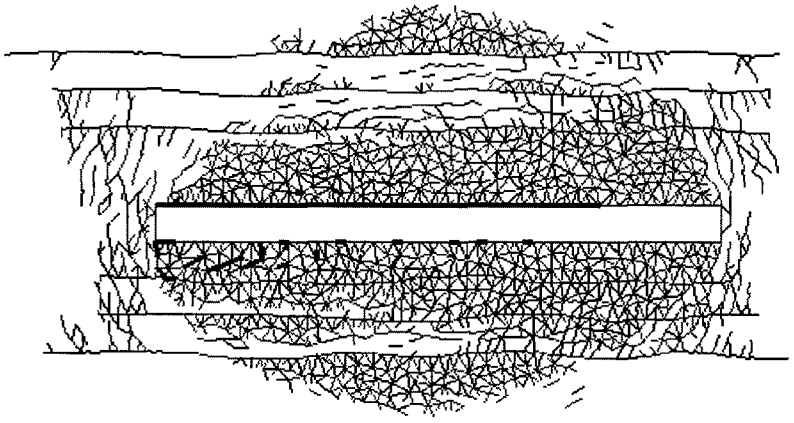

Figure 4.4.2.13 A typical fracture pattern when including time-dependent material properties.

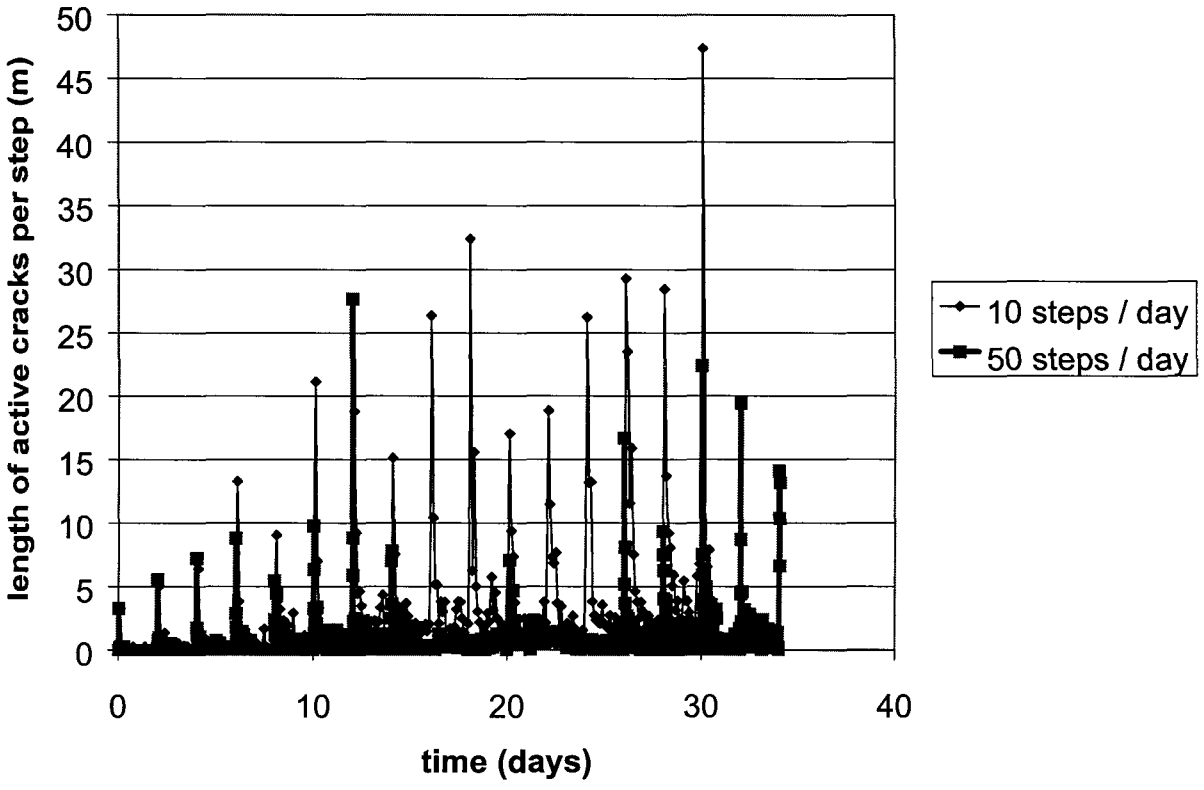

Figure 4.2.2.14 The influence of time step size on the length of cracks activated during a simulation of mining of the Carbon Leader Reef.

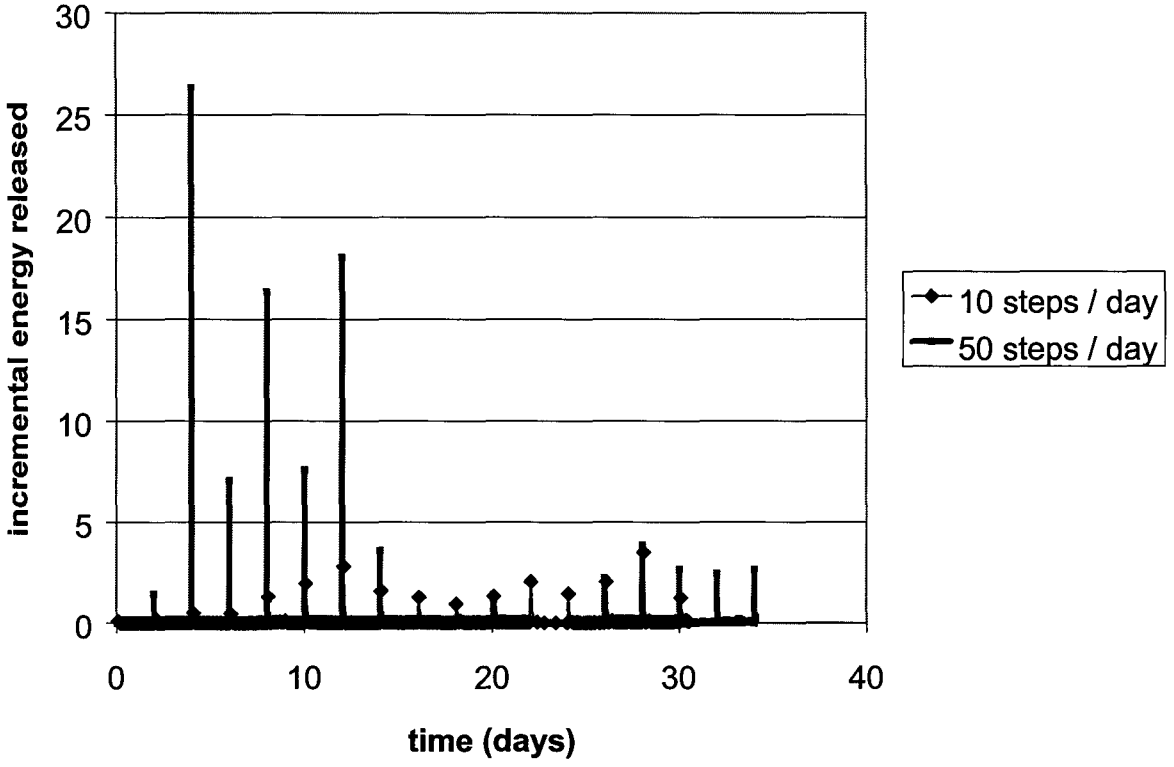

Figure 4.4.2.15 The influence of time step size on the incremental energy released during a simulation of mining of the Carbon Leader Reef.

4.4.2.9 Tension - sliding flaw model for fracture activation

The tension - flaw concept detailed in Section 2.4.3 has been applied to model the Carbon Leader stope environment. The tessellation is similar to that of the stope with laboratory material parameters discussed in Section 4.4.2.3. A set of elements was randomly selected and specified to be flaws, with a lower cohesion. When the friction angle on the parting planes is low, the fracture pattern is very similar to that of Figure 4.4.2.1b, with steeply dipping fractures at the stope face (see Appendix 4.4). This further emphasizes that the fracturing in that model is due to the induced tension arising from the slip on the parting planes and the bending of the hangingwall and footwall beams into the stope. When the friction angle is higher, then fracturing occurs behind the stope face, and is less steeply dipping. Removal of the flaws results in a similar fracture pattern, suggesting that the fracturing is occurring in response to the overall deformation of the rock mass, and not as much as a result of the presence of flaws. The fractures dip at about 60° towards the face.

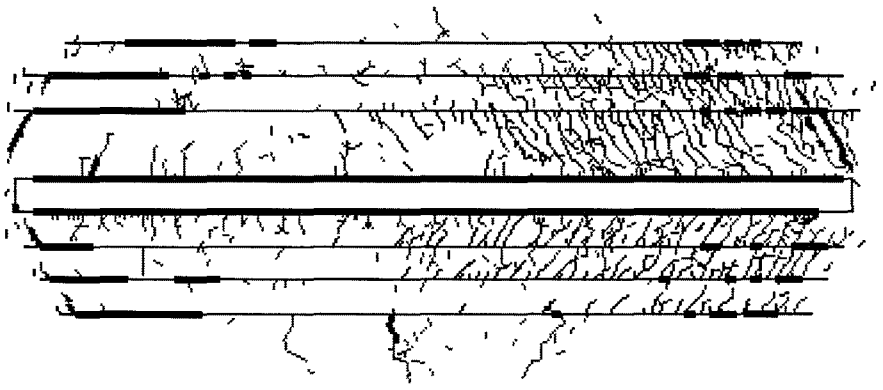

Figure 4.4.2.16 Simulation of the development of fracture patterns around a Carbon Leader stope using the sliding flaw - tension crack concept. (Model with high tensile strength and high parting plane friction.)

Table 4.4.2.2 Material properties for Carbon Leader rocks simulated with the tension- sliding flaw concept

	Flaw S_0	S_0	ϕ	S_m	ϕ_m	T
	MPa	**MPa**	**degrees**	**MPa**	**degrees**	**MPa**
Hangingwall	5	1E5	52	10	30	15
Green Bar	5	1E5	32	10	20	0
Green Bar Parting			30		30	
Footwall	5	1E5	45		25	10
Other partings			40		40	

4.4.2.10 Summary

The following similarities and differences with underground observations are observed in the models:

- Fractures are more frequent with increasing friction angles of the parting planes.
- Fractures are more prominent in the vicinity of the stope, and flatten away from the excavation.
- Shear fractures are more continuous in competent strata and more widely spaced than the extension fractures in competent footwall or hangingwall rock.
- Less intense fracturing is predicted by the model in competent horizons in comparison with weaker, bedded counterparts. This is possibly in disagreement with underground observations.
- Stress transfer ahead of the face, and periodic bands of fracturing, may be caused by irregular bedding planes (King, et al 1990) and not by low friction on flat parting planes as often used in models. Models incorporating irregular bedding planes with realistic friction angles appear to be in agreement with underground observations

4.4.3 Use of time-dependent closure as a hazard indicator

4.4.3.1 Time-dependent closure data

Time-dependent closure data of tabular excavations is a good reflection of the localised rock response and may provide important information which may be more difficult to obtain with other methods. It also provides important additional data to calibrate the viscoplastic models developed in this study. To analyse the true time-dependent behaviour of the rock mass, data for this study was collected using clockwork closure instruments which record the stope closure continuously as described in Section 4.3.2. Figure 4.4.3.1 illustrates a typical installation of this instrument in a stope.

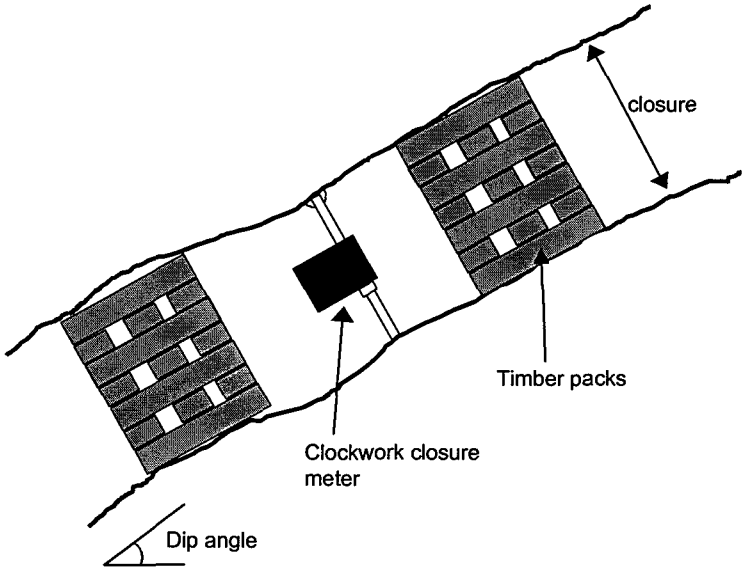

Figure 4.4.3.1 Installation of the clockwork closure meter normal to the plane of the excavation.

Closure data of the Ventersdorp Contact Reef

Closure data was collected in the South Shaft area of Western Deep Levels Mine near Carletonville. The hangingwall of the VCR at this mine consists of hard lava. The general mining layout in this area is given in Figure 4.4.3.2. The instrumentation was installed in the W3 panel of the 87-49 longwall. An enlarged view of this panel is given in Figure 4.4.3.3. The dip of the reef is 22° and the depth below surface is approximately 2570 m. Timber packs are used as back-area support in this panel. Five clockwork closure meters were installed at any one time, with their positions before the blast on 15/4/97 illustrated in Figure 4.4.3.3. Typical recorded time-dependent closure is illustrated in Figure 4.4.3.4. Note that there is a sudden increase in the closure after the blast consisting of an instantaneous jump and a period ($\approx$ 5 hours) of decelerating rate of closure. This will be called the primary closure. This is followed by a more gradual steady-state closure rate. If there is no mining activity for a number of days, the rate of steady-state closure appears to remain constant in the short term ($\approx$ 48 hours after the last blast), but then gradually starts declining again until the next blast occurs. Typically, after a period of two weeks with no blasting, the rate of steady-state closure is reduced to 10 % of its short term value. Of interest is that if seismic events occur close to the panel, time-dependent closure behaviour similar to the response which follows a blast is observed as depicted in Figure 4.4.3.4. The magnitude of the primary closure after a seismic event is dependent on the

magnitude of the event and on how close its source was located to the panel. A further closure data set is given in Figure 4.4.3.5. The rate of steady-state closure is defined as

$$\dot{S}_{ss} = \frac{\Delta S_{ss}}{\Delta t} \tag{4.4.3.1}$$

with the parameters ΔS_{ss} and Δt defined in Figure 4.4.3.6. The period Δt for the calculation is usually taken between 10 to 24 hours after the blast to avoid the effect of the primary closure phase.

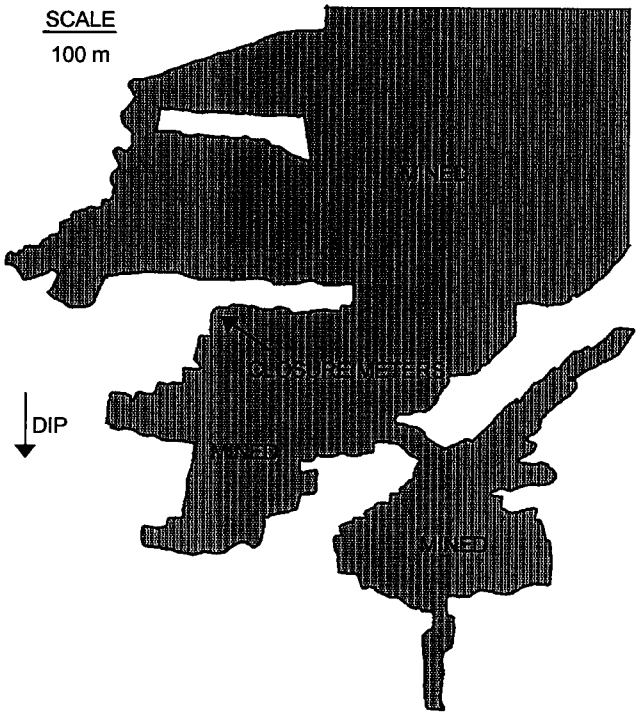

Figure 4.4.3.2 Plan view of the mining geometry in the area where the closure data was collected at Western Deep Levels Mine.

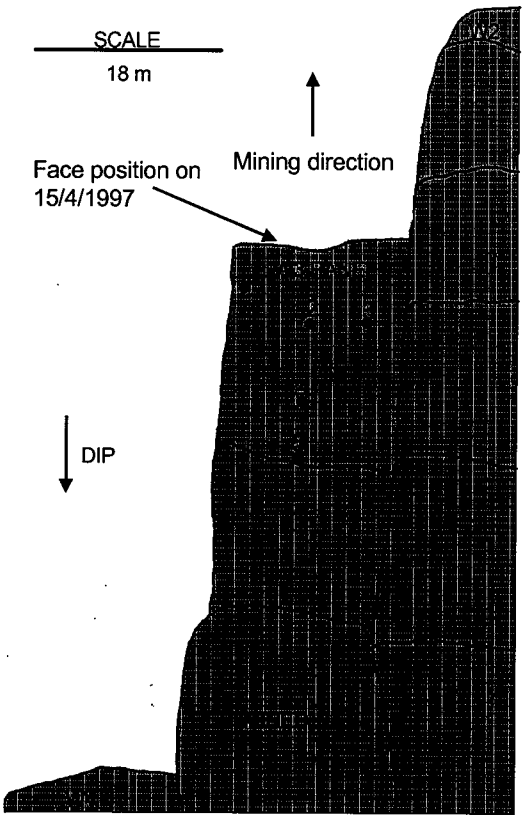

Fig. 4.4.3.3 Enlarged plan view of the W3 up-dip panel in the 87-49 longwall with the positions of the closure meters indicated.

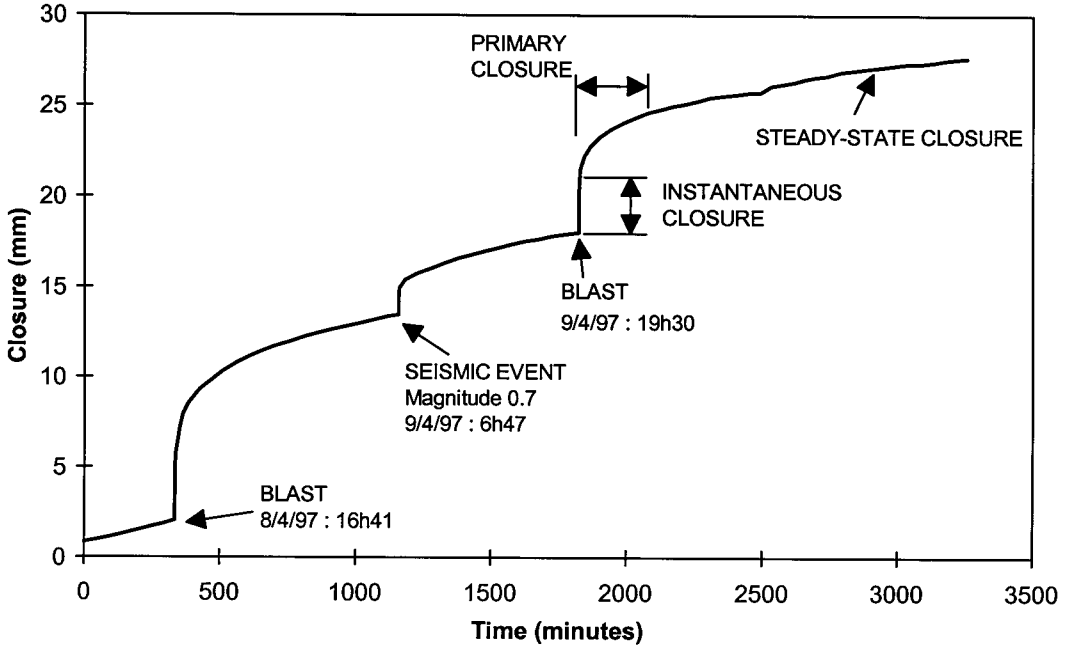

Figure 4.4.3.4 Typical time-dependent stope closure of the Ventersdorp Contact Reef at Western Deep Levels Mine. This was for a closure station at a distance of 8,7 m from the face.

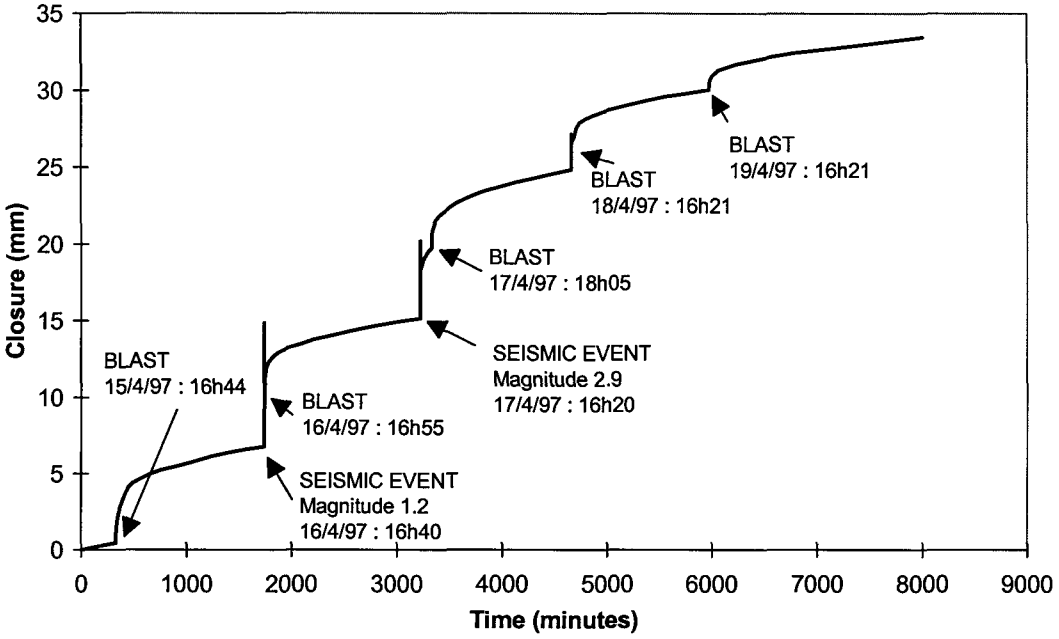

Figure 4.4.3.5 Time-dependent closure measured at Western Deep Levels Mine. This was for instrument no. 1 which was 4,1 m from the face before the blast on 15/4/97. The overshoot behaviour after seismic events is a response of the closure meter due to dynamic loading and not a reflection of the true rock mass behaviour.

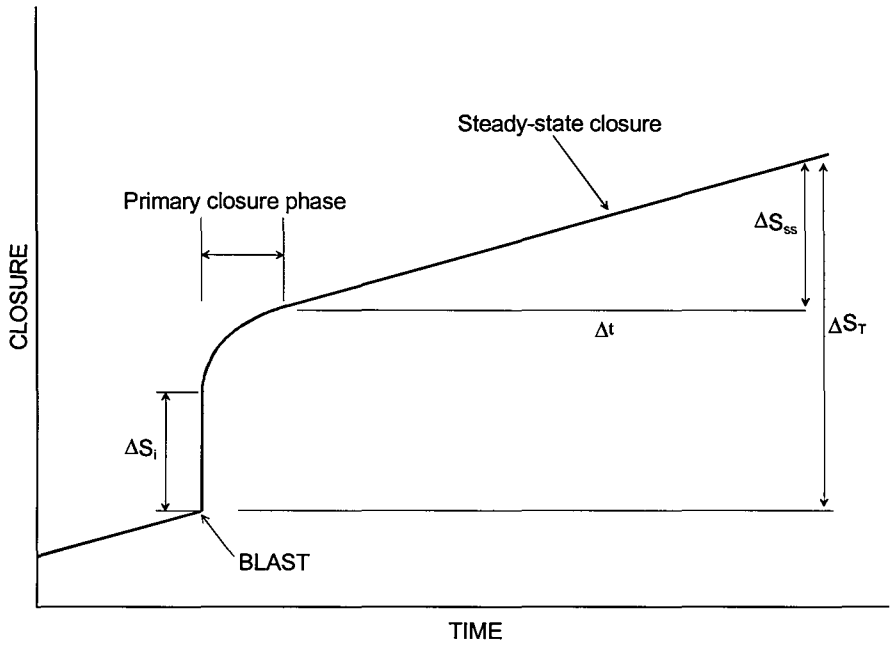

Figure 4.4.3.6 Definition of closure terms.

After any particular blast, the increase in closure is a function of the distance to the face, position in the panel and the length of the face advance increment. Figure 4.4.3.7 illustrates the incremental closure for stations no. 2, 4 and 5 (see Figure 4.4.3.3) after the blast on 15/4/97. The primary closure is large close to the face, but smaller as the distance to the face increases. The rate of steady-state closure also decreases into the back area. Figure 4.4.3.8 compares the behaviour after the same blast for the row of stations approximately parallel to the face (no. 1, 2

and 3). Although the steady-state closure rate is essentially similar for these three stations, the magnitude of primary closure increases from the solid abutment (no. 1) to the previously mined side (no. 3) of the panel. As it is difficult to determine the onset of the steady-state closure phase, the closure rates given in Figure 4.4.3.7 and Figure 4.4.3.8 were calculated for a period from 600 minutes after the blast to the end of the data set.

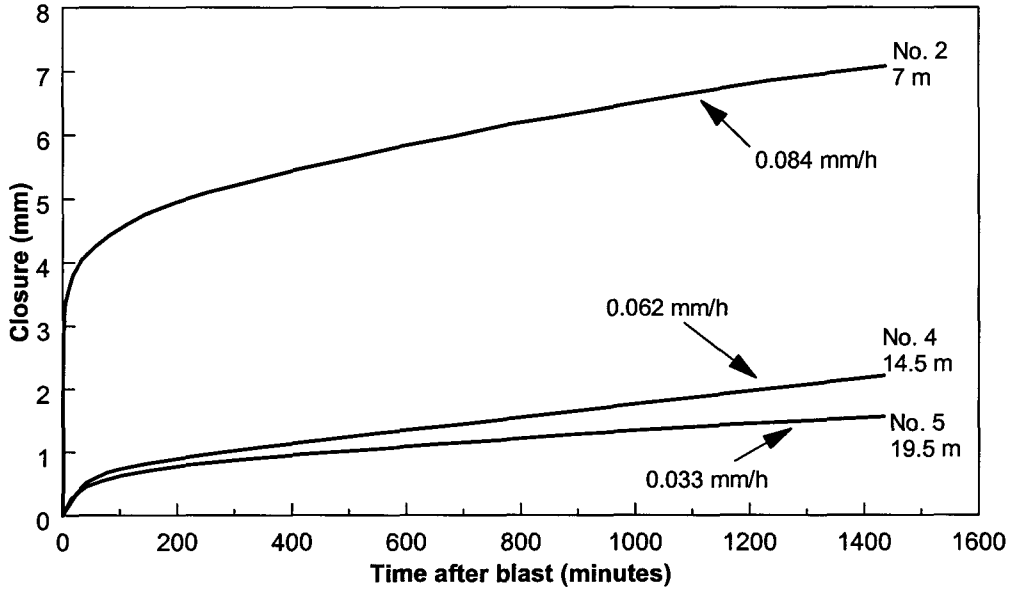

Figure 4.4.3.7 Closure as a function of time for different positions in the panel following the blast on 15/4/97. The distances given in the graph are the distances from the closure instruments to the face before the blast (see Figure 4.4.3.3).

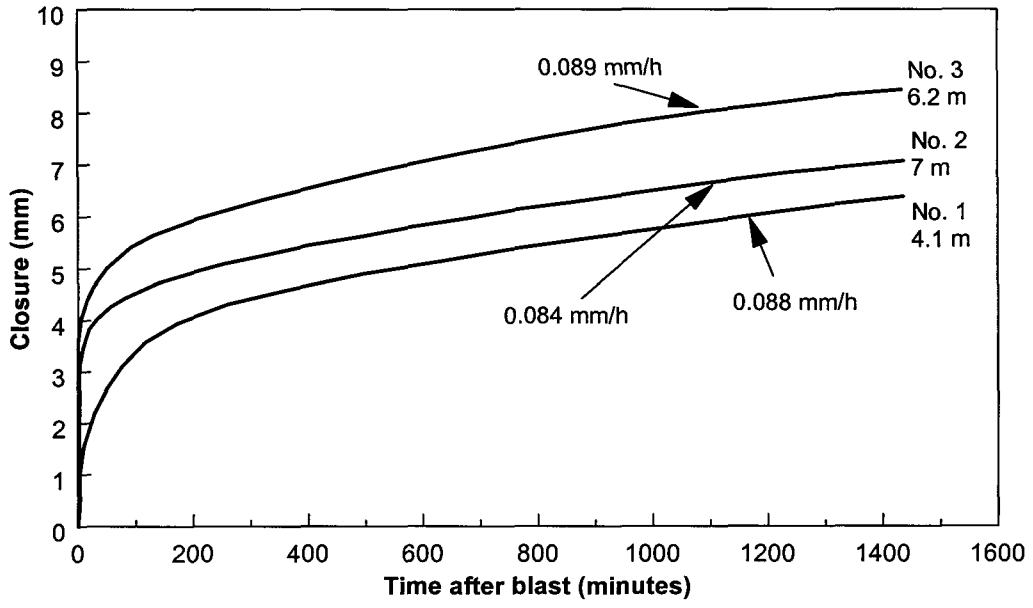

Figure 4.4.3.8 Closure as a function of time for different positions approximately parallel to the face following the blast on 15/4/97. The distances given in the graph are the distances from the closure instruments to the face before the blast (see Figure 4.4.3.3).

Closure data was also collected at Kloof Mine to compare the behaviour of the VCR with the hard lava hangingwall described above to those areas with a soft lava hangingwall. For the soft

lava at Kloof Mine, the behaviour was similar to that of the Vaal Reef as described below. The data from Kloof Mine is given in Appendix 4.5.

Closure data of the Vaal Reef

To contrast the relatively low closure rates of the Ventersdorp Contact Reef with areas experiencing significant closure, data was collected from the No. 6 shaft pillar area at Hartebeestfontein Mine in the Klerksdorp area. A schematic diagram of the shaft pillar area is given in Figure 4.4.3.9. A single closure meter was installed in the position illustrated in Figure 4.4.3.10. The dip in this area was 7° and the depth approximately 2350 m. Timber packs were used as back-area support in this panel. This shaft area is known to have some of the highest closure rates in the gold mining industry. Of significance are the well-defined bedding planes in the quartzite. The nature of infilling of these discontinuities makes conditions less favourable for stable mining excavations. The overall competency of the rock mass and its ability to provide stable mining excavations for prolonged periods appears to be less favourable than the rock types encountered in Ventersdorp Contact Reef mining operations. The quartzites of the Ventersdorp Contact Reef appear to be less bedded and substantially more siliceous than those present at Hartebeestfontein Mine. As a result of this greater strength, the rock in other mines would appear to be more susceptible to strain bursting under high stress conditions.

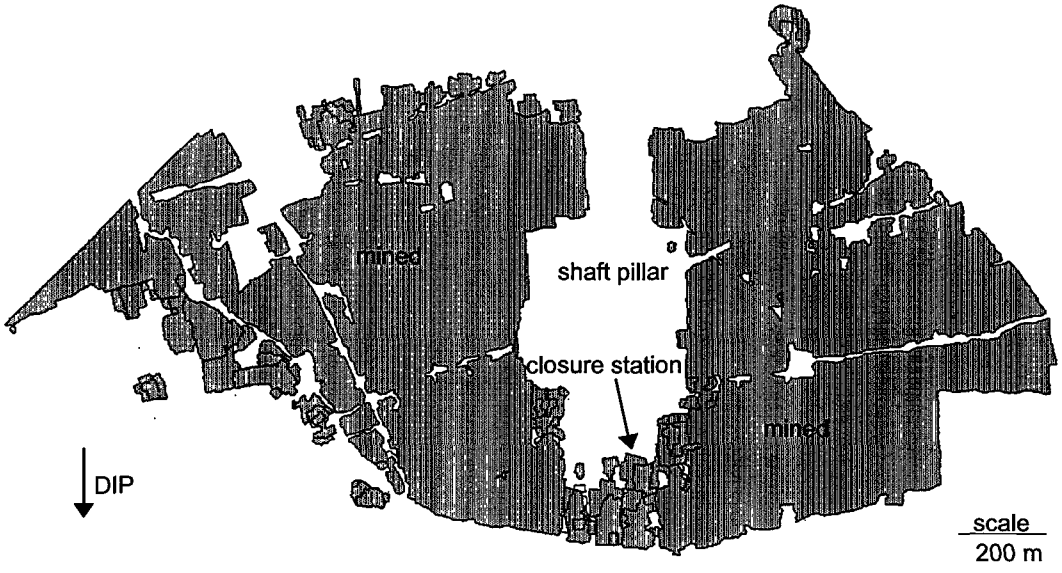

Figure 4.4.3.9 Plan view of the mining geometry at No. 6 shaft pillar area, Hartebeestfontein Mine where the closure data was collected.

A typical time-dependent closure profile is given in Figure 4.4.3.11. Evident is the high steady-state closure rate compared to that of the Ventersdorp Contact Reef, while the instantaneous closure at the time of blasting is small. A second data set is given in Figure 4.4.3.12. Note that the rate of steady-state closure increased as the instrument moved further away from the face. This is unlike measurements taken in the Ventersdorp Contact Reef stopes. A significant difference in the geotechnical properties of this area compared to the Ventersdorp Contact Reef is the presence of well-defined bedding planes. It appears that slip and dilation of these bedding planes is an important mechanism controlling the closure behaviour. This, coupled with the rapid deterioration of the hangingwall due to time-dependent fracture processes, may explain

the increase in steady-state closure rates for larger distances from the face. Control of the hangingwall strata is difficult in these areas and risks of falls of ground are pronounced.

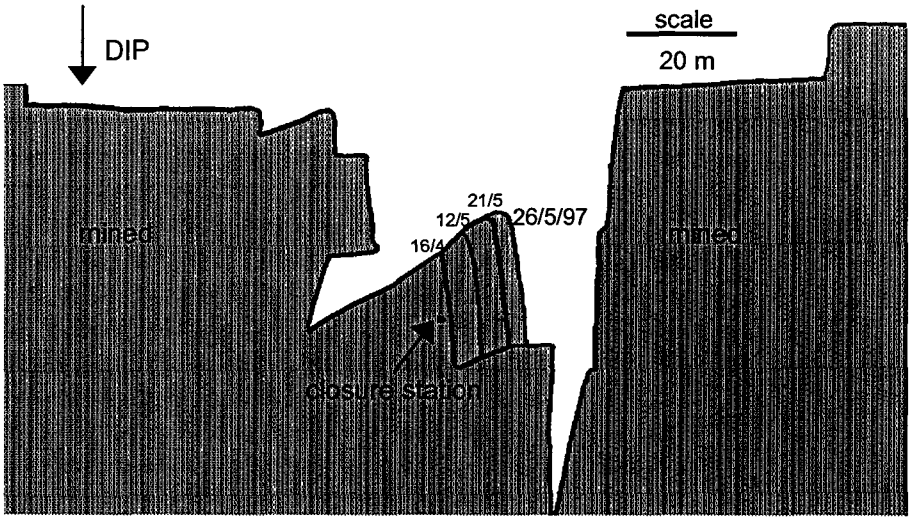

Figure 4.4.3.10 Location of the clockwork closure instrument in the 78N23 longwall at No. 6 shaft, Hartebeestfontein Mine.

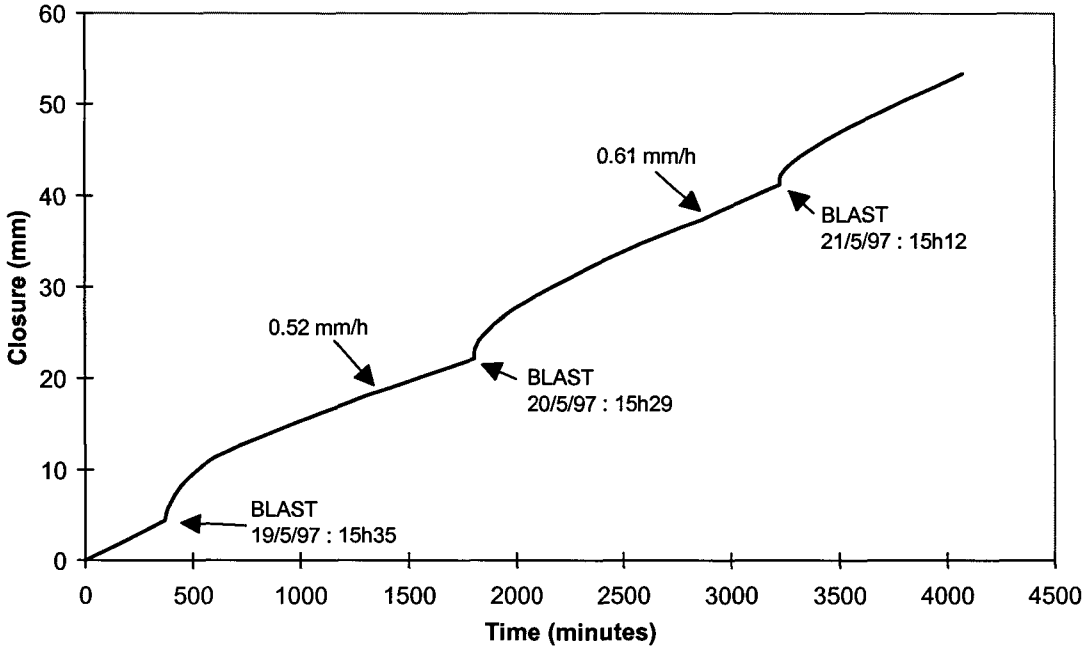

Figure 4.4.3.11 Closure measured at Hartebeestfontein Mine. The instrument was 10,9 m from the face before the blast on 19/5/97. The steady-state closure rates were calculated for the periods from approximately 600 minutes after the blast until the next blast occurred.

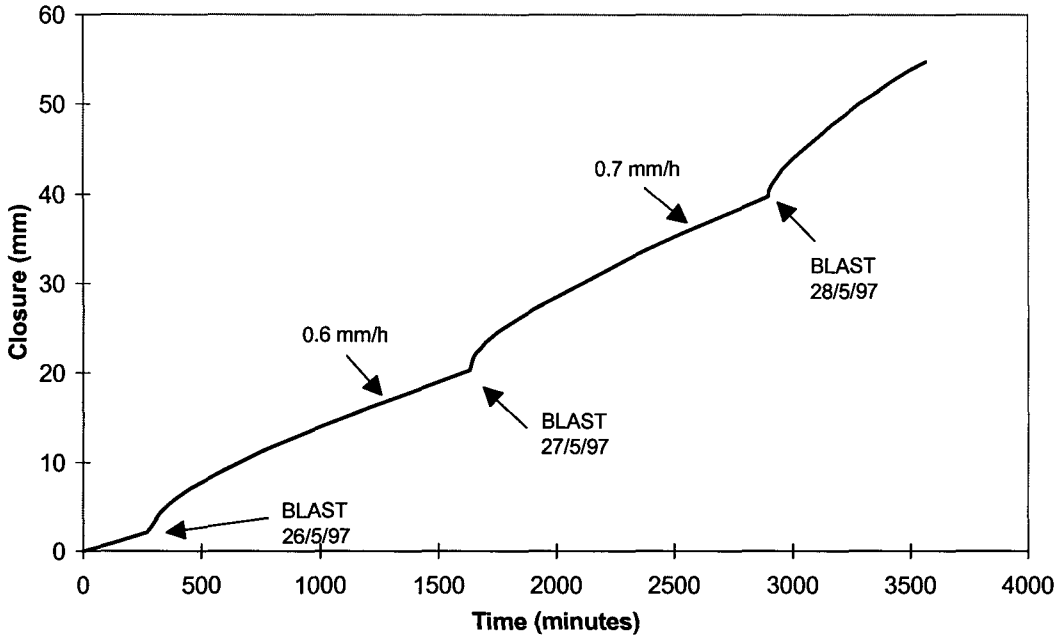

Figure 4.4.3.12 Closure measurements at Hartebeestfontein Mine for a larger distance to face than that in Figure 4.4.3.11. The instrument was 14,2 m from the face before the blast on 26/5/97.

4.4.3.2 Use of closure data as a diagnostic measure of face stress

When comparing typical results of the Vaal Reef in Figure 4.4.3.11 with those of the Ventersdorp Contact Reef in Figure 4.4.3.4, it is clear that significant differences exist between the continuous closure profiles of these different geotechnical areas. For a more direct comparison, typical closure increments after blasts for these two areas are plotted in Figure 4.4.3.13. The two experimental sites are approximately at the same depth and for these specific data sets, the closure instruments were approximately the same distance from the face. Although care should be taken when comparing these sites directly, owing to different mining geometries, the following important differences are noted. The closure behaviour of the Ventersdorp Contact Reef is characterised by a large instantaneous jump after blasting, followed by a low closure rate. These areas also appear to be prone to face bursting. In contrast, for the Vaal Reef, the closure is characterised by a small instantaneous jump after blasting, followed by a high rate of closure. The risk of face bursting is apparently lower in these areas, although the risk of falls of ground is pronounced. Further work is however necessary to quantify the face bursting and falls of ground hazard in the respective areas.

The instantaneous jump in closure after blasting is the result of the immediate redistribution of stress following the removal of an increment of rock in the face. The more significant the disturbance to the stress field, the more pronounced the immediate response will be. If the increment of rock removed by blasting carries no load (in essence loose rock lying at the face) no change in the stress field will take place and no change will be noticed in the closure behaviour. The instantaneous closure response after blasting therefore appears to indicate the role the removed rock played in maintaining the stress equilibrium before the blast. For the Ventersdorp Contact Reef, the significant instantaneous closure after blasting is probably an indicator of a more highly stressed face area than the Vaal Reef. This may explain why face bursting appears to be more pronounced on this reef than the Vaal Reef.

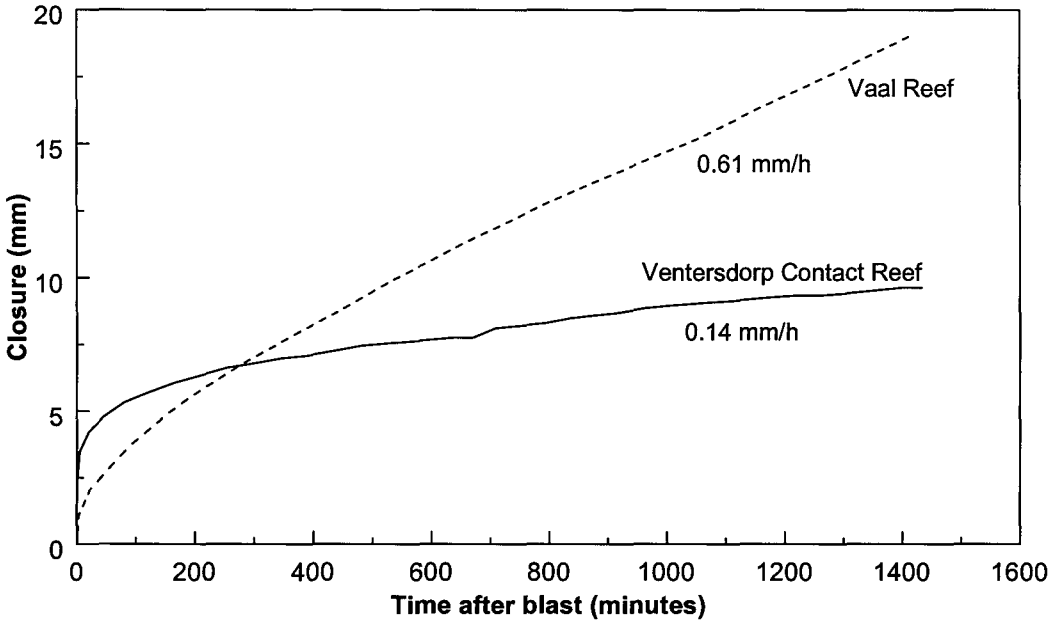

Figure 4.4.3.13 Comparison of typical closure profiles of the Ventersdorp Contact Reef and Vaal Reef. For the Vaal Reef measurements the instrument was 11,5 m from the face before the blast while it was 10 m from the face for the Ventersdorp Contact Reef measurements.

A further difference in behaviour between these areas is the high rate of steady-state closure of the Vaal Reef stopes compared to the Ventersdorp Contact Reef stopes. The high steady-state closure rate is an indication of efficient stress redistribution through mobilization and growth of the fracture zone and slip on discontinuities such as bedding planes. This in turn may result in low face stresses. Although the face bursting hazard might be low in areas with high steady-state closure rates, the large time-dependent behaviour of the fracture zone might lead to a rapid deterioration of hangingwall increasing the fall of ground hazard. Further work is however necessary to quantify this hazard.

It was suggested above that the instantaneous closure after blasting is an indication of the proximity of the stress peak to the face. This hypothesis was tested by simulating two stopes (A and B) using the viscoplastic model described in Section 2.4.5. The parameters used are given in Table 4.4.3.1. The only difference between these stopes is a different rate of cohesion decay. This resulted in the rock ahead of the face of Stope B losing its strength much faster than the rock ahead of Stope A and therefore carrying less load. This is illustrated in Figure 4.4.3.14 where the major principle stress is plotted against distance ahead of the original face position just before an increment is mined. Visible in this figure is the stress peak for both stopes some distance ahead of the face. With sufficient distance from the face, the stress magnitude is reduced to the virgin value. For Stope A the peak is closer to the face. The next increment of mining will remove the first metre of rock thereby forcing the stress carried by this increment to be instantaneously redistributed. As the average stress in this increment of rock is larger for Stope A than Stope B, it is expected that the instantaneous closure will be bigger for A. This is confirmed by the closure that followed this increment in Figure 4.4.3.15. For Stope A the instantaneous closure was 3,7 mm compared to the 2,5 mm for Stope B. Following the instantaneous closure, the steady-state closure for Stope B is larger as the failed rock loses its strength faster resulting in greater time-dependent deformation.

Figure 4.4.3.14 illustrates the position of the peak stress 24 hours after mining an increment. This position is not stationary but moves as the time-dependent fracture processes occur in the rock. This is illustrated in Malan (1998).

Table 4.4.3.1 Parameters used in the simulation to obtain the results in Figure 4.4.3.14 and Figure 4.4.3.15. As the stope span was small in this simulation, large stresses and weak rock properties were used to ensure a representative fracture zone ahead of the face.

Parameter	Value
Vertical stress	110 MPa
Horizontal stress	55 MPa
Bulk modulus	38,9 GPa
Shear modulus	29,2 GPa
Density	2700 kg/m^3
Cohesion of intact rock	10 MPa
Friction angle (Both peak and residual)	30°
Residual cohesion	3 MPa
Cohesion decay	Stope A : $1x10^{-10}$ h^{-1} Stope B : 0,01 h^{-1}
Dilation angle	15°
Fluidity coefficient	$1x10^{-10}$ $Pa^{-1}.h^{-1}$

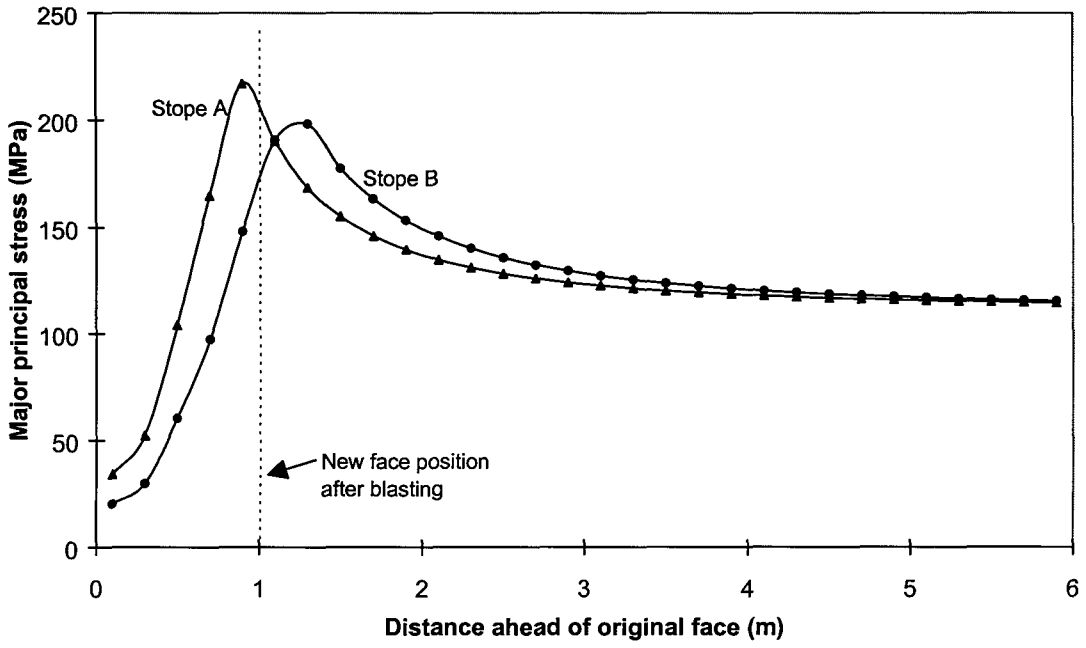

Figure 4.4.3.14 Major principal stress as a function of distance ahead of the face for the two simulated stopes. These stresses were calculated in the centre of the reef.

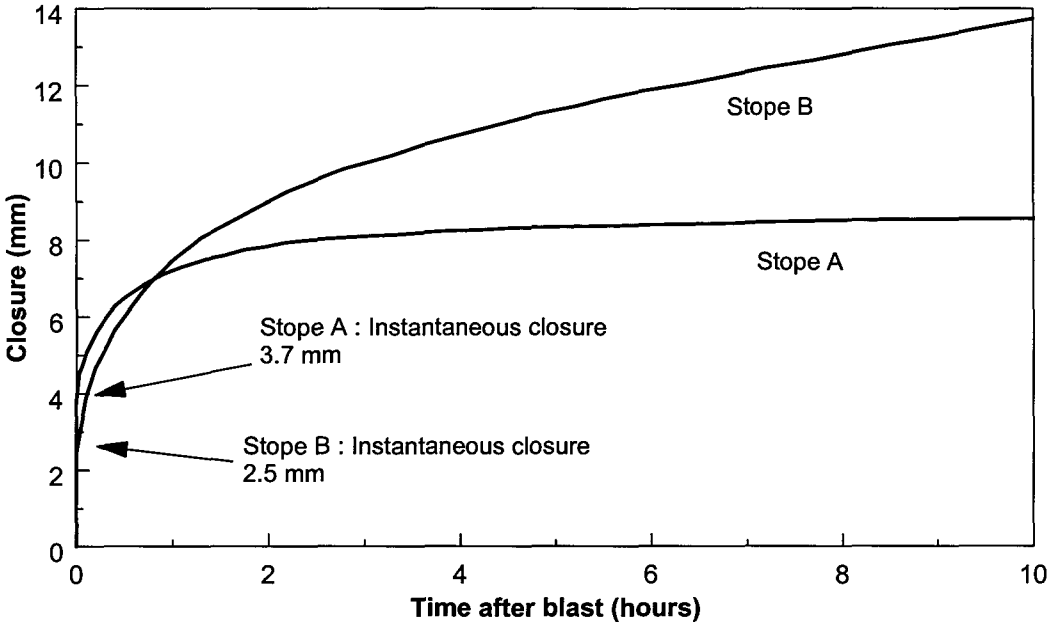

Figure 4.4.3.15 Comparison of the simulated closure behaviour as a function of time after the blast. The measurement position was 0,5 m behind the original face.

It appears then that the instantaneous closure observed underground can be used as an indication of the stress magnitude in the face area and may therefore also be an indicator of the face bursting hazard. It should however be emphasised that the instantaneous closure response after a blast is a reflection of the face stress BEFORE the blast and not after it. Underground measurements (Figure 4.4.3.19) indicate that the instantaneous closure appears to include a random component and is therefore not deterministic. This random component might be caused by the varying rock properties (and therefore varying stress magnitudes) ahead of the face although mining technique and measurement position also play a strong role. If only a portion of the face is blasted and not the entire length, the instantaneous closure at a particular measurement position will be smaller. The uninformed observer might then be deceived into concluding that the face stress is dropping. Due to these factors, prediction of face bursting would be very difficult or impossible. The value of these closure measurements should rather be seen as the possible identification of hazardous areas. An average value of instantaneous closure taken over a specified period will be very useful to define a face bursting risk. This can be seen from the data collected underground where the average instantaneous closure of the Ventersdorp Contact Reef is clearly much higher than that of the Vaal Reef. As mentioned before, this might be developed into a hazard indicator. One possibility is the closure ratio CR for n blasts given by

$$CR = \frac{1}{n}\sum_{j=1}^{n}\frac{\Delta S_i{}^j}{\Delta S_T{}^j} \qquad (4.4.3.2)$$

where ΔS_T is the total closure for a period of approximately 24 hours after the blast. The measurements are restricted to fall in an area 5-15 m from the face. For the Vaal Reef at Hartebeestfontein Mine, the value calculated is CR = 0,06 while for the Ventersdorp Contact Reef (hard lava), CR = 0,27. Further work is necessary to examine the influence of stope span, layout geometry and face advance per blast on this closure ratio.

It was shown in Section 2.4.6 that the viscoplastic displacement discontinuity model can simulate the time-dependent closure behaviour of tabular excavations. This program was used to simulate a narrow width stope mined in one metre increments. The properties of this model

are given in Napier et al, (1998). This model was used to plot the initial step closure, arising in each mining step, against the previous average stress acting on the stope face immediately prior to the stope face advance. This plot is shown in Figure 4.4.3.16 and suggests that the initial jump in the stope closure is in fact related to the existing average face stress. It is also found that the peak energy release increment in the first time interval following each face advance increment, is correlated to the initial step closure. The elastic stope face stiffness k_e can be determined for a given averaging length)L ahead of the face by dividing the average face stress $\overline{\sigma}_v$ by the average closure $\overline{D}_v$. Napier et al, 1998 showed that for L/)L >> 1,

$$k_e \approx \frac{E}{C(1-\nu^2)}\left(\frac{1}{\Delta L}\right) \qquad (4.4.3.3)$$

L is the stope span, E is Young's modulus, ν is Poisson's ratio and C is an asymptotic constant (C ≈ 8/3). Equation (4.4.3.3) indicates that the elastic face stiffness is independent of the panel span L and that when the averaging interval)L becomes very small, the face stiffness tends to infinity. With)L = 1 m, E = 70000 MPa, < = 0,2 and C = 8/3, it is found that k_e = 27,3 MPa / mm. Plotting this trend through the centroid of the data in Figure 4.4.3.16 shows that the average face stiffness in the inelastic analysis is very similar to the elastic face stiffness.

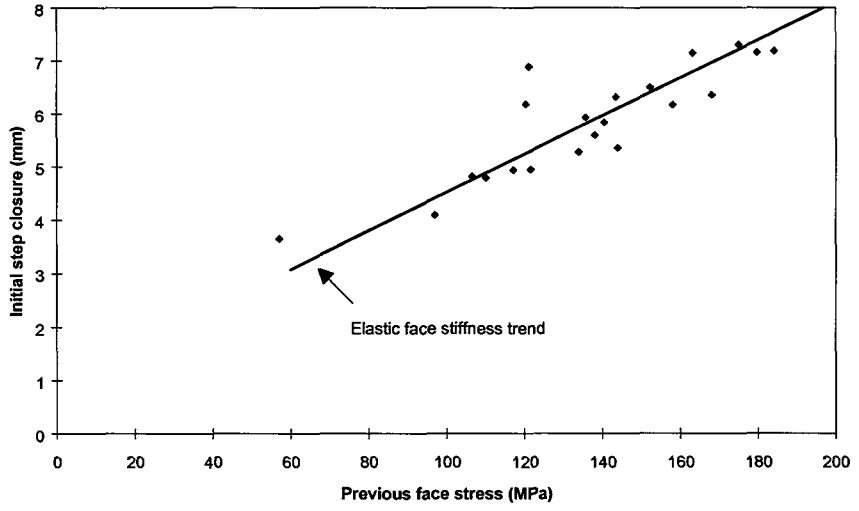

Figure 4.4.3.16 Initial average closure in the first time interval following each mining step plotted against the average stress ahead of the stope face, prior to the mining step.

The effect of preconditioning on time-dependent closure behaviour

Preconditioning was not used in the stopes described in Section 4.4.3.1 above and the closure data presented therefore does not include the effect of preconditioning. Since collection of this data, preconditioning was introduced in the 87-49 longwall at Western Deep Levels Mine. Measurements were taken in a panel not far from those depicted in Figure 4.4.3.3. Typical results are illustrated in Figure 4.4.3.17. Note that the steady-state closure rate increases significantly after the onset of preconditioning. This is further illustrated in Figure 4.4.3.18 which compares the rate of steady state closure as a function of distance from the face for panels with and without preconditioning. These rates were calculated for 10 hours to approximately 24 hours after each blast. It is clear from this that the steady-state creep rate is significantly increased with preconditioning. This is an indication of enhanced time-dependent deformation of

the rock mass that reduces the amount of strain energy stored close to the face and therefore also the likelihood of face bursting.

It is not clear at this stage what the effect of preconditioning is on the instantaneous closure response after blasting. In Figure 4.4.3.17, the instantaneous response after the first preconditioning blast was significantly higher than the previous blasts. This might be the result of the 2,4 m deep preconditioning blasts affecting a larger volume of stressed rock compared to ordinary production blasting. Figure 4.4.3.19. compares the instantaneous closure after blasting with and without preconditioning. Note that there is not a distinct difference for the two cases, although the values for the preconditioning appear to be slightly higher. Also note that there appears to be a poor correlation between magnitude of instantaneous closure and distance to face. One factor causing this is the position of the closure instrument in the direction parallel to the face. This geometrical effect is illustrated in Figure 4.4.3.8. The length of face advance for the particular blast and whether the entire face or only a portion of the face is blasted, also plays a role. For a fixed position in the direction parallel to the face it is found that the instantaneous closure typically reduces in magnitude as the distance to the face increases.

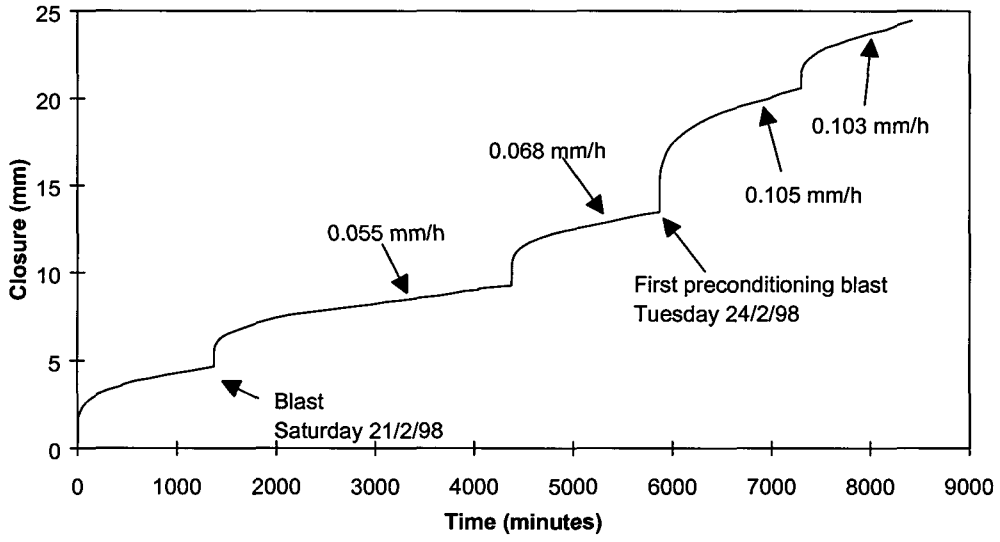

Figure 4.4.3.17 The effect of preconditioning on the time-dependent closure of a stope in the Ventersdorp Contact Reef. The values indicated in the figure are the steady-state closure rates and were calculated for the periods of 800 minutes after the blast until the next blast occurred. The instrument was 7,2 m from the face at the beginning of this data set and 10,5 m from the face after the last blast in the figure.

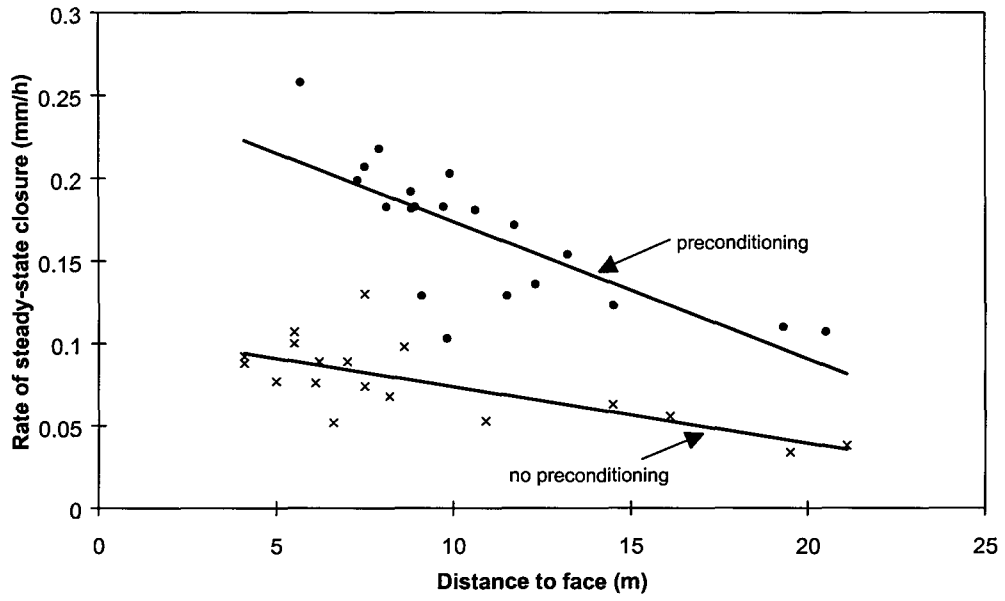

Figure 4.4.3.18 The effect of preconditioning on the rate of steady-state closure for panels in the Ventersdorp Contact Reef.

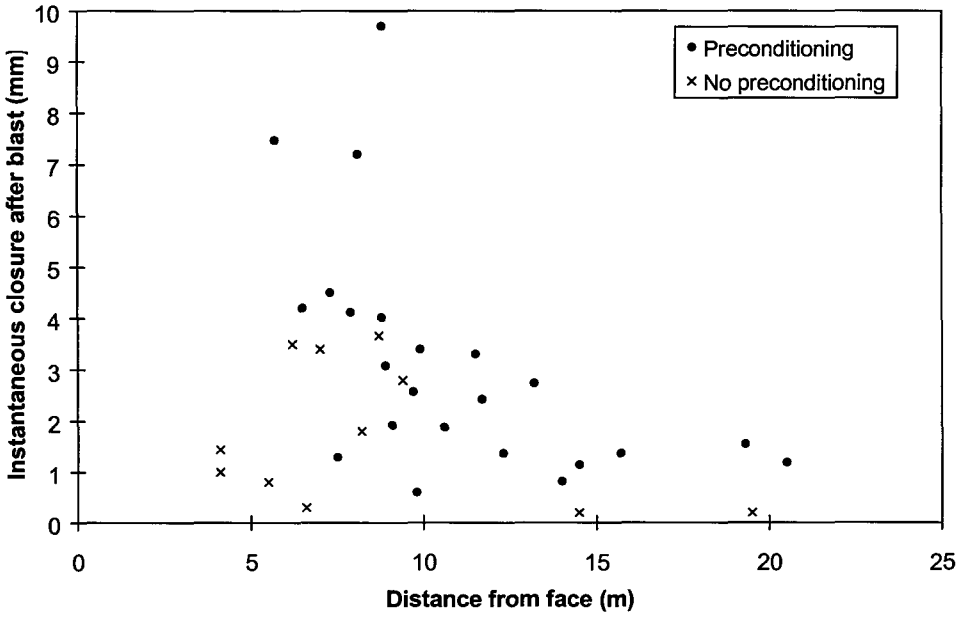

Figure 4.4.3.19 The effect of preconditioning on the instantaneous closure after blasting of the Ventersdorp Contact Reef.

4.4.4 Effect of rate of mining

4.4.4.1 Introduction

The stable formation of the fracture zone ahead of working faces is deemed necessary to reduce the amount of strain energy stored close to the excavation and therefore the likelihood of so-called face-bursting events. The rate of face advance might interfere with the formation of the fracture zone as the growth of this zone after blasting does not occur instantaneously, but as a time-dependent process. For very high production rates, the stope face might therefore catch up with the fracture zone and the increased maximum stress peak could lead to an increase in face-bursting potential. Furthermore, the time-dependent behaviour of the rock mass is also important in relation to the stability of the hangingwall and to the potential for falls of ground.

4.4.4.2 Simulating the effect of mining rate on seismic energy released

As described in Section 2.4.6, a viscoplastic displacement discontinuity method was developed to provide a direct mechanistic simulation of seismic activity and stress transfer effects in deep level mines. These models consist of multiple interacting displacement discontinuities with a prescribed viscoplastic relaxation law to relate the rate of slip on the cracks to the shear stress. As these models proved successful in simulating the observed time-dependent rock behaviour such as time-dependent closure and seismic energy release patterns, they were subsequently used to investigate the effect of mining rate.

A series of mining advance rates were analysed for a parallel-sided stope panel by specifying different numbers of time steps between each mining step. The parameters used for this model are given in Table 2.4.6.2 (Section 2.4.6). Figure 4.4.4.1 shows a cumulative plot of seismic energy released as a function of the mined length for three different face advance rates of 2 m/day, 1 m/day and 1 m/two days. The method of calculating the seismic energy released is also given in Section 2.4.6. The nominal mining depth is 2200 m with a vertical primitive stress of 60 MPa at the mining horizon. The horizontal primitive stress is assumed to be 30 MPa at this position. Up to a face advance of 16 m there appears to be little difference in the seismic energy release in each case. After this point, the highest mining rate (2 m/day) is seen to release significantly more energy. At the same time it is of great interest to examine the cumulative length of mobilized fractures shown in Figure 4.4.4.2. Here, it is apparent that at mining distances greater than 14 m, more fractures are mobilized at the slower mining rate. Significantly, it can be seen that when the mining has advanced to 28 m, approximately 20 percent more fractures are mobilized if the slowest rate of 1 m/two days is pursued as compared to the mining rate of 1 m/day, although, from Figure 4.4.4.1, there is little difference in the cumulative released energy. This illustrates the important point that while slow mining may lead to a smaller cumulative release of seismic energy, more damage or slip movements may arise in the rock mass which in turn may lead to local support difficulties in terms of rock falls and shake out.

It should be noted that the simulations were carried out using a discontinuity relaxation parameter of 1×10^{-5} $m.MPa^{-1}.h^{-1}$. In future, work is necessary to calibrate this parameter for different geotechnical environments and also to validate the assumed viscoplastic relaxation law.

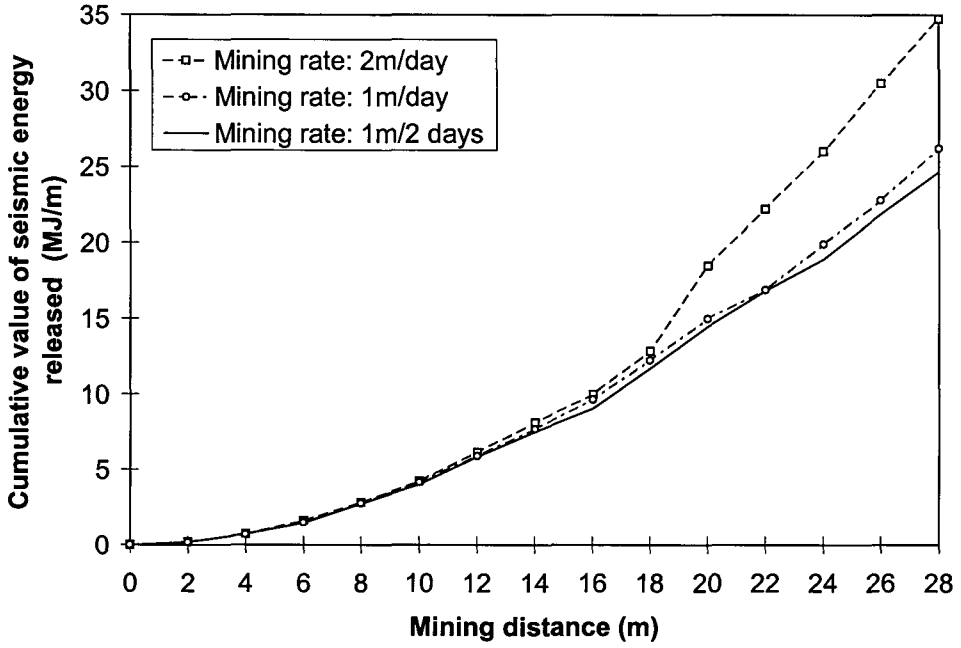

Figure 4.4.4.1 The effect of mining rate on seismic energy released.

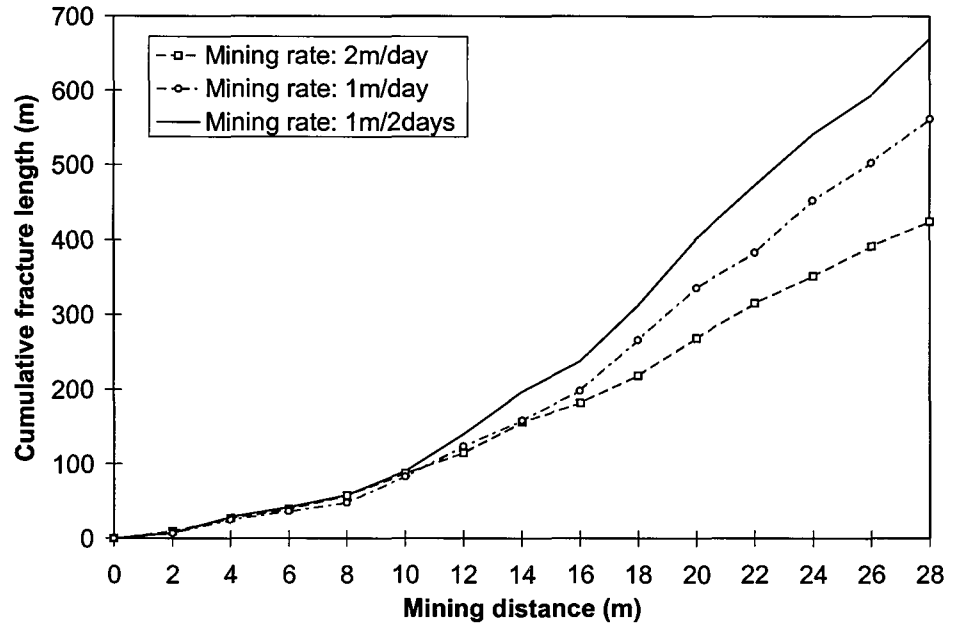

Figure 4.4.4.2 The effect of mining rate on cumulative fracture length mobilization.

4.4.4.3 Simulating the effect of mining with a weekend break on seismic energy released

The viscoplastic displacement discontinuity model was applied to the case of mining a horizontal panel which is enlarged in 40 mining steps of one metre per step. The panel is surrounded by a rectangular region covered by a random mesh of potential crack segments. For convenience the mesh was generated as a Delaunay triangulation. The total length of mesh segments is 5912 m and is confined to a vertical section 60 m wide and 30 m high (Figure 4.4.4.3). The lines marked A in Figure 4.4.4.4 depict the highly stressed region where new

fractures are formed in response to the last face advance step. The regions B and C above and below the stope have low stresses and are pervasively fractured by previous mining steps.

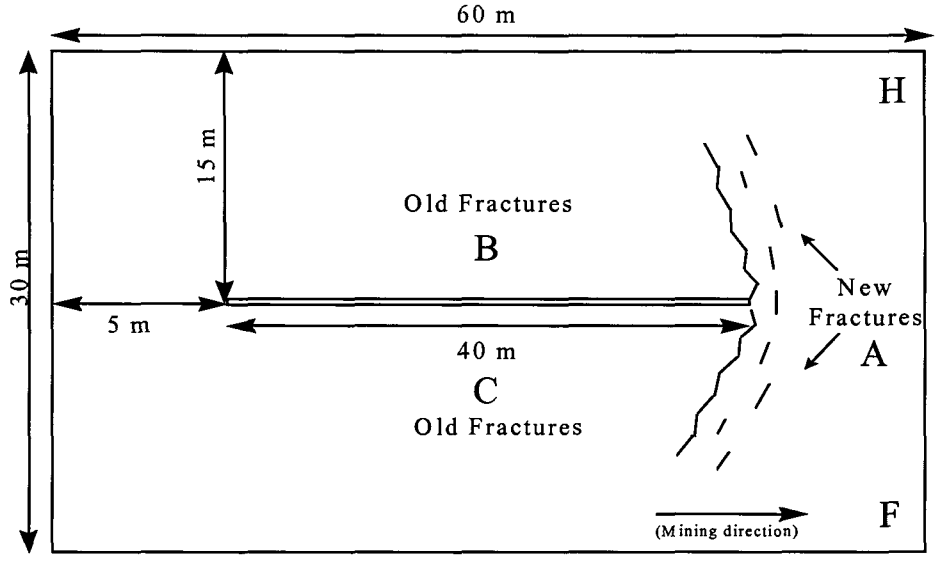

Figure 4.4.4.3 Illustrative mining problem of a parallel-sided panel.

Table 4.4.4.1 Material properties of H and F regions in the mining problem above.

Region	Cohesion (MPa)	Friction (degrees)	Mobilized Cohesion (MPa)	Mobilized Friction (degrees)	Tension Cut-off (MPa)
H	25	45	0	30	10
F	10	45	0	30	5

The far-field stress is assumed to have a vertical component of 60 MPa and a horizontal component of 30 MPa. The intact elastic material has a Young's modulus of 70 GPa and a Poisson's ratio of 0,2. It is assumed that the segments of the mesh behave in a viscoplastic manner in shear with a discontinuity relaxation constant of 0,0005 m MPa^{-1} day^{-1}. Figure 4.4.4.4 shows the estimated recurrence of seismic energy release when 40 mining steps are carried out at a face advance rate of one metre per day. The time step interval is 0,1 days implying that 400 successive problems are solved. Following each face advance step there is a sharp increase in released energy followed generally by a monotonic decay in activity until the next face advance increment. The sizes of the initial five peaks in Figure 4.4.4.4 are seen to increase steadily but thereafter become progressively more erratic as the mining face advances. Small sub-peaks of activity are also observed to occur between successive advance steps as the panel span is increased. This behaviour shows an encouraging correspondence to actual observations in the deep level gold mines. It can also be seen from Figure 4.4.4.4 that the minimum level of activity displays an increasing trend as the span of the panel is increased.

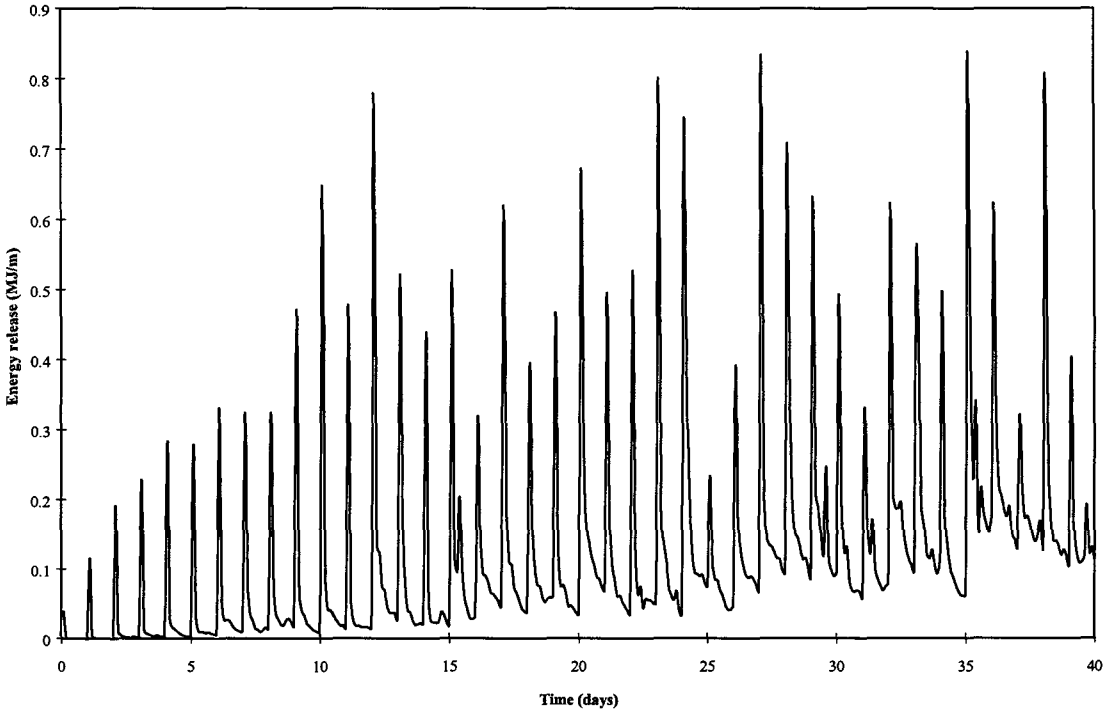

Figure 4.4.4.4 Energy release per time step - mining seven days per week.

The analysis shown in Figure 4.4.4.4 was repeated with 20 relaxation time steps being introduced after every six face advance steps to simulate the weekend break. The results are shown in Figure 4.4.4.5. Again it is clear that the general level of activity increases steadily as the panel span is increased. The cumulative energy released, at the end of each face advance step, is compared in Figure 4.4.4.6 for the two cases of continuous mining (filled squares) and mining with a weekend break (open triangles). Over the first 30 mining steps there seems to be little difference, although after step 30 slightly more seismic activity appears to be associated with the continuous mining cycle.

It is also important to consider whether, in each week, the seismic activity increases during the week. The successive mean values of the peak seismic energy release shown in Figure 4.4.4.5 are quoted in Table 4.4.4.2 and do suggest that the seismic activity increases towards the end of each week. However, it must be recalled that in this case the increasing span of the panel tends to impose a trend of increasing seismic activity over the simulated period of seven weeks. In future the analysis should be repeated for the case of a mature stope of wide span with a fully developed fracture zone.

Table 4.4.4.2 Peak energy release averaged for each day of the week.

DAY	Mon	Tues	Wed	Thu	Fri	Sat
Average Peak Energy	0,375	0,307	0,483	0,483	0,512	0,586

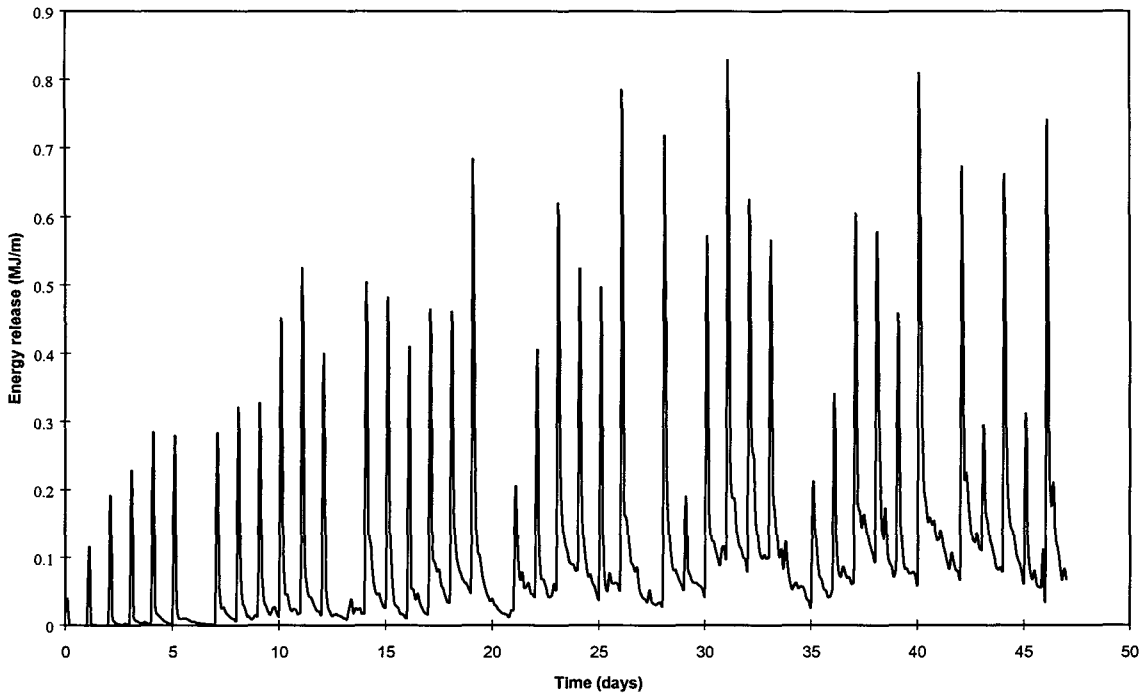

Figure 4.4.4.5 Energy release per time step - no mining every seventh day.

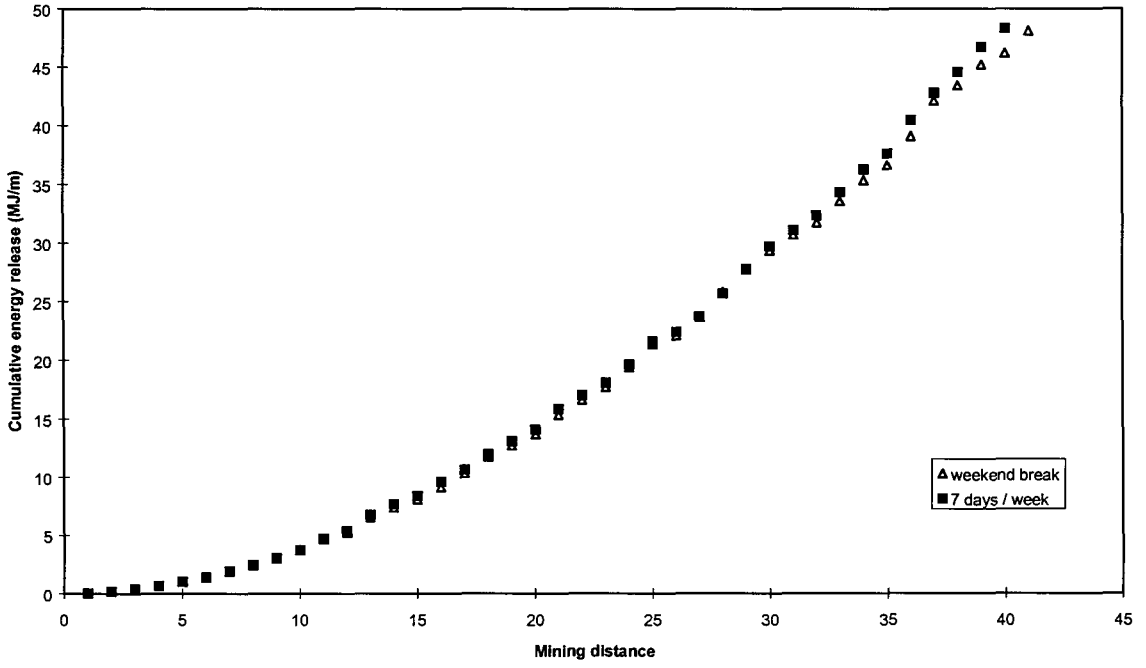

Figure 4.4.4.6 Comparison of cumulative energy released for continuous mining and mining with a break every seventh day.

4.4.4.4 The effect of rate of mining on the volume of stope closure per area mined

When discussing the effects of rate of mining, emphasis is mostly placed on the aspect of increased worker exposure to possible rockbursts. On the positive side, however, a potential benefit of the higher mining rate will be a reduction in the volume of closure per area mined.

Large magnitudes of closure are undesirable as this reduces the energy absorbing capabilities of hydraulic and other support units that remain in the same position for too long. Large magnitudes of closure might also be associated with a deterioration in hangingwall conditions that increases the risk of falls of ground and the potential for shake-out during seismic events. From Figure 4.4.3.12 (Section 4.4.3) and Appendix 4.5, the significant steady-state closure rates in certain areas of the Vaal Reef and Ventersdorp Contact Reef (soft lava) are evident. It is known that if all mining activity stops, this steady-state closure rate will persist for many days before it gradually starts to decline. The effect of this on the volume of closure per area mined was illustrated by using the discontinuum viscoplastic model developed for this project. Two stopes are mined up to a span of 20 m with the one subjected to blasting operations throughout the whole week while in the other no mining takes place on both Saturdays and Sundays. The model parameters used in these simulations are given in Table 4.4.4.3. Figure 4.4.4.7 illustrates the effect of these mining strategies on the volume of stope closure. It is clear that the slower mining rate which accompanies mining with a weekend break, leads to a significant increase in closure.

Table 4.4.4.3 Parameters used in the stope simulation to investigate the effect of a weekend break on the volume of stope closure per area mined.

Parameter	**Value**
Vertical stress	60 MPa
Horizontal stress	30 MPa
Young's modulus	70 GPa
Poisson's ratio	0,2
Cohesion	25 MPa
Friction	45°
Mobilized cohesion	0 MPa
Mobilised friction	30°
Discontinuity fluidity	1×10^{-5} m MPa^{-1} day^{-1}

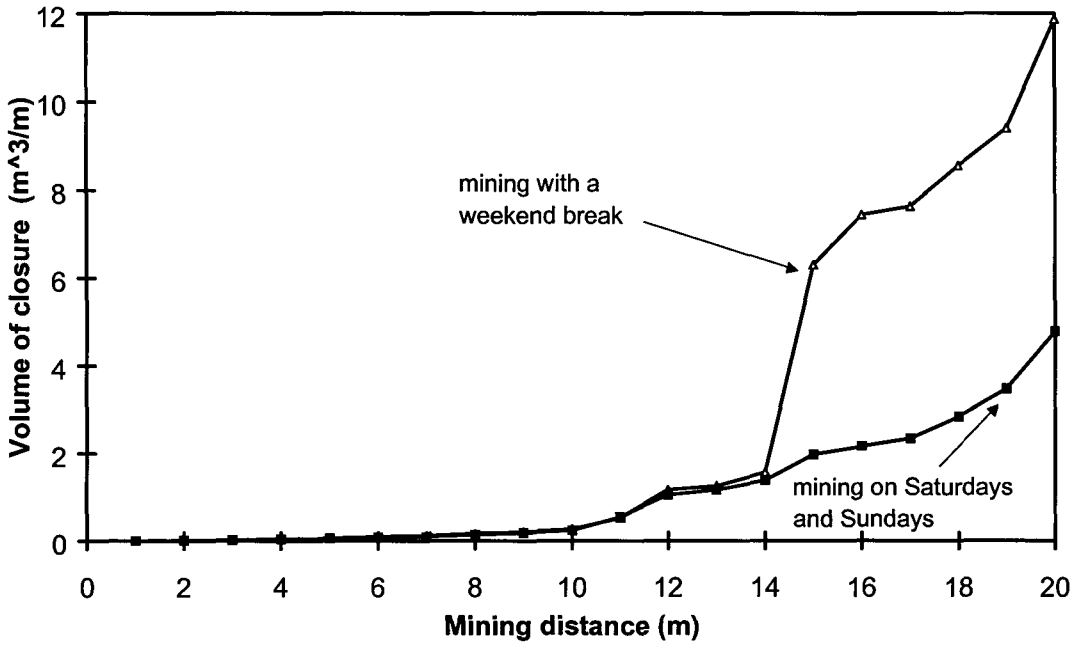

Figure 4.4.4.7 Volume of stope closure as a function of mining distance for mining which includes blasting on Saturdays and Sundays and mining with a weekend break.

To obtain actual values of closure increase due to a break on Sundays, underground closure data was analysed. The calculations are restricted to the first 20 m behind the face (Figure 4.4.4.8). Assume the volume of closure in region A to be S_T on Sunday morning when the workers enter the stope (after an increment was mined on Saturday).

It was noted from underground measurements that the rate of steady-state closure $\dot{S}_{ss}$ (see Figure 4.4.3.6 and Equation 4.4.3.1 for a definition of the closure terms) is a function of the position in the panel. Therefore the volumetric increase in steady-state closure, ΔS^{v}_{ss}, in the rectangular area from x_1 to x_2 perpendicular to the face and y_1 to y_2 parallel to the face, for the period Δt when there is no mining, will be given by

$$\Delta S^{v}_{ss} = \Delta t \int_{x_1}^{x_2} \int_{y_1}^{y_2} \dot{S}_{ss}(x,y)\,dy\,dx \qquad (4.4.4.1)$$

$\dot{S}_{ss}(x,y)$ is a function describing the spatial dependence of the rate of steady-state closure. The preliminary measurements indicated that $\dot{S}_{ss}$ varies significantly with distance to face (therefore in the x-direction) but not significantly in the face-parallel direction (y-direction). Therefore, when assuming that $\dot{S}_{ss}(x,y)$ remains constant in the y-direction, Equation (4.4.4.1) can be simplified to

$$\Delta S^{v}_{ss} = Y \Delta t \int_{x_1}^{x_2} \dot{S}_{ss}(x)\,dx \qquad (4.4.4.2)$$

where $Y = y_2 - y_1$ is the distance of the rectangular area parallel to the face.

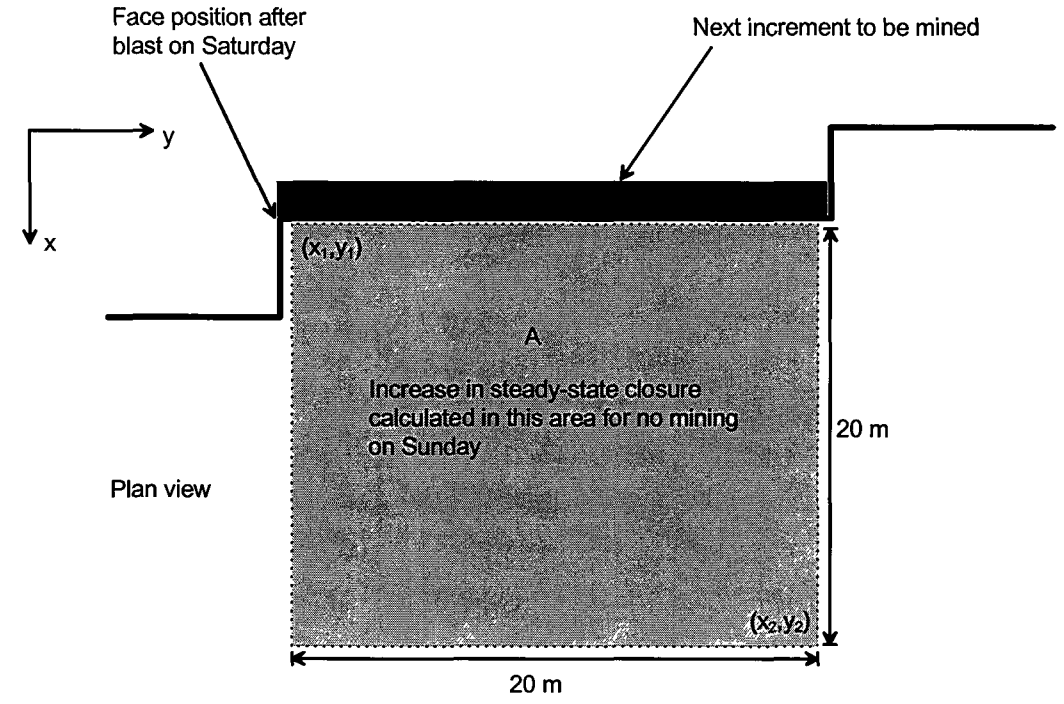

Figure 4.4.4.8 Region where the increase in volume of steady-state closure is calculated.

Note that for these initial calculations, a linear function between closure rate and distance to face in the region 0-20 m is assumed. Further measurements are however needed to verify this assumption. For the Vaal Reef at Hartebeestfontein Mine, only the steady-state closure rates for distances from the face between approximately 10 m and 16 m are known. These closure rates are plotted in Figure 4.4.4.9 as a function of distance from the face. Note that this data suggests that the steady-state closure rates increase as the distance to face increases.

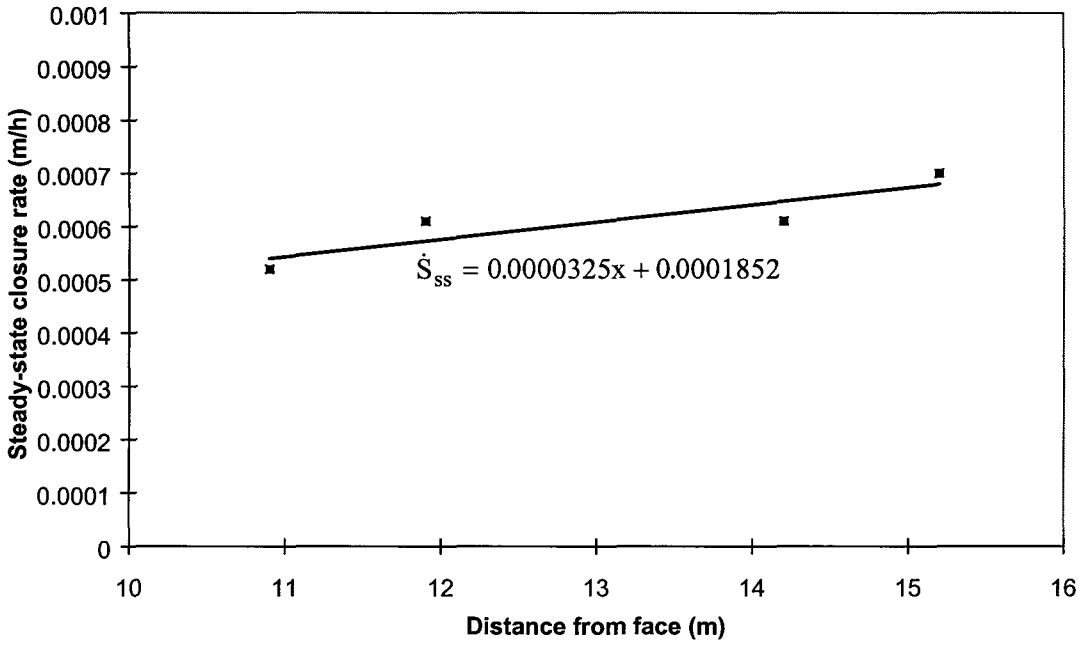

Figure 4.4.4.9 Steady-state closure rate as a function of the distance to face for the Vaal Reef.

The volume of steady-state closure increase over a 24 hour period for a distance of 0-20 m from the face and a panel length of 20 m can then be calculated from Equation (4.4.4.2) as $\Delta S^{v}_{ss} = 4{,}9m^3$. Referring to Figure 4.4.4.8 then, if the next increment after Saturday blasting is mined on Sunday, the volume of closure in region A will be S_T when the workers enter the stope. If there is however a weekend break and they only return on Monday, the volume of closure will be (S_T + 4,9 m^3) for the same area mined. If there was no mining on Saturday either, the increase would double to $\Delta S^{v}_{ss} = 9{,}8\ m^3$.

In comparison, Figure 4.4.4.10 illustrates steady-state closure rates for the Ventersdorp Contact Reef where the lava is hard. Note that the closure rates are significantly lower than those in Figure 4.4.4.9. The volume of increase in steady-state closure can again be calculated from Equation (4.4.4.2) as $\Delta S^{v}_{ss} = 1{,}36\ m^3$ for no mining on Sunday and $\Delta S^{v}_{ss} = 2{,}7\ m^3$ for no mining on both Saturday and Sunday.

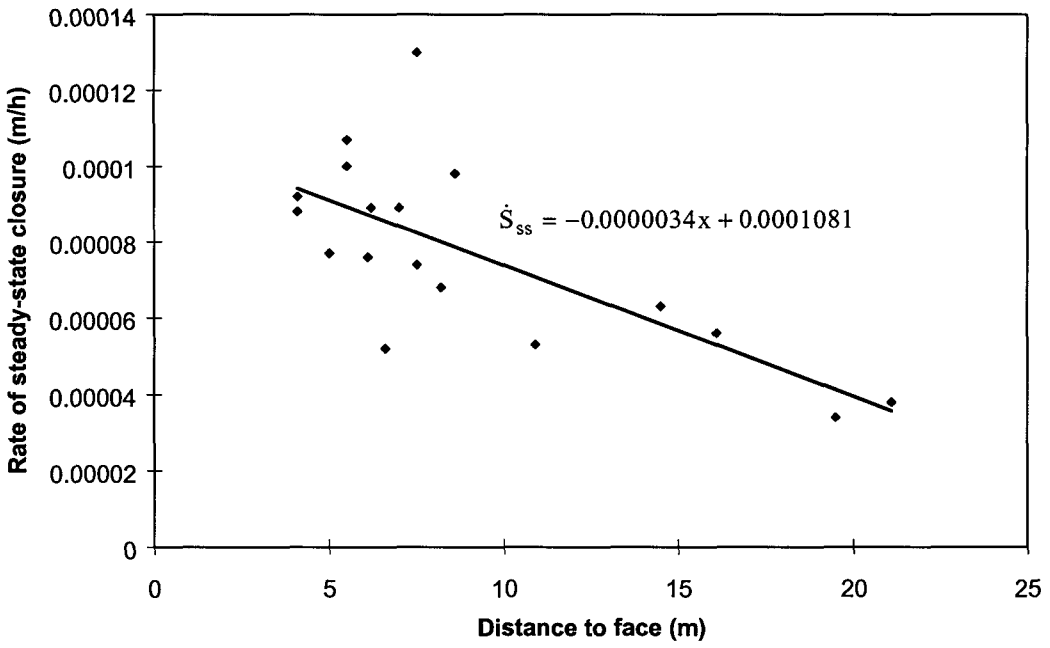

Figure 4.4.4.10 Steady-state closure rate as a function of the distance to face for the Ventersdorp Contact Reef.

To summarise, it is clear that increased mining rates in areas with high steady-state closure rates will have the distinct benefit of decreasing the volume of closure per area mined with a possible improvement in hangingwall conditions. This is in agreement with work done by Arnold (1993) who noted that increased rates of face advance, decreased the time-dependent loosening or unravelling of hangingwall blocks and improved hangingwall stability. Due to the lower steady-state closure rates, increased mining rates in the Ventersdorp Contact Reef (hard lava) stopes will however not be as effective in reducing the volume of closure per area mined as in areas with a high steady-state closure rate. When considering the effect of increased mining rates (such as implementation of mining operations over weekends) in a particular area, the parameter ΔS^{v}_{ss}, might be a useful measure of possible improvements in hangingwall conditions. Further work is necessary to establish a quantitative correlation between $\dot{S}_{ss}$ and the

unravelling of the hangingwall for slow mining. The mechanisms of deterioration in hangingwall condition should also be investigated.

4.4.5 Time to failure and prediction of future energy release

In assembling appropriate numerical techniques to be used to represent the stope fracture zone it is essential to understand the potential mechanisms for material instability in relation to the representation of the rock fabric and pre-existing fractures. In this respect it is interesting to compare the time-dependent failure of two uniaxially loaded samples in which the grain structure is represented by fracture paths favouring splitting (the Delaunay tessellation) and fracture that is interrupted by rounded particles (a Voronoi tessellation). Previous studies of this type have revealed that the Delaunay structure promotes strong load shedding at the yield point of the sample, whereas the Voronoi structure promotes plastic hardening behaviour beyond the yield point. Incorporation of time-dependent attributes on existing fractures can be used to study questions of stand up time and time to failure. In addition, investigation of these problems relates to the potential for the prediction of rapid failure in the stoping environment. To gain some preliminary insight into these questions numerical simulations of two uniaxially loaded rectangular specimens were compared. In the one case the sample was loaded suddenly with $\sigma_1 / \sigma_c = 0{,}41$ where σ_c represents the uniaxial strength equivalent to the Mohr-Coulomb parameters associated with the initially intact crack segments in the specimen. The consequent failure sequence, shown in Figures 4.4.5.1a to 4.4.5.1d, indicates the progressive formation of a splitting crack parallel to the loading direction. Figure 4.4.5.2 shows the time sequence of incremental strain energy release in each time step. Following an initial period of activity the incremental energy release continues at a relatively low level. (The released energy could be considered to correspond to acoustic emission counts). Just after time 50, the energy release increments display a rapid oscillation which is then followed, at approximate time 56, by very large amplitude release cycles culminating in failure at time 87,4 (this situation is depicted in Figure 4.4.5.1d).

In the second numerical experiment, the sample was covered by a grid of Voronoi polygons having the same nominal failure properties as the Delaunay mesh. Loading this sample with $\sigma_1 / \sigma_c = 0{,}41$ resulted in very small incremental energy release events and very little damage in the sample. When the load was doubled to $\sigma_1 / \sigma_c = 0{,}82$ the sample still appeared to deform in a gradual manner with the resultant damage pattern at time 36,6 shown in Figure 4.4.5.3. It is interesting to note that the damage pattern shown in Figure 4.4.5.3 is more diffuse than that shown in Figure 4.4.5.1c although incipient shear banding can be observed in Figure 4.4.5.3 and the predominant fracture direction is aligned to the loading direction. The corresponding incremental energy release in each time step is plotted in Figure 4.4.5.4 showing a relatively uniform trend of energy release up to the time of run termination as compared to the unstable behaviour shown in Figure 4.4.5.2.

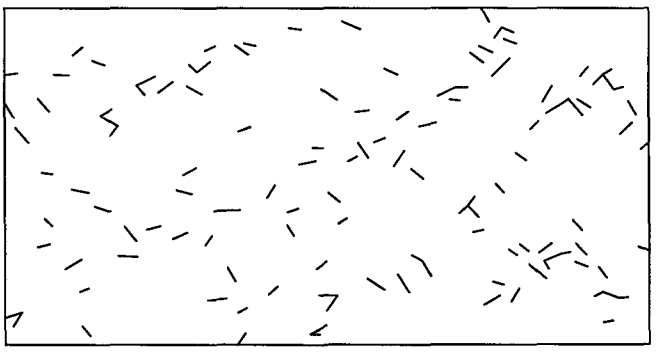

a) Time = 5

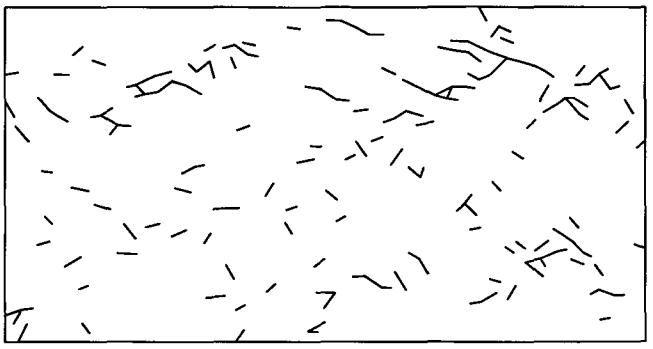

b) Time = 45

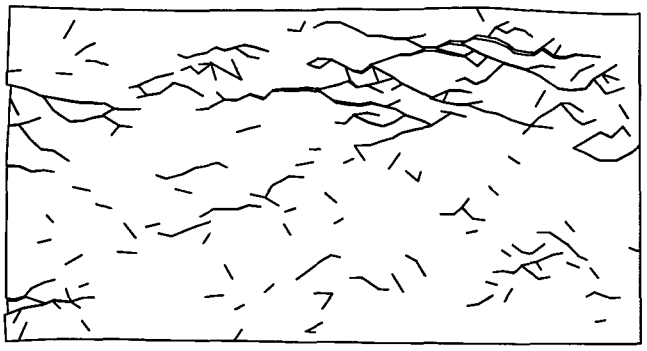

c) Time = 85

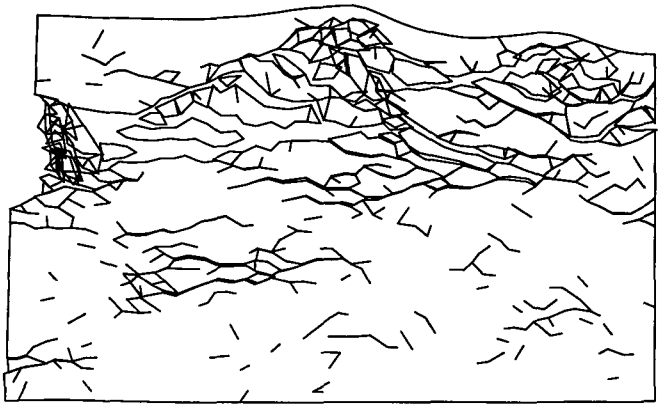

d) Time = 87,4 (Time of failure)

Figure 4.4.5.1 Fractures mobilized at different times following a sudden horizontal load applied to a rectangular sample.

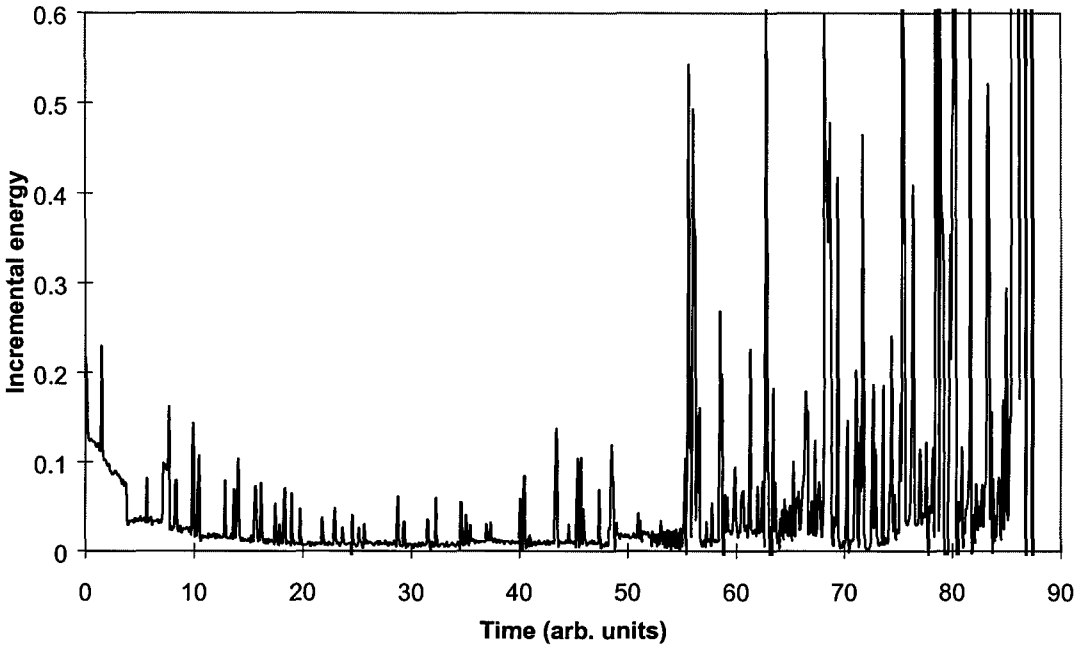

Figure 4.4.5.2 Incremental strain energy released as a function of time for the specimen depicted in Figure 4.4.5.1.

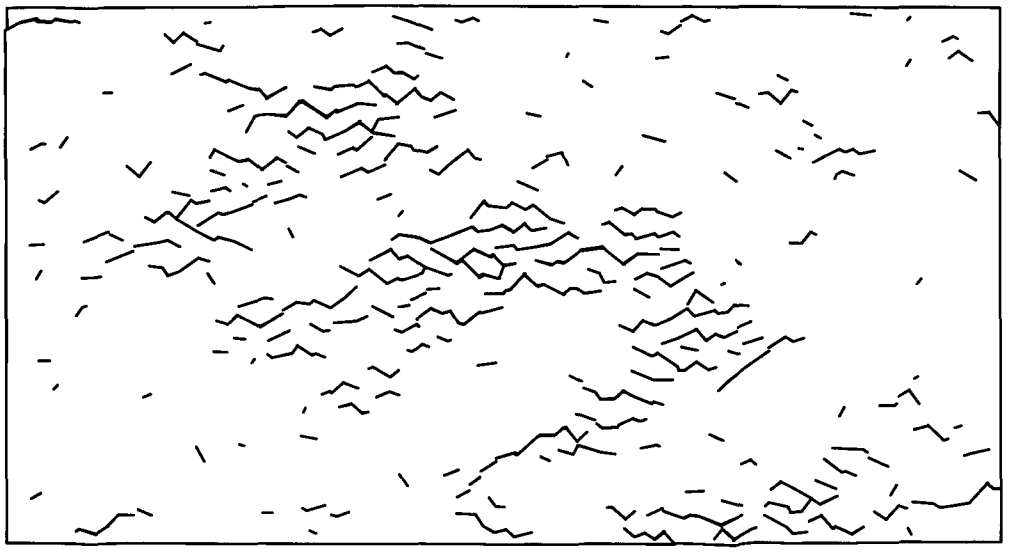

Figure 4.4.5.3 Damage pattern in a deformed sample arising from a Voronoi tessellation.

The most significant point of these initial investigations is that strongly different energy release signatures are associated with the two different sample fabrics represented by the Delaunay and Voronoi tessellations respectively. This raises the question of whether the failure time can be predicted. For example, the diffuse localization of failure observed in Figure 4.4.5.3 may have a predictable time to ultimate failure whereas the time to failure of strongly localized phenomena, as shown in Figures 4.4.5.1a to 4.4.5.1d, may be inherently unpredictable. A

further question of practical interest is whether the time-dependent nature of the fracture zone response can be engineered to reduce the uncertainty of sudden failure episodes.

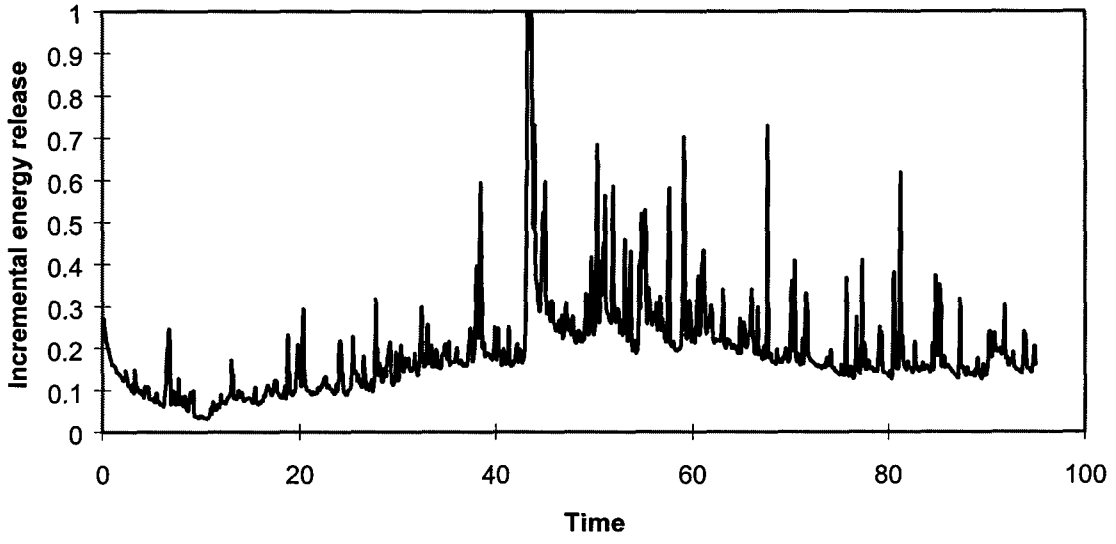

Figure 4.4.5.4 Incremental strain energy released as a function of time for the specimen shown in Figure 4.4.5.3.

It follows from Section 4.4.3 that time-dependent stope closure following a mining increment is a reflection of the face stress before mining the particular increment. The question of the predictability of future stope face stress from detailed observations of the stope closure is also of considerable interest. The time-dependent tessellation model can be used to explore, for example, the case of a narrow width stope that is mined according to a cycle of one blast per day in incremental steps of one metre per step. The stope panel is surrounded by a random mesh of potential crack segments which are generated as a Delaunay triangulation to allow load shedding following failure. In the particular case described here, the average length of the mesh segments is 1,12 m with a standard deviation of 0,28 m. The mesh segments above the panel horizon are assumed to be stronger than the segments below the panel. The specific strength and viscoplastic properties are summarised in Section 2.4.6 and by Napier & Peirce (1997). The far-field stress is assumed to have a vertical component of 60 MPa and a horizontal component of 30 MPa. The intact elastic material has a Young's modulus of 70 GPa and a Poisson's ratio of 0,2.

Figure 4.4.5.5 shows the estimated recurrence of seismic energy release for 30 mining steps at a face advance rate of one metre per day. The time step interval is 0,1 days implying that 10 time steps occur between each face advance increment. Following each face advance step there is a sharp increase in released energy followed, generally, by a monotonic decay in activity until the next face advance increment. Small sub-peaks of activity are also observed to occur between successive advance steps of the panel span. This behaviour is qualitatively very similar to that observed in deep level South African gold mines (McGarr, 1971). The sizes of the initial five peaks in Figure 4.4.5.5 are seen to increase steadily but thereafter become progressively more erratic as the mining face advances. It can also be seen from Figure 4.4.5.5 that the minimum level of activity displays an increasing trend as the span of the panel is

increased. An analysis of the successive energy release peaks (Napier & Peirce, 1997) shows that their successive magnitudes beyond step 9 are effectively uncorrelated.

Consider next the time-dependent closure profile measured at a fixed point 24 m from the starting edge of the panel. This profile is plotted in Figure 4.4.5.6 as the stope span is increased to 25 m, 26 m, 27 m and 28 m respectively and is encouragingly similar to the closure profiles observed in practice (see Section 4.4.3). For the purposes of further analysis, it is useful to define the change in closure during the first time step following the incremental mining step as the initial step closure and the final closure just prior to the next mining step as the total step closure.

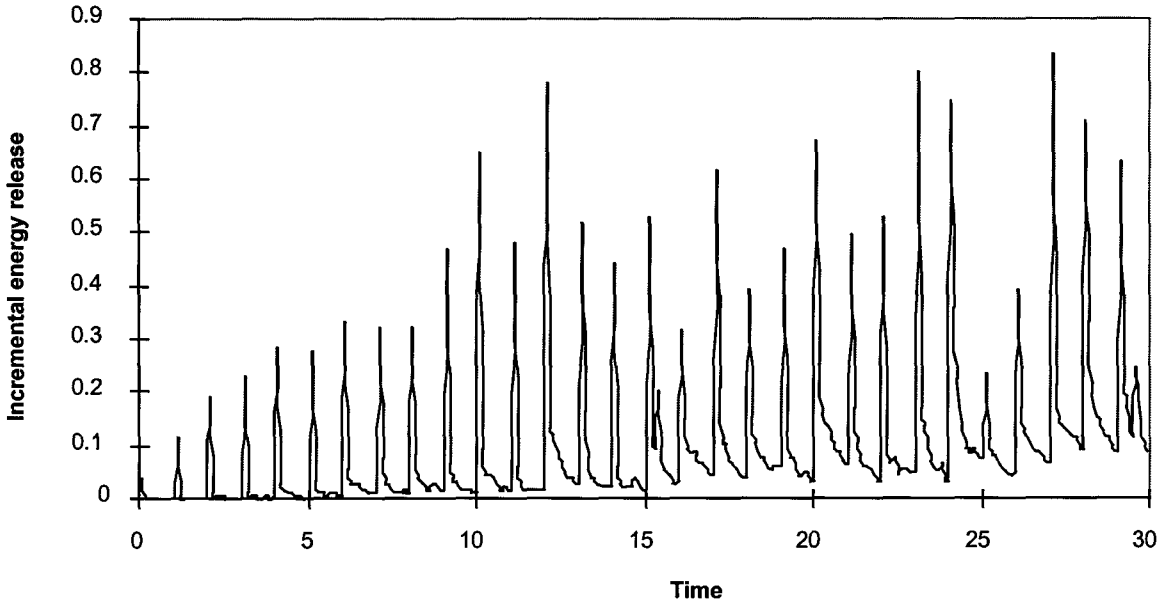

Figure 4.4.5.5 Energy release cycles accompanying mining step increments for a parallel sided panel.

The initial step closure and the total step closure, averaged over a distance of one metre behind the stope face, are plotted from mining step 9 to mining step 30 in Figure 4.4.5.7. It is seen that the initial step closure fluctuates with no clear trend whereas the total step closure apparently increases as the panel span increases. To place some interpretation on these results it is useful to recall the analytical expressions for the closure of a parallel sided, narrow width opening in an infinite elastic medium (Salamon, 1974). Integrating these expressions it can be shown that for a panel of span $L+\Delta L$, the average closure $\overline{D_v}$ over the interval ΔL immediately behind the stope face is given by the approximate relation :

$$\overline{D_v} \approx C(1-\nu^2)(P_v / E)\sqrt{L\Delta L} \qquad (4.4.5.1)$$

where P_v = Virgin vertical stress (MPa)

E = Young's modulus (MPa)

ν = Poisson's ratio

C = Asymptotic constant (C . 8/3)

Similarly, the average stress $\overline{\sigma}_v$ over the interval)L ahead of a panel of span *L* is given by

$$\overline{\sigma}_v = P_v\sqrt{(1 + L/\Delta L)} \qquad (4.4.5.2)$$

Equation (4.4.5.1) is plotted in Figure 4.4.5.7 for)L=1 m, using the field stress P_v = 60 MPa and elastic constants E = 70 GPa and ν = 0,2. The average elastic closure shows a similar trend to the total step closure. However, the total step closure always exceeds the elastic closure as might be expected. The average stress over a distance of 1m ahead of the stope face is plotted in Figure 4.4.5.8 together with the values obtained for the elastic case given by Equation (4.4.5.2). It is interesting to note that the average stress ahead of the stope face in the inelastic analysis appears to be bounded and, in particular, does not follow the increasing stress trend shown by the elastic analysis.

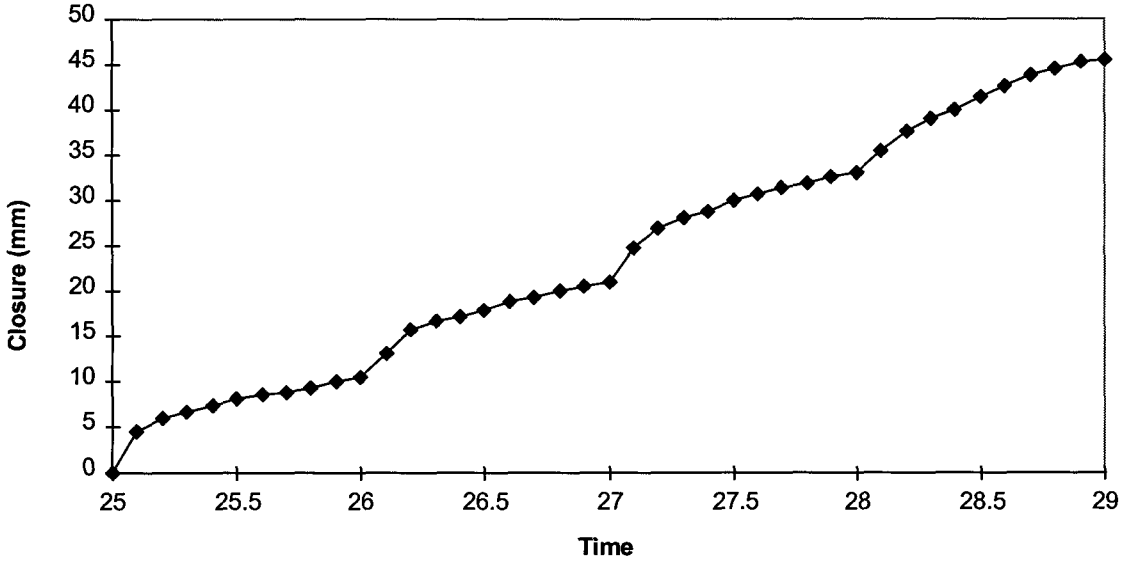

Figure 4.4.5.6 Time-dependent closure at a fixed point in the modelled stope.

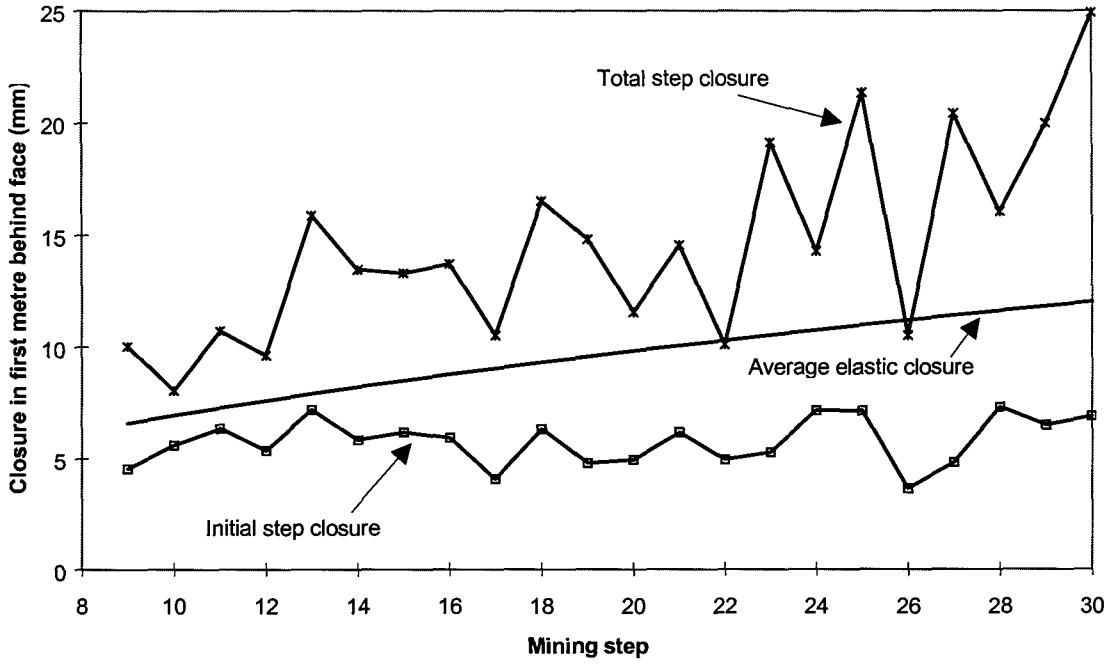

Figure 4.4.5.7 Average initial and total step closure compared to the average elastic closure one metre behind the stope face, for successive mining steps.

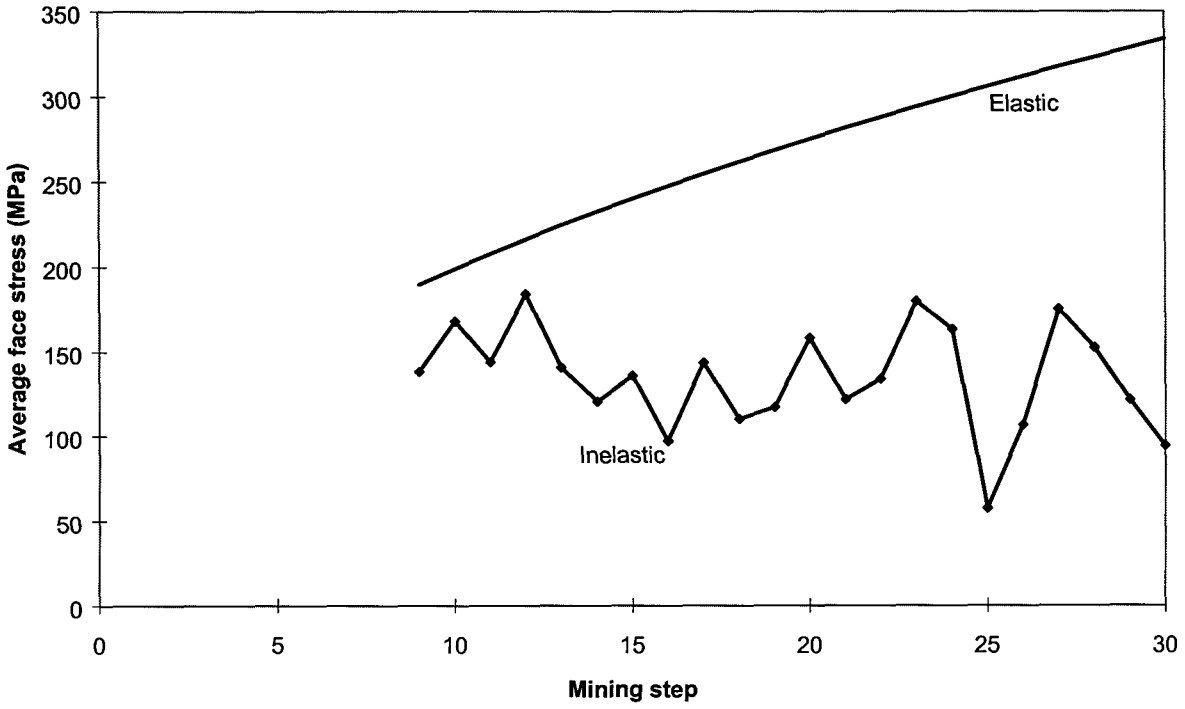

Figure 4.4.5.8 Average stress ahead of the stope face compared to the average stress calculated using an elastic analysis.

A question of considerable interest is whether the continuous time-dependent closure measurements can be used to predict the *future* energy release or face stress buildup. At present no definitive predictor has been found. In particular, no correlation is found, for example, between the change in closure after the initial jump and the subsequent energy release peak. However, it appears that the change in closure after the initial jump in closure, divided by the initial closure jump, shows a tenuous inverse correlation to the stope face stress as shown in Figure 4.4.5.9. It is also clear that this relationship will probably have to be supplemented by additional information, such as regions of intense damage, which might be inferred from seismic data. The random viscoplastic discontinuity simulation of face advance processes seems to be a useful tool that can be used to gain insight into the mechanisms of stress redistribution and energy release cycles. This offers the hope that this type of analysis can be applied routinely to layout sequencing problems and to understanding how hazardous face stress conditions can be identified. In this regard it must be emphasized that three dimensional effects have not yet been simulated. These are expected to be important in devising optimal tradeoffs between available face length and total shaft production rate as well as questions concerning the extent of the fracture zone in ultra deep level mining operations.

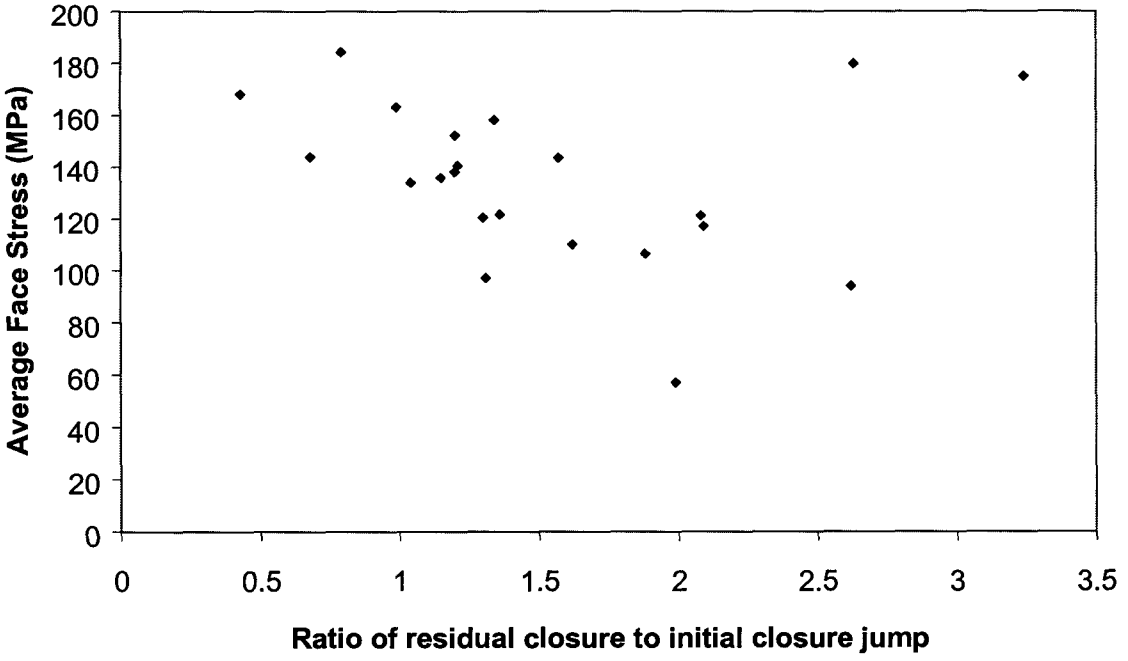

Figure 4.4.5.9 Plot of average stress ahead of the stope face against the ratio of the residual closure divided by the initial jump in closure following the previous mining step.

4.5 Conclusions

An important objective of the studies described in this section was the calibration and validation of the DIGS fracture zone simulator using physical modelling, underground observations and closure measurements. Subsequently the code was used to investigate rate of mining strategies. It was found that detailed monitoring of stope closure profiles can provide a useful signature of the geotechnical response of the rock mass to the mining process.

As described in Section 2, two approaches to modelling fracture growth have been incorporated in the DIGS displacement discontinuity element program. The first involves discrete fracture growth from seed points and the second considers a pre-defined tessellation of potential sites which activate sequentially as the failure criterion is exceeded. The physical models and underground experiments were used to test the validity of these two approaches.

Regarding the laboratory work, encouraging correspondence has been obtained between various physical experiments and the numerical simulations. The results of experiments on blocks of quartzite containing a tabular slot under triaxial loading show that the presence of interfaces significantly alters the position and inclination of the resulting fractures. It was found that these fractures can be simulated using the discrete fracture growth approach in DIGS. The three dimensional acoustic emission location technique provides useful information regarding the sequence of fracture growth and growth direction, which correlate well with the numerical simulations. In the samples without discontinuities, shear fractures are observed to extend ahead of the stope in the experiments. The shear fracture criterion of DIGS correctly predicts corresponding fractures in the numerical models. In the models with a pre-existing discontinuity, fractures extending from the tip of the slot are observed to terminate on the discontinuities. The analysis with a tensile fracture criterion correctly predicted the final fracture directions. The requirement to pre-select the seed point may however bias the final fracture pattern. The physical experiments demonstrate that the fracturing may occur in shear or tension depending on the presence of interfaces and closure behaviour of the stope.

When using the alternative tessellation approach in DIGS, there is no need to choose the appropriate failure criterion beforehand. This approach was evaluated with physical tests of fracture formation processes below a rectangular strip punch. The results suggest that some confidence can be placed in the use of a random mesh to represent complex failure processes near mine openings in hard rock. It is found that the post-failure cohesion of each activated crack in the random assembly is a particularly important parameter controlling the pattern of failure. A related concept is the use of an incremental procedure to select the sequence of crack initiation in the random mesh. The use of an incremental activation rule implies some form of weakest link breakage mechanism and can also be viewed as an alternative manifestation of general cohesion and tension weakening behaviour. In general, the residual cohesion and incremental growth rules allow a balance to be established between plastic and brittle failure modes in the material. Additional work is required to clarify the choice of cohesion and tension weakening rules in relation to particular rock types.

As a further validation of the fracture growth methodologies in DIGS, the laboratory work was supplemented with underground observations of the fracture zone around deep level gold mine stopes. It was found that the numerical stability problems associated with discrete fracture growth from seed points can be overcome by using a tessellation approach. Modification of the material properties assigned to each element of the tessellation mesh permits the modelling of different rock types The memory and run time limitations of the standard boundary element formulation can be largely overcome with the multipole solution technique. A method of selecting the parameters for the multipole grid has been developed.

Sequential solution of the problem permits the use of large tessellated regions as only the active elements are included in the solution. The incremental method produces the most well-defined fracture paths, at the expense of solving the problem after the activation of each element. An activation rule in which many parallel growth stages are permitted for each mining step, makes allowance for the migration of the fracture zone associated with stress redistribution and is the suggested method for the solution of larger stoping widths in a reasonable time.

Dilation on the fractures resulted in higher compressive stresses in the hangingwall, and hence less closure. The relative strength of the rock types depends on both the unconfined strength and the friction angle, not directly on the cohesion. Good correspondence with the fracture patterns observed underground is obtained if stress redistribution is permitted and, in particular, if low friction parting planes are included above and below the stope. The trends of the

deformations and stresses agree with the measurements of Legge (1986) for the rock mass behaviour around a Carbon Leader stope.

Some distance ahead of the stope, the rock mass contains solid blocks separated by fracture zones. Dilation begins and the stress increases. Closer to the face relative movements between the hangingwall, reef and footwall are evident as the rock mass is translated towards the face. Immediately ahead of the face, the reef is highly fractured. The rock mass dilates into the excavation. The vertical and horizontal stresses reduce significantly. Most displacement on fractures, joints or bedding planes occurs within a few metres of the face. Behind the face, the horizontal and vertical stresses are slightly compressive and the rock mass contracts.

The comparison of modelling predictions with underground observations has shown that the tessellation approach is suitable for the prediction of the distribution and direction of fracturing induced by the interaction of the mining with primary geological structures such as bedding planes and layers of different strength rocks. Currently, however, the fracture intensity is not correctly predicted. The method can also predict the influence of closely spaced joints on the direction of the mining induced fracturing, suggesting that mining induced fracturing may align with mining activated jointing and other secondary geological structures. Methods for distinguishing the induced fractures from the geological features are required to provide unambiguous input parameters for computer modelling. This will lead to a better understanding of the interaction of discontinuities in the stope hangingwall and, therefore, to improvements in support design methodologies.

The discrete growth method is able to model the dependence of the fracturing on the direction of the major principal stress and can be used to investigate ways of overcoming the observed dependence of the rockfall hazard on the mining direction. The tessellation approach can predict a similar response, however, the initial mobilisation of diffuse fracture zones, corresponding to pre-existing faults, is further evidence for the need to incorporate the ability to predict shear localisation and fracture spacing.

Significant improvements in the modelling and understanding of the complex mining environments has been achieved by comparing numerical models with detailed geological and rock mechanics information. Further comparison with the available data is difficult as the current computers permit the analysis of small spans, and most *in situ* observations have been undertaken at large spans. In many cases, the data obtained underground does not have sufficient information to uniquely distinguish between proposed mechanisms. For example, closure measurements may have been taken, but no record of stress or geological environment is available. To be able to make meaningful comparisons, the geological structure, stress magnitudes and directions, and the deformation response should be known. The models have the potential to model realistic stope lengths. In addition, numerical schemes that capture the rock mass response on a small scale and provide equivalent representations on a large scale, e.g. the lumping methods investigated in Section 2, should be developed and implemented.

The observation and modelling of underground fracture patterns was supplemented by the monitoring of time-dependent stope closure in various geotechnical areas. The continuous closure data contains much information that is lost with the more conventional daily closure measurements. Although excavations in hard rock are not usually perceived to undergo significant time-dependent deformation due to the low creep rate of intact rock, the collected stope closure data illustrated behaviour to the contrary. Continuous closure measurements in tabular excavations indicate significant time-dependent deformation. Although the excavations are developed in brittle quartzite and lava, the rate of time-dependent closure can be as high as 0,6 mm/h in certain areas. The continuous closure behaviour of these excavations typically consists of an instantaneous response at blasting time followed by a primary phase of decelerating closure lasting approximately five hours and a steady-state closure phase. This pattern is repeated after the next blast. This closure behaviour is the result of the rheological behaviour of the fracture zone that surrounds these excavations. After a mining increment, the fracture zone extends in a time-dependent fashion ahead of the working faces. The majority of

new fractures appear to form within approximately the first 5 hours after the blast. Thereafter the number of new fractures decreases until the next blast occurs.

For tabular excavations in the Ventersdorp Contact Reef, the instantaneous closure response is very prominent, but decreases in magnitude as the distance from the face to the measurement position increases. The steady-state closure rate also decreases in magnitude with distance to the face. By contrast, for excavations in certain areas of the Vaal Reef, the rate of steady-state closure can be as high as 15 mm/day. For these excavations the instantaneous closure response at blasting time is virtually absent. Unlike the Ventersdorp Contact Reef, the steady-state closure rate of the experimental panel in the Vaal Reef increases with increasing distance to the face. This difference in behaviour is caused by the presence of prominent bedding planes in the hangingwall of the Vaal Reef.

Both the continuum and discontinuum viscoplastic models developed in this project allow for the direct simulation of the time-dependent fracture zone behaviour. Experiments indicate that these models are successful in simulating the time-dependent closure behaviour of tabular excavations, giving both the instantaneous response at blasting time and the primary and steady-state closure phases.

An important finding of this study is that the time-dependent closure data can possibly be used to deduce important information about the behaviour of the rock mass and the stress in the fracture zone ahead of the face. Although estimation of absolute stresses may not be feasible, the closure may be used to identify areas with large average face stresses and therefore a high risk of face bursting. It appears that the instantaneous closure response at blasting time gives an indication of the magnitude of stress in the face area. The larger the stress, the bigger the instantaneous closure response following the mining increment. This hypothesis was succesfully tested by simulating two stopes with different rock conditions using the continuum viscoplastic approach. Numerical studies using the discontinuum viscoplastic model also indicated that the initial jump in closure after blasting is correlated with the face stress before the blast. Some confirmation of this possible use of time-dependent closure data to determine a face burst hazard indicator was obtained from initial underground observations. The Ventersdorp Contact Reef (hard lava) stopes appear to be prone to face bursting and, as mentioned above, the closure behaviour of these excavations typically includes a large instantaneous response after blasting. By comparison, in some areas of the Vaal Reef with an apparent lower risk of face bursting, the instantaneous closure response after blasting is small. One useful hazard parameter might be the initial jump in closure after blasting divided by the total daily closure (called the closure ratio). Further work is however necessary to validate this concept, to quantify the face burst and falls of ground hazards for different geotechnical areas and to investigate how different values of closure ratio correlate with these hazards.

Following the success of the discontinuum viscoplastic model in simulating the time-dependent formation of the fracture zone and seismic energy release patterns, preliminary studies of the effect of rate of mining were conducted. It was found that a balance must be struck between higher energy release rates (potentially damaging rockbursts) at high face advance rates and greater deformation of the rock mass, with greater potential for local rockfalls, at slower mining rates. Numerical experiments indicated that slightly more seismic activity is associated with a seven day mining cycle when compared with mining with a weekend break. Optimum rates of face advance will however depend on the geotechnical area. Further work is therefore necessary to calibrate the models for the different areas and to determine appropriate mining rates for these areas.

An important aspect of higher face advance rates is the reduction in volume of closure per area mined. Slow mining rates are undesirable as the time-dependent increase in closure reduces the energy absorption capabilites of support units. Large magnitudes of closure are also associated with a deterioration of hangingwall conditions that increase the risk of falls of ground and the potential for shake-out during seismic events. The continuous closure measurements allowed for an estimation of increases in closure on days where faces are left standing.

Calculations showed that an increase in face advance rates in areas with large time-dependent closure (e.g. some areas of the Vaal Reef) will lead to a significant reduction in closure volumes per area mined. This might lead to a significant improvement in hangingwall conditions. This phenomenon might be less noticeable on the VCR with a hard lava hangingwall where the time-dependent closure is significantly less.

4.6 References

Adams, G. R., Jager, A. J. & Roering, C., 1981. Investigation of rock fractures around deep-level gold mine stopes, *2nd US Symposium on Rock Mechanics*, MIT, 213-218.

Arnold, D.A. 1993. An evaluation of cave mining in weak hangingwall conditions at Hartebeestfontein Gold Mining Company, Limited. *M.Sc. Thesis*, University of the Witwatersrand.

Atkins, A.R. & Keen, M.A. 1984. The measurement of rock deformation about excavations in hard rock mining. *SANGORM. Monitoring for Safety in Geotechnical Engineering,* 47-52.

Berlenbach, J.W. 1993. The mechanics of bedding-parallel faulting associated with the Ventersdorp Contact Reef on Kloof Gold Mine. *PhD Thesis*, Rand Afrikaans University.

Berlenbach, J.W., & J.K. Schweitzer 1996. Geotechnical environments associated with the auriferous Vaal Reef and Carbon Leader, Witwatersrand Basin, South Africa, *Interim SIMRAC Report GAP 332*, CSIR-Miningtek.

Briggs, D.J., 1983. Mechanical properties of quartzites and associated rock-types, *Report 13/83*, Chamber of Mines of South Africa.

Brummer, R.K. & Rorke, A.J., 1984. Mining induced fracturing around deep gold mines stopes, *Report 38/84,* Chamber of Mines of South Africa.

Chen, G., Kemeny, J.M. & Harpalani, S. 1992. Fracture propagation and coalescence in marble plates with pre-cut notches under compression. In: *Proceedings of fractured and jointed rock masses*, Lake Tahoe, California.

Cook, N.G.W., Hoek, E., Pretorius, J.P.G., Ortlepp, W.D. & Salamon, M.D.G. 1966. Rock mechanics applied to the study of rockbursts. *J. S. Afr. Inst. Min. Metall.*, vol. 66, 435-528.

Cundall, P.A. 1989. Numerical experiments on localization in frictional materials. *Ingenieur-Archiv*, vol. 59, 148-159.

Dyskin, A.V., Gemanovich, L.N., Jewell, R.J., Joer, H., Krasinski, J.S., Lee, K.K., Roegiers, J.C., Sahouryeh, E. & Ustinov, K.B. 1995. Some experimental results on three-dimensional crack propagation in compression. In: H.P. Rossmanith (ed.) *Proceedings Mechanics of Jointed and Faulted Rock 2*, Balkema, 91-96.

Gay, N.C. 1973. Fracture growth around openings in thick-walled cylinders of rock subjected to hydrostatic compression. *Int. J. Rock Mech. Min. Sci. & Geomech. Abstr.*, vol. 10, 209-233.

Gay, N.C. 1976. Fracture growth around openings in large blocks of rock subjected to uniaxial and biaxial compression. *Int. J. Rock Mech. Min. Sci. & Geomech. Abstr.*, vol. 13, 231-243.

Gay, N.C. & A.J. Jager 1986. The influence of geological features on problems of rock mechanics in Witwatersrand mines. In: Anhaeusser, C.R., Maske, S. (eds.) *Mineral Deposits of Southern Africa, Geol. Soc. S. Afr.*, 753-772.

Gay, N.C., Jager, A.C., Ryder, J.A. & Spottiswoode, S.M., 1995. Rock engineering strategies to meet the safety and productivity needs of the South African mining industry in the 21st century. *J. S. Afr. Inst. Min. Metall.* vol. 95, 115-135.

Gay, N.J., Spencer, D., Van Wyk J.J. & Van der Heever, P.K. 1984. The control of geological and mining parameters in the Klerksdorp Gold Mining district. In Gay, N.C., Wainwright, E.H. (eds.) *Proceedings of the 1st International Congress on Rockbursts and Seismicity in Mines*, Johannesburg, SAIMM: 107-120.

Germanovich, L.N., Salganik, R.L., Dyskin, A.V. & Lee, K.K. 1994. Mechanisms of brittle fracture of rocks with multiple pre-existingcracks in compression. *Pure and Applied Geophysics*, vol. 143, 117-149.

Germs, G.J.B. & Schweitzer, J.K. 1994. A provisional model for the regional morphostratigraphy of the Venterspost Conglomerate Formation in the West Rand and Carletonville Goldfields. *S.Afr. J. Geol.* vol. 97, 279-287.

Güler, G. 1997. Analysis of the rock mass behaviour as associated with Ventersdorp Contact Reef stopes, South Africa. *M.Sc dissertation*, University of the Witwatersrand, Johannesburg.

Gürtunca R.G. 1989. Results of a classified tailings monitoring programme at Vaal Reefs. *COMRO (now CSIR Miningtek) Internal Report*, no. 614.

Gürtunca R.G., Jager A.J., Adams D.J. & Gonlag M. 1989. The in situ behaviour of backfill materials and the surrounding rock mass in South African gold mines. In: HASSANI, F. (ed.) *Proc. 4th Int. Symp. of Mining with Backfill.*, Balkema, Rotterdam, 187-197.

Gürtunca, R.G. & Adams, D.J., 1991. Determination of the in situ modulus of the rock mass by the use of backfill measurements, *J.S. Afr. Inst. Min. Metall.* vol. 91 81-88.

Handley, M.F. 1996. The constitutive behaviour of a simple granular model as determined from numerical experiment. *Proceedings of the Second North American Rock Mechanics Symposium*, Balkema, Rotterdam.

Hodgson, K. 1967. The behaviour of the failed zone ahead of a face, as indicated by continuous seismic and convergence measurements, *Chamber of Mines Research Report 31/61*, Transvaal and Orange Free State Chamber of Mines Research Organisation.

Jaeger, J.C., & Cook, N.G.W., 1979. Fundamentals of rock mechanics. Chapman and Hall. : London.

Jager, A.J. & Turner, P.A. 1986. The influence of geological features and rock fracturing on mechanised mining systems in South African gold mines. *Gold 100, Proceedings of the International Conference on Gold, Gold Mining Technology,* Johannesburg, SAIMM, 89-103.

Johnson, R.A. & Schweitzer, J.K. 1996. Mining at ultra-depth: evaluation of alternatives. In: Aubertin, Hassani, Mitri (eds.) *Rock Mechanics*, Balkema, Rotterdam, 359-366.

King, R.G., Jager, A.J., Roberts, M.K.C. & Turner, P.A. 1989. Rock mechanics aspects of stoping without back-area support. *COMRO (Now CSIR Miningtek) Research Report,* no. 17/89.

Kuijpers, J.S. & Napier, J.A.L., 1991. The effect of loading history on stress generation due to inelastic deformation around deep-level tabular stopes, *J. S. Afr. Inst. Min. Metall.* vol. 91,183-194.

Leeman, E.R. 1958. Some measurements of closure and ride in a stope of the East Rand Proprietary Mines. *Pap. Ass. Min. Mngrs. S.Afr.,* vol. 1958-1959, 385-404.

Legge, N.B., 1986. Rock deformation in the vicinity of deep gold mine stopes and its relation to fracture, *Report 14/86.* Chamber of Mines of South Africa.

Legge, N.B. & Spottiswoode, S.M., 1987. Fracturing and microseismicity of a deep gold mind stope in the pre-remnant and remnant stages of mining, *IRSM 6th Int. Congr. Rock Mech.* Montreal, 1071-1077.

Lightfoot, N., Leach, A.R., & Kullman, D.H., 1994. A conceptual model of a hard rock, deep level, tabular ore body. *1st North American Rock Mechanics Symposium.* Balkema: Rotterdam.

Linkov, A.M. 1996. Rockbursts and the instability of rock masses - Schlumberger Award Lecture. *Int. J. Rock Mech. Min. Sci & Geomech Abstr.,* vol. 33, 727-732.

Malan, D.F. 1998. An investigation into the identification and modelling of time-dependent behaviour of deep level excavations in hard rock. *PhD Thesis*, University of the Witwatersrand, Johannesburg.

Malan, D.F. & Napier, J.A.L. 1997. Viscoplastic Discontinuum Model of Time-Dependent Fracture and Seismicity, *Int. J. Rock Mech. Min. Sci.* vol. 34, 1075-1089.

Martin, C.D. 1997. Seventeenth Canadian Geotechnical Colloquium: The effect of cohesion loss and stress path on brittle rock strength. *Can. Geotech. J.* vol. 34, 698-725.

Mcgarr, A. 1971. Stable deformation near deep-level tabular excavations. *J. Geophys. Res.*, vol. 76, no. 29, 7088-7106.

McWha, M. 1994. The influence of landscape on the Ventersdorp Contact Reef at Western Deep Levels South Mine. *S.Afr. J. Geol.,* vol. 97, 319-332.

Mendecki, A.J. 1997. Keynote lecture: Principles of monitoring seismic rock mass response to mining. In: Gibowicz, S.J. & Lasocki, S. (eds) *Proc. 4th Int. Symp. Rockbursts and Seismicity in Mines*, Balkema, Rotterdam, 69-80.

Napier, J.A.L. 1990. Modelling of fracturing near deep level gold mine excavations using a displacement discontinuity approach. *Proceedings of Conference on Mechanics of Jointed and Faulted Rock.* Vienna, Balkema, Rotterdam, 709-715.

Napier, J.A.L., 1998. Three dimensional modelling of seismicity in deep level mines. *Proceedings of Conference on Mechanics of Jointed and Faulted Rock.* Vienna, Balkema, Rotterdam, 285-290.

Napier J.A.L. & Stephansson, S.J., 1987. Analysis of deep level mine design problems using the MINSIM-D Boundary element program, *Proc. 20th Symp on application of computers and mathematics in the mineral industries*, SAIMM, Johannesburg, 3-19.

Napier, J.A.L. & Peirce, A.P. 1995. Simulation of extensive fracture formation and interaction in brittle materials, In: H.P. Rossmanith (ed), *Mechanics of jointed and faulted rock - 2,* Balkema, Rotterdam, 63-75.

Napier, J.A.L. & Peirce, A.P. 1997. The use of a multipole expansion technique to analyse large scale fracture processes and seismic recurrence effects in deep level mines. In: Hudson, J.A. (ed.) *Proc. NYRocks '97* ISRM International Symposium, 680.

Napier, J.A.L. & Hildyard, M.W. 1992. Simulation of fracture growth around openings in highly stressed, brittle rock, *J. S. Afr. Inst. Min. Metall.* vol. 92,159-168.

Napier, J.A.L., & Ozbay, M.U. 1993. Application of the Displacement Discontinuity Method to the Modelling of Crack Growth Around Openings in Layered Media. *Proc. Int. Symp. Assessment and Prevention of Failure Phenomena in Rock Engineering.* Istanbul, Turkey, 947-956.

Napier, J.A.L., Malan, D.F. & Sellers, E.J. 1998. Implications of fracture zone behaviour in deep level gold mines. Submitted to SIMRAC Symposium.

Nawrocki, P.A. 1995. One-dimensional semi-analytical solution for time-dependent behaviour of a seam. *Int. J. Num. Anal. Meth. Geomech.*, vol. 19, 59-74.

Peirce, A. P. & Napier, J.A.L. 1995. A spectral multipole method for efficient solution of large-scale boundary element models in elastostatics, *Int. J. Num. Methods Eng.* vol. 38, 4009-4034.

Raffield, M. P., James, J.V., Humphreys, I., & Issacs, A., 1993. Model input parameter selection through instrumentation and back analysis of large excavation failure, In: Bawden & Archibald (eds), *Innovative Mine Design for the 21st Century*, Balkema, 641-652.

Roberts, M.K.C. & Jager, A.J. 1991. An analysis of falls of ground and rockburst fatalities in three mining districts. *Mine Safety and Health Congress*, Chamber of Mines of South Africa.

Roering, C., Berlenbach, J & Schweitzer, J.K. 1991. Guidelines for the classification of fault rocks. *COMRO, User Guide No. 21.*

Schweitzer, J. K. & Johnson, R. A., 1997. Geotechnical classification of deep and ultra-deep Witwatersrand mining areas, *Mineralium Deposita*, vol. 32, 335-348.

Sellers, E.J. 1997. A tessellation approach for the simulation of the fracture zone around a stope. *Proceedings of Southern African Rock Engineering Symposium (SARES),* 143-154, Johannesburg.

Sellers, E. & Napier, J.A.L. 1997. A comparative investigation of micro-flaw models for the simulation of brittle fracture in rock. *Comp. Mechanics*, 20, 164-169.

Squelch A. P., 1990. Horizontal stresses in the face area hangingwall of backfilled and conventional stopes at Vaal Reefs, *Report R16/80*, Chamber of Mines of South Africa.

Toper, Z. 1997. Personal communication.

Van der Heever, P. 1982. The influence of geological structure on seismicity and rockbursts in the Klerksdorp Goldfield. *M.Sc. Thesis*, Rand Afrikaans University.

Walsh, J.B., Leyde, E.E., White, A.J.A. & Carragher, B.L. 1977. Stope closure studies at West Driefontein gold mine. *Int. J. Rock Mech. Min. Sci & Geomech. Abstr.*, vol. 14, 277-281.

Wiggill, R.B. 1965. The effects of different support methods on strata behaviour around stoping excavations. *Symposium on Rock Mechanics and Strata Control in Mines: J. S. Afr. Inst. Min. Metall.,* pp. 1-35.

Wilson, S.A., Henderson, J.R. & Main, I.G. 1996. A cellular automaton fracture model: the influence of heterogeneity in the failure process. *J. Struct. Geol.*, vol. 18, 343-348.

5 Conclusions

The main conclusions relating to each planned enabling output for project GAP332 are summarised in this section.

5.1 Gain sufficient knowledge of the fundamental physics of fracture initiation and growth to characterise and model the fracture zone around deep level gold mine excavations and engineer the fracture zone (Enabling output 1)

The study of microfractures in rock samples tested in laboratory triaxial extension experiments has provided a wealth of information regarding the nucleation, growth and coalescence of fractures. The consideration of thin sections of these samples as well as the surface fractography has resulted in a full three dimensional picture of fracture growth. Fracture surfaces that appear to grow in one direction have many component microfractures, some even growing towards the expanding fracture front. Numerical modelling of a two dimensional section through the samples using the standard DIGS displacement discontinuity program has proved that the numerical techniques are able to capture the nucleation from flaws and the effect of larger scale stress re-distributions by grain boundaries.

The coalescence of the fractures depends on a complicated process whereby tensile stresses produced ahead of growing fractures initiate other fractures and lead to a localized failure surface on a larger scale. In certain cases, the compressive stress regions induced by the flaws, perpendicular to the initiated fractures, can halt the growth of other fractures. Thus, the presence of flaws can both induce and inhibit fracture growth and the final fracture density will depend on the flaw density, and hence the rock fabric. The observation of these features from surface fractography provides a basis for the development of three dimensional modelling programmes, and also enables forensic studies of fractures that will assist in identifying the origin of fractures that have caused, or arisen from, rockfalls and rockbursts.

5.1.1 Incorporate creep-like time-dependent effects in prototype boundary element computer codes such as DIGS or MINSIM (Enabling output 1.1)

The time-dependent behaviour of the rock mass has been identified as an important factor controlling the closure of stopes and the potential for face bursting. Laboratory studies of the uniaxial creep of intact rock samples indicated that the hard rocks of the South African gold mines exhibit measurable creep strains and follow the characteristic primary, secondary and tertiary creep phases. Ultimate failure of the sample arises when the load is greater than about 90 per cent of the uniaxial strength. The quartzites were found to be more prone to creep, and hence allow non violent dissipation of energy, than hard lavas. The dependence of the strain rate on the stress level can be modelled successfully with a power law. Discontinuities exhibit an instantaneous response to shear stress followed by primary creep and then a steady state response. Extension fractures in lava exhibit negligible creep compared to bedding planes or gouge filled discontinuities. This is a reason for the low time dependent closure rates in VCR (hard Lava) stopes, compared to stopes in layered rock, such as the Carbon leader and Vaal Reefs.

A continuum viscoplastic model, based on the Mohr-Coulomb failure criterion, was developed to allow simulation of the, time-dependent, fracture zone behaviour. The model includes a novel time-dependent cohesion weakening rule to simulate time-dependent failure. The model

predicts that regions around an excavation with high stresses, exceeding the failure state, will fail first and will be followed by a gradual transfer of stress to the unfailed rock until an equilibrium state is attained. The instantaneous response to blasting, and subsequent primary and steady state closure phases observed in tabular stopes can be well represented.

A shortcoming of the continuum approach is the inability to consider the creep response of specific discontinuities. The framework for a discontinuum viscoplastic model was developed to be able to model the rate of slip on individual fractures, partings or other discontinuities. The rock fabric is represented by a random mesh of interacting discontinuities that can reproduce the primary, secondary and tertiary creep response of the overall rock mass. The method is applied to the modelling of stopes and the investigation of the rate of mining on energy release.

5.2 Study and model the interaction of seismic waves with the fracture zone so as to understand and improve the design of rockburst resistant mining strategies (Enabling output 2)

Combined experimental and theoretical approaches are developed in this work to study various aspects of the dynamic behaviour of rock. Specifically, the interaction of stress waves with rock mass discontinuities and dynamic fracturing due to blasting is investigated. Full details of the work are given in supplementary document number 2 attached to the present report. Theoretical concepts of elastodynamics and dynamic fracture mechanics are reviewed, and a comprehensive analysis of stress wave interaction with interfaces modelling various rock joint types is given. Important parameters and effects such as joint pre-stress, wave amplitude, non-linear interface conditions and energy dissipation are studied and discussed.

A brief overview is given of experimental methods and techniques, which are suitable to examine transient phenomena such as stress wave propagation and dynamic fracturing. These techniques are subsequently applied to investigate by experimental means wave interactions with mining excavations. The laboratory experiments are back-analysed by numerical simulations, and upon finding close correlation, the numerical programs are further applied to investigate parameters influencing rock mass instabilities and dynamic fracturing.

Blast induced fracturing is studied using cubic shaped laboratory specimens of PMMA to determine the effect of charge geometry and the relative importance of stress wave versus gas driven fracturing. Analytical as well as numerical methods are applied to investigate the dynamic stress field radiated by a progressively detonating column charge. Gas driven fracturing is simulated by means of a hybrid analytical/numerical model, and mechanisms and parameters which govern the final gas driven fracture extent in rock are identified and discussed.

5.2.1 Produce a report on dynamic fracture propagation, physical and numerical modelling (Enabling output 2.1) (Refer to supplementary document 2)

An important aspect of rock dynamics is blast induced fracturing. The blasting process is investigated by means of laboratory experiments and mathematical modelling. Specific attention is given to blast induced stress waves and gas pressurisation mechanisms that drive comparatively few fractures for a distance of many borehole radii. Some of the principal findings of the study are as follows:

- Laboratory experiments were conducted using cubic shaped specimens fabricated from PMMA and dynamically loaded with explosives. The resulting stress wave and fracture evolution was recorded by means of high speed photography. The experiments have provided new insights into the evolution of fracture systems due to detonation of various charge geometries.

- Photographs of the lag between the gas and crack front were obtained. This lag has previously been predicted theoretically, however this is the first direct physical evidence of the vacuum behind the propagating crack tip.

- The transient stress field due to the progressive detonation of a column charge is quantitatively studied by means of numerical analyses. It is shown that the shape of the pressure profile acting on the borehole walls has a relatively small influence on the dynamic stress field.

  When the velocity of detonation of the explosive exceeds the shear wave speed of the material, it is found that the maximum tensile stress initially acts in a tangential direction. At a distance of two to three borehole radii, the maximum tensile stress acts in an approximately axial direction and fracture re-orientation is likely. This fracture kinking has been observed in laboratory blasting experiments. At a detonation velocity below the Rayleigh wave speed of the material, the borehole is effectively pressurised quasi-statically, and the dynamic stresses are low in magnitude.

- Descriptions of blast induced fractures obtained under controlled conditions in the laboratory are valuable for developers of dynamic fracture codes to validate and check their results. Here, upon recognising that stress waves rapidly outpace the slower dynamic fractures and the majority of fracturing occurs due to pressurisation by detonation gases, a coupled solid, fluid and fracture mechanics numerical model is used to analyse the gas driven fracture propagation phase. The model is verified by back-analysing laboratory experiments, and good correlation between numerical and experimental data is observed. The analytical/numerical model is able to predict fracture propagation rates and the final fracture extent. The model gives insights into pressure profiles and gas velocities within fractures, incorporates dynamic material properties and quasi-dynamic fracture mechanics. Previously, a similar analysis was checked by limited post-blast data. In the present investigation a detailed verification is possible by correlating data obtained during the complete gas driven fracturing process.

- Using a combined analytical and numerical model, it is found that, for a given volume of gas, the fracture extent is similar for a wide range of initial peak borehole pressures. A method is proposed to estimate the final lengths of radial fractures for a given volume of combustion gases, where the gas volume is related to the explosive type and borehole diameter or charge mass. The method is applied to investigate various parameters governing the extent of blast induced fractures in confined rock. The influence of gas pressure, temperature, in-situ stress, rock fracture toughness, number of fractures and gas leak-off due to seepage on the final fracture extent is illustrated. The study quantitatively assesses the effect of these parameters on fracture extent related to explosive type and amount.

Various thermodynamic models are assessed and the importance of incorporating heat transfer from the hot combustion gases to the surrounding rock is demonstrated.

The results given here have important practical implications for blasting in confined rock, well-bore stimulation and rock pre-conditioning as is currently practiced in some deep-level mines in South Africa, the USA and Canada.

- Gas driven conical cracks extend typically from the ends of cylindrical cavities containing sealed charges and have not been investigated in detail previously. Here, the combined analytical/numerical method is further enhanced to model gas driven conical cracks. Practical results are given to relate the final fracture extent of sealed charges, at various levels of in-situ stress, to the type and amount of explosives.

5.2.2 Produce a report on the numerical modelling of experimental and field data, studying the interaction of seismic waves with the fracture zone (Enabling output 2.2) (See supplementary document 2)

5.2.2.1 Wave interactions with rock joints

Determining the nature of the interactions between stress waves and rock fractures/joints is an important area of research forming the basis of many rock dynamics problems. Notable progress has been made, particularly since the investigations of M. Schoenberg, who first investigated the comparatively simple interface stiffness model in detail. The validity of this model was further confirmed in later work by L.J. Pyrak-Nolte, N.G.W. Cook and L. Myer, and the stiffness model was successfully correlated to data obtained by means of reduced scale laboratory experiments. The interface stiffness model had, before the current study, not yet been applied in a general manner to actual rock joints, with stiffness related to measurable rock joint properties.

Principal findings

- In this work the joint stiffness model is further developed to incorporate non-linear normal and tangential interface stiffness, where the relations governing the stiffness are based on actual joint properties. For typical joints analysed here, stress waves with a frequency of $\pm$ 100 Hz are predominantly transmitted, whereas at a comparatively high frequency of $\pm$ 2000 Hz most of the incident energy is reflected.

  Previously, although reflection and transmission coefficients were available for constant stiffness interface models, the coefficients were not related to actual joint properties and no lower to higher end frequency limits were established. The method developed here can be used to establish the approximate reflection – transmission characteristics for other joint types, provided the interface surface properties have been determined by means of field or laboratory testing.

- An essential aspect of studies dealing with joint – wave interactions is the influence of joint pre-stress. This effect has previously been neglected. Based on actual interface properties, it is shown in this work that at even comparatively low levels of pre-stress, the joint reflection and transmission characteristics are altered significantly. With increasing pre-stress, more energy is transmitted across the joint and the amplitude of reflected waves is reduced. These results have important implications in deep level mining applications and numerical simulations of wave propagation through fractured rock.

- The generalised Kelvin model is used to investigate the dynamic behaviour of fluid filled interfaces. The reflection and transmission as well as energy dissipation characteristics of this model are quantified, and are found to depend on the joint stiffness, viscosity and wave frequency.

- Further novel work dealing with joint – wave interactions examines approximate energy dissipation at frictional joints, failure envelopes for joints with cohesive filler materials, undulating joints and the influence of wave amplitudes.

5.2.2.2 Wave interactions with mining excavations

Seismic stress waves interacting with mining excavations are the most severe mining hazard associated with deep level mines. The complicated radiation field resulting from stope – wave interaction leads to stress wave superposition, which can result in rock mass instabilities. Here, numerical and photoelastic investigations are used to identify zones of high dynamic stress concentrations and parameters influencing stress wave driven fracturing in the vicinity of the stope.

Principal findings

- Dynamic photoelasticity is used to visualise the complex stope – wave interactions and, by means of back-analyses, the numerical codes WAVE and ELFEN are verified to be able to model stress wave interactions and dynamic fracturing.

- This work has demonstrated that parting planes in general are found to reflect a portion of the incident energy and thus shield the stope. However, non-cohesive parting planes trap energy within the hangingwall beam, and wave superposition associated with dense energy channeling gives rise to dynamic stress concentrations, which are likely to initiate fracturing and lead to rock mass instabilities.

- Numerical and experimental parametric studies are conducted to investigate stress wave driven fracturing in the stope vicinity. It is shown that fracturing occurs primarily due to reflected waves, and individual fractures are most likely to be oriented parallel to the free surface of the mining excavation. The polarity of incident shear waves affects the extent of fracturing significantly, and shear waves with wave front motion towards the excavation promote more extensive fracturing than incident *S*-waves with reversed polarity. Stiff stope support transmits a higher portion of energy across the stope; hence the amplitude of reflected waves is reduced, and less fracturing occurs. However, the stiffness that is required to reduce fracturing substantially must be approximately the same magnitude as the rock mass stiffness (e.g. pillars) and, comparatively, support in the form of timber packs is too soft to reduce fracturing to a significant extent.

5.3 Assess the knowledge gained of fracture mechanisms to formulate strategies to be used to pursue the goal of reducing fall of ground injuries and fatalities (Enabling output 3)

An important objective of the studies described in this section was the calibration and validation of the DIGS fracture zone simulator using physical modelling, underground observations and closure measurements. Subsequently the code was used to investigate rate of mining strategies. It was found that detailed monitoring of stope closure profiles could provide a useful signature of the geotechnical response of the rockmass to the mining process. These main conclusions are discussed below in greater detail.

As described in Section 2, two approaches to modelling fracture growth have been incorporated in the DIGS displacement discontinuity element program. The first involves discrete fracture growth from seed points and the second considers a pre-defined tessellation of potential sites which are activated sequentially using a specified failure criterion. The physical models and underground experiments were used to test the validity of these two approaches.

Regarding the laboratory work, encouraging correspondence has been obtained between various physical experiments and the numerical simulations. The results of experiments on blocks of quartzite containing a tabular slot under triaxial loading show that the presence of interfaces significantly alters the position and inclination of the resulting fractures. It was found that these fractures can be simulated using the discrete fracture growth approach in DIGS. The three dimensional acoustic emission location technique provides useful information regarding the sequence of fracture growth and the growth directions, which correlate well with the numerical simulations. In the samples without discontinuities, shear fractures are observed to extend ahead of a narrow slot. The shear fracture criterion of DIGS correctly predicts corresponding fractures in the numerical models. In the models with a pre-existing discontinuity, fractures extending from the tip of the slot are observed to terminate on the discontinuities. The analysis with a tensile fracture criterion correctly predicted the final fracture directions. The requirement to pre-select the seed point may however bias the final fracture pattern. The physical experiments demonstrate that the fracturing may occur in shear or tension depending on the presence of interfaces and closure behaviour of the stope.

When using the tessellation approach in DIGS, there is no need to choose the appropriate growth direction mode beforehand. This approach was evaluated with physical tests of fracture formation processes below a rectangular strip punch. The results suggest that some confidence can be placed in the use of a random mesh to represent complex failure processes near mine openings in hard rock. It is found that the post-failure cohesion of each activated crack in the random assembly is a particularly important parameter controling the pattern of failure. A related concept is the use of an incremental procedure to select the sequence of crack initiation in the random mesh. The use of an incremental activation rule implies some form of “weakest link” breakage mechanism and can also be viewed as an alternative manifestation of general cohesion and tension weakening behaviour. In general, the residual cohesion and incremental growth rules allow a balance to be established between plastic and brittle failure modes in the material. Additional work is required to clarify the choice of cohesion and tension weakening rules in relation to particular rock types.

As a further validation of the fracture growth methodologies in DIGS, the laboratory work was supplemented with underground observations of the fracture zone around deep level gold mine stopes. It was found that the numerical stability problems associated with discrete fracture growth from seed points could be overcome by using the tessellation approach. Modification of the material properties assigned to each element of the tessellation mesh permits the modelling of different rock types The memory and run time limitations of the standard boundary element

formulation can be largely overcome with the multipole solution technique. A method of selecting the parameters for the multipole grid has been developed.

Sequential solution of the problem permits the use of large tessellated regions as only the active elements are included in the solution. The incremental selection of one growth element at a time produces the most well-defined fracture paths, at the expense of solving the problem after the activation of each element. An activation rule in which many parallel growth stages are permitted for each mining step, makes allowance for the migration of the fracture zone associated with stress redistribution and is the suggested method for the solution of larger scale problems in a reasonable time.

Dilation on the fractures resulted in higher compressive stresses in the hangingwall, and hence less closure. The relative strength of the rock types depends on both the unconfined strength and the friction angle, not directly on the cohesion. Good correspondence with the fracture patterns observed underground is obtained if stress redistribution is permitted and, in particular, if low friction parting planes are included above and below the stope. The trends of the deformations and stresses agree with the measurements of Legge (1986) for the rockmass behaviour around a Carbon Leader stope.

The comparison of modelling predictions with underground observations has shown that the tessellation approach is suitable for the prediction of the distribution and directions of fracturing induced by the interaction of the mining with primary geological structures such as bedding planes and layers of different strength rocks. Currently the fracture intensity is however not correctly predicted. The method can also predict the influence of closely spaced joints on the direction of the mining induced fracturing, suggesting that mining induced fracturing may align with mining activated jointing and other secondary geological structures. Methods for distinguishing the induced fractures from the geological features are required to provide unambiguous input parameters for computer modelling. This will lead to a better understanding of the interaction of discontinuities in the stope hangingwall and, therefore, to improvements in support design methodologies.

Significant improvements in the modelling and understanding of the complex mining environments has been achieved by comparing numerical models with detailed geological and rock mechanical information. Further comparison with the available data is difficult as the current computers permit the analysis of small spans, and most in situ observations have been undertaken at large spans. In many cases, the data obtained underground does not have sufficient information to distinguish uniquely between proposed mechanisms. For example, closure measurements may have been taken, but no record of stress or geological environment is available. To be able to make meaningful comparisons, the geological structure, stress magnitudes and directions, and the deformation response should be known. The models have the potential to model realistic stope lengths if numerical schemes that capture the rock mass response on small scales and provide equivalent representations at a large scale, e.g. the lumping methods investigated in section 2, are developed and implemented.

The observation and modelling of underground fracture patterns was supplemented by the monitoring of time dependent stope closure in various geotechnical areas. The continuous closure data contains much information that is lost with the more conventional daily closure measurements. Although excavations in hard rock are not usually perceived to undergo significant time dependent deformation due to the low creep rate of intact rock, the collected stope closure data illustrated behaviour to the contrary. Continuous closure measurements in tabular excavations indicate significant time dependent deformation. Although the excavations are developed in brittle quartzite and lava, the rate of time dependent closure can be as high as 0,1 mm/h in certain areas. The continuous closure behaviour of these excavations typically consists of an instantaneous response at blasting time followed by a primary phase of decelerating closure lasting approximately five hours and a steady-state closure phase. This pattern is repeated after the next blast. This closure behaviour is the result of the rheological behaviour of the fracture zone that surrounds these excavations. After a mining increment, the fracture zone extends in a time dependent fashion ahead of the working faces. The majority of

new fractures appear to form within approximately the first 5 hours after the blast. Thereafter the number of new fractures decreases until the next blast occurs.

For tabular excavations in the Ventersdorp Contact Reef, the instantaneous closure response is very prominent, but decreases in magnitude as the distance from the face to the measurement position increases. The steady-state closure rate also decreases in magnitude with distance to the face. By contrast, for excavations in certain areas of the Vaal Reef, the rate of steady-state closure can be as high as 15 mm/day. For these excavations the instantaneous closure response at blasting time is virtually absent. Unlike the Ventersdorp Contact Reef, the steady-state closure rate of the experimental panel in the Vaal Reef increases with increasing distance to the face. This difference in behaviour is caused by the presence of prominent bedding planes in the hangingwall of the Vaal Reef.

Both the continuum and discontinuum viscoplastic models developed in this project allow for the direct simulation of the time dependent fracture zone behaviour. Experiments indicate that these models are successful in simulating the time dependent closure behaviour of tabular excavations, giving both the instantaneous response at blasting time and the primary and steady-state closure phases.

An important finding of this study is that the time dependent closure data can possibly be used to deduce important information about the behaviour of the rock mass and the stress in the fracture zone ahead of the face. Although estimation of absolute stresses may not be feasible, the closure may be used to identify areas with large average face stresses and therefore a high risk of face bursting. It appears that the instantaneous closure response at blasting time gives an indication of the magnitude of stress in the face area. The larger the stress, the bigger the instantaneous closure response following the mining increment. This hypothesis was successfully tested by simulating two stopes with different rock conditions using the continuum viscoplastic approach. Numerical studies using the discontinuum viscoplastic model also indicated that the initial jump in closure after blasting is correlated with the face stress before the blast. Some confirmation of this possible use of time dependent closure data to determine a face burst hazard indicator was obtained from initial underground observations. The Ventersdorp Contact Reef (hard lava) stopes appear to be prone to face bursting and, as mentioned above, the closure behaviour of these excavations typically includes a large instantaneous response after blasting. By comparison, in some areas of the Vaal Reef with an apparent lower risk of face bursting, the instantaneous closure response after blasting is small. One useful hazard parameter might be the initial jump in closure after blasting divided by the total daily closure (called the closure ratio). Further work is however necessary to validate this concept, to quantify the face burst and falls of ground hazards for different geotechnical areas and to investigate how different values of closure ratio correlate with these hazards.

Following the success of the discontinuum viscoplastic model to simulate the time dependent formation of the fracture zone and seismic energy release patterns, preliminary studies of the effect of rate of mining was conducted. It was found that a balance must be struck between higher energy release rates (potentially damaging rockbursts) at high face advance rates and greater deformation of the rock mass, with greater potential for local rockfalls, at slower mining rates. Numerical experiments indicated that slightly more seismic activity is associated with a seven day mining cycle when compared with mining with a weekend break. Optimum rates of face advance will however depend on the geotechnical area. Further work is therefore necessary to calibrate the models for the different areas and to determine appropriate mining rates for these areas.

An important aspect of higher face advance rates is the reduction in volume of closure per area mined. Slow mining rates are undesirable as the time dependent increase in closure reduces the energy absorption capabilites of support units. Large magnitudes of closure are also associated with a deterioration of hangingwall conditions that increase the risk of falls of ground and the potential for shake-out during seismic events. The continuous closure measurements allowed for an estimation of increases in closure on days where faces are left standing. Calculations showed that an increase in face advance rates in areas with large time dependent

closure (e.g. some areas of the Vaal Reef) will lead to a significant reduction in closure volumes per area mined. This might lead to a significant improvement in hangingwall conditions. This phenomenon might be less noticeable on the VCR with a hard lava hangingwall where the time dependent closure is significantly less.

5.3.1 Produce a computer based fracture zone simulator to evaluate mining strategies and automatic mining sequence generator (Enabling output 3.1)

The tessellation approach to modelling, developed in projects GAP029 and GAP332, is a major advance in the modelling of rock fracture processes. This allows the fracture pattern to develop with the minimum input from the program user as opposed to the standard DIGS method that requires the user to pre-select the fracture initiation sites. A new fracture activation concept has been developed to apply in the tessellation models that includes only the sliding resistance and tensile strength that can be considered to be fundamental parameters of the rock. Flaws, with only a sliding resistance, placed randomly throughout the mesh, induce local zones of tension, and initiate potential tensile fractures. The method can model the transition from axial splitting to localized shear failure and finally multiple shear band formation with increasing confining pressure, that is observed in laboratory tests. The method is able to respond to different stress paths, e.g. the extension test, and correctly predict the fracture pattern. The method can be extended into three dimensions, and can be applied within the context of 3D boundary element analysis methods that have been developed and implemented as part of this project. The 3D program 3DIGS is still in an early stage of development, but the results from the fracture studies will provide excellent data with which to verify three-dimensional fracture formation mechanisms.

The tessellation method has been applied in the modelling of stope scale problems. The multipole method developed in project GAP029 is applied to obtain memory savings that permit the analysis of an order of magnitude more elements, than are allowed in the standard boundary element formulation. The stope scale problems highlighted the need for a more systematic approach to the selection of the multipole parameters to optimize the memory saving. A scheme that produces a saving that is close to optimal was developed and included in a prototype user interface to facilitate the building of models. Studies of the fracture zone behaviour predicted by the models and the comparisons with underground observations are presented in the final section of this report.

The methods developed so far, have considered only the strength properties of the rock, and neglected the differences in elastic material properties. A three layer method, based on superposition schemes, has been developed and implemented into a version of the DIGS code. The model has been applied to the modelling of fracture zone development on different reefs and has demonstrated that in certain areas there can be a significant effect of the geology on the fracture pattern.

The extension of the modelling capabilities to three dimensions has been initiated with the development of the framework for a three-dimensional boundary element programme 3DIGS. A lumping scheme for far-field influence computations has been introduced to enable large scale problems to be analysed. The influences of small cracks are represented as an “equivalent crack” set to effect efficient influence transmission. The method provides an initial step for dealing with the interaction of fractures over a range of physical scales. A preliminary application to the mining of a lead lag stope layout has been considered.

A particular application of the 3DIGS code is to evaluate the optimum choice of mining sequences. Such sequences can be generated with the next increment to be mined determined

by a pre-selected criterion such as minimum normal stress in the block to be mined. The optimal mining sequence can be evaluated by permitting the program to select mining blocks automatically according to the preset criterion. This work is at an early stage and no firm conclusion can be drawn, other than that the optimum overall mining policy does not necessarily result from the policy that seems best at a local mining step point of view. The implications of this work need to be considered further, but have great potential for mining strategy evaluation and selection.

Appendix 2.1

Studies of rock fracture in extension

This appendix presents the results of a number of laboratory tests performed to investigate how different rocks will fracture under a stress state similar to that expected ahead of a deep level tabular stope. The experiments are listed and the stress - strain results are described. Some photographs of the failure planes are included for comparison. The second section presents a set of DIGS numerical modelling studies to investigate fracture growth within a grain in siliceous quartzite.

A2.1.1 Extension tests to determine the effect of rock fabric on the mode of fracture

The extension test device was developed by the former Chamber of Mine Research Laboratories to simulate the stress conditions ahead of the face. Considering a sample of rock some distance ahead of the face, it may be expected that there will be a high major principal stress in the vertical direction. The horizontal stresses will steadily decrease as the stope approaches. This could lead to fracture formation parallel to the stope face. A test was devised, in which a cylindrical sample of rock is confined in the radial direction using an oil emulsion confining medium. The axial loading is increased to maintain a hydrostatic stress in the sample. Once the desired hydrostatic stress has been achieved, the axial loading is reduced until the sample fails.

A series of triaxial tests was carried out on examples of different rock types associated with the hangingwall and footwall strata of deep mines. Three siliceous quartzites: Timeball Hill, Orange Grove and Black Reef, were selected and compared with the more argillaceous Elsburg quartzite. These were contrasted with hard (Alberton) lava and two types of soft (Westonaria) lava. In most cases, the specimens were obtained from surface to reduce the possibility of pre-existing microcracks that would obscure the test induced cracking. The results of the test are best presented as graphically of deviatoric stress against deviatoric strain. The deviatoric stress is calculated by subtracting the confinement from the axial stress. Thus,

$$\sigma_d = \sigma_{axial} - ((\sigma_{axial} + 2\sigma_{radial})/3) \qquad \text{(A2.1.1)}$$

Some tests were taken to failure, and others were unloaded close to failure. The aim of these tests was to investigate the degree of microfracturing in the sample just prior to failure. Table A2.1.1 presents a list of the sucessful tests, the confinement and the failure stress. Most samples failed in a state of all round compression. Since the samples are dry, this is significantly different to the

conventional view of fracture, e.g. Olsen and Pollard (1991), that requires a state of tension, or internal hydrostatic pressure, for fracture to occur. The deviatoric stress – deviatoric strain curves of the rocks are shown in Figures A2.1.1.1 to A2.1.1.8. Figure A2.1.1.1 compares the four quartzite rock types. The more silieous rock types are found to exhibit more brittle response and higher strengths. The Orange Grove and Timeball Hill quartzites (Figure A2.1.1.2 and Figure A2.1.1.3) each show a consistent, and very brittle response and fail at an angle less than 10° from the direction of the major principal stress. The Elsburg quartzites (Figure A2.1.1.4) show a consistent, but more ductile stress – strain response. The failure angle is larger, being up to 25° from the direction of the major principal stress. The Black Reef quartzite shows significant differences in strength (Figure A2.1.1.5) that may be due to the anisotropic fabric of the material.

The hard (Alberton) lava shows a consistent response (Figure A2.1.1.6). The deformation measurements of test H28 are incorrect due to data acquistion problems, but the ultimate strength agrees with that of the other tests. The soft lava (Figure A2.1.1.7) demonstrates considerabl;y different results, depending on the material. More tuffaeous rock exhibits more ductile response and lower strengths. The confinement of the lava of test S18 has exceeded the brittle ductile transistion pressure, and the material has failed in a plastic manner.

The relative strengths of the hard lava and quartzite can be obtained from Figure A2.1.1.8. The moduli can not be compared directly due to the small machine dependent kink in the early stages of some of the tests. The hard lava is the strongest.

The fracture surfaces of some of the test samples are shown in Figures A2.1.1.9 to A2.1.1.16. The hard lava (Figure A2.1.1.9) fails due to a single crack that extends from a weakness on the boundary. The Orange Grove sample exhibits a clean fracture, consisting of a number of microfractures (Figure A2.1.1.10). Thus, even though failure occurs in a state of compression, the fractures exhibit no shear deformation.

In contrast, one type of soft lava failed in a ductile manner, as a set of slip planes. The fracture surface (Figure A2.1.1.11) shows that the final failure plane is at an angle to the slip planes. The series of slip lines, shown in Figure A2.1.1.12, are at an angle of 45° to the major stress, implying an internal friction angle of 0°, as associated with ductile flow of a perfectly plastic material.. These mineralogy-dependent rock behaviours have important implications to the response of the rock in VCR stopes, and may explain the anomalous fracturing observed in soft lava stopes. If the stresses ahead of the face are sufficient to cause the soft lava to exceed the brittle-ductile transition it may be expected that the hangingwall would consist of a multitude of slip planes and may unravel when exposed.

The Elsburg quartzite exhibits more ductile response than the other quartzites, but fails in a brittle manner. In this case, the final failure plane is a shear fracture at 26° to the major principal stress. The shear plane consists of a series of en echelon extension fractures, each in the direction of the major principal stress. The friction angle obtained from triaxial compression tests is 36°, which implies a Mohr-Coulomb localization angle (45° - $\varphi/2$) of 26°, very close to the measured values in extension. In contrast, the stonger quartzites have friction angles in the region of 62°, implying that the localization angle is about 14°, higher than observed in the extension tests. Thus, the material response must change from extension cracking in the direction of the major principal stress to shear localization as the material becomes more ductile. For a given stress state, with two different rock types, it may be expected that the fracture directions could be considerably different. Thus, there can be differences in the fracture pattern between, for example, the strong quartzite hangingwall and the weaker, argillaceous footwall in the Carbon Leader stopes.

An intermediate lava, unloaded just prior to failure also exhibited a shear type failure plane, at an angle of 20° to the major principal stress (Figure A2.1.1.14). The section of the incipient failure

surface was a fine line on the surface of the sample, and exhibited a tendency to bifurcate, as shown in Figure A2.1.1.14). The failure surface of a similar rock type is shown in Figure A2.1.1.15 and shows a series of slickensides due to the relative sliding of the two parts of the samples after failure. The surface of the Timeball Hill quartzite (Figure A2.1.1.16) clearly exhibits the en echelon microfractures formed through each grain in the rock, in the more brittle failure mode.

Table A2.1.1 Summary of extension tests performed and ultimate strengths (note that compression stress is positive).

TEST 1780 -	ROCK	CONFINING STRESS (MPa)	FAILURE STRESS (MPa)	MODULUS (MPa)	FINAL STATE
11	Black Reef Quartzite	797	29	90	Failed
10	Black Reef Quartzite	596	9.9	91	Failed
21	Elsburg Quartzite	599	86,12	87	Failed
22	Elsburg Quartzite	601	93	89	Unloaded
23	Elsburg Quartzite	603	89,9	89	Unloaded
26	Hard Lava	600	40	74	Failed
27	Hard Lava	605	32	92	Failed
28	Hard Lava	600	6.9	103	Failed
29	Hard Lava	603	32,8	103	Unloaded
13	Orange Grove Quartzite	605	495	77	Error
12	Orange Grove Quartzite	601	9,3	74	Failed
14	Orange Grove Quartzite	604	45	89	Failed
31	Orange Grove Quartzite	603	60	86	Unloaded
18	Soft Lava	599	297	76	Failed

15	Timeball Hill Quartzite	603	21.8	93	Failed
16	Timeball Hill Quartzite	599	3	?	Failed
17	Timeball Hill Quartzite	598	49.5	94	unloaded
	* note that modulus is the deformation modulus calculated from the LVDT displacement outside the cell and the volume change and is calculated from a range of values in the apparently linear region of the curve.				

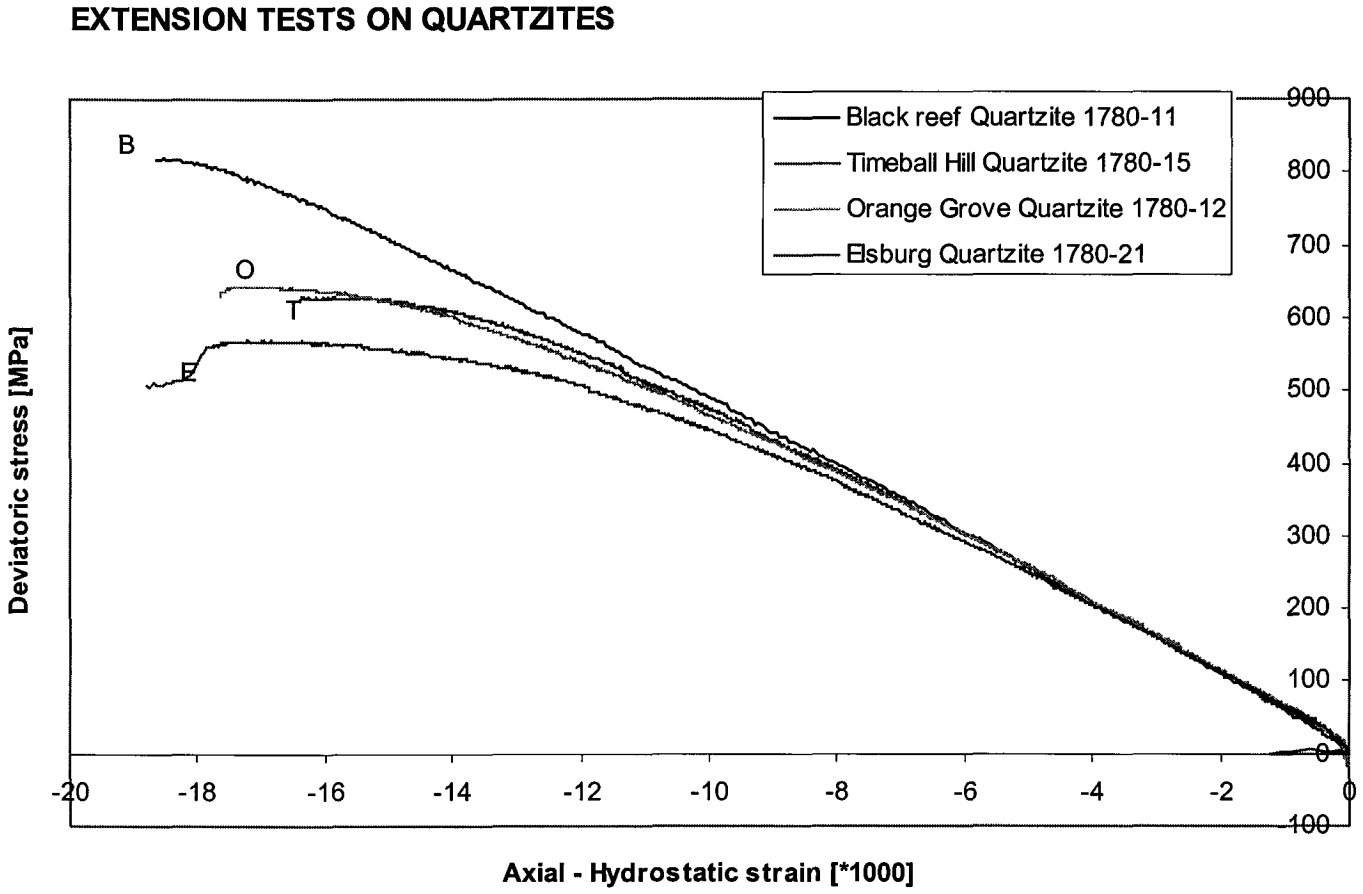

Figure A2.1.1.1 Comparison of extension test on four different quartzite rock types.

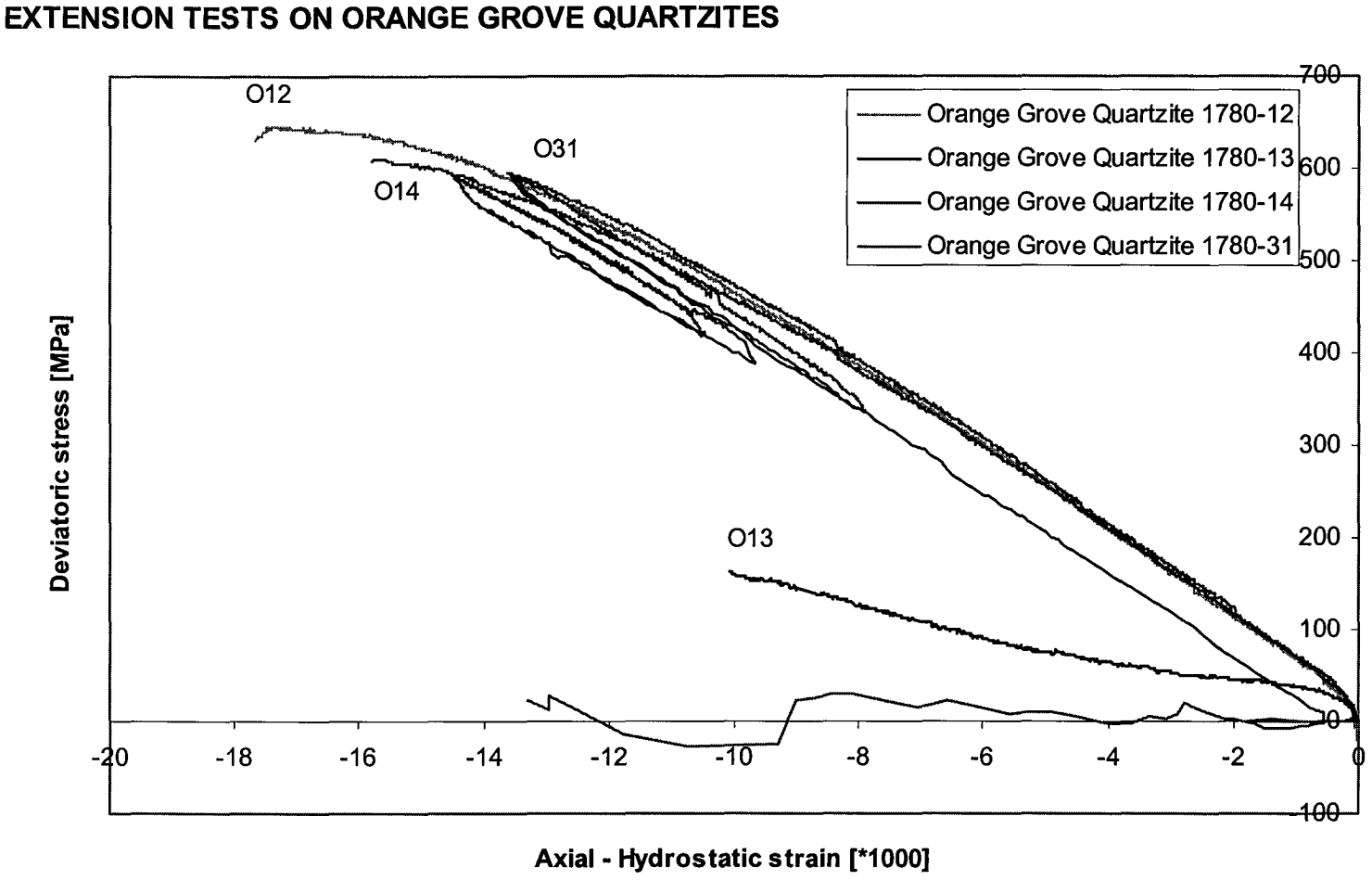

Figure A2.1.1.2 Comparison of four extension tests on Orange Grove quartzite.

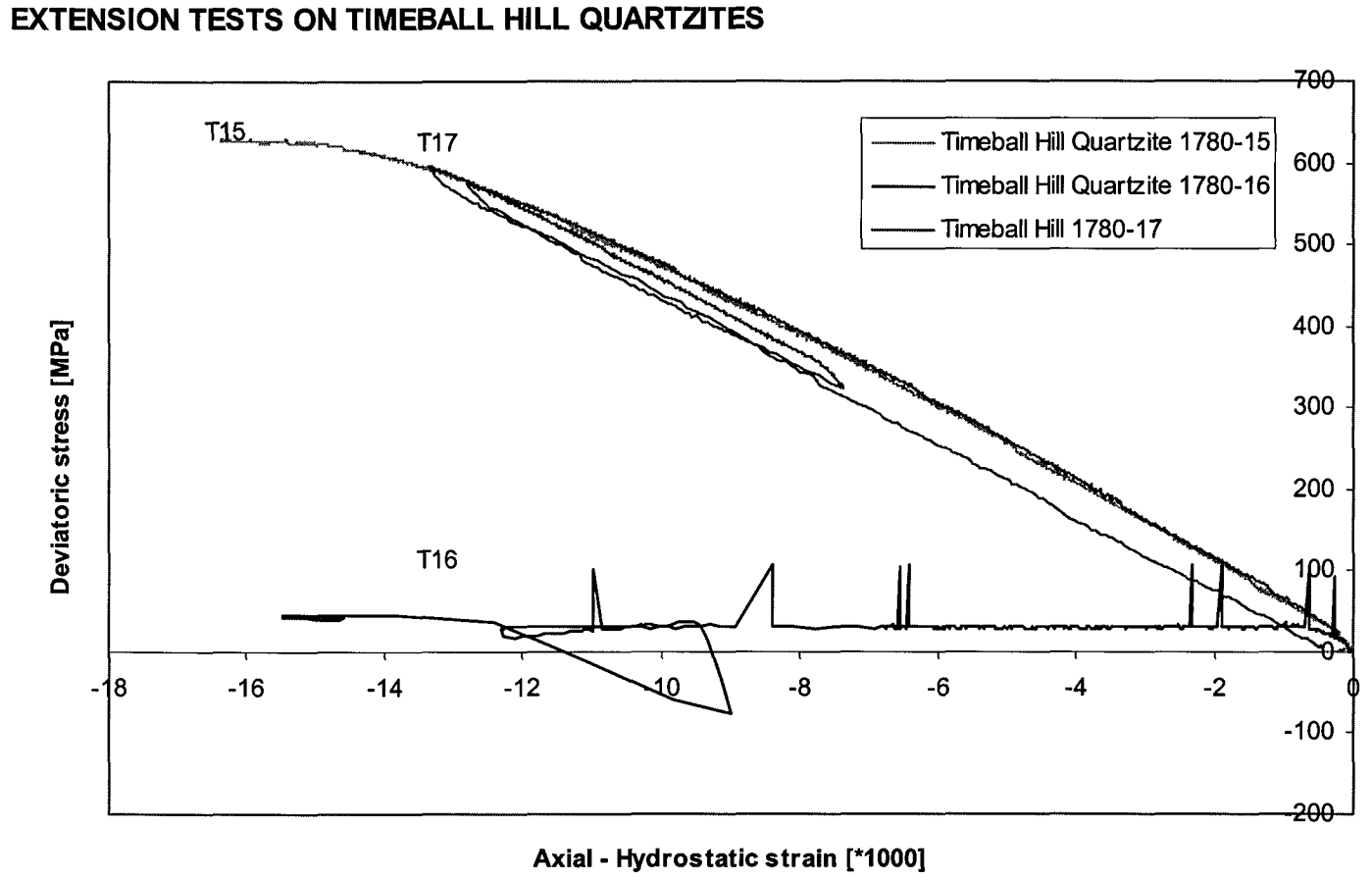

Figure A2.1.1.3 Comparison of three extension tests on Timeball Hill quartzite.

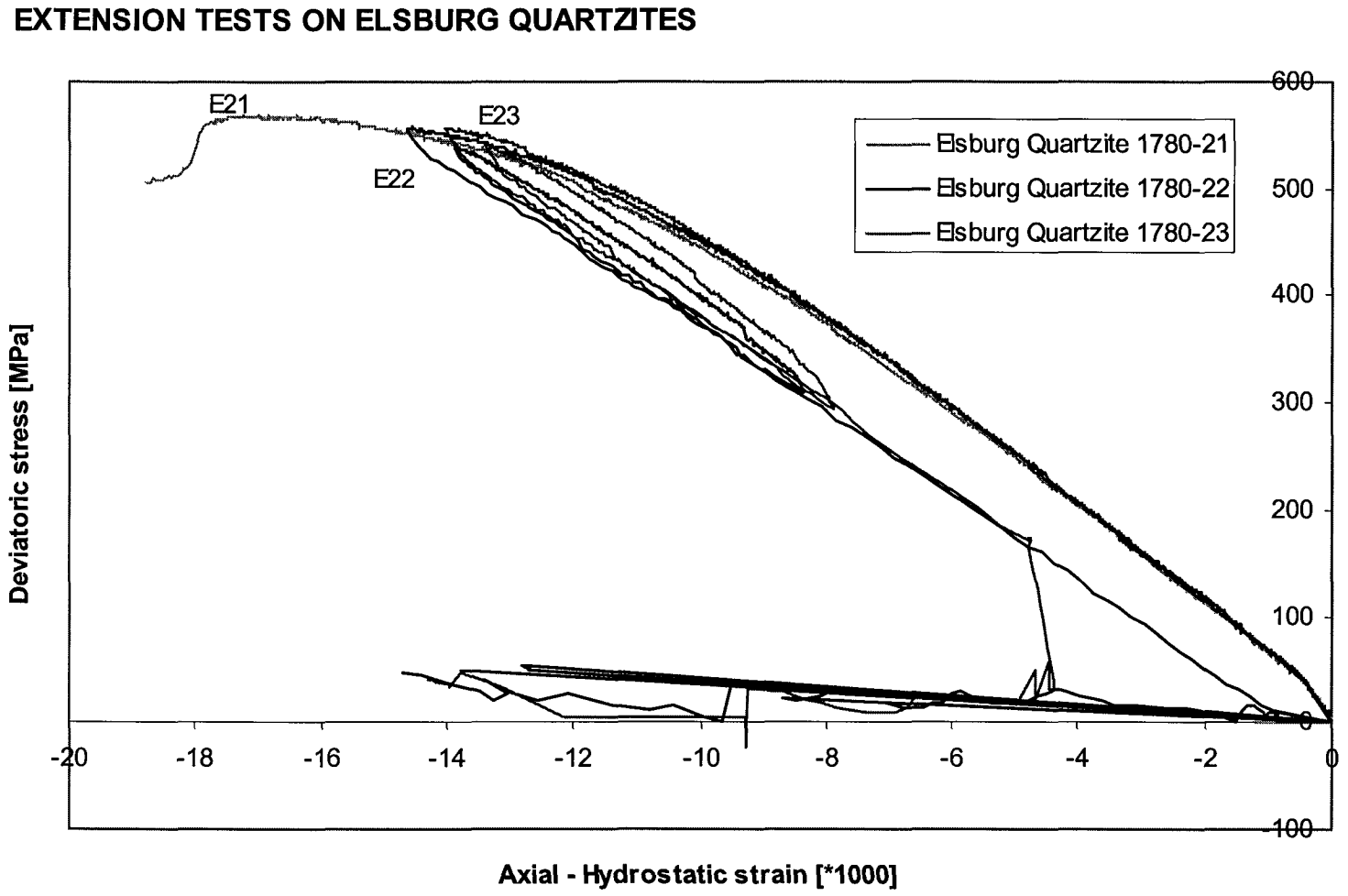

Figure A2.1.1.4 Comparison of three extension tests on Elsburg quartzite.

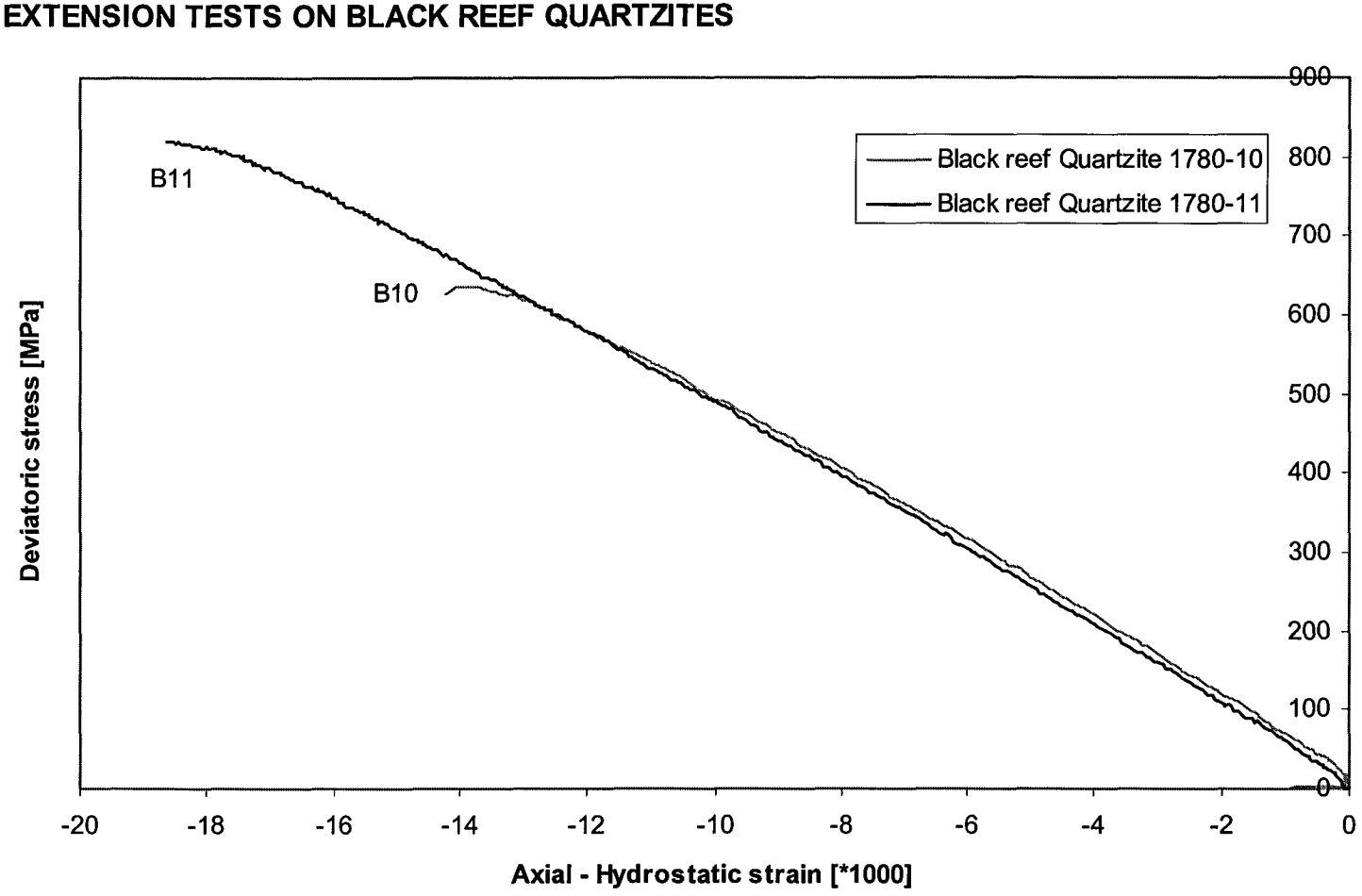

Figure A2.1.1.5 Comparison of two extension tests on Black Reef quartzite.

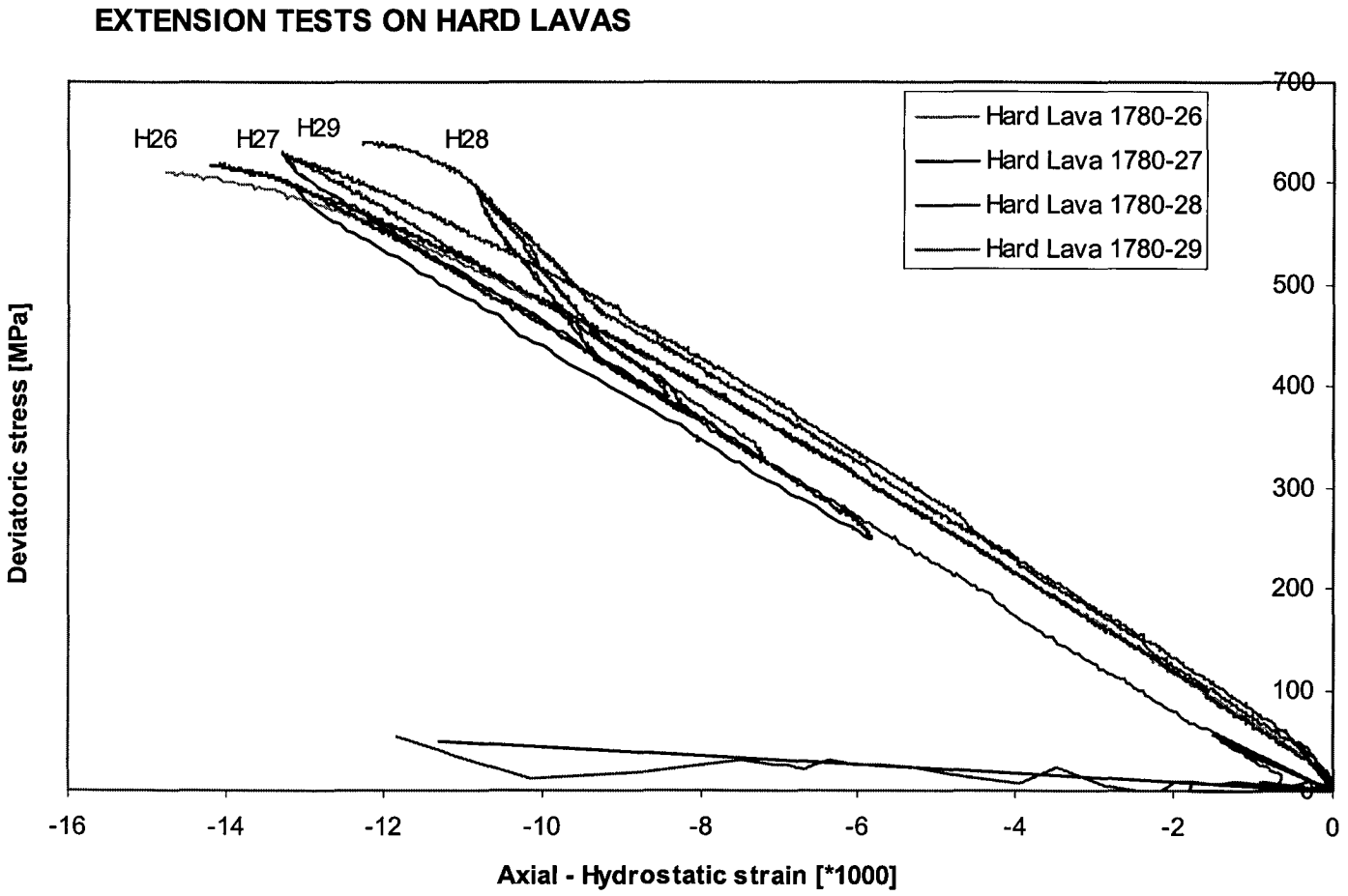

Figure A2.1.1.6 Comparison of four extension tests on hard lava.

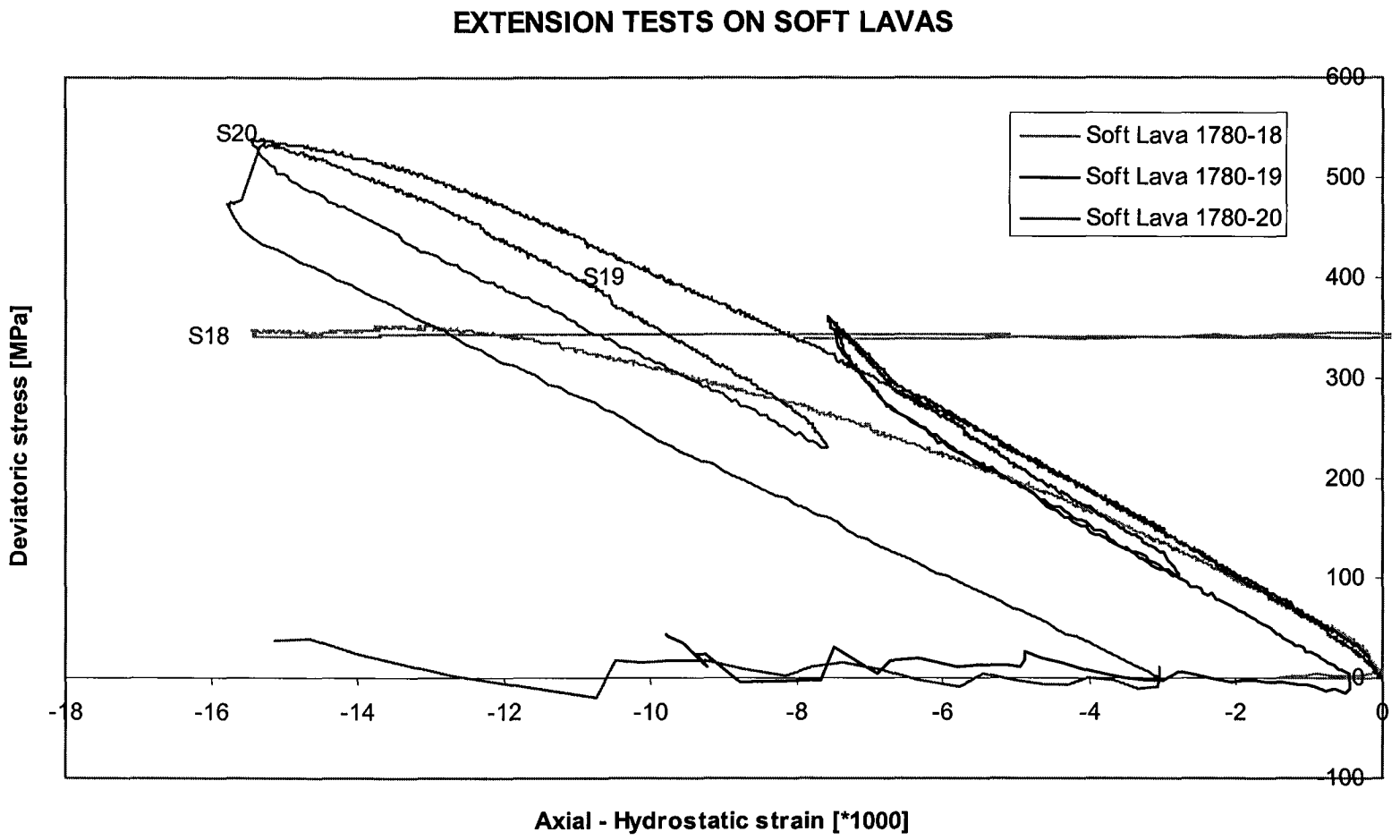

Figure A2.1.1.7 Comparison of three extension tests on soft lava.

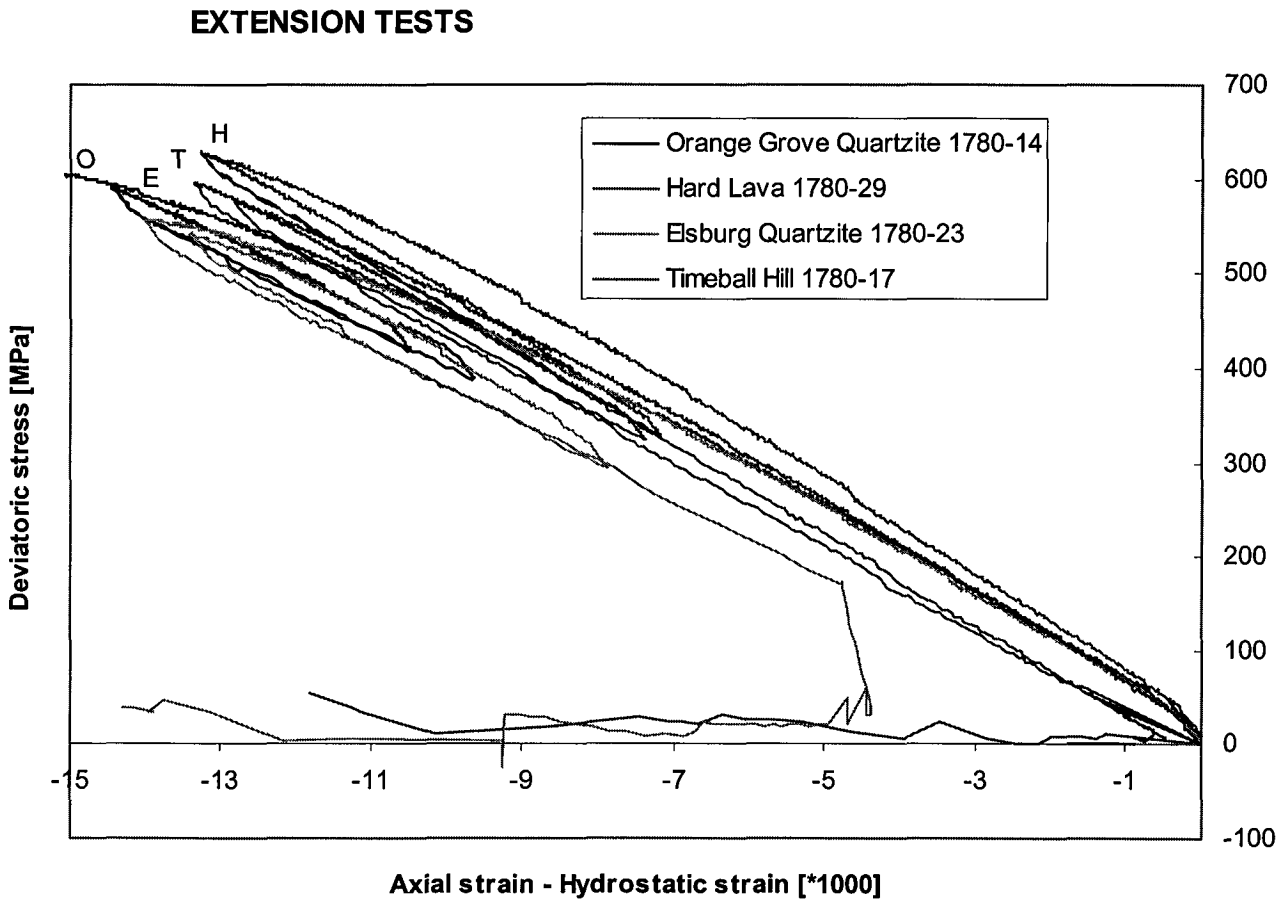

Figure A2.1.1.8 Comparison of extension tests on three quartzites and hard lava.

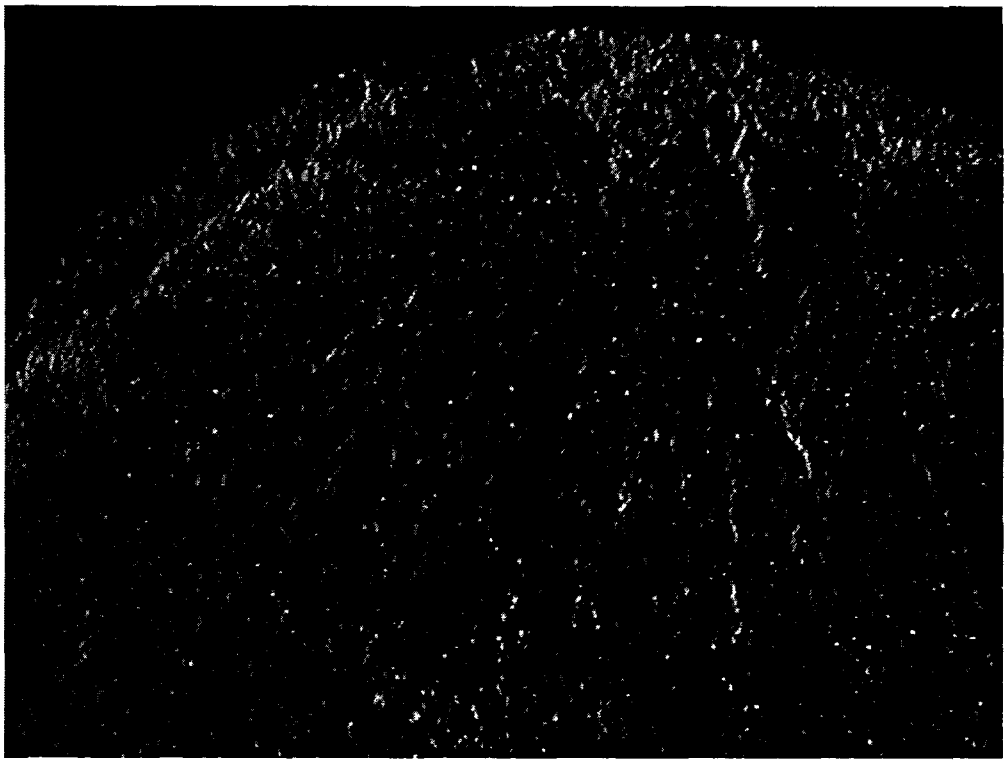

Figure A2.1.1.9 Fracture surface from hard lava sample with single fracture initiating from nucleus at the sample edge (top of picture).

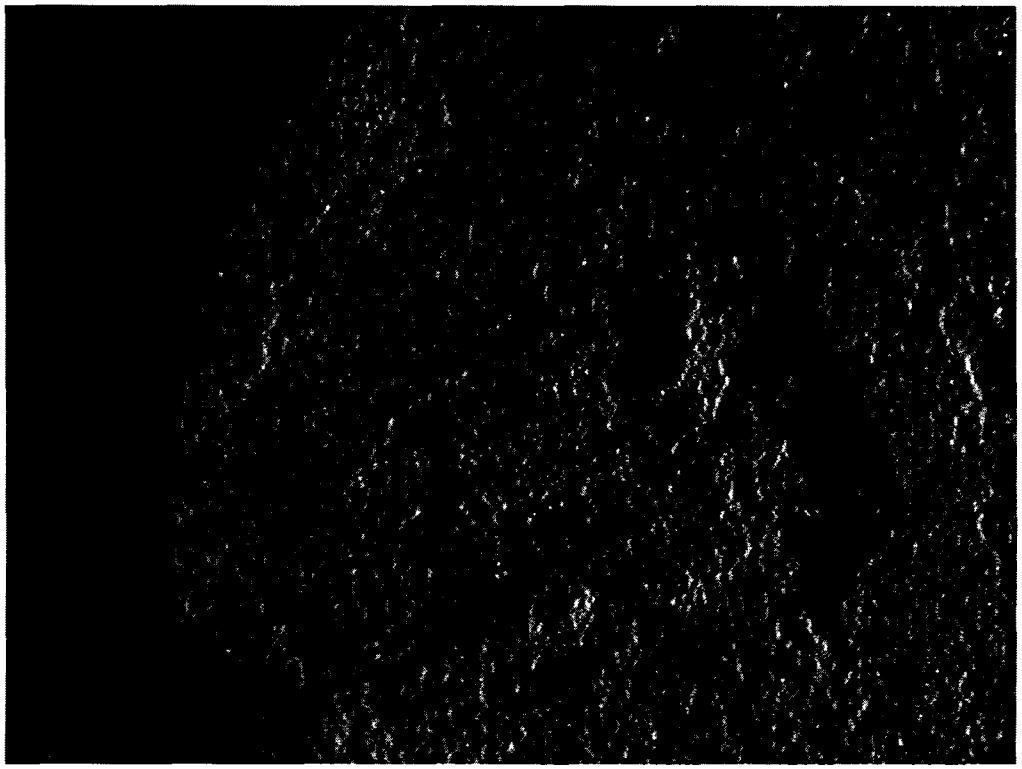

Figure A2.1.1.10 Fracture surface from Orange Grove quartzite sample.

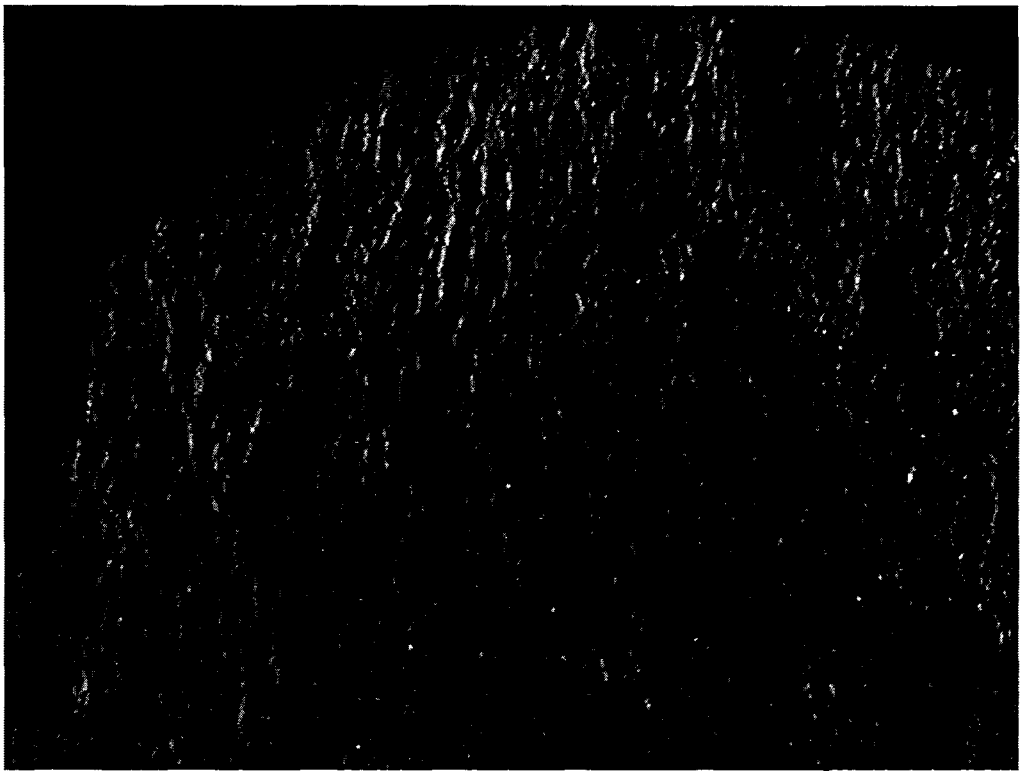

Figure A2.1.1.11 Fracture surface from soft lava sample showing intersections of slip planes.

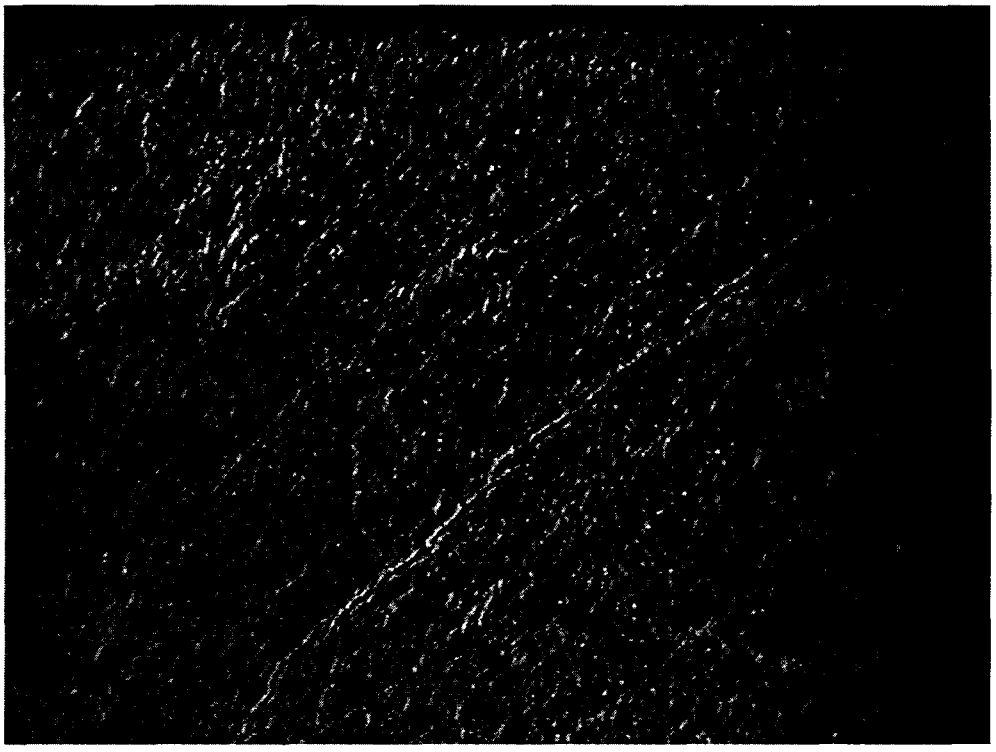

Figure A2.1.1.12 Side of soft lava surface showing slip planes.

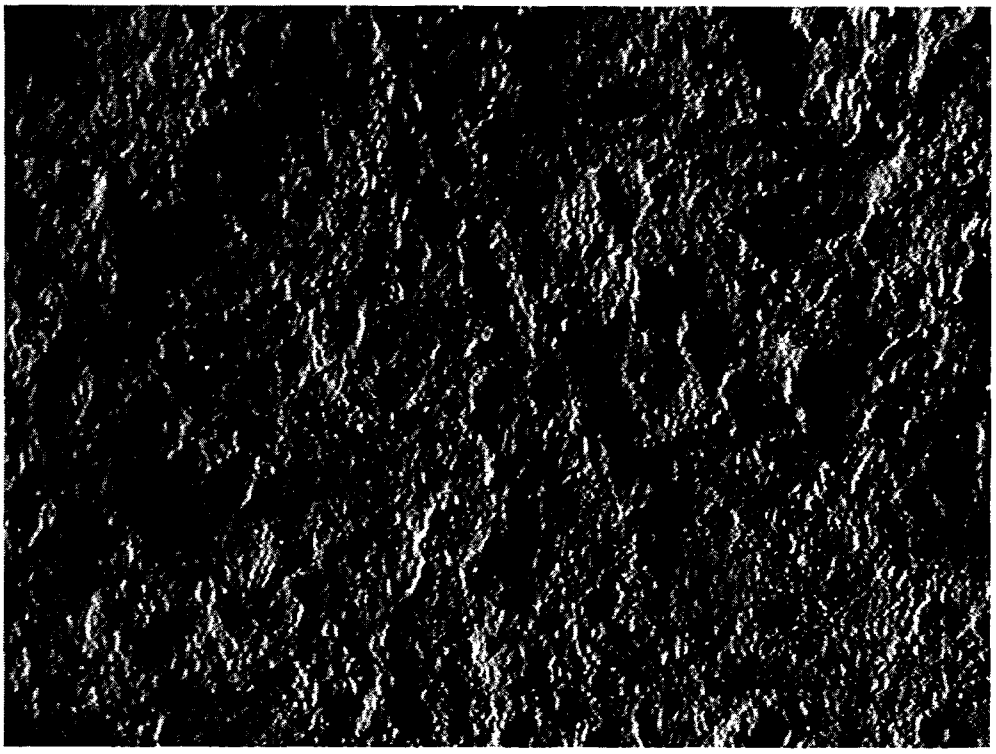

Figure A2.1.1.13 Fracture surface from Elsburg quartzite sample. Oblique lighting emphasizes the stepped nature of the surface.

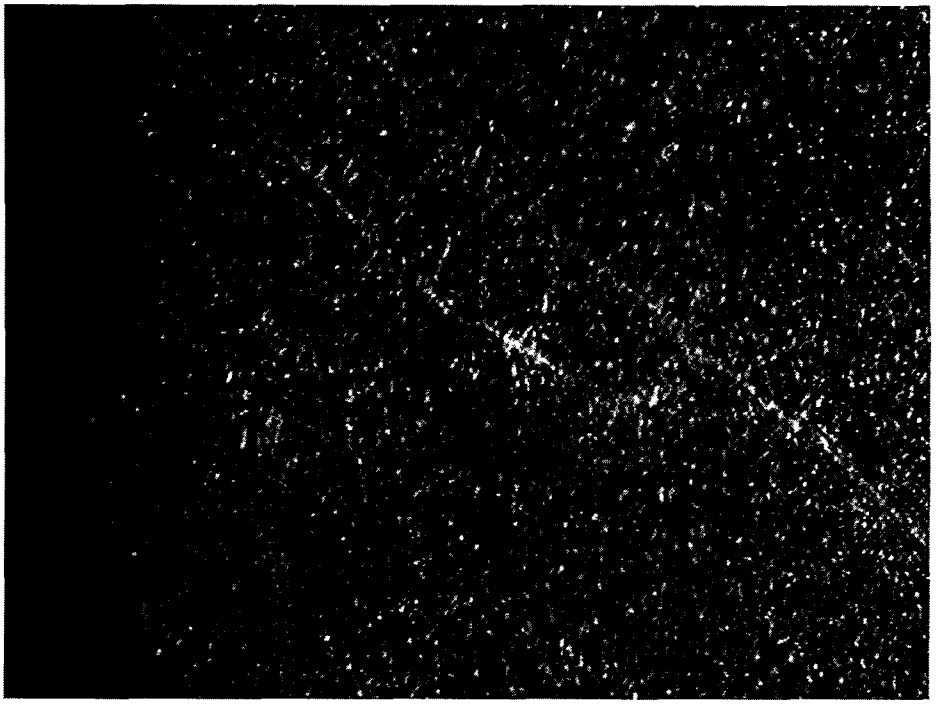

Figure A2.1.1.14 Section of incipient failure plane from stronger soft lava sample.

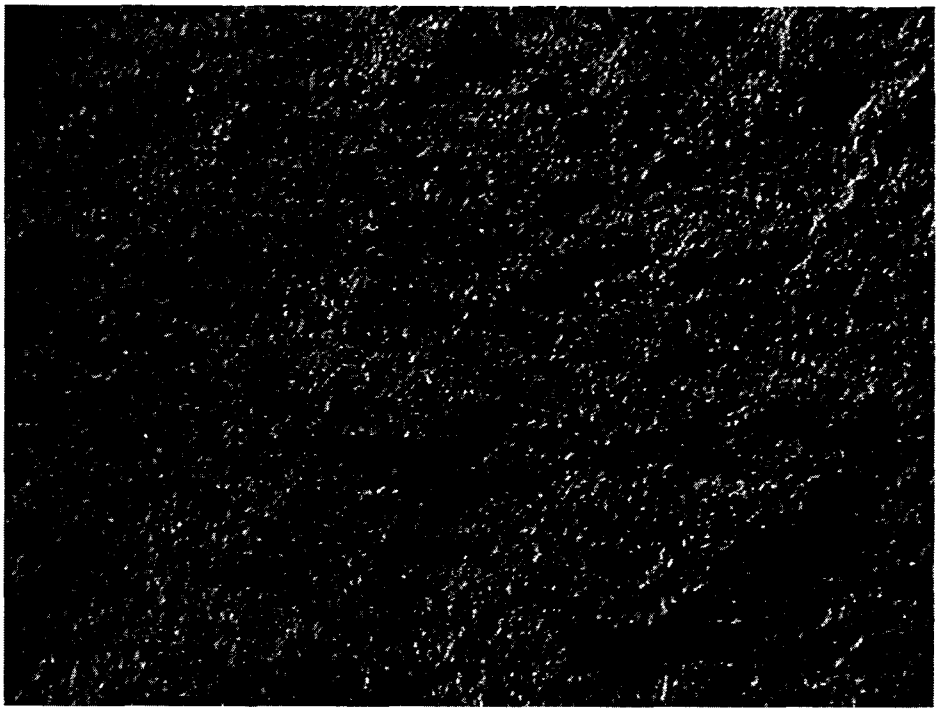

Figure A2.1.1.15 Fracture surface from stronger soft lava sample. Note slickensides in direction of sliding (horizontal in picture).

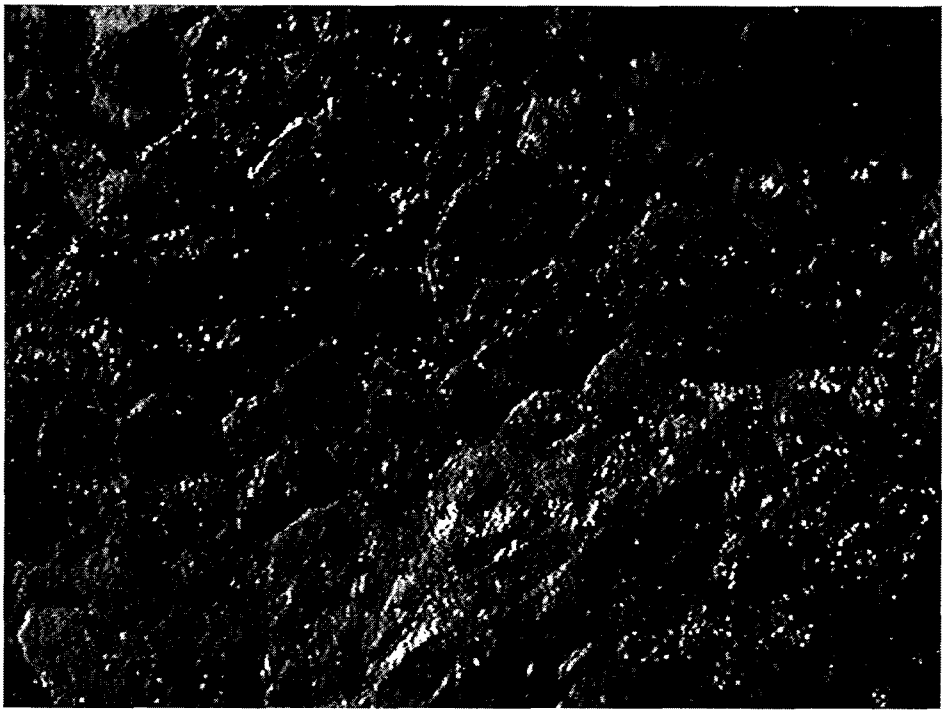

Figure A2.1.1.16 Fracture surface from Timeball Hill quartzite sample. Oblique lighting emphasizes the stepped nature of the surface.

A2.1.2 Modelling of the growth of fractures from flaws under extension test stress conditions

The growth of fractures under tension has been considered in a number of studies. Olsen and Pollard (1991), for example, consider the tension cracks to extend when the stress intensity factor exceeds the fracture toughness. The stress intensity factor is calculated based on an approximation of the weight function. In DIGS, the crack growth is controlled by the tensile strength of the material around the crack. The crack direction is determined as being perpendicular to the direction of the most tensile principle stress ahead of the crack tip. This corresponds to the well known maximum tensile stress criterion. A crack element is included when the stress at a distance of $\frac{b}{2}\left(\frac{\sqrt{2}-1}{\sqrt{2}}\right)$, where b is the element length, ahead of the current crack tip exceeds the specified tensile strength. In a uniform stress state with a single far-field tensile stress, a single crack will extend in a straight line perpendicular to the stress direction. This stress state is equivalent to a crack growing with an internal pressure of the same magnitude as the tensile stress. When a number of seed points are placed in the material, the cracks initially extend perpendicular to the stress, but then interact as the crack tips approach, as shown in Figure A2.1.2.1a.

In this model, the cracks deviate away from each other as the two tips approach, then change direction and approach each other. In this model, the tips are not allowed to intersect and so the cracks grow alongside each other. This characteristic deviation of the crack path was also observed by Pollard. This can provide a diagnostic for field or microscopic observations to determine if the crack grew in a pure tension field. The cracks grow straighter and interact less when the tensile stress is reduced. As expected, no cracks are observed to grow under the action of a compressive stress field (Figure A2.1.2.1b). The introduction of a stress raiser does however introduce tensile cracks, even in the highly compressive stress field of 600 MPa compressive stress in the horizontal direction, and 10 MPa in the vertical direction, as shown in Figure A2.1.2.2. The sliding surface flaw shown in Figure A2.1.2.2a, exhibits the well studied wing cracks extending from each tip of the flaw. The cracks in the numerical model initiate at an angle of 45°, which corresponds to the angle of 70,4° calculated in theory (Lehner and Kachanov, 1996). The wing cracks grow towards the direction of the principle stress and then terminate. The introduction of a diamond shaped hole with stress free boundaries causes tension cracks at the tips of the stress raiser in the direction of the major stress (Figure A2.1.2.2). The size and shape of the stress raiser and the specified tension strength determines the length of the cracks Figure A2.1.2.2 and Figure A2.1.2.3a. The sides of the grain influence the fracture activation, as shown in Figure A2.1.2.3c, where a tensile fracture is initiated on a re-entrant grain boundary.

A group of flaws stacked in a line perpendicular to the major principle stress demonstrates the effect that the interaction of the wing cracks may have on the length of tension cracks within the material (Figure A2.1.2.4). The wing cracks extend different lengths to form a diamond shape that is slightly asymmetrical (Figure A2.1.2.4a). When a crack approaches from the right, the longest cracks begin to extend in opposite directions (Figure A2.1.2.4b). Thus, the set of cracks acts as a diamond shaped stress raiser, similar to those shown in Figure A2.1.2.2, at a larger scale than the original sliding flaw stress raisers. The crack growing towards the right extends a significant distance and then stops as it interacts with the advancing crack (Figure A2.1.2.4c). The array of flaws thus acts to affect the fracture growth on a number of scales. This interaction is difficult to capture in continuum damage models for representing the growth of microfractures in a continuum.

The inclusion of larger stress raisers alters the growth patterns considerably. In this case, the boundaries of a grain are included to investigate the effect on the growth of the wing cracks

from a sliding flaw (Figure A2.1.2.5) . The boundaries included in the analysis are based on the example of a grain in a siliceous quartzite. The grain is welded to neighbouring grains along the top and bottom, and surrounded by micaceous material along the two sides. The boundaries are modelled by displacement discontinuity elements that are permitted to interpenetrate a certain amount to simulate a softer material on the boundary. A friction angle of 30^{o} is specified on the elements once closure occurs. A small triangular stress raiser is included on the left hand boundary to investigate the effect of a non smooth boundary.

The central flaw induces wing cracks that are similar in length to the crack in the uniform stress field (Figure A2.1.2.5). The flaw placed on the right exhibits very different behaviour. The left hand wing crack growing towards the centre of the grain stopes after a short length, but the right hand wing crack extends until it reaches the right hand boundary. Increasing the distance of the boundary from the flaw increases the wing crack length. Thus, the wing crack extends into a region of tension. Translating the boundary to the right results in the right hand crack extending further, to the new boundary. Moving the flaw position some distance lower has little effect on the crack, which still grows to the boundary. However, when positioned even lower in the grain, the crack extends a shorter distance, and is more symmetrical. Thus, the position of the flaw can influence the extent of cracking within the grain.

The stresses have been applied as field stresses and therefore act on every point in the body. To investigate the shielding effect of the grain boundaries, a box of displacement discontinuity elements was placed around the grain, as shown in Figure A2.1.2.6a. The cracks induced under the field stresses are shown in Figure A2.1.2.6b. When the stresses are applied via the boundaries of the box, the crack growth is significantly reduced (Figure A2.1.2.6c). Thus, the grain boundaries have a shielding effect on the crack growth. The actual, three-dimensional stress state will be somewhere in between the two states, as the grain boundaries have a finite depth in the third dimension, and will have variations in the area of contact and hence the stress transfer will vary through the sample thickness. Figure A2.1.2.7a shows a single crack growing from the centre that has intersected the boundary. If a fracture initiation point is placed at the boundary, the cracks growing away from the boundary prevent the central crack from extending completely to the boundary (Figure A2.1.2.7b).

The induced stresses surrounding the flaws can be observed by calculating the difference in the stresses between two growth increments. The tensile stresses induced by the interaction of two wing cracks are shown in Figure A2.1.2.8a. The initial induced tensile stresses are perpendicular to the direction of major compression. As the cracks extend, the zones of induced tension extend outwards from the crack tip. The greatest area of tensile stress extends between the approaching wing crack tips. The induced tension on the outer sides of the cracks is limited in extent. At some stage the zone of induced tension extends between the two wing cracks, this tensile stress would activate smaller flaws in tension and produce a stepped fracture surface.

Taking the difference in the stresses between the first and second (Figure A2.1.2.9) or the first and sixth growth steps (Figure A2.1.2.10) indicates the change in the stress state and suggests the reasons for the termination of crack growth. The overall stress state is reduced in the zone between the cracks, as evidenced by the extensive regions of induced tension (reduced compression) stress. The lighter stress vectors in Figures 2.4.1.9 and 10 indicate the induced compression. These vectors are directed along the original flaw towards the crack tip. This shows that the compressive stress has increased in the line of the flaw. The compressive stresses are able to clamp the tips of the wing cracks, preventing further growth.

The tensile stresses between the grains remain perpendicular to the growth direction i.e. parallel to the major principal stresses. Figure A2.1.2.11 shows that a crack may grow between the two extending fractures, but will be parallel to them. Thus, it is not an induced tension stress that causes linking of the fractures. Fracture linking must be due to the shearing of the thin region of rock between the induced fractures. This is similar to the observed samples that exhibit en echelon steps linked by a set of smaller en echelon fractures, at a steeper angle.

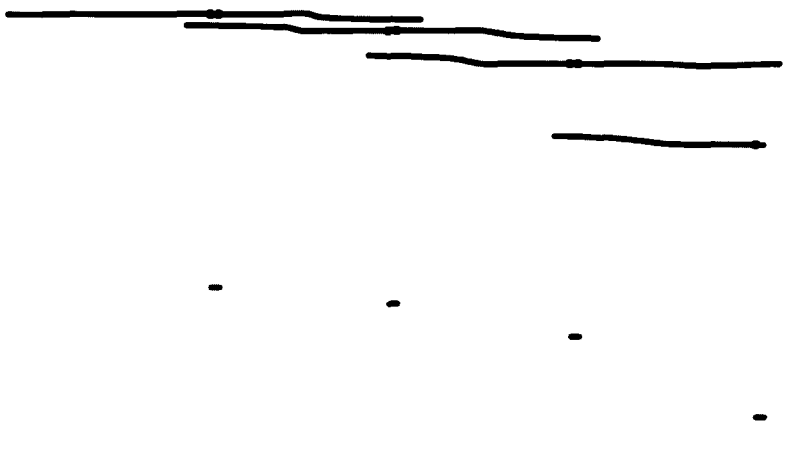

Figure A2.1.2.1 Crack growth from seed points in DIGS under 600 MPa compression in horizontal direction a: 10 MPa tensile stress in vertical direction b: 10 MPa compressive stress in vertical direction.

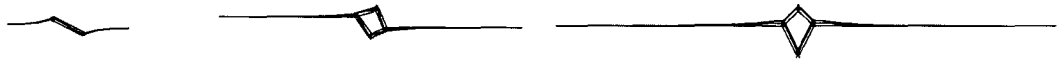

Figure A2.1.2.2 Crack growth from flaws in DIGS under 600 MPa compression in horizontal direction and 10 MPa compressive stress in vertical direction.

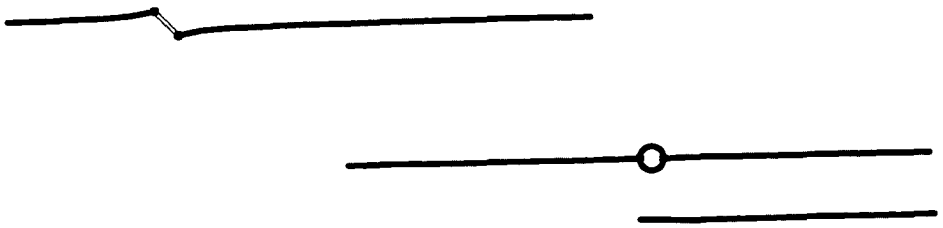

a:

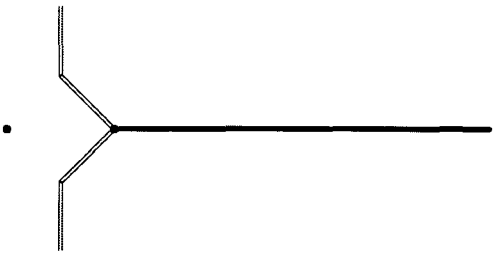

b:

Figure A2.1.2.3 Crack growth from a: hole and slider elements and b: re-entrant corner in a grain under 600 MPa compression in horizontal direction and 10 MPa compressive stress in vertical direction.

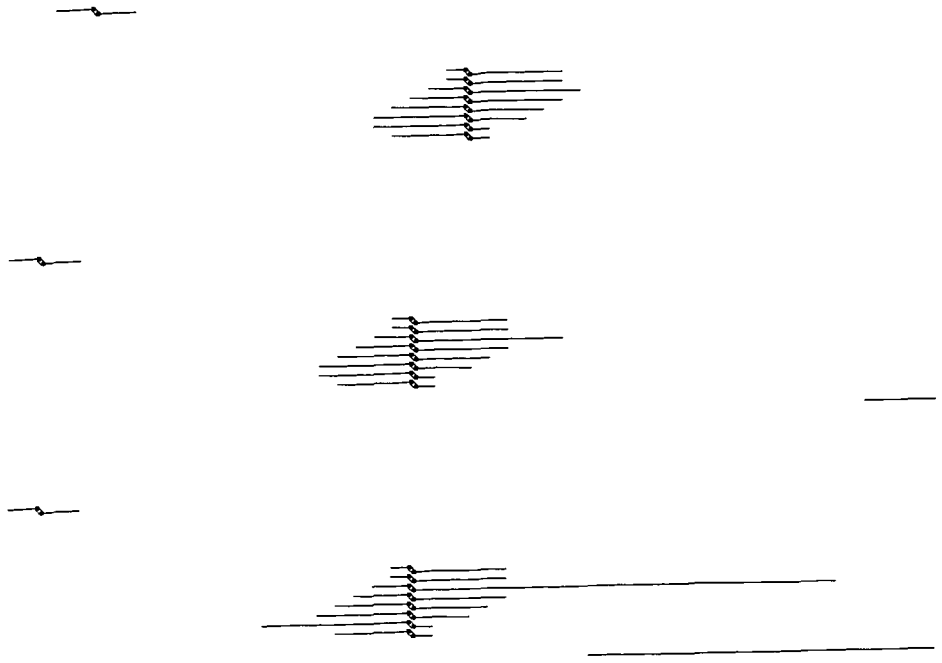

Figure A2.1.2.4 Crack growth sequence at two scales from array of slider elements in a grain under 600 MPa compression in horizontal direction and 10 MPa compressive stress in vertical direction.

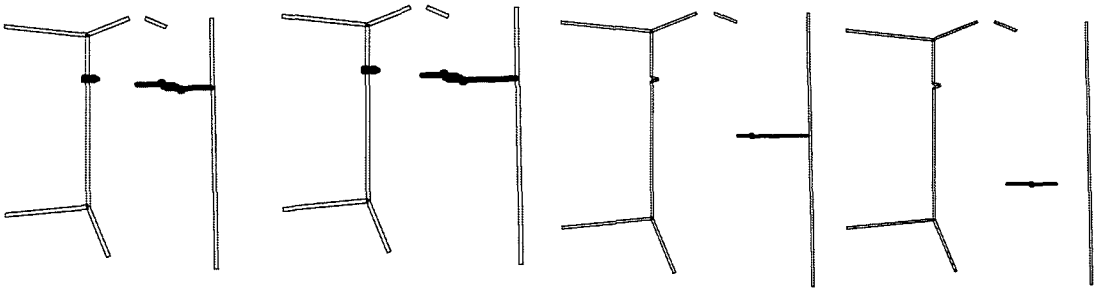

Figure A2.1.2.5 Effect of flaw position on crack growth in a grain under 600 MPa compression in horizontal direction and 10 MPa compressive stress in vertical direction.

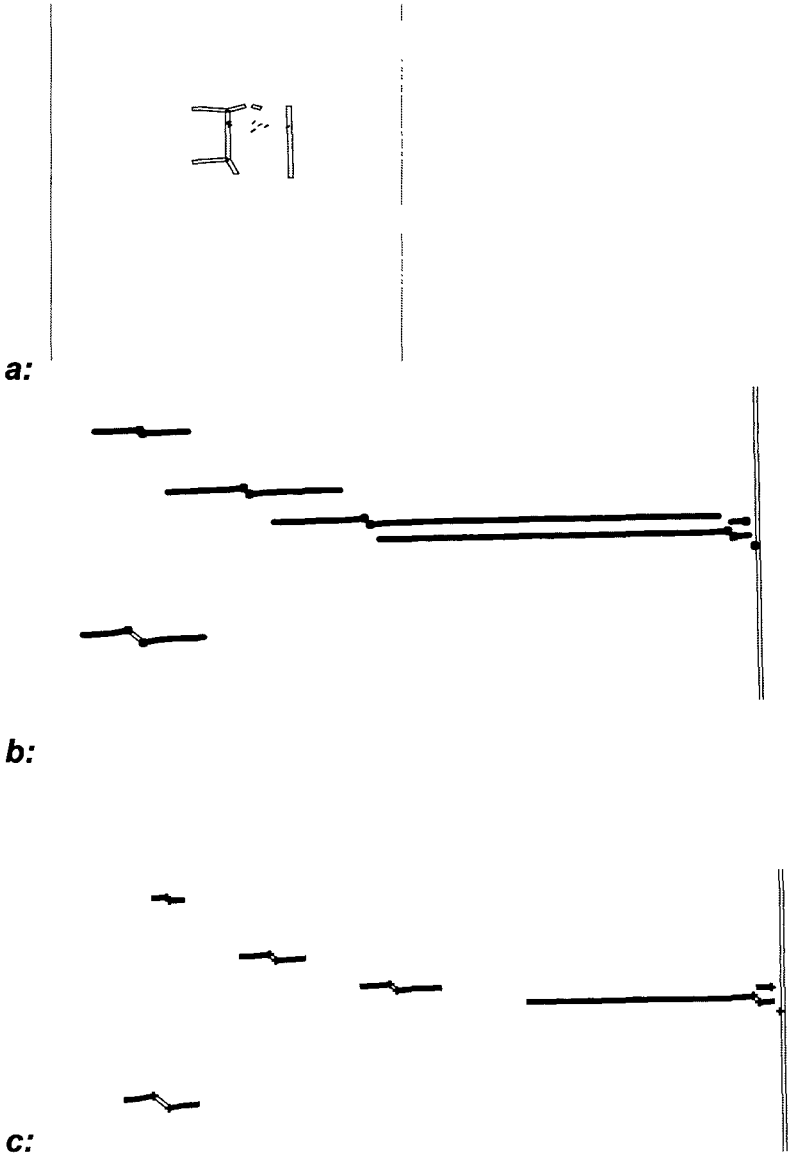

Figure A2.1.2.6 Effect of boundary stresses on crack growth in a grain under 600 MPa compression in horizontal direction and 10 MPa compressive stress in vertical direction a: model with rectangle for applied stresses b: stresses applied as overall field stresses c: stresses applied to box.

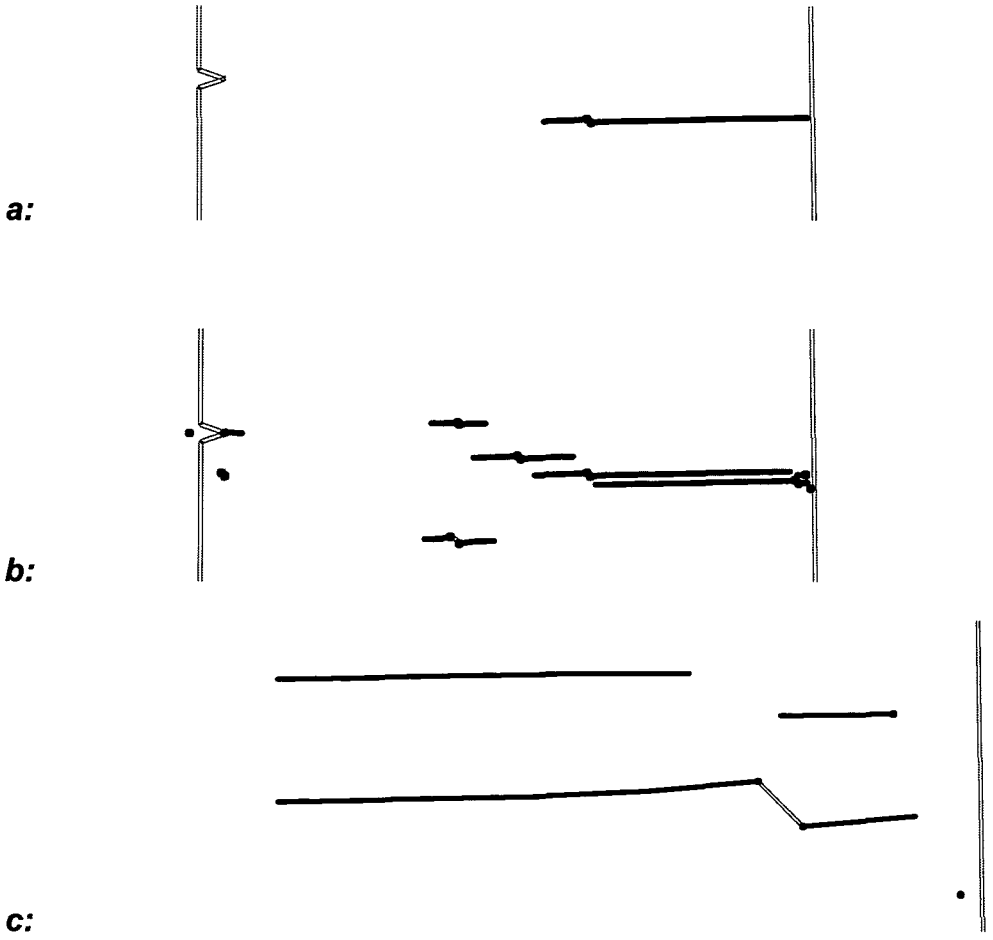

Figure A2.1.2.7 Shielding of crack growth in a grain under 600 MPa compression in horizontal direction and 10 MPa compressive stress in vertical direction a: single flaw in grain b: multiple flaws in grain c: detail of multiple flaw model showing edge cracks shielding crack growth from the grain centre.

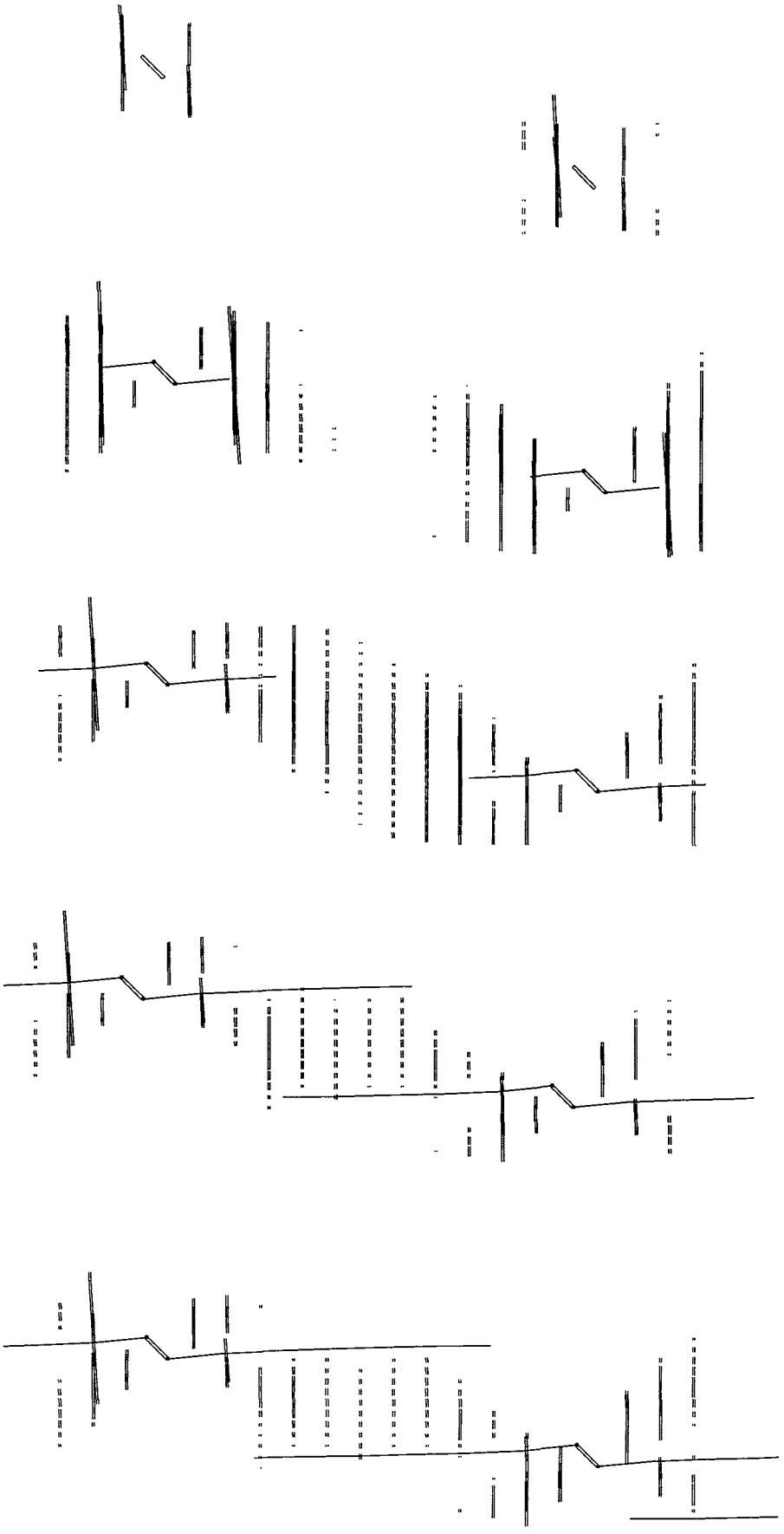

Figure A2.1.2.8 Progress of induced tensile stress around interacting wingcracks.

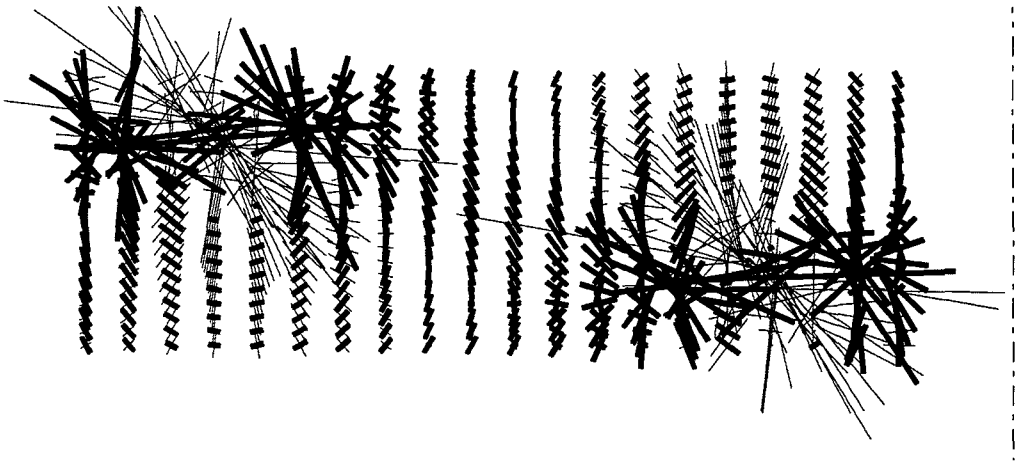

Figure A2.1.2.9 Stress change between steps 1 and 2.

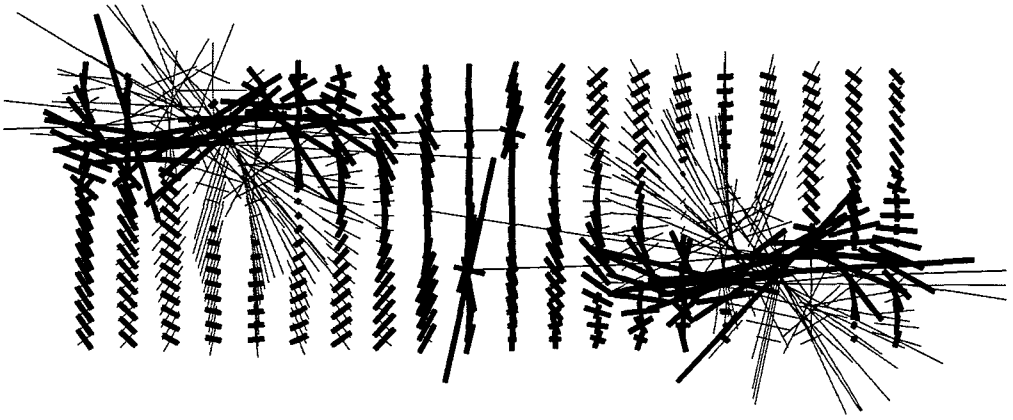

Figure A2.1.2.10 Stress change between steps 1 and 6.

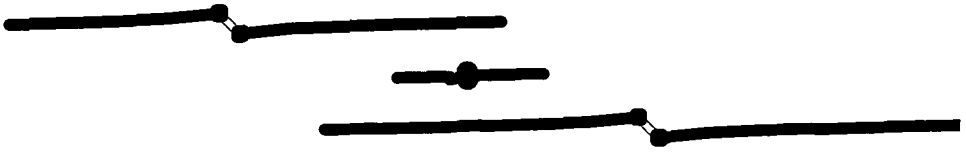

Figure A2.1.2.11 A smaller, en echelon, crack induced between two interacting wings cracks.

Appendix 2.2

Development of a discontinuum viscoplastic model

A2.2.1 Introduction

The link between seismic activity and mining operations in deep level mines has been well established (Cook *et al.,* 1966). Elastic models of tabular mining operations have been used to delineate regions of potential seismic activity in terms of the implied stress drop on geological weaknesses near the edges of mine excavations (Ryder, 1988; Spottiswoode, 1990a). Further extensions to this approach were proposed by Spottiswoode (1990b) in terms of the direct modelling of volumetric deformation processes around tabular excavations. More recently, Salamon (1993) has stressed the necessity to quantify the relationship between mining activity and induced seismicity. Salamon (1993) has proposed a novel procedure to establish this relationship by postulating the existence of populations of randomly disposed flaw sites surrounding the mine workings. The potential seismic stress drop on the flaws is calculated when the mine excavations are enlarged in progressive steps and Salamon's method provides a simulation tool to assess the expected seismic activity accompanying each mining step. Time-dependent constitutive effects are not considered.

In hard rock mining, carried out in the sedimentary deposits of the South African gold fields, it is often found that both seismic activity and significant closure of the excavation surfaces can arise not associated only with changes to mining face positions. Time-dependent deformations have been observed over periods of hours, days or longer periods (Leeman, 1958; McGarr, 1971; Malan, 1995). Seismic activity in highly stressed regions is found, also, to migrate spatially, presumably as a result of time-dependent fracturing and attendant stress transfer processes (Mendecki, 1993; Van Aswegen & Butler, 1993). These effects have been highlighted in the case of rock mass preconditioning experiments where seismic activity moves away from a mining face that has been subjected to a preconditioning blast, towards adjacent areas that are more highly stressed (Lightfoot *et al.,*1996). The role of time-dependent deformation in relation to the stability of mine workings and the recurrence of seismic activity has been emphasized by Linkov (1995). In particular, Linkov has noted the importance of creep on discontinuity contacts. This time-dependent behaviour is highlighted also by investigators concerned with the modelling of earthquake phenomena (Scholz *et al.,*1996; Lehner *et al.,* 1981; Rice, 1980; Ben-Zion & Rice, 1993).

In order to account for time-dependent seismic recurrence effects and to link these effects mechanistically to mining activity, it is necessary to represent in an explicit manner the rheological deformations that take place in the rock mass over periods of hours, days or weeks as well as rapid elastodynamic excitations. This study describes a framework for the incorporation of viscoplastic effects on random discontinuities which allows for the relaxation of the discontinuities according to a postulated law. Sudden stress drop or elastodynamic effects are approximated by allowing rapid cohesion loss (softening) to be accommodated in the solution scheme but no attempt is made to include elastodynamic wave propagation effects in the current study. The most important aspect of the work is that explicit interaction between the mine openings and mobilized discontinuities is accounted for as an evolutionary time process. This allows realistic questions concerning practical mining problems to be addressed. Specifically, it becomes possible to investigate problems such as the consequences of varying the mining face advance rate, the effects of mining at greater depths, the desirability of continuous or punctuated mining cycles and questions relating to the rate of extraction of remnant areas and the expected recurrence of rockbursts and seismic energy release cycles.

A variety of discontinuity structures are present in the vicinity of deep level South African gold mines. These depend generally on the geological formation of the reef horizon that is extracted and may also be induced by blasting operations which form part of the mining cycle. In the case of sedimentary reef deposits, such as the Carbon Leader and Vaal Reef, it is often found that parting planes parallel to the reef horizon are readily mobilized by the mining operations (King et al., 1989). In some cases the parting planes contain pre-existing gouge material which facilitates slip on the discontinuities (Malan et al., 1998). It is also found that other gold bearing reefs such as the Ventersdorp Contact Reef, are overlain by lava deposits which contain multiple joint structures which show less propensity for movement. Pre-existing fault structures are also encountered which behave differently in response to stress changes induced by mining operations. In some cases fault exposures have been observed to be continually mobilized (Van Aswegen & Butler, 1993) but in other cases sudden slip occurs resulting in large scale damage to underground excavations. Little data is currently available to characterise the manifold properties of these discontinuities. Experimental work currently underway suggests that mining induced extension fractures and joints in lava may exhibit very long relaxation times whereas discontinuities with gouge infilling may readily creep when shear loading is suddenly applied to the joint (Malan et al., 1998).

The approach presented here outlines a method for modelling the viscoplastic behaviour of discontinuities by incorporating a simple time-dependent slip rule on explicit crack interfaces that are represented by small strain dislocations as embodied in the displacement discontinuity boundary integral method (Crouch & Starfield, 1983). This approach facilitates the analysis of multiple interacting cracks such as joints, parting planes and faults which are characteristic of mining problems. It is demonstrated that realistic seismic energy release and stope closure trends can be simulated using a random mesh of potential discontinuity sites surrounding a tabular mining excavation. The justification for employing a random mesh representation is based on some success in modelling physical experiments of brittle rock failure (Napier & Dede, 1997) as well as the realistic replication of fracture patterns near mine openings (Sellers, 1997). Specific geological structures such as faults or parting planes are not considered. The approach used to estimate seismic energy release levels is described and the application of the model is illustrated by comparing simulated seismic energy release trends and stope closures to actual observations. The potential of the model to examine the effect of varying the mining face advance rate is illustrated. Although a simple time-dependent slip rule is used, it can easily be adapted within the developed framework to simulate behaviour appropriate to different discontinuity types.

A2.2.2 Viscoplastic displacement discontinuity model formulation

In previous work, carried out by Crawford & Curran (1983), the displacement discontinuity method was employed in conjunction with the correspondence principle to analyse viscoelastic intact rock behaviour with inelastic joints or elastic intact rock with viscoelastic joints. Malan (1995) also analysed time-dependent stope closure using an analytical model of a tabular opening in a viscoelastic medium. In the present development, it is postulated that the intact rock material behaves in an essentially elastic manner and that all inelastic behaviour, including viscoplastic effects, is controlled by the presence of multiple interacting discontinuities. In this approach, explicit slip is modelled as a time-dependent (but not elastodynamic) process and progressive redistribution of stress can occur near the edges of mine openings both as a function of time and in response to changes to the size of the openings.

To make the analysis explicit, suppose that the problem region of interest is covered by a specified mesh of potential crack surfaces S_d and assume that each arc of the mesh is a straight line segment that is divided into one or more elements. It is assumed that the displacement vector may be discontinuous at any point Q of the surface S_d. The displacement discontinuity vector $D_i(Q)$ at point Q is defined to be

$$S \qquad _d \tag{A2.2.1}$$

where $u_i^-(Q)$ and $u_i^+(Q)$ represent the displacement vectors on the "negative" and "positive" sides of the surface S_d with respect to a defined normal $n_i(Q)$ at point Q. The displacement and stress influence of each element can be defined as described in Napier & Malan (1997) (also see Crouch & Starfield, 1983). In the following development it is convenient to consider the stress values that arise at a given point within an element of length *2b* which is centred on the *y*-axis of a local co-ordinate system *y-z* as shown in Figure A2.2.1. In this system, the *x*-axis is assumed to be the direction of plane strain. Assuming that the displacement discontinuity varies linearly over the element of length $2b$, shown in Figure A2.2.1, the local displacement discontinuity vector components can be expressed as

$$D_i(\eta) = \alpha_i + \beta_i \eta \tag{A2.2.2}$$

where $i = y$ or z and α_i and β_i are constants.

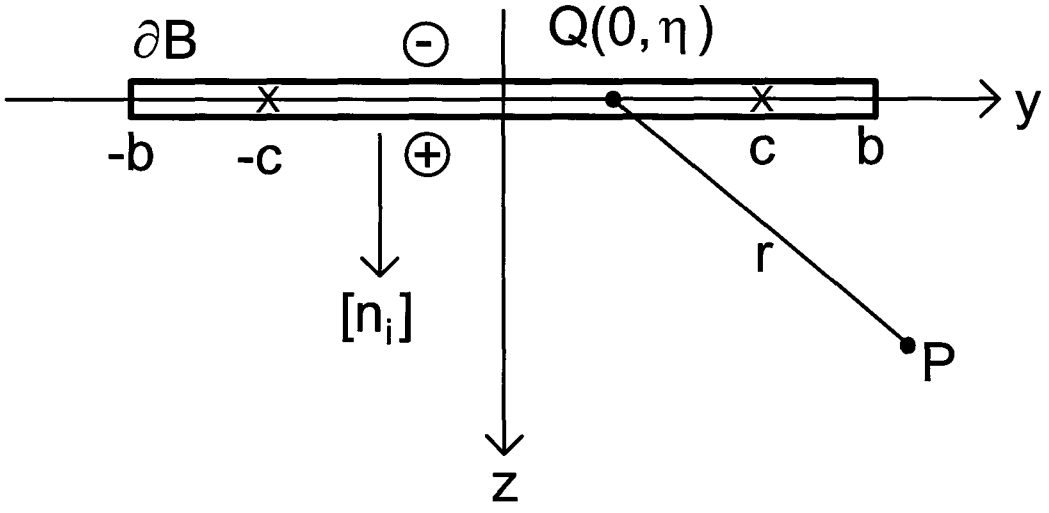

Figure A2.2.1 Local co-ordinate system defining a plane strain displacement discontinuity element of length 2b and having two collocation points located at y = ±c.

The linear variation shape is more accurate than constant variation displacement discontinuities (Crawford & Curran, 1983) and also allows direct estimates of crack-parallel stresses to be made without requiring numerical differentiation of adjacent element discontinuity values.

Let the shear and normal stress tractions at a designated collocation point, $y = c$, within a given element, be written in the form

$$\begin{bmatrix} T_y(c) \\ T_z(c) \end{bmatrix} = \frac{K_0}{b}\begin{bmatrix} D_y(c) \\ D_z(c) \end{bmatrix} + \frac{\bar{K}_0}{b}\begin{bmatrix} D_y(-c) \\ D_z(-c) \end{bmatrix} + \begin{bmatrix} E_y'(c) \\ E_z'(c) \end{bmatrix} \tag{A2.2.3}$$

where E_y' and E_z' represent the total shear and normal stress tractions, at the designated point, due to primitive stresses and due to the stress induced by all other mobilized displacement discontinuity elements.

The values of K_0 and $\overline{K}_0$ depend on the collocation factor $c_f = c/b$ and it was shown that for $y = c$ and $z = 0$ (Napier & Malan, 1997)

$$K_0 = \frac{G}{4\pi(1-\nu)}\left[\frac{4}{1-c_f^2} + \frac{1}{2c_f}\log\left(\frac{1+c_f}{1-c_f}\right)^2\right] \tag{A2.2.4}$$

$$\overline{K}_0 = -\frac{G}{4\pi(1-\nu)}\left[\frac{1}{2c_f}\log\left(\frac{1+c_f}{1-c_f}\right)^2\right] \tag{A2.2.5}$$

In cases of frictional sliding or creep relaxation, it is convenient to define the total external stress vector by

$$\begin{bmatrix} E_y(c) \\ E_z(c) \end{bmatrix} = \frac{\overline{K}_0}{b}\begin{bmatrix} D_y(-c) \\ D_z(-c) \end{bmatrix} + \begin{bmatrix} E_y'(c) \\ E_z'(c) \end{bmatrix} \tag{A2.2.6}$$

Substituting Equation (A2.2.6) into Equation (A2.2.3) and assuming implicit reference to a particular collocation point, Equation (A2.2.3) becomes

$$\begin{bmatrix} T_y \\ T_z \end{bmatrix} = \frac{K_0}{b}\begin{bmatrix} D_y \\ D_z \end{bmatrix} + \begin{bmatrix} E_y \\ E_z \end{bmatrix} \tag{A2.2.7}$$

or, in vector form

$$\boldsymbol{T} = (K_0/b)\,\boldsymbol{D} + \boldsymbol{E} \tag{A2.2.8}$$

Solution procedure

The determination of D_y and D_z will depend on the nature of the boundary condition imposed on each displacement discontinuity element. It is assumed that all elements are designated as elastic or as viscoplastic.

Let *L* designate the total set of defined elements. At each specific instance in time, t_i (*i*=1,2,...,*N*), let M_i represent the set of mobilized elements and $\overline{M}_i$ the complementary set of elements which have not been activated. Hence,

$$L = M_i \cup \overline{M}_i \tag{A2.2.9}$$

The set of active elements M_i arising at time t_i, will comprise a subset E_i of elastic elements and a subset V_i of viscoplastic elements. The classification of each element depends on the constitutive boundary conditions that are defined for the element as well as special rules which can be specified to control the transition of an element from elastic to viscoplastic status or vice versa. For example, a viscoplastic element may become elastic if it is subjected to a tensile stress component that causes the crack to open. E_i and V_i are non-intersecting sets and

$$M_i = E_i \cup V_i \qquad \text{(A2.2.10)}$$

The complete solution to the problem is defined by the displacement discontinuity values that are associated with each element in the sequence of sets $M_1 \ldots M_N$ that arise at the designated times $t_1 \ldots t_N$ respectively. The displacement discontinuity values are determined in an evolutionary manner from time step to time step. At the start of time step *i*, elements are selected for mobilization from the set $\overline{M}_{i-1}$ by computing the stress values at each collocation point in each element. Assuming that compressive stresses are negative, the element will be selected for mobilization if the stress state ***T*** at either collocation point falls on or outside the bilinear Mohr-Coulomb envelope shown in Figure 2.4.6.2 (Section 2.4.6 of the main report).

S_o' and ϕ' designate the unmobilized values of the cohesion and friction angle respectively and S_o and ϕ designate the residual mobilized values. T_c designates the tensile strength of the element and is assumed to fall to zero if failure occurs.

The evolution of the solution proceeds in the following steps.

i) At the start of time step *i* (time t_{i-1}) select all elements in $\overline{M}_{i-1}$ which can be mobilized. The selected elastic elements are designated as $\overline{E}_{i-1}$ and the selected viscoplastic elements are designated as $\overline{V}_{i-1}$

ii) Form the provisional sets of elastic, $\hat{E}_i$, and viscoplastic, $\hat{V}_i$, elements for step *i* from the relations

$$\hat{E}_i = E_{i-1} \cup \overline{E}_{i-1} \qquad \text{(A2.2.11)}$$

$$\hat{V}_i = V_{i-1} \cup \overline{V}_{i-1} \qquad \text{(A2.2.12)}$$

iii) Solve for the mutual interactions in set $\hat{E}_i$, using fixed external influences from the set $\hat{V}_i$, by iteratively adjusting the discontinuity values of $\hat{E}_i$.

iv) Apply a viscoplastic relaxation step to adjust the discontinuity at every collocation point in the set of elements $\hat{V}_i$.

v) Form the final sets E_i and V_i for time step *i* by checking for a change in status of each element in $\hat{E}_i$ and $\hat{V}_i$ which results from the adjusted displacement discontinuity values determined in steps (iii) and (iv).

vi) Return to step (i) for the next time step.

The iterative solution in step (iii) proceeds by computing external stress values E_y, E_z at each collocation point and then accelerating these values. For simple Jacobi iteration, this procedure is as follows (Ryder, 1991).

Let $E_y^{(k-1)}$ and $E_z^{(k-1)}$ represent external influences used in the *k-1*st iteration. Current estimates of $\hat{E}_y^{(k)}$ and $\hat{E}_z^{(k)}$ are determined from the discontinuity values existing at the end of the *k-1* st iteration. New estimates of $\hat{E}_y^{(k)}$ and $\hat{E}_z^{(k)}$ for the current step are determined from

$$\begin{bmatrix} E_y^{(k)} \\ E_z^{(k)} \end{bmatrix} = \begin{bmatrix} E_y^{(k-1)} \\ E_z^{(k-1)} \end{bmatrix} + \omega \begin{bmatrix} \hat{E}_y^{(k)} - E_y^{(k-1)} \\ \hat{E}_z^{(k)} - E_z^{(k-1)} \end{bmatrix} \tag{A2.2.13}$$

where the multiplier ω is a defined relaxation factor. The residual error of the estimates is given by

$$\begin{bmatrix} r_y^{(k)} \\ r_z^{(k)} \end{bmatrix} = \begin{bmatrix} \hat{E}_y^{(k)} - E_y^{(k-1)} \\ \hat{E}_z^{(k)} - E_z^{(k-1)} \end{bmatrix} \tag{A2.2.14}$$

Current estimates of $D_y^{(k)}$ and $D_z^{(k)}$ are determined from specific boundary conditions imposed at the collocation point. For example, for an open crack or for the case of a tabular mine opening approximated as an open crack, tractions defined by Equation (A2.2.7) should be zero and therefore,

$$\begin{bmatrix} D_y^{(k)} \\ D_z^{(k)} \end{bmatrix} = -\frac{b}{K_0} \begin{bmatrix} E_y^{(k)} \\ E_z^{(k)} \end{bmatrix} \tag{A2.2.15}$$

Once a discontinuity is mobilized it is assumed that the tensile strength is zero. Hence in the case of sliding friction contact it is required that

$$|T_y| = S_o - \tan\phi T_z \;\; ; \;\; T_z < 0 \tag{A2.2.16}$$

Define a slip direction indicator, e, to be such that $e = 1$ if $E_y < 0$ and $e = -1$ if $E_y > 0$ then

$$|T_y| = -eT_y \tag{A2.2.17}$$

For a sliding crack it is assumed that the discontinuity opening displacement is given by

$$D_z = -\tan\psi |D_y| \tag{A2.2.18}$$

where ψ is the sliding dilation angle, then the equilibrium condition (A2.2.16) is satisfied if

$$D_y = \frac{-[E_y + e(S_o - \tan\phi E_z)]b}{K_0[1 + \tan\phi\tan\psi]} \tag{A2.2.19}$$

Other contact conditions, such as cohesion or friction weakening expressed as a function of slip D_y, or the inclusion of discontinuity stiffness values, can be treated using a similar formulation to that of Equation (A2.2.7) in which the collocation point self-effect and the external influence components of stress are decoupled and the external influence components are iterated as implied by Equations (A2.2.13) and (A2.2.14). It is also possible to formulate more elaborate schemes to improve the iterative efficiency. This involves optimizing the choice of ω in each iteration step by successively approximating the nature of the residual error structure (Ryder, 1991; Peirce, 1993).

Viscoplastic relaxation and timestep bounds

In order to resolve the viscoplastic relaxation step (iv) above, it is necessary to assume a specific functional dependence of the slip rate on the current stress state at each collocation point. Each slip element is assumed to be in quasi-static equilibrium at each instant in time, with the rate of slip being a function of the stress state and the resistance to slip. Specifically, define the resistance to slip, ρ, to be given by

$$\rho = S_\circ - \tan\phi T_z \quad ; \quad T_z < 0 \tag{A2.2.20}$$

where $S_\circ$ and ϕ are the residual cohesion and friction angle parameters. The excess driving shear stress, τ_e, is defined to be

$$\tau_e = \left|T_y\right| - \rho \tag{A2.2.21}$$

Using Equations (A2.2.7) and (A2.2.17), Equation (A2.2.21) becomes

$$\tau_e = -e(\frac{K_0}{b} D_y + E_y) - (S_\circ - \tan\phi T_z) \tag{A2.2.22}$$

From the definition of the slip direction indicator variable, *e*, the sign of the rate of change of slip, dD_y/dt is equal to *e*. It is now postulated that the rate of slip is proportional to the driving shear stress τ_e. Specifically,

$$\frac{dD_y}{dt} = e\kappa\tau_e \tag{A2.2.23}$$

where κ is defined to be a parameter playing a similar role to the fluidity parameter of classical viscoplasticity theory (Perzyna, 1966). This parameter will be designated as the *surface fluidity* having units of $m/(Pa \cdot s)$. Substituting Equation (A2.2.22) into Equation (A2.2.23) and noting that $e^2 = 1$,

$$\frac{dD_y}{dt} = -\kappa[\frac{K_0}{b} D_y + E_y + e(S_\circ - \tan\phi T_z)] \tag{A2.2.24}$$

In discrete form,

$$D_y^{t_i} \approx D_y^{t_{i-1}} - \kappa\Delta t[\frac{K_0}{b} D_y^{t_{i-1}} + E_y + e(S_\circ - \tan\phi T_z)] \tag{A2.2.25}$$

where

$$\Delta t = t_i - t_{i-1} \tag{A2.2.26}$$

The value of the confining stress T_z in Equations (A2.2.20) and (A2.2.25) is assumed to be approximately constant over the time step Δt. The functional form of Equation (A2.2.24) is essentially equivalent to the relationship proposed by Wesson (1988). The cohesion $S_\circ$ and friction angle ϕ can, in general, depend on the velocity dD_y/dt, the current slip D_y and time, *t*.

(Wesson, 1988; Ruina, 1983; Rice, 1980). In the present study, S_o and ϕ are assumed to be constant. Equation (A2.2.25) can be written in the more compact form

$$\Delta D_y^{t_{i-1}} = e\kappa\tau_e\Delta t \tag{A2.2.27}$$

Similarly, Equation (A2.2.19), with the dilation angle ψ set to zero, can be written for an incremental change in slip as

$$\Delta D_y = e\tau_e b/K_0 \tag{A2.2.28}$$

Due to the discrete nature of the time step in Equations (A2.2.25) and (A2.2.27) it is necessary that the magnitude of the change in Equation (A2.2.27) should be less than the maximum possible elastic slip relaxation given by (A2.2.28). This implies a bound on the product of the timestep Δt and the surface fluidity parameter κ such that

$$\kappa\Delta t < b/K_0 \tag{A2.2.29}$$

This bound on the timestep is analogous to the timestep bound identified by Cormeau (1975) for volumetric viscoplastic stress relaxation. It is clearly possible to extend the crude time stepping procedure given by Equation (A2.2.25) to a higher order Runge-Kutta scheme with automatic timestep selection (Press *et al.*,1986).

A2.2.3 Estimation of seismic energy release

In the analysis of mining or earthquake problems it is convenient to define the gravitational body forces and far-field tectonic forces as loading forces. In the course of mining or fault slip, the earth is deformed and the loading forces perform work. Let the incremental work done by the loading forces during a given time interval be ΔW_L. In the particular case of an elastic body, conservation of energy requires that

$$\Delta W_L = \Delta U + \Delta W_A \tag{A2.2.30}$$

where ΔU is the change in internal strain energy and ΔW_A represents kinetic energy changes and energy dissipated by frictional sliding on discontinuities or consumed in creating new discontinuity surfaces. Consider in particular the transition between two states *p* and *t* which are associated with equilibrated stress and displacement fields $\tau_{ij}^{\ p}(Q), u_i^{\ p}(Q)$ and $\tau_{ij}^{\ t}(Q), u_i^{\ t}(Q)$ respectively at each point Q of the body. In each case the body force field components $F_i(Q)$ remain the same. The work done by the loading forces are shown in Napier & Malan (1997) to be given by

$$\Delta W_L = \Delta W_{Le} + \int_{S_d}[T_i^t(Q)D_i^{\ p}(Q) - T_i^p(Q)D_i^{\ t}(Q)]dS_Q \tag{A2.2.31}$$

where

$$\Delta W_{Le} = \int_{S_e}[T_i^t(Q) - T_i^p(Q)][u_i^t(Q) + u_i^p(Q)]dS_Q \tag{A2.2.32}$$

In Equations (A2.2.31) and (A2.2.32), repeated subscripts imply summation over the requisite number of spatial components, S_d designates the internal discontinuity surfaces and S_e designates the external boundary surface of the body. $T_i^s(Q)$ represent, for time step *s*, the traction vector components at a given point Q of the internal or external surface with respect to a normal vector $n_i(Q)$ as defined in Napier & Malan (1997). ΔW_{Le} represents the effect of the external surface S_e on the incremental work of the loading forces. In mining problems S_e can be considered to comprise both the earth's surface, where the tractions are zero, and a remote surface where the tractions are fixed ($T_i^t = T_i^p$) or where the displacement is zero. In this case ΔW_{Le} will be zero. The internal surface S_d can include narrow tabular openings which are approximated as cracks.

Equation (A2.2.31) provides a means for computing the incremental loading work which accompanies a transition from state *p* to state *t*. The crucial assumption is now made that the equilibrated states *p* and *t* can be sufficiently well approximated using the static solution procedure outlined in the previous sections. Having identified two equilibrium states of the system, it is possible to compute the incremental work done by the loading forces ΔW_L and the change in the strain energy ΔU. Since the two states *p* and *t* are computed using a quasi-static solution procedure, there will generally be an unaccounted gap ΔW_A between ΔW_L and ΔU. By conservation of energy, ΔW_A must be assumed to comprise both kinetic energy and other dissipated energy. ΔW_A can be loosely termed released energy. If some estimate can be made of the energy that is dissipated by frictional sliding during the transition from state *p* to state *t*, it is possible to infer the maximum level of kinetic energy that could exist in the body during the transition. The kinetic energy is itself assumed to be dissipated by unspecified material damping and radiation mechanisms. The validity of this approximation rests on the assumption that elastodynamic stress waves do not give rise to significant additional fracture formation and that there is little overshoot in computing the final discontinuity values. The difference between ΔW_L and ΔU in Equation (A2.2.30) then provides a measure of the released energy which arises in the transition from state *p* to state *t*. This difference, ΔW_A, is shown in Napier & Malan (1997) to be given by

$$\Delta W_A = \tfrac{1}{2}\Delta W_{Le} - \tfrac{1}{2}\int_{S_d}[T_i^t(Q) + T_i^p(Q)][D_i^t(Q) - D_i^p(Q)]dS_Q \qquad \text{(A2.2.33)}$$

The level of kinetic or seismic energy, ΔW_S, that arises during the transition from state *p* to state *t* can be expressed as

$$\Delta W_S = \Delta W_A - \Delta W_D \qquad \text{(A2.2.34)}$$

where ΔW_D is the energy dissipated by frictional sliding or by the creation of new fracture surfaces. In the specific examples considered in this study, it is assumed that in local discontinuity co-ordinates, as shown in Figure A2.2.1, the dissipated energy is predominantly frictional and is given by

$$\Delta W_D = \int_{S_d}\tan\phi T_z(\eta)\left|D_y^t(\eta) - D_y^p(\eta)\right|d\eta \qquad \text{(A2.2.35)}$$

where T_z is the local stress component normal to the discontinuity surface S_d.

Equations (A2.2.33) and (A2.2.35) can be evaluated at each time step *i* by associating state *p* with the set of elements M_{i-1} mobilized at t_{i-1} and state *t* with the set of elements M_i mobilized at t_i. Approximate numerical values of (A2.2.33) and (A2.2.35) are obtained for each

element by using the traction and displacement discontinuity vector components at the element collocation points in the following discrete sums.

$$\Delta W_A^{el} \approx -\tfrac{b}{2}\sum_{k=\pm 1}[T_i^p(kc)+T_i^t(kc)][D_i^t(kc)-D_i^p(kc)] \qquad \text{(A2.2.36)}$$

$$\Delta W_D{}^{el} \approx -\tfrac{b}{2}\tan\phi\sum_{k=\pm 1}T_z(kc)\left|D_y^t(kc)-D_y^p(kc)\right| \qquad \text{(A2.2.37)}$$

where *kc* is the collocation position in the local co-ordinate system defined in Figure A2.2.1 and $T_z(kc) < 0$ for compressive stress normal to the element surface.

A2.2.4 Example

It is of interest to consider the viscoplastic response of an isolated straight crack in an infinite medium. Suppose that the crack lies on the *y*-axis of the local co-ordinate system shown in Figure A2.2.1. The total shear traction T_y acting at position *y* within the crack is obtained by adding the induced shear stress $\tau_{yz}(y,0)$ (see Napier & Malan, 1997), to the primitive far-field shear stress component P_y. Specifically,

$$T_y(y) = \frac{G}{4\pi(1-\nu)}\int_{-b}^{b}\varphi_{,zz}(\eta,0)D_y(\eta)d\eta + P_y \qquad \text{(A2.2.38)}$$

where $\varphi(y,z) = -\log[(y-\eta)^2+z^2]$. The net driving shear stress, τ_e, acting on the crack is obtained by substituting Equations (A2.2.38), (A2.2.20) and (A2.2.17) into Equation (A2.2.21). This gives

$$\tau_e = -e\left\{\frac{G}{4\pi(1-\nu)}\int_{-b}^{b}\varphi_{,zz}(\eta,0)D_y(\eta)d\eta + P_y\right\} - S_\circ + \tan\phi T_z \qquad \text{(A2.2.39)}$$

The slip rate dD_y/dt at any point inside the crack is given by Equation (A2.2.23). When the crack has ceased to slip, $dD_y/dt = 0 = \tau_e$. The solution to Equation (A2.2.39) with $\tau_e = 0$ is given by (Sneddon & Lowengrub [30]),

$$D_y^*(\eta) = -\frac{2(1-\nu)}{G}\left[e(S_\circ - \tan\phi T_z) + P_y\right]\sqrt{b^2-\eta^2} \qquad \text{(A2.2.40)}$$

The slip motion on a single crack can be solved numerically, using the scheme corresponding to Equation (A2.2.25), for any particular choice of the surface fluidity parameter κ. Figure A2.2.2 shows the time evolution of the normalised maximum slip value at the centre of the crack when κ is set to 2×10^{-4} m/(MPa·day) and the crack is modelled using twenty equal length displacement discontinuity elements, with linear variation, described previously. The maximum slip values are scaled by the maximum asymptotic value $D_y^*(0)$ given by Equation (A2.2.40).

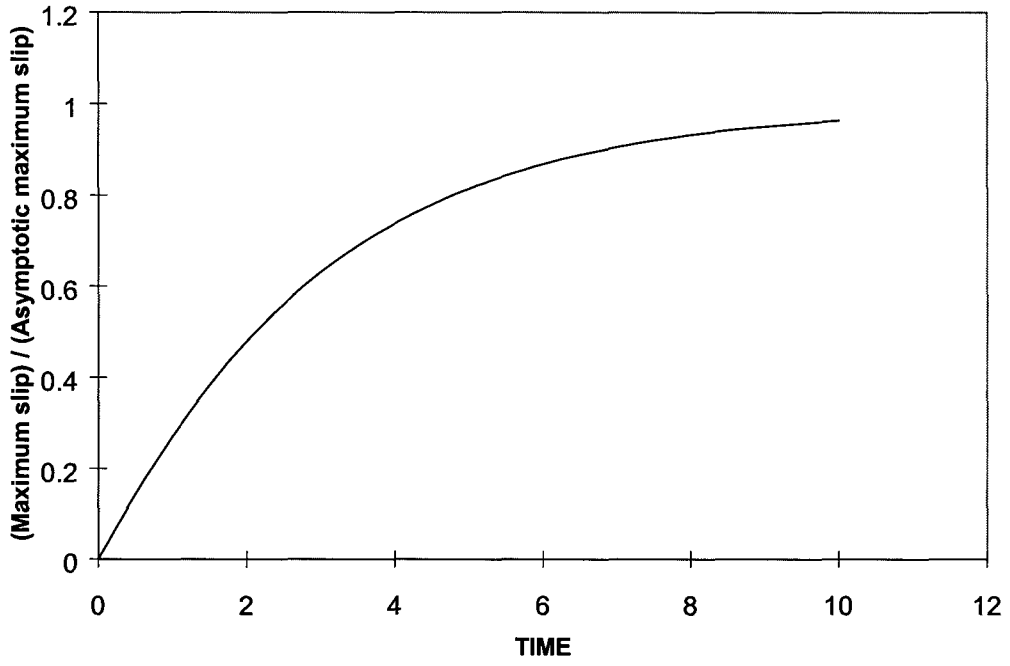

Figure A2.2.2 Maximum slip evolution on a single crack.

A2.2.5 References

Ben-Zion, Y. & Rice, J.R. 1993. Earthquake failure sequences along a cellular fault zone in a three-dimensional elastic solid containing asperity and nonasperity regions. *J. Geophys. Res.*, vol. 98, 14109-14131.

Cook, N.G.W., Hoek, E., Pretorius, J.P.G., Ortlepp, W.D. & Salamon, M.D.G. 1966. Rock Mechanics applied to the study of rockbursts. *J. S. Afr. Inst. Min. Metall.* vol. 66, 435-528.

Cormeau, I. 1975. Numerical stability in quasi-static elasto/visco-plasticity. *Int. J. Num. Methods Eng.*, vol. 9, 109-127.

Crawford A.M. & Curran J.H. 1983. A displacement discontinuity approach to modelling the creep behaviour of rock and its discontinuities. *Int. J. Num. Anal. Meth. Geomech.*, 245-268.

Crouch S.L. & Starfield A.M. 1983. *Boundary element methods in solid mechanics.* 1st ed. London, George Allen & Unwin.

King R.G., Jager, A.J., M.K.C. Roberts & Turner, P.A. 1989. Rock mechanics aspects of stoping without back-area support. Unpublished COMRO (Chamber of Mines Research Organization, now CSIR Miningtek) research report, no. 17/89.

Leeman, E.R. 1958. Some measurements of closure and ride in a stope of the East Rand Proprietary Mines. *Pap. Ass. Min. Mngrs. S.Afr.* 1958-1959, 385-404.

Lehner, F.K. Li, V.C. & Rice, J.R. 1981. Stress diffusion along rupturing plate boundaries, *J. Geophys. Res.*, vol. 86, 6155-6169.

Lightfoot, N., Goldbach, O.D., Kullmann, D.H. & Toper, A.Z. 1996. Rockburst control in the South African deep level gold mining industry. In: M. Aubertin, F. Hassani & H. Mitri (eds.) Rock Mechanics Tools and Techniques, *Proc. 2nd North American Rock Mechanics Symposium: NARMS '96*, 295-303.

Linkov, A. M. 1995. Keynote address: Equilibrium and stability of rock masses. In: T. Fujii (ed.) *Proc. 8th Int. Congress on Rock Mechanics*, vol. III, Japan, Balkema.

Malan, D.F. 1995. A viscoelastic approach to the modelling of the transient closure behaviour of tabular excavations after blasting. *J. S. Afr. Inst. Min. Metall.*, 95, 211-220.

Malan, D.F. & Spottiswoode, S.M. 1997. Time-dependent fracture zone behaviour and seismicity surrounding deep level stoping operations. In: S.J. Gibowicz & S. Lasocki (eds) *Proc 4th Int. Symp. Rockbursts & Seismicity in Mines*, Krakow, Poland, Balkema, pp. 173-177.

Malan, D.F. Drescher, K. & Vogler, U.W. 1998. Shear creep of discontinuities in hard rock surrounding deep level excavations. In: H.P.Rossmanith (ed.) *Proceedings Third International Conference on Mechanics of Jointed and Faulted Rock*, Vienna, Balkema, pp. 473-478.

Malan, D.F., Vogler, U.W. & Drescher, K. 1997. Time-dependent behaviour of hard rock in deep level gold mines. *J. S. Afr. Inst. Min. Metall.*, vol. 97, pp. 135-147.

Mcgarr, A. 1976. Dependence of magnitude statistics on strain rate. *Bull. Seism. Soc. Am.*, vol. 66, 33-44.

Mcgarr, A. 1971. Stable deformation near deep-level tabular excavations *J. Geophys. Res.* vol. 76, 7088-7106.

Mendecki, A.J. 1993. Real time quantitative seismology in mines. Keynote Lecture. In: R.P. Young (ed.) *Proc. 3rd Int Symp. Rockbursts and Seismicity in Mines*, Balkema, 287-295.

Napier, J.A.L. 1991. Energy changes in a rock mass containing multiple discontinuities. *J. S. Afr. Inst. Min. Metall.*, vol. 91, 145-157.

Napier J.A.L. & Dede T. 1997. A comparison between random mesh schemes and explicit growth rules for rock fracture simulation. Accepted for publication in *Proc. 36th US Symp. Rock Mech.*, New York.

Napier, J.A.L. & Malan, D.F. 1997. A viscoplastic discontinuum model of time-dependent fracture and seismicity effects in brittle rock. *Int. J. Rock Mech. Min. Sci. & Geomech. Abstr.*, vol. 34, pp. 1075-1089.

Peirce, A. 1993. Optimal iteration of discretized boundary element equations, CSIR, Division of Mining Technology project report.

Perzyna, P. 1966. Fundamental problems in viscoplasticity. *Adv. Appl. Mech.*, vol. 9, 243-377 (1966).

Press, W.H., Flannery, B.P., Teukolsky, S.A. & Vetterling, W.T. 1986. *Numerical recipes*, Cambridge University Press.

Rice, J.R. 1980. The mechanics of earthquake rupture. In: A.M. Dziewonski & E. Boschi (eds.) *Physics of the earth's interior*, Italian Physical Society, Bologna, Italy, 555-649.

Ruina, A. 1983. Slip instability and state variable friction laws. *J.Geophys. Res.*, vol. 88, 10359-10370.

Ryder, J.A. 1988. Excess shear stress in the assessment of geological hazardous situations. *J. S. Afr. Inst. Min. Metall.* vol. 88, 27-39.

Ryder, J.A. 1991. Optimal iteration schemes suitable for general non-linear boundary element modelling applications. In: Beer, Booker & Carter (eds.), *Computer Methods and Advances in Geomechanics*, 1079-1084.

Salamon, M.D.G. 1984. Energy considerations in rock mechanics: Fundamental results, *J. S.Afr. Inst. Min. Metall.*, vol. 84, 223-246.

Salamon, M.D.G. 1993. Keynote address: Some applications of geomechanical modelling in rockburst and related research. In: R.P. Young (ed.) *Proc. 3rd Int. Symp. Rockbursts and Seismicity in Mines*, Balkema, 297-309.

Salamon, M.D.G. 1974. Rock mechanics of underground excavations. *Proc. 3rd Cong. International Society for Rock Mechanics,* 951-1099.

Scholz, C.H., Wyss, M. & Smith, S.W. 1969. Seismic and aseismic slip on the San Andreas Fault, *J. Geophys. Res.*, vol. 74, 2049-2069.

Sellers E. 1997. A tessellation approach for the simulation of the fracture zone around a stope. In: G. Gürtunca & T.O. Hagan (eds) Proceedings 1st Southern African Rock Engineering Symposium, Johannesburg, pp. 143-154.

Sneddon, I.N. & Lowengrub, M. 1969. *Crack problems in the classical theory of elasticity*, John Wiley and Sons, New York.

Sokolnikof, I.S. 1956. *Mathematical theory of elasticity*, McGraw-Hill, New York.

Spottiswoode, S.M. 1990. Towards 3D modelling of inelastic deformation around deep-level mines. In: H.P. Rossmanith (ed.) *Proc. Int. Conf. Mechanics of Jointed and Faulted Rock*, Balkema, 695-707.

Spottiswoode, S.M. 1990. Volume of excess shear stress and cumulative seismic moments. In: C. Fairhurst (ed.) *Proc. 2nd Int. Symp. Rockbursts and Seismicity in Mines*, Balkema, 39-43.

Van Aswegen, G. & Butler A.G. 1993. Applications of quantitative seismology in South African gold mines. In: R.P. Young (ed.) *Rockbursts and Seismicity in Mines*, Balkema, 261-266.

Wesson, R.L. 1988. Dynamics of fault creep, *J. Geophys. Res.*, vol. 93, pp. 8929-8951.

Appendix 2.3

Derivation of the fundamental displacement discontinuity solution for a multiple layered medium

In order to demonstrate more clearly the establishment of the fundamental solution for a displacement discontinuity element in a three-layer medium, the solution for a displacement discontinuity element in an infinite plane, a half-plane, and bonded half-planes are presented briefly for completeness.

A2.3.1 Solution for an infinite plane

The solution for the displacements and stresses at a point (x,y) due to displacement discontinuity (D_x , D_y) over the line segment $|x| \leq a$, y = 0, can be expressed as

$$u_x = [2(1- \nu)f_{x,y} - yf_{x,xx}] + [-(1-\nu)f_{y,x} - yf_{y,xy}]$$

$$u_y = [(1-\nu)f_{x,x} - yf_{x,xy}] + [2(1- \nu)f_{y,y} - yf_{y,yy}]$$

$$\sigma_{xx} = 2G\,[2f_{x,xy} + yf_{x,xyy}] + 2G\,[f_{y,yy} + yf_{y,yyy}] \qquad \text{(A2.3.1)}$$

$$\sigma_{yy} = 2G\,[-yf_{x,xyy}] + 2G\,[f_{y,yy} - yf_{y,yyy}]$$

$$\sigma_{xy} = 2G\,[f_{x,yy} + yf_{x,yyy}] + 2G\,[-yf_{y,xyy}]$$

where

$$f_i(x,y) = \frac{1}{4\pi(1-\nu)} \int_{-a}^{a} D_i(\xi) \ln \sqrt{(x-\xi)^2 + y^2}\, d\xi \quad i=x,y \qquad \text{(A2.3.2)}$$

G is the shear modulus, and ν is the Poisson's ratio.

In the original displacement discontinuity formulation, i.e, the constant strength element presented by Crouch & Starfield (1983), the mid-element stresses and displacements were assumed to represent the effective values over the length of the discontinuity. For the linear variation element, with four degrees of freedom, two nodes within the discontinuity must be chosen at which the representative measures of stresses and displacements are evaluated. In this study, the two Gauss-Chebyshev integration points (at $x= \pm a/\sqrt{2}$, y=0) are used and the local displacement discontinuity components can be expressed as

$$D_i(\xi)=N_1(\xi)D_i(1)+ N_2(\xi)D_i(2) \quad i=x,y \qquad \text{(A2.3.3)}$$

where

$$N_1(\xi)=\frac{1}{2}-\frac{\xi}{\sqrt{2}}$$

$$N_2(\xi)=\frac{1}{2}+\frac{\xi}{\sqrt{2}} \qquad \text{(A2.3.4)}$$

and $D_i(j)$ (i=x,y and j=1,2) are the nodal displacement discontinuities.

A2.3.2 Solution for a half-plane

The fundamental solution for a constant strength displacement discontinuity element in a semi-infinite region $y \leq 0$ can be obtained by using the method of images (Salamon, 1963, Crouch and Starfield, 1983). Based on the principle of superposition, the method of images can be used to find the solution to the problem in two steps. In the first step, consider a displacement discontinuity element, the actual element, in the region $y < 0$ and suppose that a second element representing its image, reflected about $y = 0$, exists in $y > 0$. By symmetry, this setting ensures zero shear traction on $y = 0$, however, the normal traction is not zero. In the second step, a supplementary solution, related to a prescribed normal traction on $y = 0$, is obtained to make the normal traction vanish (see Figure A2.3.1). Therefore, the complete solution for the half-plane $y \leq 0$ can be written as:

$$u_i = (u_i)_A + (u_i)_I + (u_i)_S$$

$$\sigma_{ij} = (\sigma_{ij})_A + (\sigma_{ij})_I + (\sigma_{ij})_S \qquad \text{(A2.3.5)}$$

where subscripts A, I, and S denote the displacements and stresses due to the actual element, the image element, and the supplementary solution.

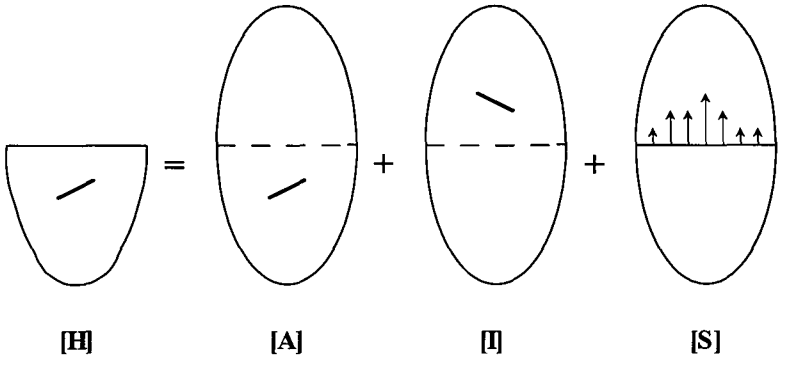

Figure A2.3.1 The composition of the half-plane solution.

A2.3.3 Solution for bonded half-planes

For a displacement discontinuity element within one of two bonded half-planes, the fundamental solution can be obtain by the method of images with one more step (see Figure A2.3.2) to the half-plane solution. This is accomplished by introducing a general form of solution u_i^* and σ_{ij}^* for the upper half-plane and an additional supplementary solution u_i^{**} and σ_{ij}^{**} for the lower half-plane. Superposing the lower and upper half-planes, the induced boundary conditions at the surface y = 0, which ensure that the stresses and displacements are continuous at the interface are as follows.

$$u_x = u_x^*$$

$$u_y = u_y^*$$

$$\sigma_{xy} = \sigma_{xy}^*$$

$$\sigma_{yy} = \sigma_{yy}^* \quad \text{for } -\infty<x<\infty,\ y=0 \tag{A2.3.6}$$

where

$$u_i = (u_i)_A + (u_i)_I + (u_i)_S + u_i^{**}$$

$$\sigma_{ij} = (\sigma_{ij})_A + (\sigma_{ij})_I + (\sigma_{ij})_S + \sigma_{ij}^{**} \tag{A2.3.7}$$

is the complete solution for the half-plane $y \leq 0$, and where u_i^{**} and σ_{ij}^{**} represent the displacement and stress components in the lower half-plane due to the stresses applied to the negative side of the interface $y = 0^-$. The complete solution for the upper half-plane is u_i^* and σ_{ij}^*, which depends only upon the normal and shear stresses applied to the positive side of the interface $y = 0^+$. Based on the theory of elasticity (Fang, 1965), the solutions u_i^{**}, σ_{ij}^{**}, u_i^*, and σ_{ij}^* can be expressed in terms of displacement potential functions. We can derive these potential functions by considering the continuity conditions specified by Equation (A2.3.6). The solutions u_i and σ_{ij} can be obtained by introducing the terms u_i^{**} and σ_{ij}^{**} in Equation (A2.3.7).

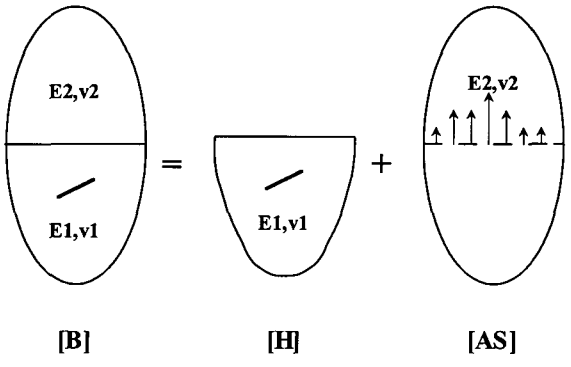

Figure A2.3.2 The composition of the solutions of bonded half-planes.

A2.3.4 Solution for a three-layer medium

In this study, the solution of a displacement discontinuity element within a three-layer medium is derived by a superposition procedure, which is based on the appropriate combination of appropriate bonded half-plane solutions. In particular, a three-layered elastic region, with Young's moduli E_1, E_2, and E_3, can be obtained by superposing two sets of bonded half-plane regions and an infinite plane. This is accomplished by introducing two sets of bonded half-plane solutions with different elastic modulus sets (E_2, E_3) and (E_1, E_2), and subtracting a supplementary infinite domain solution, as shown in Figure A2.3.3. The complete solution can be written as:

$$u_i = (u_i)_{[A]} + (u_i)_{[B]} - (u_i)_{[C]}$$

$$\sigma_{ij} = (\sigma_{ij})_{[A]} + (\sigma_{ij})_{[B]} - (\sigma_{ij})_{[C]} \qquad \text{(A2.3.8)}$$

For each layer, the solution can be expressed in more detail as:

(1) Layer 1 ($y > H$)

$$u_i^{[1]} = (u_i)_{[AU]} + (u_i)_{[BU]} - (u_i)_{[C]}$$

$$\sigma_{ij}^{[1]} = (\sigma_{ij})_{[AU]} + (\sigma_{ij})_{[BU]} - (\sigma_{ij})_{[C]} \qquad \text{(A2.3.9)}$$

(2) Layer 2 ($H \geq y \geq 0$)

$$u_i^{[2]} = (u_i)_{[AU]} + (u_i)_{[BL]} - (u_i)_{[C]}$$

$$\sigma_{ij}^{[2]} = (\sigma_{ij})_{[AU]} + (\sigma_{ij})_{[BL]} - (\sigma_{ij})_{[C]} \qquad \text{(A2.3.10)}$$

(3) Layer 3 ($y < 0$)

$$u_i^{[3]} = (u_i)_{[AL]} + (u_i)_{[BL]} - (u_i)_{[C]}$$

$$\sigma_{ij}^{[3]} = (\sigma_{ij})_{[AL]} + (\sigma_{ij})_{[BL]} - (\sigma_{ij})_{[C]} \qquad \text{(A2.3.11)}$$

where subscript [A] represents the bonded half-planes with parameters (E_2, ν_2) and (E_3, ν_3), [B] represents the bonded half-planes with parameters (E_1, ν_1) and (E_2, ν_2), and [C] represents the infinite plane with parameters (E_2, ν_2). The additional subscripts U and L represent the solutions for upper and lower half-planes, as the bonded half-planes solutions are different for the upper and lower half-planes.

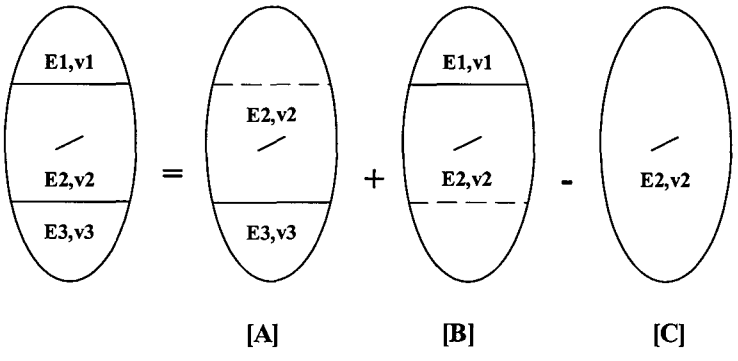

Figure A2.3.3 The superposition scheme to obtain the solutions for a three-layered media.

A2.3.5 References

Crouch, S.L. and Starfield, A.M. 1983. *Boundary Element Methods in Solid Mechanics.* Allen & Unwin, London.

Fang, Y.C. 1965. *Foundation of Solid Mechanics.* Englewood Cliffs, New York.

Salamon, M.D.G. 1963. Elastic analysis of displacements and stresses induced by mining of seam or reef deposits, Part I. *J. S. Afr. Inst. Min. Metall.,* 64, 128-149.

Appendix 4.1

Fracture growth in numerical and physical models

A4.1.1 Introduction

The objective of the work presented in this Appendix was to calibrate and validate DIGS using results obtained from laboratory tests. This section gives additional results not covered in Section 4.4.1. As mentioned previously, these well-controlled physical tests allow extensive studies of the mechanism of fracture formation in brittle rock. This verification process is essential before embarking on the analysis of fracturing around underground excavations where qualitative data relating the boundary conditions to the fracture pattern is difficult to obtain. The physical experiments were conducted using cubic blocks of rock containing tabular slots to represent a stope (see Figure 4.4.1.1). The models were prepared from Elsburg quartzite, Black Reef quartzite and norite and the properties of these rock types were already given in Table 4.4.1.1.

A description of the biaxial test rig developed for the laboratory experiments is given in Section 4.3 of the main report. A standard sequence was used for the tests: The MTS actuator piston applied the vertical stress to the specimens. Two independent confining stresses were applied via pistons embedded in the biaxial cell. A centrifugal pump drove the pistons and the pressure was controlled manually using two valves. As a first step, the samples were confined triaxially to a pressure of 27 MPa. Once this was achieved, the valves on the cell were closed. This resulted in increasing confinement as the sample deformed in the horizontal direction. Vertical loading continued at a rate of 0,005 mm/s until a vertical pressure of 80 MPa was reached. This stress conditon was maintained for approximately 5 minutes after which the vertical stress was slowly reduced to 27 MPa. Both vertical and horizontal stresses were then reduced to zero. To simulate incremental mining of the stope, the specimen was removed from the cell, the slot was extended by 1 mm and the process repeated.

A4.1.2 Results

A total of 25 laboratory tests with a corresponding DIGS model for each were performed. These tests can be grouped under four major categories:

- Effect of closure
- Mining steps in a solid block
- Mining steps in the presence of a natural discontinuity
- Mining steps in the presence of pre-defined parting planes

A summary of the tests conducted is given in Table A4.1.1.

Table A4.1.1 Summary of the different tests conducted.

Step, Specimen, stoping width (mm)	Vertical Load (MPa)	Confinement (MPa)		Closure from face (mm)		Stress/Strain ratio at maximum load (GPa)
		Initial	Final	Lab. test	Num mod.	
Effect of Closure						
1, EQ, 0,2	384	27,00		7	7.58	35
1, EQ, 2,0	160	27,00		None	None	16
1, EQ, 3,0	115	27,00		None	None	17
Mining steps in a solid block						
1, EQ, 0,5	261	27,00		14	8	27
2, EQ, 0,5	260	27,00		14	9	26
3, EQ, 0,5	262	27,00		15	7	24
4, EQ, 0,5	257	27,00		16	7	23
5, EQ, 0,5	264	27,00		14	8	22.5
6, EQ, 0,5	267	27,00		14	9	23.2
7, EQ, 0,5	260	27,00		14	9	22
Mining steps with a natural discontinuity						
1, EQ, 0,5	100	27,00		22	12	32
2, EQ, 0,5	80	27.00	28.13	23	13	30
3, EQ, 0,5	80	27.65	28.28	23	11	30
4, EQ, 0,5	80	27.60	28.30	24	12	19
5, EQ, 0,5	80	27.68	28.40	25	13	17
6, EQ, 0,5	80	27.16	27.81	23	13	16
7, EQ, 0,5	80	27,00		25	14	15
8, EQ, 0,5	80	25.87	28.14	22	15	15.5
9, EQ, 0,5	80	27.49	28.24	22	15	14.6
10, EQ, 0,5	80	27		24		15
Mining steps with cut parting planes						
1,BRQ, 2x0.25	80	27.16	27.05	None	8	17
2,BRQ, 2x0.25	100	27.32	27.22	None	9	30
3,BRQ, 2x0.25	100	26.78	26.68	None	9	19
4,BRQ, 2x0.25	100	28.08	27.49	None	8	20
5,BRQ, 2x0.25	120	26.46	25.81	None	9	22

A4.1.2.1 Effect of Closure

These tests were performed to study the effect of closure of the slot on the fracture patterns occurring around the face area. Three tests were carried out on specimens having slot widths of 0,2 mm, 2 mm and 3 mm.

The specimen with a 0,2 mm slot width was loaded up to 384 MPa and total closure was observed in the slot 7 mm from the face. For the cases of 2 mm and 3 mm slot widths, total closure was not observed. Similar results were obtained from DIGS numerical modelling in that the 0,2 mm slot closed up to 7 mm from the face, while total closure did not occur in the 2 mm and 3 mm slot width models as shown in Figure A4.1.1. Based on these observations, the slot width was kept at 0,5 mm to ensure that closure occurred in the slot for the remainder of the experiments.

The fracture patterns observed from testing and modelling are compared in Figure A4.1.2. As seen, the tests with total closure resulted in fractures forming ahead of the slot. In the case where total closure did not occur, the fracturing formed behind the face of the slot. The fracture patterns produced by DIGS were observed to be dependent on the location of seed points and

the type of failure criterion used. The fracturing resulting from the extension failure criterion tends to grow behind the face of the slot while shear fractures develop ahead of the slot. Closure in the slot limits the extent of extension fracturing and also causes shear fractures with a shallower angle than for the case with no closure.

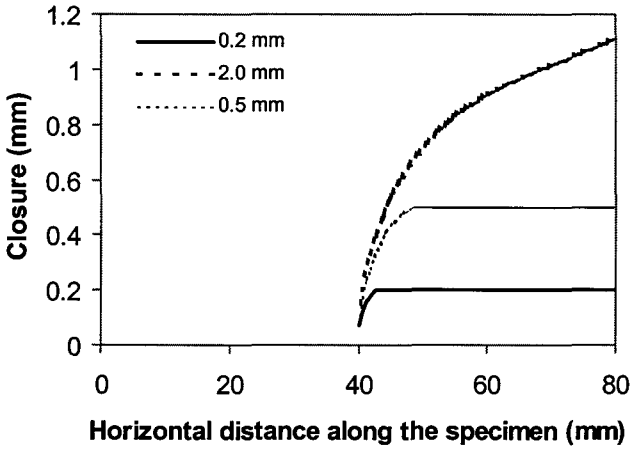

Figure A4.1.1 Simulated closure of the slot as modelled with DIGS.

A4.1.2.2 Mining steps in a solid block

For these tests, the specimens were also prepared from Elsburg quartzite. Mining steps were simulated by extending the length of the slot by about one millimetre after each test. A total of seven increments were mined and the resulting fracture patterns and the extent of the closed area in the slot were recorded for each of the increments. For the DIGS modelling, the fracture seed points were positioned close to the slot where the fracturing was expected to occur. The shear growth rule was specified on each crack with an initial cohesion of 35 MPa, initial friction angle of 35°, dilation angle of 5° , no residual cohesion, a residual friction angle of 32°, and a tensile cut-off of 5 MPa. A termination rule is specified so that the growth of a fracture would be terminated on intersection with other fractures.

Figures A4.1.3 and A4.1.4 summarize the results from this series of testing. In both the physical and the numerical models, the fractures, which form in the first step, extended ahead of the face and grew towards the outer boundary. Subsequent steps in both the physical experiment and the numerical simulation resulted in secondary fractures, in much the same direction as the initial fracture. Figure A4.1.4 shows the fracture patterns observed from modelling and testing after the last mining step. The orientation and length of fractures show overall similarities in both cases, although more damage at grain size level is prevalent in the physical model. Also, in the physical model, the major fractures were observed to consist of sets of small en echelon fractures. These en echelon fractures would indicate that the mode of failure was shear fracture (Kranz, 1983; Lockner et al. 1992). This indicates that the shear criterion used in the numerical solution is probably valid for modelling shear fractures in the quartzite rock.

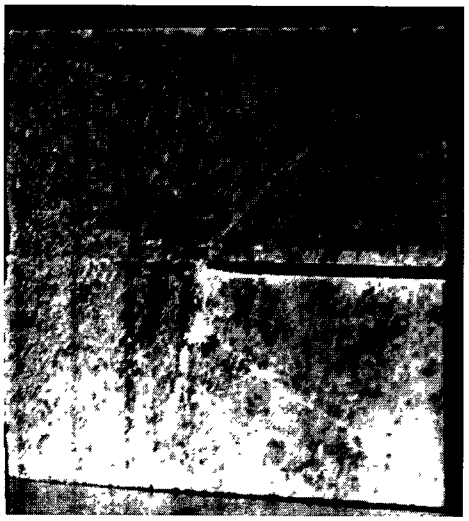

Without total closure (slot width = 2 mm)

With total closure (slot width = 0.2 mm)

Experimental results.

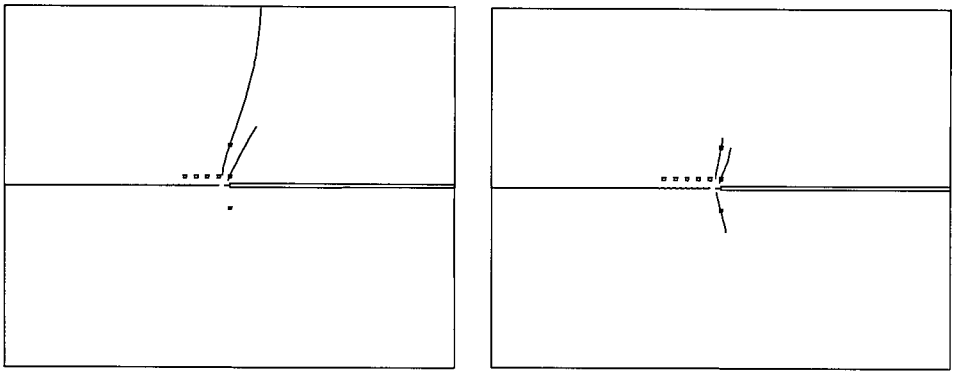

DIGS – Extension failure criterion.

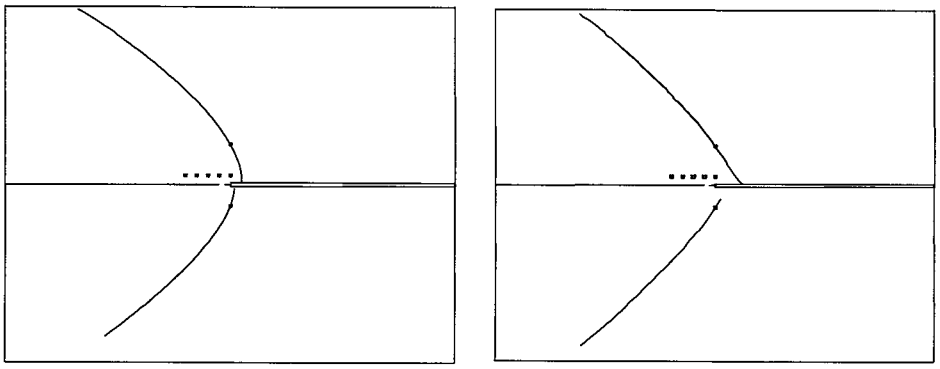

DIGS – Shear failure criterion.

Figure A4.1.2 Results of the stoping width experiments.

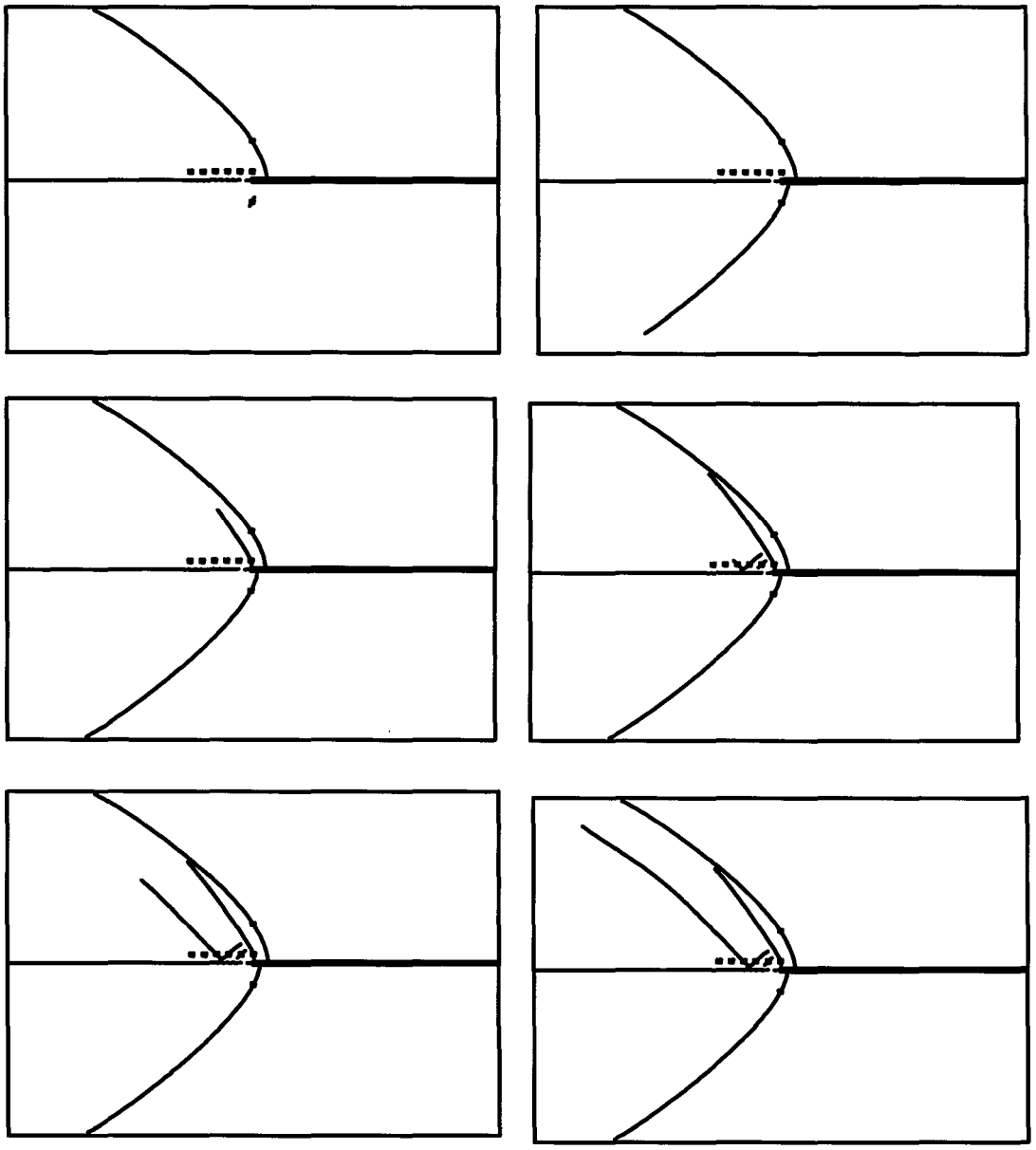

Figure A4.1.3 Fracture patterns around a slot obtained from DIGS modelling.

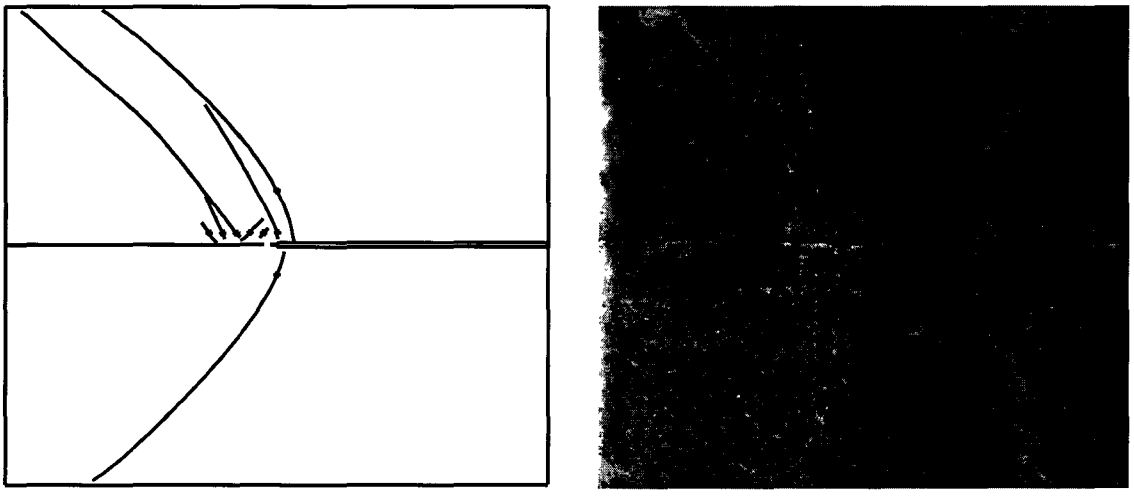

Figure A4.1.4 Comparison of solid block experiments at the seventh mining step.

A4.1.2.3 Mining steps with a natural discontinuity

In this test, the model prepared from Elsburg quartzite contained a natural discontinuity in the top block for the objective of investigating the influence of a pre-existing discontinuity on the fracture pattern around the slot. The top block was machined with an existing discontinuity at an angle to the slot. The discontinuity consisted of a welded joint with quartz infilling and was angled so that it passed through the centre point of one side of the sample. The test involved sequential extension of the slot towards the discontinuity.

The fracture patterns obtained after the last mining step from the numerical and physical modelling experiments are shown in Figure A4.1.5. For numerical modelling, two analyses were required to investigate the effect of discontinuities because of the different distances between the slot and the angled discontinuity on different sides of the sample. The numerical modelling results of the individual steps for the two different cases are presented in Figures A4.1.6 and A4.1.7.

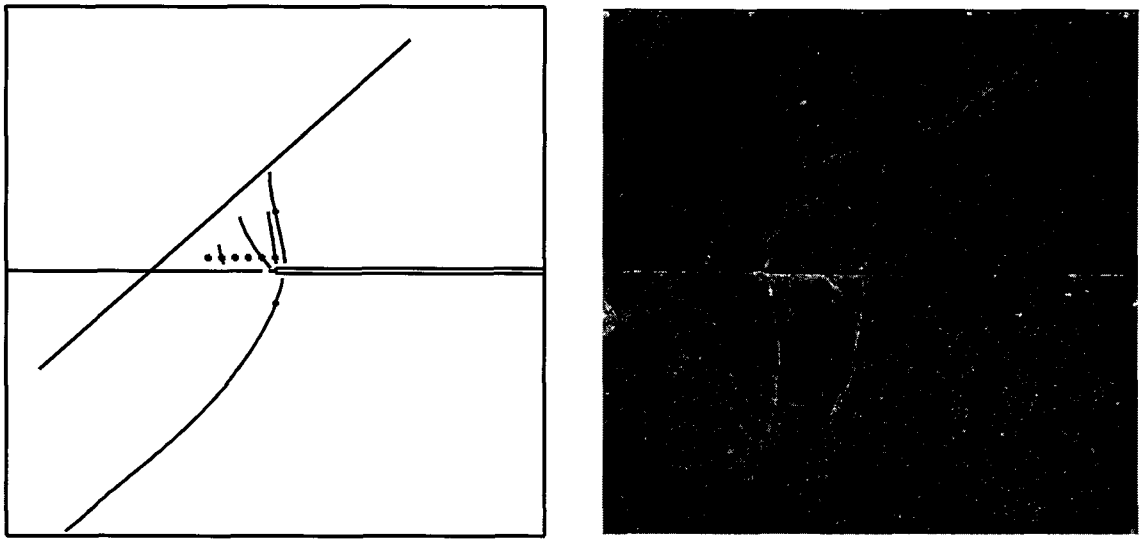

Figure A4.1.5 Final fracture patterns observed from numerical and physical modelling of the block with a natural discontinuity (on the side of the specimen where the discontinuity was furthest from the slot).

The physical and numerical models show similar fracture patterns. In all cases, a footwall fracture extends ahead of the face in the first step, as was observed in the case without a discontinuity. A difference in the fracture pattern is apparent in the hangingwall block. The initial fracture was formed in much the same way as the homogeneous sample and terminated at the discontinuity. The fracture terminating at the point of intersection between the fracture and the discontinuity suggests that either the quartz infilling of the joint was too tough to fracture, or that the deformation was accommodated by activation of the discontinuity. The tested samples showed evidence that the discontinuity had been activated.

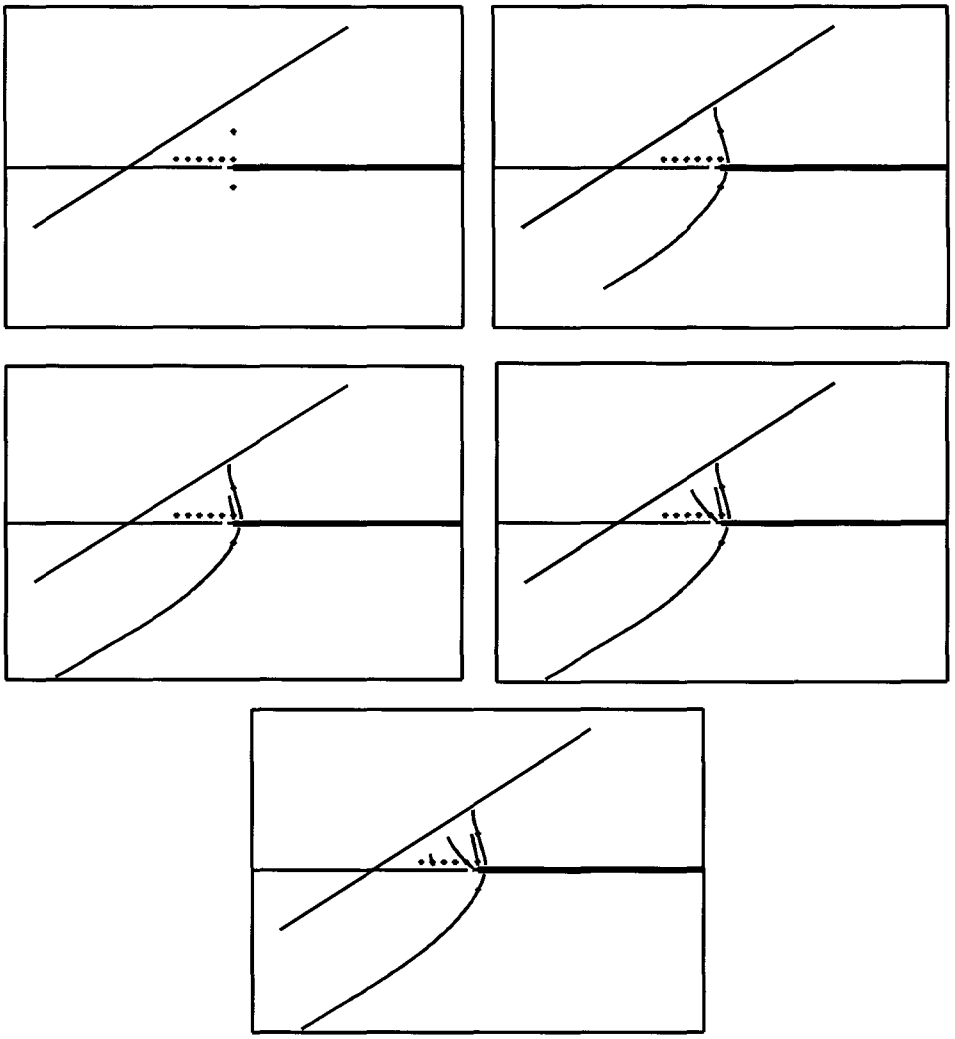

Figure A4.1.6 Results from the numerical modelling of the sample with a natural discontinuity (on the side of the block where the discontinuity was far from the slot).

On the side of the block where the discontinuity intersects the slot, subsequent steps in the experiment showed little fracturing occurring in either the footwall or the hangingwall. In the numerical solution, (see Figure A4.1.7), a single fracture extended to the discontinuity, and continued mining induced no further fracturing. On the other side of the block (see Figure A4.1.6), smaller fractures extended in the same direction as the initial fracture, increasing in length with each mining step. The eighth mining step produced an extended fracture in the footwall, and no fracturing in the hangingwall. Finally, in the tenth step, one fracture extended from the corner of the slot to the discontinuity in the hangingwall, and another grew in the footwall towards the large fracture formed in the previous step. These results suggest that the deformation will occur preferentially on the largest existing weakness (e.g. fracture or discontinuity), until the stress state has been altered sufficiently to require the formation of new fractures.

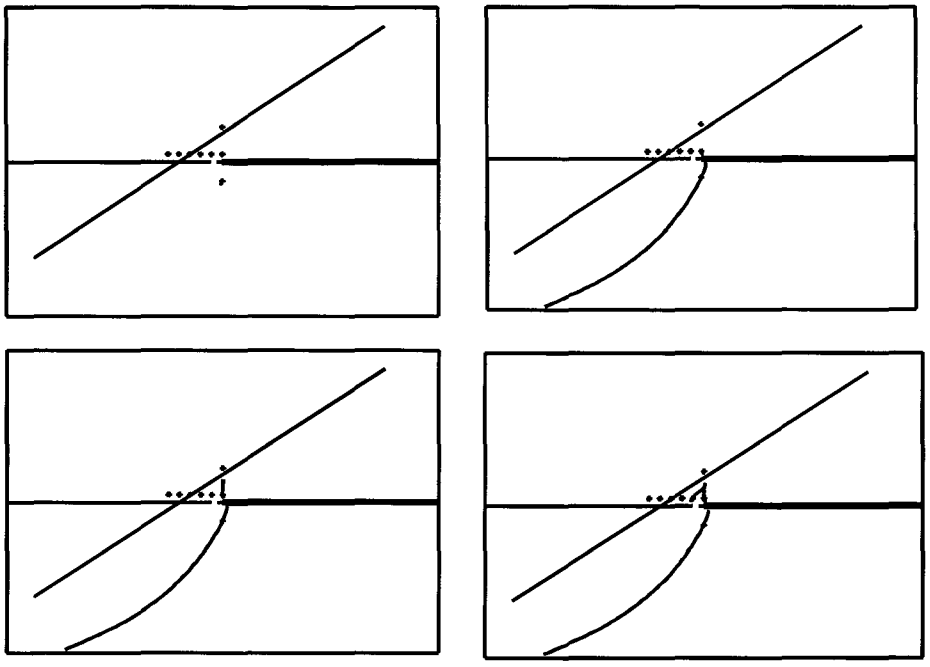

Figure A4.1.7 Results from the numerical modelling of the sample with a natural discontinuity (on the side of the block where the discontinuity was close to the slot).

A4.1.2.4 Mining steps with pre-defined parting planes

In this series, the sample contained two prepared parting planes located at the mid-height of the top and bottom blocks as shown in Figure A4.1.8. To ensure horizontal symmetry, the slot was machined in both the top and bottom blocks to a depth of 0,25 mm to give a total slot width of 0,5 mm. A specimen without any parting planes was also prepared and tested for comparison.

The specimens were prepared from Black Reef quartzite. The parting plane specimen consisted of four 20 mm thick blocks. The friction angle on each interface was measured as 26°.

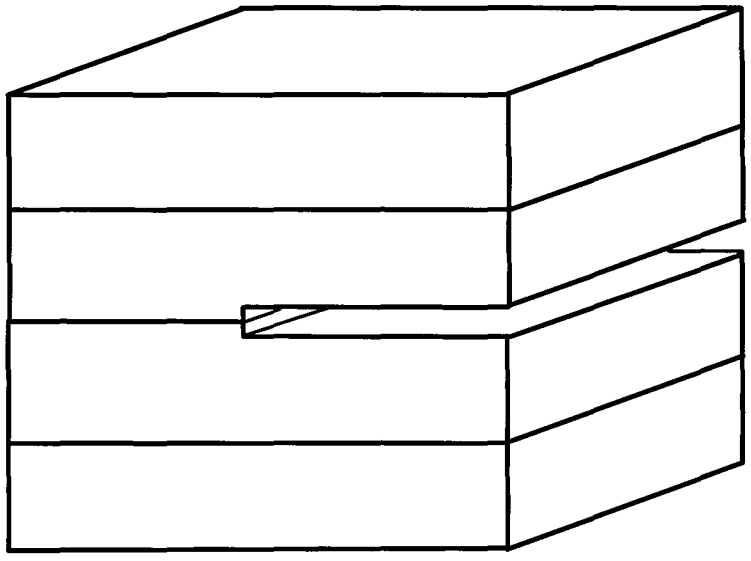

Figure A4.1.8 A schematic diagram of the parting plane specimen.

Figure A4.1.9a shows the located AE events in the sample without parting planes. The events are clustered in the same regions as the observed fractures. The events in the centre of the sample correspond to the fractures, which curve into the hangingwall from the edge of the slot. The vertical fractures ahead of the slot, in the hangingwall and footwall are also evident. A cluster of events at the edge of the sample corresponds to the small horizontal fracture in the hangingwall.

Two steps were mined with the sample containing parting planes and, in each step, the positions of the AE events correspond closely to the cracks observed (Figure 4.1.9.b). It is interesting to note that there is not any significant AE activity concentrated on the parting planes. In the first step, the vertical cracking is evident in the two footwall blocks, ahead of the slot. There is less AE activity in the immediate hangingwall block, and the located events correspond to the angled crack extending from the slot tip, and the small fractures which are initiated at the upper parting planes. In the top block, the events relate to the two vertical fractures ahead of the face. In the second step, the vertical fractures ahead of the slot extended through the sample and the angled cracks in the hangingwall connected the slot and the parting plane above, as shown by the AE events above the slot.

The results from numerical modelling of the parting plane case are summarized in Figure A4.1.10. A tension mode of failure was selected for the cracks with zero tensile strength and a residual friction of 20°. In Figure A4.1.10, the fractures extend behind the advancing slot. Two fractures occur in the hangingwall at angles of 70° and 79° to the slot. In the footwall, a single fracture is angled at 81° to the slot. These crack angles are very close to those predicted in the model which are 71° and 80° in the hangingwall and 74° in the footwall, as can be seen in Figure 4.1.10.b. On the parting plane in the hangingwall of the test sample, there appears to be a slight shift of the fracture from left to right of about 2 mm across the parting plane, and another fracture extends almost vertically to intersect with the boundary.

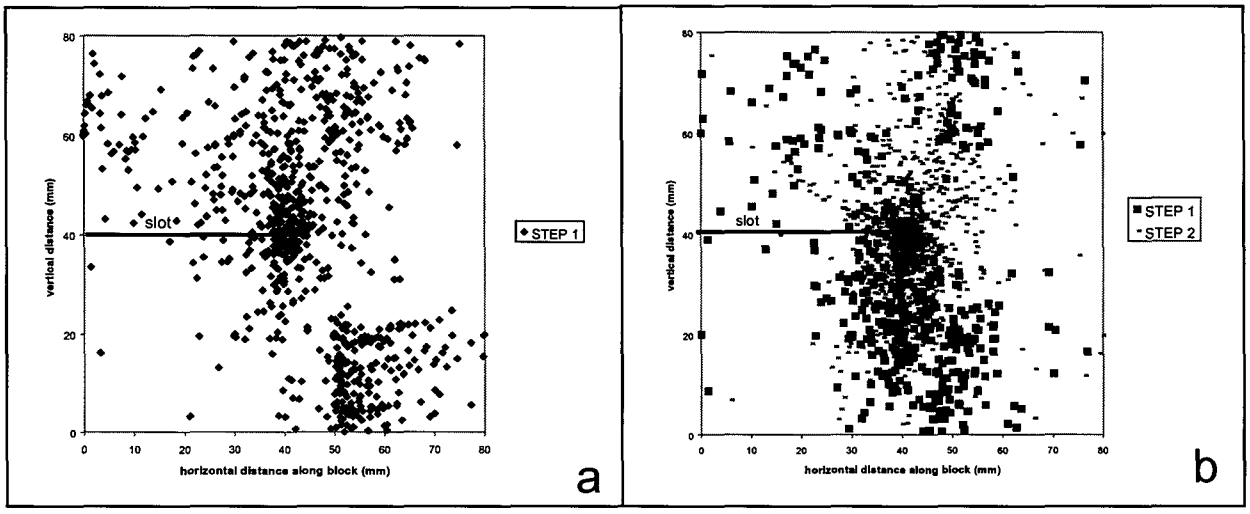

Figure A4.1.9 Locations of acoustic emissions determined in physical models using Black Reef quartzite. a: block without discontinuity, b: block with parting planes

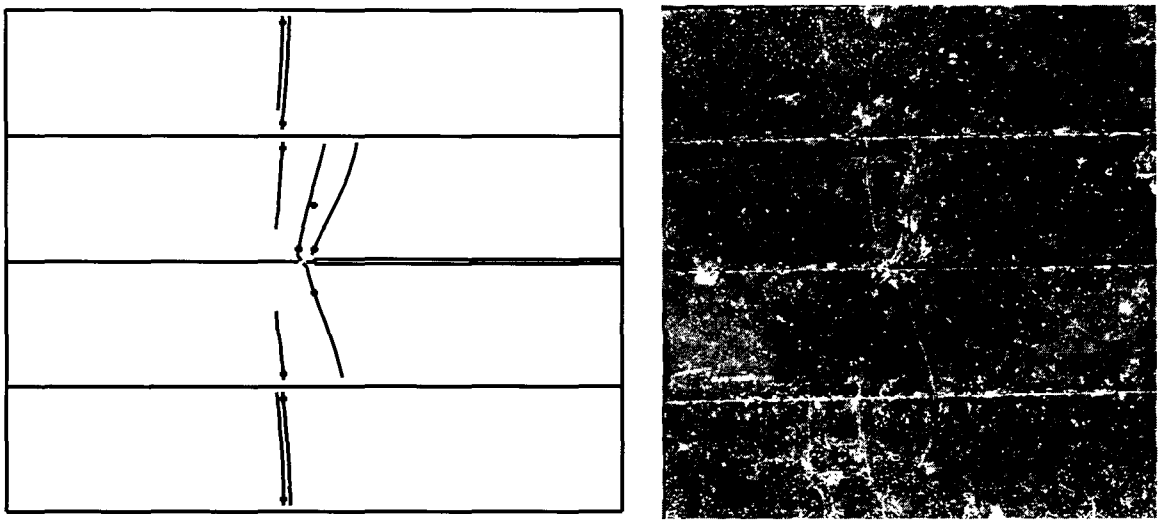

Figure A4.1.10 Comparison of the results from the numerical and physical modelling of parting planes.

The direction of fracture growth is not clear from the physical model, but comparison of the AE results (Figure A4.1.9) with the numerical modelling (Figure A4.1.11) suggests that each crack has grown downwards, one from the top boundary and the other from the parting plane. This supports the numerical modelling of Napier and Hildyard (1992), who suggest that it is the presence of parting planes that causes extension fractures to initiate above and ahead of a stope and not in the high stress region at the stope face.

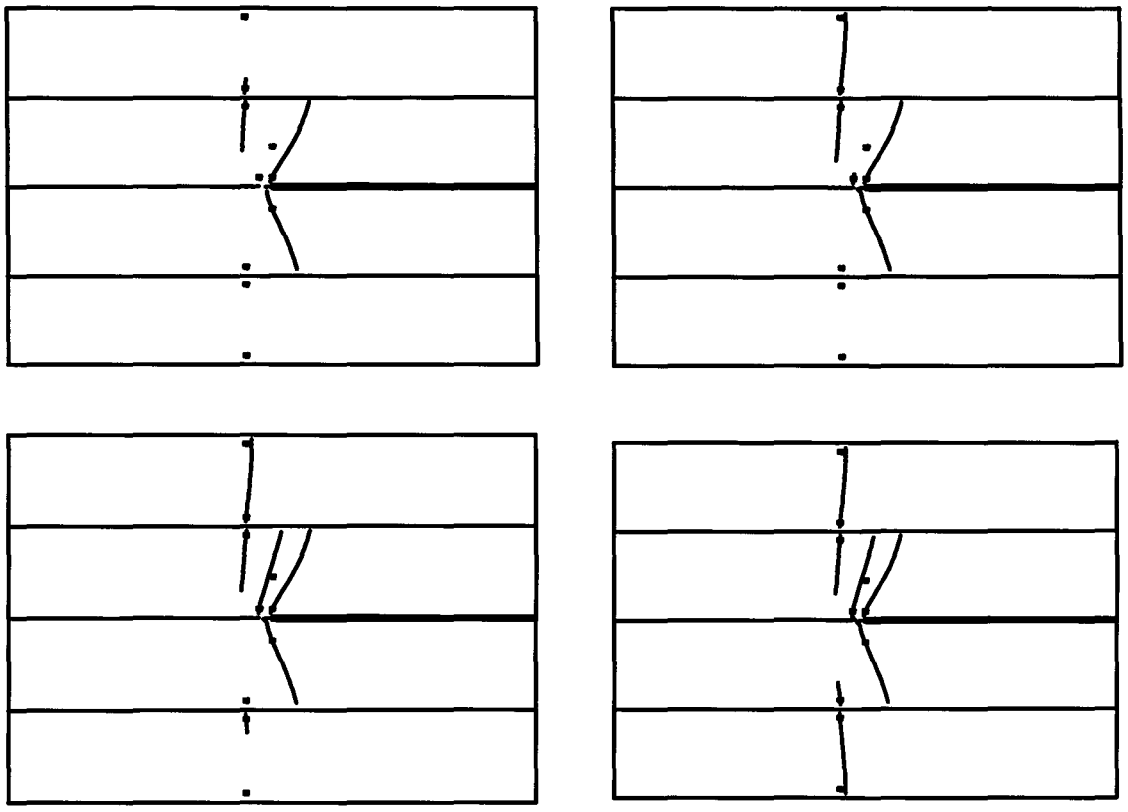

Figure A4.1.11 Numerical modelling results of the parting plane model.

A4.1.3 Summary

The resulting fracture pattern is observed to be dependent on whether or not the slot closes. When there is significant closure in the slot, the shear fractures are observed to extend ahead of the slot in the experiments. A similar dependence of the fracture pattern on slot width has also been observed in the numerical simulations. The shear failure criterion correctly predicts corresponding fractures in the numerical models. The analysis with a tensile fracture criterion correctly predicted the final fracture directions when the slot remained open.

The physical experiments demonstrate that the fracturing may occur in shear or tension depending on whether the slot is closed, or remains open respectively. The logic to decide on the appropriate fracture criterion needs further consideration.

The results of experiments on blocks of rock containing discontinuities indicate that interfaces significantly alter the position and inclination of the resulting fractures. In these experiments fractures extending from the tip of the slot are observed to terminate on the discontinuity. No fractures are evident once the slot passes through the discontinuity suggesting that the deformation is occurring on the discontinuity. Similar trends are evident in the numerical simulations.

Fractures were apparently initiated at horizontal parting planes in both the physical and numerical models, indicating that the discontinuity can alter the stress distribution within the sample, depending on the interface properties.

The observed three-dimensional acoustic emission locations provide useful information regarding the sequence of fracture growth and the growth directions, which correlate well with the numerical simulations.

The displacement discontinuity program DIGS can therefore replicate the fracture patterns in these samples, and the influence of the various interfaces. The requirement to pre-select seed point positions limits the capacity for predictive simulation of fracture growth patterns.

A4.1.4 References

Kranz, R.L. 1983. Microcracks in rocks: a review. *Tectonophysics,* vol. 100, 449-480.

Lockner, D.A., Moore D.E. & Reches, Z. 1992. Microcrack interaction leading to shear fracture. *Rock Mechanics.* Tillerson & Wawersik (eds). Balkema, Rotterdam, 807-816.

Napier, J.A.L. 1990. Modelling of fracturing near deep level gold mine excavations using a displacement discontinuity approach. *Proceedings of Conference on Mechanics of Jointed and Faulted Rock.* Vienna, Balkema, Rotterdam, 709-715.

Napier, J.A.L. & Hildyard, M.W. 1992. Simulation of fracture growth around openings in highly stressed , brittle rock. *Journal of the South African Institute of Mining and Metallurgy.* Vol. 92, 159-168.

Appendix 4.2

A comparison between random mesh schemes and explicit growth rules for rock fracture simulation

A4.2.1 Introduction

A central theme in this study is the modelling of failure processes in brittle rock. It is generally found that tensile failure in brittle homogeneous materials such as PMMA or glass can be modelled by explicit representations of crack paths using incrementally modified finite element meshes (Swenson & Ingraffea, 1987) or by displacement discontinuity methods (Thomas & Pollard, 1993, Napier, 1990). In two-dimensional problems in which the crack speed is much slower than the Rayleigh wave speed, these approaches are able to mimic observed fracture patterns with some success. A much more difficult problem arises in the modelling of splitting fractures or the formation of shear bands in granular materials such as concrete or rock. Failure patterns are observed to occur as intricate hierarchical structures over a wide range of scales. In these cases, it is also apparent that the micro-fabric of the rock can play a role in controlling the detailed coalescence patterns. Unfortunately, in mine design applications it is generally the characteristics of the failed material that are of the greatest concern in the design of support systems for the excavations.

The difficulty in modelling the failure processes in brittle materials is consequently associated with making a suitable choice of building block which can be used to synthesize large scale patterns of failure. In the case of a continuum plasticity formulation it is necessary to postulate the flow rule for the basic continuum element and to calibrate the details of the flow rule parameters against suitable laboratory tests. An alternative approach is to assume that the fundamental composition of the rock fabric is in the form of interacting particles (Cundall, 1989; Handley, 1996) or some generalised cellular structure, Wilson et. al.(1996). This appendix describes an approach in which the basic failure mechanism is assumed to be a sliding crack. Failure is then modelled by tracking the successive mobilization of a random assembly of such cracks. The specific case where the cracks are associated with the arcs of a Delaunay triangulation is investigated. The model is applied to the problem of a rectangular strip punch which is pressed onto the surface of a laterally confined cubic block of Witwatersrand quartzite. The effect of allowing the cracks to initiate sequentially or simultaneously is investigated and the results are compared to the experimentally observed fracture patterns. The possibility of formulating a macro shear fracture growth rule that is equivalent to the detailed coalescence processes is examined.

A4.2.2 Explicit fracture modelling using a Delaunay tessellation

Previous numerical investigations carried out by Napier & Peirce (1995) and by Napier & Kuijpers (1995) have shown that in simple rectangular shaped samples that are uniformly loaded or displaced on opposite edges, it is possible to reproduce many of the important characteristics of brittle rock failure if the region of interest is covered by a Delaunay triangulation and if failure is limited to the defining arcs of the mesh. In particular, it has been demonstrated that rapid load shedding occurs once failure is initiated with accompanying dilation of the sample. More importantly, the localization of failure appeared to be controlled by the sequence in which cracks were permitted to fail. If fracturing was allowed to initiate simultaneously at all potential sites, failure was distributed in non-localized patterns throughout the sample. If failure was controlled by selecting each crack element in turn, according to a

given ranking of its likelihood of failure, it was found that in a sample with no lateral confinement a splitting fracture was formed parallel to the loading direction. When confinement was applied to the sample, failure tended to form in a band structure diagonally across the sample. Similar effects have also been reproduced by Sellers & Napier (1997) where an initial population of weak flaws is present and where fractures are distinguished as being either on the boundaries of grains or as being within grains.

The question arises, however, as to the applicability of the Delaunay tessellation when modelling fracturing in circumstances where the stress field is rapidly varying as is the case near the edge of a mining excavation or in the vicinity of a stabilizing pillar. Sellers (1997) has performed a number of simulations of fracturing near tabular shaped openings in layered and unlayered strata, using Delaunay tessellations to represent the fracture paths. In the cases studied, an encouraging qualitative agreement has been obtained between modelled and observed fracture patterns. A more quantitative test for the approach is afforded by experiments that were carried out by Dede (1996) to examine the pattern of fracturing induced below a rigid rectangular punch pressed onto the surface of a cubic rock sample.

A special purpose Delaunay mesh generation program has been written to prepare the problem data files. In order to generate a mesh, the overall region of interest is bounded by a series of straight line segments forming a closed polygon. Random points or centres are generated within the region at a specified minimum spacing. In addition, a pad distance is defined to prevent the points being placed too close to the boundary segments. The mesh generation proceeds by defining an internal seed triangle and by successively adding triangles to each edge of the seed triangle. In this respect the successive triangles are selected according to the Delaunay property that the circumscribed circle around each triangle should not contain any random centres other than those defining the vertices of the triangle. Adjacent to the defined region boundaries this condition is relaxed to allow the triangular mesh to include each boundary segment. It is important to define each boundary segment to have a length that is of the order of the minimum spacing between each random centre. Extended straight line boundaries are thus made up of a number of aligned segments having the required minimum length. In general, internal boundaries may also be defined to create openings or approximately circular holes. This simple form of mesh generation is found to be effective for relatively small scale problems but is obviously much cruder than the refined techniques used in finite element analyses.

A4.2.3 Experimental procedure

A test rig comprising a circular steel ring was constructed to allow a cubic shaped rock sample to be confined laterally on four sides and to be supported on a rigid base. A cubic shaped sample was prepared with a raised strip milled across the centre of the top face as shown in Figure A4.2.1. Samples were prepared from Witwatersrand Elsburg quartzite and the vertical sides of the sample were coated with stearic acid as a friction reducing agent.

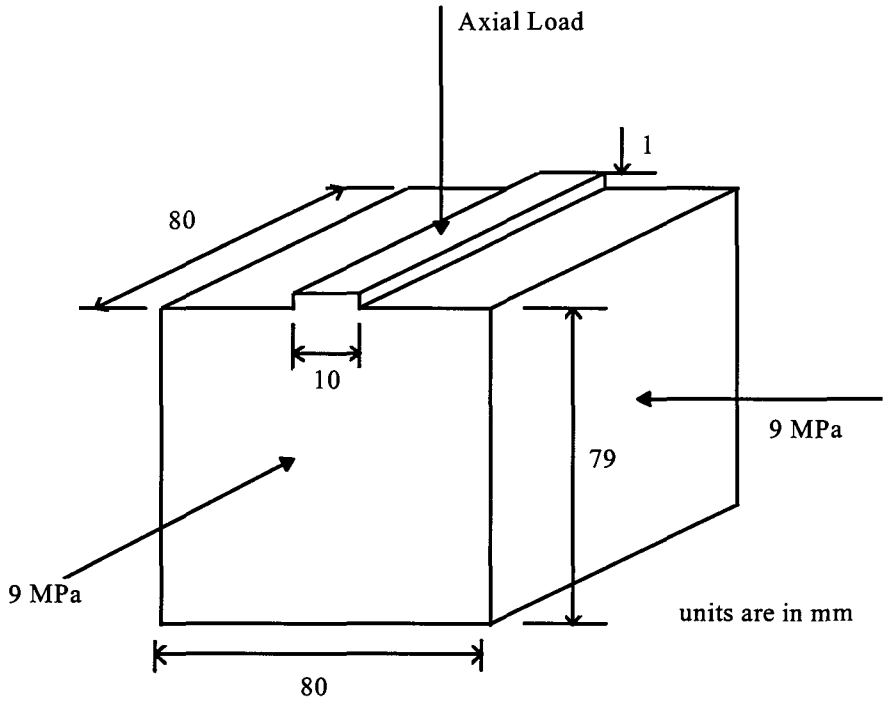

Figure 4.2.1 Dimensions of strip punch test specimen.

The sample was placed in the test rig and a rectangular shaped platen was then pressed onto the raised strip across the centre of the sample.

The axial load on the punch was increased in a series of loading steps while adjusting the lateral confinement up to a maximum level of 9 MPa. The axial load was then increased further while maintaining the confining stress at 9 MPa. The axial deformation of the punch was monitored. A typical load-displacement curve is shown in Figure A4.2.2.

The sample was observed to fail at a nominal stress of about 500 MPa beneath the loading punch. Several tests were also conducted with the loading halted at an intermediate level before the final failure. Following each test, the sample was removed from the rig and the fracture pattern formed beneath the punch was photographed and mapped. Figures A4.2.3a and A4.2.3b show the pattern of fracturing developed at an intermediate and at the ultimate stage of loading of two different samples. It can be seen that an intact wedge shaped region forms below the punch and that a tensile splitting fracture is formed below the wedge. The tensile fracture ultimately intersects the lower boundary of the sample.

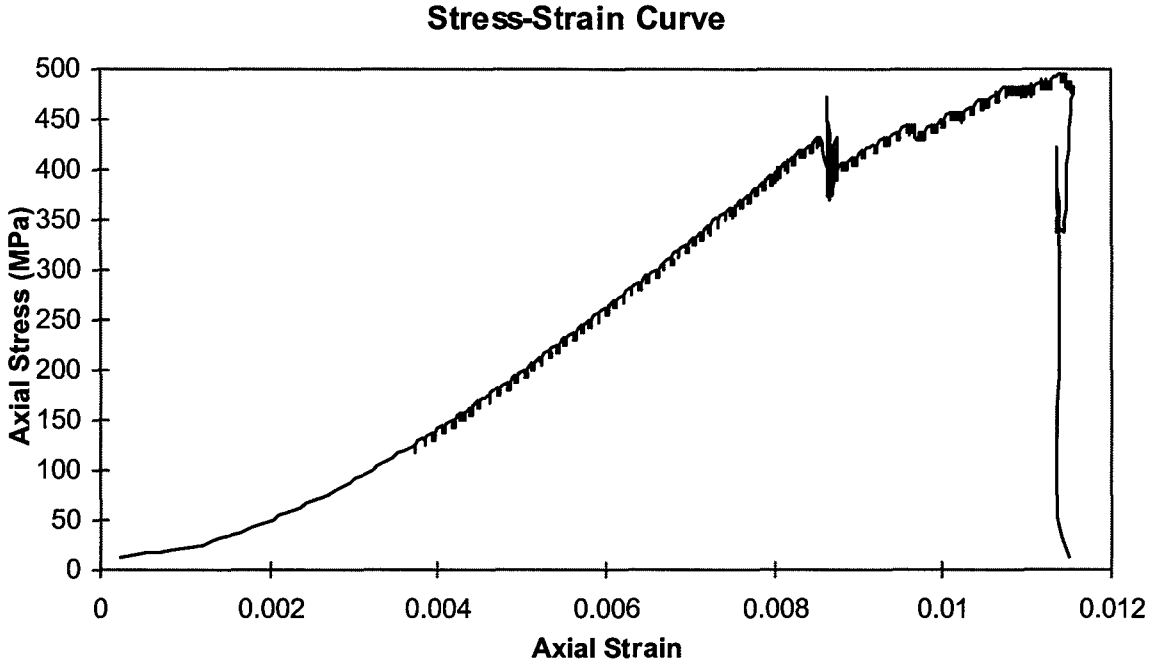

Figure A4.2.2 Typical axial stress strain curve observed in punch loading test.

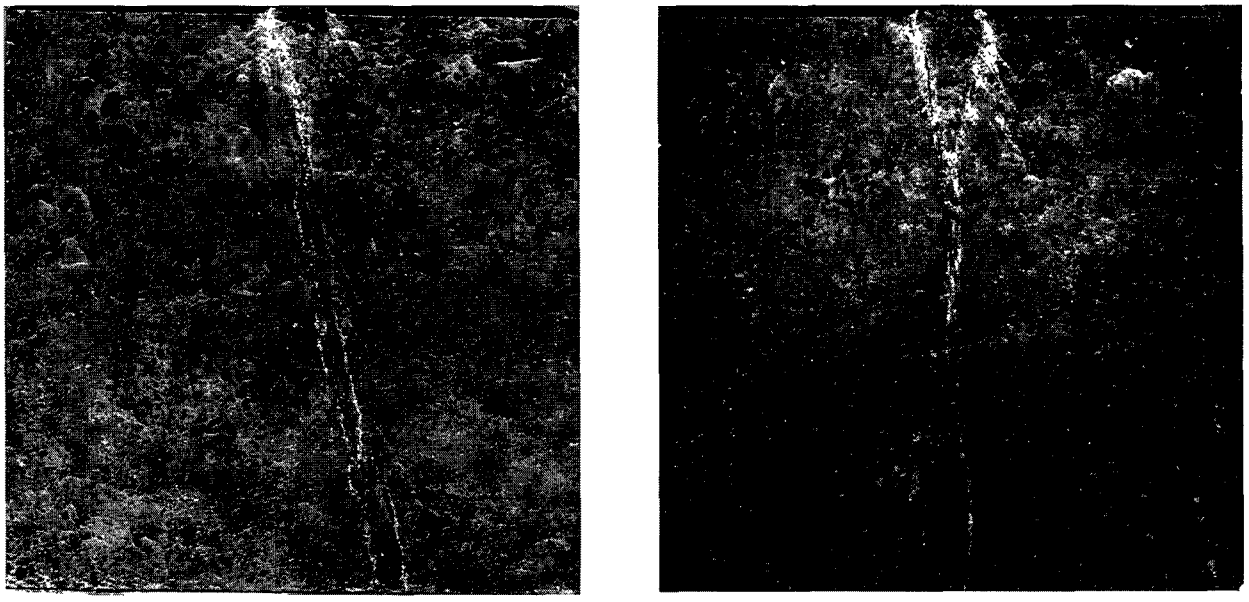

(a) (b)

Figure A4.2.3 a) Damage pattern below punch at intermediate load b) Damage pattern at ultimate load.

A4.2.4 Numerical simulations

The cubic sample profile described in the previous section was modelled with a rectangular boundary comprising 320 displacement discontinuity boundary elements. The edge below the

loading platen comprised ten elements. This edge was displaced uniformly in a series of eight loading steps such that the final displacement yielded an average stress of approximately 500 MPa below the loading platen. A sub-region of the sample, 30 mm wide and nominally 80 mm high, was selected below the loading platen and filled with a random mesh of Delaunay triangles generated from approximately 1500 random centres in the region. This resulted in a tessellation comprising 4444 segments with a total length of 6257,8 mm. The statistics of the mesh segments are given in Table A4.2.1.

Table A4.2.1 Class interval and other statistics of segments comprising the tessellation used in the punch loading problem.

Size interval (mm)	0,0-0,4	0,6	0,8	1,0	1,2	1,4	1,6	1,8	2,0	2,2	2,4	2,6	2,8	3,0
Number of Segments	0	0	18	508	898	902	847	664	367	181	44	13	2	0

minimum length = 0,72 mm

mean length = 1,41 mm

maximum length = 2,73 mm

standard deviation = 0,34 mm

The mobilization of each element is controlled by a bilinear Mohr-Coulomb failure criterion depending on two functions F_1 and F_2 defined by

$$F_1 = |\tau| - \tan\phi\sigma_n - S_o \qquad \text{(A4.2.1)}$$

$$F_2 = -\sigma_n - T_c \qquad \text{(A4.2.2)}$$

where τ is the shear stress and σ_n is the normal stress acting across the crack (compressive stress positive). ϕ is the angle of friction prior to crack mobilization and S_o is the unmobilized cohesion. T_c is the absolute strength of the crack if tensile stresses are applied across the crack in the normal direction. Failure is assumed to occur if either $F_1 \geq 0$ or $F_2 \geq 0$. Once failure has occurred, the crack is allowed to open or to slide to satisfy the equilibrium condition

$$|\tau^*| = \tan\phi_m\sigma_n^* + S_m \qquad \text{(A4.2.3)}$$

where τ^* and σ_n^* are the mobilized shear and normal stresses respectively. ϕ_m is the mobilized friction angle and S_m is the mobilized cohesion. If the crack opens in tension, Equation (A4.2.3) is replaced by the condition $\tau^* = 0$ and $\sigma_n^* = 0$.

Within each loading step, particular collocation points are examined on each edge of the random array of triangles defined by the tessellation structure. Following this scan, a selection is made of those segments which are to be mobilized according to two growth strategies. In the parallel strategy (designated as P) all segments which satisfy the mobilization condition $F_1 \geq 0$ or $F_2 \geq 0$ are selected and the problem is re-solved with these elements interacting with one another. This procedure is continued for a specified number of growth steps or until no further segments are selected. In the incremental strategy (designated as I), all segments are again

examined but only the most over-stressed segment is chosen for mobilization. The ranking is made according to the distance in stress space of the particular points examined in each segment outside the Mohr-Coulomb envelope defined by the region $F_1 = 0$ and $F_2 = 0$. The problem is then re-solved with the single selected crack being allowed to interact with existing cracks. This procedure is again repeated for a specified number of steps or until no further cracks are selected.

A series of numerical simulations were carried out to investigate the effect of the growth strategy, P or I, and to examine the effect of the choice of the failure parameters on the fracture pattern in relation to the observed patterns shown in Figures A4.2.3a and A4.2.3b. The combinations studied are given in Table A4.2.2. The failure parameters correspond to a material having a uniaxial compressive strength of 200 MPa and a tensile strength of 25 MPa. These are representative but not exact values for the quartzite specimens described previously. The Young's modulus and Poisson's ratio of the intact material was assumed to be 68 GPa and 0,19 respectively.

Table A4.2.2 Fracture growth simulation parameters.

Run	ϕ	S_o	ϕ_m	S_m	T_c	Growth Strategy	Figure
PUN 1A	51	35,4	30	0	25	P	A4.2.4a
PUN 1B	51	35,4	30	30	25	P	A4.2.4b
PUN 1C	51	35,4	30	0	5	P	A4.2.4c
PUN 1D	51	35,4	30	30	5	P	A4.2.4d
PUN 9	35	35,4	30	30	25	P	A4.2.4e
PUN 6	51	35,4	30	0	25	I	A4.2.5a
PUN 7	51	35,4	30	30	25	I	A4.2.5b
PUN 5	51	35,4	30	0	5	I	A4.2.5c
PUN 8	35	35,4	30	30	25	I	A4.2.5d

Consider first the series of runs where the parallel growth strategy **P** is used. Figure A4.2.4a shows the fracture pattern that results after two parallel growth steps where the residual cohesion of the mobilized cracks is zero (PUN 1A). A widely dispersed region of fracturing is observed below the punch and does not generally follow the observed patterns in Figures A4.2.3a and A4.2.3b. If the tensile strength is reduced to 5 MPa (PUN 1C) it is seen in Figure A4.2.4c that the fracture pattern becomes somewhat less dispersed as the fractures grow towards the lower boundary of the platen.

A very significant role, however, appears to be played by the level of the residual cohesion S_m (Kuijpers, 1997). The mobilization of each sliding crack in the tessellation assembly can be thought to represent the coalescence of smaller scale fracture processes into localized plastic bands or can be considered to arise from pre-existing weaknesses in the material that are favourably disposed for mobilization. Figure A4.2.4b shows the fracture pattern that occurs when the residual cohesion is 30 MPa (PUN 1B) and is a more satisfactory representation of the actual fracture patterns shown in Figures A4.2.3a and A4.2.3b If the residual cohesion is set to

30 MPa but the tension cut off is reduced to 5 MPa (PUN 1D) then a less realistic fracture pattern emerges as shown in Figure A4.2.4d where excessive tensile damage occurs in the lower half of the specimen. Finally, retaining the residual cohesion of 30 MPa and the tension cut off of 25 MPa, but reducing the initial material internal friction ϕ to 35° (PUN 9) results in the fracture pattern shown in Figure A4.2.4e. This is very similar to that of Figure A4.2.4b. These simulations suggest that the residual cohesion S_m and the tension cut off T_c are the most sensitive parameters that control the extent and localization of the failure zone.

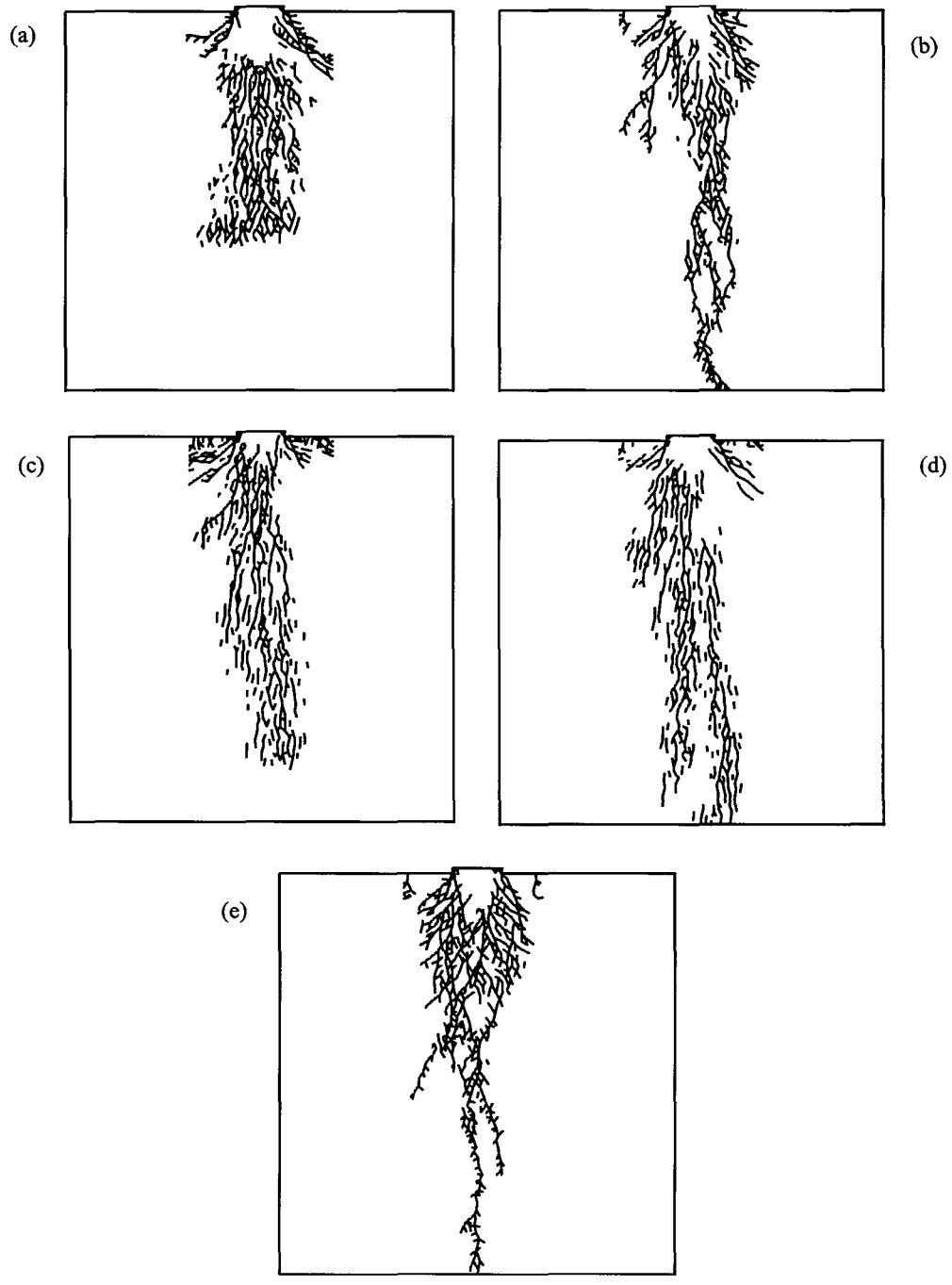

Figure A4.2.4 Fracture pattern results after parallel growth steps.

It is of some interest to consider the effect of the incremental crack growth strategy **I**. The runs PUN 1A, PUN 1B and PUN1C of Table A4.2.2, shown in Figures A4.2.4a, A4.2.4b and A4.2.4c, were repeated and are shown in Figures A4.2.5a, A4.2.5b and A4.2.5c respectively. (See

entries PUN 6, PUN 7 and PUN 5 in Table A4.2.2). If Figure A4.2.5a is contrasted to Figure A4.2.4a, it is apparent that the incremental growth mode provides a much more satisfactory representation of the true fracture pattern shown in Figures A4.2.3a and A4.2.3b even if the residual cohesion is reduced to zero. However, the very nature of the incremental growth strategy will have the effect of preventing a simultaneous loss of cohesion at many sites and can, in fact, be considered to be an indirect means of simulating cohesion and tension weakening. Figure A4.2.5b shows the case where the incremental growth strategy is followed and the residual cohesion is retained (PUN 7). The fracture pattern shows the formation of a single extension fracture in the lower part of the sample and a more intense zone of damage below the loading platen than in the case of Figure A4.2.5a (PUN 6). If the tension cut-off is reduced (PUN 5) the fracturing becomes more intense in the lower half of the sample (Figure A4.2.5c). Finally, if the initial material strength is reduced as in PUN 9, the fracture pattern of Figure A4.2.5d results (PUN 8) which should be compared to that of Figure A4.2.4.e. Figure A4.2.5d shows a generally closer correspondence to the observed fracture patterns (Figures A4.2.3.a and A4.2.3b) with the formation of a more clearly defined wedge structure below the loading platen.

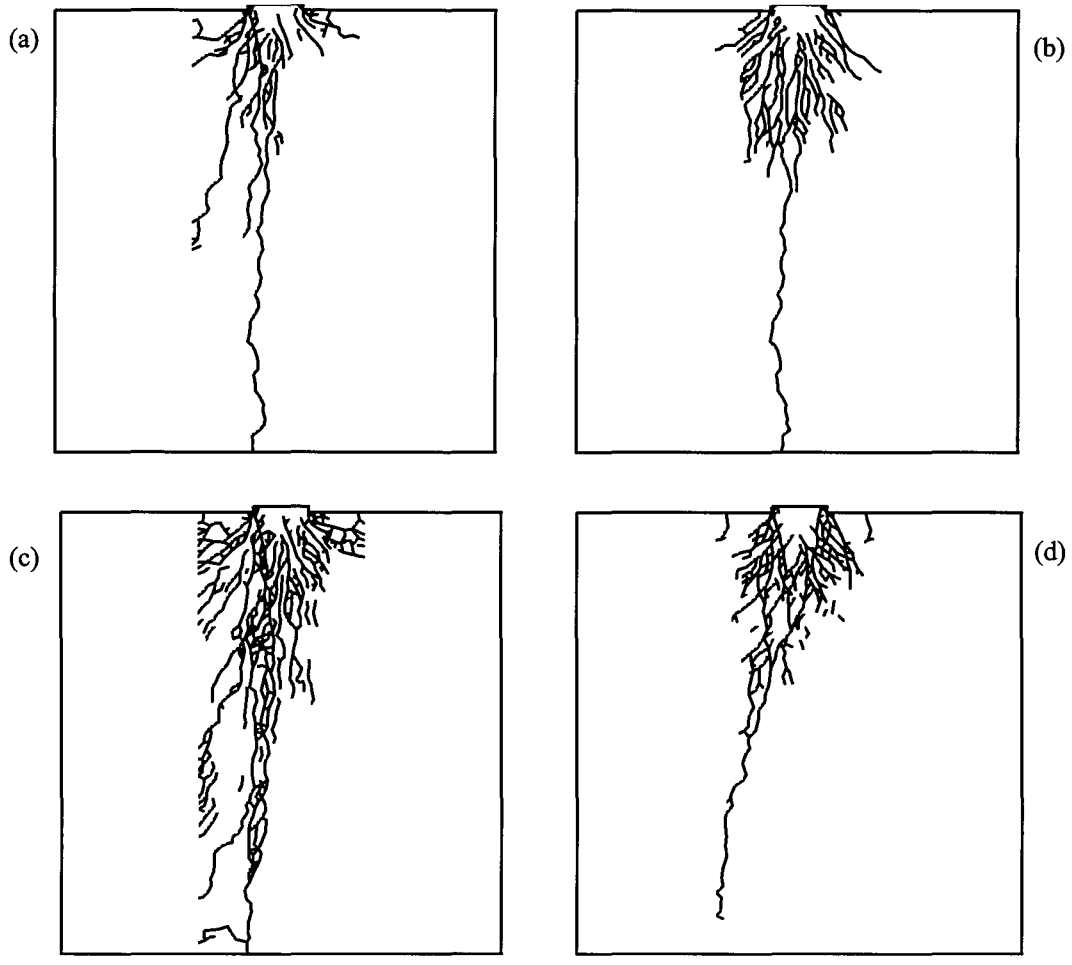

Figure A4.2.5 Fracture pattern results after incremental growth steps.

A4.2.5 Formulation of equivalent shear band models

It is apparent that the incremental growth strategy applied to a tessellation scheme can result in rather long computer run times if very dense tessellation meshes are used. It is useful to investigate whether some macro shear growth rule can be formulated which could replace this

multi-site explicit search process. One difficulty in the use of such a rule is that the initial growth point must be pre-selected. An automated choice of initiation point could require, in principle, a detailed search of the problem region and may become as time consuming as the selection of elements from a random mesh. At present, it has not been possible to deduce an equivalent shear band growth rule from the numerical simulations described previously. However, one possibility that has been investigated is to consider a growth rule in which the growth direction is chosen to maximize the strain energy release rate. Specifically, suppose that the shear band is to be extended at an angle θ relative to the current direction of the shear band. Designate the shear and normal stress components, with respect to the proposed direction as $\tau_{r\theta}$ and $\tau_{\theta\theta}$ respectively. It may then be demonstrated that the strain energy release rate G, evaluated at a fixed distance ahead of the end of the band, is given approximately by

$$G = [\tau_{r\theta}^2 - \tan^2 \phi \tau_{\theta\theta}^2] / 2K_0 \qquad \text{(A4.2.4)}$$

where K_0 is a constant related to the elastic constants of the material and to the length of the growth increment.

The results of applying Equation (A4.2.4) are illustrated in Figure A4.2.6a where two shear initiation sites are chosen at the edges of the punch. The material properties were chosen to be the same as those for run PUN1A in Table A4.2.2. It is clear from Figure A4.2.6a that no wedge structure is formed in this case. Introducing a residual cohesion of 30 MPa and reducing the intact material friction angle to 35°, yields the growth pattern shown in Figure A4.2.6b. This shows the formation of a wedge structure as well as a possible continued region of failure in the form of a slip line. As yet it is not clear whether the concept of attempting to formulate explicit shear band growth rules is physically well-founded. More detailed results of using the explicit shear band growth model are reported by Dede (1996).

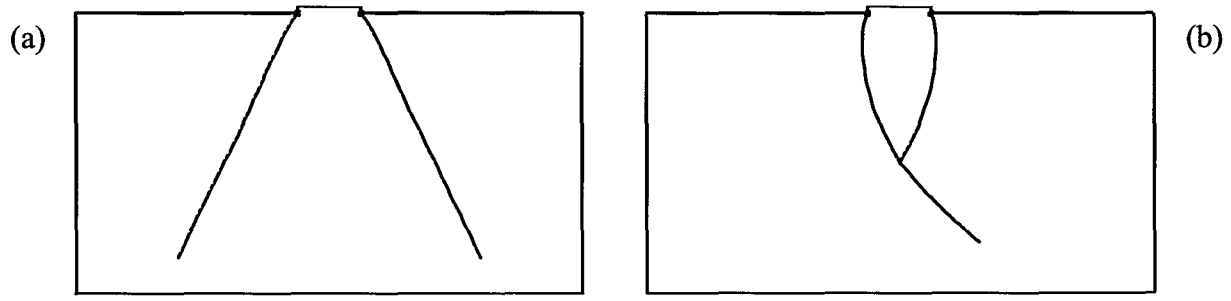

Figure A4.2.6 Fracture pattern results after incremental growth steps.

A4.2.6 Summary

Encouraging correspondence has been obtained between physical experiments and numerical simulations of fracture formation processes below a rectangular strip punch. The results suggest that some confidence can be placed in the use of a random mesh to represent complex failure processes near mine openings in hard rock. It is found that the post-failure cohesion of each activated crack in the random assembly is a particularly important parameter which controls the pattern of failure. A related concept is the use of an incremental procedure to select the sequence of crack initiation in the random mesh. The use of an incremental activation rule implies some form of weakest link breakage mechanism and can also be viewed as an alternative manifestation of general cohesion and tension weakening behaviour. In general, the residual cohesion and incremental growth rules allow a balance to be established between plastic and brittle failure modes in the material. Additional work is required to clarify the choice of cohesion and tension weakening rules in relation to particular rock types.

The use of equivalent shear band growth models has been explored in some limited studies using an energy based shear growth rule. Although this approach can be made to produce a superficial pattern of fracturing that is equivalent to the observed patterns, no direct justification of the mechanistic validity of the proposed growth rule has been established. However, it appears that in this case the effect of residual cohesion still plays a central role in controlling the equivalent shear band growth direction.

A4.2.7 References

Cundall, P.A. 1989. Numerical experiments on localization in frictional materials. *Ingenieur-Archiv*, 59, 148-159.

Dede, T. 1996. *Fracture onset and propagation in layered media.* M.Sc. Thesis, University of the Witwatersrand, Johannesburg.

Handley, M.F. 1996. The constitutive behaviour of a simple granular model as determined from numerical experiment. *Proceedings of the Second North American Rock Mechanics Symposium*, Balkema, Rotterdam.

Kuijpers, J.S. 1997. *Identification of inelastic deformation mechanisms around deep level mining stopes and their application to improvements in mine design.* Unpublished Ph.D. Thesis, University of the Witwatersrand, Johannesburg.

Napier, J.A.L. 1990. Modelling of fracturing near deep level gold mine excavations using a displacement discontinuity approach. In : H.P. Rossmanith (ed.), *Mechanics of Jointed and Faulted Rock*. Balkema, Rotterdam, 709-715.

Napier, J.A.L. & Pierce, P.A. 1995. Simulation of extensive fracture formation and interaction in brittle materials. In : H.P. Rossmanith (ed.), *Mechanics of Jointed and Faulted Rock -MJFR-2.* Balkema, Rotterdam, 63-74.

Napier, J.A.L. & Kuijpers, J.S. 1995. Simulation of fracture in brittle rock. In unpublished proceedings *South African Institute of Mining And Metallurgy SIMRAC Symposium*, September, Mintek, Johannesburg.

Sellers, E.J. & Napier J.A.L. 1997. A comparative investigation of micro-flaw models for the simulation of brittle fracture in rock. *J. Computational Mechanics.* 120, 164-169.

Sellers, E.J. 1997. A tessellation approach for the simulation of the fracture zone around a stope. *Proceedings of Southern African Rock Engineering Symposium (SARES),* 143-154, Johannesburg.

Swenson, D.V. & Ingraffea, A. 1987.. A finite element model of dynamic crack propagation with an application to intersecting cracks, in *Proceedings of Fourth International Conference on Numerical Methods in Fracture Mechanics*, Pineridge, Swansea, United Kingdom, 191-204.

Thomas, A.L. & Pollard, D.D. 1993.. The geometry of echelon fractures in rock: implications from laboratory and numerical experiments. *J. Struct. Geol.,* 15, 323-334.

Wilson, S.A., Henderson, J.R. & Main, I.G. 1996. A cellular automaton fracture model: the influence of heterogeneity in the failure process. *J. Struct. Geol.,* 18, 343-348.

Appendix 4.3

Physical and numerical modelling of three-dimensional fracture processes

Despite the successful advances that have been made in design procedures for underground excavations, a complete understanding of the fundamental three-dimensional mechanisms of rock fracture and deformation has not been achieved yet. With a better knowledge of these mechanisms, design procedures can be enhanced and mining methods can be altered to achieve more favorable conditions in terms of both safety and production. As described in Section 2.4.8, a three-dimensional version of DIGS has been developed. The work presented in this appendix describes the physical experiments performed to validate this code and to guide the formulation of theories of brittle rock failure.

A4.3.1 Numerical modelling

A4.3.1.1 Stress analysis

The physical and numerical experiments focussed on a lead-lag stress raising geometry as depicted in Figure A4.3.1. Three-dimensional modelling of this lead-lag geometry was carried out using MAP3D (Wiles, 1996) and 3DIGS (Napier, 1998). Three different sizes of lead-lag were modelled namely 5 mm, 10 mm and 20 mm using the above mentioned numerical codes. The results were similar. Figures A4.3.2 to A4.3.4 illustrate the results obtained. The vertical stresses are plotted in Figure A4.3.5 to compare the MAP3D and 3DIGS results for the 20 mm lead-lag case.

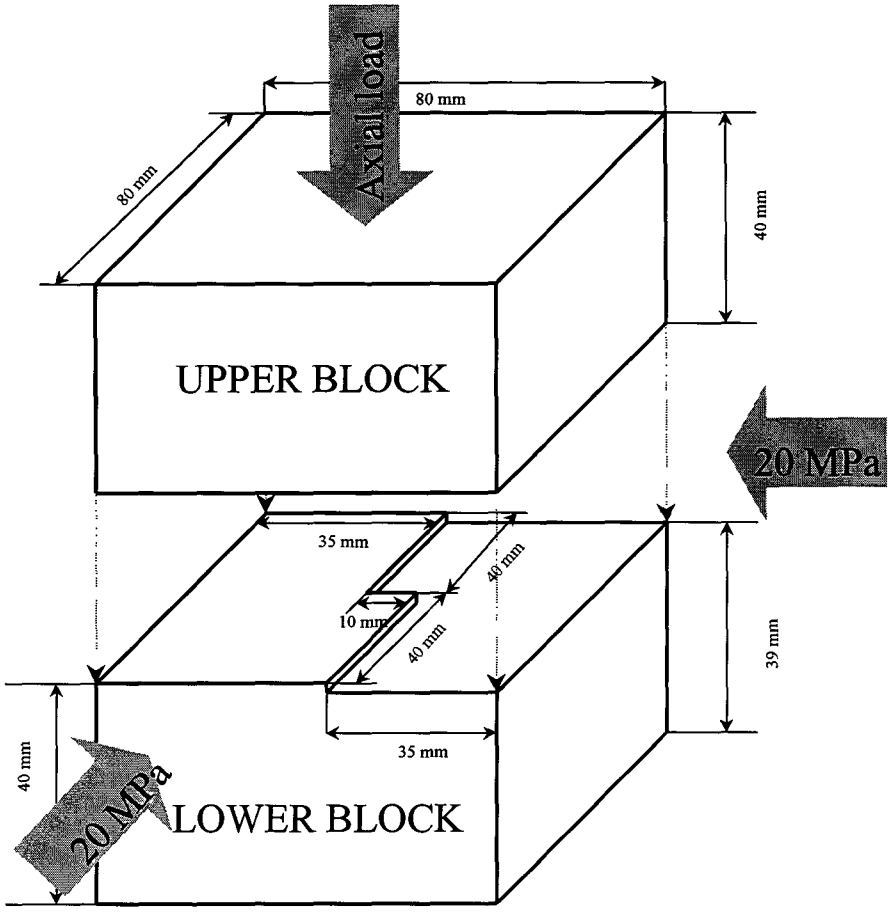

Figure A4.3.1 The geometry simulated in 3DIGS and MAP3D.

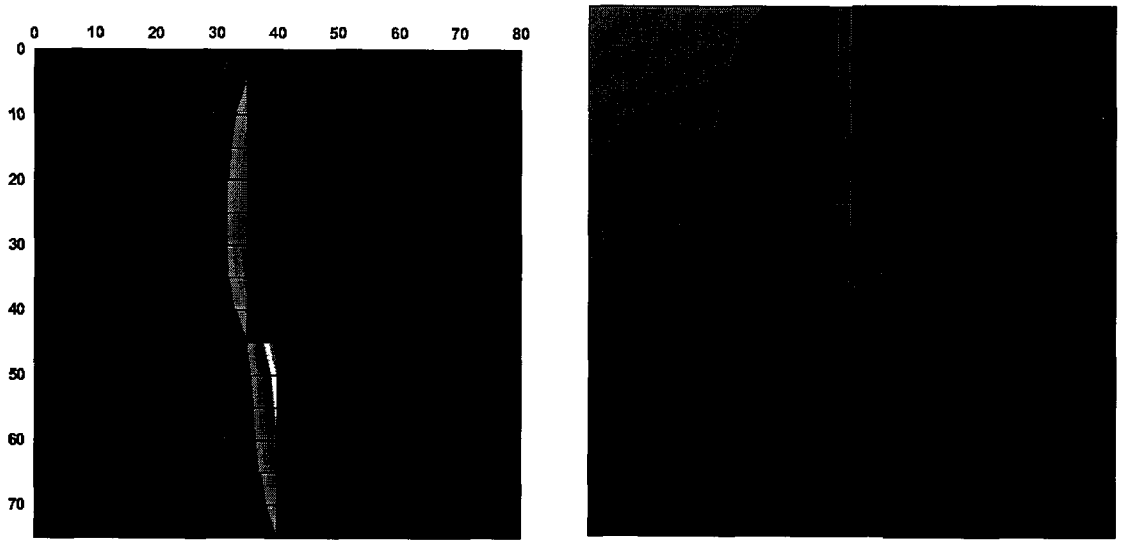

(a) 3DIGS (b) MAP3D

Figure A4.3.2 Vertical stress distribution ahead of face obtained from (a) 3DIGS (b) MAP3D for a lead-lag of 5 mm.

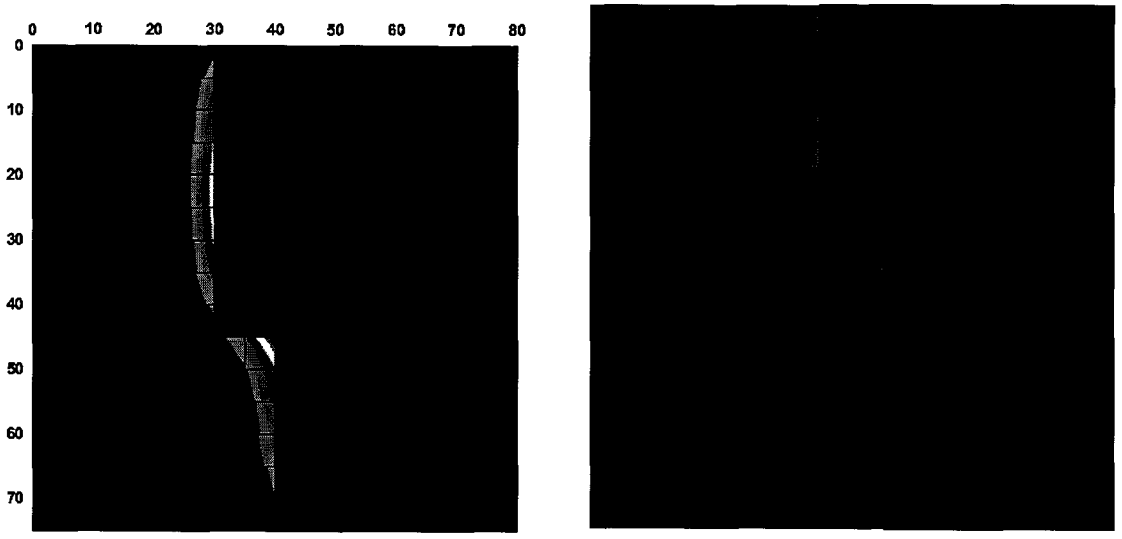

(a) 3DIGS (b) MAP3D

Figure A4.3.3 Vertical stress distribution ahead of face obtained from (a) 3DIGS (b) MAP3D for a lead-lag of 10 mm.

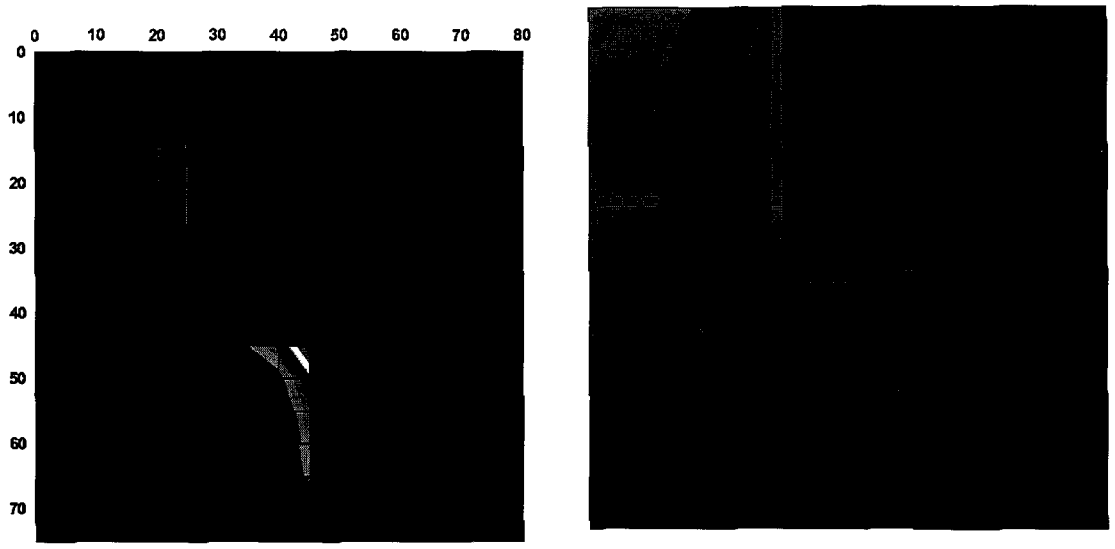

(a) 3DIGS (b) MAP3D

Figure A4.3.4 Vertical stress distribution ahead of face obtained from (a) 3DIGS (b) MAP3D for a lead-lag of 20 mm.

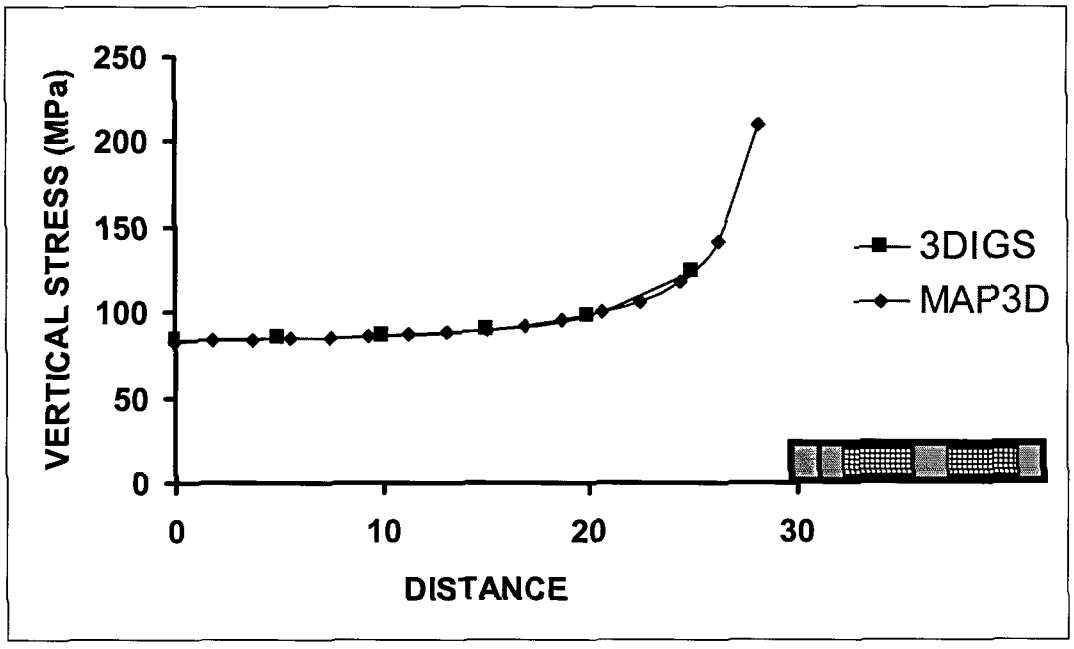

Figure A4.3.5 Vertical stresses ahead of the face (along the dashed line in Figure A4.3.4) obtained from MAP3D and 3DIGS for a 20 mm lead-lag.

A4.3.1.2 Fracture growth simulations

Initial runs using 3DIGS were conducted to obtain a typical fracture pattern around the test geometry. Figure A4.3.6 illustrates this geometry. The initial 3D tessellation pattern used before fracturing is given in Figure A4.3.7.

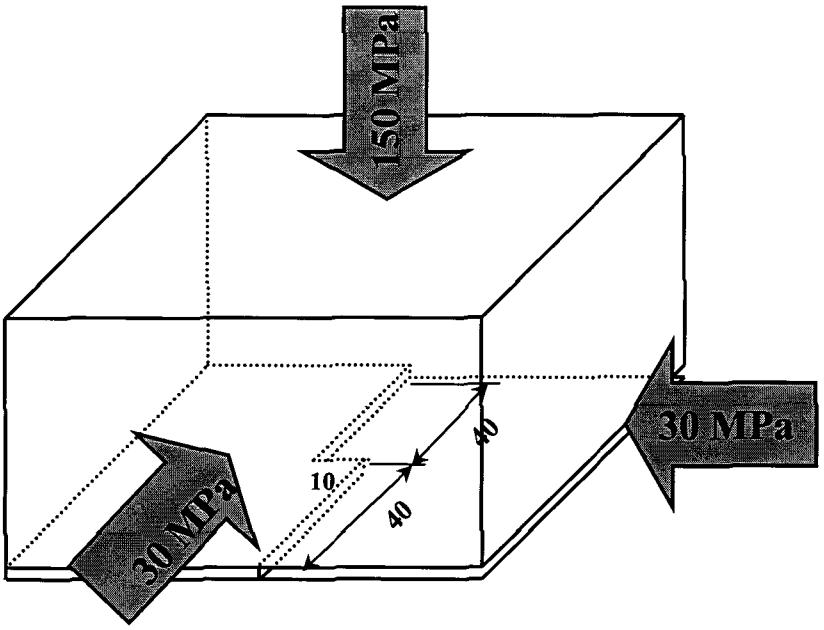

Figure A4.3.6 Model used for 3D fracturing of lead-lag in 3DIGS.

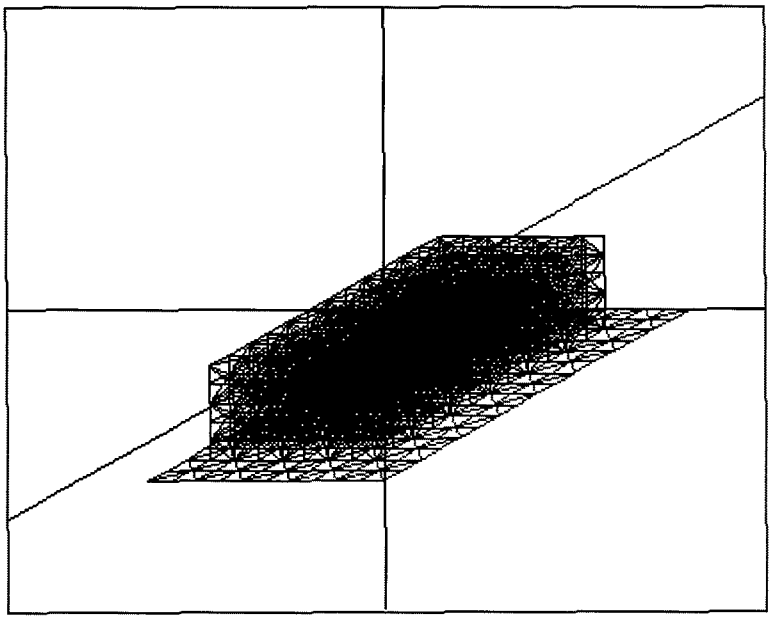

Figure A4.3.7 Initial 3D tessellation used in the simulation.

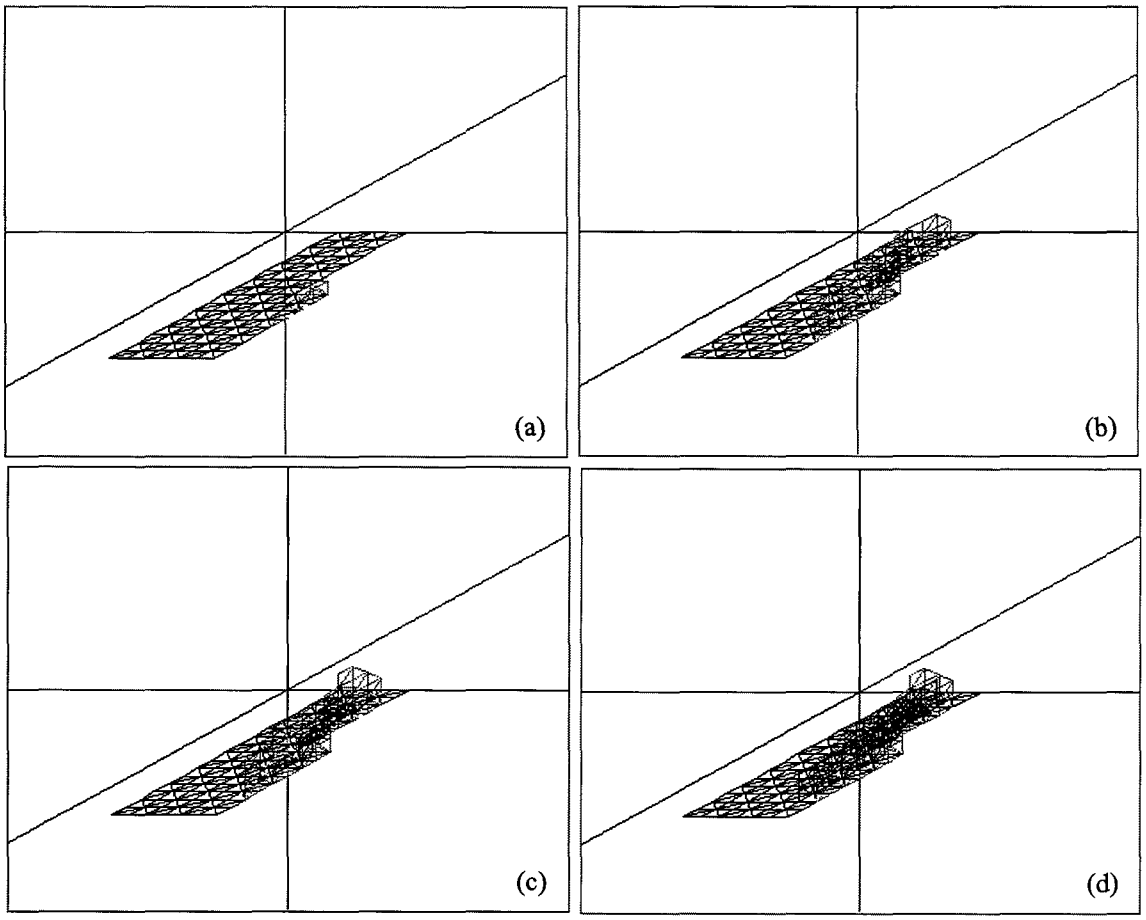

Figure A4.3.8 Fracture propagation at different stages of the mining.

The resultant fracture pattern is shown in Figure A4.3.8. These initial attempts to model three-dimensional fracture growth simulations have highlighted the need to develop higher order element formulations for the simulation of crack growth processes. It is also not possible, at present, to state when 2D modelling can be used in place of a full 3D analysis.

A4.3.2 Laboratory experiments

A4.3.2.1 Specimens

The models were prepared from Elsburg quartzite with the material properties given in Table A4.3.1.

Table A4.3.1 Properties of the Elsburg quartzite used for the experiments.

Property	Value
Uniaxial compressive strength	180 MPa
Elastic modulus	69,6 GPa
Poisson's ratio	0,2
p-wave velocity	5200 m/s

The models were cubic blocks with a side length of 80 mm. Three different geometries were tested:

1. A lead-lag geometry with different lead-lag distances (Figure A4.3.9)
2. Pillar modelling with different spacing of pillars (Figure A4.3.10)
3. A thin slot (Figure A4.3.11)

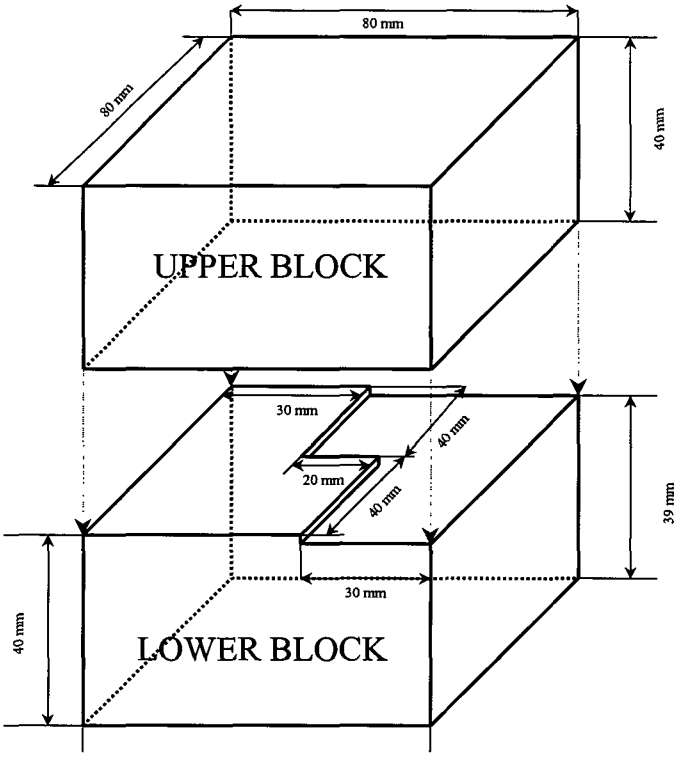

(a)

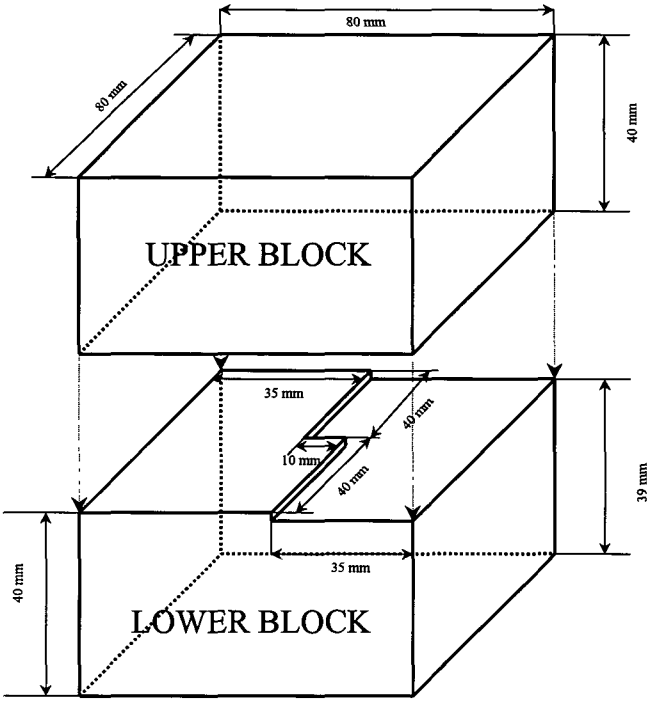

(b)

Figure A4.3.9 Geometry of the lead-lag specimens (a) 10 mm, (b) 20 mm.

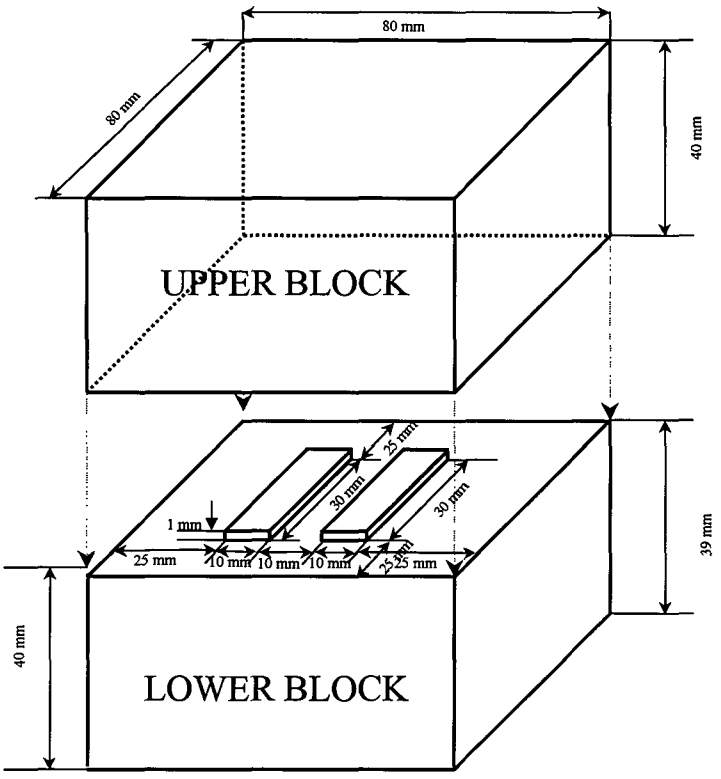

(a)

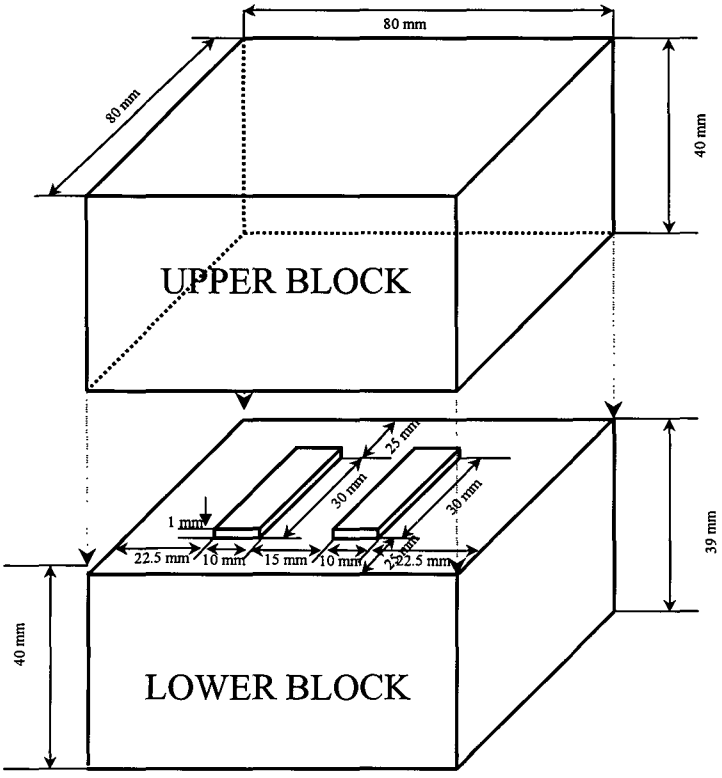

(b)

Figure A4.3.10 Geometry of the pillar specimens. (a) 15 mm and (b) 10 mm pillar spacing.

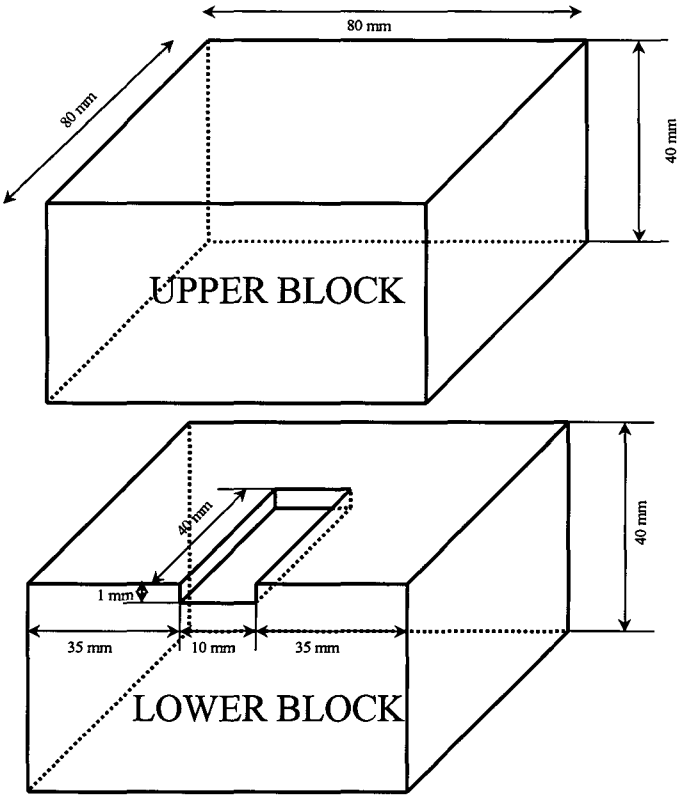

Figure A4.3.11 Laboratory specimen layout with a thin slot in the lower block.

The testing procedure was similar to that described in Section 4.3 and Appendix 4.1 and 4.2.

A4.3.2.2 Lead-lag geometries

Figure A4.3.12 shows the plan view of the sample and Figure A4.3.9b illustrates the general outline of the sample. The sample was axially loaded up to 250 MPa with 20 MPa confinement in both directions. Figure 4.3.13 illustrates the axial strain versus axial stress and axial strain versus cumulative energy released graphs, obtained from the acoustic emission observations. The graph of the confinement loading as a function of axial stress is shown in Figure A4.3.14.

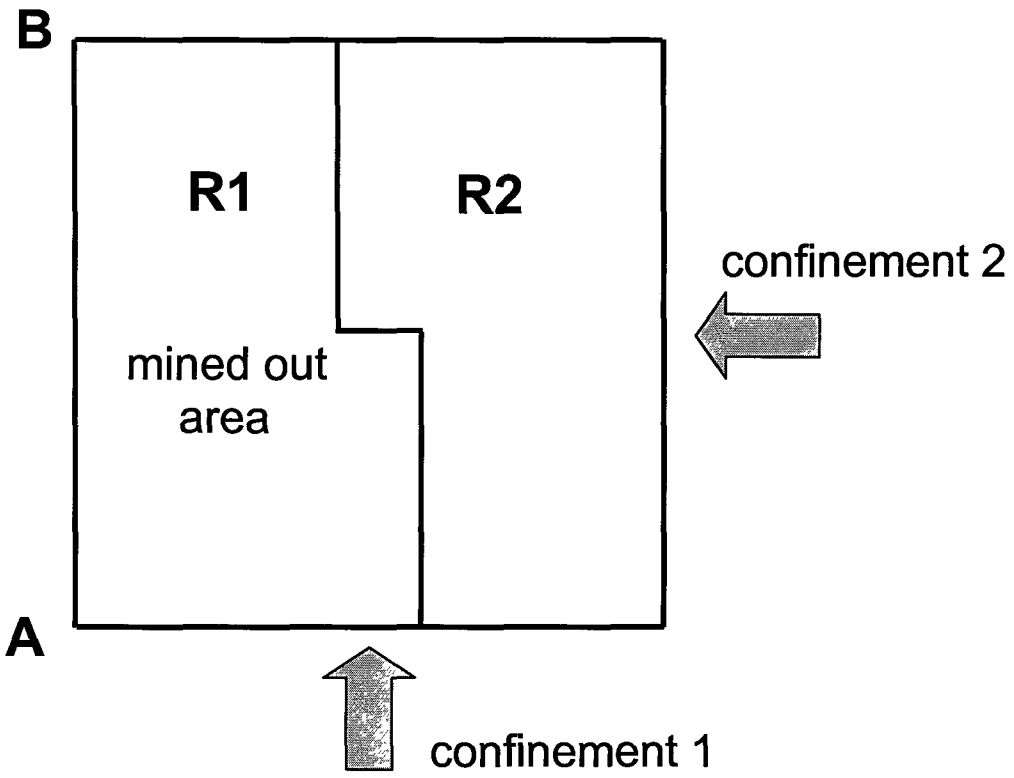

Figure A4.3.12 Plan view of the lead-lag geometry.

The cumulative energy release is seen to increase significantly at axial strain of 0,005, 0,0125 and 0,017. These values coincide with the significant change in confinement levels (see Figure A4.3.13 and A4.3.14). These confinement changes reflect increased dilation in the sample caused by the fracture initiations at a micro and macro level. Figure A4.3.15 illustrates the final fracture pattern of the sample. Above the axial stress level of 100 MPa, the slope of the stress-strain curve becomes steeper (Figure A4.3.13). Acoustic emission also gives high values of energy released at these stress values (Figure 4.3.16). There was evidence of total closure along the edge *AB* in Figure A4.3.12 as indicated by the pressure film which was inserted between the two layers of the sample. Figure A4.3.17 shows the darker the area the higher the stress in the region of the initially open slot where contact occurs.

At lower stresses (0-25 MPa), the fracturing takes place in the area around the slot, however, at the higher stresses (60-100 MPa) the fracturing moves to the region around the contact area R2 (Figure A4.3.12). Figure A4.3.18 illustrates the fracture initiation as a function of axial stresses. The energy released distributions are shown in Figure A4.3.19 at three orthogonal planes through the centre of the sample.

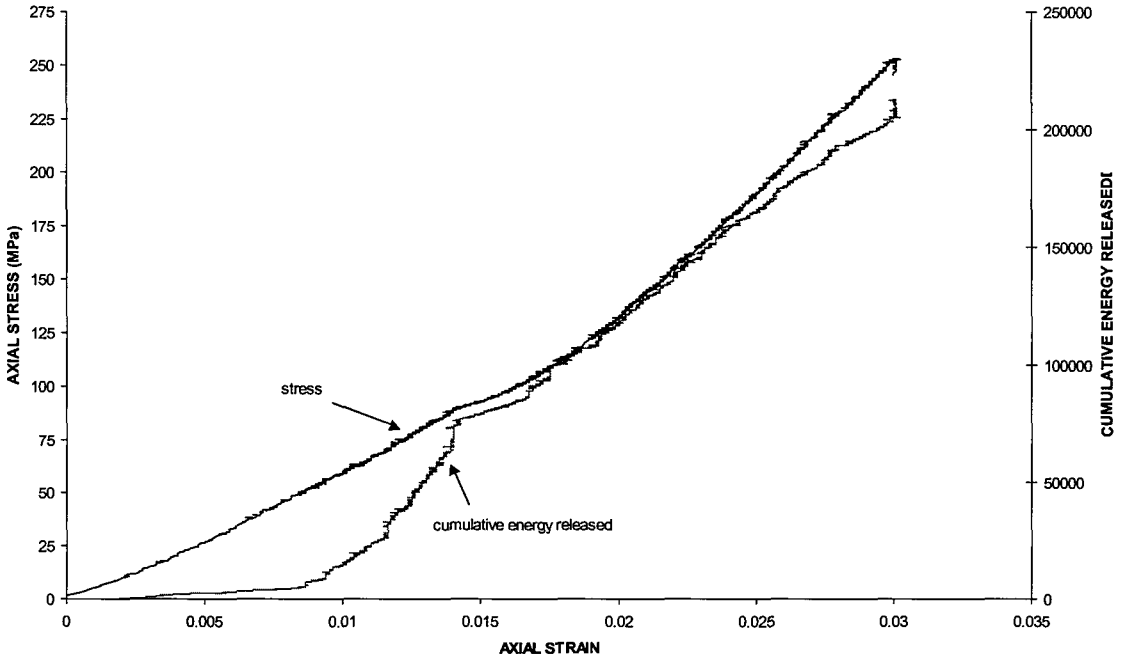

Figure A4.3.13 Axial strain versus axial stress graph and axial strain versus cumulative energy released for the lead-lag experiment.

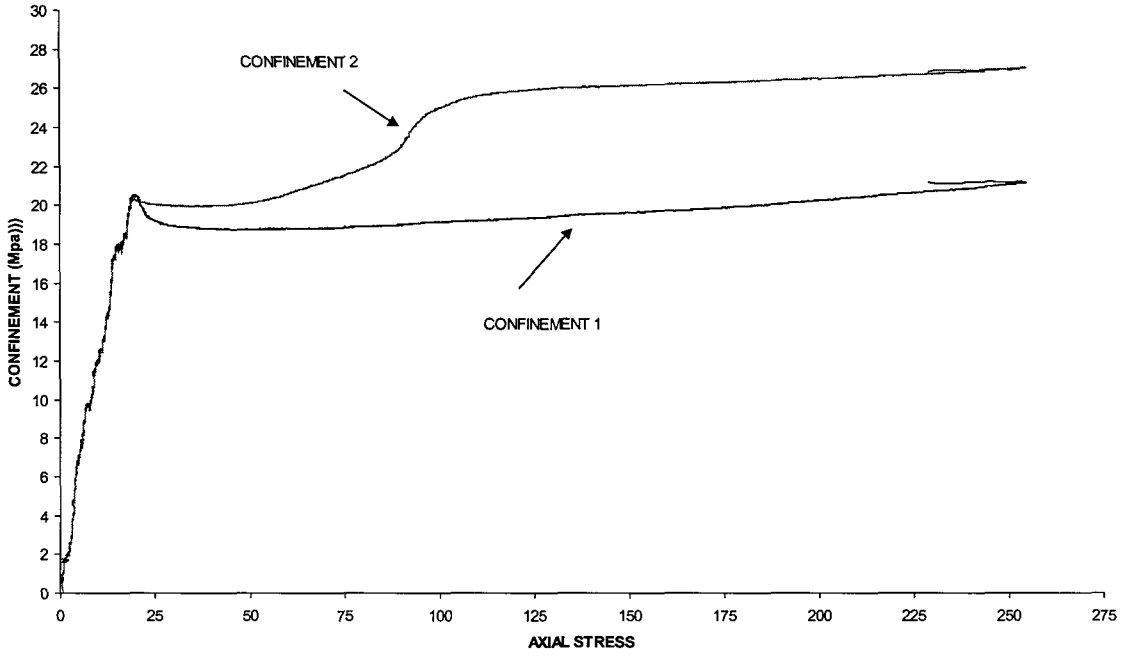

Figure A4.3.14 Axial stress versus confinement for the lead-lag experiment.

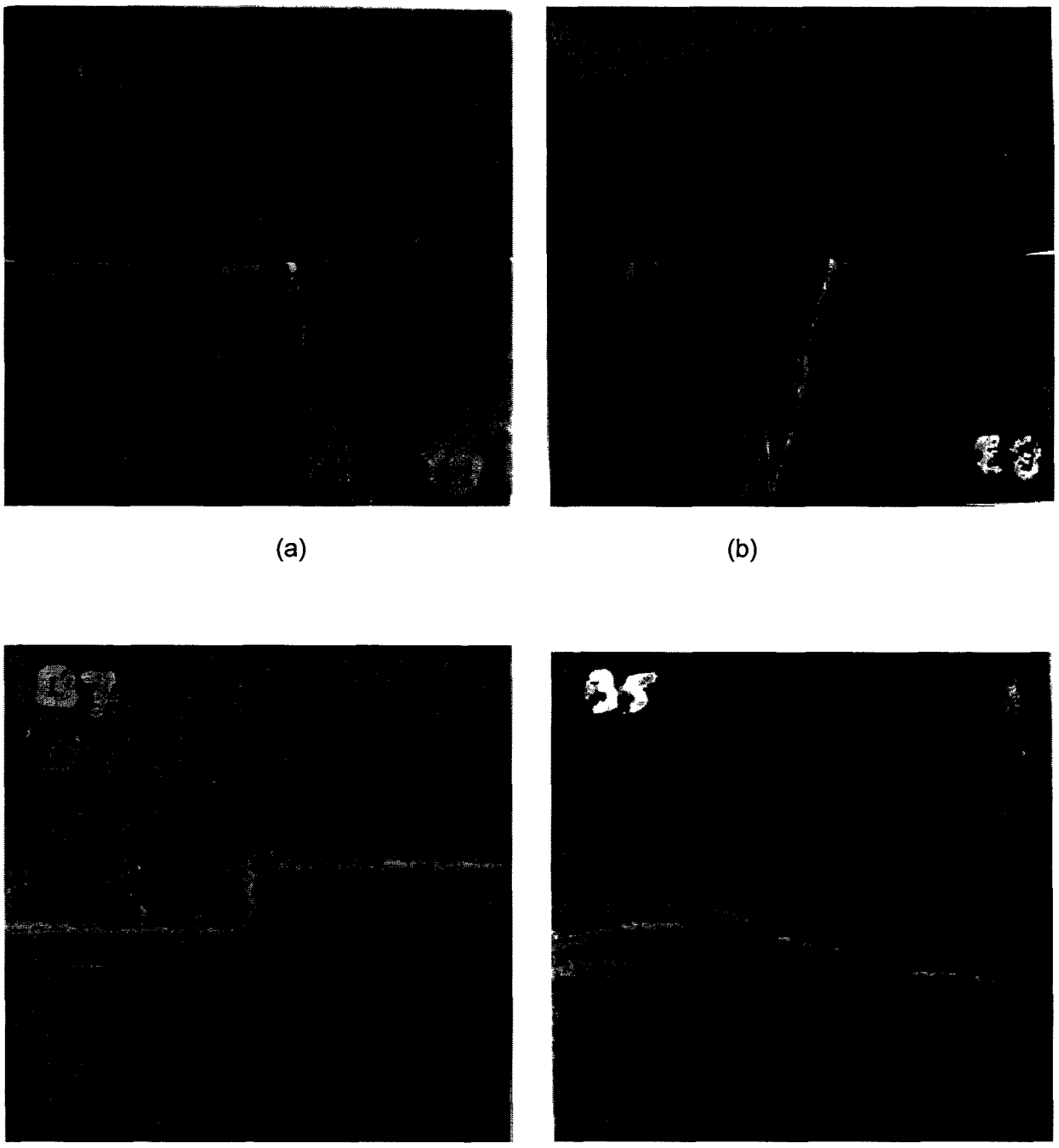

(a) (b)

(c) (d)

Figure A4.3.15 Laboratory results for the lead-lag experiment (a) side view (b) side view, (c) view from the bottom and (d) top view of lower portion of the sample.

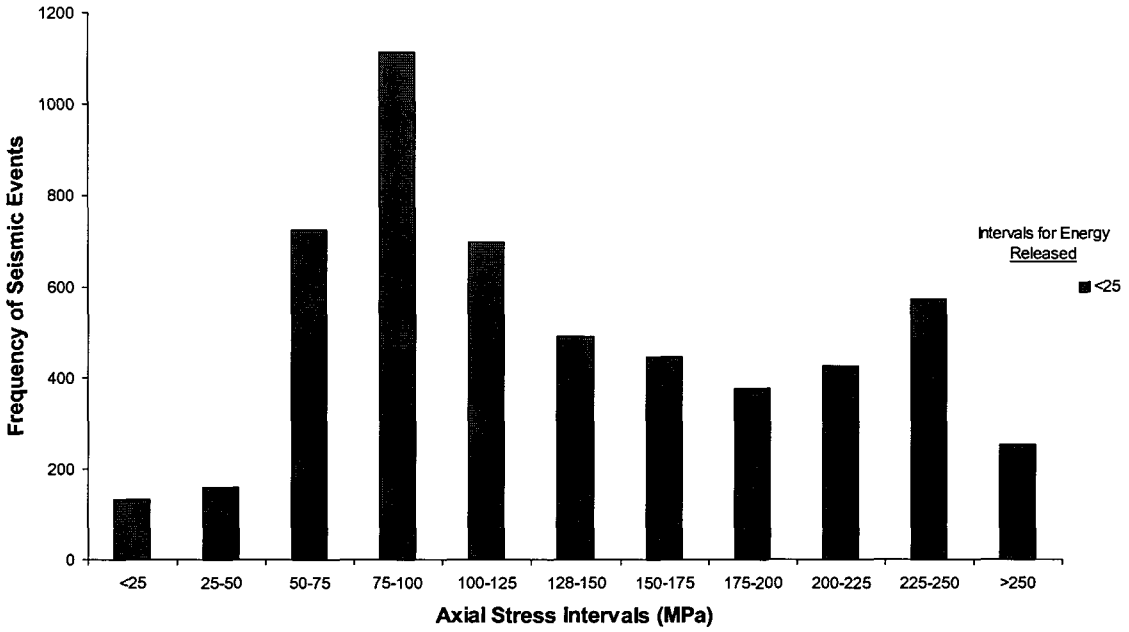

(a)

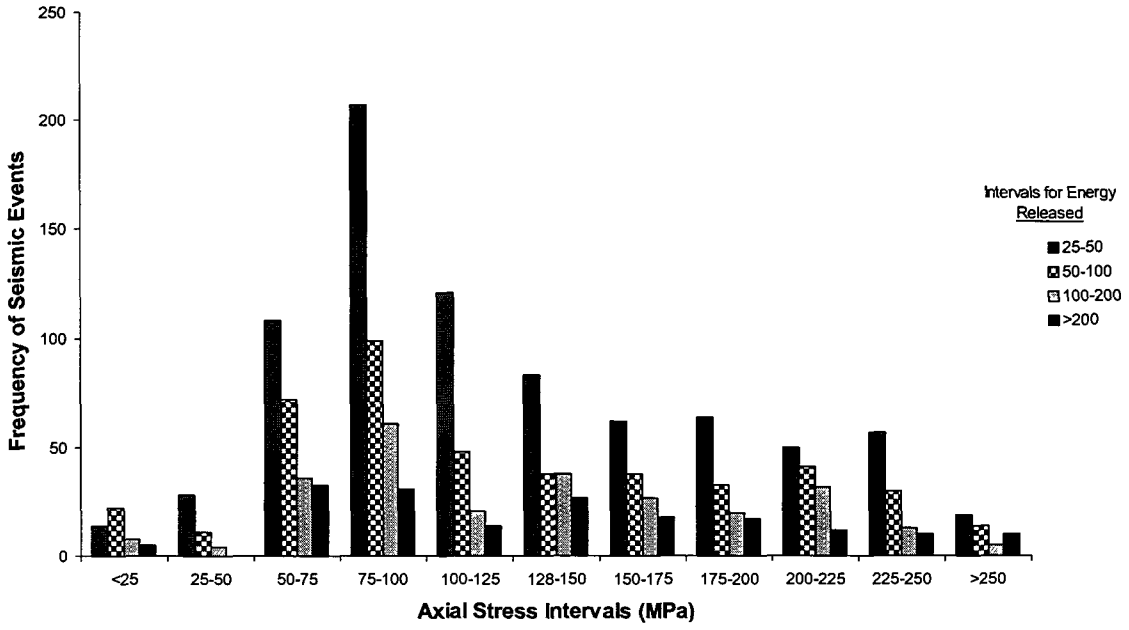

(b)

Figure A4.3.16 Frequency of seismic events as a function of axial stress and energy released for the lead-lag sample ((a) the energy released value less than 25, (b) the energy released value greater than 25).

Figure A4.3.17 Stress distribution obtained from the pressure film at the interface.

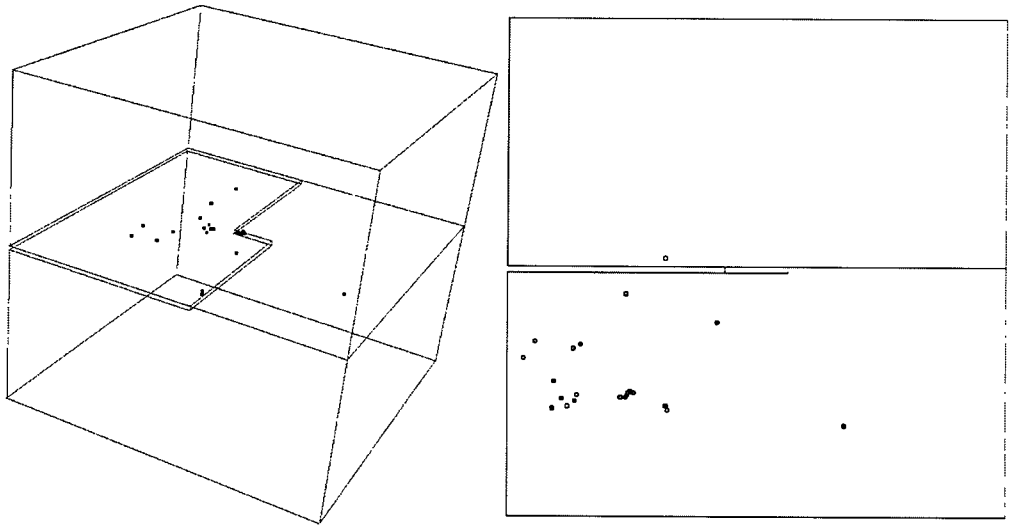

(a) Event locations at an axial stress level from 15 to 25 MPa,

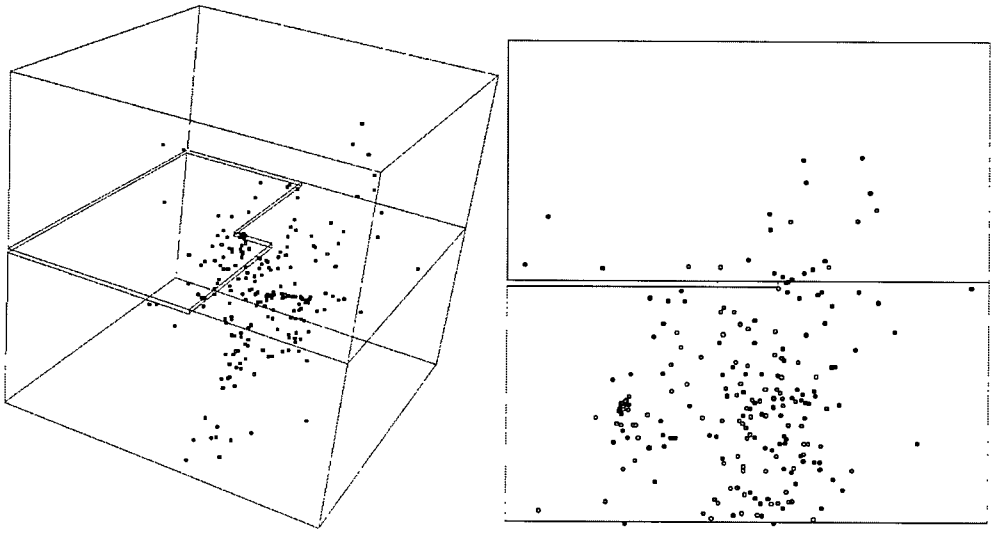

(b) Event locations at an axial stress level from 60 to 80 MPa,

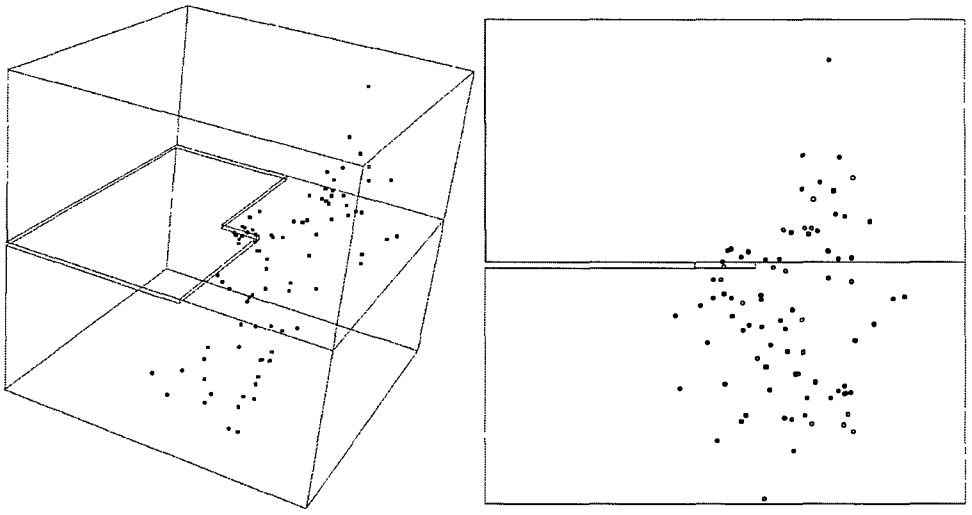

(c) Event locations at an axial stress level from 90 to 100 MPa,

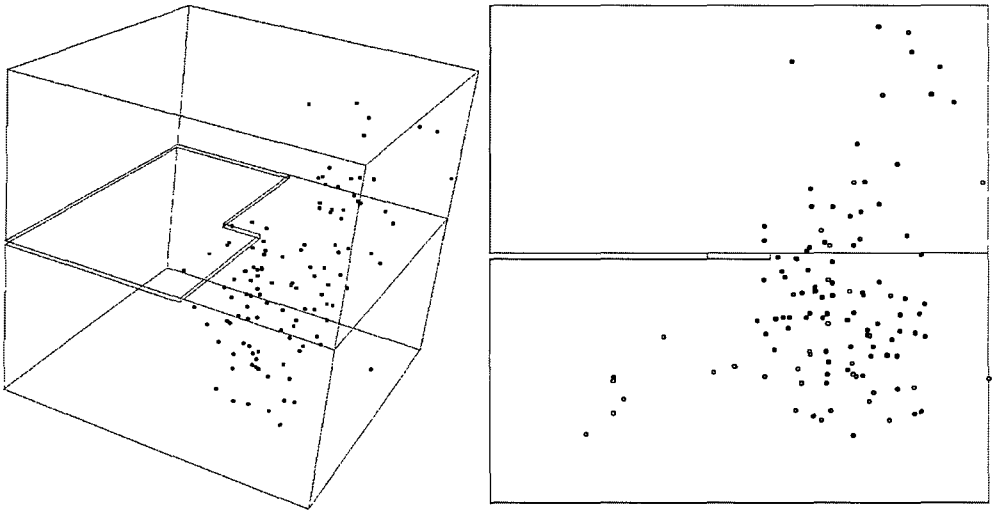

(d) Event locations at an axial stress level from 105 to 120 MPa,

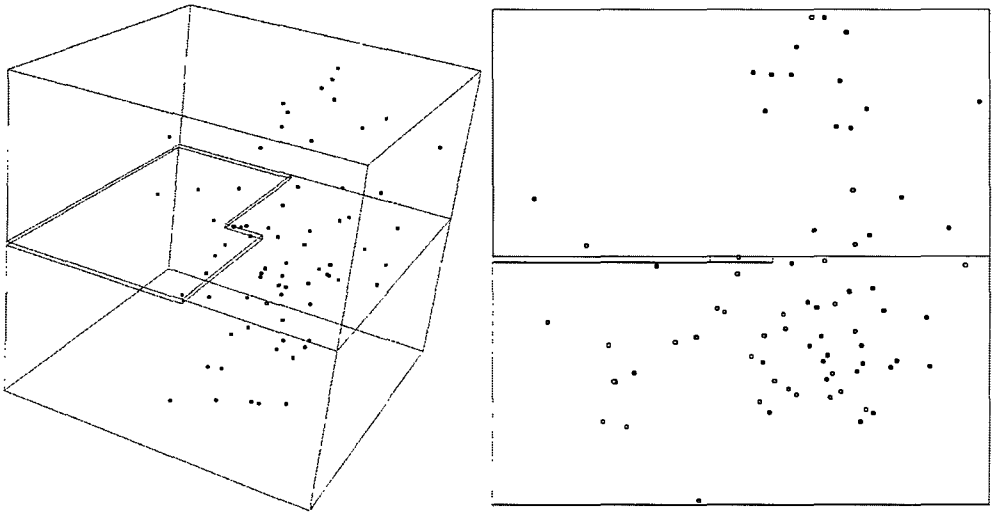

(e) Event locations at an axial stress level from 125 to 130 MPa,

Figure A4.3.18 Locations of events at different axial stress levels (energy released values greater than 30 are illustrated).

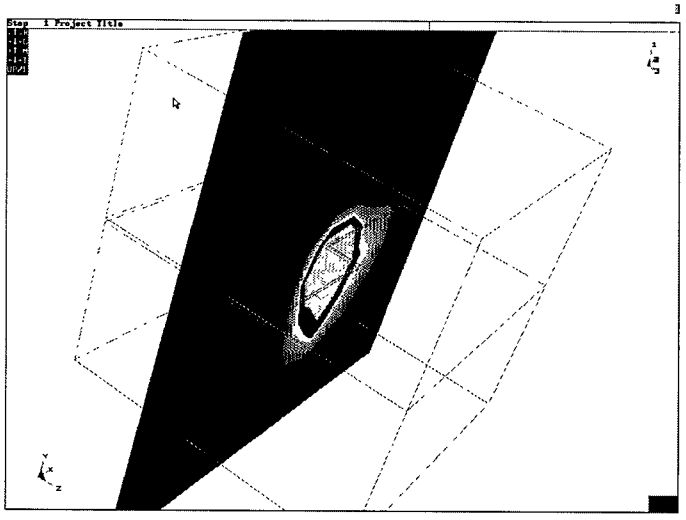

(a)

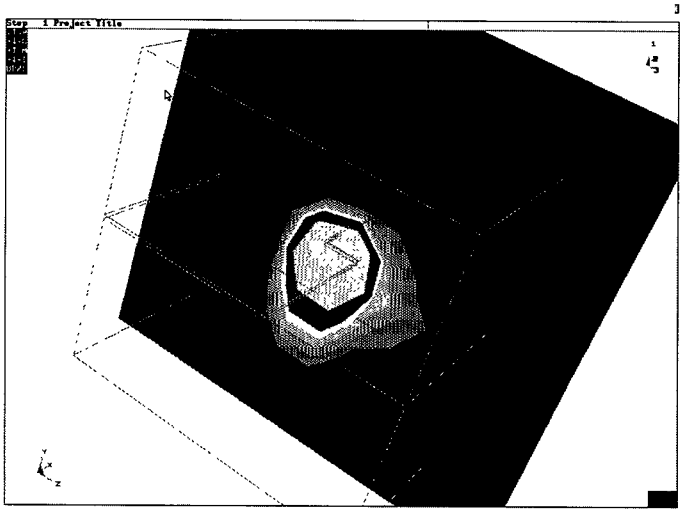

(b)

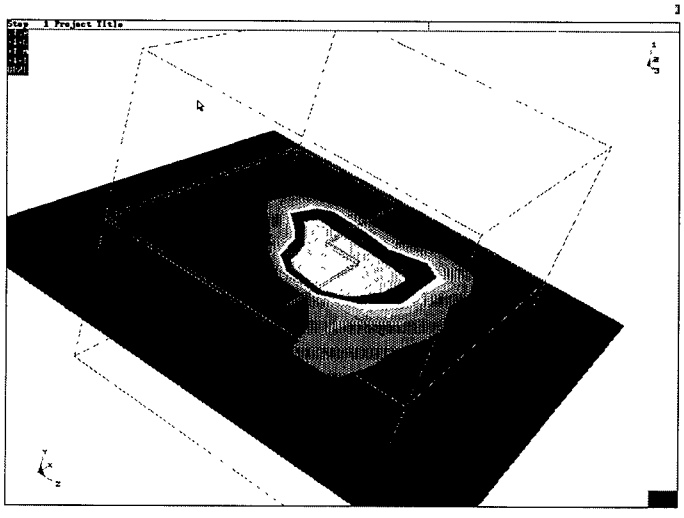

(c)

Figure A4.3.19 Energy released distributions at the three orthogonal planes.

A4.3.2.3 Pillar modelling

In order to investigate the three-dimensional fracture patterns around pillars, a series of laboratory experiments was carried out. Figure A4.3.20 shows the plan view of the sample and Figure A4.3.10b illustrates the general outline of the sample. The sample was loaded up to 230 MPa of axial loading with 20 MPa confinement. Figure A4.3.21 illustrates the axial strain versus axial stress and axial strain versus cumulative energy released graphs, obtained from the acoustic emission observations. The graph of the confinement loading graph as a function of axial stress is shown in Figure A4.3.22.

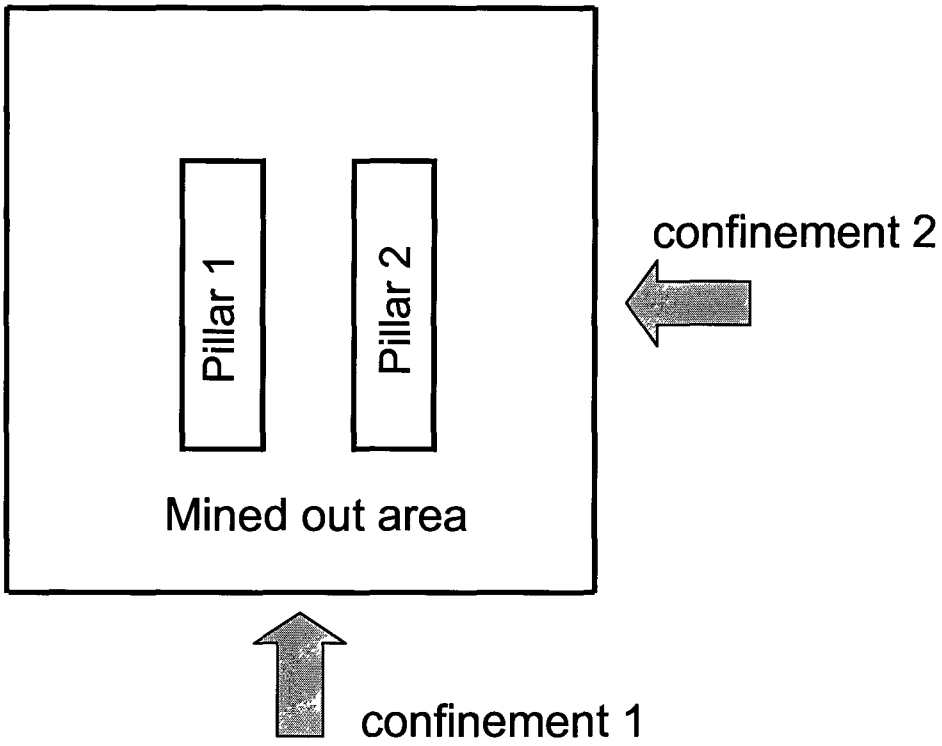

Figure A4.3.20 Plan view of the laboratory sample used for pillar modelling.

There are sudden energy changes in the sample at axial strain levels of 0,003 and 0,018. These values coincide with the significant changes in the confinement levels (Figure A4.3.22). These confinement changes are the result of dilation of the sample caused by the fracture growth. Figure A4.3.22 shows distinctly 3D behaviour, on the confining stress changed, in both confining directions, when the axial stress is approximately 100 MPa, as compared to Figure A4.3.14. Figure A4.3.23 illustrates the final fracture pattern of the sample. After the axial strain level of 0,018, the slope of the stress-strain curve becomes steeper (Figure A4.3.21). Acoustic emission also gives high energy released at these stress levels (Figure A4.3.24).

At lower axial stresses (0-50 MPa), the fracturing takes place in the lower block where most of the damage occurred (see Figure A4.3.25.b). Once the pillars fail, the fractures start to propagate into the hangingwall. Figure A4.3.25 illustrates the events picked up by the acoustic emission system for the different stress levels. The energy released distributions for the final load are shown in Figure A4.3.26 at three orthogonal planes in the centre of the sample.

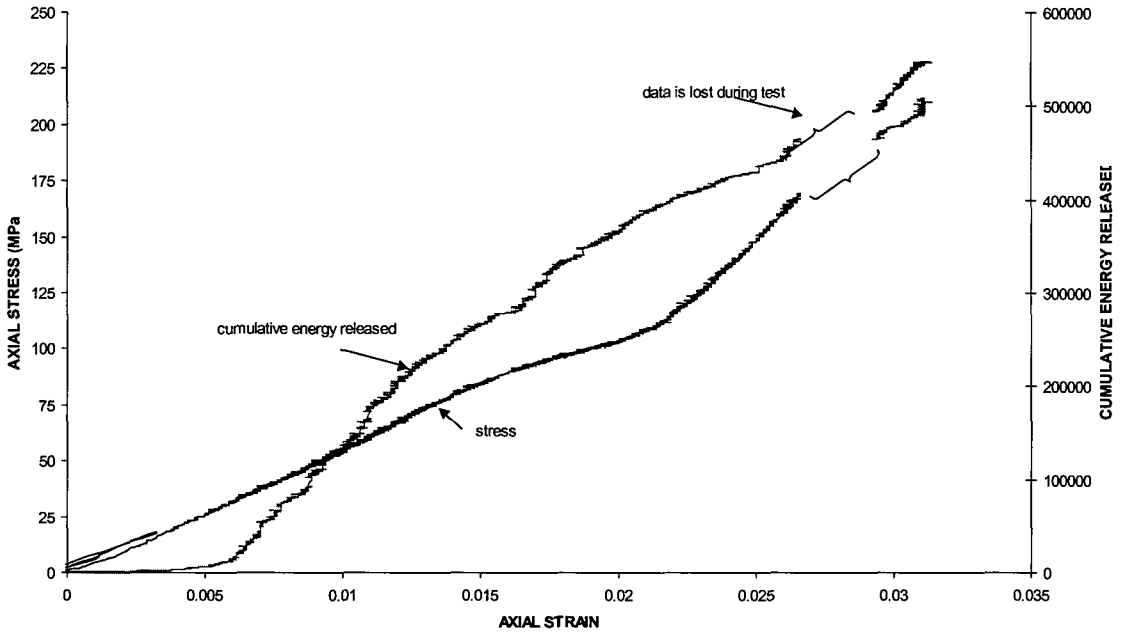

Figure A4.3.21 Axial strain versus axial stress and axial strain versus cumulative energy released for the pillar experiment.

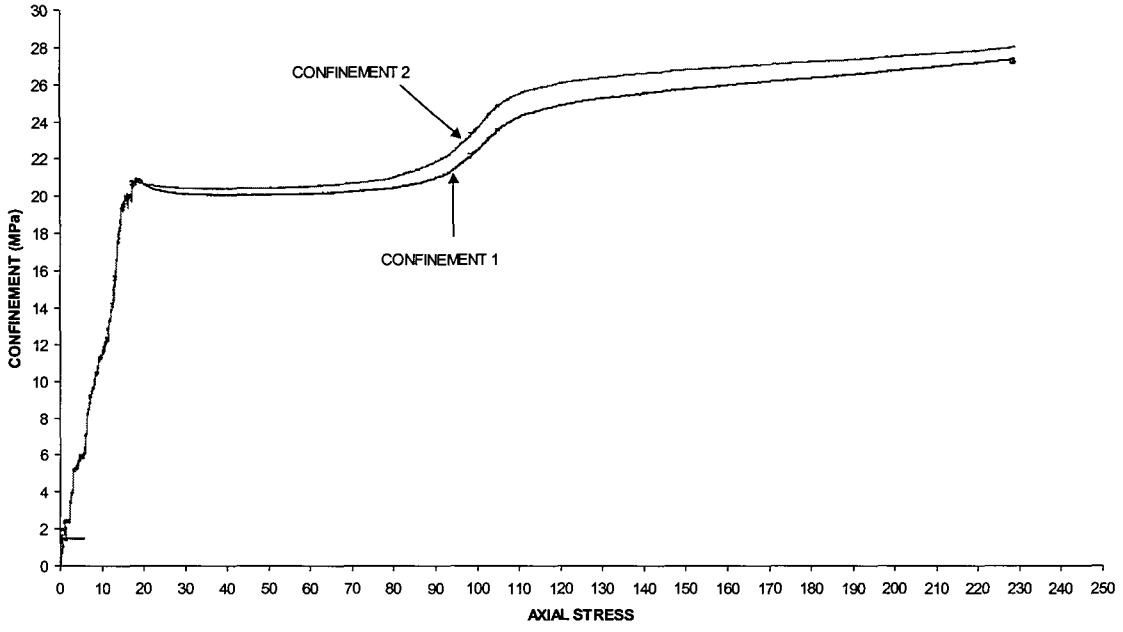

Figure A4.3.22 Axial stress versus confinement for the pillar experiments.

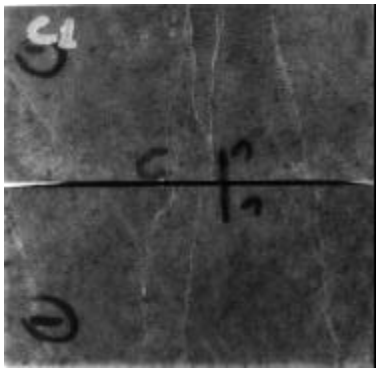

(a) side view

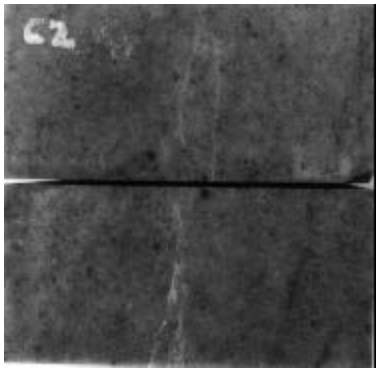

(b) side view

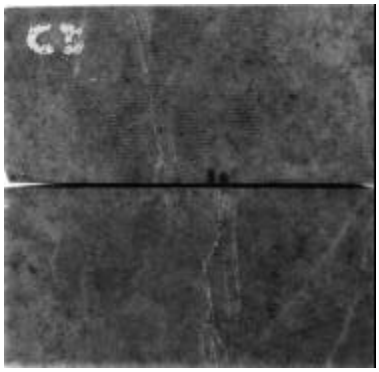

(c) side view

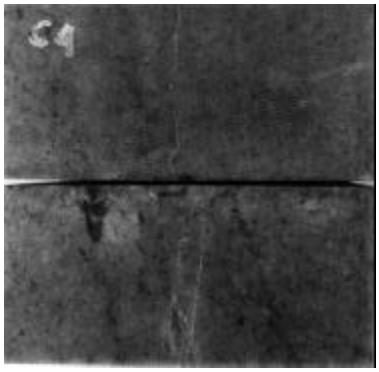

(d) side view

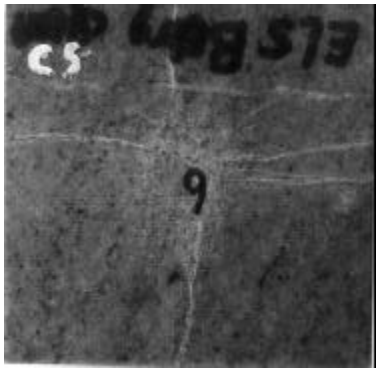

(e) top view

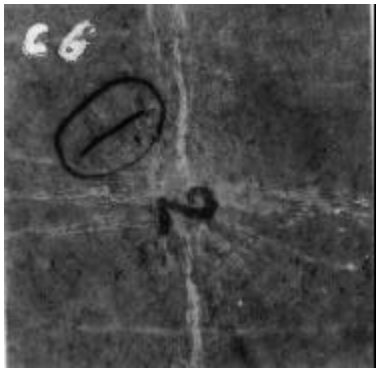

(f) bottom view

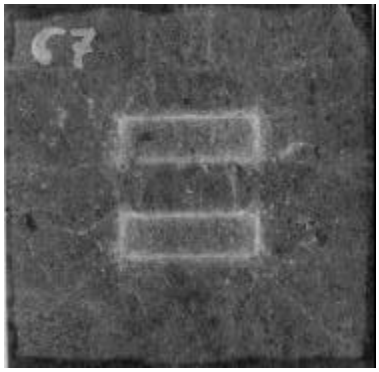

(g) plan view of upper block

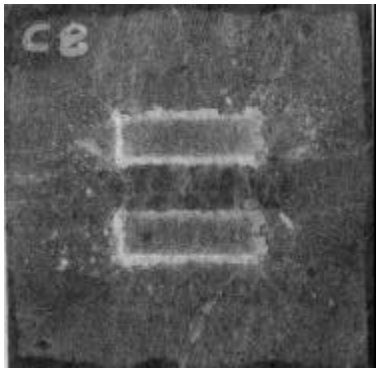

(h) plan view of lower part inside sample

Figure A4.3.23 Laboratory results of the pillar experiment.

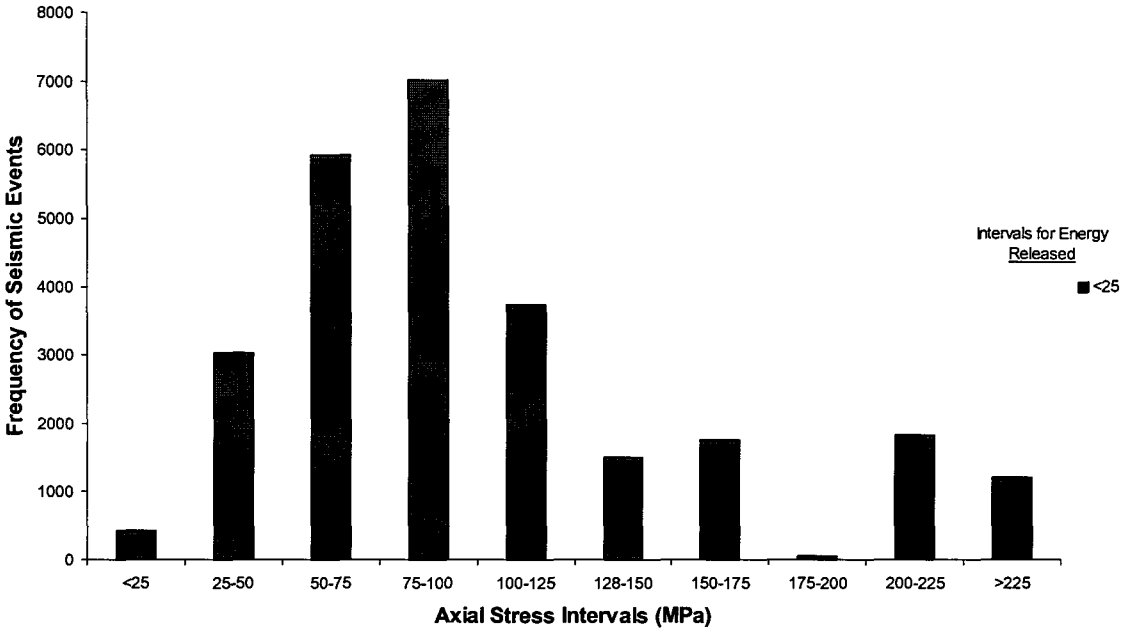

(a)

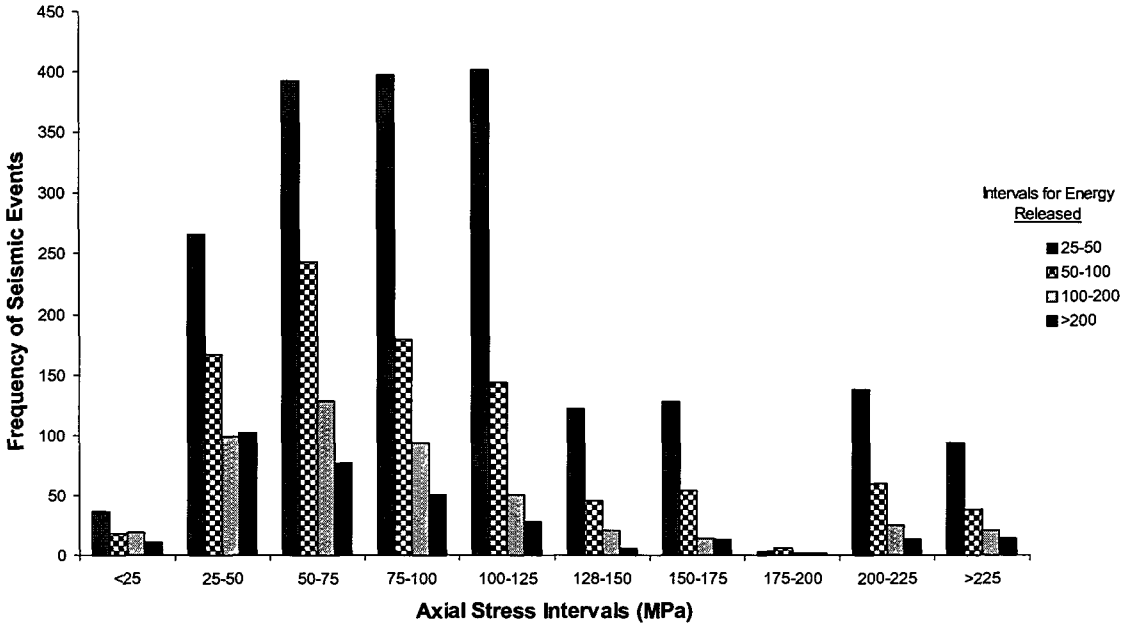

(b)

Figure A4.3.24 Frequency of seismic events as a function of axial stress and energy released for the pillar sample: (a) the energy released for values less than 25, (b) the energy released for values greater than 25.

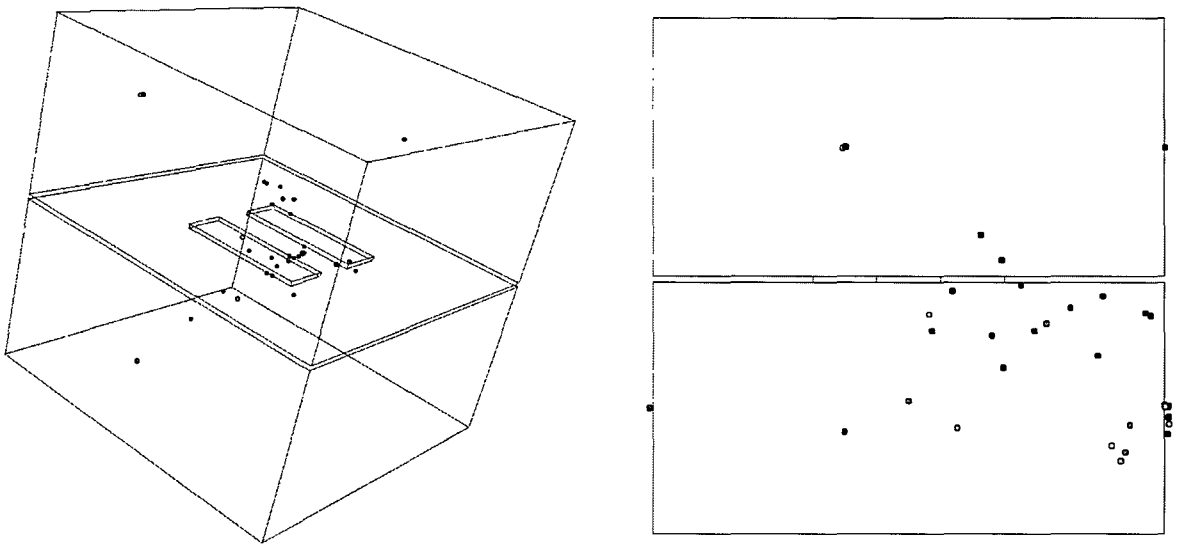

(a) Event locations at an axial stress level from 0 to 25 MPa,

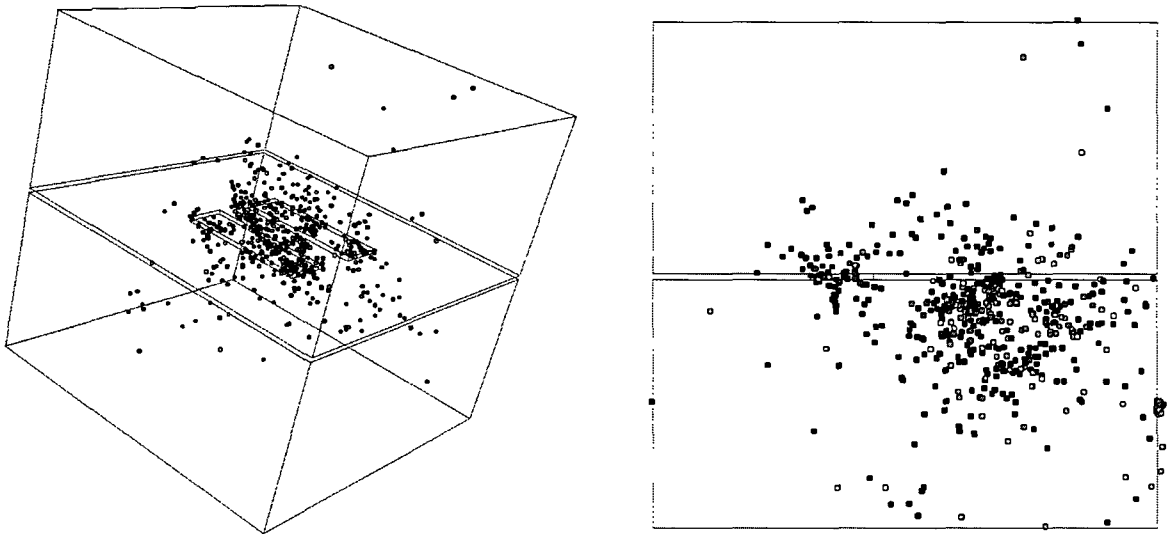

(b) Event locations at an axial stress level from 25 to 50 MPa,

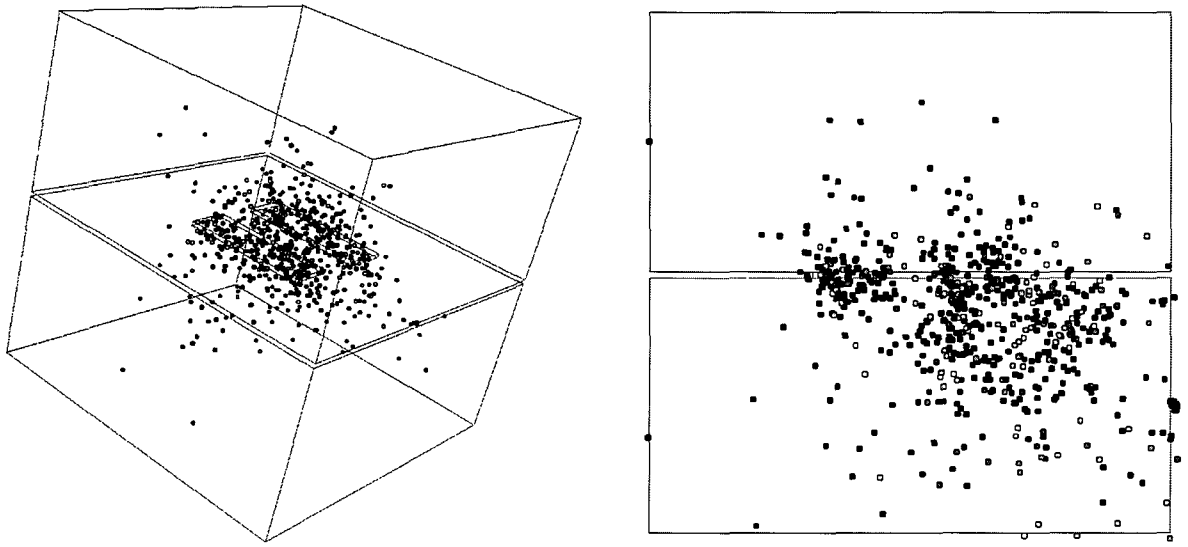

(c) Event locations at an axial stress level from 50 to 75 MPa,

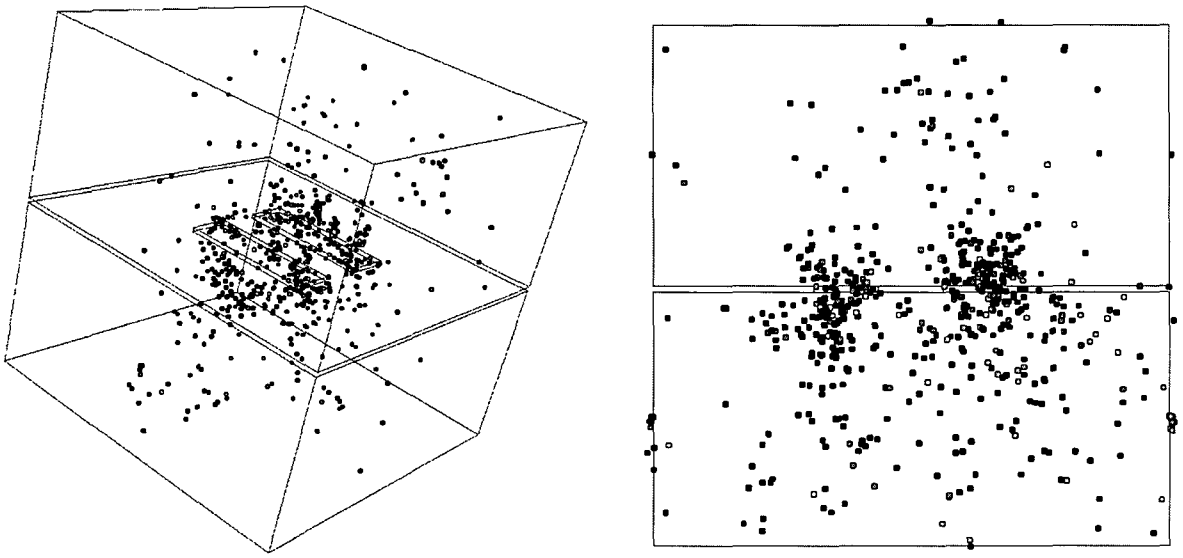

(d) Event locations at an axial stress level from 75 to 100 MPa,

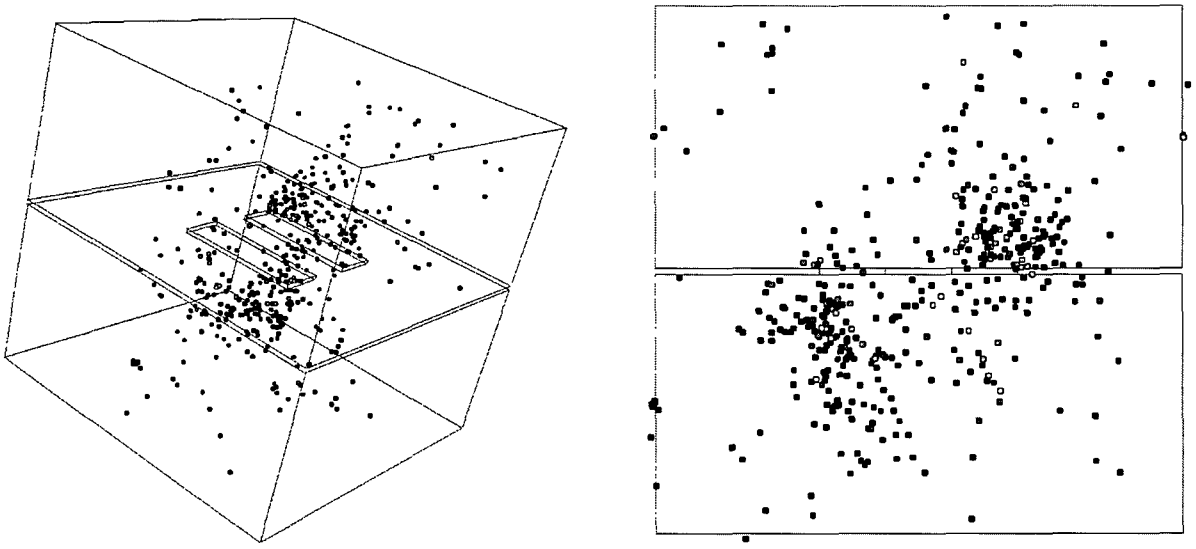

(e) Event locations at an axial stress level from 100 to 125 MPa,

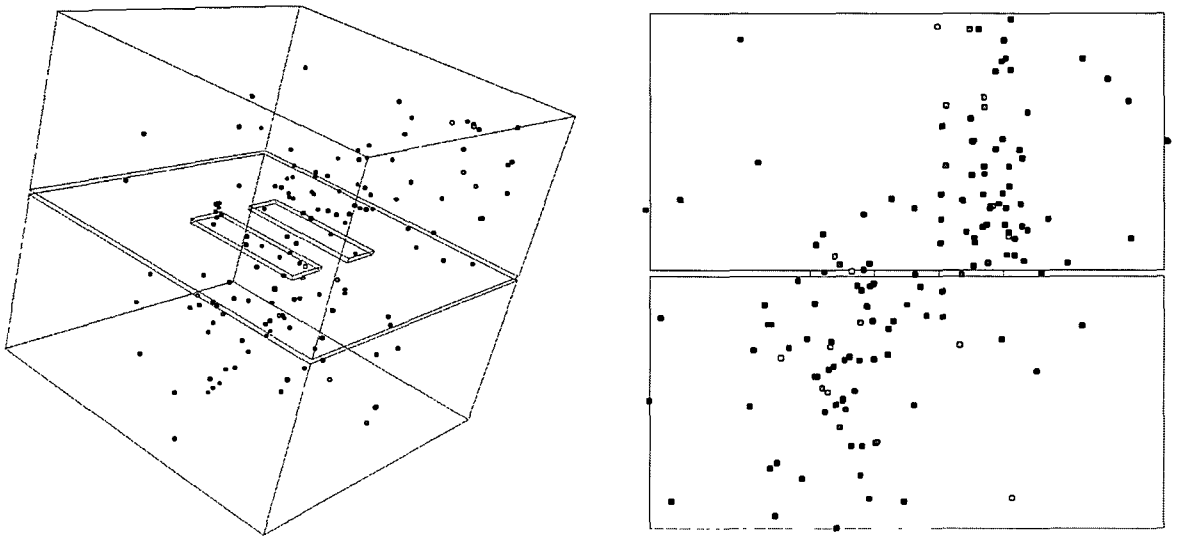

(f) Event locations at an axial stress level from 125 to 150 MPa,

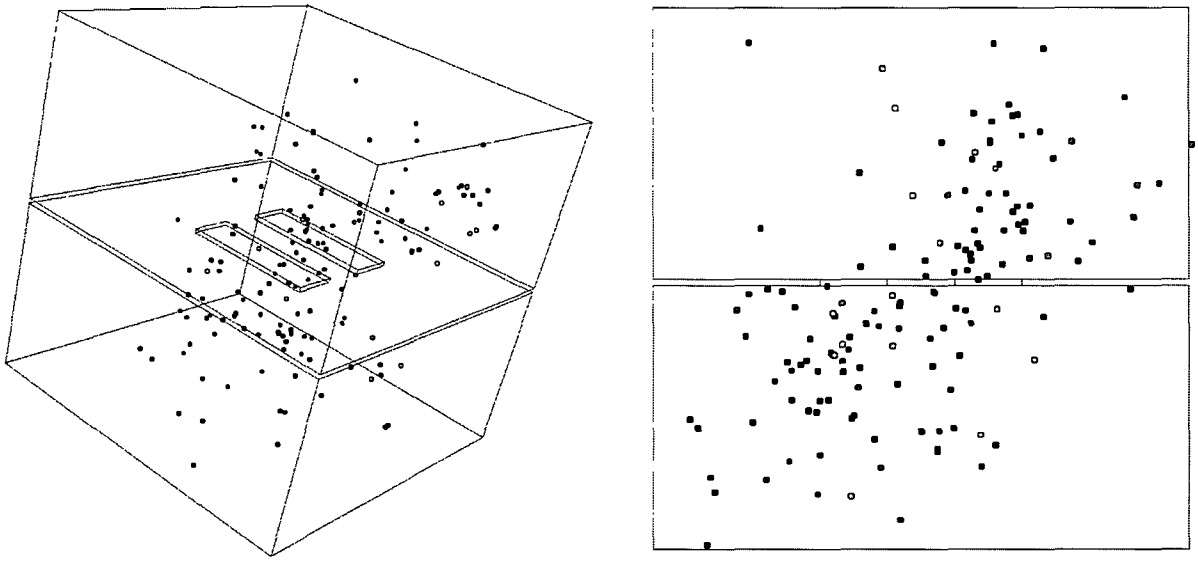

(g) Event locations at an axial stress level from 150 to 175 MPa,

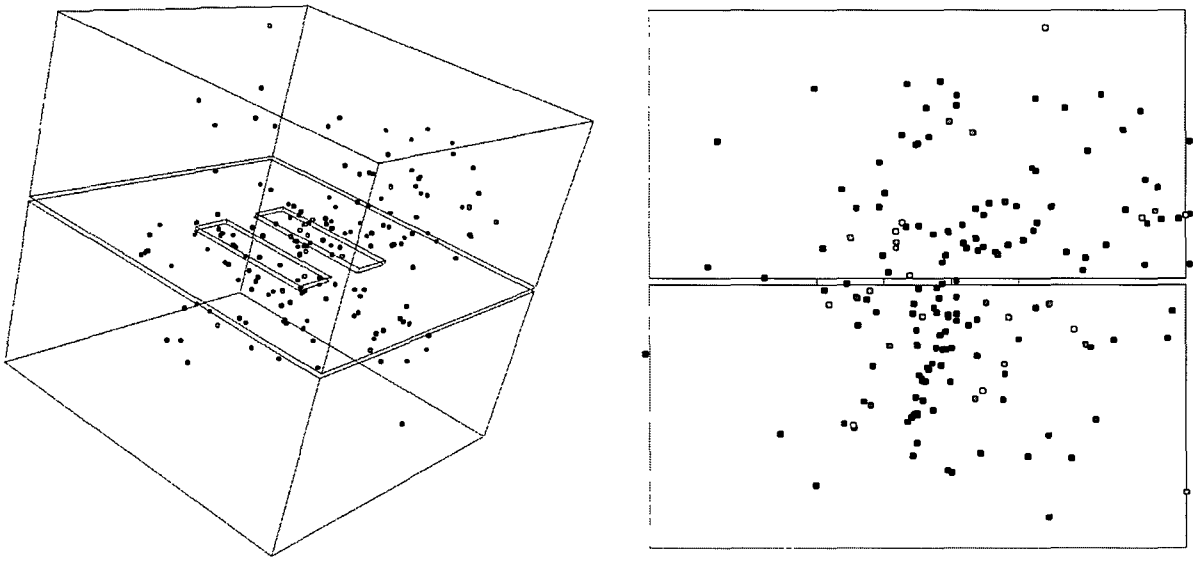

(h) Event locations at an axial stress level from 175 to 200 MPa,

Figure A4.3.25 Locations of events at different axial stress levels (energy released values greater than 30 are illustrated).

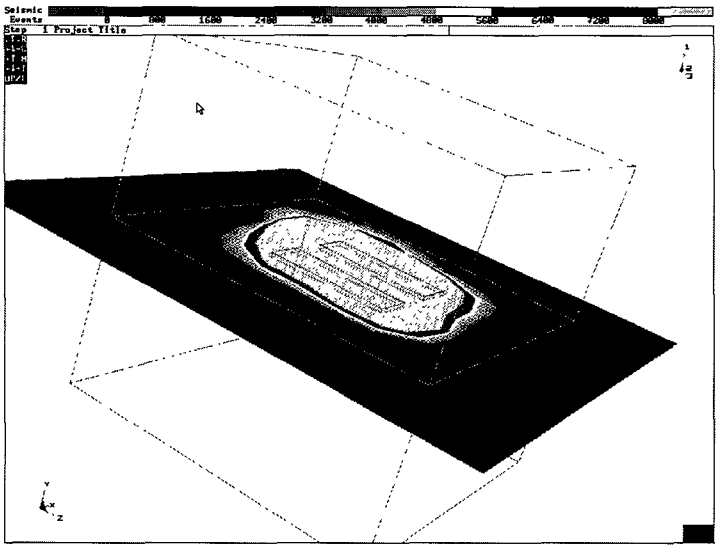

(a)

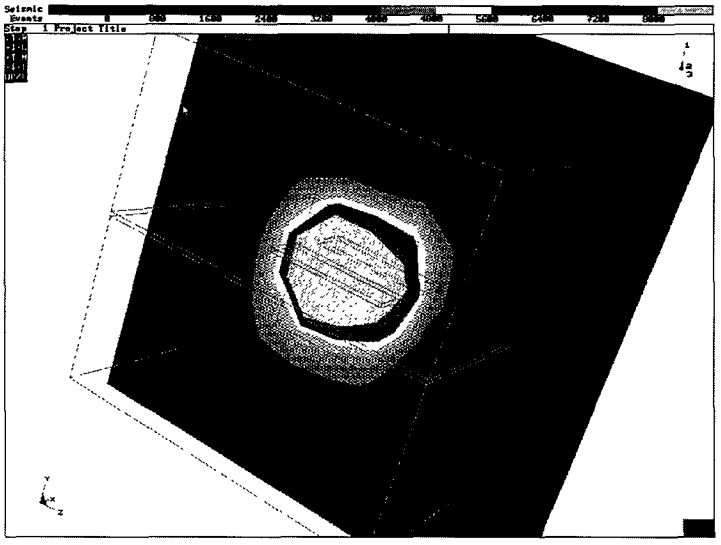

(b)

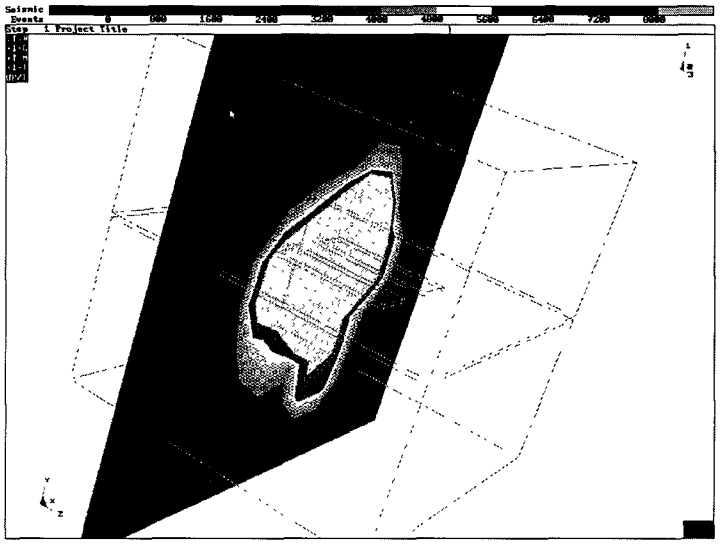

(c)

Figure A4.3.26 Energy released distributions at three orthogonal planes.

A4.3.2.4 Experiments with a thin slot in the lower block

The sample with a thin slot in the lower block was loaded axially with a confinement of 20 MPa in both directions. The outline of the sample is given in Figure A4.3.11, and the plan view of the sample is shown in Figure A4.3.27. The maximum axial stress was 360 MPa. Figure A4.3.28 illustrates graphs of the axial strain versus axial stress and axial strain versus cumulative energy released. These results were obtained from the acoustic emission equipment. The graph of the confinement loading as a function of axial stress is shown in Figure A4.3.29.

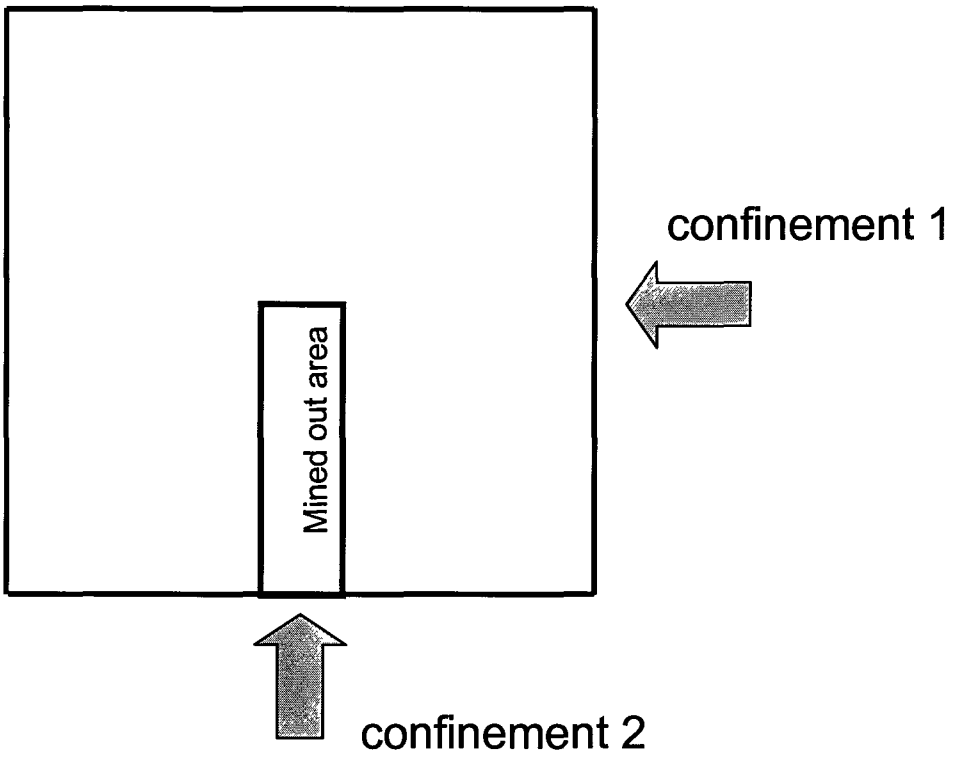

Figure A4.3.27 Plan view of the sample used for the thin slot experiment.

There is little dilation in the sample as concluded from Figure A4.3.29. Figure A4.3.30 illustrates the final fracture pattern of the sample, viewing the opening in the direction of the confinement 2 loading. Initially, fracturing took place in the lower block below the opening and as the axial stresses increased the fracturing migrated to the upper block. Figures A4.3.31 and A4.3.32 show the distributions of the seismic events recorded by the acoustic emission equipment. The distributions of energy released for the final load are shown in Figure A4.3.33 at three orthogonal planes in the centre of the sample.

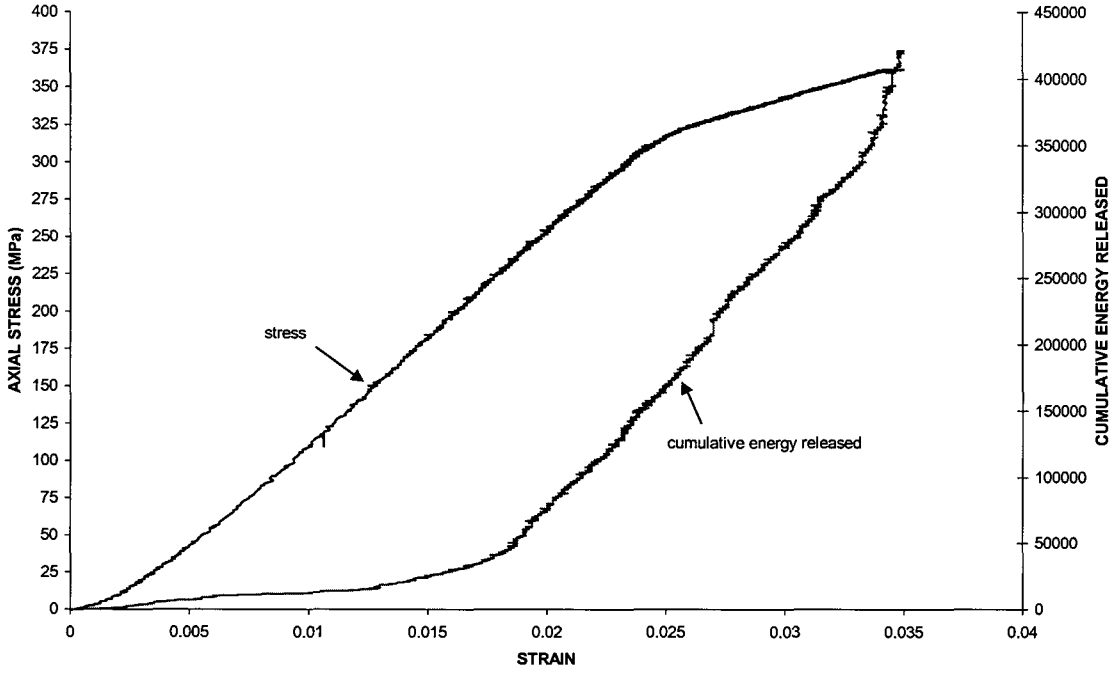

Figure A4.3.28 Axial strain versus axial stress and axial strain versus cumulative energy released for the thin slot experiment.

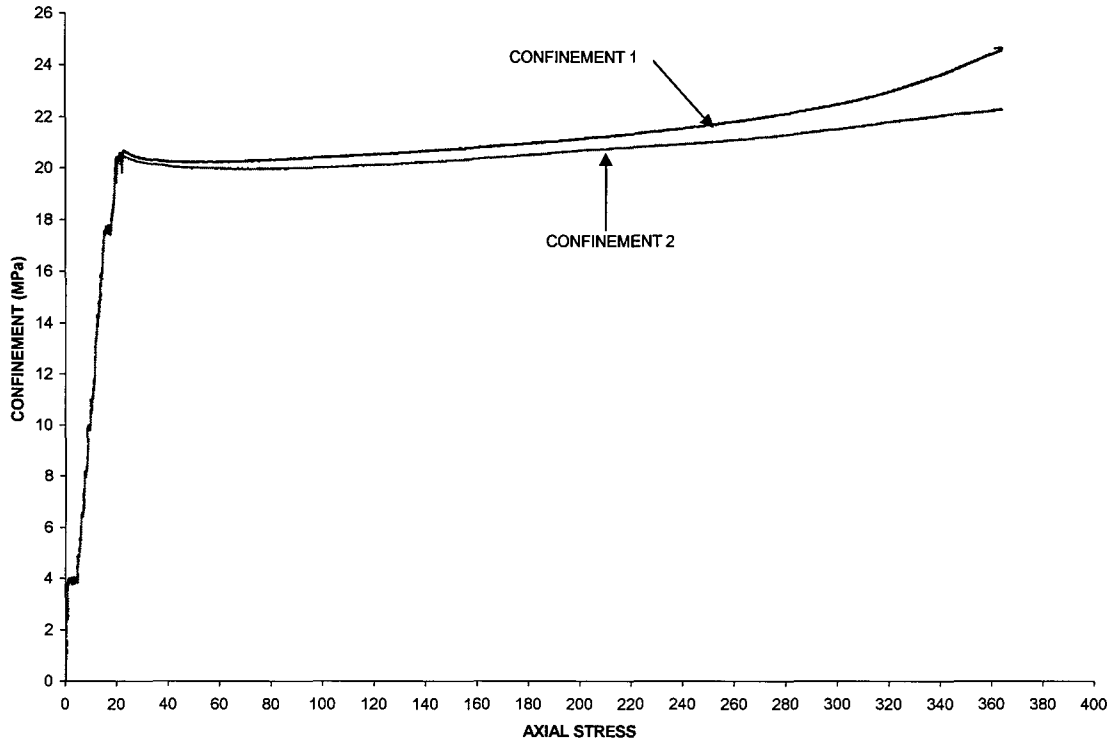

Figure A4.3.29 Axial stress versus confinement for the thin slot experiment.

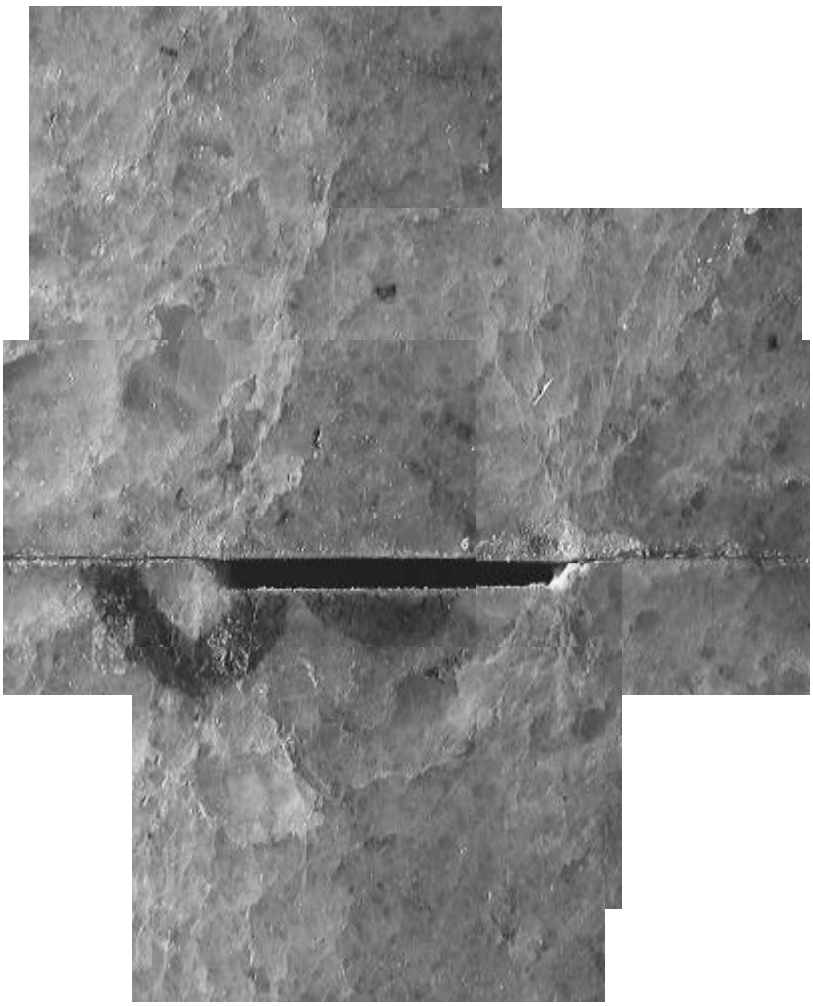

(a) Detail picture of fracturing around the narrow slot

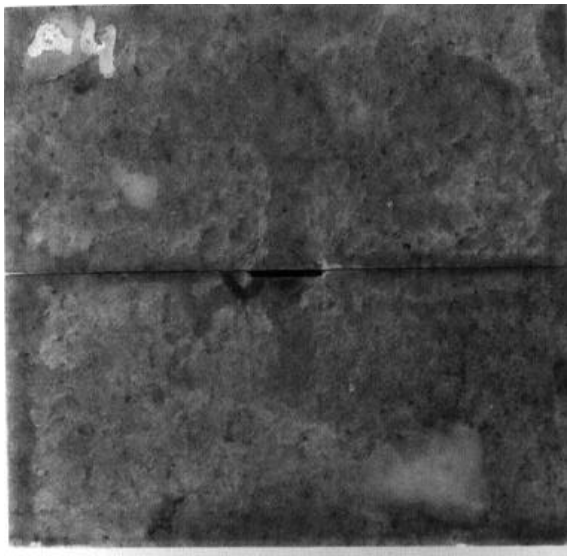

(a) Side view

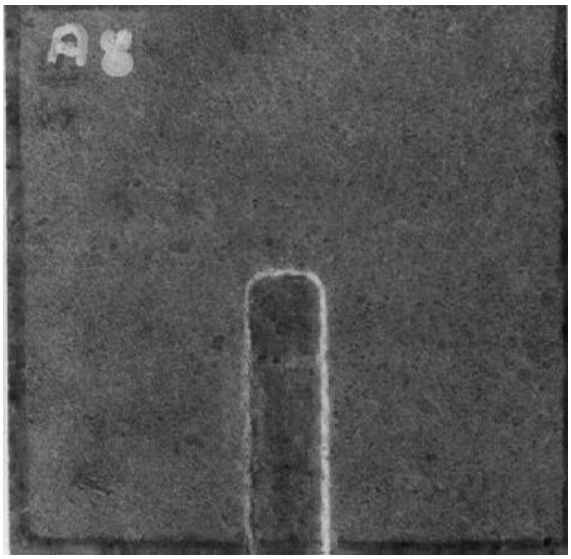

(b) Plan view of lower block

Figure A4.3.30 Laboratory results of the thin slot experiment.

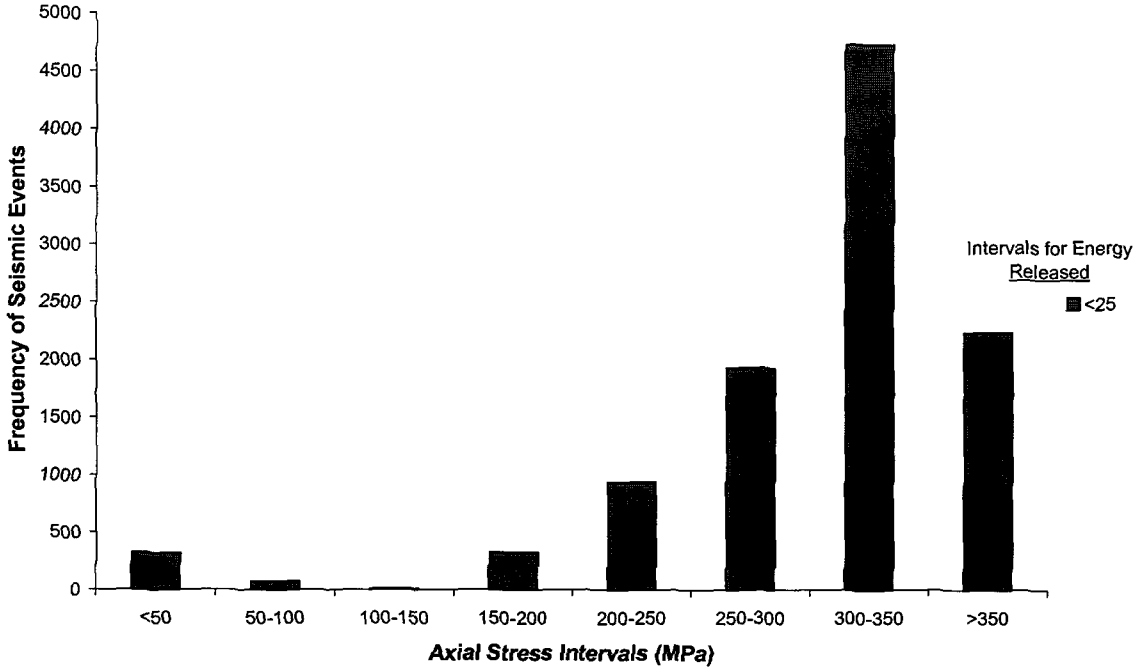

(a)

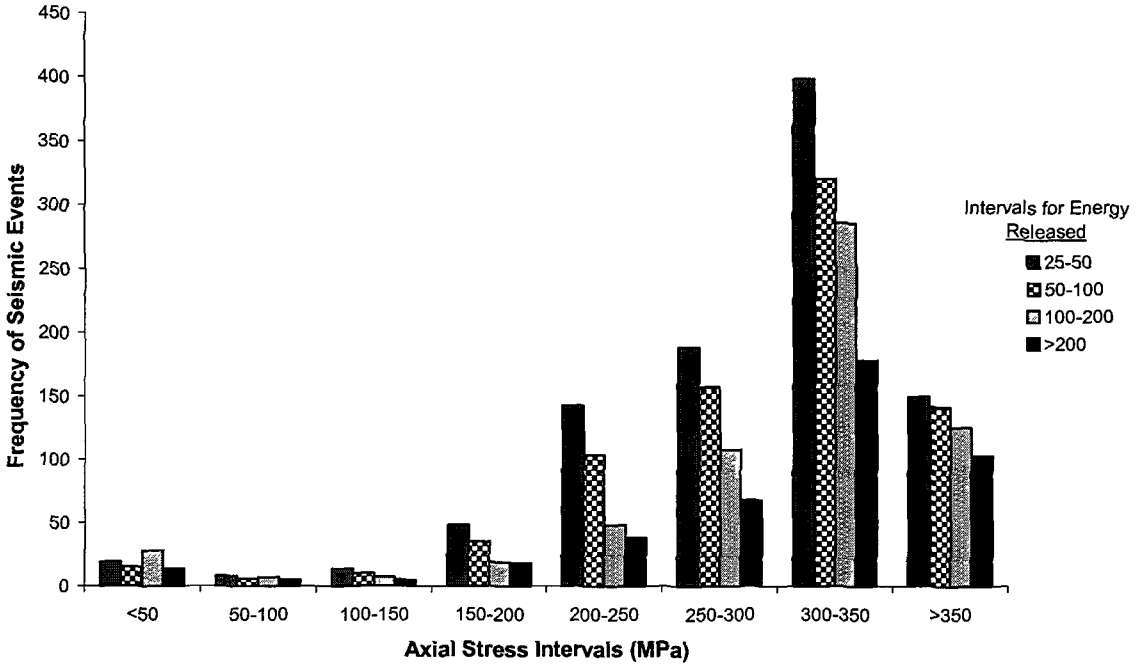

(b)

Figure A4.3.31 Frequency of seismic events as a function of axial stress and energy released for the thin slot sample ((a) the energy released value less than 25, (b) the energy released value greater than 25).

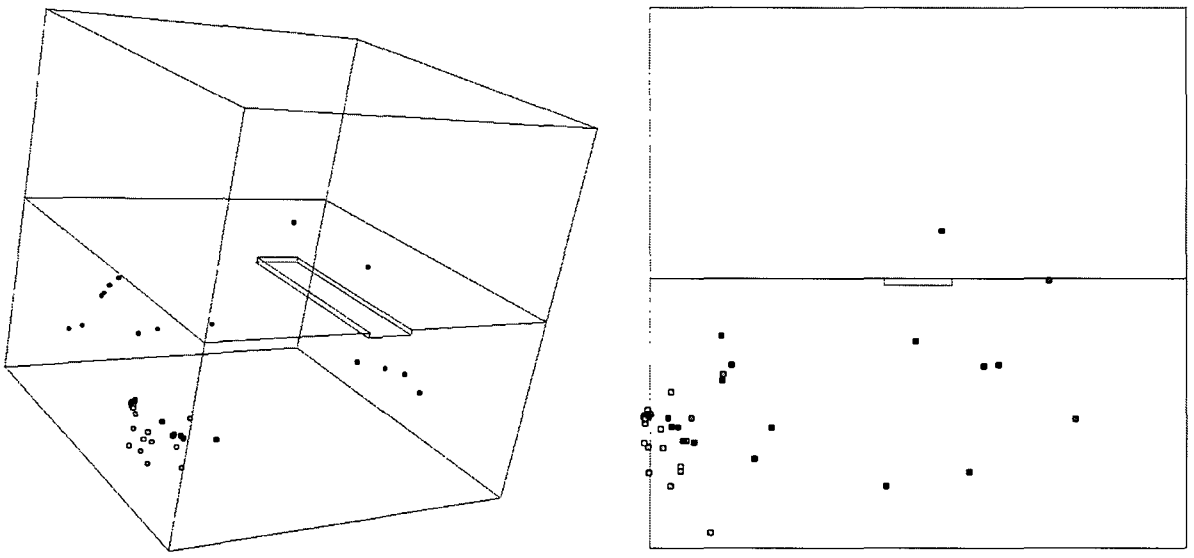

(a) Event locations at an axial stress level from 0 to 50 MPa,

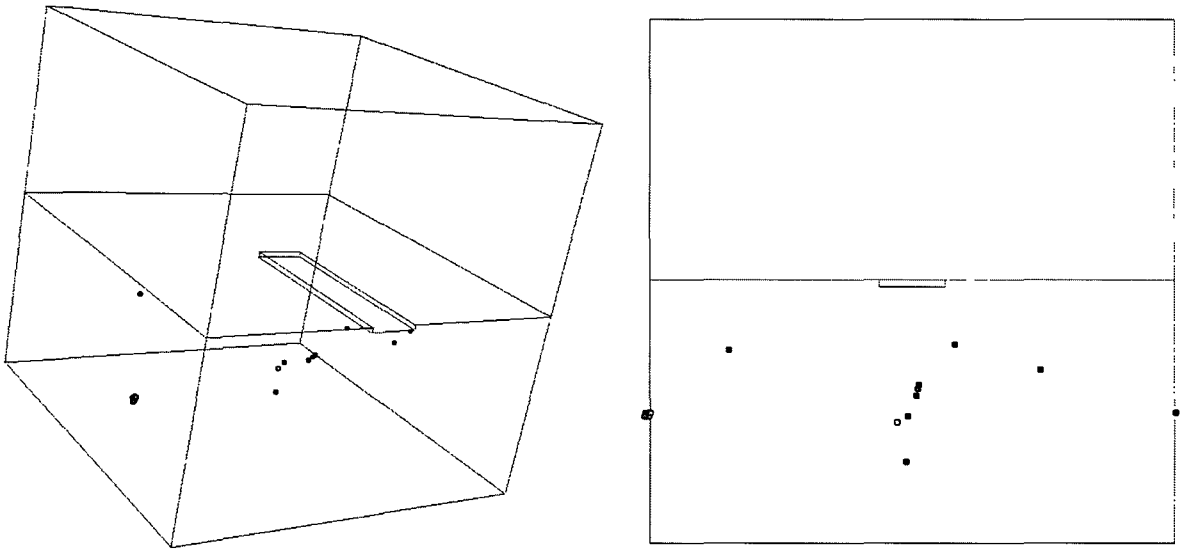

(b) Event locations at an axial stress level from 50 to 75 MPa,

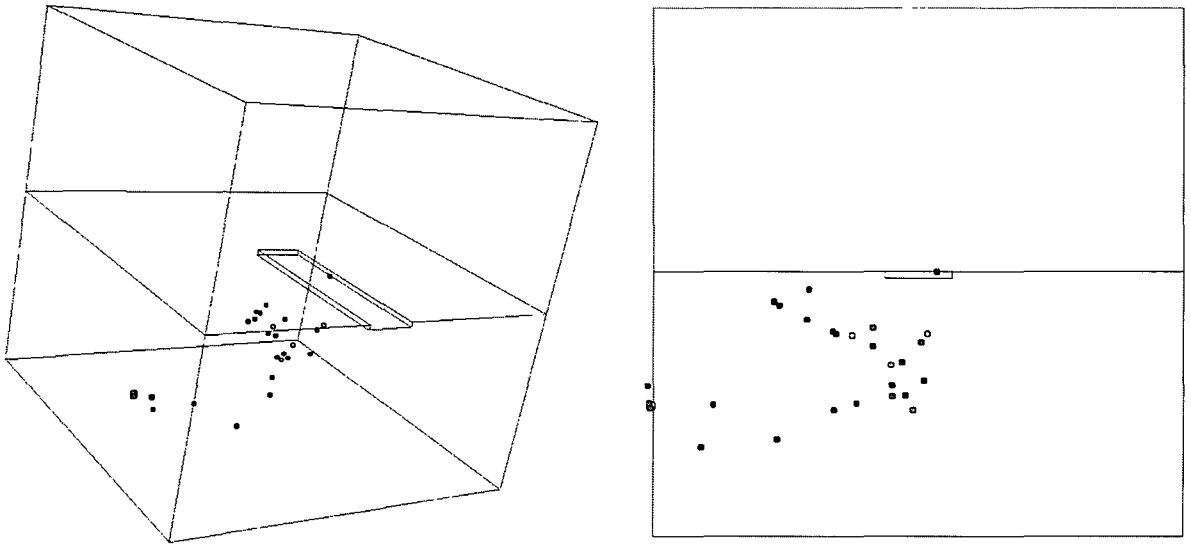

(c) Event locations at an axial stress level from 75 to 100 MPa,

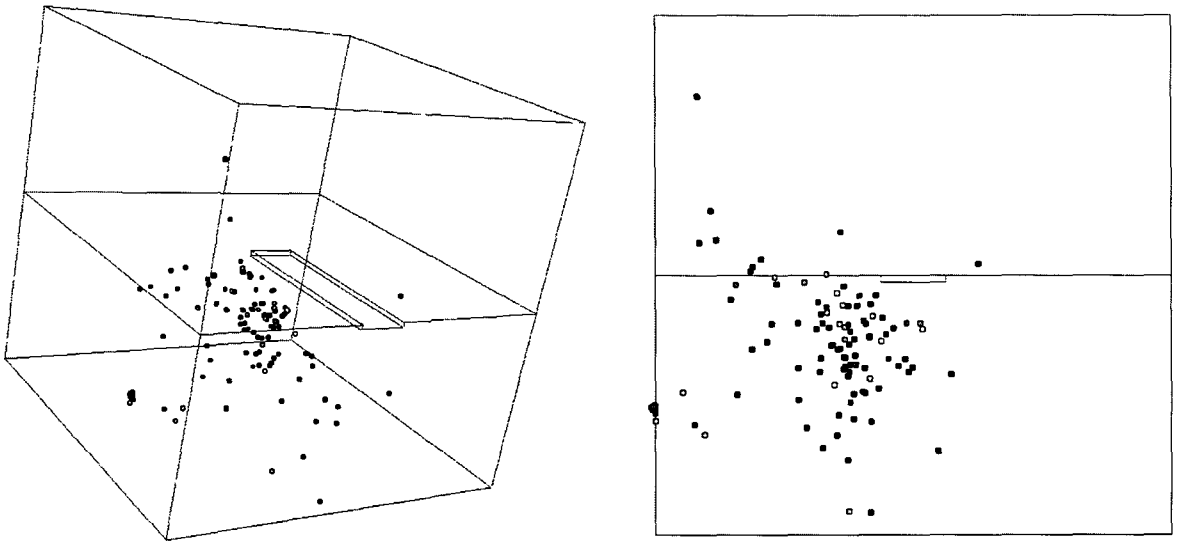

(d) Event locations at an axial stress level from 100 to 150 MPa,

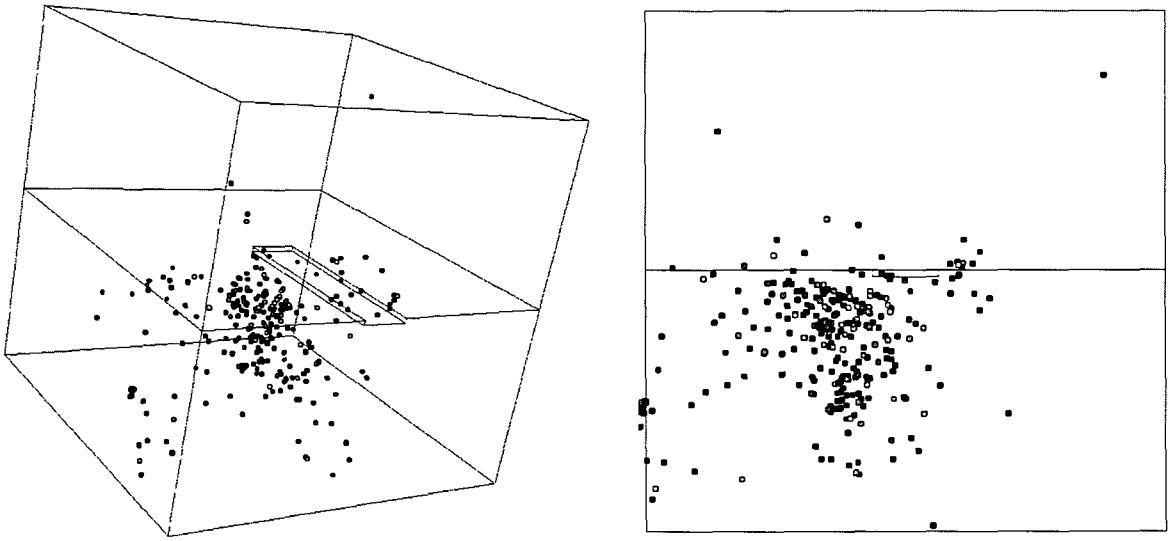

(e) Event locations at an axial stress level from 150 to 200 MPa,

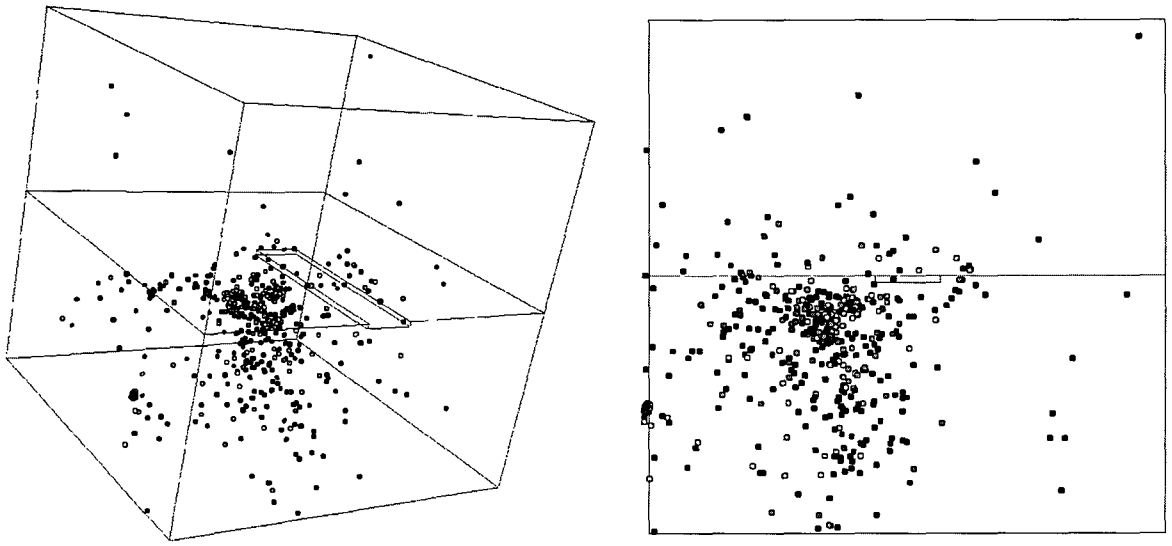

(f) Event locations at an axial stress level from 200 to 250 MPa,

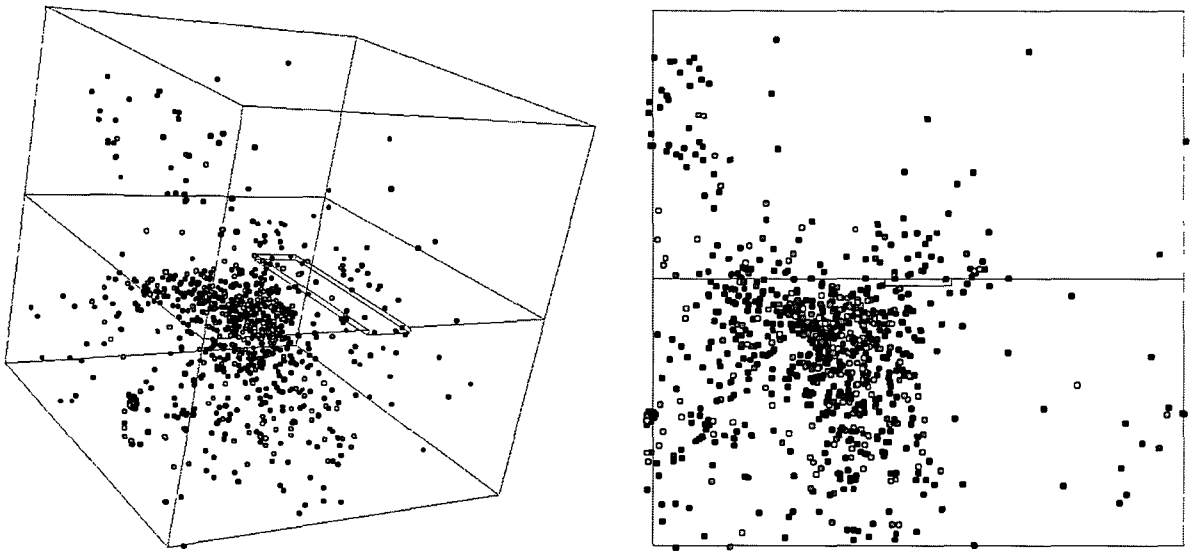

(g) Event locations at an axial stress level from 250 to 300 MPa,

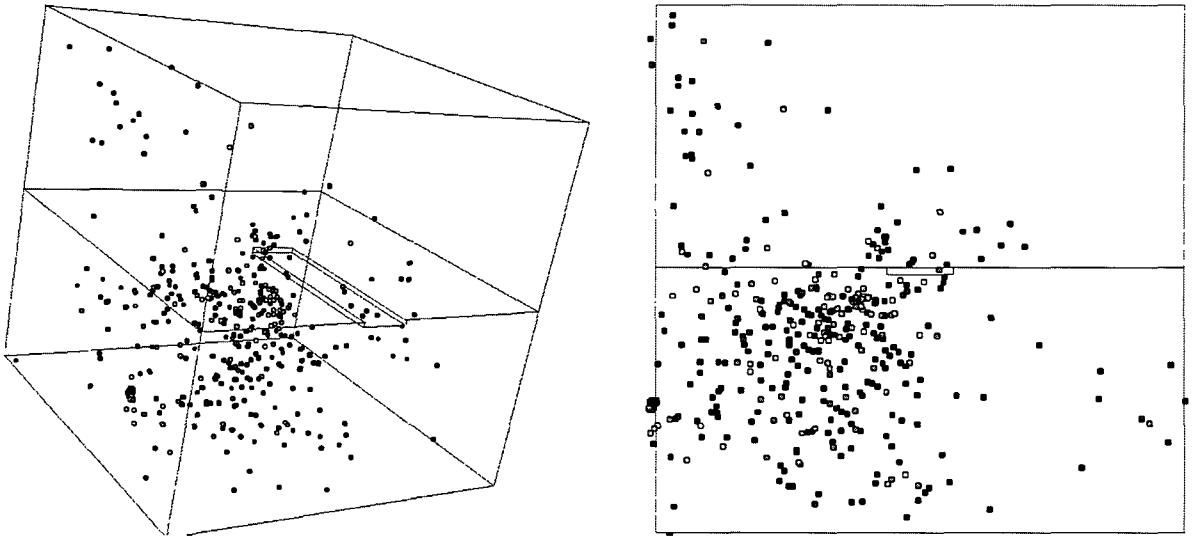

(h) Event locations at an axial stress level from 300 to 350 MPa,

Figure A4.3.32 Locations of events at different axial stress levels (only energy released values greater than 30 are illustrated).

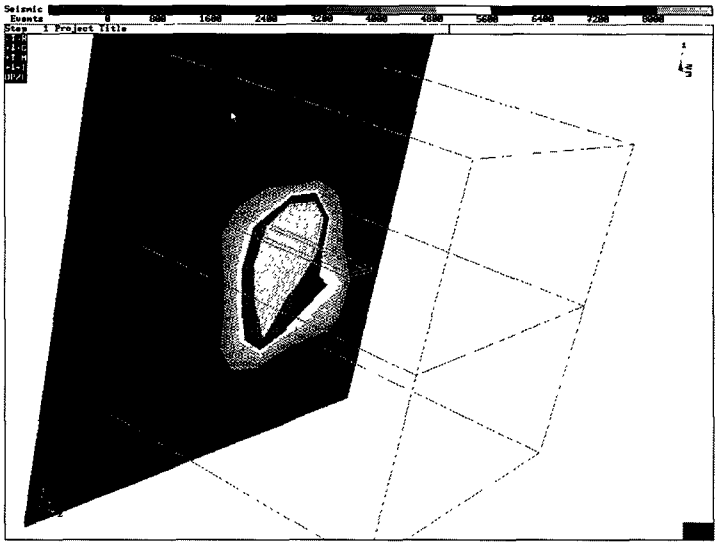

(a)

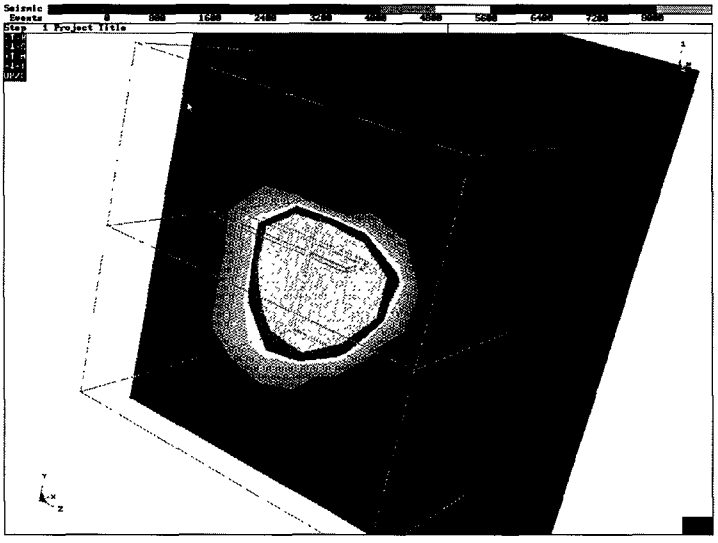

(b)

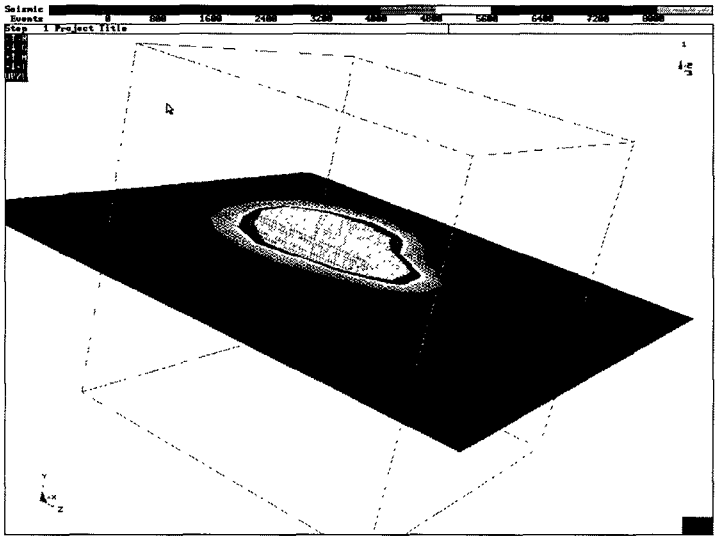

(c)

Figure 4.3.33 Energy released distributions at three orthogonal planes.

A4.3.3 References

Napier, J.A.L., 1998. Three-dimensional modelling of seismicity in deep level mines. *Proceedings of Conference on Mechanics of Jointed and Faulted Rock.* 709-715. Vienna, Balkema, Rotterdam.

Wiles, T. 1996. MAP3D User's Manual. Mine Modelling Limited, Canada.

Appendix 4.4

Studies of the fracture zone surrounding deep level stopes

A4.4.1 Introduction

The prediction of the development of the fracture zone around deep level stopes has been the goal of rock engineering research in the South African gold mining industry for a number of years. Crucial to any of the rock engineering strategies proposed for safe and efficient mining of ultradeep orebodies is the ability to predict the response of the rock mass to a planned mining layout (Gay et al., 1995). For example, the design of effective support systems depends on the fracture directions and spacing in the hangingwall, which in turn are influenced by the rock properties and the geological structures in a particular geotechnical area (Schweitzer and Johnson, 1996). The development of the fracture pattern around the stope and the seismicity associated with mining is also influenced by the primary geological structures, such as faults and dykes, in the vicinity of the stope (e.g. Legge and Spottiswoode, 1987). Monitoring of the seismicity can possibly identify potential hazards once mining has started, however the evaluation of alternative mining strategies requires the ability to simulate the development of the fracture zone in a given geological environment.

Elastic modelling of mine excavations has been successfully implemented in two and three-dimensional boundary element programs such as DIGS (Napier, 1990) and MINSIM (Napier and Stephansson, 1987). Correlation of observed stope closures with numerical results can be obtained if the damage due to the fracture zone is represented by reducing the Young's Modulus of the rock mass by about 40 to 50 per cent (Gurtunca and Adams, 1991). Regions of high stress and hence potential failure can be indicated using the excess shear stress concept, but the elastic models cannot include the stress re-distribution associated with the development of the fracture zone as mining progresses (Legge and Spottiswoode, 1987).

Elastic modelling techniques are useful for overall mine planning, but their inability to predict the fracture direction and frequency is a shortcoming for the prediction of hangingwall conditions and design of support at the scale of a single excavation. The past few years have seen a number of advances towards this goal. Plasticity and ubiquitous joint models suggest that most deformation occurs at the stope face (Kuijpers and Napier, 1991) and do not predict the formation of fracture bands ahead of the stope, as observed in underground studies (Adams et al., 1981). Discrete element methods can cope with large numbers of blocks arising from a complex jointing pattern in a rock mass. The mining induced fracturing can be modelled as sets of initially welded discontinuities, at pre-defined angles, which activate ahead of the excavation as mining progresses (Lightfoot et al., 1994). A mechanism for fracture initiation ahead of the face was postulated by allowing for activation of bedding planes ahead of the stope face (Napier and Hildyard, 1992). The discrete fracture growth concept was incorporated in the DIGS boundary element program. A solution to the problem of requiring explicit fracture initiation points has been proposed (Napier and Peirce, 1995) in which the region of interest is covered by a random mesh, or tessellation, of potential fractures. In addition, large scale problems, involving thousands of crack segments, can be analysed using a special method of influence transmission termed the multipole method (Peirce and Napier, 1995). Tessellation models have been applied in studies of micro-mechanics of fracture in laboratory tests

(Sellers and Napier, 1997) as well as mine models with the stope modelled as a single slit (Malan and Napier, 1997).

The tessellation method has been further developed for modelling large scale mining simulations with a finite stope width, and a method for selection of the multipole parameters for the most efficient memory allocation has been developed. The ability of the tessellation approach to model fracturing around stopes in various geotechnical environments is demonstrated with examples of Carbon Leader stope. This appendix sets out the results of the stope modelling performed during the course of the project. The figures are described briefly. Further analysis and interpretation of the work is provided in the main document.

A4.4.2 Stope fracture models and the multipole method

A considerable step towards the possibility of predicting the fracture directions around stopes was achieved using the concept of discrete fracture growth in the boundary element program DIGS (Napier, 1990). A mechanism for fracture initiation ahead of the face was postulated by allowing for activation of bedding planes ahead of the stope face (Napier and Hildyard, 1992). The success of the discrete fracture growth models has been limited by the need to choose the position of the seed points from which the fractures initiate and the computational effort required for searching for each crack direction at each crack increment. The choice of fracture growth mode is also left to the user to decide and can considerably alter the fracture pattern (Figure A4.4.2.1)

The problems of pre-selection of fracture initiation sites and computational effort required for modelling discrete fracture growth are compounded by the possibility of numerical instabilities arising from the linking of cracks at small angles, and the insertion of very small elements at crack intersection points. These shortcomings led to the development of the tessellation approach in which the region of interest is covered by a random tessellation of inactive elements. Fractures form in the model when induced stresses on crack segments exceed a specified failure criterion. The linking of preferentially aligned segments provides an approximation of a discrete fracture path. The segment lengths and angles of intersection are controlled by the choice of tessellation pattern (Figure A4.4.2.2). Applying a Delaunay or Voronoi triangulation scheme can control the numerical instabilities arising from the intersections of cracks at small angles. The models of fracturing around stopes use tessellations based on the Delaunay triangulation scheme.

The number of elements that can be solved using the multipole method and with given memory and a given average triangulation size is still limited. If all the elements are immediately included in the solution, the size of the tessellated region and the multipole grid must be carefully selected. The only alternative for saving memory is to reduce the size of the pad region, resulting in lower accuracy of the solution. However, when modelling the progressive excavation of a tabular stope, it is possible to include in the solution only crack elements that have been activated. The fracture patterns depends to some extent on the size of the tessellation selected for the analysis. As shown in Figure A4.4.2.3, the finer tessellation produces a more distinct fracture pattern. The type of fractures appear to depend on the rock fabric and therefore the finer grid may be more suited to the modelling of the siliceous quartzites, and the more coarse patterns may be required for argillaceous materials.

Three schemes have been developed to permit sequential activation of elements (Sellers and Napier,1997, Sellers, 1997). The first method involves an incremental activation procedure, in which the crack having a stress state, which is furthest beyond the failure limit, is activated and the problem is solved again. This sequence of crack activation and solution continues until there are no more elements with stress states beyond the failure limit (Figure A4.4.2.4a). The second method is a parallel activation procedure and all elements, which are outside the failure envelope, are activated simultaneously, the problem solved and then the next mining step is made (Figure

A4.4.2.4b). Thirdly, the parallel activation sequence is extended so that once the first set of fractures has been activated, and the solution determined, the stress is redistributed into the unfractured regions, and may cause failure of another set of fractures. This process continues a number of times before the fracture pattern stabilizes (Figure A4.4.2.5). The Mohr-Coulomb failure criterion is applied at each collocation point in each element, the shear and normal stress being calculated in the local co-ordinate system of the element. The element activates when the driving shear traction exceeds the shear resistance, calculated using the cohesion C and the friction angle ϕ. After activation, the element is assigned the specified mobilized friction angle ϕ_m, dilation angle φ_m, and cohesion S_o.

The incremental activation procedure requires a considerable amount of solution time, as the problem must be solved again after every fracture activation increment. As the stope length increases, this can require hundreds of solutions per mining step. Fortunately, the addition of a single element does not alter the equilibrium significantly and each solution converges in a few iterations.

The parallel activation rule requires only one solution cycle per mining step, but leads to a significantly different fracture pattern. The fractures generally occur in the same regions around the stope as in the case of incremental activation. However, the fracturing is more diffuse and occurs in larger zones of activated elements (compare Figures A4.4.2.4a and b). The fractures in the hangingwall do not extend across the entire beam. Few fractures form ahead of the face. An analysis with residual cohesion on the activated fractures resulted in slightly more distinct fracture zones but did not cause fractures to form ahead of the face.

	C	ϕ	ϕ_m	T	G M
HW	10	43	25	1	S
PP 2		10	5		
FW	10	43	25	1	S
PP 1,3,4,5		5	2		

a:

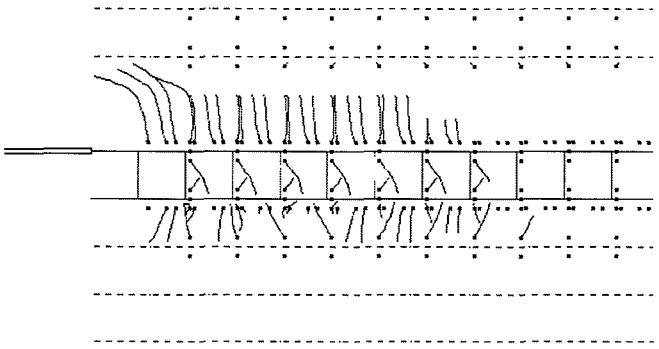

	C	ϕ	ϕ_m	T	G M
HW	18	52	30	5	T
PP 2		10	5		
FW	10	43	25	1	T
PP 1,3,4,5		5	2		

b:

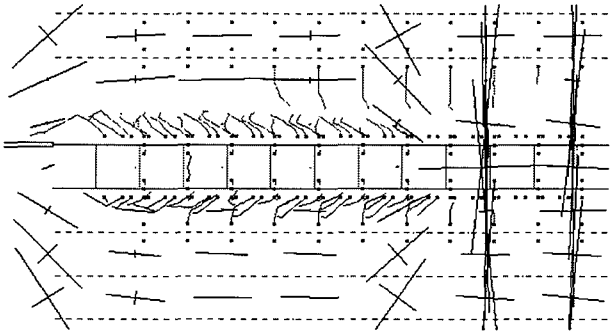

	C	ϕ	ϕ_m	T	G M
HW	18	52	30	5	S
PP 2		10	5		
FW	10	43	25	1	S
PP 1,3,4,5		5	2		

c:

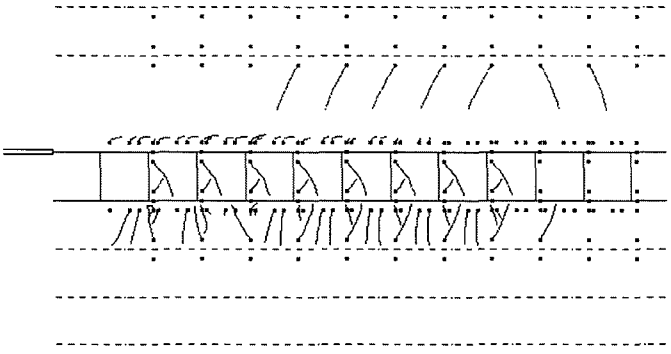

Figure A4.4.2.1 Modelling of a Carbon Leader stope with the standard DIGS discrete fracture growth rule. a: shear S growth mode cracks, b: tension T growth mode c: shear S growth mode with different material in the hangingwall and the footwall. (stope width 1 m)

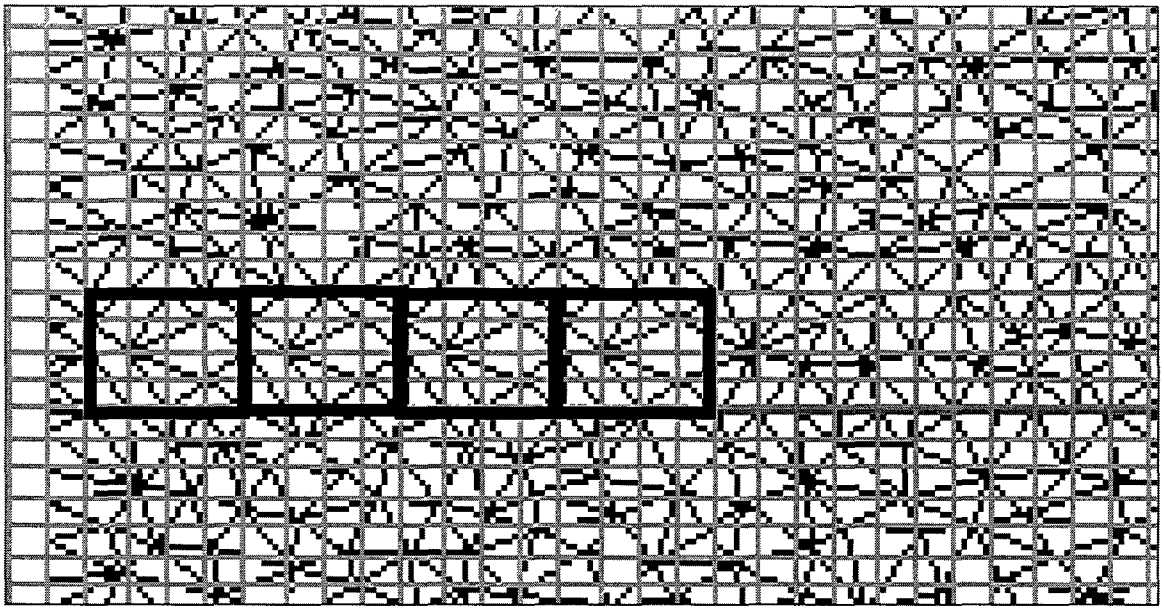

Figure A4.4.2.2 A detail of a tessellation showing the stope, mining steps and the multipole grid.

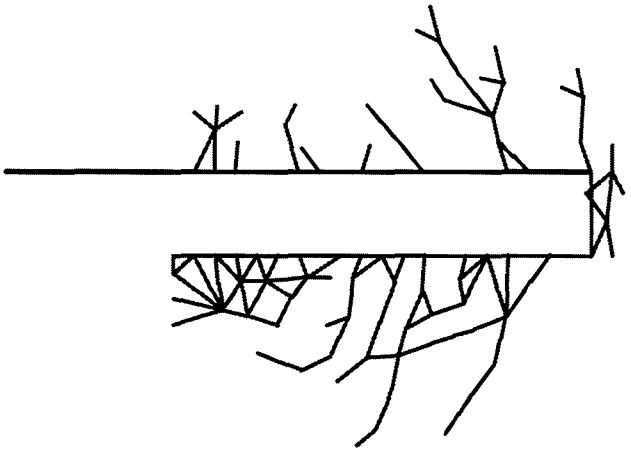

a:

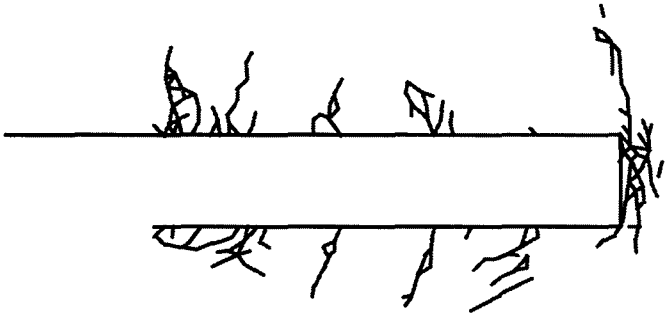

b:

Figure A4.4.2.3 Effect of tessellation size on predicted fracture pattern around a stope (stope width 1 m). a: 0,25m tessellation b: 0,1m tessellation grid size.

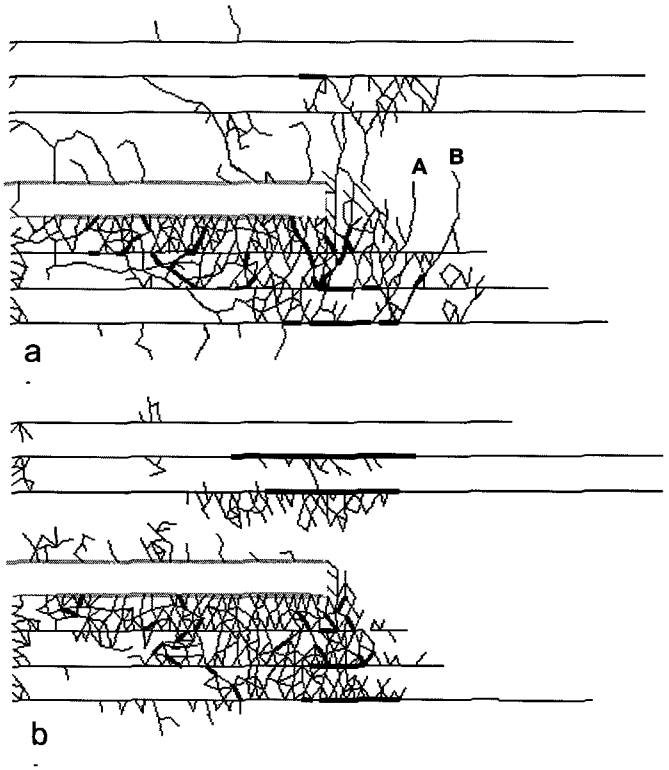

Figure A4.4.2.4 Influence of activation rule on the fracture pattern. a: Incremental activation, b: Parallel activation.

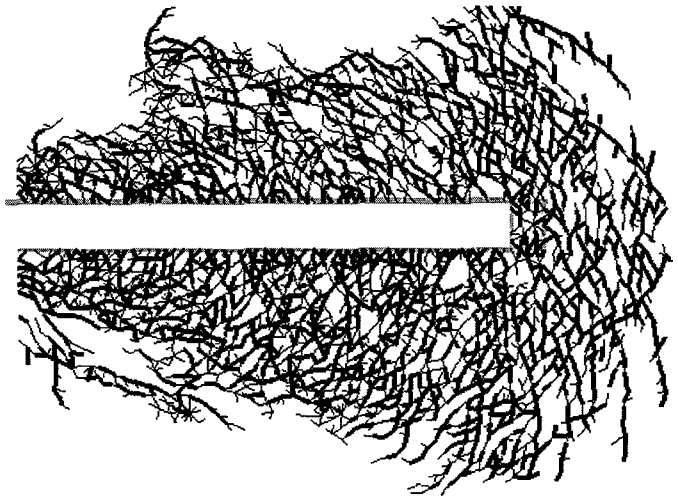

Figure A4.4.2.5 Fracture pattern in a homogeneous rock mass using parallel activation and permitting a number of increments for stress redistributions. (stope width 1,5 m)

A4.4.3 Effect of different material responses

The effect of a variable rock mass strength was investigated by dividing a square tessellation into a series of 0,5 m strips, dipping at 80 degrees, as shown in Figure A4.4.3.1. When the entire rock mass is given the same material properties, the pattern is as shown in Figure A4.4.3.2. The reduction in strength of the strips leads to a failure of the weakest strip after nine mining steps. This is equivalent to the failure of altered materials along a dyke interface and demonstrates that the tessellation approach is able to capture the effect of different rock strengths.

An incremental analysis was performed for a stope, with the material properties given in Table A4.4.3.1, corresponding to the Carbon Leader reef. The fracture pattern after fourteen mining steps is shown in Figure A4.4.3.4. This corresponds to the patterns reported from fracture mapping studies in Carbon Leader stopes (Adams et al., 1981; Brummer and Rorke, 1984). The dilation in the rock can be quantified by considering the relative displacements of three sets of grid points, 0,5 m apart, similar to the calculation of dilation from measurements between extensometer anchor points (Legge, 1986). The first set is situated 0,5 m into the hangingwall, the second is at the centre of the reef, and the third is 0,5 m into the footwall. Figure A4.4.3.5 shows the deformation increments between adjacent grid points. The vertical stress distributions for the same set of grid points are shown in Figure A4.4.3.6. The horizontal stresses, shown in Figure A4.4.3.7, reduce within the fracture zone, and are slightly compressive in the hangingwall, as observed by Squelch (1990). The closure profiles after ten and fourteen mining steps are shown in Figure A4.4.3.8.

The cohesion applied in the analysis of Figure A4.4.2.4 and given in Table A4.4.3.1 had been reduced to 30 per cent of the laboratory values to simulate in situ properties. The analysis was then performed using the laboratory values of cohesion and the fracture pattern is given in Figure A4.4.3.9. The fractures initiate ahead of the stope, and often grow from the first parting towards the stope, as in the mechanism postulated by Napier and Hildyard (1985). The details of the fracture pattern for the final span of 31m are shown in Figure A4.4.3.10 and the stress state is shown in Figure A4.4.3.11. The dilation of the hangingwall, reef and footwall, calculated from grid points representing extensometers , is shown in Figure A4.4.3.12. The distribution of dilation between grid points is given in Figure A4.4.3.13. The values can not be directly compared with measurements e.g. those by Legge (1985) since the underground measurements relate to a mature stope with a span of 480m. The change in the angle of the principal stress for the hangingwall, reef and footwall is shown in Figure A4.4.3.14. The vertical and horizontal stress distributions for the situations with in situ and laboratory properties are shown in Figure A4.4.3.15 and Figure A4.4.3.16. As the fracturing extends 6m ahead of the face, in the case with in situ material properties, and only 1m ahead of the face in the model, using laboratory material properties, these two figures can be used to compare the stress states due to different amounts of fracturing ahead of the face. The case with more fracturing shows a lower stress further ahead of the face.

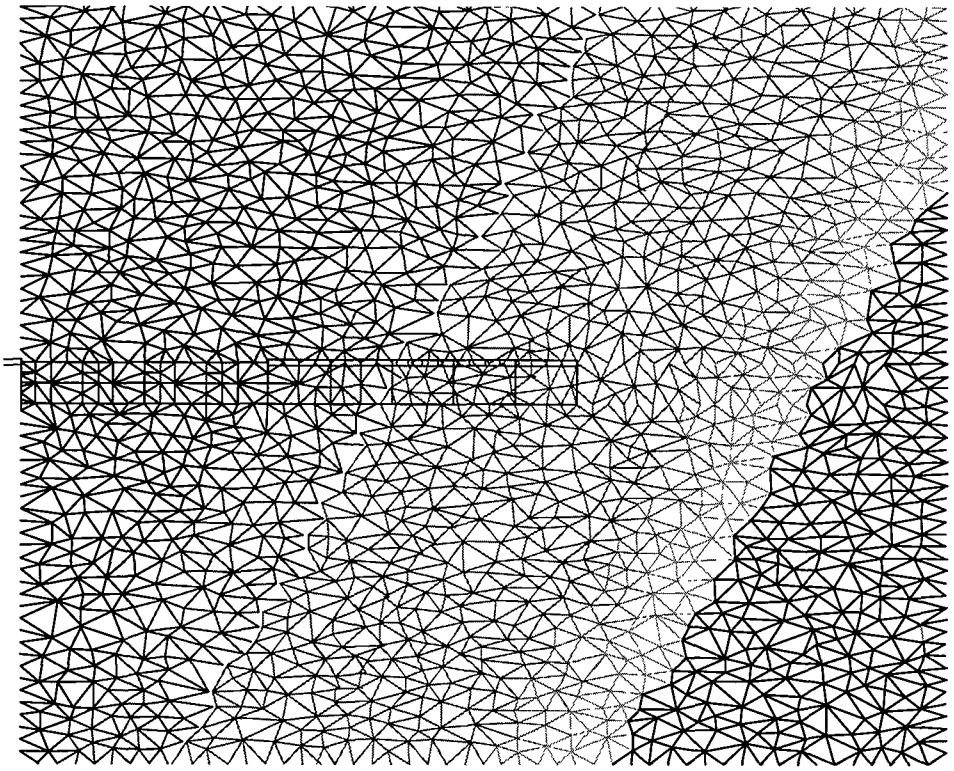

Figure A4.4.3.1 A tessellation with layers of different strength, simulating the degradation in strength towards a dyke or fault. Triangular regions, at top left and bottom right, have the same (high) strength. The strength of the layers decreases in 0.5 m steps towards right.

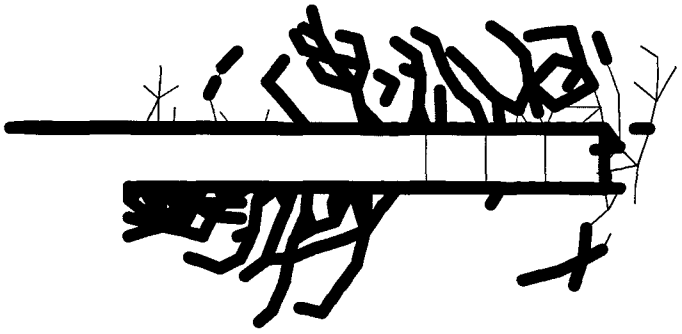

Figure A4.4.3.2 The fracture pattern arising from the tessellation in Figure A4.4.3.1 assuming uniform rock mass strength

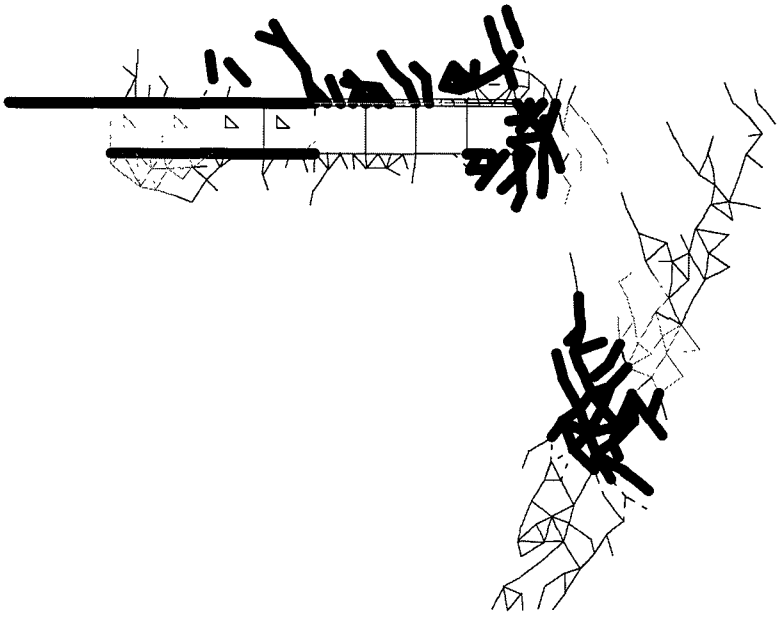

Figure A4.4.3.3 The fracture pattern arising from the tessellation in Figure A4.4.3.1 assuming decreasing rock mass strength

Table A4.4.3.1 Material properties for Carbon Leader rocks calculated from laboratory tests (Briggs, 1982) with the UCS reduced to 30% for calculation of the in-situ cohesion

Rock type	UCS	In-situ cohesion	Friction angle		tensile strength
	MPa	MPa	initial	mob	MPa
Hangingwall Quartzite	320	18	52	30	5
Footwall Quartzite	200	18	43	25	5
Greenbar	180	18	32	20	5

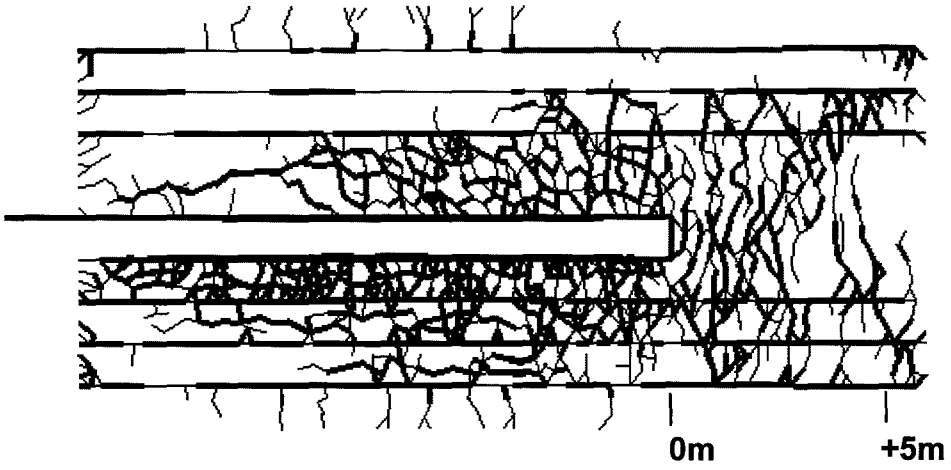

Figure A4.4.3.4 Fracture pattern around Carbon Leader stope after 14 mining steps. Fracture properties given in Table A4.4.3.1.

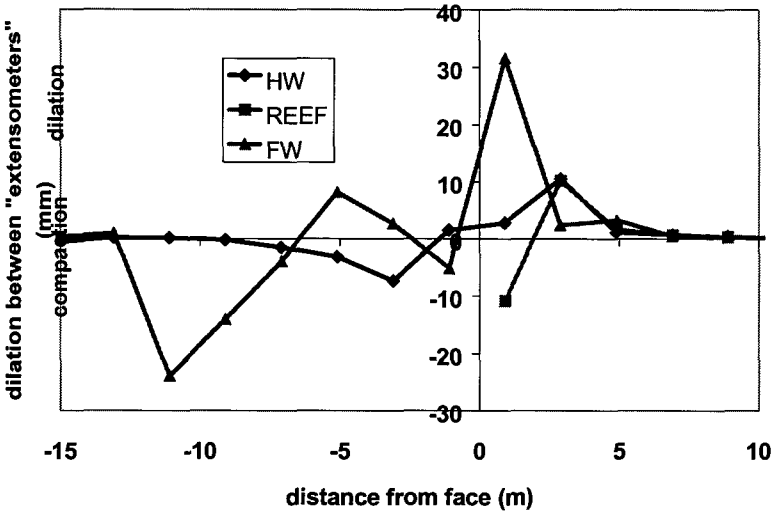

Figure A4.4.3.5 Dilation between grid points in hangingwall, reef and footwall of a simulated Carbon Leader stope.

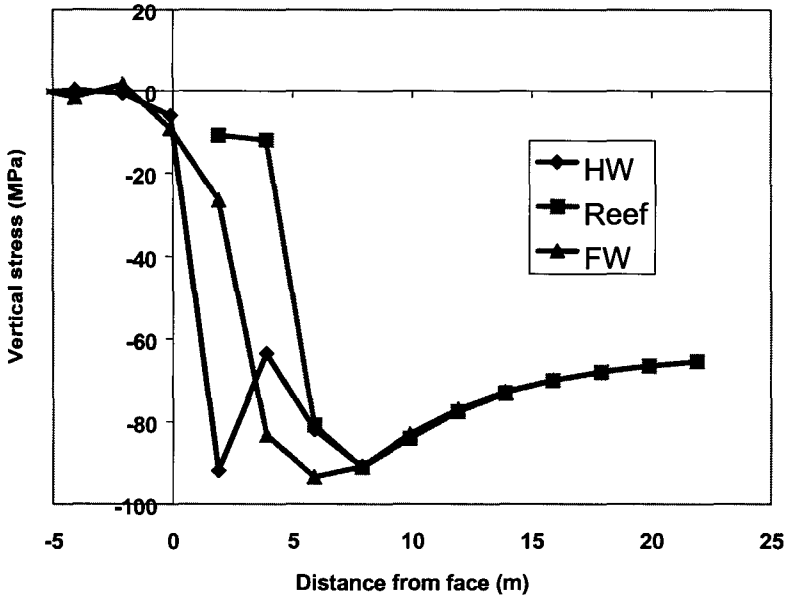

Figure A4.4.3.6 Vertical stress calculated at grid points in hangingwall, reef and footwall of a simulated Carbon Leader stope

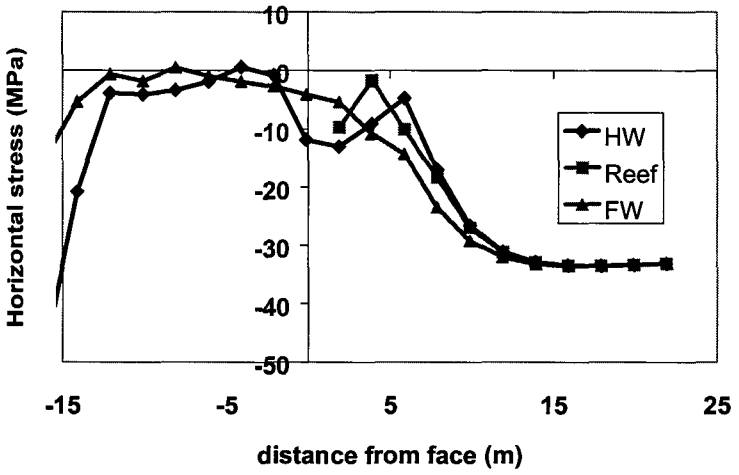

Figure A4.4.3.7 Horizontal stress calculated at grid points in hangingwall, reef and footwall of a simulated Carbon Leader stope

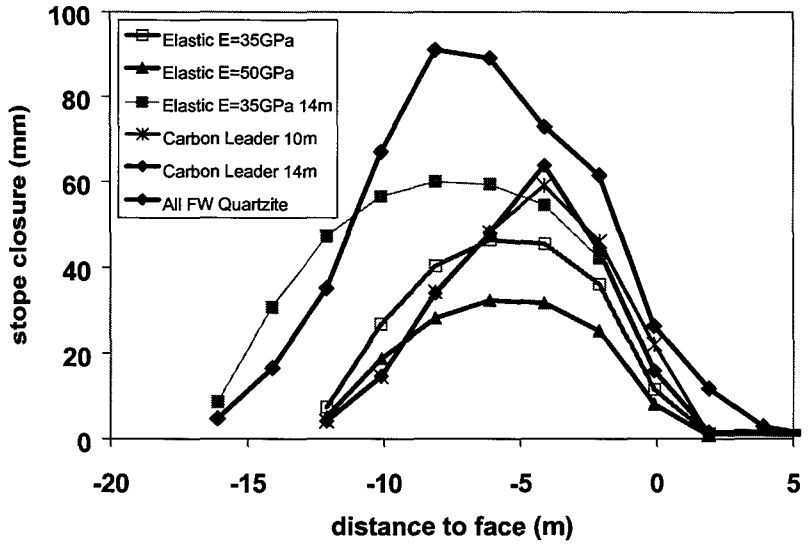

Figure A4.4.3.8 Stope closure calculated between grid points in hangingwall and footwall of a simulated Carbon Leader stope

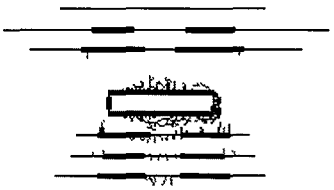

a:

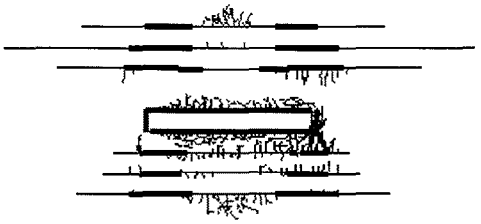

b:

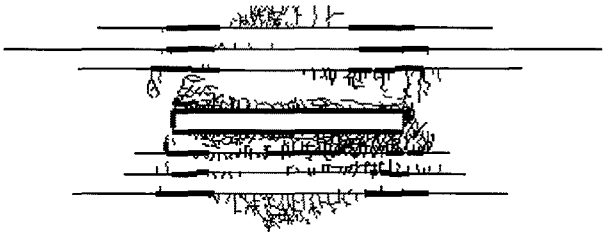

c:

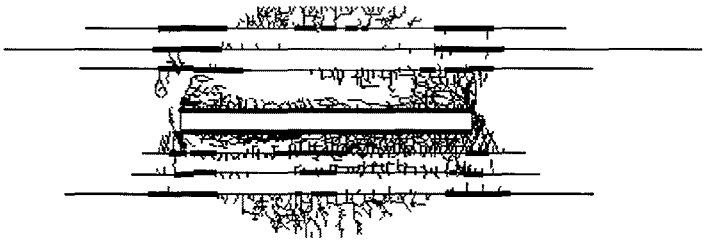

d:

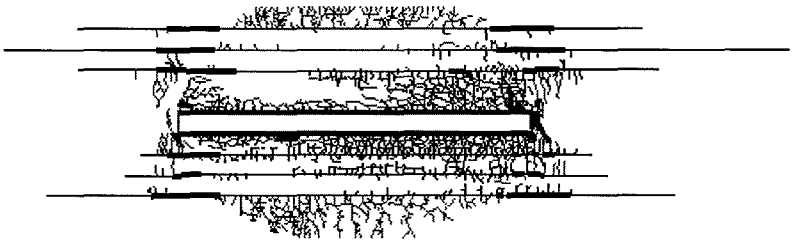

e:

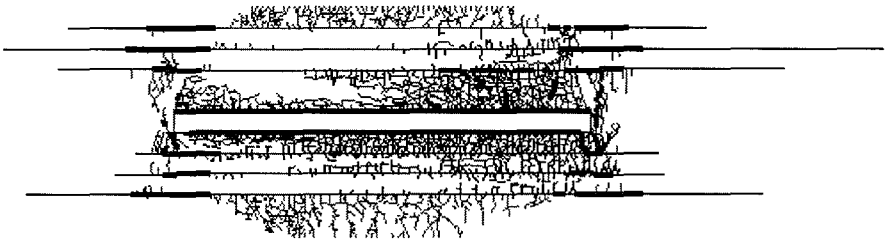

f:

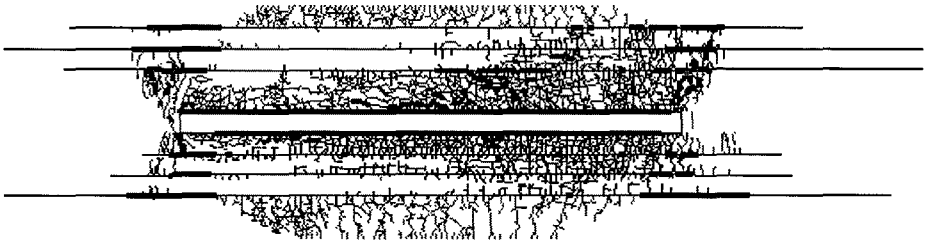

g:

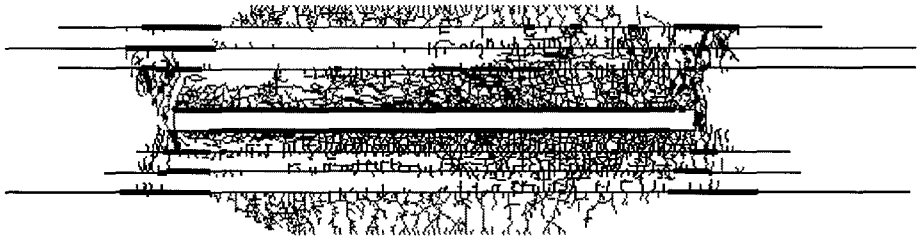

h:

Figure A4.4.3.9 Simulation of the development of fracture pattern around a Carbon Leader stope (laboratory material properties). a: 5m span, b: 7m span, c: 11 m span, d: 14 m span, e: 1 7m span, f: 20 m span, g: 24 m span, h:25 m span.

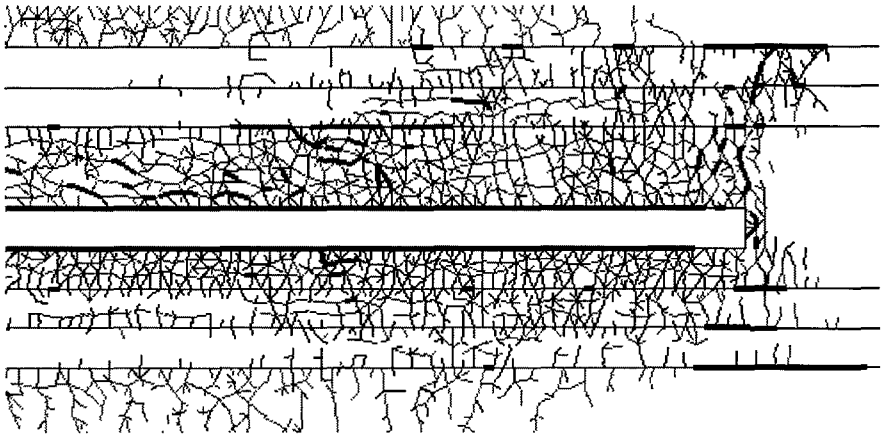

Figure A4.4.3.10 Detail of fracture pattern around the stope face, in a simulation of the development of fracture pattern around a Carbon Leader stope. (at a span of 25 m)

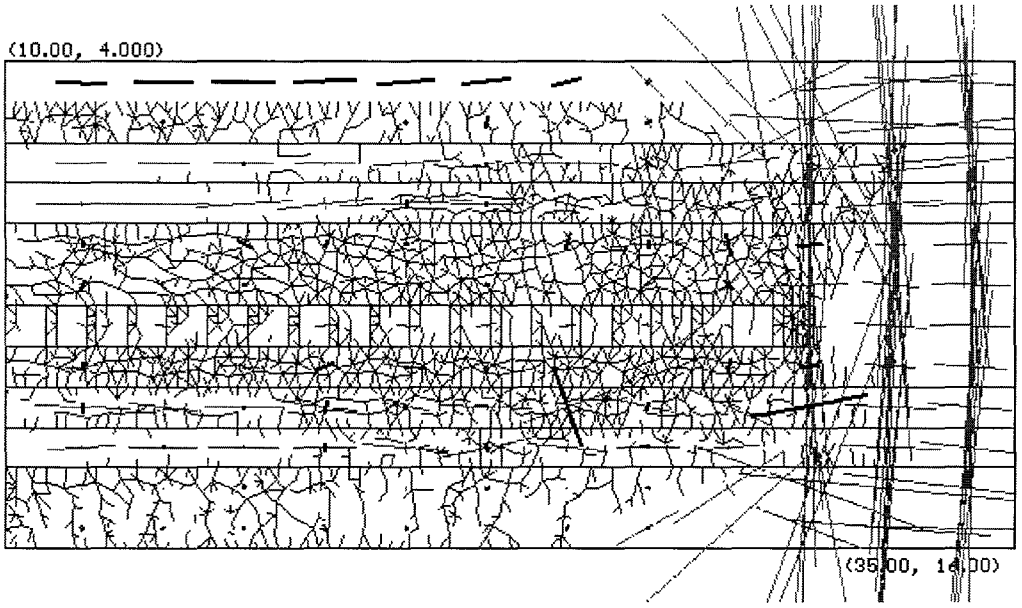

Figure A4.4.3.11 Detail of fracture pattern and stress state around the stope face, in a simulation of the development of fracture pattern around a Carbon Leader stope. (at a span of 25 m)

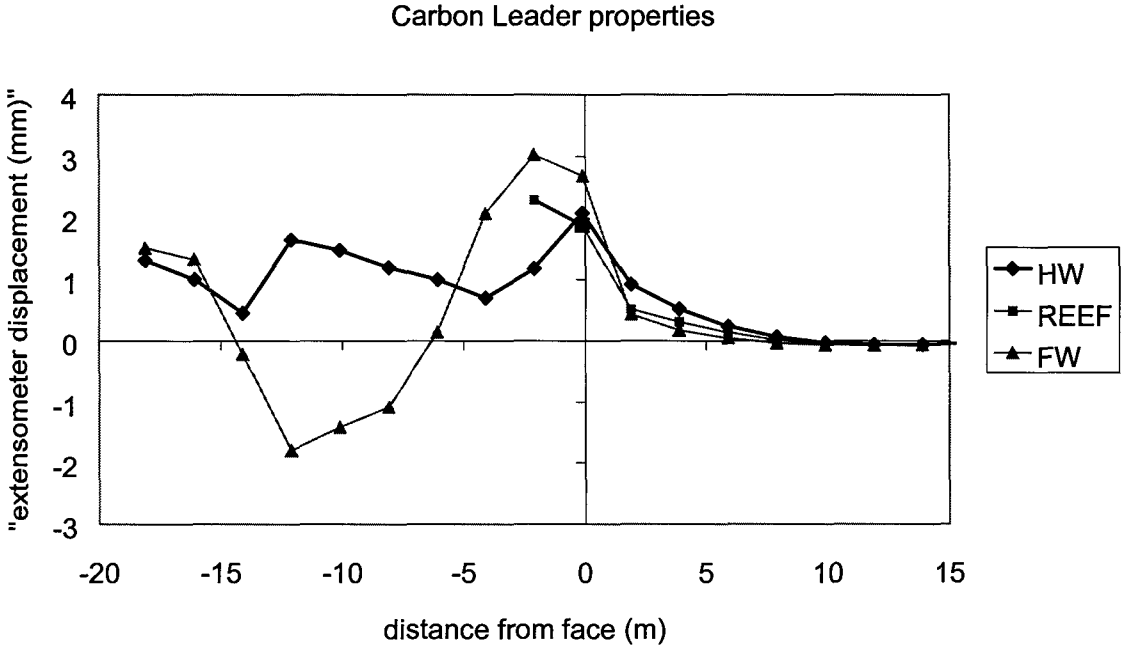

Figure A4.4.3.12 Calculated extensometer displacement in stope models with flat parting planes and laboratory material properties, at a span of 14 m.

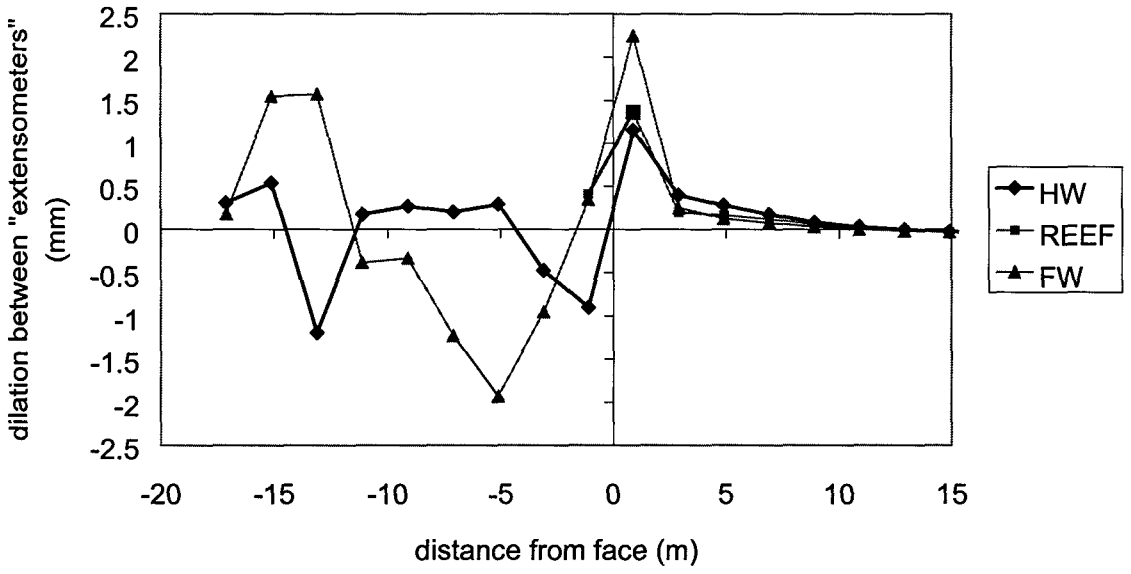

Figure A4.4.3.13 Distribution of calculated dilation between extensometer grid points for a stope model with flat parting planes and laboratory material properties, at a span of 14 m.

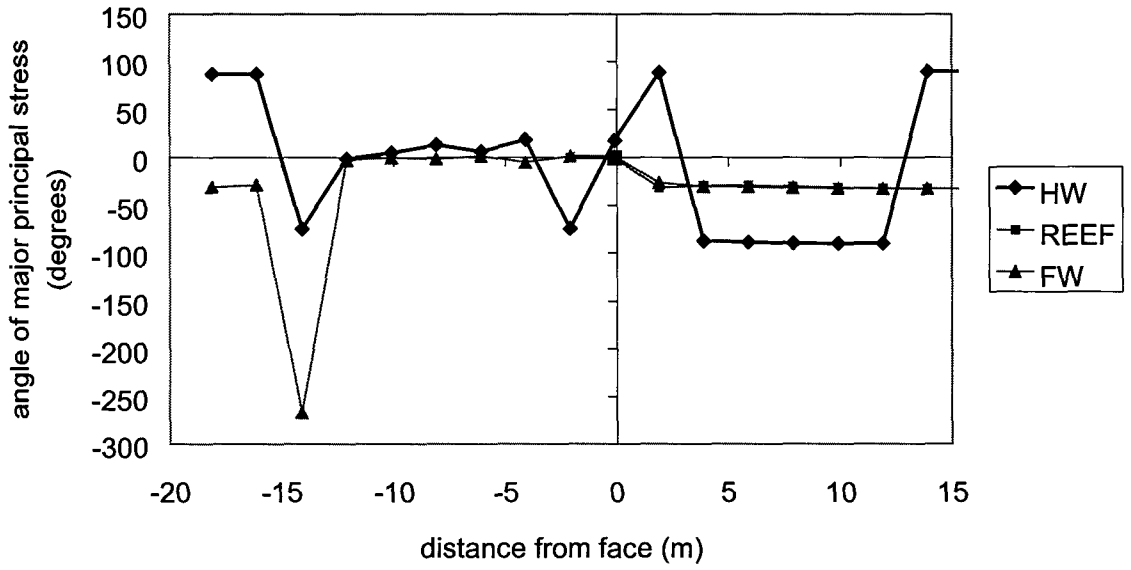

Figure A4.4.3.14 Angle of principal stress, anticlockwise from horizontal, in a stope model with flat parting planes and laboratory material properties, at a span of 14 m.

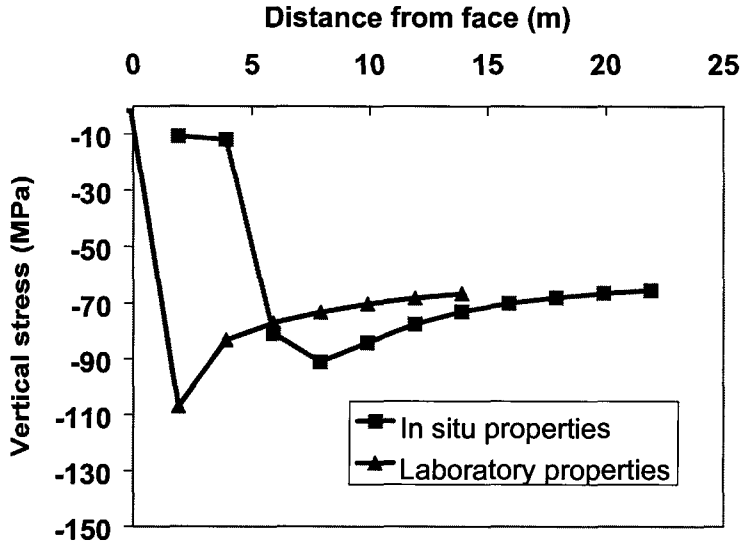

Figure A4.4.3.15 Comparison of vertical stress distribution for stope models with laboratory and in situ material properties at a span of 14 m.

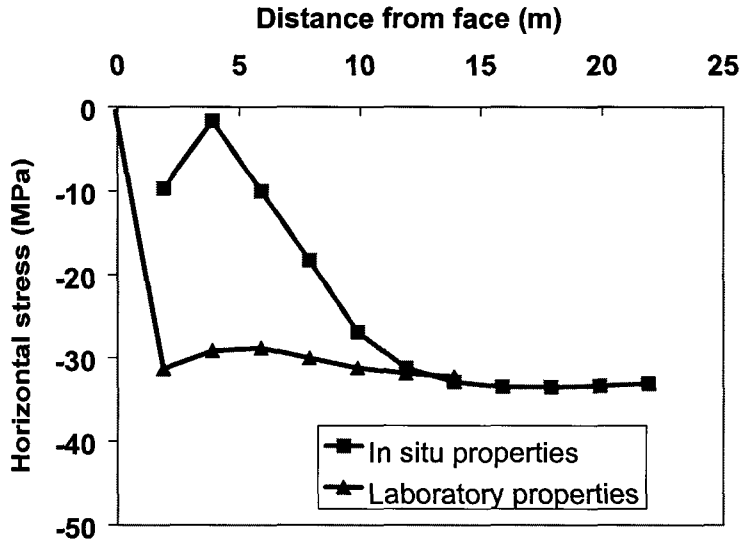

Figure A4.4.3.16 Comparison of vertical stress distribution for stope models with laboratory and in situ material properties at a span of 14 m.

A4.4.4 Sliding flaw and Tension model of fracturing

One source of randomness in the rock mass is the presence of flaws or pre-existing planes of weakness. As shown previously, for laboratory test specimens, the random flaws can introduce tension (Sellers and Napier, 1997). In this case, the pre-existing flaws is mobilized first and further fracture activation may be assumed to occur only if the stress normal to the fracture exceeds a specified tension limit. Analyses of Carbon Leader stopes with flat parting planes were performed by including a set of randomly distributed weak flaws. All other potential elements in the tessellation may only activate in tension. The fracture patterns are similar to those produced using the Mohr-Coulomb fracture rule. Low friction on the parting planes leads to vertical fractures in the immediate hanging- and footwall (Figure A4.4.4.1). Higher friction produces dipping fractures (Figure A4.4.4.2). Increasing the tensile strength of the fractures increases the length of the hangingwall beam that remains unfractured after ledging (Figure A4.4.4.3). This could indicate a means of testing the in situ tensile strength of the rock. Removal of all flaws from the rock mass results in a fracture pattern that is still very similar to the case with flaws (Figure A4.4.4.4). Thus, the structures at a higher scale i.e. the bedding planes are more influential than the smaller flaws.

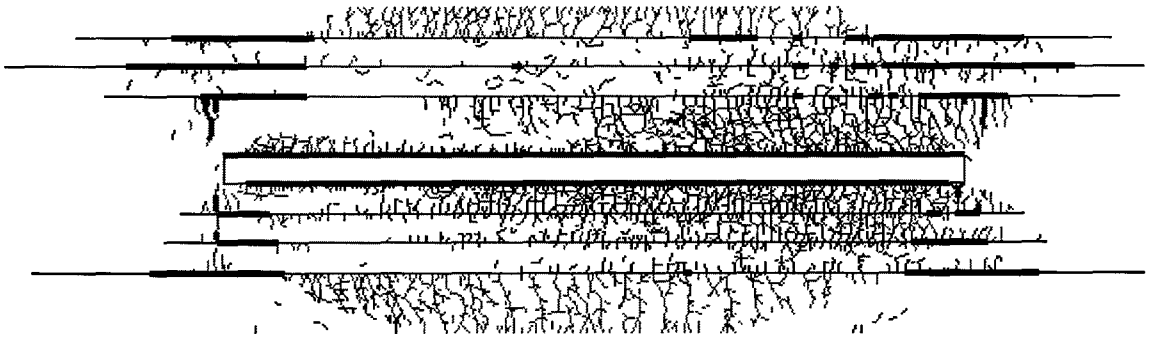

	FC	C	ϕ	C_m	ϕ_m	T
HW	5	1E5	52	10	30	5
GB	5	1E5	32	10	20	5
GB P			5		2	
FW	5	1E5	45		25	5
PP			10		5	

Figure A4.4.4.1 Simulation of the development of fracture pattern around a Carbon Leader stope using sliding flaw - tension crack concept. Model with low tensile strength and low parting plane friction (stope width is 1 m).

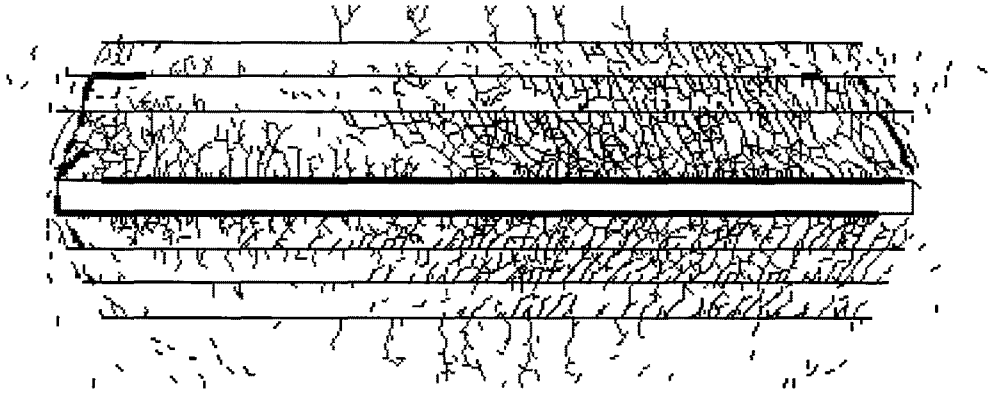

	FC	C	ϕ	C_m	ϕ_m	T
HW	5	1E5	52	10	30	5
GB	5	1E5	32	10	20	5
GB P			30		30	
FW	5	1E5	45		25	5
PP			40		40	

Figure A4.4.4.2 Simulation of the development of fracture pattern around a Carbon Leader stope using sliding flaw - tension crack concept. Model with low tensile strength and high parting plane friction (stope width is 1 m).

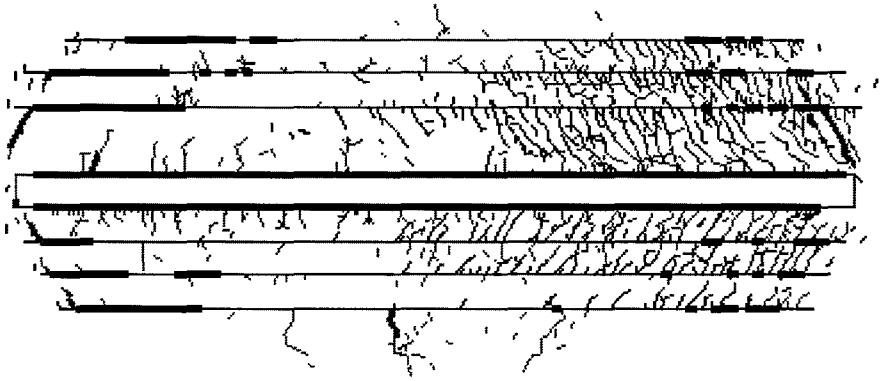

	FC	C	ϕ	C_m	ϕ_m	T
HW	5	1E5	52	10	30	15
GB	5	1E5	32	10	20	0
GB P			30		30	
FW	5	1E5	45		25	10
PP			40		40	

Figure A4.4.4.3 Simulation of the development of fracture pattern around a Carbon Leader stope using sliding flaw - tension crack concept. Model with high tensile strength and high parting plane friction (stope width is 1 m).

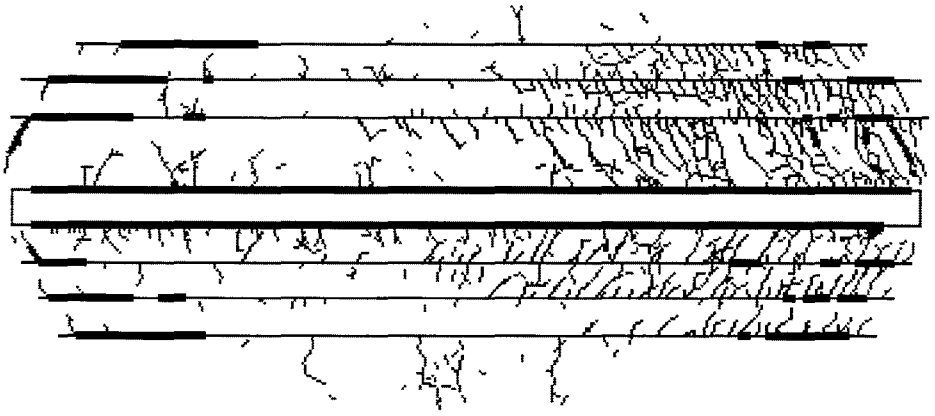

	FC	C	ϕ	C_m	ϕ_m	T
HW	1E5	1E5	52	10	30	5
GB	1E5	1E5	32	10	20	5
GB P			30		30	
FW	1E5	1E5	45		25	5
PP			40		40	

Figure A4.4.4.4 Simulation of the development of fracture pattern around a Carbon Leader stope using sliding flaw - tension crack concept. Model with low tensile strength and high parting plane friction, but no flaws (stope width is 1 m).

A4.4.5 Effect of parting planes

The presence of primary geological features such as bedding planes, parting planes or lithological contacts is known to affect the fracturing around deep level stopes (Schweitzer and Johnson, 1996). The effect of these partings on the development of the fracture zone was investigated by the introduction of three horizontal parting plane discontinuities at 1m intervals, above and below the stope. The partings are of limited extent, to reduce the size of the multipole grid required, and extend to a distance of 6 m ahead of the final stope face postion.

The fracture pattern determined from an analysis with 12 mining steps in a uniform rock mass with a 0,25m average tessellation is shown in Figure A4.4.5.1a. The initial vertical stress is 60 MPa and the horizontal stress is 30 MPa, corresponding to a depth of approximately 2000 m. Each potential fracture is assigned a cohesion of 15 MPa, friction angle of 45 degrees, and a tensile strength of 5 MPa. After fracture, the friction angle is set to the residual value of 30 degrees and there is no cohesion.

The size of the zone of activated fractures increases as the excavation progresses. At each step, individual fractures initiate around the excavation. As the stope lengthens, the individual active segments link to form longer fractures. The majority of these fractures dip at a steep angle towards the face in the hangingwall and away from the face in the footwall. The dips of the fractures decrease with distance away from the stope. Thus, a fracture zone front forms about 1 m ahead of the face and extends behind the stope, following the arching of the compressive principal stresses. The fracture zone is approximately symmetric, but the random nature of the tessellation results in the formation of longer fractures only when the potential cracks are preferentially aligned.

When the initial friction angle on the parting plane is high, φ = 30 degrees and φm = 30 degrees, corresponding in practice to lithological contact on the parting planes, the fracture zone is found to extend behind the stope face, as shown in Figure A4.4.5.1b, in a similar manner to the analysis without partings. Slip on the partings is only evident, above and below the excavated region and the length of parting plane that has experienced slip decreases away from the stope. The active fractures tend to be aligned in the vertical direction, especially in the immediate hangingwall and footwall. The fractures are observed to be continuous across the parting planes. Lowering the friction angle to 5 degrees and the residual angle to 2 degrees, causes the fracture zone to extend ahead of the stope face, as shown in Figure A4.4.5.1c.

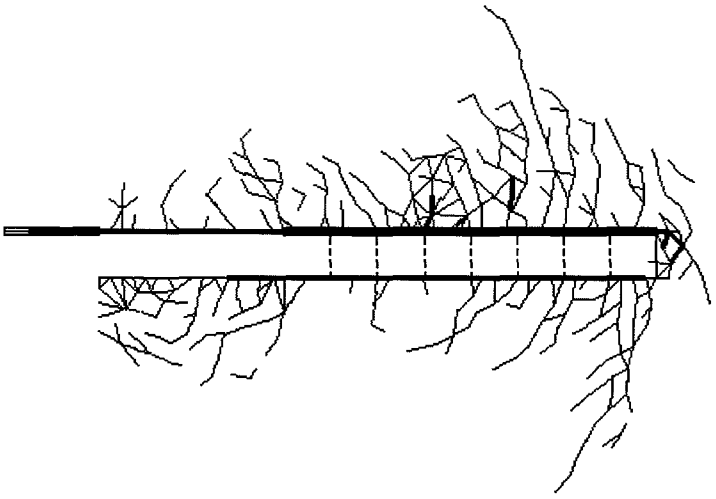

a:

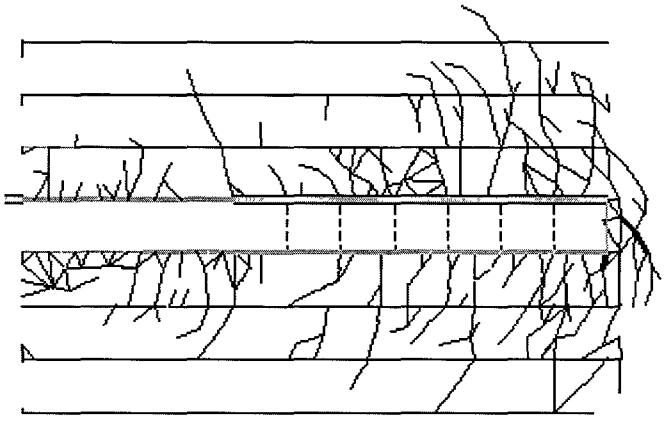

b:

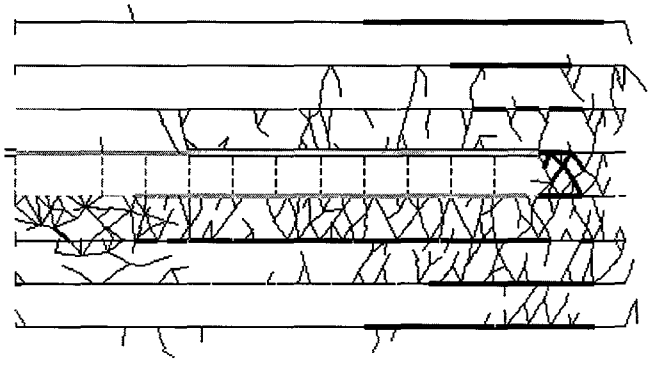

c:

Figure A4.4.5.1 The effect of parting planes on the fracture pattern around a stope. a: : Fracture pattern after 14 mining steps of 1 m in a uniform rock mass, with all elements active simultaneously b: high friction angles on parting planes with $\phi = \phi_m = 30^o$, c: low friction angle parting planes with $\phi = 5^o$,$\phi_m = 4^o$. Thicker lines denote fractures with displacements within 1% of the maximum (stope width is 1 m).

A4.4.6 Effect of introducing random amplitude parting planes.

The numerical modelling studies of the Carbon Leader stopes have shown that fractures can form ahead of the stopes face, but only if the parting plane friction is reduced to less than 10 degrees. Observations of friction angles suggest that surfaces such as gouge, which may be considered to be much lower than quartzite - quartzite interfaces, have friction angles of about 30 degrees. In addition, underground observations of partings show that the partings are not flat, but vary in amplitude (see Figures A4.4.6.1 and A4.4.6.2). The question arises as to whether the variation in amplitude of a parting plane, with a high friction angle, could induce fracturing due to different portions of the parting having a low friction angle with respect to the stope. Parting planes with discontinuities that have a variation in amplitude with distance, based on a randomised sine wave, smoothed by a running average have been implemented. The randomised sine wave, is smoothed by a moving average of the n previous points, so that the vertical (z co-ordinate) of a point k is a function of the horizontal (y co-ordinate)

$$z_k = \sum_{k-n}^{k} \left[(a + f_a a(R_a - 0.5)) \sin\left(\left(\frac{y_k}{L + f_l L(R_l - 0.5)} \right) 2\pi \right) \right] / n. \quad \text{(A4.4.6.1)}$$

The amplitude a and period L are selected and each has a random component which is a factor f_a or f_l, of the amplitude or period, respectively ($0 \leq f_a \leq 1$, $0 \leq f_l \leq 1$). The amplitude and period are assigned different random numbers R_a and R_l. Studies of a number of similar functions showed that this one provided reasonably realistic shapes (if n=5), although this has not been confirmed quantitatively. This function and some others have been included in the user interface that has been developed for automatic mesh generation.

The random sine function was found to provide realistic shapes, and can now be included into the tessellation from the DIGS program user interface. An analysis was set up for comparison with the other carbon leader simulations. Six partings, each with a different random variation in amplitude, up to 0,25m, were placed on either side of the stope (Figure A4.4.6.3). After 14 mining steps of 1m, using incremental activation, there is considerable fracturing ahead of the face (Figure A4.4.6.4). Thus, it is most likely that it is the randomness in the rock mass that induces stress distributions that make it possible for tensile/extension fracturing to occur. The vertical stress distribution (Figure A4.4.6.5.) shows a slight increase in stress with random partings, but the horizontal stress is increased significantly and the peak stress moves ahead of the face (Figure A4.4.6.6).

The dilation, as measured by extensometers derived from grid points at 0,5m spacing in the hangingwall, footwall and reef, indicates dilation and contraction values of up to 10mm (Figure A4.4.6.7) compared with the 2mm from the flat parting model. The distribution of the dilation is given in Figure A4.4.6.8, and shows a similar distribution as for the flat partings, but with higher magnitudes. The angle of principal stress (Figure A4.4.6.9) changes in a similar manner for the active face, but is different on the passive face. The closure in the case of the random partings (Figure A4.4.6.10) is nearly twice that obtained with the flat partings. The displaced shapes of the hangingwall and footwall partings are shown in Figure A4.4.6.11 and A4.4.6.12, respectively. The side of the parting closest to the stope moves into the stope, as expected. The roughness of the parting is increased at a small scale. This would be due to the breaking up of the parting by intersecting cracks. The shear displacements of the footwall parting at a span of 16m are shown in Figure A4.4.6.13, and the corresponding opening displacements are shown in Figure A4.4.6.14. The shearing on the partings shows an overall shear towards the centre of the stopes, but there are differences in the magnitude of the shear on a small scale. Similarly, there appears to be more opening where the parting is further from the stope (Figure A4.4.6.14), but the correlation between the displacements and the parting shape have not been investigated. Figures A4.4.6.15 and

A4.4.6.16 show similar response of the hangingwall parting. The difference in the shear and normal displacements after a mining step is given in Figure A4.4.6.17 and Figure A4.4.6.18. The shear maintains the same sense, but some places on the parting open whilst others close. The parting in the hangingwall shows similar changes (Figure A4.4.6.19 and Figure A4.4.6.20)

The difference in fracture pattern between incremental and parallel activation can be observed by comparing Figure A4.4.6.4d and A4.4.6.21. The rock had no tensile strength in these analyses, and the introduction of tensile strength (Figure A4.4.6.22) causes less fracturing in the hangingwall and footwall and moves the fracturing ahead of the face.

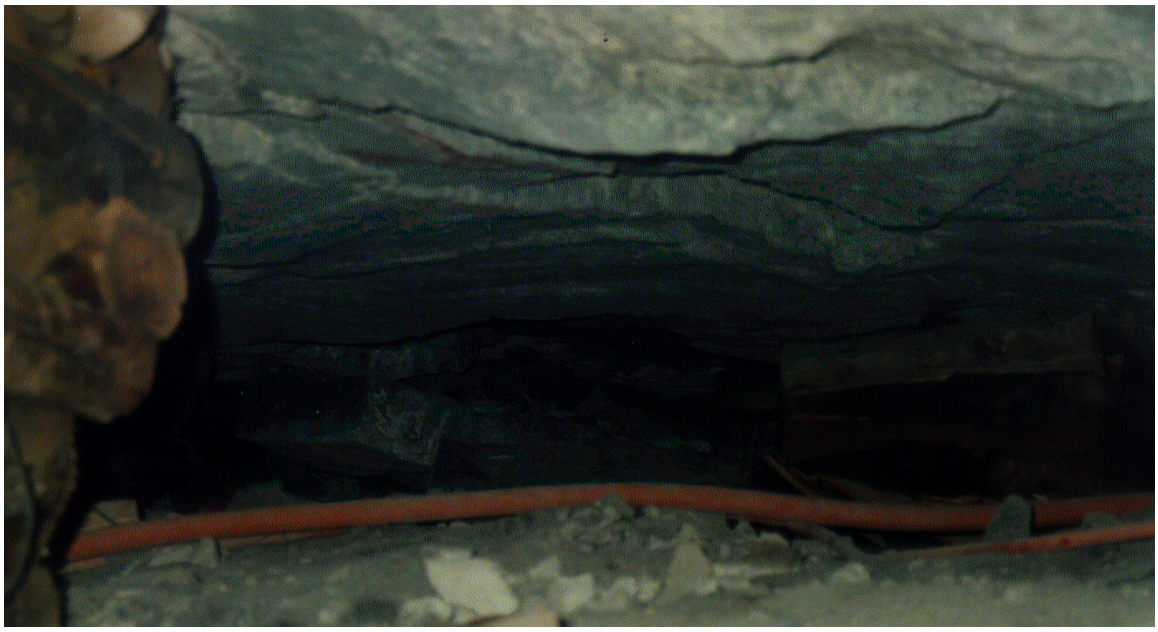

Figure A4.4.6.1 Photograph of a Carbon Leader stope showing the variation in the hangingwall parting plane amplitude

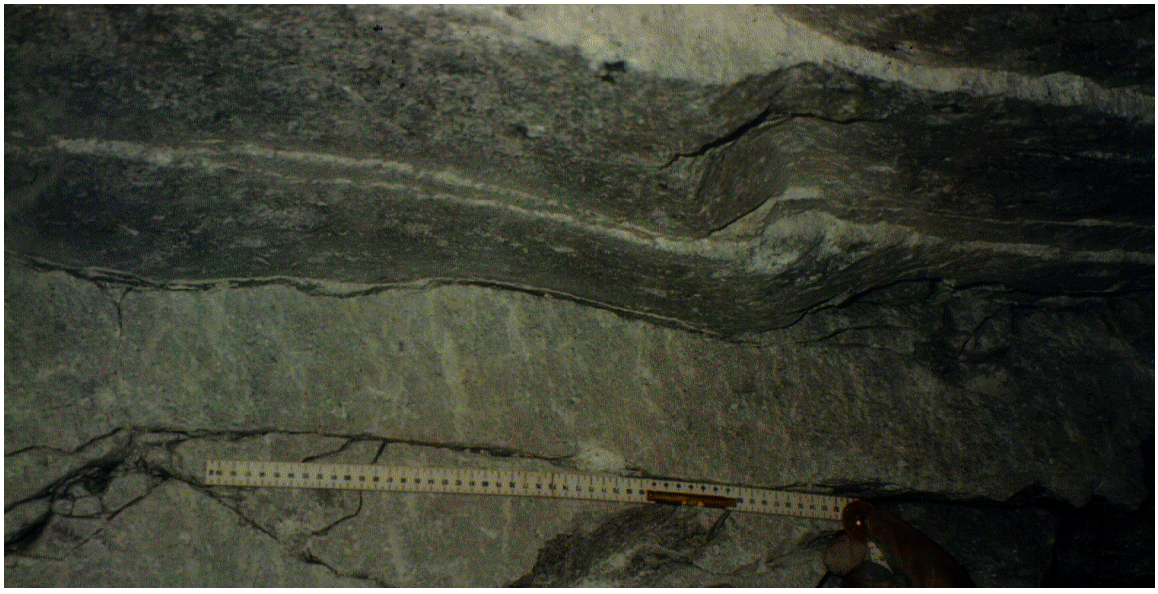

Figure A4.4.6.2 Photograph showing the variation in amplitude of a parting plane

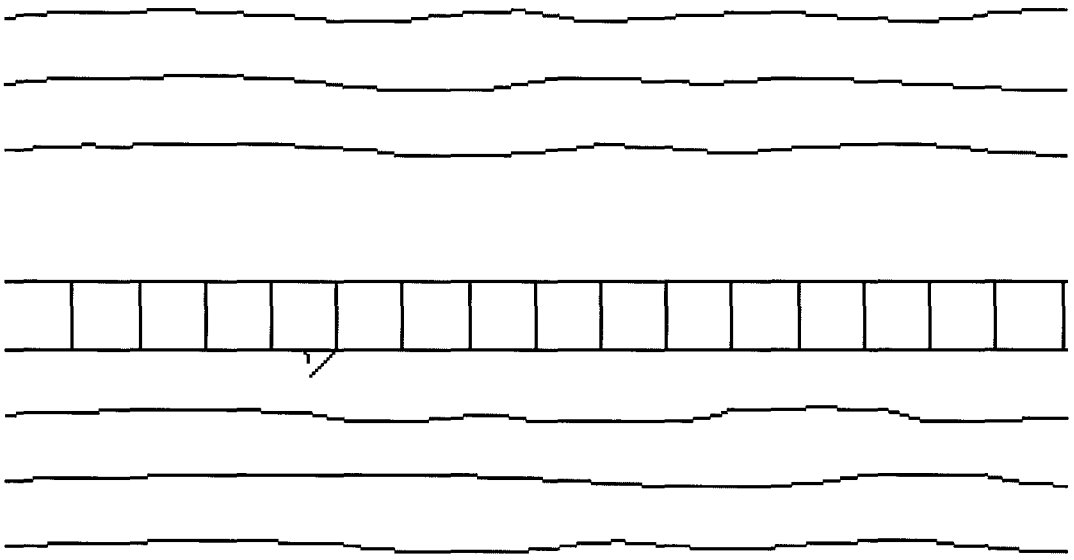

Figure A4.4.6.3 The parting planes and mining steps in a model of a Carbon Leader stope

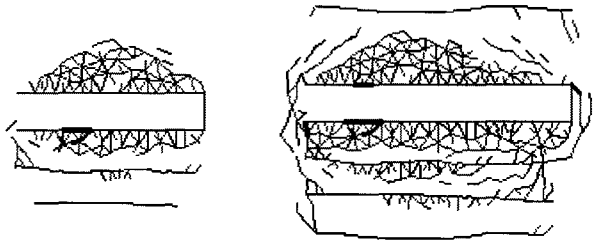

a: *b:*

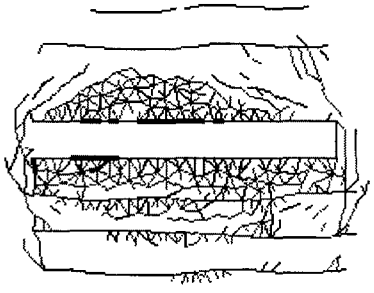

c:

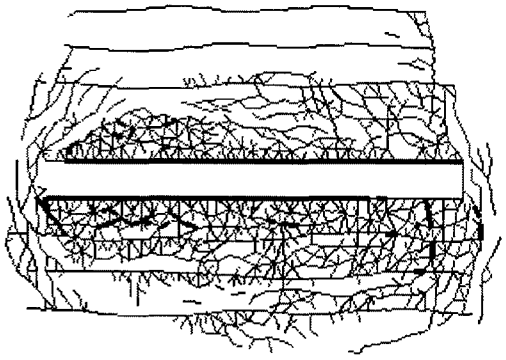

d:

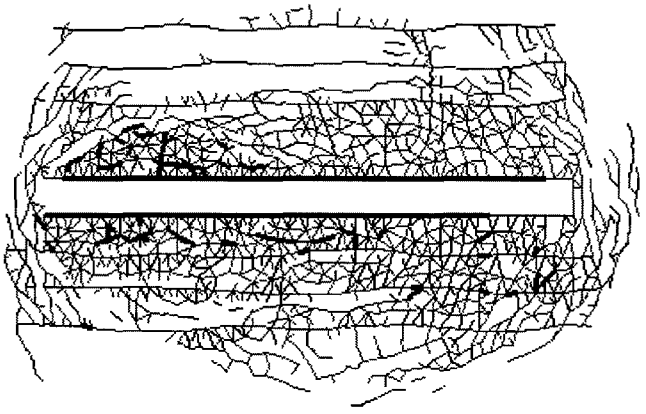

e:

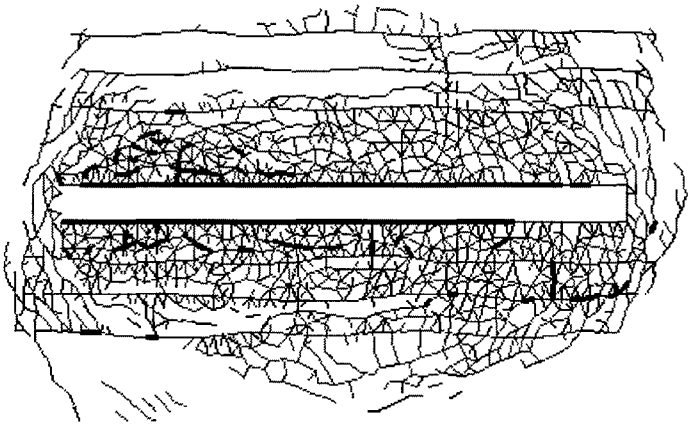

f:

Figure A4.4.6.4 Simulation of the development of fracture pattern around a Carbon Leader stope (laboratory material properties). a: 5 m span, b: 7 m span, c: 11 m span, d: 14 m span, e: 17 m span, f: 18 m span. Incremental fracture activation.

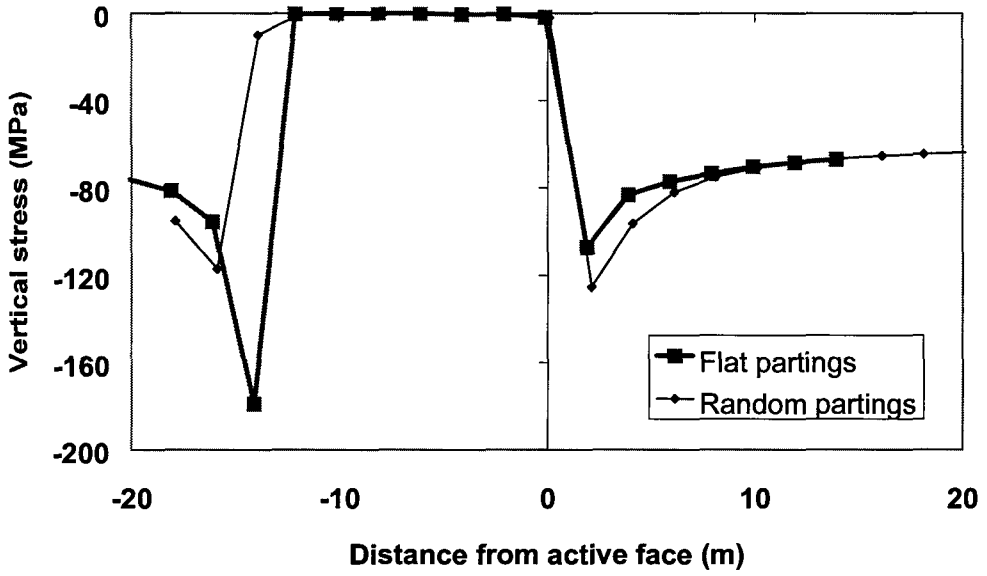

Figure A4.4.6.5 Comparison of vertical stress distribution for stope models with flat and random parting planes at a span of 14 m.

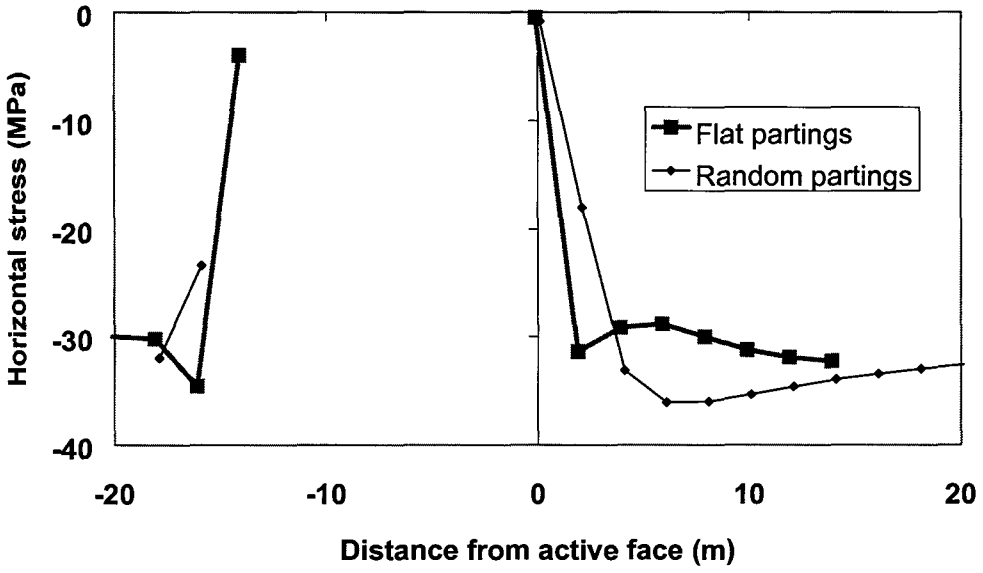

Figure A4.4.6.6 Comparison of horizontal stress distribution for stope models with flat and random parting planes at a span of 14 m.

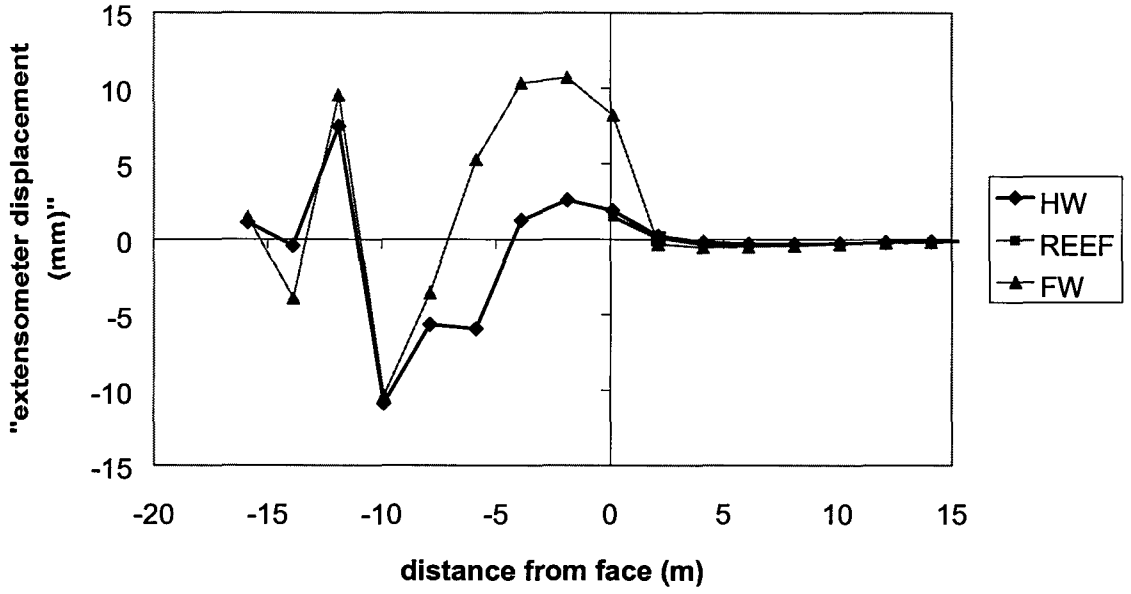

Figure A4.4.6.7 Calculated extensometer displacement distributions in stope models with random partings at a span of 14 m.

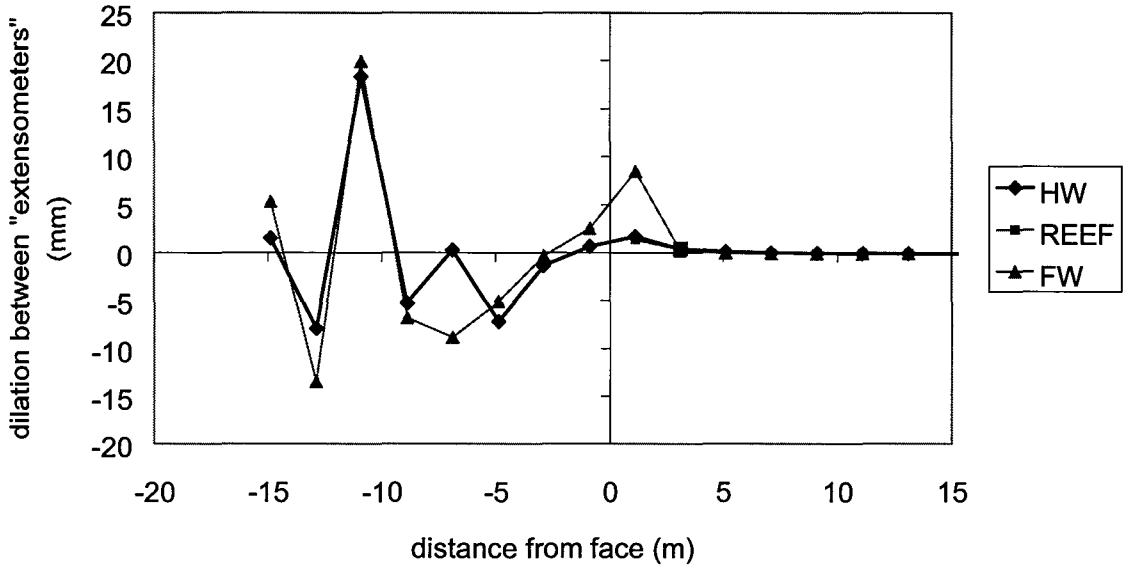

Figure A4.4.6.8 Distribution of calculated dilation between extensometer grid points for a stope model with random parting planes at a span of 14 m.

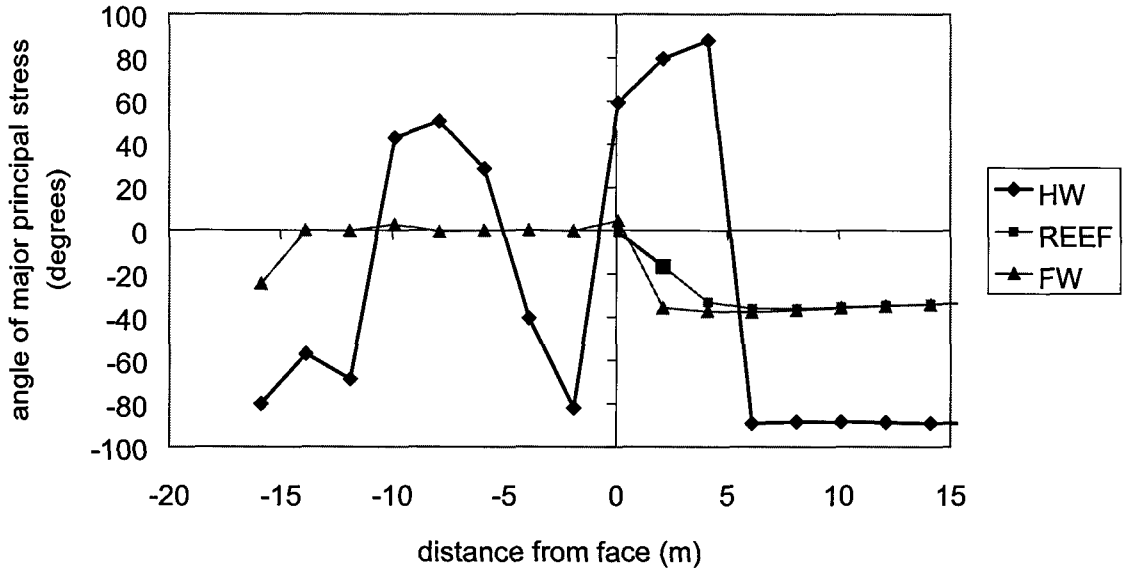

Figure A4.4.6.9 Angle of principal stress, anti-clockwise from horizontal, in a stope model with random parting planes at a span of 14 m.

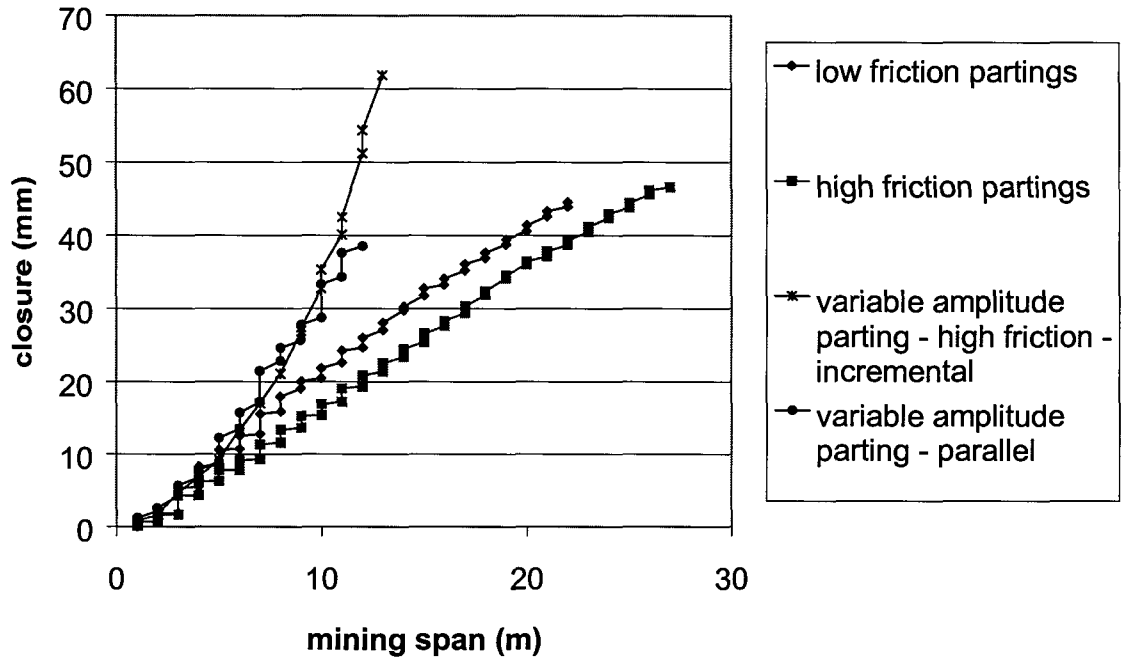

Figure A4.4.6.10 Comparison of maximum closure with span for flat and random partings with different friction angles

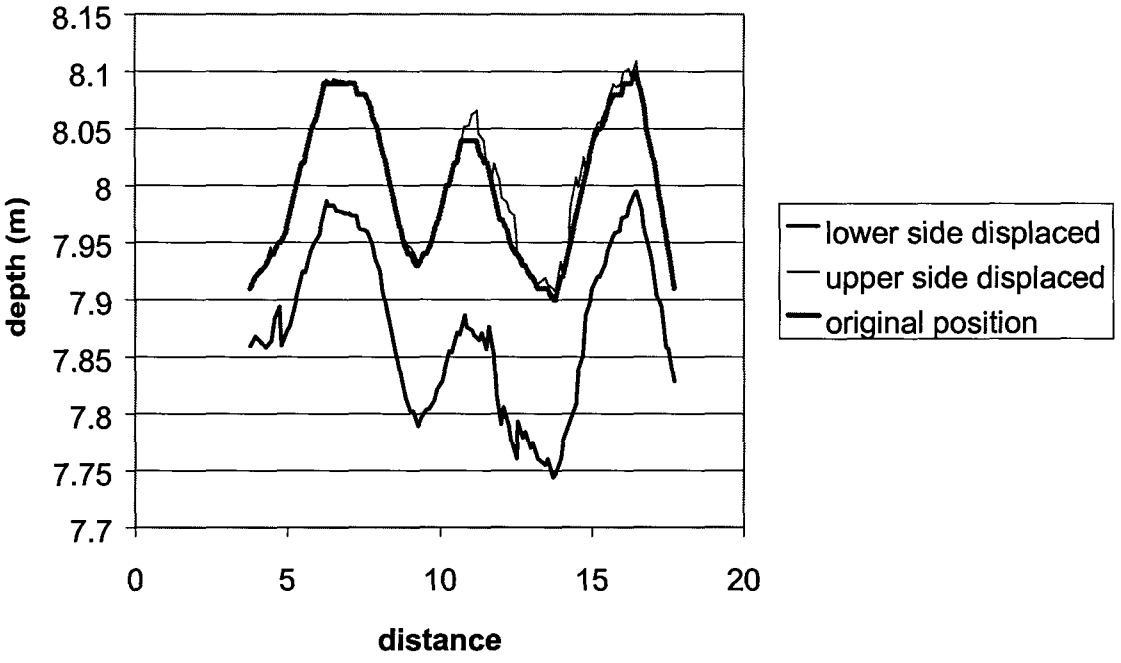

Figure A4.4.6.11 Displaced shape of the random parting plane immediately in the hangingwall, after 16 m of mining

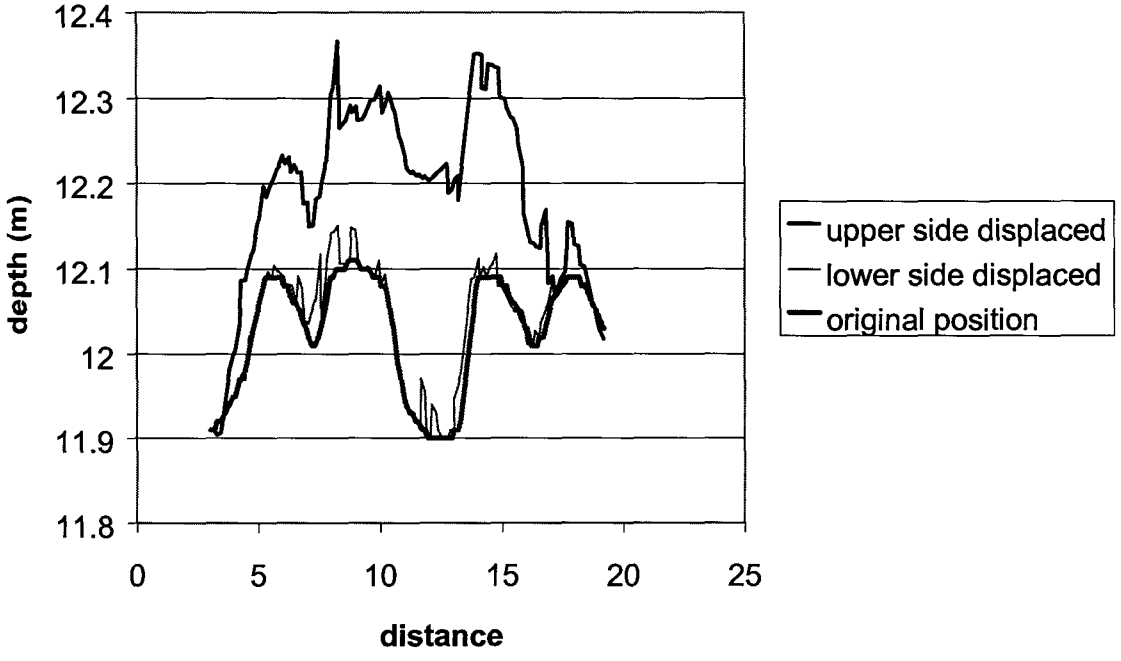

Figure A4.4.6.12 Displaced shape of the random parting plane immediately in the footwall, after 16 m of mining

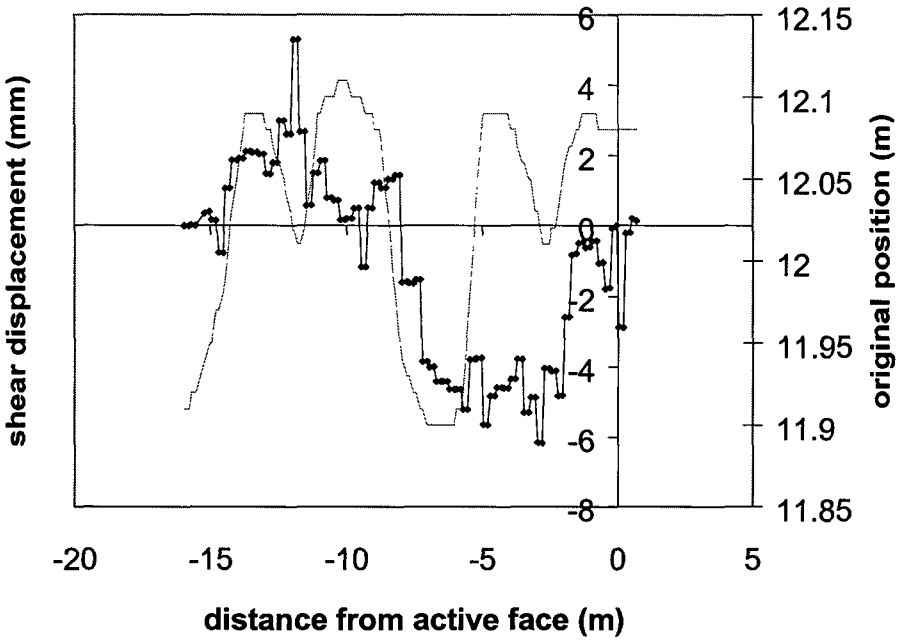

Figure A4.4.6.13 Shear displacements of the random parting plane immediately in the footwall, after 16 m of mining, and compared to the original shape (with magnified vertical position).

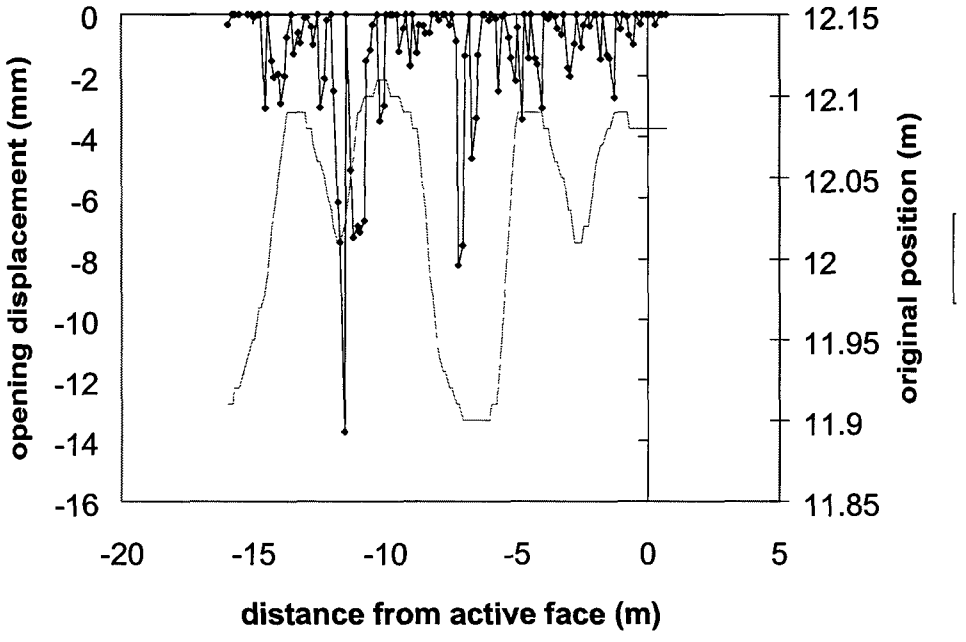

Figure A4.4.6.14 Opening displacements of the random parting plane immediately in the footwall, after 16 m of mining, and compared to the original shape (with magnified vertical position)

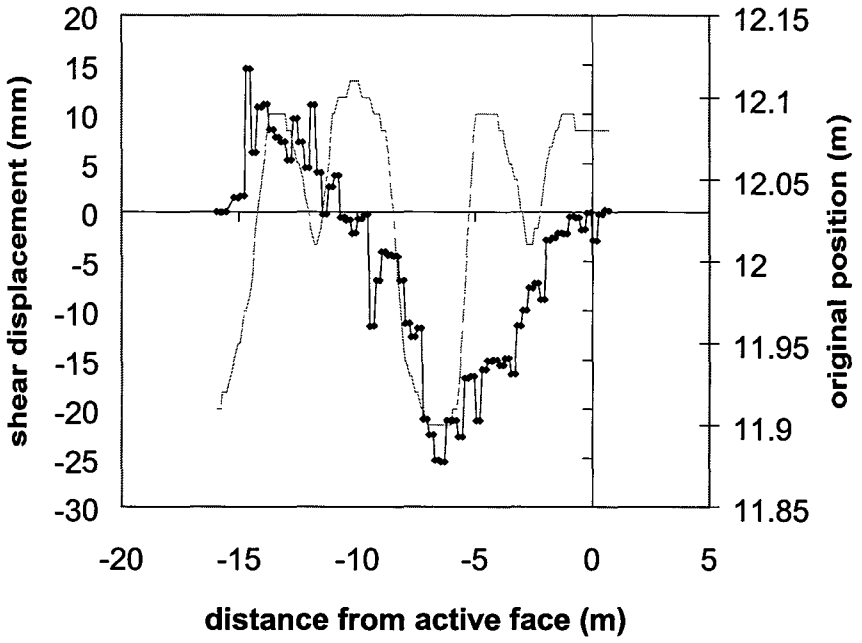

Figure A4.4.6.15 Shear displacements of the random parting plane immediately in the footwall, after 16 m of mining, and compared to the original shape (with magnified vertical position)

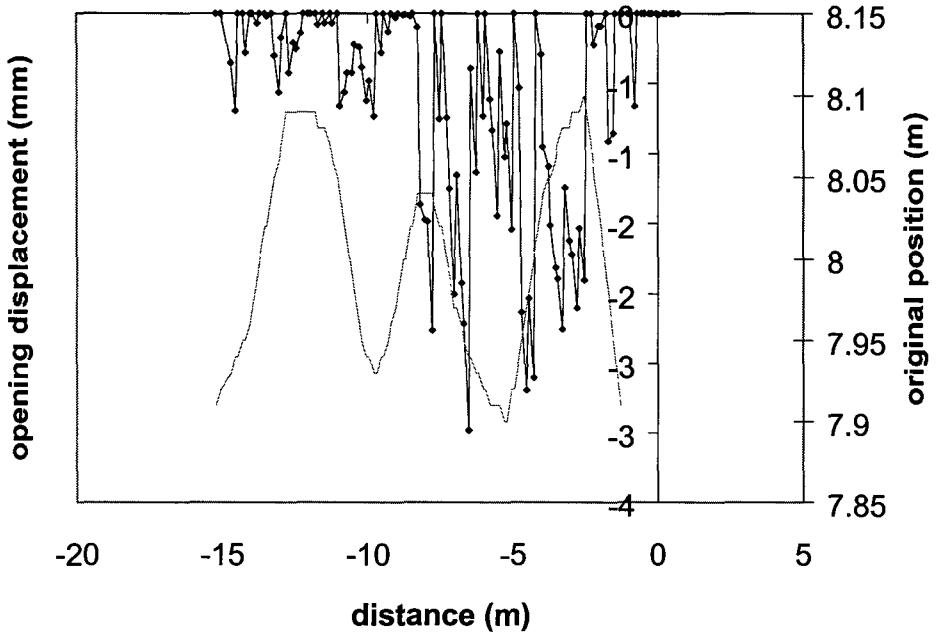

Figure A4.4.6.16 Opening displacements of the random parting plane immediately in the hangingwall, after 16 m of mining, and compared to the original shape (with magnified vertical position)

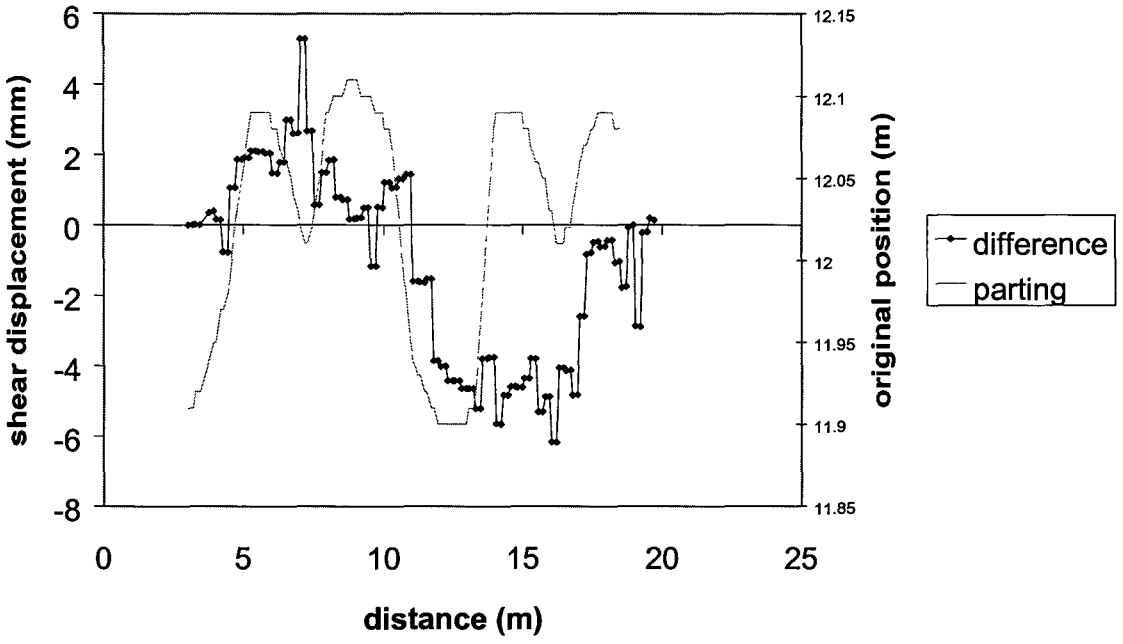

Figure A4.4.6.17 Difference in shear displacements of the random parting plane immediately in the footwall, due to a mining step increasing the span from 15 m to 16 m of mining, and compared to the original shape (with magnified vertical position)

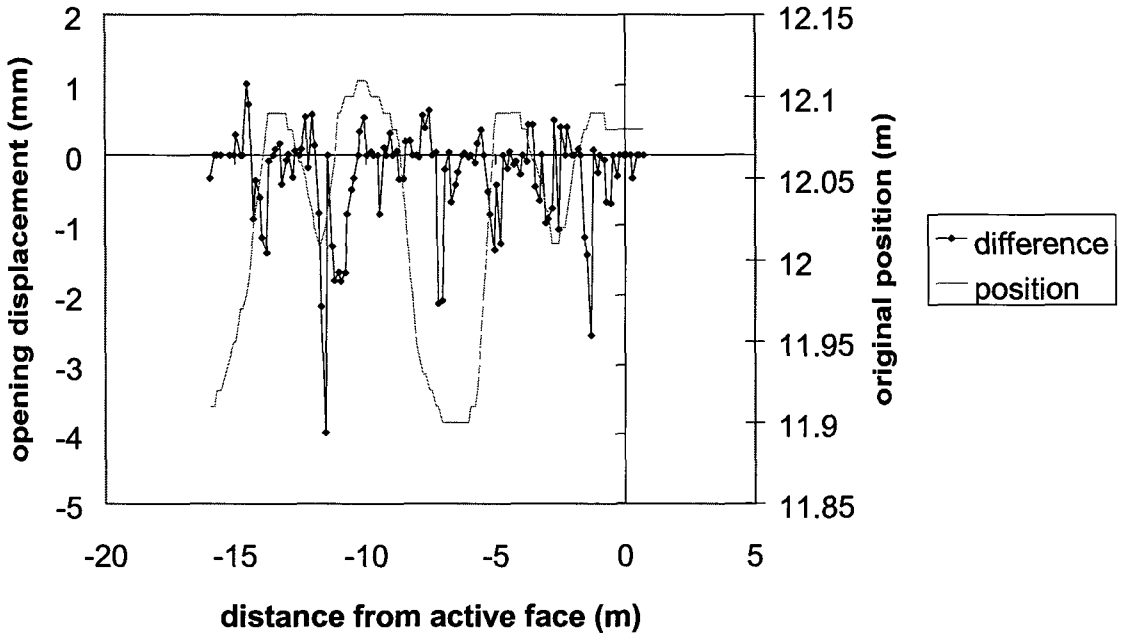

Figure A4.4.6.18 Difference in opening displacements of the random parting plane immediately in the footwall, due to a mining step increasing the span from 15 m to 16 m of mining, and compared to the original shape (with magnified vertical position)

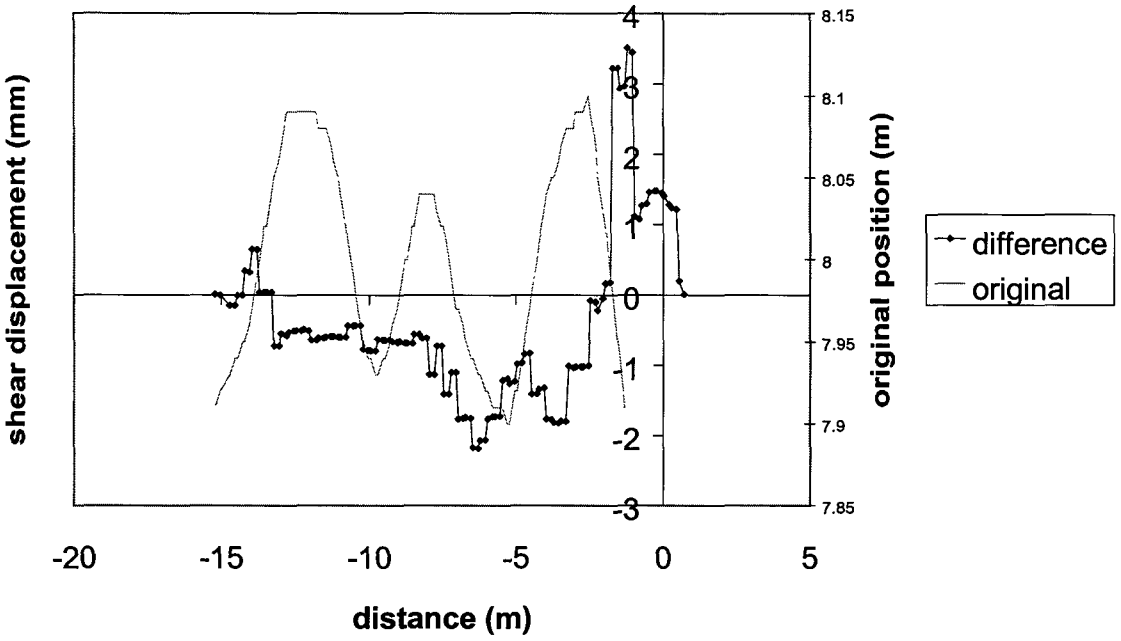

Figure A4.4.6. 19 Difference in shear displacements of the random parting plane immediately in the hangingwall, due to a mining step increasing the span from 15 m to 16 m of mining, and compared to the original shape (with magnified vertical position)

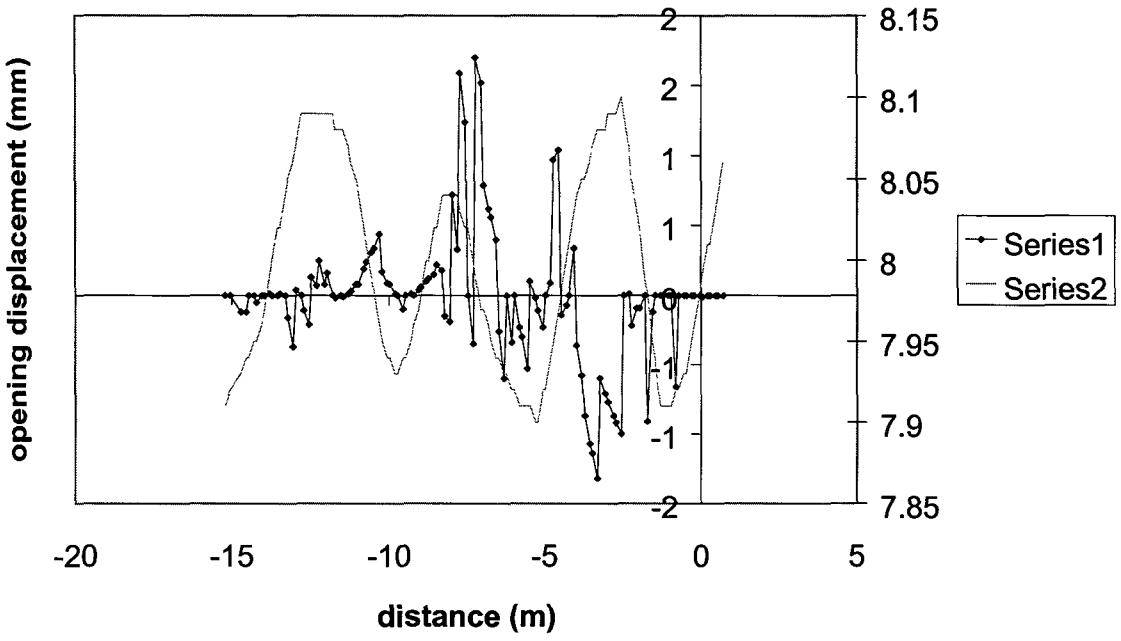

Figure A4.4.6.20 Difference in opening displacements of the random parting plane immediately in the hangingwall, due to a mining step increasing the span from 15 m to 16 m of mining, and compared to the original shape (with magnified vertical position)

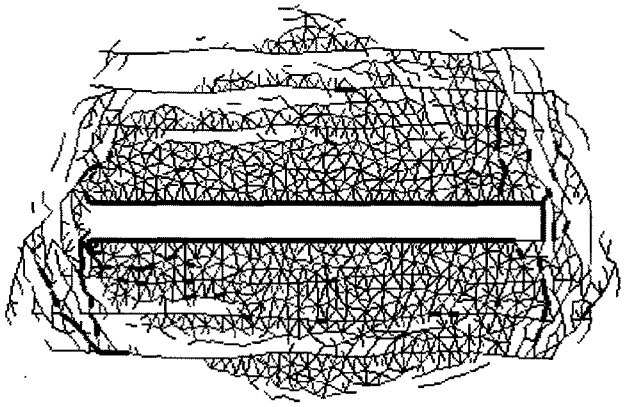

Figure A4.4.6.21 Simulation of the development of a fracture pattern around a Carbon leader stope (zero tensile strength). Parallel fracture activation.

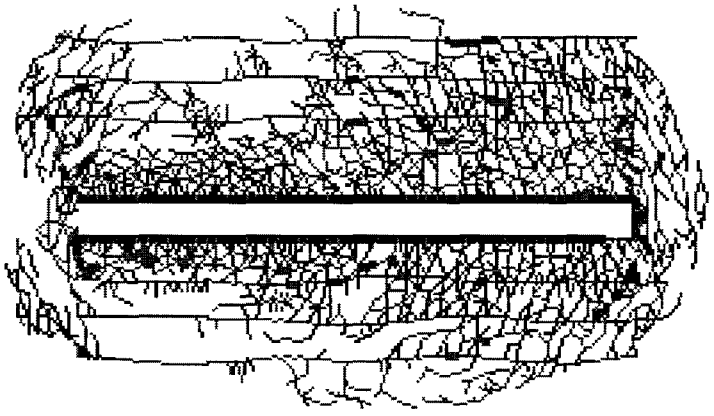

Figure A4.4.6.22 Simulation of the development of a fracture pattern around a Carbon leader stope (tensile strength of 5 MPa). Parallel fracture activation.

A4.4.7 Effect of Pre-existing joints

A4.4.7.1 Tessellation models

The rock mass within the Witwatersrand basin contains a number of secondary geological features, which can alter the fracture patterns induced by mining (Schweitzer and Johnson, 1997). A model was developed to investigate the relationship between the fracturing and the direction of a pre-existing joint set in the hangingwall, dipping at 80 degrees away from the face with a spacing of 0,5 m, see Figure A4.4.7.1. Due to computer memory limitations, each joint is assumed to extend only 4m into the hangingwall. No jointing is included in the footwall for comparison. Each joint is assumed to have healed and to have a cohesion value of 5 MPa. The friction angle is initially 20° and is assumed to reduce to 15^0 degrees upon activation. In this case, the average element size is 0,1 m. The tessellation grid is considerably refined in comparison to the previous examples and so only six mining steps were possible with the available memory.

The incremental activation procedure was applied. As the mining progressed, the joints slightly ahead of the face failed by sliding. Fractures formed ahead of the face and extended into the hangingwall sub-parallel to the jointing. Horizontal fracturing formed above and within the jointed zone to accommodate the sliding of the joints into the excavated region. Fracturing in the footwall is similar to the uniform rock mass in Figure A4.4.2.3. The dip decreases with distance from the stope and the fractures tend to become sub-horizontal within 1 m to 2 m.

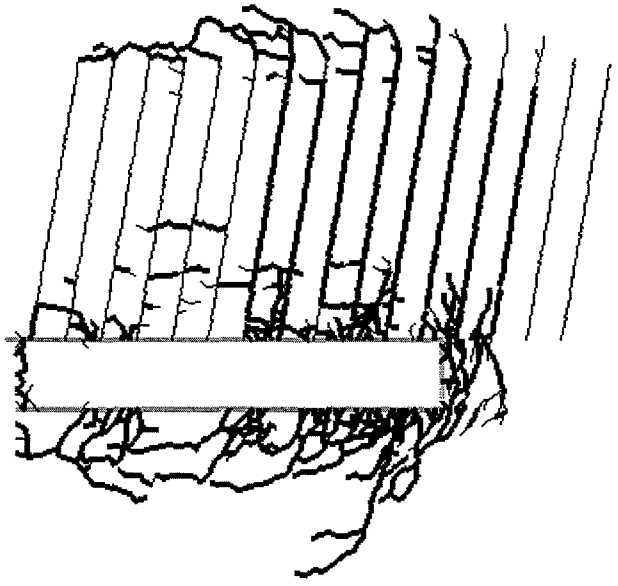

Figure A4.4.7.1 Fracture initiation in a stope with a set of steeply dipping healed joints in the hangingwall

A4.4.7.2 Standard DIGS models

A model was set up using standard DIGS to investigate the effect of duplex ramp structures in the hangingwall. These are found in soft lava hangingwalls due to tectonic thrust events (Berlenbach,

1995), and can alter the mining induced fracturing (Quaye and Guler, 1998), as shown in Figure A4.4.7.2. In the model, the fractures in the hangingwall dip away from the face (Figure A4.4.7.3), but this is due to the shear activation rule applied in the model (Figure A4.4.7.4). The thrust events do not have a significant effect on the fracture direction, but do result in the formation of blocks in the hangingwall. Rotating the major principal stress into the horizontal plane results in fractures dipping towards and away from the face, depending on the face position relative to the ramp structure (Figure A4.4.7.5). Extension tests on soft lava indicate that the lava fails on a series of slip planes, not a discrete fracture plane. Thus, the anomolous fracture pattern could be ascribed to the pre-existing jointing, the material failure mode, the induced stress, or a combination of the above.

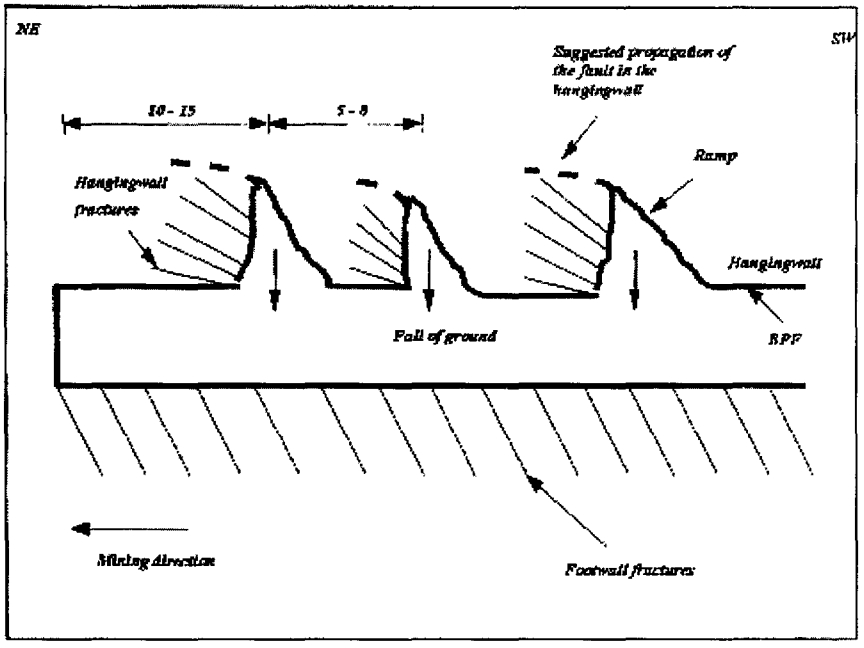

Figure A4.4.7.2 Fracture patterns in a soft lava stope are influenced by the pre-existing thrust ramp structures (Quaye and Guler, 1998)

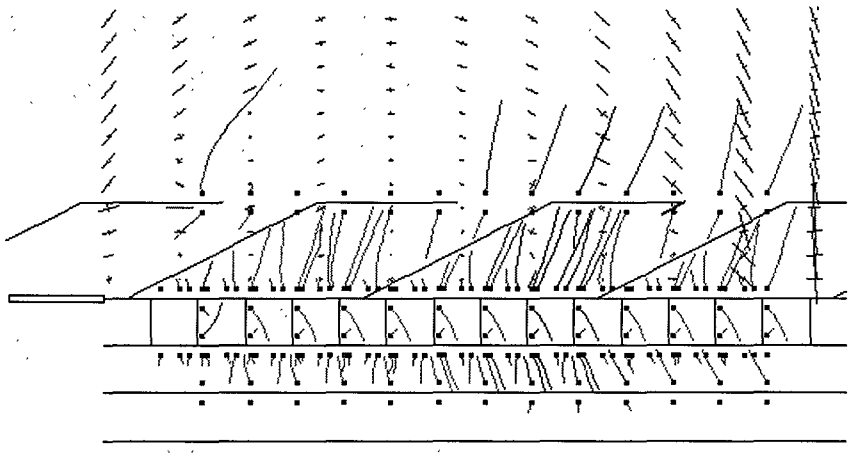

***Figure A4.4.7.3* Fracture initiation in a soft lava stope with pre-existing thrust ramp structures in the hangingwall.**

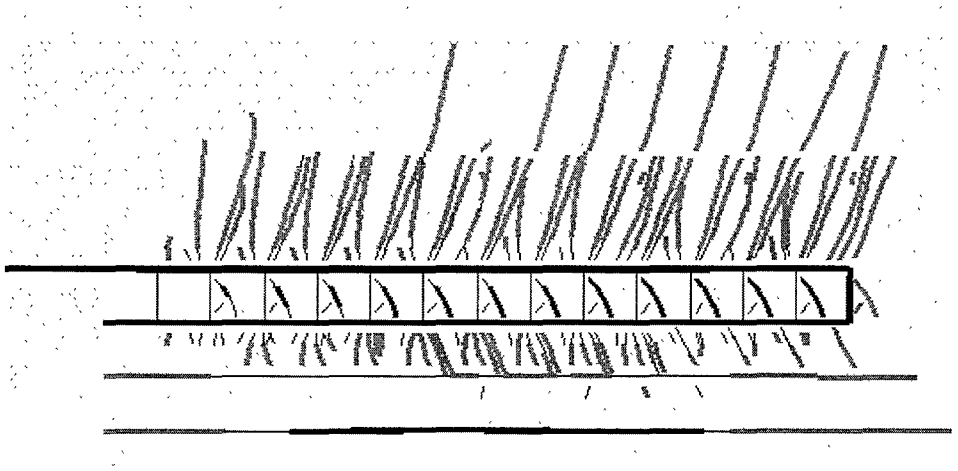

Figure A4.4.7.4 Fracture initiation in a soft lava stope with shear fractures in the hanging and footwall.

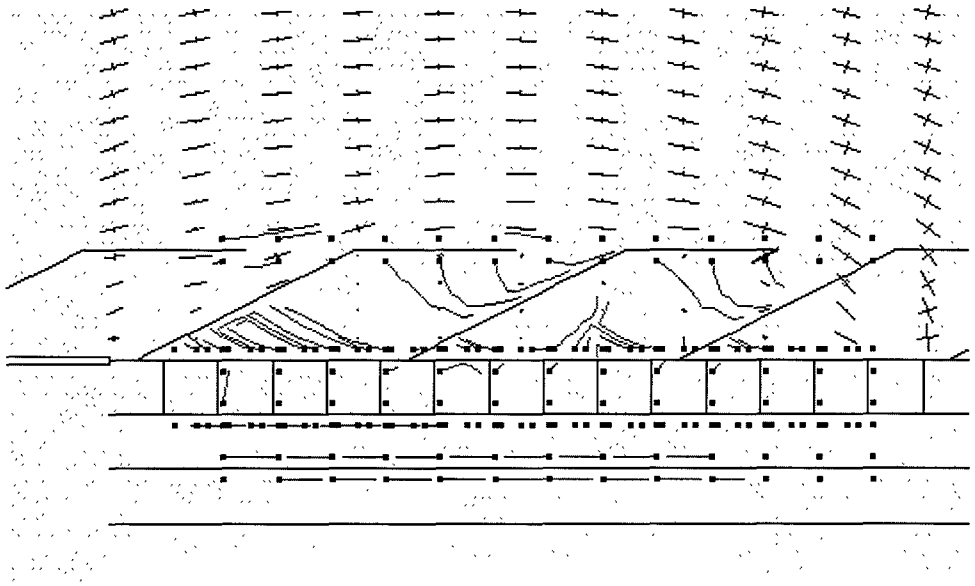

Figure A4.4.7.5 Fracture initiation in a stope with a set of steeply dipping healed joints in the hangingwall. Major stress is horizontal.

Table A4.4.7.1 Material properties used in the DIGS analyses of soft lava stope

	C	ϕ	C_m	ϕ_m	T	GM
HW	12	30	10	20	5	S
J	20	5		5		
FW	15	45		25	5	S
PP		5		2		

A4.4.8 Effect of in situ stress

The effect of a non-vertical in situ stress in a uniform rock mass is considered in Figure A4.4.8.1. Mining in a stress state with the opposite plunge of the major principal stress is shown in Figure A4.4.8.2. The induced stresses can activate fractures some distance into the rock mass. The angle of fracturing is different, being shallower when mining in the direction of the plunge of the stress. Similar effects are observed in the presence of bedding planes, as shown in Figure A4.4.8.3. The tessellation approach indicates similar response, depending on the ratio of major to minor principal stress, and the bedding plane friction. If the stress ratio is too high, the tessellation activates as a fault zone and the actual mining induced fracture pattern is difficult to deduce. For low parting plane friction, little effect is observed (Figure A4.4.8.4), but as the friction increases, the partings activate closer to the stope and the effect is more pronounced (Figure A4.4.8.5).

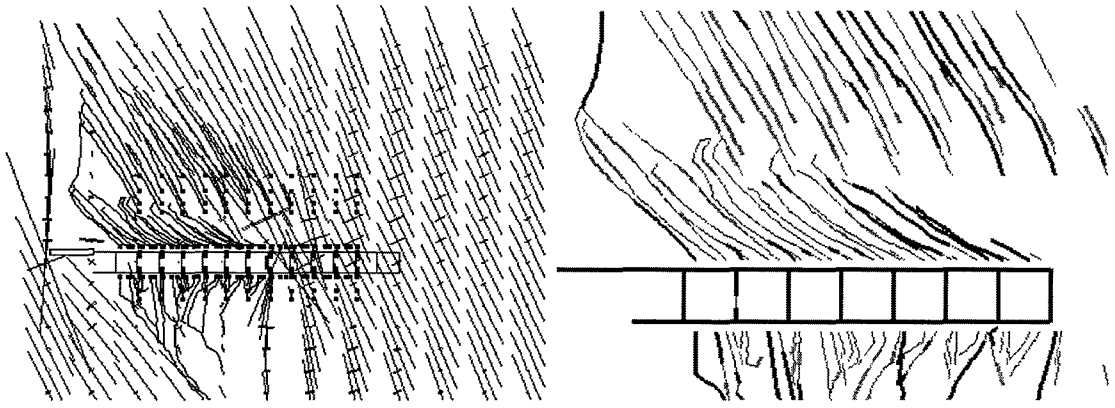

	C	ϕ	C_m	ϕ_m	T	GM
HW	18	45	0	25	5	T
FW	18	45	0	25	5	T

Figure A4.4.8.1 DIGS model of mining towards the plunge of the principal stress in a uniform rock mass a: stress pattern b: detail of fracture pattern.

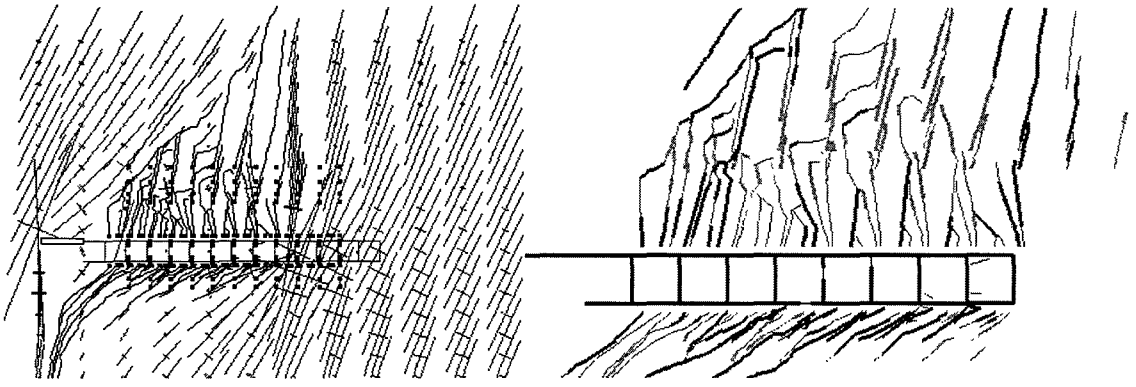

Figure A4.4.8.2 DIGS model of mining away from the plunge of the principal stress in a uniform rock mass a: stress pattern b: detail of fracture pattern.

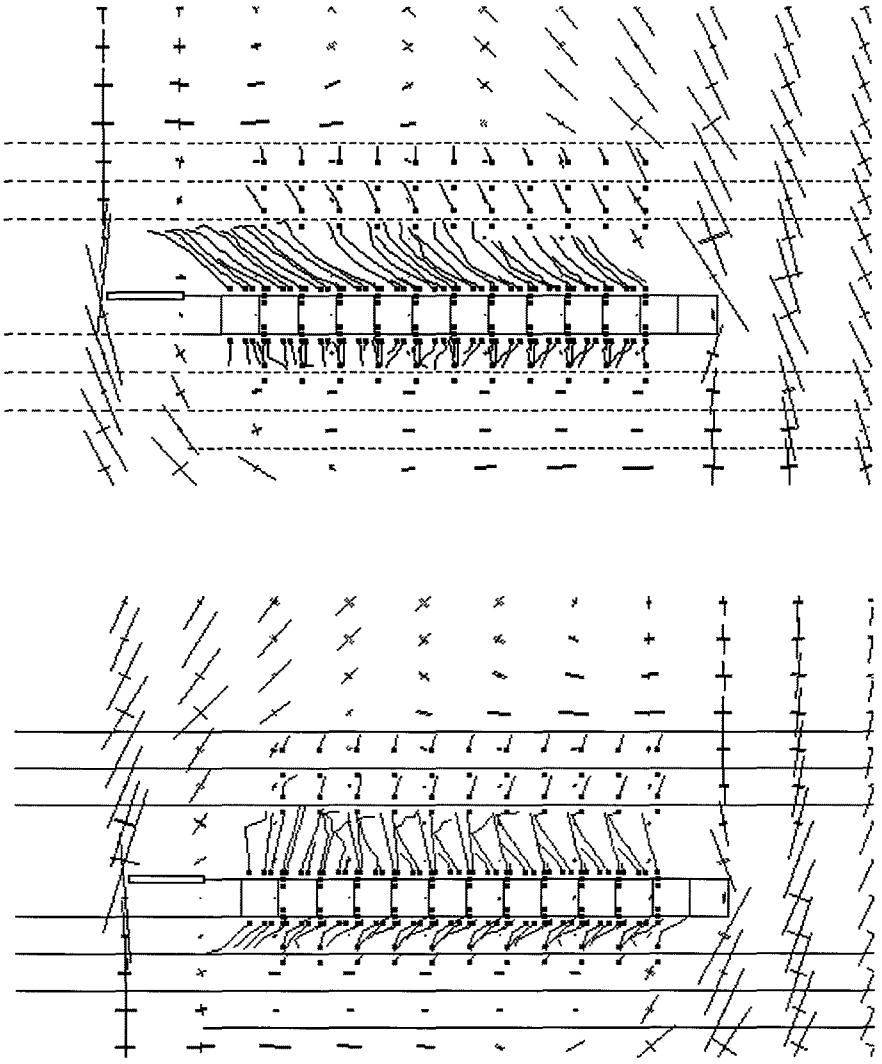

Figure A4.4.8.3 DIGS model of mining in Carbon Leader environment with plunging principal stress a: mining towards the plunge of the principal stress a: mining away from the plunge of the principal stress

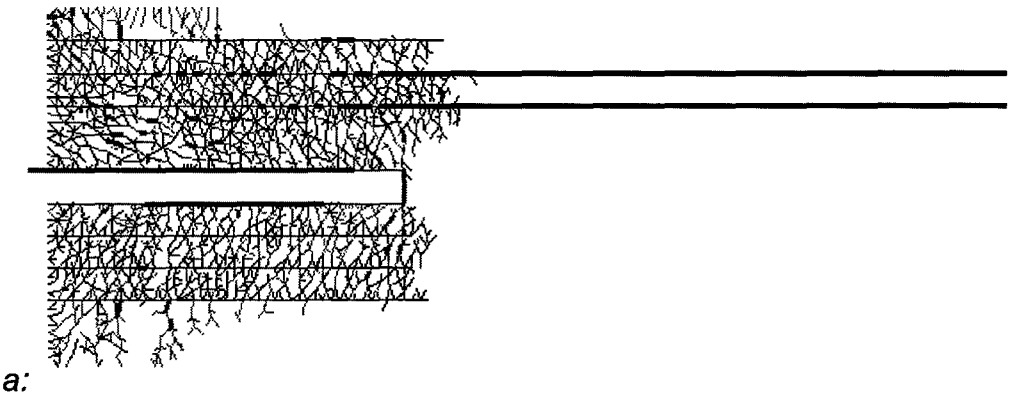

a:

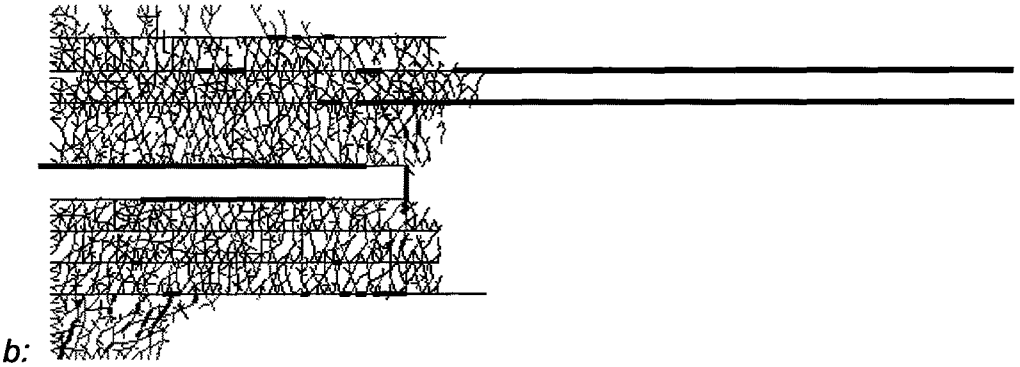

b:

Figure A4.4.8.4 Tessellation model of mining in Carbon Leader environment with plunging principal stress and low friction on partings a: mining towards the plunge of the principal stress b: mining away from the plunge of the principal stress

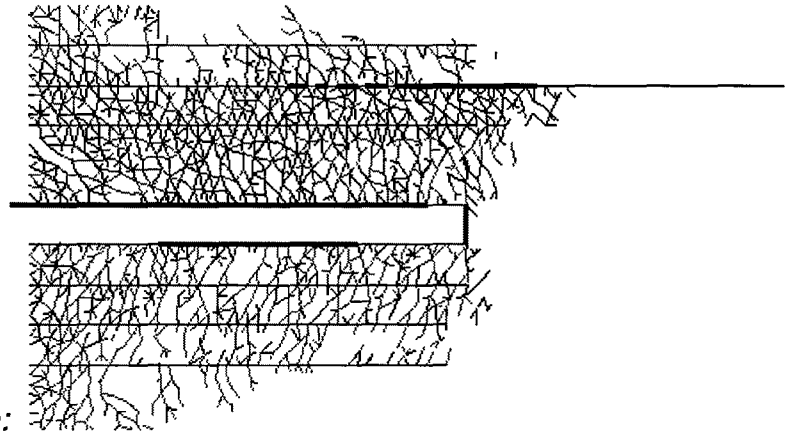

a:

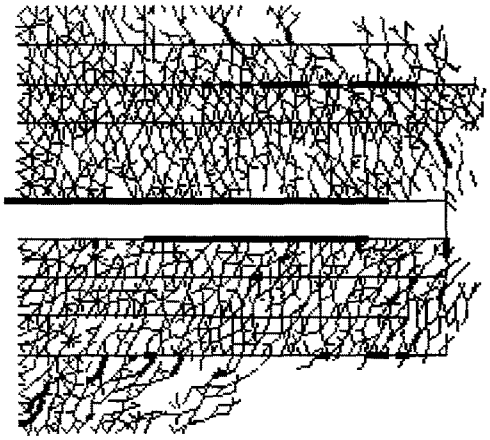

b:

Figure A4.4.8.5 Tessellation model of mining in Carbon Leader environment with plunging principal stress and high friction on partings a: mining towards the plunge of the principal stress b: mining away from the plunge of the principal stress

A4.4.9 Stope analyses with time-dependent rock mass response.

The viscoplastic method of discontinuity relaxation (Malan and Napier, 1997) has been applied using the stope models. Initial studies suggested that there was no effect of the fluidity parameter on energy release. Subsequently, the energy release and activated crack length have been found to depend on the time step used in the analysis. Thus, if the time step is small enough, viscoplastic response can be observed. An increase in the number of time steps leads to a reduced length of activated fractures, but a higher energy release. The stope fracture pattern for a parallel activation is shown in Figure A4.4.9.1. The partings activate ahead of the face and induce a realistic looking fracture pattern. The fracture zone increases in size with successive time increments after taking a mining step. A lower friction angle of 20 degrees on the partings causes slip ahead of the stope face (Figure A4.4.9.2). The time-dependent material model is based on an explicit time integration scheme. Thus, it can be expected that the response depends on the number of time steps selected. The fracture patterns for an analysis with 50 time steps of 0,02 days per mining step (Figure A4.4.9.3) does not differ much from the patterns with 10 steps of 0,1 days (Figure A4.4.9.2a).

Increasing the fluidity of the parting planes alters the pattern of the incremental energy release as shown in Figure A4.4.9.4. Also, with more time steps per day, there is less fracture activation (Figure A4.4.9.5), but considerably more energy released (Figure A4.4.9.6). The implications of the numerical time stepping scheme and path dependence of the parting plane creep model must still be investigated. Not only are the fracture length and energy release affected, but the time at which the fractures activate and the amount of energy is also different (Figure A4.4.9.7).

In a uniform rock mass, the fracture pattern increases with span (Figure A4.4.9.11). At certain stages, large fractures form and extend outside the main fracture envelope. The incremental energy release (Figure A4.4.9.12) shows the characteristic pattern of random amounts of energy release on excavation of the mining step. The energy released subsequently, before the next mining step is taken, is observed to increase with span. A tenfold lower fluidity parameter does not alter the energy release significantly, but exhibits some changes in the distribution of the peak energy release values. The cumulative fracture length remains very similar (Figure A4.4.9.13).

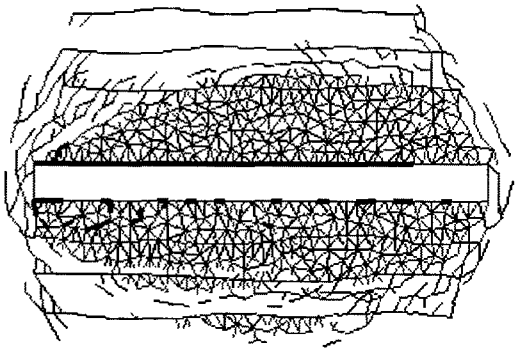

a:

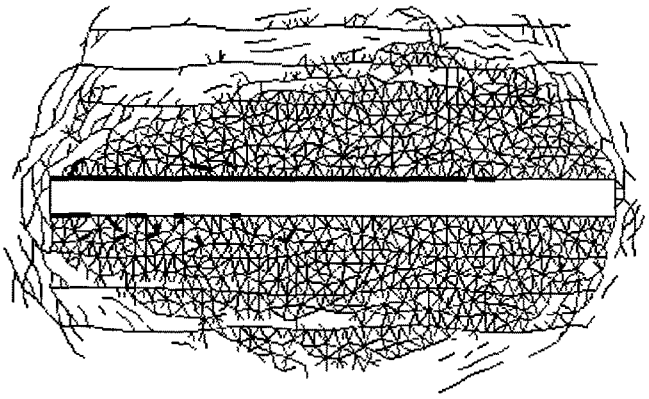

b:

Figure A4.4.9.1 Fracture pattern for a stope with random parting planes, parallel activation and time-dependent rock mass. A friction angle of 40° is specified on the partings. a: 14 m span b: 17 m span.

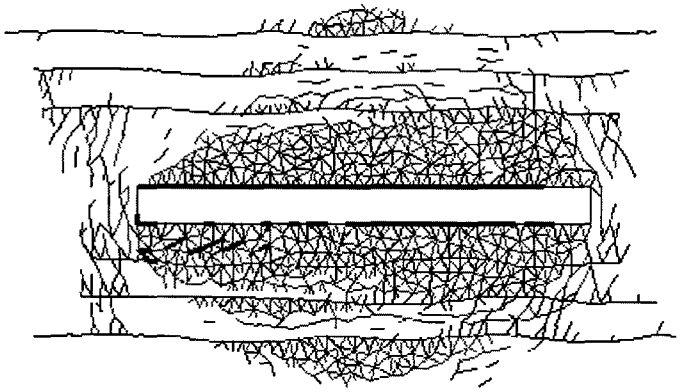

a:

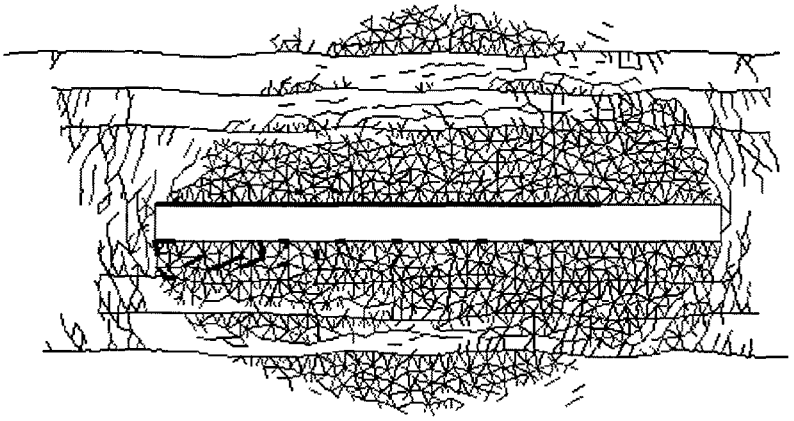

b:

Figure A4.4.9.2 Fracture pattern for a stope with random parting planes, parallel activation and time-dependent rock mass. A friction angle of 20° is specified on the partings. a: 14 m span b: 17 m span.

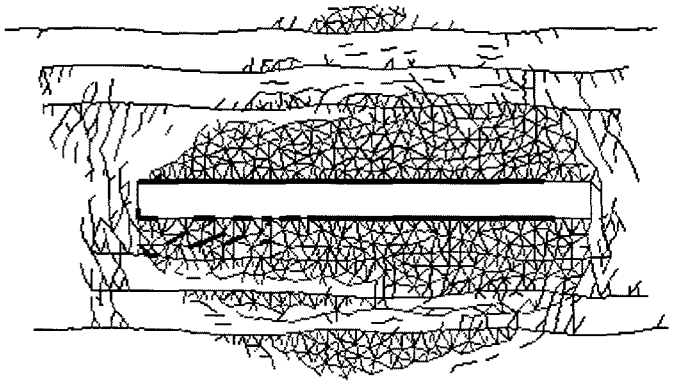

Figure A4.4.9.3 Fracture pattern for a stope with random parting planes, parallel activation and time-dependent rock mass. A friction angle of 20° is specified on the partings. Number of time increments increased from 10 to 50 per day (14 m span).

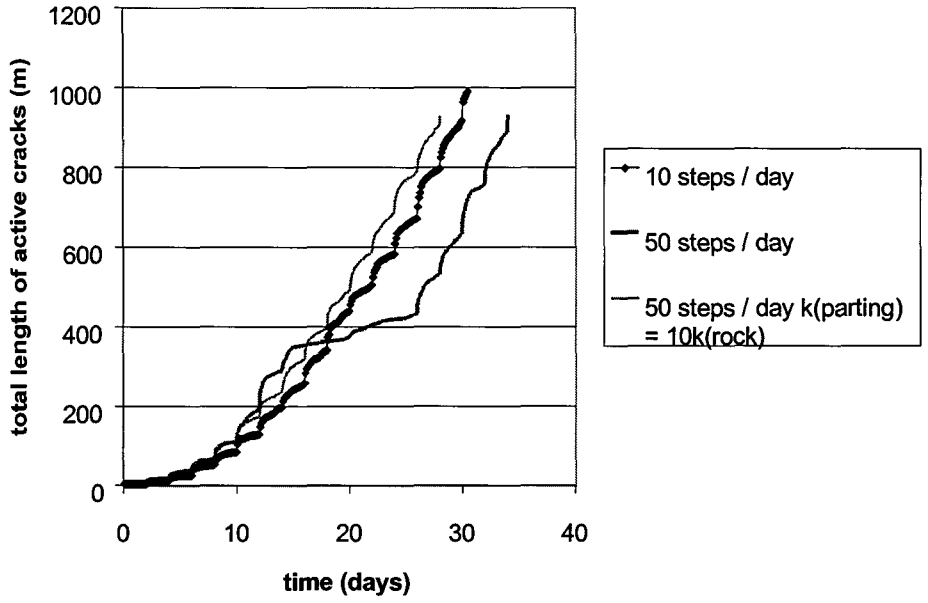

Figure A4.4.9.4 Comparison of the length of cracks activated in three simulations of a Carbon Leader stope with random partings. The first simulation is calculated using a time increment of 0,1 day and the second and third are calculated with a time step of 0,02 day. The third simulation has higher fluidity on the parting planes.

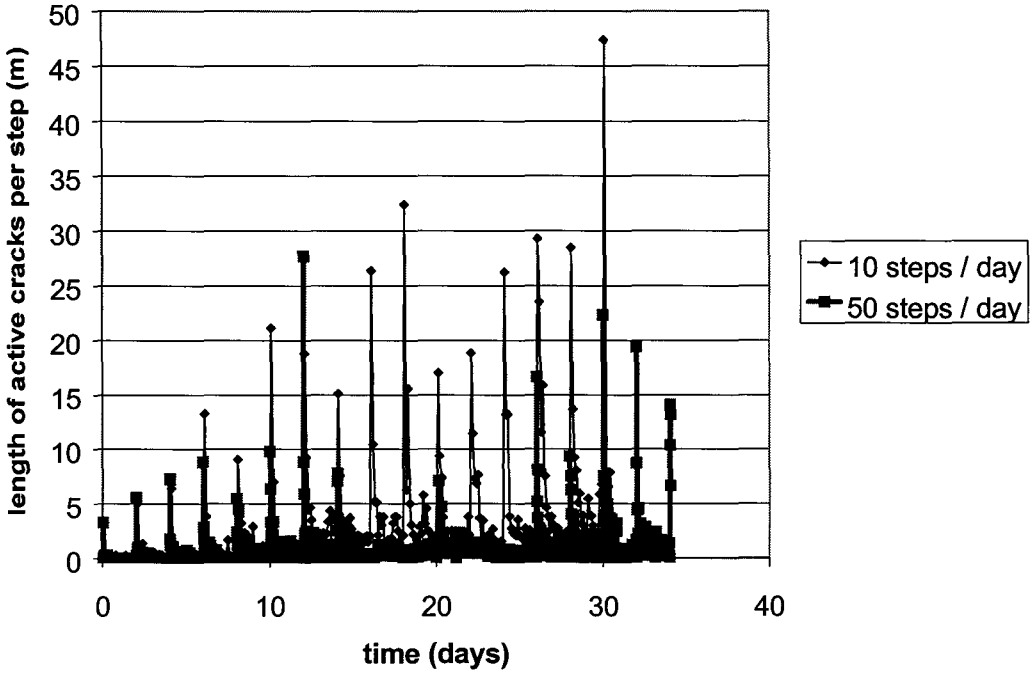

Figure A4.4.9.5 The influence of time step size on the length of cracks activated during a simulation of mining of the Carbon Leader Reef.

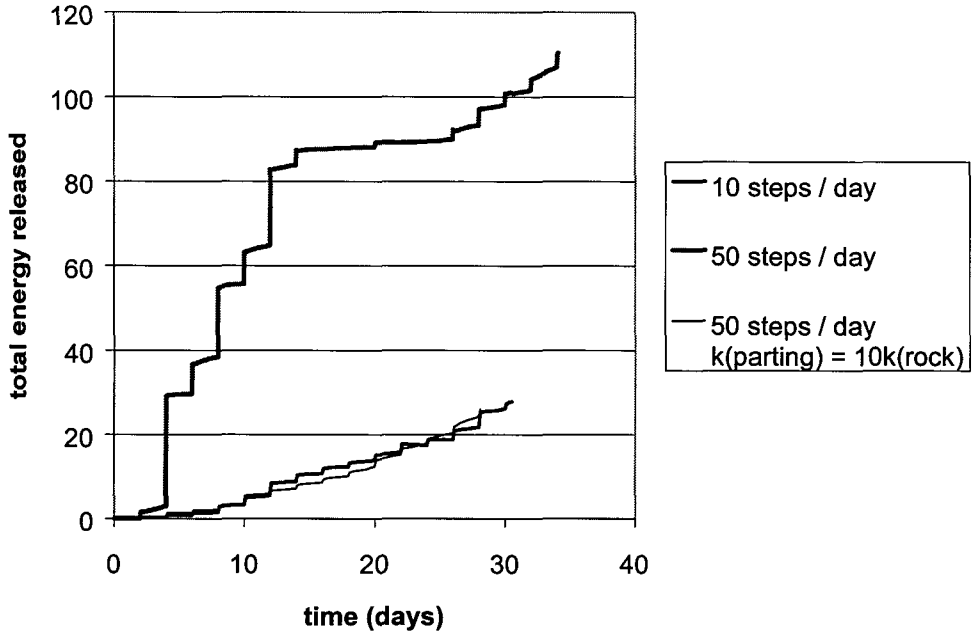

Figure A4.4.9.6 Comparison of the total energy released in three simulations of a Carbon Leader stope with random partings. The first simulation is calculated using a time increment of 0,1 day and the second and third are calculated with a time step of 0,02 day. The third simulation has higher fluidity on the parting planes.

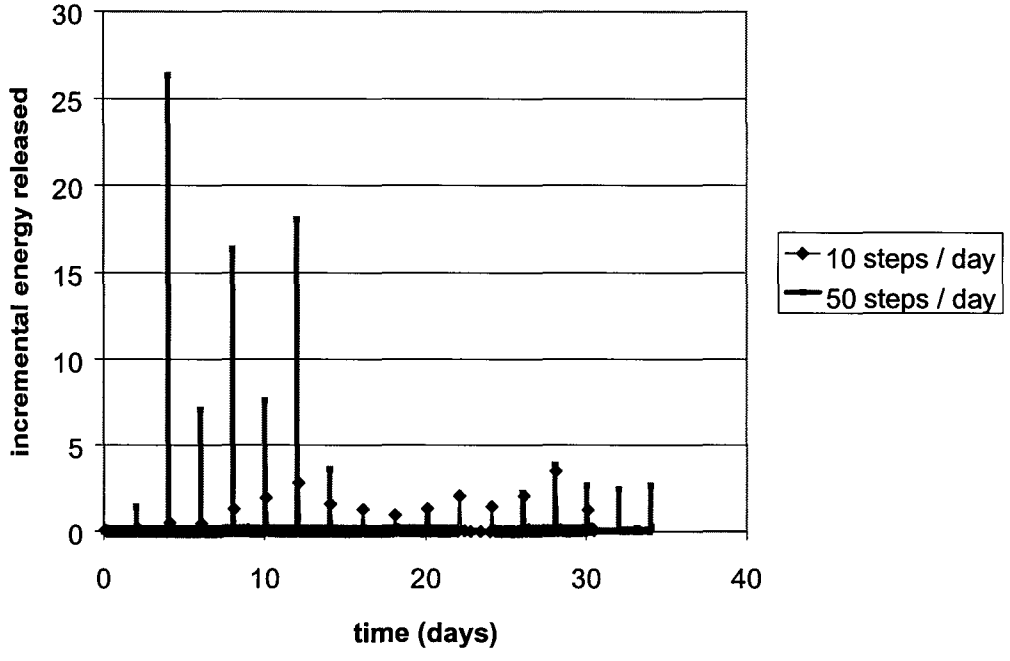

Figure A4.4.9.7 The influence of time step size on the incremental energy released activated during a simulation of mining of the Carbon Leader Reef.

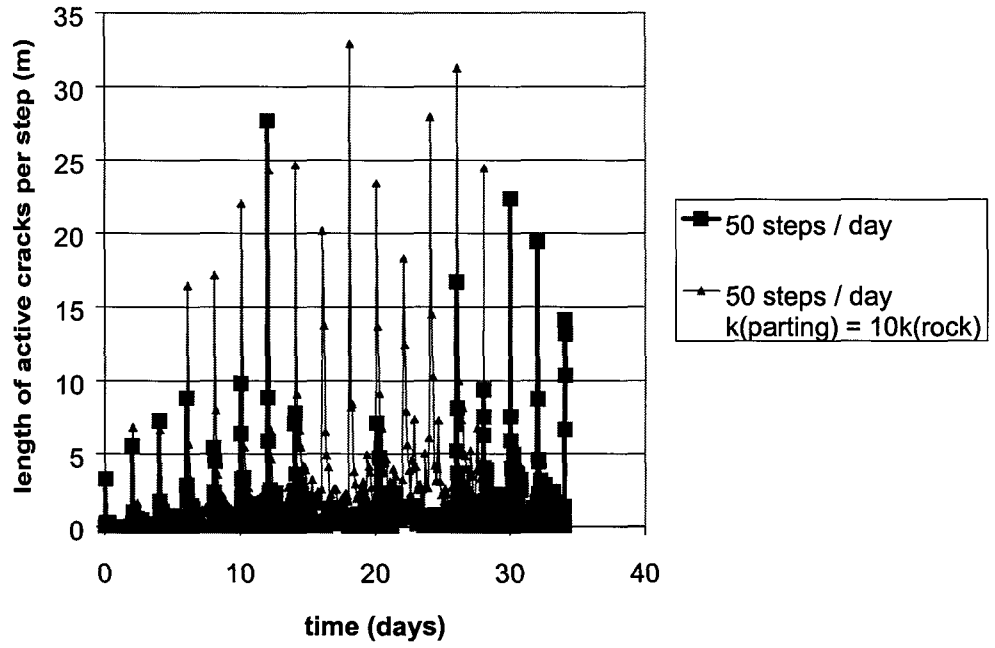

Figure A4.4.9.8 Comparison of the length of cracks activated per time step in two simulations of the Carbon Leader stope with random partings. The second simulation has higher fluidity on the parting planes.

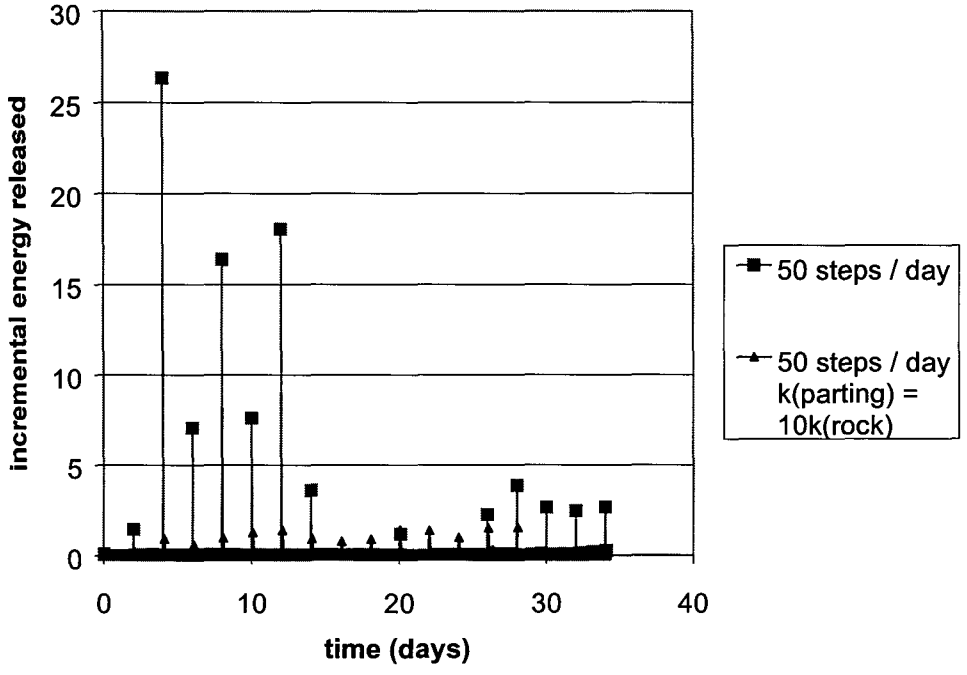

Figure A4.4.9.9 The influence of fluidity parameter on the incremental energy released during a simulation of mining of the Carbon Leader Reef.

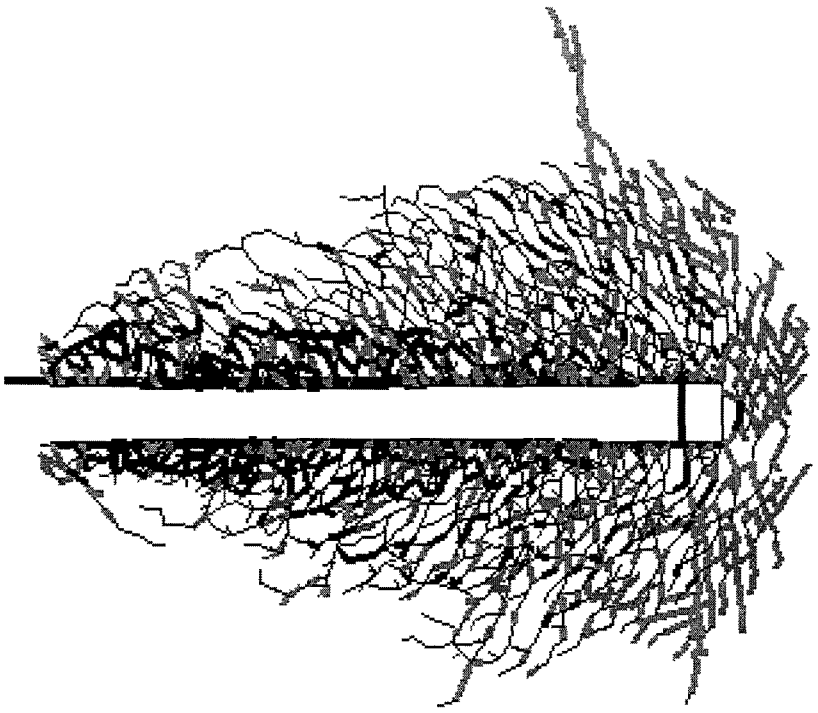

Figure A4.4.9.10 Fracture pattern in a uniform rock mass after 16 mining steps using the viscoplastic fracture logic. Viscosity set to 0,0005 m/day/MPa and mined at a rate of 1m/2 days

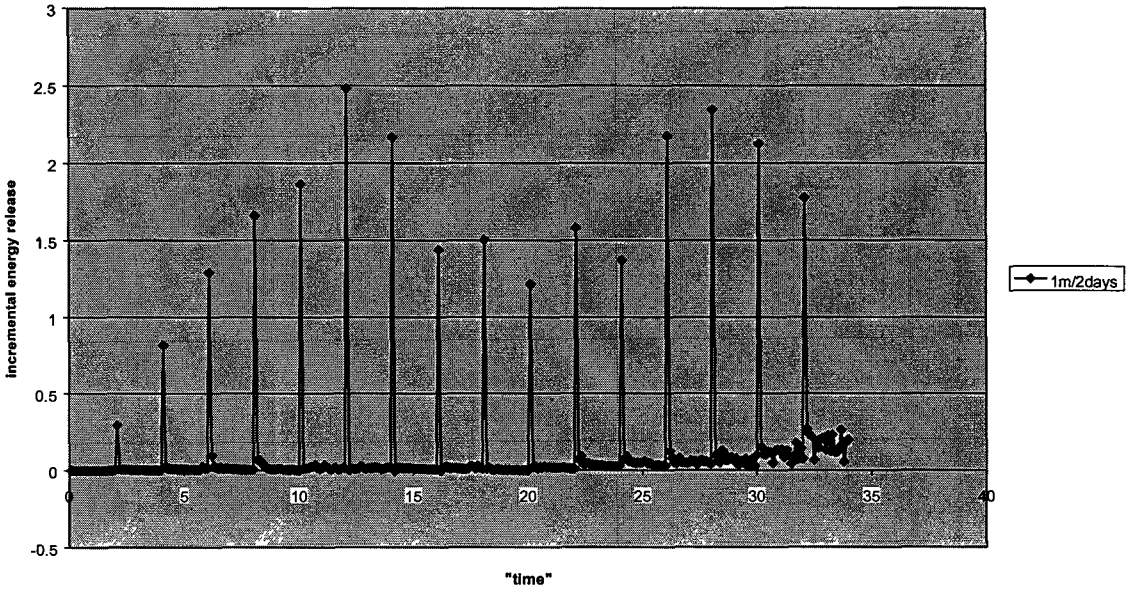

Figure A4.4.9.11 Incremental energy release with time using the viscoplastic fracture logic in a uniform rock mass. Viscosity set to 0,0005 m/day/MPa and mined at a rate of 1m/2 days

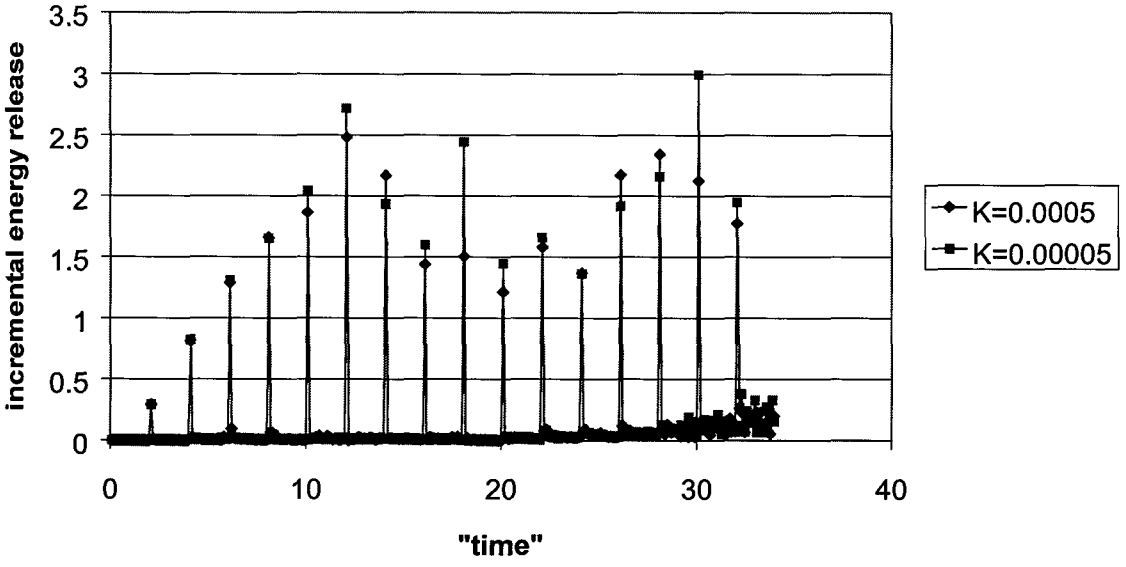

Figure A4.4.9.12 Comparisons of the incremental energy release predicted in a model of a stope in a uniform rock mass for two different fluidity parameters for the rock mass. Stope width is 1,5 m.

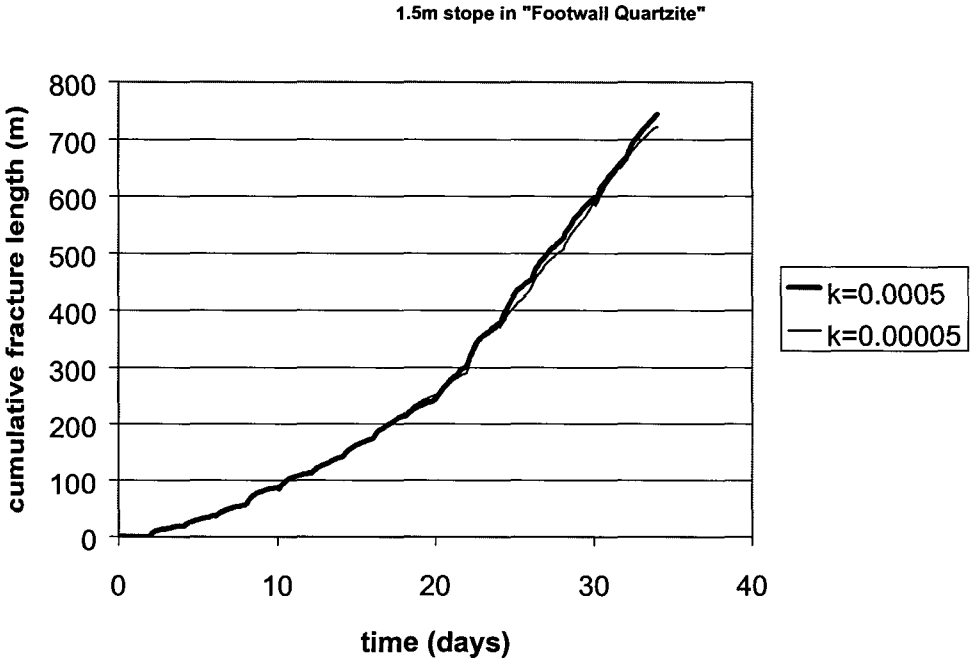

Figure A4.4.9.13 Comparisons of the cumulative fracture length predicted in a model of a stope in a uniform rock mass for two different fluidity parameters for the rock mass. Stope width is 1,5 m.

A4.4.10 References

Adams, G. R. & Jager, A. J. & Roering, C. 1981. Investigation of rock fractures around deep-level gold mine stopes, *22nd US Symposium on Rock Mechanics*, MIT, 213-218.

Adams, G. R., Jager, A. J. & Roering, C., 1981. Investigation of rock fractures around deep-level gold mine stopes, *2nd US Symposium on Rock Mechanics*, MIT, 213-218.

Berlenbach, J.W. 1993. The mechanics of bedding-parallel faulting associated with the Ventersdorp Contact Reef on Kloof Gold Mine. *PhD Thesis*, Rand Afrikaans University.

Berlenbach, J.W., & J.K. Schweitzer 1996. Geotechnical environments associated with the auriferous Vaal Reef and Carbon Leader, Witwatersrand Basin, South Africa, *Interim SIMRAC Report GAP 332*, CSIR-Miningtek.

Brummer, R.K. & Rorke, A.J., 1984. Mining induced fracturing around deep gold mines stopes, *Report 38/84,* Chamber of Mines of South Africa.

Gay, N.C. & A.J. Jager 1986. The influence of geological features on problems of rock mechanics in Witwatersrand mines. In: Anhaeusser, C.R., Maske, S. (eds.) *Mineral Deposits of Southern Africa, Geol. Soc. S. Afr.*, 753-772.

Gay, N.C., Jager, A.C., Ryder, J.A. & Spottiswoode, S.M., 1995. Rock engineering strategies to meet the safety and productivity needs of the South African mining industry in the 21st century. *J. S. Afr. Inst. Min. Metall.* vol. 95, 115-135.

Gay, N.J., Spencer, D., Van Wyk J.J. & Van der Heever, P.K. 1984. The control of geological and mining parameters in the Klerksdorp Gold Mining district. In Gay, N.C., Wainwright, E.H. (eds.) *Proceedings of the 1st International Congress on Rockbursts and Seismicity in Mines*, Johannesburg, SAIMM: 107-120.

Gürtunca, R.G. & Adams, D.J., 1991. Determination of the in situ modulus of the rock mass by the use of backfill measurements, *J.S. Afr. Inst. Min. Metall.* vol. 91 81-88.

Kuijpers, J.S. & Napier, J.A.L., 1991. The effect of loading history on stress generation due to inelastic deformation around deep-level tabular stopes, *J. S. Afr. Inst. Min. Metall.* vol. 91,183-194.

Legge, N.B., 1986. Rock deformation in the vicinity of deep gold mine stopes and its relation to fracture, *Report 14/86*. Chamber of Mines of South Africa.

Legge, N.B. & Spottiswoode, S.M., 1987. Fracturing and microseismicity of a deep gold mind stope in the pre-remnant and remnant stages of mining, *IRSM 6th Int. Congr. Rock Mech.* Montreal, 1071-1077.

Lightfoot, N., Leach, A.R., & Kullman, D.H., 1994. A conceptual model of a hard rock, deep level, tabular ore body. *1st North American Rock Mechanics Symposium*. Balkema: Rotterdam.

Linkov, A.M. 1996. Rockbursts and the instability of rock masses - Schlumberger Award Lecture. *Int. J. Rock Mech. Min. Sci & Geomech Abstr.,* vol. 33, 727-732.

Malan, D.F. & Napier, J.A.L. 1997. Viscoplastic Discontinuum Model of Time-Dependent Fracture and Seismicity, *Int. J. Rock Mech. Min. Sci.* vol. 34, 1075-1089.

Napier, J.A.L. 1990. Modelling of fracturing near deep level gold mine excavations using a displacement discontinuity approach. *Proceedings of Conference on Mechanics of Jointed and Faulted Rock.* Vienna, Balkema, Rotterdam, 709-715.

Napier J.A.L. & Stephansson, S.J., 1987. Analysis of deep level mine design problems using the MINSIM-D Boundary element program, *Proc. 20th Symp on application of computers and mathematics in the mineral industries*, SAIMM, Johannesburg, 3-19.

Napier, J.A.L. & Peirce, A.P. 1995. Simulation of extensive fracture formation and interaction in brittle materials, In: H.P. Rossmanith (ed), *Mechanics of jointed and faulted rock - 2,* Balkema, Rotterdam, 63-75.

Napier, J.A.L. & Peirce, A.P. 1997. The use of a multipole expansion technique to analyse large scale fracture processes and seismic recurrence effects in deep level mines. In: Hudson, J.A. (ed.) *Proc. NYRocks '97* ISRM International Symposium, 680.

Napier, J.A.L. & Hildyard, M.W. 1992. Simulation of fracture growth around openings in highly stressed, brittle rock, *J. S. Afr. Inst. Min. Metall.* vol. 92,159-168.

Napier, J.A.L., Malan, D.F. & Sellers, E.J. 1998. Implications of fracture zone behaviour in deep level gold mines. Submitted to SIMRAC Symposium.

Napier, J.A.L., Daehnke, A., Hildyard, M.W., Kuijpers, J.S., Malan, D.F., Sellers, E.J. & Turner, P.A.T. 1996. Quantification of stope fracture zone behaviour in deep level gold mines, *J. SAIMM.*

Napier, J.A.L., Hildyard, M.W., Kuijpers, J.S., Daehnke, A., Sellers, E.J., Malan, D.F., Siebrits, E., Ozbay, M.U., Dede, T. & Turner, P.A. 1995. *Develop a quantitative understanding of rock mass behaviour near excavations in deep mines.* SIMRAC Final Project Report, Project GAP029.

Quaye, G.B., & Guler, G., 1998, The importance of both geological structures and mining induced stress fractures on the hangingwall stability in deep mines. *J.SAIMM*, 98, 157-162

Schweitzer, J. K. & Johnson, R. A., 1997. Geotechnical classification of deep and ultra-deep Witwatersrand mining areas, *Mineralium Deposita*, vol. 32, 335-348.

Sellers, E.J. 1997. A tessellation approach for the simulation of the fracture zone around a stope. *Proceedings of Southern African Rock Engineering Symposium (SARES),* 143-154, Johannesburg.

Sellers, E. & Napier, J.A.L. 1997. A comparative investigation of micro-flaw models for the simulation of brittle fracture in rock. *Comp. Mechanics*, 20, 164-169.

Squelch A. P., 1990. Horizontal stresses in the face area hangingwall of backfilled and conventional stopes at Vaal Reefs, *Report R16/80*, Chamber of Mines of South Africa.

Appendix 4.5

Continuous closure measurements of VCR stopes with a soft lava hangingwall

Continuous closure data was collected at Kloof Mine to compare the time-dependent rock mass response of the VCR with a soft lava hangingwall to other mining areas where the lava is hard. The measurements described in this Appendix were taken in the 31-34 longwall at Main Shaft, Kloof Mine. The depth of the area of interest is approximately 2600 m and the dip is 26°. A schematic diagram of the instrumented panel is given in Figure A4.5.1 to illustrate the position of the closure meters. As the clockwork closure meters were not very reliable in high temperature and humidity environments, two meters were installed to ensure that at least one set of data was collected every week. The support in this area consists of brick composite packs and backfill some distance behind the face. According to the production personnel, the risk of strain bursting in this area is low, but the risk of falls of ground is pronounced. It is very difficult to support the soft lava hangingwall in this area with significant fallouts occurring between the packs (Figure A4.5.2).

Figure A4.5.3 illustrates closure data collected during the first week of measurement. A small jump in instantaneous closure at blasting time and a high steady-state closure rate is noticeable. This steady-state closure rate is the highest measured so far in the South African gold mining industry. Note that the closure profiles are entirely different from the profiles observed for the VCR with hard lava (Figure 4.4.3.5). Further work is necessary to quantify the effect of layout geometry and span. The steady-state closure rate is very dependent on the blast history. If there are no blasts for a number of days, this rate decreases steadily as seen for the first 7000 minutes in Figure A4.5.6. After a blast, this rate increases again. Due to poor hangingwall conditions, the rate of steady-state closure also varied from position to position in the panel. Typical values for a relatively stable area in this panel and regular blasting are 0,6 mm/h. Total daily closure after regular blasting (for a distance of typically 5-10 m from the face) would be 20-30 mm/day.

Although the clockwork closure instruments are designed to record the closure continuously for a period of at least a week, the very high closure rates at this site exceeded the closure range of the instruments after only two or three days. Figures A4.5.3 to A4.5.7 illustrate all the closure data collected at this site during the four week period of monitoring.

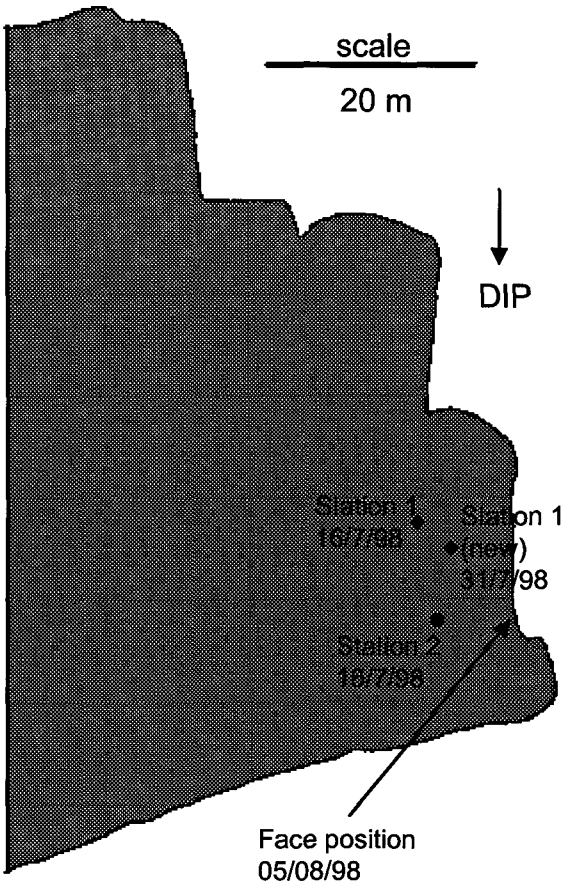

Figure A4.5.1 View of the instrumented panel and the position of the closure meters in the 31-34 longwall north.

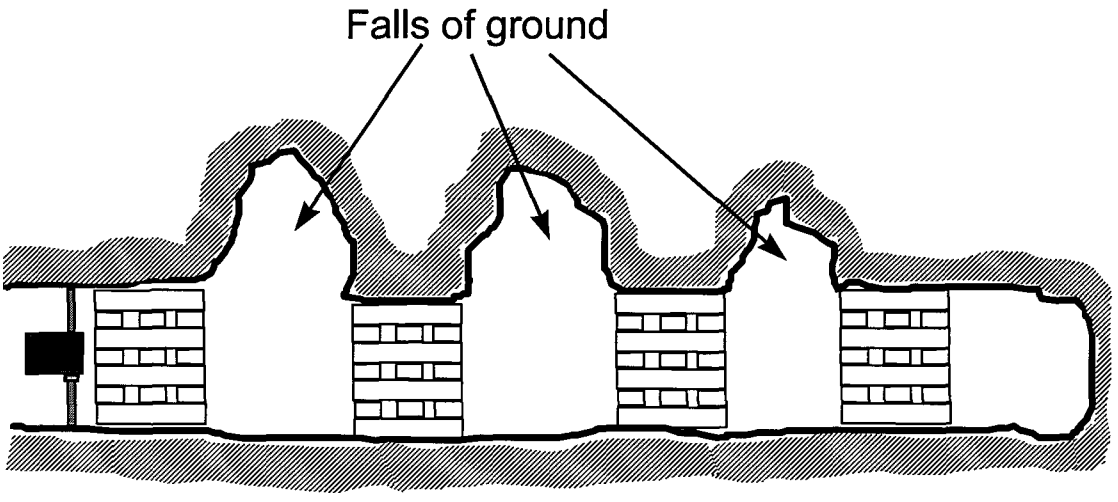

Figure A4.5.2 Typical fallout of the soft lava between the packs. This hangingwall behaviour made it rather difficult to find a stable area to install the closure meters.

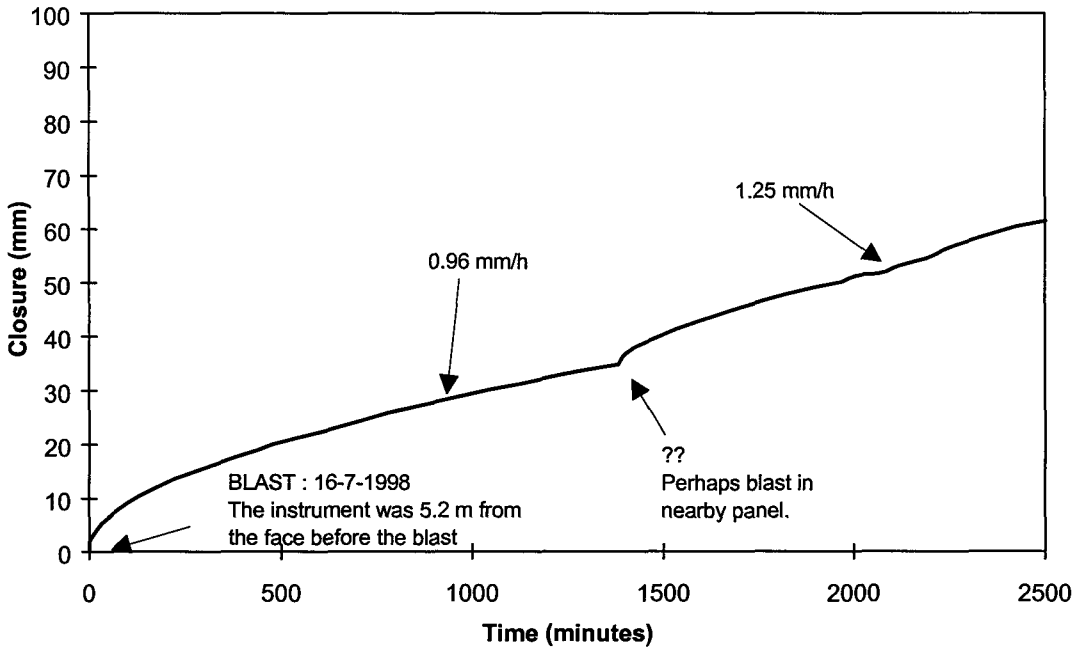

Figure A4.5.3 Continuous time-dependent closure data collected in the 31-34 longwall site. The rates of steady-state closure given in the figure were calculated for the periods from approximately 600 minutes after the blast until the next blast occurred. This is for instrument no 1 (see Figure A4.5.1). Note the very high steady-state closure rates.

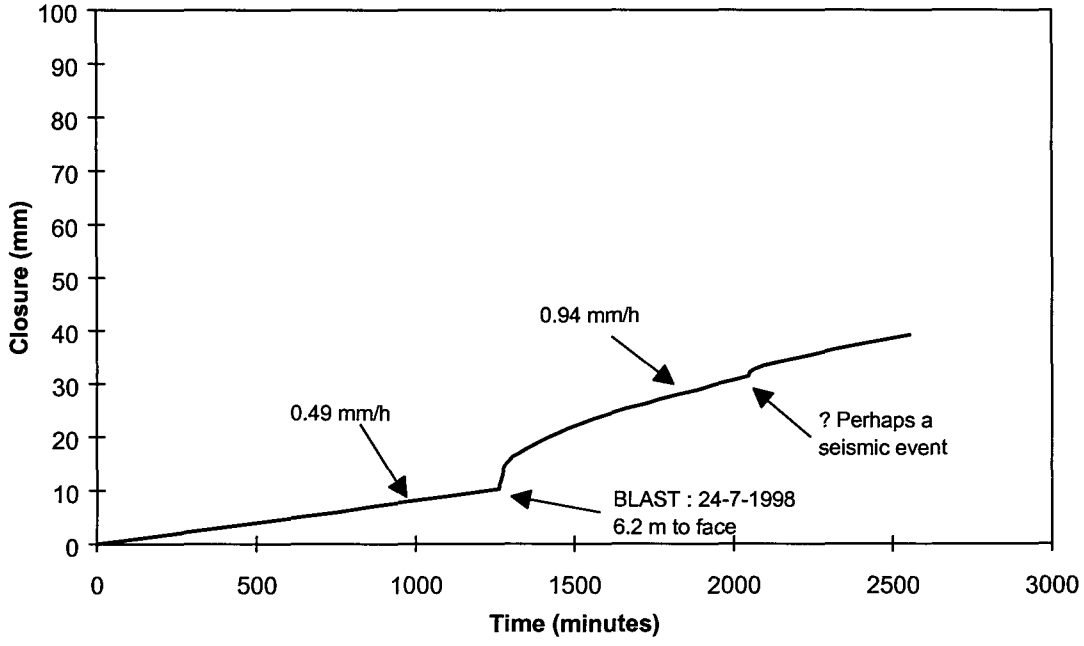

Figure A4.5.4 Continuous closure data collected by instrument no 2. Note how the steady-state closure rate increases after the blast.

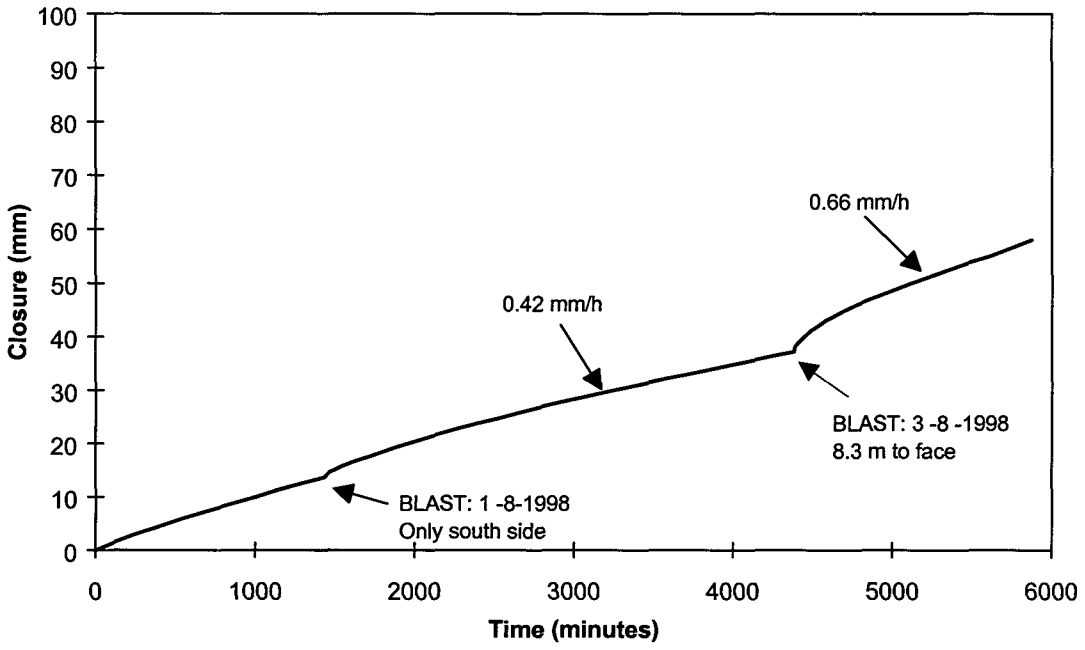

Figure 4.5.5 Continuous closure data collected by instrument no. 2. Again note the increase in steady-state closure after the blast on 3-8-1998.

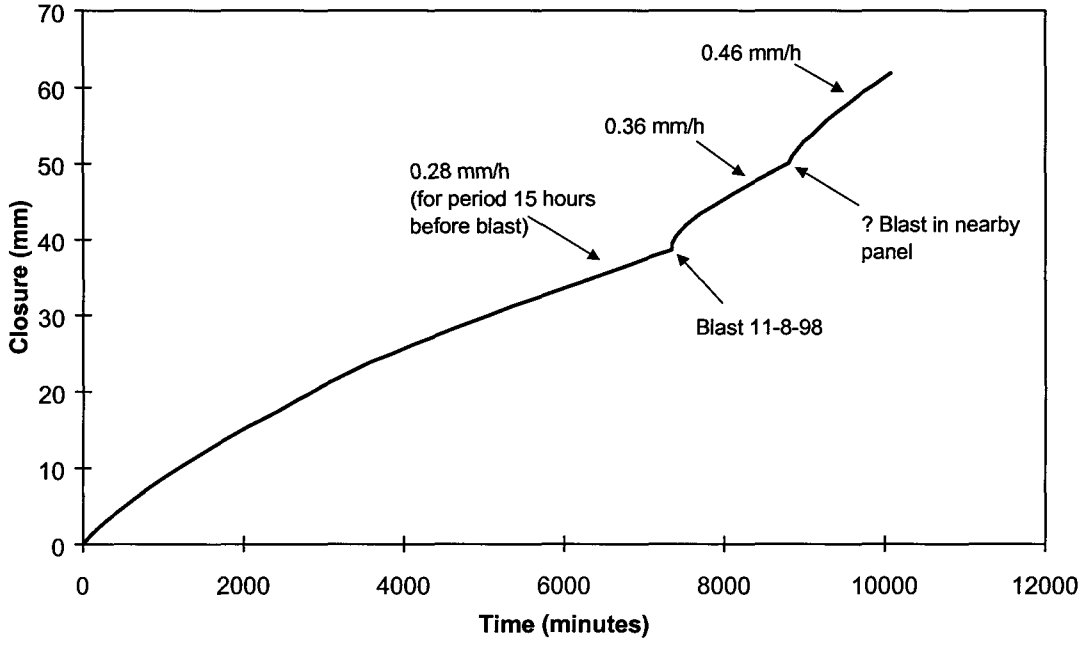

Figure A4.5.6 Continuous closure data collected by instrument no. 2 which was 8,8 m from the face before the blast on 11-8-1998.

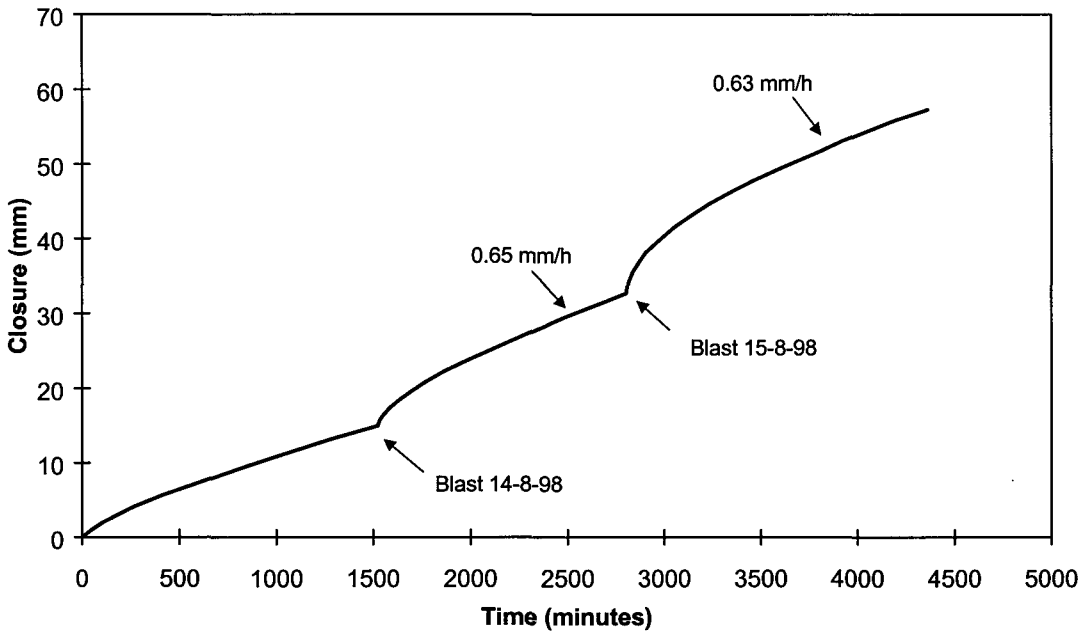

Figure A4.5.7 Continuous closure data collected by instrument no 1 which was 8,5 m from the face before the blast on 14-8-1998.

Summary

It appears from these measurements that the time-dependent closure response of VCR stopes with the soft lava hangingwall (Westonaria Formation lava) is distinctly different from mines where the lava is hard (Alberton Porphyry Formation lava). The continuous closure in the 31-34 longwall at Kloof Mine (soft lava) is characterised by a small instantaneous closure at blasting time followed by a high rate of steady-state closure. This closure response is similar to that observed in some areas of the Vaal Reef. Due to the highly discontinuous nature of the hangingwall at this site in Kloof Mine, the magnitude of closure varies from position to position in the panel. Typical values of steady-state closure and total daily closure after regular blasting are 0,6 to1 mm/h and 20 to 30 mm/h respectively. If there is no blasting for a week or longer, the daily closure rate will reduce to approximately 7 mm/day. This value is still high since the daily closure rate, after the same period of no blasting, typically reduces to 0,5 mm/day for VCR with the hard lava hangingwall. A high rate of face advance might be beneficial in these high closure areas to improve the condition of the hangingwall and therefore reduce the risk of falls of ground. It is unclear at this stage how high rates of face advance will affect the levels of seismicity and further work is necessary.

List of supplementary documents

The following additional documents, available on request, describe work conducted in the GAP332 project and these are also submitted as it gives a more detailed account of some of the work areas described in the main report.

1. An investigation into the identification and modelling of time-dependent behaviour of deep level excavations in hard rock. PhD thesis. University of the Witwatersrand.

2. Stress wave and fracture propagation in rock. PhD thesis, Technical University of Vienna.